Crystallography Reports, Vol. 47, No. 5, 2002, pp. 709–719. Translated from Kristallografiya, Vol. 47, No. 5, 2002, pp. 775–784.

CRYSTAL SYMMETRY

Generalized Crystallography of Diamond-Like Structures: II. Diamond Packing in the Space of a Three-Dimensional Sphere, Subconfiguration of Finite Projective Planes, and Generating Clusters of Diamond-Like Structures

A. L. Talis

Institute of Synthesis of Mineral Raw Materials, Aleksandrov, Vladimir oblast, Russia

e-mail: ofi@vniisims.elcom.ru

Received April 24, 2001

Abstract—An enantiomorphous 240-vertex "diamond structure" is considered in the space of a three-dimensional sphere S^3, whose highly symmetric clusters determined by the subconfigurations of finite projective planes $PG(2, q)$, $q = 2, 3, 4$ are the specific clusters of diamond-like structures. The classification of the generating clusters forming diamond-like structures is introduced. It is shown that the symmetry of the configuration, in which the configuration setting the generating clusters is embedded, determines the symmetry of diamond-like structures. The sequence of diamond-like structures (from a diamond to a BC8 structure) is also considered. On an example of the construction of $PG(2, 3)$, it is shown with the aid of the summation and multiplication tables of the Galois field $GF(3)$ that the generalized crystallography of diamond-like structures provides more possibilities than classical crystallography because of the transition from groups to algebraic constructions in which at least two operations are defined. © *2002 MAIK "Nauka/Interperiodica".*

INTRODUCTION

Earlier [1], it was shown that the adequate mapping of the symmetry of diamond-like structures requires a change of the Euclidean basis of the structural crystallography to a more general basis of algebraic (projective) geometry. In particular, the incidence graphs of specific subconfigurations of finite projective planes PG, $q = 2, 3, 4$ turned out to be isomorphous to the graphs of the specific clusters of a diamond-like structure. These graphs are mapped onto themselves by the groups of projective geometry and contain the orthogonal groups of the classical crystallography as their subgroups.

The present article is the second of a series dedicated to the construction of the generalized crystallography of diamond-like structures as a particular structural application of algebraic geometry, which includes as the limiting case the respective sections of the classical crystallography [2, 3]. For diamond-like structures, the penta-, hexa-, and heptacycles are the most realistic [4–6]. Therefore, the present study is dedicated mainly to the determination of the symmetrically possible types of generating clusters of diamond-like structures containing only these cycles. In the general case, the specific clusters of a diamond-like structure are the combinations of various generating clusters, whereas the diamond-like structures themselves are constructed from a certain set of generating clusters in a way similar to the construction of a three-dimensional Penrose division from four types of tetrahedra [7].

The most highly symmetric diamond-like structure is such a combination of two three-dimensional lattices that can be implemented in the Euclidean space E^3 as a diamond and in the space of a three-dimensional sphere S^3 as an "enantiomorphous diamond" or an irregular {240} polytope [4, 5, 8]. This shows the importance of those specific clusters of the {240} polytope in the generalized crystallography of diamond-like structures that are defined by the corresponding subconfigurations $PG(2, q)$ considered in detail in the present study.

The frequent detailed citation of [1] allows the author to use the definitions introduced in [1] and the results obtained there. For clarity, the author often sacrifices mathematical rigor and uses numerous illustrations to be able to compare directly the mathematical constructions with the clusters they determine. The results obtained make the basis for constructing the system of generating clusters, which allows the author to derive diamond-like structures and determine all the symmetrically possible structural phase transitions between these structures.

1063-7745/02/4705-0709$22.00 © 2002 MAIK "Nauka/Interperiodica"

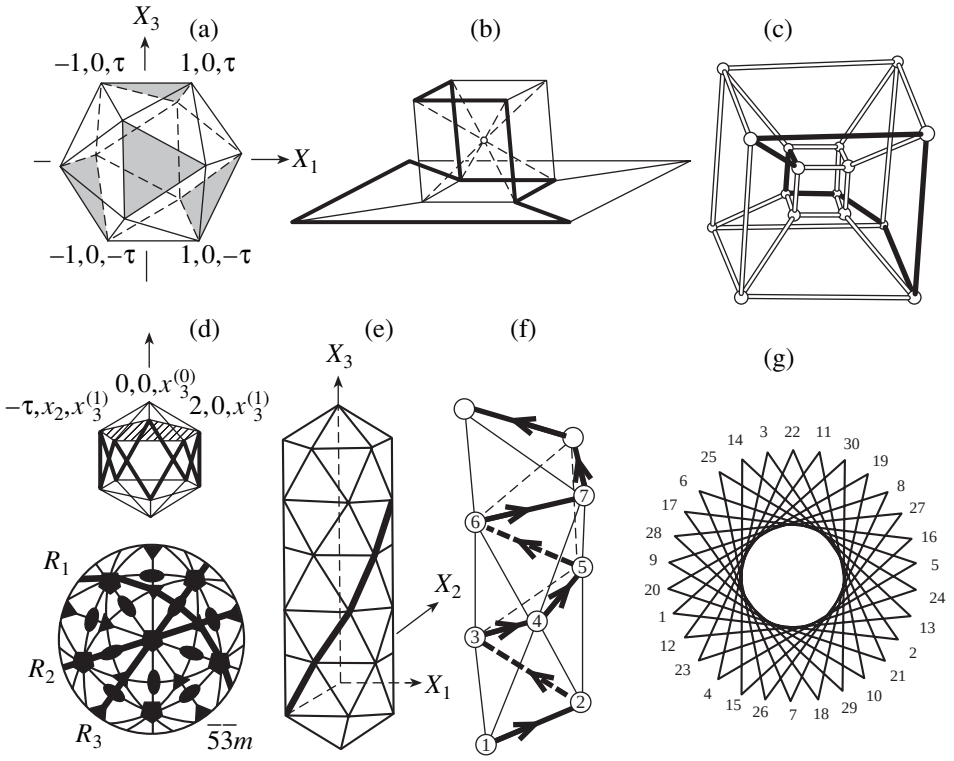

Fig. 1. Mapping of substructures of polytopes in E^3 [5, 10, 12]: (a) {3, 5} icosahedron whose three twofold axes coincide with the X_1-, X_2-, and X_3 axes of the Cartesian coordinate system (four hatched triangles and the center of the icosahedron belong to four tetrahedra whose centers form a tetrahedron); (b) {4, 3} cube and its projection onto the plane represented in the form of a Schlegel diagram (six-edge Petrie's polygon of the cube and its Schlegel diagrams are shown by solid lines); (c) the projection of the {4, 3, 3} polytope in E^3; solid lines show its eight-edge Petrie's polygon; (d) the icosahedron and the stereographic projection of the $\bar{5}\bar{3}m$ group, whose fundamental domain is separated by the reflection planes R_1, R_2, and R_3 shown by solid lines (the fivefold axis of the icosahedron coincides with the X_3-axis of the Cartesian coordinate system; the sections of the icosahedron by the plane normal to X_3-axis are the $(0, 0, x_3^{(0)})$ point, the hatched pentagon, etc.; a 10-edge Petrie's polygon of the {3, 5} icosahedron is shown by solid lines); (e) the rod of icosahedra sharing the fivefold axis (the part of the helix determined by the 10_1 screw axis of the {3, 3, 5} polytope is shown by a solid line); (f) Bernal's chain of tetrahedra; the 30/11 irrational screw helix corresponding to Petrie's polygon of the {3, 3, 5} polytope is shown by solid arrows; (g) the starlike polygon formed as a result of the orthogonal projection of 30 vertices of the {3, 3, 5} polytope along the 30/11 axis.

A 240-VERTEX "DIAMOND" STRUCTURE IN THE SPACE OF A THREE-DIMENSIONAL SPHERE S^3—AN IRREGULAR {240} POLYTOPE

Three-dimensional Platonic solids can be generalized to projective Platonic solids—finite projective planes $PG(2, q)$. Taking into account the metric relationships, this generalization requires the transition from the space E^3 to the space E^n, $n > 3$. At $n = 4$, the Platonic solids in the Schläfli notation $\{p, q\}$ (Figs. 1a, 1b, 1d) are extended to the four-dimensional Platonic solids—$\{p, q, r\}$ polytopes built by the $\{p, q\}$ cells in such a way that each face $\{p\}$ is shared by two cells and each edge, by r cells. The location of the cells at the vertex $\{p, q, r\}$ corresponds to the location of the faces of the $\{q, r\}$-vertex polyhedron of the polytope (Fig. 1c) [9–12].

The most important characteristic of the n-dimensional polyhedron is its Petrie polygon; for the $\{p, q\}$-polyhedron, it is a "zig-zag" consisting of h edges ($\cos^2(\pi/h) = \cos^2(\pi/p) + \cos^2(\pi/q)$) in which any three successive sides do not belong to one face. Thus, for a {4, 3} cube, $h = 6$ (Fig. 1b). For a {3, 5} icosahedron, Petrie's polygon consists of $h = 10$ "side" edges of a pentagonal antiprism (Fig. 1d). For a $\{p, q, r\}$ polytope, Petrie's polygon is a set of edges in which any successive three (and not four) edges belong to the Petrie's polygon of the $\{p, q\}$ cell [10]. For example, the Petrie's polygon of a four-dimensional cube (the {4, 3, 3} polytope) is an octacycle, any three successive edges of which belong to one cubic {4, 3} cell of this polytope (Fig. 1c).

The division of E^3 into regular tetrahedra is impossible because the dihedral angle of the regular tetrahedron equals $70.53° < 72° = 360°/5$. The "angular deficit" of the connected tetrahedra can be avoided if one "sacrifices" their regularity by connecting 20 tetrahedra into an icosahedron (Fig. 1a), which can be made only

by using two types of edges with the length ratio ~0.951 in the tetrahedra. In this case, 12 vertices of an {3, 5} icosahedron provide the regular triangulation of the sphere S^2, which is mapped onto itself by the orthogonal group $\bar{5}\bar{3}m$ of order 120 set by the following defining relationships for the generating elements (code):

$$R_i^2 = (R_1R_2)^3 = (R_2R_3)^5 = (R_1R_3)^2 = (R_1R_2R_3)^{10} = 1, \quad (1)$$

where R_i, $i = 1, 2, 3$ are the generating reflection planes that single out the fundamental domain of the group $\bar{5}\bar{3}m$; R_1R_2, R_2R_3, R_1R_3 are the rotations by the angles of $2\pi/3$, $2\pi/5$, and π, and $R_1R_2R_3 = 5$ is the Coxeter element whose degree $h = 10$ coincides with the number of edges in the Petrie's polygon of an icosahedron (Fig. 1d) [13, 14].

In the space of a three-dimensional sphere S^3 embedded in E^4, the angular deficit of regular tetrahedra is avoided because of a constant positive curvature; in this case, the sphere is divided into 600 regular tetrahedra forming the {3, 3, 5} polytope (four-dimensional icosahedron). One hundred and twenty vertices of the polytope {3, 3, 5} are determined by the unit vectors (with the origin at the center of S^3) in E^4 to which there corresponds the set Y' consisting of 120 specific quaternions–icosians

$$Y' = \{(\pm1, 0, 0, 0)^*, 1/2(\pm1, \pm1, \pm1, \pm1), 1/2(0, \pm1, \pm\sigma, \pm\tau)^A\}, \quad (2)$$

where A indicates that all the even permutations of coordinates are allowed, $\sigma = 1/2(1 - \sqrt{5})$, and $\tau = 1/2(1 + \sqrt{5})$. With respect to the multiplication operation of icosians, the set Y' is a binary icosahedral group isomorphous to the subgroup of the special unitary group $SU(2)$. The set J of all the finite sums $q_1 + \ldots + q_t + \ldots + q_n$ (where each q_t is an occasion from (2)) is a ring $(\alpha, \beta, \gamma, \delta)$ of icosians, where α, β, γ, and δ belong to the ring of the golden section $Q(\tau) = \{a + b\sqrt{5}\}$, $a, b \in Z$, where Z is a set of integers [14, 15].

All the motions in E^4 that bring the vertices of the {3, 3, 5} polytope into coincidence form the subgroup [3, 3, 5] of the orthogonal four-dimensional group $O(4)$. The group [3, 3, 5] of order 14 400 is the direct product $Y' \times Y'$ that can be embedded in $SU(2) \times SU(2)$. The group [3, 3, 5] is defined by the code

$$R_i^2 = (R_1R_2)^3 = (R_2R_3)^3 = (R_3R_4)^5 = (R_1R_4)^2 = Q^6 = P^{10} = S^{30} = 1, \quad (3)$$

where R_i, $i = 1, 2, 3, 4$ are the generating reflection planes, $R_1R_2R_3 = Q$, $R_1R_3R_4 = P$, and $R_1R_2R_3R_4 = S$ is the Coxeter element whose degree $h = 30$ coincides with the number of edges of the Petrie's polygon of the {3, 3, 5} polytope [13, 14]. Code (3) determines the presence in the polytope {3, 3, 5} of the axes which in E^3 coincide with the axes of rotation by $2\pi/n$, $n = 2, 3, 5$ (Fig. 1d), the conventional (rational) screw axes n_1, $n = 6, 10$ (Fig. 1e), and the irrational screw axis 30/11, which provides the rotation by about $2\pi 11/30$ around 11/30 with the subsequent translation along this axis (Fig. 1g). The 30/11 axis reflects the symmetry of a 30-edge Bernal helix composed by tetrahedra (Fig. 1f) and corresponding to the Petrie's polygon of the {3, 3, 5} polytope [9, 10, 15].

In the {3, 3, 5} polytope, one can select 120 tetrahedra whose centers form the congruent $\varphi\{3, 3, 5\}$ polytope, where φ is the enantiomorphous rotation in E^4 and $O(4) \ni \varphi \notin [3, 3, 5]$; in this case, in each icosahedron from the {3, 3, 5} polytope, four tetrahedra are centered so that their centers form a tetrahedron (Fig. 1a). The connection of "white vertices" of the initial {3, 3, 5} polytope with the closest "black vertices" of the $\varphi\{3, 3, 5\}$ polytope results in the formation in S^3 of an enantiomorphous structure consisting of 240 tetrahedrally coordinated vertices connected by 480 edges forming nonflat hexacycles (twist-boats). This structure is called an irregular {240} polytope [4, 5, 8]. The group of motion in E^4 mapping the {240} polytope onto itself is the subgroup of rotations $(O' \times Y')/Z_2$ of the group $O(4)$, where O' is the binary octahedral group of order 48. The order of $(O' \times Y')/Z_2$ is 2880; the group of the {240} polytope of the opposite chirality is the group $(Y' \times O')/Z_2$ [5].

The isomorphism of the group $SU(2)$ to the sphere S^3 [5, 15] indicates that the definition $SU(2) \times SU(2)$ is eight-dimensional and, in the final analysis, determines the imbedding of {3, 3, 5} in E_8—the close packing of spheres S^7 in E^8 [14]. In this case, the isomorphism between the set of 240 icosians $Y' \cup \tau Y'$, $\tau Y' = \{\tau q_t | q_t \in Y'\}$, and 240 vectors of the first coordination sphere in E_8 provides the isomorphism (in the Euclidean norm) E_8 and the ring of icosians J. The crystallographic root lattice in E_8 (the system of vectors E^8) determines the maximum specific simple Lie algebra e_8 and allows one to obtain the MOG construction [1] whose boundedness for the generalized crystallography of diamond-like structures [14] can be considered as mapping of the maximality of e_8. The isomorphism of the groups Y', $\varphi Y'$, and $\tau Y'$ indicates that the {240} polytope also reflects the limiting symmetry of E_8. Thus, the finite projective plane $PG(2, 4)$ embedded in MOG and the {240} polytope reflect the limiting symmetry of E_8, which signifies that the maximum super-Euclidean symmetry of the specific clusters of a diamond-like structure is determined by the maximum [1] subconfigurations $PG(2, q)$, $q \le 4$, which also determine the clusters of the {240} polytope.

Sections of the {3, 3, 5} polytope by the hyperplane beginning with the vertex and with the cell (Table 5 from [10])

{3, 3, 5} sections	x_4	(x_1, x_2, x_3)	Number of vertices	Polyhedron
0_0	2	(0, 0, 0)	1	Point
1_0	τ	$(1, 0, \tau^{-1})$	12	Icosahedron
2_0	1	(1, 1, 1)	20	Dodecahedron
…		$(\tau, \tau^{-1}, 0)$		
{3, 3, 5} sections	$x_4\sqrt{2}$	$(x_1, x_2, x_3)\sqrt{2}$	Number of vertices	Polyhedron
1_3	τ^2	$(\tau^{-1}, \tau^{-1}, \tau^{-1})$	4	Tetrahedron
2_3	$\sqrt{5}$	(–1, 1, 1)	4	Tetrahedron
3_3	2	(2, 0, 0)	6	Octahedron
4_3	τ	(τ, τ, τ^{-2})	12	Cuboditetrahedron
…				

SPECIFIC CLUSTERS OF THE {240} POLYTOPE DETERMINED BY THE SELF-DUAL SUBCONFIGURATIONS OF FINITE PROJECTIVE PLANES

The incidence graph $PG(2, 2)$ determines the regular division of a torus into hexacycles and is a $\{6, 3\}_{2,1}$ map. The removal of set 4 consisting of three edges (three empty circles in the incidence table of $PG(2, 2)$) results in the formation of the subgraph $\{6, 3\}_{2,1}^{3(4)}$, which provides the irregular division of the sphere into hexacycles and which is the graph of the parallelohedron of the diamond structure [1]. The interpretation of the {240} polytope as an "enantiomorphous diamond" in S^3 allows us to repeat the reasoning in [1] and obtain the enantiomorphous graph $\{6, 3\}_{2,1}^{3(4)}$, which differs from $\{6, 3\}_{2,1}^{3(2)}$ (by removing set 2 consisting of three empty circles from the incidence table of $PG(2, 2)$), which in E^3 has the form of a 14-vertex combination of six twist-boats (Figs. 2a, 2b) under the condition of the equality of the edges (without their intersection) and the angles formed by these edges [16].

The Petrie's polygon of the {240} polytope can be defined as the combination of two (white and black) Bernal helices whose vertices form the 30/11 channel (Fig. 2c). The generating cluster of this channel (generating 30/11 clusters) is a 14-vertex $\{6, 3\}_{2,1}^{3(3)}$ cluster uniquely determined by the reject of set 3 of three empty circles in the incidence table of $PG(2, 2)$. To these empty circles there correspond the bonds forming a trigonal handle and supplementing the sphere to make it a torus. As for the $\{6, 3\}_{2,1}^{3(4)}$ and $\{6, 3\}_{2,1}^{3(2)}$ clusters, the rejection of this handle allows one to obtain a generating cluster whose graph provides the irregular division of the sphere into hexacycles.

The $\{6, 3\}_{2,1}^{3(2)}$ cluster was determined in [2, 3] as the projection in E^3 of the "cell" of the {240} polytope, which, in the Schläfli notation $\{p, q, r\}$, is represented as

$$\{240\} = \{3, 3, 5\} \cup \varphi\{3, 3, 5\} = \{\{6, 3\}_{2,1}^{3(2)}, 3\}, \quad (4)$$

where 6 is the symbol of the face of the hexacycle $\{p\}$ shared by two cells, $\{p, q\} = \{6, 3\}_{2,1}^{3(2)}$; 3 is the number r of the cells at the shared edge; and the corresponding {3, 3} tetrahedron provides the tetrahedral coordination of each vertex of the {240} polytope and the formation of the vertex {240} figure consisting of four $\{6, 3\}_{2,1}^{3(2)}$ cells. The inner braces in (4) indicate the irregularity of the {240} polytope, and rejecting these braces, we arrive at the symbol {6, 3, 3} of specific hyperbolic honeycomb cells [4].

The section of a polygon by the $E^2(x_3)$ plane normal to the X_3-axis and cutting the segment x_3 on it is a polygon whose center lies at the height x_3 above the $X_1X_2 = E^2(0)$ plane (Fig. 1d). In a similar way, the section of the polytope by the hyperplane $E^3(x_4)$ is a polygon whose center lies at a "height" x_4 above the space $X_1X_2X_3 = E^3(0)$. The upper section of the polytope {3, 3, 5} (increased by a factor of two in comparison with (2)) is a point of the "north pole" (0, 0, 0, 2), and, therefore, the sections $\{3, 3, 5\} \cap E^3(x_4)$ are the sections of the {3, 3, 5} polytope originating from its top. The orthogonal transformation φ rotates the {3, 3, 5} polytope in such a way that its upper section is a tetrahedron, the {3, 3, 5} cell, and, therefore, the $\varphi\{3, 3, 5\} \cap E^3(x_4)$ sections

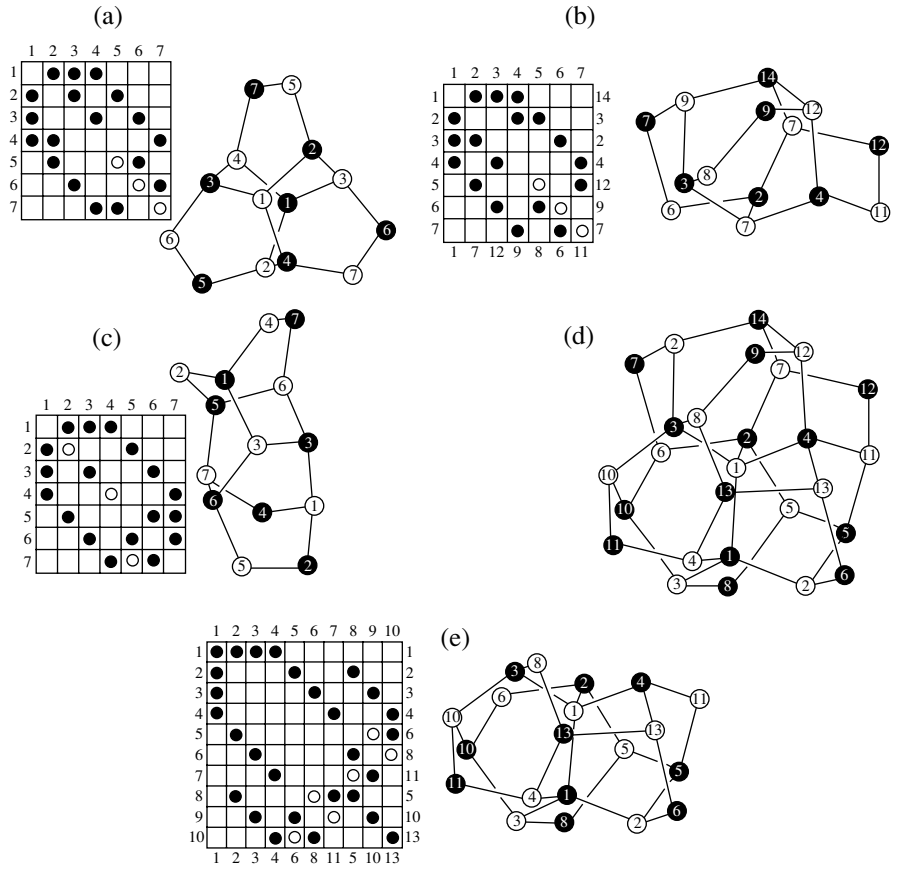

Fig. 2. The vertex figure of the {240} polytope and its parts determined by the incidence tables of the corresponding subconfigurations: (a) the cell of the "left" {240} polytope determined by the incidence table 7_3 without set 2 of three empty circles; (b) the cell of the "right" {240} polytope determined by the incidence table of the cell of the "left" polytope in which the rows are replaced by columns (the numbers of the corresponding vertices of the vertex figure shown in (d) are shown on the right and below the incidence table); (c) the generating clusters of the Petrie's polygon of the right {240} polytope consisting of white and black Bernal's helices (the twofold axis relating these helices is perpendicular to the middle of the 3–3' edge); the cluster is determined by the incidence table 7_3 without set 3 consisting of three empty circles; the replacement of the rows by the columns corresponds to the enantiomorphous modification; (d) the vertex figure of the right {240} polytope as a combination of four cells shown in (b); vertices 1, 2–13 and 1'–4'; 5', 10', 13', 14'; and 6', 7', 8', 9', 11', 12' (the primed numbers enumerate black vertices) correspond to the sections 0_0–1_0 and 1_3–3_3 of the {3, 3, 5} polytope by the $E^3(x_4)$ hyperplane indicated in the table (the sections n_0 and n_3 begin with the vertex and the cell of the {3, 3, 5} polytope, respectively); (e) the layer part of the cluster shown in (d) determined by the incidence table of the extended Desargues configuration 10_3^4 without empty circles; the numbers of corresponding rows and columns of the incidence table of $PG(2, 3)$ (Fig. 6) containing it are indicated on the right and below of the incidence table.

coincide with the sections of the {3, 3, 5} polytope beginning with the cell [10]. In virtue of (4), we have

$$\{240\} \cap E^3(x_4) = (\{3, 3, 5\} \cap E^3(x_4^{(0)})) \cup (\varphi\{3, 3, 5\}) \cap E^3(x_4^{(3)})), \quad (5)$$

where the first and second parentheses indicate the sections of the {3, 3, 5} polytope beginning with the vertex (a zero-dimensional object) and the cell (a three-dimensional object). At $x_4^{(0)} = 2, \tau$, the sections are a point and an icosahedron; at $x_4^{(3)} = \tau^2/\sqrt{2}$, $\sqrt{5/2}$, and $\sqrt{2}$, the sections are tetrahedron, a tetrahedron, and an octahedron, respectively. The projection of these sections onto $E^3(x_4 = 2)$, which here is assumed to be the physical space E^3, results in the formation of a 27-vertex cluster that is the combination of the point and the following polyhedra: a tetrahedron, an icosahedron, a tetrahedron, and an octahedron (see table). This cluster is characterized by the symmetry 23 and is the combination of 18 twist-boats [8, 5, 16, 17] and is also the projection in E^3 of the figure of the {240} polytope centered by the vertex—the combination of four $\{6, 3\}_{2,1}^{3(2)}$ cells.

Without vertex 14' (the primed numbers indicate black vertices), this cluster corresponds to the "edge figure" of the {240} polytope—the combination of three $\{6, 3\}_{2,1}^{3(2)}$ cells sharing the 1–1' edge (Fig. 2d; cf.

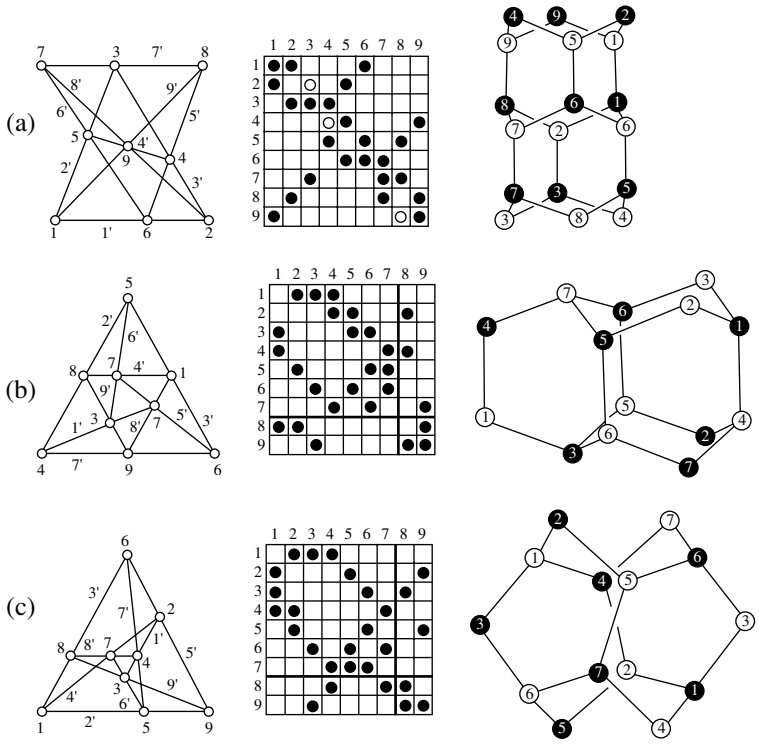

Fig. 3. Configurations 9_3, their incidence tables [12, 18], and the clusters of diamond-like structures determined by their subtables: (a) Pappus configuration $(9_3)_1$, whose incidence table without three empty circles determines an 18-vertex cluster of the lonsdaleite structure; (b) configuration $(9_3)_2$ of three triangles inscribed one into another: {7, 2, 3}, {1, 8, 9}, and {4, 5, 6} (subtable 7×7 is indicated by solid lines; its incidence table determined the generating clusters of the lonsdaleite structure); (c) irregular configuration $(9_3)_3$ (subtable 7×7 is indicated by solid lines, its incidence table determines the generating clusters of the core of a screw dislocation in the diamond structure). The primed numbers enumerate the straight lines corresponding to the black vertices of the clusters of a diamond-like structure.

Fig. 5a from [1]). It was shown [1] that this 26-vertex polyhedron is uniquely determined by the incidence table of the maximum specific configuration $\{13_4\}^{15}$ which arises from the incidence table of $PG(2, 3)$ upon the rejection of 15 incidence signs.

The projective plane $PG(2, 3)$ also contains the extended Desargues configuration 10_3^4, whose 10×10 incidence table contains 34 incidence signs, i.e., our signs more than the incidence table of the Desargues configuration 10_3 [18]. The intersection $\{13_4\}^{15} \cap 10_3^4$ uniquely determines a 20-vertex cluster—the layer part of the vertex figure of the {240} polytope (Fig. 2e), which is the building block of the assembly of diamond-like structures that are not the traditional crystallographic objects [16, 17].

A 27-atom cluster (Fig. 2d) "straightened" from the {240} polytope in E^3 shows the deviations from the ideal tetrahedral coordination (the angles formed by the bonds are not equal to 109.47°), but it is still more energetically advantageous than a 27-atom cluster in the diamond structure [5]. Obviously, further growth of this cluster by the strengthening of clusters of ever increasing dimensions in E^3 from the {240} prototype should result in ever less energetically advantageous clusters with an icosahedral order and, finally, in the attainment of a certain limit at which the crystal cluster with almost ideal tetrahedral coordination restored due to icosahedron deformation becomes more energetically advantageous.

The $x_4^{(0)} = \tau$ and $x_4^{(3)} = \sqrt{2}$ sections in the {3, 3, 5} polytope are followed by the section $x_4^{(0)} = 1$ (dodecahedron) and section $x_4^{(3)} = \tau/\sqrt{2}$ (cuboditetrahedron) (Fig. 2d). Therefore, if one limits the choice of the vertices by eight rotational dodecahedron vertices most remote from the center forming a cube, the projections of these sections in E^3 would yield a 47-atom cluster (Fig. 6c from [1]). Deformation of an octahedron formed by white atoms transforms this cluster straightened from the {240} polytope into the combination of a 21-atom unit cell and a 26-atom Pauling polyhedron of the cubic Frank–Kasper phases A15 and C15, respectively [1, 19]. The unit cell of a hypothetical tetrahedrally coordinated crystal described by the sp. gr. $P\bar{4}3n$ [19] is also embedded in this cluster. One can assume that this cluster is energetically advantageous, which is provided by the outer cube of white atoms,

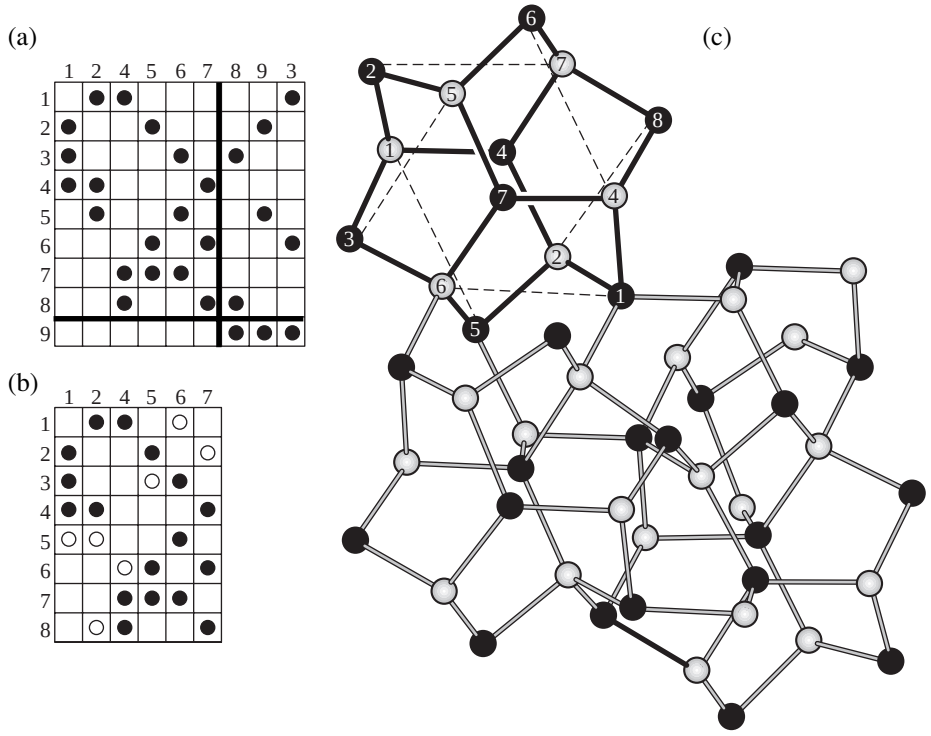

Fig. 4. A BC8 crystal generated by a 14-vertex generating cluster determined by the intersection of the configurations $(9_3)_3$ and $(6_4, 8_3)$: (a) the location of the 3rd right incidence table $(9_3)_3$ behind the 9th column results in an isomorphous incidence table whose subtable 6×8 (solid lines) determines the generating clusters of the BC8 structure; (b) the incidence table of the nongeometric $(6_4, 8_3)$ configuration without empty circles determining the generating clusters of the BC8 structure; (c) the BC8 structure formed by the generating clusters of BC8 are indicated by solid lines. Generating clusters of BC8 are uniquely determined by the subtable 8×6—the intersection of the incidence table $(9_3)_3$ and the incidence table $(6_4, 8_3)$ shown in (a) and (b). The graph of the generating cluster of BC8 with the edges of the incidence graph of the configuration $(6_4, 8_3)$ (empty circles in the incidence table $(6_4, 8_3)$) (shown by dashed line) coincides with the graph of a rhombododecahedron.

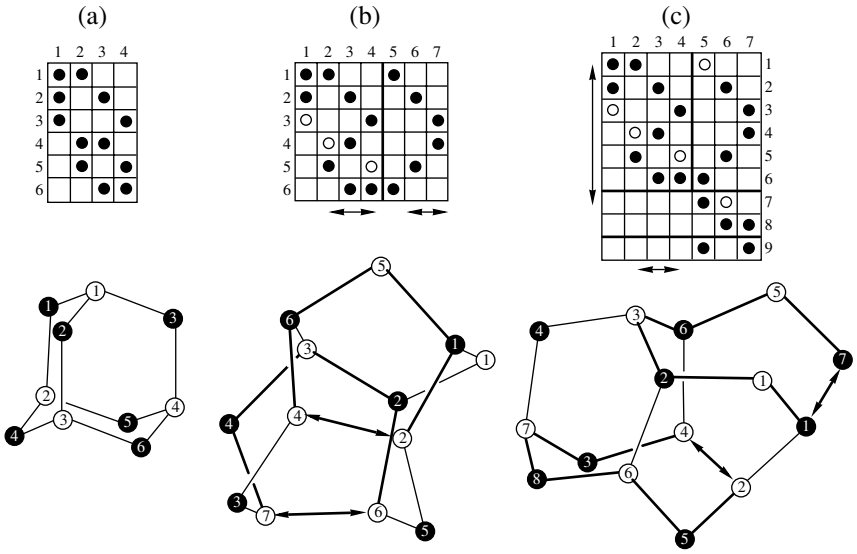

Fig. 5. Finite non-Arguesian planes [18] and the generating clusters with penta-, hexa-, and heptacycles determined by the subtables of their incidence tables: (a) the incidence table of the configuration $(4_3, 6_2)$ of the tetragon and the generating clusters of the adamantane structure determined by this configuration; (b, c) the incidence tables of the finite non-Arguesian planes extended with the aid of arrows and clusters with penta-, hexa, and heptacycles determined by their 6×7 and 8×7 subtables. The sequence of the incidence tables (without arrows) shown in (a–c) is the sequence of the steps T_1, T_2, and T_3 formed during the alternating addition of columns and rows to the previous step. The subtable of the previous step is indicated by the solid line on the subsequent step. Penta- and heptacycles are indicated by solid lines. The bonds between the vertices of the same color are indicated by arrows.

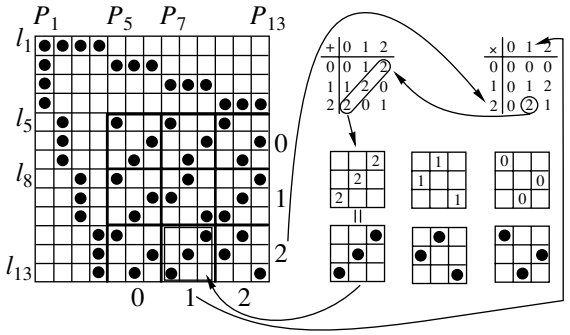

Fig. 6. Construction of the incidence table of finite projective plane $PG(2, 3)$ based on the summation and multiplication tables of the Galois field $GF(3)$. The square C^{21} shown by double lines corresponds to the intersection of row 2 and column 1 of the multiplication table of the Galois field $GF(3)$ determining element 2 whose distribution in the summation table of $GF(3)$ is the distribution of the incidence signs in the square C^{21}. The squares C^{mx} with the zero values either of m or x are the same and are, in fact, the distribution of zeroes in the summation table of $GF(3)$. The square consisting of 3^2 C^{mx} squares with $m, x = 0, 1, 2$ is the Q-contents of the table. The first four rows and columns form a Γ hook [18].

which, unlike an icosahedron, can ensure the division of E^3.

If rows 1, 2, 3, 6, 7, 8, 10, 11, 14, and 16 and columns 1, 2, 3, 4, 6, 7, 8, 10, 11, and 12 in the incidence table of $PG(2, 4)$ (Figs. 6a, 6c in [1]) are rearranged as 6, 1, 2, 3, 7, 10, 11, 8, 14, 16 and 1, 2, 3, 6, 7, 10, 3, 7, 11, 4, 8, 12, then the intersections of the changed rows and columns form the incidence table of the extended Desargues configuration 10_3^3 [18]. This incidence table can be embedded only in $PG(2, 4)$ and determines a specific 20-vertex cluster of a diamond-like structure, which belongs to the unit cell [19] but does not belong to the 27-vertex cluster shown in Fig. 2d.

CLASSIFICATION OF THE GENERATING CLUSTERS OF DIAMOND-LIKE STRUCTURES BY CONFIGURATION TYPE

The finite projective plane $PG(2, q)$ is a self-dual configuration $n_d = (n_d, n_d)$, where $n = q^2 + q + 1$ and $d = q + 1$ [9, 18]. If (m_f, n_d) is the minimum configuration containing the given subconfigurations, then the latter can be embedded in (m_f, n_d). All the specific clusters of the diamond-like structures considered up to now contained hexacycles as the cycles of the minimum length and were determined by the subconfigurations which could be embedded into the self-dual configurations, which, in turn, could be embedded to the finite Arguesian planes [18]. Therefore, these configurations are called Arguesian. The next section is dedicated to the solution of the general problem of enumerating all types of configurations in which the subconfigurations determining the generating clusters with penta-, hexa-, and heptacycles can be embedded. Unlike the unique implementation of self-dual configurations 7_3 and 8_3, three self-dual 9_3 configurations are possible, namely, Pappus configurations $(9_3)_1$ (Fig. 3a), three triangles inscribed into one another $(9_3)_2$ (Fig. 3b), and an irregular configuration $(9_3)_3$ (Fig. 3c) [9, 12, 18]. Therefore, the solution of the problem is demonstrated on the general example of 9_3.

If the bichromatic graph of generating clusters provides the irregular division of a sphere into hexacycles, then, applying the Euler theorem for polyhedra, we arrive at the following relationships:

$$F = 1/2(m_1 + n_1) - 1, \quad E = 3F, \tag{6}$$

where m_1 and n_1 are the numbers of the white and black vertices of the graph, F is the number of hexacycles, and E is the number of edges. The self-dual configuration $n_3 = (n_3, n_3)$ can be represented in the form $((m_1 + m_2)_3, (n_1 + n_2)_3)$, which allows one to single out the subtable $m_1 \times n_1$ in the incidence table n_3. If this subtable contains not less than $3(1/2(m_1 + n_1) - 1)$ incidence signs and each row and each column has not less than two incidence signs, then, in virtue of (6), this subtable of the incidence table determines the generating clusters either directly or when the incidence signs denoted by empty circles are rejected from it.

The simplest case $m_2 = n_2 = 0$ illustrates a Pappus configuration $(9_3)_1$, whose incidence table without three empty circles (i.e., the incidence table of subconfiguration $\{(9_3)_1\}^3$) determines a 18-vertex cluster of lonsdaleite with eight hexacycles (Fig. 3a).

The variant $m_2 = n_2 = 2$ is implemented for the configuration $(9_3)_2 = ((7 + 2)_3, (7 + 2)_3)_2$, whose 7×7 subtable of the incidence table uniquely determines a 14-vertex generating cluster of lonsdaleite with six hexacycles—two chairs and four boats (Fig. 3b). Subconfiguration $(9_3)_2$ with such an incidence table is denoted as $((7 \cup 2)_3)_2$. In a similar way, the subconfiguration $((7 \cup 2)_3)_3$ of the configuration $(9_3)_3$ uniquely determines a 14-vertex generating cluster of a screw-dislocation core in the diamond structure with six hexacycles, two twist-boats, and four twist-chairs (Fig. 3c) [16, 17, 20].

At $m_2 = 3$ and $n_2 = 1$, one can single out in a self-dual configuration $(9_3)_3$ a non-self-dual subconfiguration $((6 \cup 3)_3, (8 \cup 1)_3)_3$ with the 8×6 incidence table, which is the intersection of $(9_3)_3$ and the non-self-dual configuration $(6_4, 8_3)$ (Fig. 4). The configuration $(6_4, 8_3)$ can be considered as a set of eight vertices and six faces of a cube, with each vertex being shared by three faces and each face containing four vertices. Substituting each face by a white dot, we arrive at a bichromatic graph of a rhombododecahedron; since the faces of this dodecahedron are tetragons, then $(6_4, 8_3)$ is a nongeometric configuration. The intersection $(9_3)_3 \cap (6_4, 8_3)$ is the maximum geometric subconfiguration of the con-

figuration $(6_4, 8_3)$ (Fig. 4b). The incidence table of $(6_4, 8_3)$ contains a smaller number of incidence signs than the incidence table of $(9_3)_3$ and, therefore, the subconfiguration $(9_3)_3 \cap (6_4, 8_3)$ determining a 14-vertex generating cluster with six hexacycles is embedded in the non-self-dual configuration $(6_4, 8_3)$. The graph of this generating cluster is obtained from the graph of a rhombododecahedron upon rejection of the edges shown by dashed lines (empty circles in the incidence table $(6_4, 8_3)$ (Figs. 4b, 4c). This graph is a graph of generating clusters of BC8 structure, the high-pressure body-centered Si-phase [6, 19, 21]. This structure is a diamond-like structure with distorted (up to 100°) "tetrahedral angles" (Fig. 4c). In [6, 19], the BC8 structure was considered as the approximant of an icosahedral quasicrystal.

All the generating clusters considered above are determined by the Arguesian subconfigurations of the planes of $PG(2, q)$. However, these planes can also have non-Arguesian subconfigurations. Thus, the Hall steps T_2 and T_3 (Figs. 5b, 5c) are finite non-Arguesian projective planes [18] that can be embedded in $PG(2, 2)$ and $PG(2, 3)$, respectively. Since T_2 (T_3) are non-Arguesian projective planes, which is seen from the fact that some columns (rows) do not intersect in the incidence table of $T_2(T_3)$, the bichromatic incidence graph $T_2(T_3)$ acquires the cycles absent in the $PG(2, q)$ graph. The latter cycles can be divided into smaller ones if they are connected by the edges originating from the vertices of the same color. This signifies that one can single out in the "incidence-extended" space between the points or between the straight lines of the Arguesian plane $T_2(T_3)$ the subconfiguration determining the division of a sphere into penta-, hexa-, and heptacycles.

In addition to T_2, the $PG(2, 2)$ plane also contains the subconfiguration $7_3 \cap 10_3$ considered in detail earlier, which determines the parallelohedron of the diamond structure (Fig. 3c from [1]). To the intersection of $(7_3 \cap 10_3)$ with T_2 there corresponds the rejection of two more signs from the incidence table. Rejecting one more sign from this incidence table and then establishing the "incidence" between the points 2–4 and 6–7 with the aid of the arrows, we obtain the incidence table which determines the subconfiguration $\{7_3 \cap 10_3 \cap T_2\}^{1-2}$. The superscript 1 in this subconfiguration signifies one rejected bichromatic edge, and the 2 indicates the introduction of two additional edges not belonging to the incidence graph of the subconfiguration $7_3 \cap 10_3 \cap T_2$ and connecting the vertices of the same color. The projective plane $PG(2, 3)$ contains the Hall step T_3 and the configuration 8_3, and, therefore, the incidence graph of the subconfiguration $\{8_3 \cap (9_3)_2 \cap T_3\}^{-2}$ determines the graph of a 15-vertex generating cluster with two heptacycles and four hexacycles (Fig. 5c).

It is possible to show that both in [1] and the present article, all the types of generating clusters containing only penta-, hexa-, and heptacycles have been considered, and, therefore, it is possible to classify these types over the following configuration types: Arguesian (Figs. 2–4), non-Arguesian (Fig. 5), self-dual (Figs. 2, 3), non-self-dual (Fig. 4), conventional, and extended (Fig. 2d).

Now arrange the subconfigurations determining 14-vertex generating clusters with six hexacycles in the order of lowering of their symmetry and the symmetry of the configurations in which they can be embedded,

$$\begin{array}{ccccccc} PG(2,2) = 7_3, & & (9_3)_2, & & (9_3)_3, & & (6_4, 8_3), \\ \cup & \cup & \cup & & . & & \cup \\ 7_3 \cap 10_3, & \{7_3\}^{3(i)}, & ((7 \cup 2)_3)_2, & & ((7 \cup 2)_3)_3, & & (9_3)_3 \cap (6_4, 8_3). \end{array} \quad (7)$$

Indeed, $PG(2, 2)$, being a finite projective plane, is "more symmetric" than a conventional configuration [18]; in this case, the unique configuration $7_3 \cap 10_3$ determining the generating clusters of the diamond structure is more symmetric than the subconfigurations $\{7_3\}^{3(i)} = \{6, 3\}^{3(i)}_{2,1}$, $i = 2, 3$ determining the generating clusters of the cell of the {240} polytope and the 30/11 channel. The regular configuration $(9_3)_2$ is more symmetric than the irregular one, $(9_3)_3$ [12], which, in turn is more symmetric than the non-self-dual configuration $(6_4, 8_3)$.

If a diamond-like structure is built by generating clusters of one type, one can state that its symmetry (understood at the level of the algebraic groups [14, 23, 24]) is determined by the symmetry of the subconfiguration determining the generating clusters and the configuration in which this subconfiguration is embedded. Thus, it follows from relationships (7) that the symmetry is lowered in the following sequence of diamond-like structures: diamond, structures determined by the {240} polytope, lonsdaleite, the core of a screw dislocation in the diamond structure, and BC8. In the spirit of Bernal's article on the role of geometric factors in the structure of matter [22], relationship (7) can be regarded as the specification of the "projective–geometrical factor" in diamond-like structures.

CONCLUSIONS

It is shown on numerous examples both in [1] and the present article that the graphs of the generating clusters of diamond-like structures are uniquely determined by the subtables of the incidence table of finite projective planes $PG(2, q)$, $q = 2, 3, 4$. Within the framework of classical crystallography, whose algebraic basis is the group theory, no adequate reflection of the symmetry of these graphs is possible. This signifies that the incidence table of $PG(2, q)$ reflects the symmetry of such algebraic objects as rings, fields, algebras, etc., in which, unlike the symmetry groups, at least two operations are defined [23, 24].

Indeed, the incidence tables of $PG(2, q)$ are uniquely constructed with the aid of the summation and multiplication tables of the subtraction fields modulo q—the Galois fields $GF(q)$. Consider an example of such a construction of the incidence table of $PG(2, q)$ with $q = 3$ (Fig. 6). It is well known that the distribution of numbers in the summation table of $GF(q)$ is diagonal, i.e., each column and each row of the $q \times q$ table has only one number (from 0 to $q - 1$). One can see that to each product of numbers m and x from the multiplication table, $q \times q$, there corresponds the table C^{mx} containing only the diagonal distribution of the number $t = mx$ from the summation table. In turn, all the tables C^{mx}, $m, x = 0$, and $1 \ldots q - 1$ form the table $q \times q$, which (upon the replacement of all the numbers t by the black circles) becomes the Q-contents of the incidence table of $PG(2, q)$. Upon the addition of the stepwise distribution of the incidence signs in the additional Γ-like hook (consisting of $q + 1$ rows and a column), the incidence table of $PG(2, q)$ in the form of a Γ-table is formed [18].

Thus, the transition from the classical to the generalized crystallography of diamond-like structures is, in fact, the transition from the Euclidean to the projective geometry, whereas at the algebraic level, it is the transition from a group to rings, fields, algebras, etc. Both in [1] and in the present article, we replaced the algebraic constructions by their crystallographic equivalents just as crystallographers determine the space group using the corresponding plot from the International Tables [26] instead of their group-theoretical determination [25]. In this sense, the subalgebras of different types [23] correspond to the subconfigurations of different symmetries in (7).

The conclusions following from the present study can be formulated as follows:

—highly symmetric clusters of the diamond structure in S^3, the {240} polytope, are determined by the subconfigurations of $PG(2, q)$, $q = 2, 3, 4$ and, upon their straightening in E^3, become specific clusters of diamond-like structures;

—the generating clusters, whose minimum cycles are only hexacycles, are determined by the subconfigurations which can be embedded in self-dual, non-self-dual, conventional, or extended configurations of the Arguesian finite projective planes. The generating clusters containing penta-, hexa-, and heptacycles are determined by the subconfigurations that can be embedded in the finite projective planes;

—the symmetry of diamond-like structures assembled from generating clusters of one type is determined by the symmetry of the configuration in which the setting subconfiguration of the generating clusters is embedded. This determines the lowering of the symmetry in the sequence of diamond-like structures corresponding to the lowering of the symmetry of the respective configurations. As an example, we considered the following sequence of diamond-like structures: diamond, structures determined by the {240} polytope, lonsdaleite, the core of a screw dislocation in the diamond structure, and BC8.

ACKNOWLEDGMENTS

The author expresses his deep gratitude to V.A. Koptsik, N.A. Bul'enkov, L.I. Tsinober, M.I. Samoĭlovich, V.S. Kraposhin, and M.I. Mironov for their interest in this study and stimulating discussions. The author is also grateful to V.E. Dmitrienko and N.P. Dolbilin for fruitful discussion of the results and valuable remarks.

REFERENCES

1. A. L. Talis, Kristallografiya **47** (4), 583 (2002) [Crystallogr. Rep. **47**, 527 (2002)].
2. A. L. Talis, in *Proceedings of the IV International Conference "Crystals: Growth, Properties, Real Structure, Application"* (VNIISIMS, Aleksandrov, 1999), p. 219.
3. A. L. Talis, *Synthesis of Minerals* (VNIISIMS, Aleksandrov, 2000), Vol. 3, p. 321.
4. M. Kleman, Adv. Phys. **38**, 605 (1989).
5. R. Mosseri, D. P. Di Vincenzo, T. F. Sadoc, and M. H. Brodsky, Phys. Rev. B **32**, 3974 (1985).
6. V. E. Dmitirienko and M. Kléman, Philos. Mag. Lett. **79**, 359 (1999).
7. L. Danzer, Z. Popadopulus, and A. Talis, Int. J. Mod. Phys. B **7**, 1379 (1993).
8. H. S. M. Coxeter, Philos. Trans. R. Soc. London, Ser. A **229**, 346 (1930).
9. H. S. M. Coxeter, *Introduction to Geometry* (Wiley, New York, 1961; Nauka, Moscow, 1966).
10. H. S. M. Coxeter, *Regular Polytopes* (Dover, New York, 1973).
11. H. S. M. Coxeter, Bull. Am. Math. Soc. **56**, 413 (1950).
12. D. Hilbert and S. Cohn-Vóssen, in *Descriptive Geometry* (Nauka, Moscow, 1981), p. 289.
13. H. S. M. Coxeter and W. O. J. Moser, *Generations and Relations for Discrete Groups* (Springer-Verlag, New York, 1972; Nauka, Moscow, 1980).
14. J. H. Conway and N. J. A. Sloane, *Sphere Packings, Lattices, and Groups* (Springer-Verlag, New York, 1988; Mir, Moscow, 1990), Vols. 1, 2.
15. D. R. Nelson, Phys. Rev. B **28**, 5515 (1983).

16. N. A. Bul'enkov, Biofizika **36**, 181 (1991).
17. N. A. Bul'enkov, in *Quasicrystals and Discrete Geometry*, Ed. by J. Patera (American Mathematical Society, Providence, 1998).
18. F. Karteszi, *Introduction to Finite Geometries* (Akademiai Kiado, Budapest, 1976; Nauka, Moscow, 1980).
19. V. E. Dmitrienko and M. Kléman, Kristallografiya **46** (4), 591 (2001) [Crystallogr. Rep. **46**, 527 (2001)].
20. J. Hornstra, in *Defects in Crystals of Semiconductors: Collection of Articles* (Mir, Moscow, 1969), p. 15.
21. J. Crain, G. J. Ackland, J. R. Maciean, *et al.*, Phys. Rev. B **50**, 13043 (1994).
22. J. Bernal, Kristallografiya **7** (3), 507 (1962) [Sov. Phys. Crystallogr. **7**, 410 (1962)].
23. I. R. Shafarevich, *Basic Concepts in Algebra* (Izd. Izhevskoĭ Respublikanskoĭ Tipografii, Izhevsk, 1999).
24. R. V. Moody and J. Patera, J. Phys. A **26**, 2829 (1993).
25. A. G. Kurosh, *The Theory of Groups* (Chelsea, New York, 1960; Nauka, Moscow, 1967, 3rd ed.).
26. *International Tables for Crystallography*, Vol. A: *Space-Group Symmetry*, Ed. by T. Hahn (Reidel, Dordrecht, 1983).

Translated by L. Man

Crystallography Reports, Vol. 47, No. 5, 2002, pp. 720–722. Translated from Kristallografiya, Vol. 47, No. 5, 2002, pp. 785–787.

CRYSTAL SYMMETRY

Fullerenes C_{20}–C_{60}: Combinatorial Types and Symmetry Point Groups

Yu. L. Voytekhovsky* and D. G. Stepenshchikov**

** Geological Institute, Kola Scientific Center, Russian Academy of Sciences, ul. Fersmana 14, Apatity, Murmansk oblast, 184209 Russia*

e-mail: voyt@geoksc.apatity.ru

*** Kola Branch, Petrozavodsk State University, ul. Kosmonavtov 3, Apatity, Murmansk oblast, 184209 Russia*

Received June 5, 2001

Abstract—A series of fullerenes from C_{20} to C_{60} (a total of 5770) is obtained and their characterization in terms of symmetry point groups is performed for the first time. The most symmetric forms with the sixth and higher orders of automorphism groups (a total of 80) are represented in the Schlegel projection onto one of the faces. It is noted that, among the 5770 fullerenes obtained, only 12 fullerenes exhibit noncrystallographic symmetry.

Considerable advances made in the crystallography and mineralogy of carbon over the last fifteen years are associated with the laboratory synthesis [1, 2] and the subsequent discovery [3–5] of C_{60} stable clusters in nature. Fullerenes containing less than 60 atoms are unstable; furthermore, carbon clusters involving from 20 to 36 atoms fall within the so-called "forbidden gap" [6, 7]. However, it is this type of crystallization cavities that has been revealed in different clathrate compounds over the last fifty years [8]. In the present work, we derived all combinatorial types of fullerenes containing from 20 to 60 atoms and proposed their classification in terms of symmetry point groups. It should be noted that the problem of enumeration of fullerenes is dual of the problem of triangulation of a spherical surface. The latter problem has been intensively studied in the context of the problem concerning the closest packing of identical particles on the spherical surface.

Let us now consider a fullerene in the form of a simple polyhedron (each vertex is shared by three faces) in which only pentagonal and hexagonal faces are allowed. It is assumed that f_5 and f_6 are the numbers of pentagonal and hexagonal faces, respectively, and f, e, and v are the numbers of all faces, edges, and vertices in the polyhedron, respectively. Hence, from the relationships

$$f_5 + f_6 = f, \quad 5f_5 + 6f_6 = 2e$$

we obtain

$$f_5 = 6f - 2e.$$

Next, from the relationships

$$f - e + v = 2, \quad 2e = 3v$$

we have

$$6f - 2e = 12.$$

As a result, we obtain

$$f_5 = 12, \quad f = 12 + f_6$$

at any $f_6 \geq 0$.

Similarly,

$$v = 2f - 4 \geq 20, \quad f_6 = f - 12 = v/2 - 10.$$

Thus, any fullerene can be characterized by the vertex (C_v-) and face ($5_{12}6_{v/2\text{-}10}$) formulas.

The general idea of representing a fullerene in the form of a Schlegel projection according to the face formula is as follows. Face *1* is surrounded by other faces that are numbered clockwise. The same operation is repeated with faces *2*, *3*, etc. In the favorable case, the basal face of the Schlegel projection will be generated at the penultimate step. In particular, for the simplest formula 5_{12}, the operation begins with the pentagonal face and leads to a dodecahedron (see figure, no. 1).

For fullerenes described by the formula $5_{12}6_n$, the above operation can begin with the hexagonal face. In order to exhaust all the possible variants, it is necessary to preliminarily enumerate the sequences (6, …) with all kinds of arrangement of $(n - 1)$ sextuples in $(n + 11)$ unoccupied positions. Then, pentagonal and hexagonal faces are generated in accordance with these sequences. For example, the sequence (6, 5, …, 5) with twelve quintuples does not lead to a polyhedron, because the $5_{12}6_1$ fullerene is nonexistent in nature. However, the $5_{12}6_2$ fullerene (figure, no. 2) exists and can be specified by the sequence (6, 5, …, 5, 6).

The aforementioned operation is terminated in the following cases: (i) the fullerene is constructed according to the face formula; (ii) the fullerene is constructed prior to exhaustion of the formula; (iii) the fullerene is not constructed, but the formula is exhausted; and

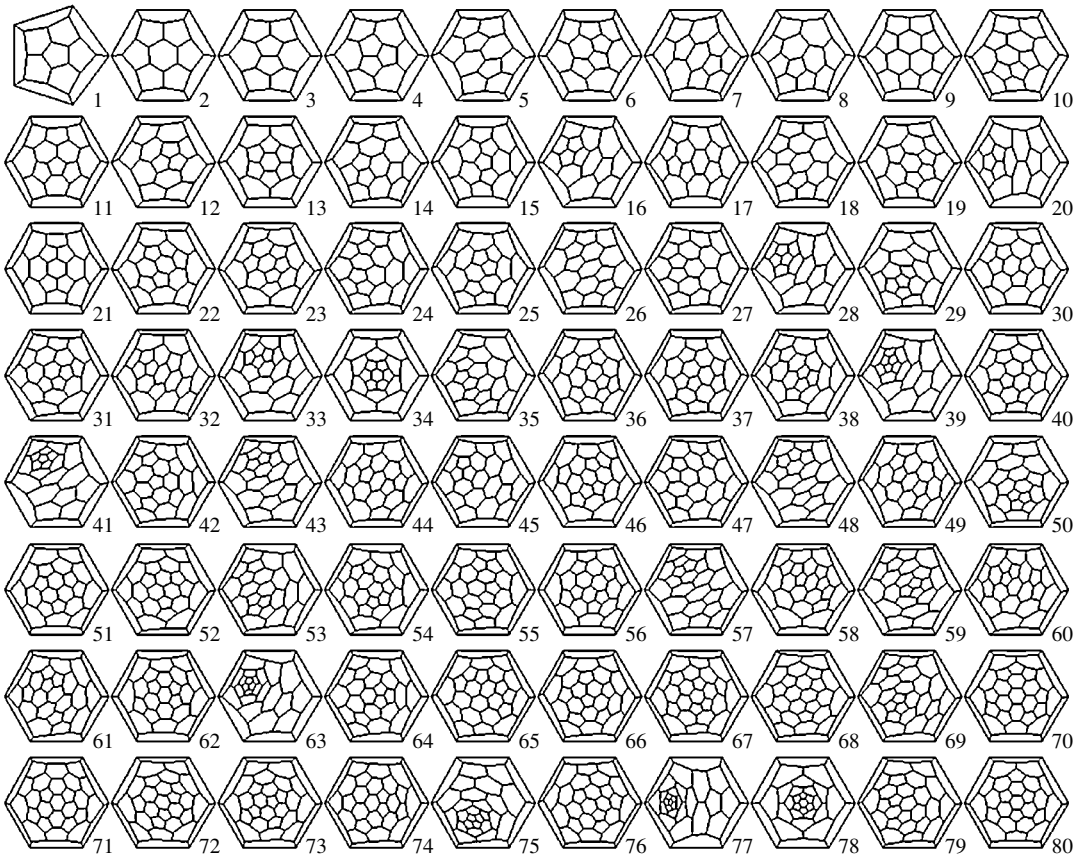

Fullerenes C_{20}–C_{60} with the sixth and higher orders of automorphism groups in the Schlegel projection onto one of the faces.

(iv) at a certain step, the required face becomes neither pentagonal nor hexagonal. All the fullerenes constructed with the use of the given formula are sorted according to combinatorial type, and repetitions are rejected.

The forms thus obtained are characterized by symmetry point groups. The algorithm of their determination is reduced to the enumeration of all kinds of redesignation of vertices retaining contiguity. By certain criteria, each redesignation is identified as a fullerene symmetry element.

After executing this algorithm, we obtained 5770 combinatorially different fullerenes in which the number of vertices ranges from 20 to 60. The distribution of the fullerenes over automorphism group orders and symmetry point groups is given in the table. The vast majority of the forms involved have the symmetry 1, 2, or *m*. For a fixed *v*, the diversity of forms drastically decreases with an increase in the order of the automorphism group. This is accompanied by an increase in the physical stability of the fullerene [1, 2, 6, 7, 9]. The most symmetric forms with the sixth and higher orders of automorphism groups are depicted in the figure. The symmetry point groups of these forms are as follows:

C_{20}: 1 ($\bar{5}\bar{3}m$); C_{24}: 2 ($\overline{12}m2$); C_{26}: 3 ($\bar{6}m2$); C_{28}: 4 ($\bar{4}3m$); C_{30}: 5 ($\overline{10}m2$); C_{32}: 6 (32), 7 ($\bar{3}m$), 8 ($\bar{6}m2$); C_{34}: 9 (3*m*); C_{36}: 10, 11 ($\bar{4}2m$), 12 ($\bar{6}m2$), 13 (6/*mmm*); C_{38}: 14 (32), 15 (3*m*), 16 ($\bar{6}m2$); C_{40}: 17 (3*m*), 18 (*mmm*), 19, 20 ($\bar{5}m$), 21 ($\bar{4}3m$); C_{42}: 22 (32); C_{44}: 23, 24 (32), 25 (23), 26–28 ($\bar{3}m$), 29, 30 ($\bar{6}m2$); C_{48}: 31 (32), 32, 33 (*mmm*), 34, 35 ($\overline{12}m2$); C_{50}: 36, 37 (32), 38 (3*m*), 39 ($\bar{6}m2$), 40, 41 ($\overline{10}m2$); C_{52}: 42, 43 (3*m*), 44, 45 (*mmm*), 46–50 ($\bar{4}2m$), 51 (23); C_{54}: 52 (32), 53 ($\bar{6}m2$); C_{56}: 54–59 (32), 60 (*mmm*), 61 ($\bar{4}2m$), 62, 63 ($\bar{3}m$), 64 ($\bar{4}3m$); C_{58}: 65, 66 (3*m*); C_{60}: 67–69 (32), 70 (3*m*), 71 (*mmm*), 72–75 ($\bar{4}2m$), 76 (52), 77 ($\bar{5}m$), 78, 79 (6/*mmm*), 80 ($\bar{5}\bar{3}m$).

Apart from the well-known form C_{60} (80), the most probable fullerenes in the physical experiments are 34, 35, 40, 41, 64, and 77–79. Judging from the number of atoms, these fullerenes fall far beyond the forbidden gap and possess high symmetry. Except for forms 1, 2, 5, 19, 20, 34, 35, 40, 41, 76, 77, and 80, the fullerenes C_{20}–C_{60} exhibit crystal symmetry and, without symmetry violation, can be considered as possible structural units of the crystalline compounds. The listed 12 forms are also encountered in crystalline compounds (for

Statistics of symmetry point groups of fullerenes C_{20}–C_{60}

AGO	TTC	20	24	26	28	30	32	34	36	38	40	42	44	46	48	50	52	54	56	58	60	Σ
1	1								2	7	8	23	42	69	117	195	307	470	700	4037	1508	4485
2	$\bar{1}$																		1			1
	2						2	3	4	5	14	11	22	22	52	37	78	62	135	98	189	734
	m							2	2		7	6	7	19	16	25	26	38	49	58	67	322
3	3										1			2		2	3		3	4		15
4	$\bar{4}$												1								2	3
	222				1		1		2		3		6		5		9		10		19	56
	2/*m*														1		1		2		4	8
	*mm*2					2			1	2	2	4	3	4	3	6	3	8	13	6	9	66
6	32						1			1		1	2		1	2		1	6		3	18
	3*m*									1	1					1	2			2	1	9
8	*mmm*							1			1				2		2		1		1	7
	$\bar{4}\,\bar{2}\,m$								2								5		1		4	12
10	52																				1	1
12	23												1				1					2
	$\bar{3}m$						1						3						2			6
	$\bar{6}\,m2$			1			1		1	1			2			1		1				8
20	$\bar{5}m$										2										1	3
	$\overline{10}\,m2$					1										2						3
24	6/*mmm*								1												2	3
	$\bar{4}\,\bar{3}\,m$				1						1								1			3
	$\overline{12}\,m2$		1												2							3
120	$\bar{5}\,\bar{3}\,m$	1																			1	2
		1	1	1	2	3	6	6	15	17	40	45	89	116	199	271	437	580	924	1205	1812	5770

Notation: AGO = automorphism group orders and SPG = symmetry point groups.

example, C_{20} dodecahedra in clathrates [8]). In this case, they are distorted and lower their own symmetry.

The schematic drawings of all 5770 fullerenes in the Schlegel projections are available from the authors in electronic form on request. In the immediate future, we will publish a systematic catalog of fullerenes with their complete characterization.

REFERENCES

1. R. F. Curl and R. E. Smalley, Science **242**, 1017 (1988).
2. H. Kroto, Science **242**, 1139 (1988).
3. A. Z. Zaĭdenberg, V. V. Kovalevskiĭ, N. N. Rozhkova, and A. G. Tupolev, Zh. Fiz. Khim. **70** (1), 107 (1996).
4. N. P. Yushkin, Dokl. Akad. Nauk **337** (6), 800 (1994).
5. M. I. Novgorodova, Dokl. Akad. Nauk **367** (2), 241 (1999).
6. J. B. Howard, J. T. McKinnon, Y. Makarovsky, *et al.*, Nature **352**, 139 (1991).
7. G. Helden, M.-T. Hsu, N. Gotts, and M. T. Bowers, J. Phys. Chem. **97**, 8182 (1993).
8. J. A. Ripmeester and Ch. I. Ratcliffe, Zh. Strukt. Khim. **40** (5), 809 (1999).
9. R. A. Dilanyan, O. G. Rybchenko, and V. Sh. Shekhtman, Kristallografiya **39** (1), 5 (1994) [Crystallogr. Rep. **39**, 1 (1994)].

Translated by O. Borovik-Romanova

Crystallography Reports, Vol. 47, No. 5, 2002, pp. 723–726. Translated from Kristallografiya, Vol. 47, No. 5, 2002, pp. 788–792.

THEORY OF CRYSTAL STRUCTURES

Tetragonal Packings of Spheres

V. V. Dolivo-Dobrovol'skiĭ

St. Petersburg Mining Institute, Vtoraya liniya 21, St. Petersburg, 199026 Russia

Received January 4, 2002

Abstract—Nine regular tetragonal packings of spheres are considered. These packings satisfy the following conditions: all the spheres have the same dimensions and environment, i.e., belong to one regular system of points with the coordination number of the packing being not less than six. The examples of the real crystal structures corresponding to seven of these packings are considered. © *2002 MAIK "Nauka/Interperiodica".*

Sphere packings with symmetry corresponding to the tetragonal system are often considered as distorted cubic or hexagonal packings. Clarke [1] described some tetragonal sphere packings as independent types and characterized 17 sphere packings, among which there were three tetragonal packings. From the crystallochemical standpoint, Clarke's study is not free of drawbacks. In particular, there are no data on the spatial symmetry of these packings, which, may account for the wrong statement that the cubic "diamond" packing is noncentrosymmetric. Later, the tetragonal packing (simple tetragonal packing, STP) with a density only slightly lower than the densities of the cubic and hexagonal close packings was described as an independent type of sphere packing [2–5].

Clarke's packings and STP are far from being a complete set of tetragonal regular sphere packings. Table 1 gives the characteristics of nine different tetragonal packings arbitrarily denoted by the symbols from T-1 to T-9 and satisfying the following conditions: all the spheres are of the same dimensions and have the same environment, i.e., belong to one regular point system (RPS); the coordination number (c.n.) of packings is not less than six, i.e., each sphere is in contact with at least six other spheres. For comparison, this table also lists the characteristics of four well-known cubic packings of spheres (from C-1 to C-4) and the hexagonal close packing (H-1). The sphere coordination in the tetragonal packings under consideration is illustrated by the figure. The characteristics of the coordination polyhedra are indicated in Table 2.

The density of the T-1 packing (STP) is only 3% lower than the densities of the cubic and hexagonal close packings. The T-1 packing is well known, because it defines the arrangement of the *B* atoms in the compounds described by the general formula AB_2, which possess rutile-type structure where the *A* atoms occupy the octahedral cavities formed by *B* atoms. The shapes and arrangement of different cavities in the T-1 packing and chemical compounds whose structures are determined by this packing were considered in detail elsewhere [3].

For an ideal T-1 packing, the c/a ratio is equal to $2 - \sqrt{2} = 0.586$, and the parameter x is half as large as this value. In the crystals of the AB_2 compounds belonging to the rutile structure type, the c/a and x_B parameters noticeably differ from their ideal values (generally, c/a varies from 0.634 to 0.705, and x_B ranges from 0.300 to 0.307). This can be considered as a certain "compromise" between the parameters of the ideal T-1 packing, which provide the regular coordination of the *A* atoms, and the parameters that ensure the regular triangular coordination of *B* atoms ($c/a = \sqrt{6}/3 = 0.8165$, $x_B = 1/3 = 0.333$) [5].

The T-2 packing (body-centered tetragonal packing described as packing no. 17 in [1]) was also considered in more recent studies [4, 5]. This packing can be readily obtained from body-centered cubic packing by contracting it along one of the fourfold axes until the c/a ratio of the tetragonal cell reaches the value $\sqrt{6}/3 = 0.8165$. Of all the known structures, the structure of metal protactinium is very close to the T-2 packing, although the c/a value for the unit cell of Pa (0.825) slightly differs from the value corresponding to the ideal T-2 packing. The high-barium modification of tin formed at pressures exceeding 11.5 GPa has an analogous structure. As far as we know, the T-2 packing has not been encountered in the structures of minerals. Conceivably, the absence of real structures with the T-2 packing is explained by the absence of regular cavities between the spheres in this packing, i.e., because all the octahedral cavities in this packing are substantially distorted [4].

The T-3 packing was also described in [1] (packing no. 14). The density of this packing is $(2 - \sqrt{2})\pi/3$. The T-3 packing, as far as we know, has not been mentioned in crystal chemistry in general and in crystal chemistry of minerals, in particular. However, this packing seems to form the basis of the structures of the group of min-

1063-7745/02/4705-0723$22.00

Table 1. Characteristics of sphere packings

Packings	Space group	RPS	q	CN	DP	c/a
Cubic:						
C-1 (close packing)	$Fm\bar{3}m$	(*a*)	4	12	0.7405	1.000
C-2 (body-centered packing)	$Im\bar{3}m$	(*a*)	2	8	0.6802	1.000
C-3 (primitive)	$Pm\bar{3}m$	(*a*)	1	6	0.5236	1.000
C-4 (diamond)	$Fd\bar{3}m$	(*a*)	8	4	0.3401	1.000
Hexagonal:						
H-1 (close packing)	$P6_3/mmc$	(*c*)	2	12	0.7405	1.633
Tetragonal:						
T-1 (STP)	$P4_2/mnm$	(*f*) [1]	4	11	0.7187	0.586
T-2 (body-centered packing)	$I4/mmm$	(*a*)	2	10	0.6981	0.816
T-3	$I4/mmm$	(*e*) [2]	4	9	0.6134	3.414
T-4	$I4_1/amd$	(*a*)	4	8	0.6046	3.464
T-5	$I4_1/amd$	(*a*)	4	6	0.5585	0.516
T-6	$I4_1/amd$	(*c*)	8	6	0.5585	0.365
T-7	$I4_1/amd$	(*f*) [3]	16	6	0.5406	0.254
T-8	$I4_1/amd$	(*h*) [4]	16	10	0.6931	0.977
T-9	$I4/mcm$	(*h*) [5]	8	7	0.6030	0.963

Note: [1] $x = 0.2929$, [2] $z = 0.1464$, [3] $x = 0.1270$, [4] $y = 0.2838$, $z = 0.9065$, [5] $x = 0.1830$; RPS is the regular point system; q is the position multiplicity; CN is the coordination number; DP is the packing density.

erals including thalcusite $Cu_3FeTl_2S_4$, murunskite $Cu_3FeK_2S_4$, and bukovite $Cu_3FeTl_2Se_4$. The c/a ratio for these minerals (3.41, 3.38, and 3.44, respectively) is very close to its ideal value for the T-3 packing ($2 + \sqrt{2}$). According to the X-ray diffraction data, these minerals are described by the space group $I4/mmm$ or the space groups $I\bar{4}2m$, $I\bar{4}m2$, $I422$, and $I4mm$ of the same diffraction class. Taking into account that the number of formula units per unit cell in these minerals equals unity, the sulfur (or selenium in bukovite) atoms may occupy RPS with a multiplicity of four. The c/a ratio indicates that these atoms occupy the (*e*) position necessary for the T-3 packing. Note also that the other above-mentioned space groups of this diffraction class contain positions analogous to the (*e*) positions in the space group $I4/mmm$ and possessing the same symmetry. Thus, the structures of these minerals can be based on the T-3 packing whether the whole structure has the $I4/mmm$ symmetry or not.

The T-4 packing was described in [1] as packing no. 13. The density of this packing is $(\sqrt{3}/9)\pi$. As far we know, the T-4 packing was not described in crystal chemistry either. However, this packing forms the basis for the structure type of thorium silicide α-$ThSi_2$, where thorium atoms occupy the (*a*) positions in the space group $I4_1/amd$ and the c/a value (3.476) is very close to the ideal value for the T-4 packing. Silicon atoms occupy the cavities formed by thorium atoms (spheres in the T-4 packing). The shapes of these cavities correspond to a trigonal prism (the coordination number of Si with respect to Th is 6). Each Th atom is surrounded by eight Th atoms of the packing and twelve Si atoms are located in the surrounding cavities.

A series of rare-earth silicides and uranium, neptunium, and plutonium silicides belong to the α-$ThSi_2$ structure type. In these structures, the c/a ratio ranges from 3.18 to 3.48.

The NbAs structure type is also described by the T-4 packing. The structure of niobium arsenide is described by the space group $I4_1md$, but both Nb and As atoms occupy the positions analogous to the (*a*) position in the space group $I4_1/amd$. For NbAs, the c/a ratio is 3.384. For the NbP and TaP structures (also of this structure type), $c/a = 3.42$.

The T-4 packing is the only packing of all the regular tetragonal sphere packings with the symmetry $I4_1/amd$. It should be noted that in terms of structural mineralogy and crystal chemistry, space group $I4_1/amd$ occupies a special position among the space groups of the tetragonal system. It can be stated that the role of space group $I4_1/amd$ in the world of tetragonal minerals is analogous to the role of space group *Pbnm* (which is the "mineralogical" aspect of space group *Pnma*) in the world of orthorhombic minerals. Without going into details, we should like to indicate that the space groups

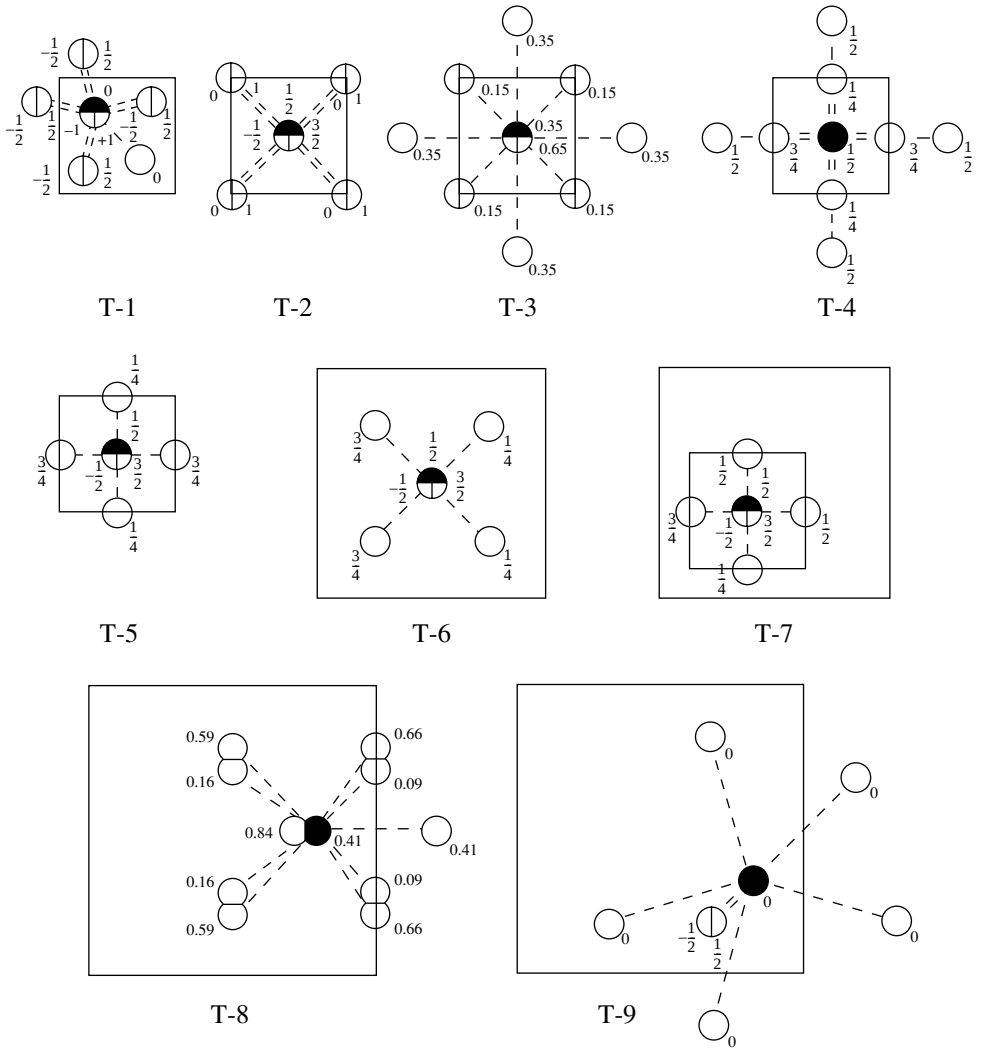

Coordination of the spheres in the T-1–T-9 tetragonal packings of spheres (projections onto the *XY* plane). The solid circle indicates the position of the center of one of the spheres; the positions of the nearest spheres are shown by empty circles. The unit cells are shown by squares.

$I4_1/amd$ and $P4/mmm$ are the only two "panautosymmetry groups" (the groups where all the possible lattice complexes have the symmetry of this group) [6] in the holohedral class of the tetragonal system. The only difference is that space group $P4/mmm$ is symmorphic and contains a large number of mirror planes *m* and fourfold rotation axes, which considerably restricts the possible arrangements of finite-size particles, whereas the nonsymmorphic group $I4_1/amd$ provides much wider possibilities for filling the space with such particles.

Like the T-4 packing, the T-5 packing is characterized by the distribution of the spheres over the (*a*) positions of the space group $I4_1/amd$. However, the *c*/*a* ratio has a different value ($2/\sqrt{15} = 0.5164$). The density of the T-5 packing is $8\pi/45$. White tin (β-Sn) is structurally similar to the T-5 packing. However, the *c*/*a* ratio in the latter structure is 0.5455, i.e., substantially different from the ideal value for the T-5 packing. As a result, each atom in the tin structure has four nearest neighbors at a distance of 3.02 Å and two neighbors at slightly larger distances (3.18 Å).

In the T-6 and T-7 packings, the sphere centers occupy the (*c*) and (*f*) positions of the same space group $I4_1/amd$, respectively. As in the T-5 packing, the coordination polyhedra in these packings can be considered as pronouncedly distorted octahedron.

The T-8 packing is somewhat more complicated. The sphere centers occupy the (*h*) positions of the space group $I4_1/amd$. The coordinates of these positions are characterized by the *y* and *z* parameters. If these parameters are assumed to be 0.2838 and 0.9065, respectively, and the *c*/*a* ratio is assumed to be 0.977, each sphere in the packing has eight nearest neighbors. In addition, two spheres are located at a distance that is only 2% larger than the eight shortest distances. Hence,

Table 2. Coordination polyhedra of the tetragonal sphere packings

Packing	Number of vertices	Number of faces	Symmetry	Simple forms and their combinations
T-1	11	13	*mm*2	Rhombic pyramid + four dihedra + monohedron
T-2	10	12	4/*mmm*	Tetragonal prism + tetragonal bipyramid
T-3	9	13	4*mm*	Tetragonal prism + two tetragonal pyramids + monohedron
T-4	8	12	$\bar{4}2m$	Tetragonal bipyramid + tetragonal tetrahedron
T-5	6	8	$\bar{4}2m$	Tetragonal scalenohedron
T-6	6	8	2/*m*	Rhombic prism + two pinacoids
T-7	6	8	2	Four dihedra
T-8	10	12	*m*	Three dihedra + six monohedra
T-9	7	10	*mm*2	Two rhombic pyramids + dihedron

it can be assumed that the coordination number of the packing is 10. The coordination polyhedron of the T-2 packing can be described as a slightly flattened cube with tetragonal pyramids above two opposite faces, whereas the coordination polyhedron of the T-8 packing can be characterized as a distorted cube with tetragonal pyramids over two adjoining faces.

The arrangement of the chlorine atoms in the thorium chloride structure, $ThCl_4$, follows the packing law of T-8. The unit-cell parameters of this structure differ from the ideal values for the T-8 packing ($y = 0.281$, $z = 0.907$, $c/a = 0.881$). A series of metal halides of the actinide group ($ThBr_4$, $PaCl_4$, UCl_4, and $NpCl_4$) belong to the $ThCl_4$ structure type.

In the T-9 packing, the sphere centers occupy the (*h*) positions of sp. gr. *I*4/*mcm*. These positions are characterized by the only parameter *x*. If this parameter is assumed to be $(\sqrt{3} - 1)/4 = 0.183$ and the *c*/*a* ratio is chosen as $\sqrt{16x - 2} = 0.963$, each sphere of the packing has seven nearest neighbors located at equal distances. The coordination polyhedron of the packing may be approximated by an irregular pentagonal bipyramid.

The arrangement of aluminum atoms in the $CuAl_2$ structure (mineral khatyrkite) corresponds to the T-9 packing (slightly distorted). The structures of a wide variety of compounds, primarily, of intermetallic compounds, belong to the $CuAl_2$ structure type. However, the *x* parameter and the *c*/*a* ratio for all these compounds substantially differ from the above-mentioned ideal values for the T-9 packing. Generally, the *x* parameter and the *c*/*a* ratio range from 0.158 to 0.167 and from 0.74 to 0.88, respectively. As a result, the coordination polyhedra in the packing are distorted. For example, the distances from the $CuAl_2$ atom to seven nearest Al atoms are 2.745 (one distance), 2.885 (two distances), and 3.115 Å (four distances). In addition, four Al atoms are located at distances of 3.22 Å [7].

An analogous arrangement of lead atoms is observed in the $PtPb_4$ structure. Although the structure of this phase is described by the sp. gr. *P*4/*nbm*, the positions of Pb atoms are very close to the (*h*) positions in the sp. gr. *I*4/*mcm*. The $PtPb_4$ structure is characterized by $x_{Pb} = 0.175$ and $c/a = 0.897$.

Apparently, other types of tetragonal packings of spheres satisfying the above-mentioned conditions can also occur in addition to the nine packings considered above. Nevertheless, it is evident that these tetragonal packings can be characterized by a wide variety of symmetry groups, coordination numbers, and coordination polyhedra. Many of the tetragonal packings are really encountered in real structures of inorganic compounds.

REFERENCES

1. J. A. R. Clarke, Nature **240** (5381), 408 (1972).
2. W. H. Baur, Mater. Res. Bull. **16**, 339 (1981).
3. A. R. West and P. G. Bruce, Acta Crystallogr., Sect. B: Struct. Crystallogr. Cryst. Chem. **38**, 1981 (1982).
4. A. West, *Solid State Chemistry and Its Applications* (Wiley, Chichester, 1984; Mir, Moscow, 1988), Part 1.
5. A. Wells, *Structural Inorganic Chemistry* (Clarendon, Oxford, 1984; Mir, Moscow, 1987), Vol. 1.
6. V. V. Dolivo-Dobrovol'skiĭ, Zap. Vses. Mineral. O–va **116** (1), 7 (1987).
7. W. B. Pearson, *Crystal Chemistry and Physics of Metals and Alloys* (Wiley, New York, 1972; Mir, Moscow, 1977), Part 2.

Translated by T. Safonova

Crystallography Reports, Vol. 47, No. 5, 2002, pp. 727–730. Translated from Kristallografiya, Vol. 47, No. 5, 2002, pp. 793–796.

THEORY OF CRYSTAL STRUCTURES

Morphogenesis of Crystal Structures in the Discrete Modeling of Packings

V. G. Rau, V. G. Zhuravlev, T. F. Rau, and A. V. Maleev

Vladimir State Pedagogical University, pr. Stroiteleĭ 11, Vladimir, 600020 Russia

e-mail: andr_mal@aport.ru

Received September 7, 2000; in final form, January 17, 2002

Abstract—Within the framework of the discrete modeling of molecular packings, a metric approach to the investigation of the mechanisms of crystal formation is proposed. This method is based on the construction of a combination of polyhedra in a space in which the space division into polyhedra (or the periodic packing of polyhedra) is specified by the multistage addition to the initial "seeding" polyhedron set of this division (packing) of the adjacent polyhedra. Crystal growth is modeled using the constructions of bounding boxes in the division of the plane into polyominoes and the three-dimensional space, into polycubes. The formation of phenomenological polygons (polyhedra) in the growth of periodic structures is revealed and theoretically grounded. © *2002 MAIK "Nauka/Interperiodica".*

The study of the mechanisms of crystal formation has become an important problem in crystallography virtually from the very beginning of its development. On the one hand, a crystal is a combination of regularly arranged atoms or molecules giving rise to a periodic symmetrical structure and, on the other hand, it is a polyhedron with a rather strictly specified set of faces. The crystal is spontaneously formed from a disordered chaotic medium surrounding the initial seed. Then, questions arise about the physical factors governing the inevitable growth of crystal structures upon the achievement of particular growth conditions in the medium. It is of interest to elucidate the (necessary and sufficient) mechanism that ensures the retention of the angles in the course of growth and also to establish the physical factors responsible for the synchronous growth of different faces. These and some others questions are still open [1].

The analysis of the geometric characteristics of the coordination spheres in the single-crystal structures of organic and heterocomplex compounds, as well as the model periodic and nonperiodic space divisions into polyhedra, forms the basis for a purely metric approach to the study of the mechanisms of crystal formation. This approach involves the construction of a combination of polyhedra in a space in which the periodic packing of polyhedra (or the periodic division into polyhedra) is specified by the multistage addition to the initial "seeding" combination of polyhedra of this packing (division) of the adjacent polyhedra. The adjacency of the polyhedra is determined by the adjacency graph proceeding from geometric or some other considerations. Below, we report an algorithm for modeling crystal formation based on the use of the so-called bounding boxes as combinations of polyhedra to be added.

To describe the structural organization of real crystals, consider as the smallest structural unit of the packing in the three-dimensional space (in the particular case of division) a polyhedron, substituting the space region occupied by an individual molecule or a complex ion. Such polyhedra can be Voronoi–Dirichlet domains [2] or polycubes (three-dimensional polyominoes) used in the discrete modeling of packings in molecular crystals [3, 4]. Polyhedra sharing at least one face are called adjacent polyhedra. In this approach, the modeling of crystal growth consists in successive enlargement of the surrounding of a chosen initial seed (a polyhedron, a, or a combination of polyhedra, A) by adding new structural units. A set of polyhedra forming this surrounding at the nth step is called the nth bounding box of the seed and is denoted by $eq(a, n)$ or $eq(A, n)$.

To determine the effects of the seed size and shape, the parameters and the symmetry of the translation lattice, and other characteristics of the division on the geometry of bounding boxes, we preliminarily analyzed growth models, based on the plane division into polyominoes and space division into polycubes. The algorithm of such a division for two-dimensional models has been reported earlier [5].

In all cases, with an increase in the number of bounding boxes, a particular phenomenological polyhedron (a polygon, in the two-dimensional case) is gradually formed. A further growth of the polyhedron proceeds with the preservation of its shape. Figure 1 shows the dynamics of this process in the two-dimensional case, where one of 14 translationally independent polyominoes of the division is used as a seed (the code of the division is 3132032232333220323212211113223113322301232201112213223 13 in the packing space $P\ 14\ 4_7$). The stages of formation of a phe-

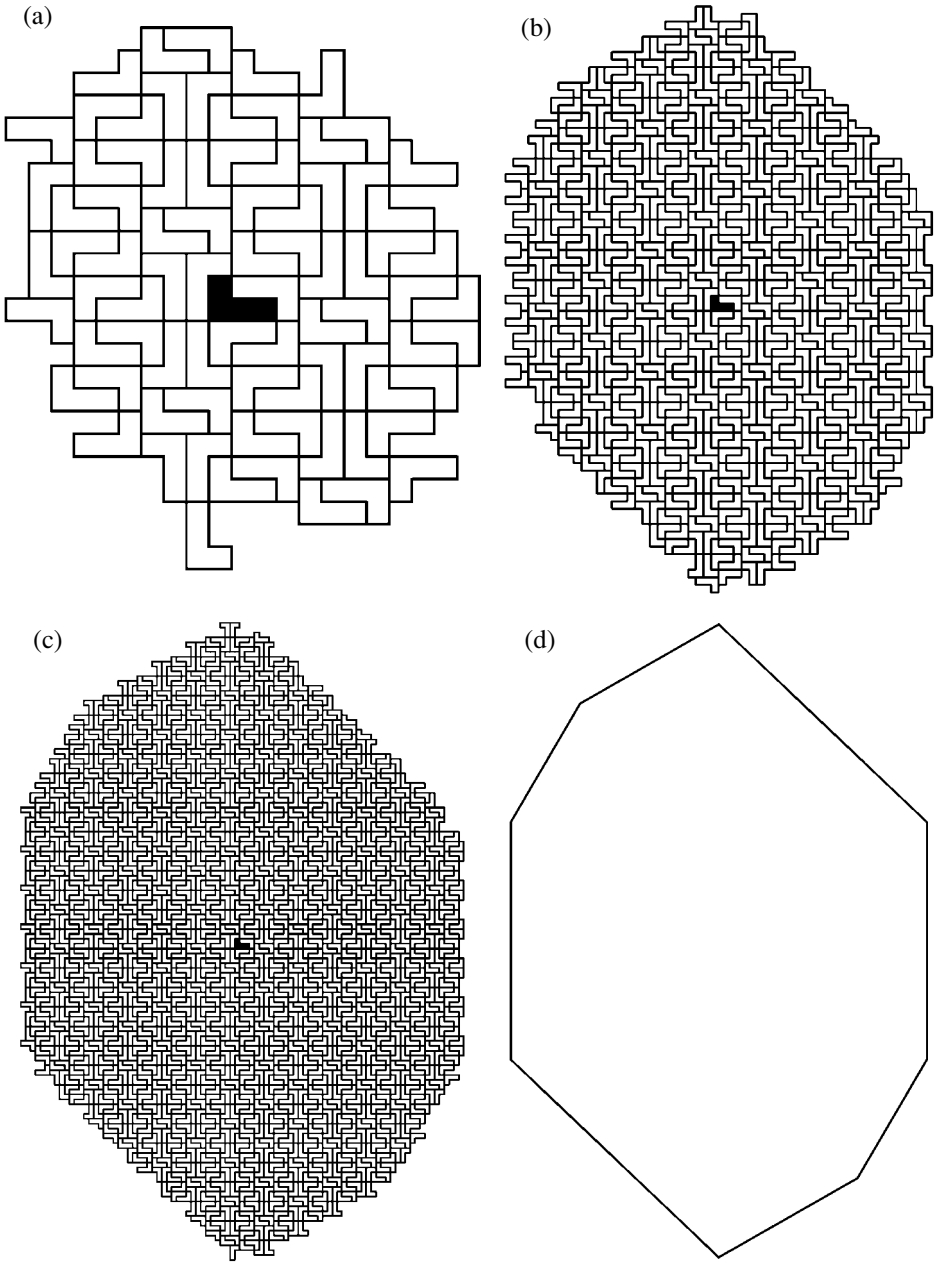

Fig. 1. Formation of a growth polygon in the division of a plane into polyominoes. The first (a) 5, (b) 15, and (c) 25 bounding boxes of the initial polyomino are blackened; (d) an octagon is a growth polygon.

nomenological octagon with a pronounced self-similarity property are also shown in Fig. 1. Similar model growth is shown for three-dimensional cases in Fig. 2, where the phenomenological 14-vertex polyhedron (Fig. 2d) is formed in the packing space $S32_12_1^2$ (the code of the division is 753667345767).

Attempts to explain the appearance of phenomenological polyhedra resulted in the formulation of the following theorems.

I. Theorem of existence. For any periodic division of a plane into polygons, there exists a centrally symmetric convex growth polygon *Pol* such that all the polygons of the *n*th bounding box $eq(a, n)$ of the seeding polygon *a* belong to the *c*-neighborhood of the polygon $n \cdot Pol$ derived from *Pol* by the homothety with the coefficient *n*:

$$eq(a, n) - a \subset (n \cdot Pol)_c.$$

II. Theorem of growth stability. The neighborhood $(n \cdot Pol)_c$ has a finite effectively calculable width *c* that is dependent on the division *Til* alone.

III. Theorem of self-similarity. Any finite subset *A* of polygons *Til* of division can be taken as a seed

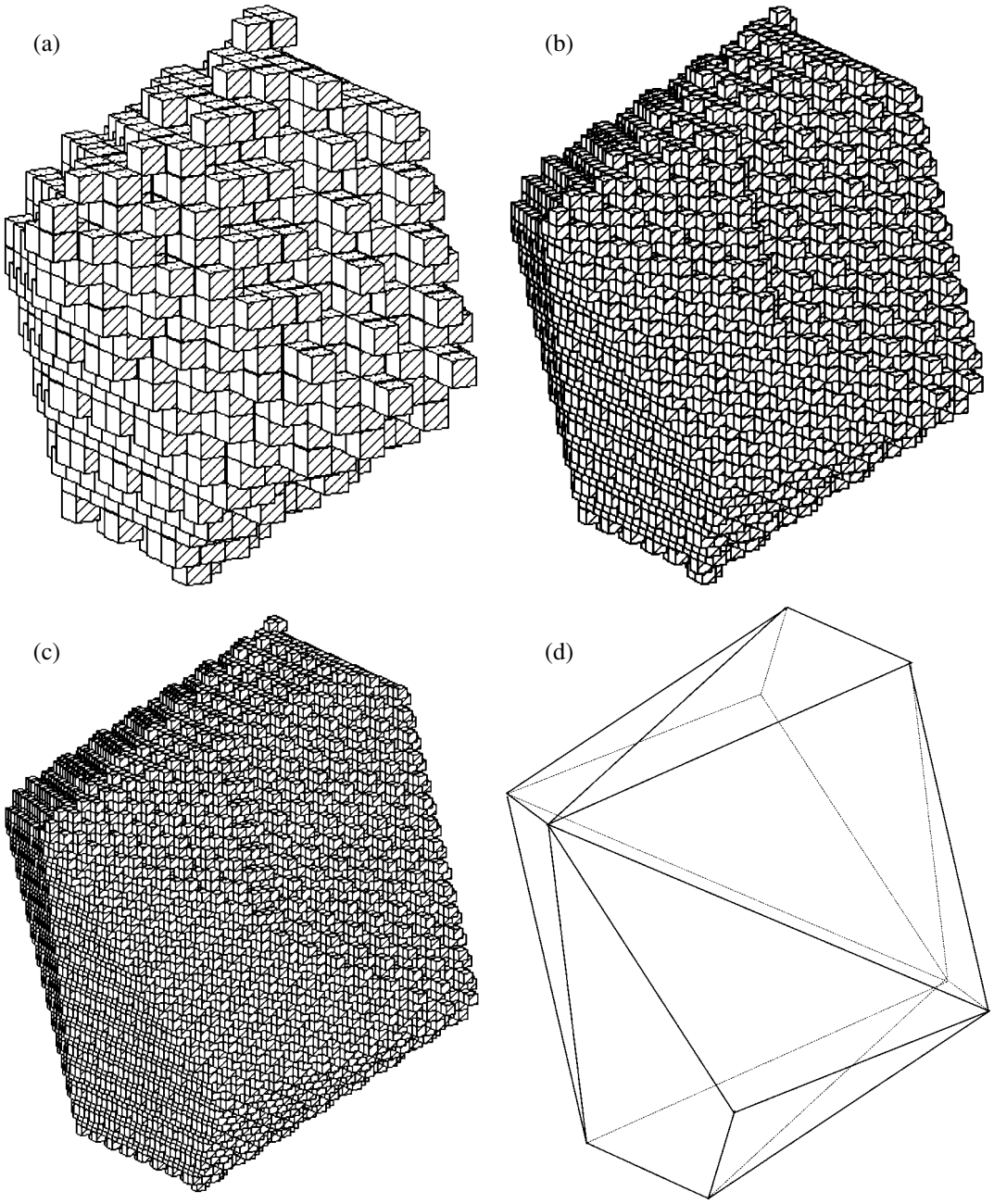

Fig. 2. Formation of a growth polyhedron in the division of the space into polycubes; the (a) 5st, (b) 10th, and (c) 15th bounding boxes of the initial polycube; (d) a 14-vertex polyhedron is a growth polyhedron.

instead of the polygon *a*. In this case, the growth polygon *Pol* preserves its shape. For the *n*th bounding box, the approximate equation $eq(A, n) - a \subset (n \cdot Pol)_c$ is valid, where *a* is a fixed polygon from *A*, and the width of the *c*-neighborhood depends only on the division *Til* and the seed *A*.

The proofs of these theorems are based on the comparison of the adjacency graph *G* and the division *Til* and the detection of the sectors of local growth in this graph. These sectors grow as a lexicographically ordered graph of a square lattice of integer points Z^2. The affine construction used for proving these theorems is extended to higher-order periodic divisions with $n \geq 3$. The theorems were proven by Zhuravlev [6].

Taking into account all the aforesaid, it can be concluded that (i) the growth of the periodic structure proceeds within the framework of the model under consideration with the formation of a convex growth polyhedron, and (ii) the polyhedron grows preserving its shape (self-similarity). It should be noted that the shape and symmetry of the growth polyhedron depend not only on

the division but also on the chosen law of adjacency (the adjacency graph). For example, the introduction of the directed adjacency graph may give rise to growth polyhedra possessing no center of symmetry.

REFERENCES

1. A. A. Vlasov, *Statistic Distribution Functions* (Nauka, Moscow, 1966).
2. W. Fischer and E. Koch, Z. Kristallogr. **150**, 245 (1979).
3. A. V. Maleev, V. G. Rau, K. A. Potekhin, *et al.*, Dokl. Akad. Nauk SSSR **315** (6), 1382 (1990) [Sov. Phys. Dokl. **35**, 997 (1990)].
4. A. V. Maleev, Kristallografiya **40** (3), 394 (1995) [Crystallogr. Rep. **40**, 354 (1995)].
5. A. V. Maleev, Kristallografiya **46** (1), 165 (2001) [Crystallogr. Rep. **46**, 154 (2001)].
6. V. G. Zhuravlev, Algebra Anal. **13** (2), 1 (2001).

Translated by T. Safonova

Crystallography Reports, Vol. 47, No. 5, 2002, pp. 731–735. Translated from Kristallografiya, Vol. 47, No. 5, 2002, pp. 797–801.

THEORY OF CRYSTAL STRUCTURES

Generation of the Structures of Molecular Crystals with Two Molecules Related by the Center of Inversion in a Primitive Unit Cell

A. V. Maleev

Vladimir State Pedagogical University, pr. Stroiteleĭ 11, Vladimir, 600020 Russia
e-mail: andr_mal@mail.ru

Received July 11, 2001; in final form, January 17, 2002

Abstract—An algorithm for the generation of possible crystal structures with two inversion-related molecules of known shape in a primitive unit cell is proposed within the method of discrete packing modeling in molecular crystals. The algorithm is based on the replacement of molecules by polycubes (geometric figures composed of identical cubes) and looking through a finite number of all the possible periodic packings of these polycubes with a given coefficient of packing. A program package for personal computers is developed on the basis of the proposed algorithm and is approved by the example of several crystal structures that were determined earlier by X-ray diffraction. © *2002 MAIK "Nauka/Interperiodica".*

INTRODUCTION

The problem of prediction (generation) of the structures of organic molecular crystals becomes more and more important. First of all, this is explained by the increasing interest in phenomena whose occurrence directly depends on the possible existence of different crystal structures of chemical compounds, namely, crystal polymorphism, phase transitions, and solid-phase reactions. Moreover, the powder methods of crystal structure investigation, which have been developing vigorously in the last few years, require specific methods of structure solution, because the experimental data sets are limited and, as a consequence, traditional methods of structure determination, namely, the direct and Patterson methods, are not efficient enough. The methods of systematic search for possible structures occupy a special place among the rapidly developing new methods of structure determination.

Earlier [1], we reported the algorithm and the program package for generation of Bravais molecular crystal structures, that is, structures in which all the molecules are translationally equivalent and, hence, identically oriented. However, according to [2], only 2% of organic homomolecular crystals have Bravais structures. The structures that contain molecules related by the center of inversion and, therefore, exhibit two molecular orientations occur more often. These are molecular crystals belonging to the following structural classes: $P\bar{1}$, $Z = 2(1)$; $P2/m$, $Z = 2(m)$; $P2/m$, $Z = 2(2)$; $P2_1/m$, $Z = 2(m)$; $C2/c$, $Z = 4(2)$; $C2/c$, $Z = 4(m)$; $Pmnm$, $Z = 2(mm)$; etc. In this paper, we discuss the algorithms for generation of molecular crystal structures of this type and the computer programs based on these algorithms.

An algorithm for the generation of structures that contain one molecule in a primitive unit cell (Bravais molecular structures) was proposed in [1]. This algorithm is based on the replacement of a molecule by a discrete model, a polycube, and the search for all the possible variants of packing (with a given coefficient of packing) according to the packing criterion that was worked out within the method of discrete modeling of molecular packings [3, 4]. We can propose two fundamentally different approaches to the extension of this algorithm to the crystal structures with two inversion-related molecules in a primitive unit cell.

The first approach involves an initial search for possible stable associates of two molecules related by the center of inversion, centrosymmetric dimers. Then, for each dimer obtained, a discrete model (polycube) is built and a search for all the possible packings of the polycube with a given coefficient of packing is performed.

The second approach consists in searching for all the possible packings of two polycubes that are discrete models of the molecules related by the center of symmetry. For this search, the packing criterion for two translationally independent polycubes with a given packing coefficient is worked out within the discrete modeling method. This criterion is similar to the packing criterion of the translationally identical polycubes proposed earlier in [3, 4].

The first approach is easier for applying the appropriate algorithms and takes shorter time to calculate, especially if the number of variants of stable dimers is small. However, the absence of stable centrosymmetric dimers in a crystal structure may become a fundamentally insurmountable barrier in the first approach. The

1063-7745/02/4705-0731$22.00 © 2002 MAIK "Nauka/Interperiodica"

second approach is more rigorous and, in our opinion, more promising. Now, we discuss some stages of the second approach in more detail.

CRITERION FOR THE EXISTENCE OF THE PACKING OF TWO TRANSLATIONALLY INDEPENDENT POLYCUBES RELATED BY THE CENTER OF INVERSION

A polycube is a connected geometric figure that consists of a limited number of identical cubes. The algorithm for the replacement of a molecule by a polycube is described in detail in [1]. A polycube that consists of p cubes can be specified by integer coordinates of the centers of these cubes $\{\mathbf{l}_i, i = 1, 2, \ldots, p\}$ in a basis whose vectors are equal in length and parallel to three perpendicular edges of the cube. If the polycube of a molecule is specified by the set $\{\mathbf{l}_i, i = 1, 2, \ldots, p\}$, the polycube of the centrosymmetrically related molecule can be specified by the set $\{-\mathbf{l}_i, i = 1, 2, \ldots, p\}$.

The packing space [3, 4] is considered a lattice in which each node is assigned a weight in such a way that all the sets of lattice nodes with identical weights form identical (except for displacement) sublattices of the initial lattice. The columns of the vector coordinates (in the basis of the initial lattice) of one of the bases of this sublattice form the integer matrix

$$Y = \begin{pmatrix} x_1 & x_2 & x_3 \\ 0 & y_2 & y_3 \\ 0 & 0 & z_3 \end{pmatrix},$$

where $0 \le x_2 < x_1$, $0 \le x_3 < x_1$, $0 \le y_3 < y_2$, and $z_3 > 0$. The Y matrix is the packing-space matrix. The order of the packing space coincides with the sublattice index and can be determined as the product of the diagonal elements of the Y matrix: $N = x_1y_2z_3$.

By analogy with the criterion of packing of one translationally independent polycube [4], we define the criterion of packing of two translationally independent inversion-related polycubes with a given packing coefficient as follows.

In order for a translational packing of two polycubes, $\{\mathbf{l}_i, i = 1, 2, \ldots, p\}$ and $\{-\mathbf{l}_i, i = 1, 2, \ldots, p\}$, with packing coefficient $k = 2p/N$ to exist, it is necessary and sufficient that, in one of the packing spaces of the Nth order, pairs of points in the totalities of the sets $\{\mathbf{l}_i, i = 1, 2, \ldots, p\} \cup \{\mathbf{r} - \mathbf{l}_i, i = 1, 2, \ldots, p\}$ have different weights. The $\mathbf{r}$ vector is one of the vectors of the fundamental region of the translation sublattice, which is specified by the packing space, for example, the vector $\begin{pmatrix} u \\ v \\ w \end{pmatrix}$, where u, v, and w are the integers satisfying the conditions $0 \le u < x_1$, $0 \le v < y_2$, and $0 \le w < z_3$.

Here, the necessity means that the translation vector cannot connect two different points within a polycube or two points of the polycubes with different orientations. The sufficiency is proved by the reconstruction of a variant of packing: if the set $\{\mathbf{l}_i, i = 1, 2, \ldots, p\} \cup \{\mathbf{r} - \mathbf{l}_i, i = 1, 2, \ldots, p\}$ satisfies the packing space criterion specified by the Y matrix, the set

$$\{Y\gamma + \mathbf{l}_i, i = 1, 2, \ldots, p\} \cup \{Y\gamma + \mathbf{r} - \mathbf{l}_i, i = 1, 2, \ldots, p\},$$

where γ varies over all the possible integer vector-columns, is the required translational packing of the polycubes.

ALGORITHM FOR LOOKING THROUGH THE POSSIBLE VARIANTS OF PACKING OF INVERSION-RELATED POLYCUBES

We assume that the initial polycube $\{\mathbf{l}_i, i = 1, 2, \ldots, p\}$, its centrosymmetric image $\{-\mathbf{l}_i, i = 1, 2, \ldots, p\}$, and the packing coefficient k are specified.

First, the order of the packing space N is calculated as the prime natural number closest to the fraction $2p/k$. The advantages of the choice of the prime order of the packing space were noted in [1]. They are associated with the substantial decrease in the computation time for the weight of a packing-space point according to the formula

$$g(u, v, w) = \{(u - vx_2 - wx_3)/N\}N \qquad (1)$$

(where $\{r\}$ is the fractional part of number r), which is simpler than that for the general case, and with the smaller number of packing spaces, which, for prime N, is equal to $N^2 + N + 1$.

For each packing space of the Nth order, the packing criterion is checked by the following procedure. First, we check the initial polycube $\{\mathbf{l}_i, i = 1, 2, \ldots, p\}$. If the weights in all the pairs of points are different, the criterion is checked for the second polycube. According to the theorem considered, the second polycube should be shifted by N vectors of the fundamental region of the translation lattice, which is specified by the packing space. However, the procedure of looking through the variants can be shortened considerably.

Prior to the checking stage, the first point of the initial polycube can be brought by a parallel shift to the (0, 0, 0) coordinates; then, the first point of the centrosymmetric polycube $\{\mathbf{l}_i, i = 1, 2, \ldots, p\}$ will also have the (0, 0, 0) coordinates. In this case, the displacement vectors (u, v, w), for which the weights of the corresponding points $g(u, v, w)$ coincide with the weight of at least one point of the initial polycube, should be excluded from consideration, because, upon shifting by the vector (u, v, w), the first point of the second polycube has the weight $g(u, v, w)$. Thus, $(N - p)$ vectors of displacement are considered instead of N vectors.

Since the order of the packing space is a prime number, the fundamental region of the translation lattice can

Table 1. Some data on the crystal structures used for the approbation of the algorithm for discrete modeling

Compound	Empirical formula	Structural class	Reference
3-*exo*-Bromo-7-*endo*-(tribromomethyl)bicyclo[3.1.1]heptane	$C_8H_{10}Br_4$	$P\bar{1}$, Z = 2(1)	[5]
4,4'-Dichlorobenzophenone*	$C_{13}H_8Cl_2O$	*C*2/*c*, *Z* = 4(2)	[6]
7-*endo*-Methyl-3-borabicyclo[3.3.1]non-3-yl 8-quinolinate	$C_{18}H_{22}BNO$	$P2_1/m$, *Z* = 2(*m*)	[7]
3-Methylbicyclo[1.1.1]pentane-1-carboxylic acid	$C_7H_{10}O_2$	*C*2/*m*, *Z* = 4(*m*)	[8]
1,3,3,5-Tetrabromopentane	$C_5H_8Br_4$	*Pmnm*, *Z* = 2(*mm*)	[9]
Methyl 2,2-dichloro-3-methylbicyclo[1.1.1]pentane-1-carboxylate	$C_8H_{10}C_{12}O_2$	$P\bar{1}$, Z = 2(1)	[10]
3,7-Diacetyl-1,5-dimethyl-3,7-diazabicyclo[3.3.1]nonan-9-one	$C_{13}H_{20}N_2O_3$	*C*2/*c*, *Z* = 4(2)	[11]
3,7-Diacetyl-1,5-dimethyl-3,7-diazabicyclo[3.3.1]nonane	$C_{13}H_{22}N_2O_2$	*C*2/*c*, *Z* = 4(2)	[11]
2-[Cyano(ethoxycarbonyl)methylene]-4,5-dimethyl-1,3-dithiole (β-form)	$C_{10}H_{11}N_1O_2S_2$	$P\bar{1}$, *Z* = 2(1)	[12]

* A temperature-induced phase transition was found in the structure. Both the initial and final phases were modeled.

Table 2. Unit cell parameters of the real crystal structure studied by X-ray diffraction and the modeled crystal structure

	a(Å)	*b*(Å)	*c*(Å)	α(deg)	β(deg)	γ(deg)
Real structure	6.312	7.968	12.082	82.09	75.07	72.03
Model	6.36	8.11	12.20	83.4	74.5	71.4

be represented as an $N \times 1 \times 1$ parallelepiped. The parallel displacement of a point of the packing space of the prime order by the vector (u, 0, 0) brings a point with the g weight to the point with the $(g + u)$ weight for $g + u < N$ or the $(g + u - N)$ weight for $g + u \geq N$. This allows us to calculate the weights of the points of the second polycube after the displacement from a simpler formula than formula (1).

CALCULATION OF A CRYSTAL STRUCTURE

After the packing criterion is checked for all packing spaces of the Nth order, each possible variant of packing of the polycubes $\{\mathbf{l}_i, i = 1, 2, \ldots, p\}$ and $\{-\mathbf{l}_i, i = 1, 2, \ldots, p\}$ is characterized by numbers N, x_2, and x_3, which specify the packing space, and number u, which specifies the vector of displacement of the polycube $\{-\mathbf{l}_i, i = 1, 2, \ldots, p\}$ with respect to the origin. In addition, the atomic coordinates of the initial molecule $\{\mathbf{r}_j, j = 1, 2, \ldots, m\}$ with respect to the orthonormal basis, which is rigidly related to the polycube, are assumed to be known. The vectors

$$\mathbf{a} = s\begin{bmatrix} N \\ 0 \\ 0 \end{bmatrix}, \quad \mathbf{b} = s\begin{bmatrix} x_2 \\ 1 \\ 0 \end{bmatrix}, \quad \mathbf{c} = s\begin{bmatrix} x_3 \\ 0 \\ 1 \end{bmatrix},$$

where s is the approximation step, specify one of the bases of the translation lattice. From this basis, we should change over to the standard crystallographic basis $\mathbf{a}_n$, $\mathbf{b}_n$, $\mathbf{c}_n$ (using, for example, the Delone reduction algorithm), which is more convenient for further calculations. Here, the traditional atomic coordinates are represented in fractions of unit cell parameters: $\mathbf{r}'_j = Y_n^{-1}(\mathbf{r}_j - 0.5\delta)$, where Y_n is the matrix of the vector-columns $\mathbf{a}_n$, $\mathbf{b}_n$, $\mathbf{c}_n$ with respect to the basis $\mathbf{a}$, $\mathbf{b}$, $\mathbf{c}$, and $\delta = s\begin{bmatrix} u \\ 0 \\ 0 \end{bmatrix}$ is the vector of displacement of the second polycube. The atomic coordinates $\mathbf{r}'_j$ correspond to the center of inversion at the origin of the coordinates.

OPTIMIZATION OF THE VARIANTS OBTAINED FOR CRYSTAL STRUCTURES

The models obtained for crystal structures at the previous stage are rather crude, because there is no point in using small approximation steps. In our program package, the approximation step is chosen in the range between 0.3 and 1.0 Å depending on the size of the molecule. The errors in determination of the unit cell parameters and positions of the molecules are of the same order. One of the procedures of crystal structure refinement is the minimization of the energy of intermolecular interactions.

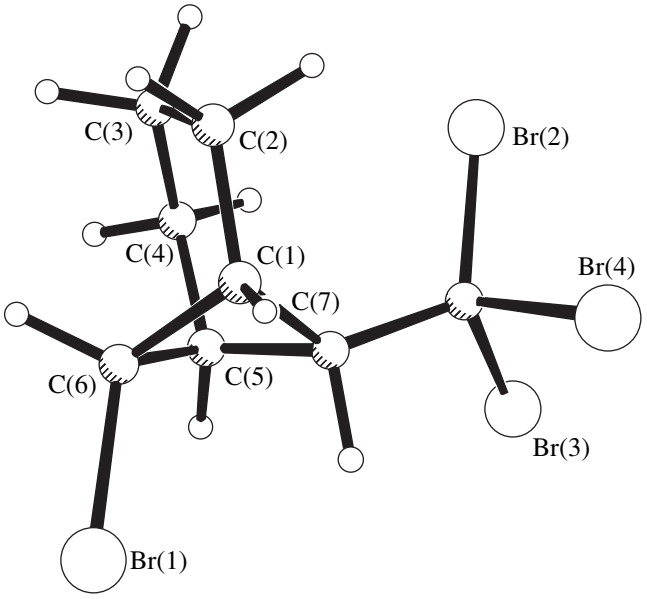

Fig. 1. A perspective view of the molecule of 6-*exo*-bromo-7-*endo*-(tribromomethyl)bicyclo[3.1.1]heptane.

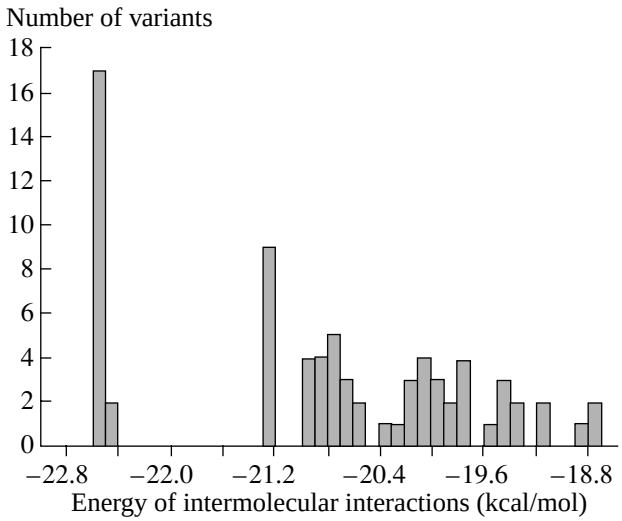

Fig. 2. Histogram of the distribution of 75 variants of modeled crystal structures over the energy of intermolecular interactions.

Let us consider the case of rigid molecules. In crystal structures with two translationally independent inversion-related molecules, the energy is a function of twelve parameters: six parameters (for example, the unit cell parameters a, b, c, α, β, and γ) specify the translation lattice, three parameters (θ, φ, and ω) specify the orientation of molecules with respect to the lattice, and the remaining three parameters (x_c, y_c, and z_c) specify the position of molecules with respect to the center of inversion. The minimization of the function $U(a, b, c, \alpha, \beta, \gamma, \theta, \varphi, \omega, x_c, y_c, z_c)$ is performed, for example, by the least-squares procedure and results, on the one hand, in some improvement in the crystal structure model and, on the other hand, in a significant simplification of the procedure of comparison of the variants obtained.

Note that the correct calculation and minimization of the energy of intermolecular interactions in crystals is a separate complex problem of crystal chemistry, which is beyond the scope of this paper.

PROGRAM PACKAGE AND ITS APPROBATION

The algorithm considered above formed the basis of the program package for IBM-compatible personal computers. The program package was evaluated using a number of crystal structures that have already been studied by X-ray diffraction. The names, empirical formulas, and structural classes for some of them are summarized in Table 1. For each structure, the discrete molecular models (polycubes) were calculated at approximation steps varying in the range 0.5–1.0 Å and the crystal structures were generated for packing coefficients 0.6–0.8. Upon the optimization of the unit cell parameters and molecular orientations, the "true" variant (corresponding to that obtained in the X-ray diffraction study) was chosen among the variants with the lowest energy of intermolecular interactions.

As an example, we consider in more detail the results of structure modeling for 6-*exo*-bromo-7-*endo*-(tribromomethyl)bicyclo[3.1.1]heptane (**I**) (Fig. 1). The crystal structure of this compound was studied earlier by X-ray diffraction [5]. It belongs to the structural class $P\bar{1}$, $Z = 2(1)$. In order to exclude possible distortions of the molecular geometry in the crystal field, the atomic coordinates for molecule **I** were not taken from [5] but were calculated within the quantum-mechanical approach using the MMX program [13]. Discrete models (polycubes) were built for nine random molecular orientations at approximation steps s = 0.70, 0.71, …, 0.90 Å. Based on the δ criterion described in [1], the five best polycubes were chosen. The possible variants of the packing of these polycubes and their centrosymmetric images were calculated for different packing coefficients k. No packings with packing coefficients larger than 0.73 were found, and for $k < 0.69$, the number of variants was very large. For packing coefficients between 0.69 and 0.73, 75 variants of packing were obtained. For all of them, the crystal structures were calculated and refined using the method of atom–atom potentials. The relationship for calculating the potential has the form

$$u_{ij} = -a_{ij}r_{ij}^{-6} + b_{ij}\exp(-c_{ij}r_{ij}),$$

where r_{ij} is the distance between the ith and jth atoms and a_{ij}, b_{ij}, and c_{ij} are the parameters taken from [14].

Table 3. Coordinates of the non-hydrogen atoms in the real and modeled crystal structures

Atom	*x*	*y*	*z*
Br(1)	0.5904	−0.2916	0.51420
	0.541	−0.289	0.518
Br(2)	0.4741	0.2023	0.79517
	0.465	0.198	0.808
Br(3)	0.9905	0.1083	0.65713
	0.976	0.093	0.657
Br(4)	0.8590	−0.0550	0.90640
	0.858	−0.072	0.902
C(1)	0.546	−0.2343	0.7553
	0.526	−0.238	0.757
C(2)	0.572	−0.331	0.8693
	0.566	−0.338	0.868
C(3)	0.816	−0.455	0.8636
	0.809	−0.467	0.851
C(4)	0.999	−0.418	0.7595
	0.983	−0.425	0.745
C(5)	0.894	−0.3036	0.6642
	0.864	−0.308	0.658
C(6)	0.687	−0.3587	0.6596
	0.652	−0.364	0.656
C(7)	0.720	−0.1261	0.7042
	0.694	−0.130	0.704
C(8)	0.760	0.0125	0.7638
	0.746	0.003	0.765

The potentials were summed over all pairs of atoms whose interatomic distances were no larger than 14 Å.

Analysis of the distribution of the variants of structures over the energy of intermolecular interactions (Fig. 2) showed that 19 variants are characterized by the lowest energy, which is approximately 1.2 kcal/mol less than the energy of the next group of variants. A comparative crystal chemical analysis revealed that all of these 19 variants are similar in mutual arrangement and orientation of molecules; that is, all of them correspond to the same model of crystal structure. Comparison of this model with the crystal structure studied earlier in [5] showed that they actually coincide. The unit cell parameters averaged over the 19 models and the parameters determined in the X-ray diffraction study are given in Table 2. The coordinates of the non-hydrogen atoms are presented (Table 3) as fractions of the corresponding unit cell parameters of these structures.

REFERENCES

1. A. V. Maleev, Kristallografiya **46** (1), 19 (2001) [Crystallogr. Rep. **46**, 13 (2001)].
2. P. M. Zorkiĭ and O. N. Zorkaya, Zh. Strukt. Khim. **39** (1), 126 (1998).
3. A. V. Maleev, V. G. Rau, K. A. Potekhin, *et al.*, Dokl. Akad. Nauk SSSR **315** (6), 1382 (1990) [Sov. Phys. Dokl. **35**, 997 (1990)].
4. A. V. Maleev, Kristallografiya **40** (3), 394 (1995) [Crystallogr. Rep. **40**, 354 (1995)].
5. A. V. Maleev, K. A. Potekhin, A. I. Yanovskiĭ, *et al.*, Dokl. Akad. Nauk SSSR **327** (3), 345 (1992).
6. V. V. Mitkevich, V. G. Lirtsman, M. A. Strzhemchny, *et al.*, Acta Crystallogr., Sect. B: Struct. Sci. **55**, 799 (1999).
7. B. M. Mikhaĭlov, M. E. Gurskiĭ, S. V. Baranin, *et al.*, Izv. Akad. Nauk SSSR, Ser. Khim., 1645 (1986).
8. K. A. Potekhin, A. V. Maleev, E. N. Kurkutova, *et al.*, Dokl. Akad. Nauk SSSR **297** (6), 1390 (1987).
9. V. I. Dostovalova, T. T. Vasil'eva, F. K. Velichko, *et al.*, Izv. Akad. Nauk SSSR, Ser. Khim., 2228 (1989).
10. K. A. Potekhin, A. V. Maleev, Yu. T. Struchkov, *et al.*, Dokl. Akad. Nauk SSSR **298** (1), 123 (1988).
11. V. A. Palyulin, S. V. Emets, K. A. Potekhin, *et al.*, Dokl. Akad. Nauk **375** (6), 782 (2000).
12. K. Nakatsu, N. Yoshie, H. Yoshioka, *et al.*, Mol. Cryst. Liq. Cryst., Sect. A **182**, 59 (1990).
13. U. Burkert and N. Allinger, *Molecular Mechanics* (American Chemical Society, Washington, 1982; Mir, Moscow, 1986).
14. D. E. Williams and D. J. Houpt, Acta Crystallogr., Sect. B: Struct. Sci. **42**, 286 (1986).

Translated by I. Polyakova

Crystallography Reports, Vol. 47, No. 5, 2002, pp. 736–743. Translated from Kristallografiya, Vol. 47, No. 5, 2002, pp. 802–809.

CRYSTAL CHEMISTRY

Synthesis and Crystal Chemical Characteristics of the Structure of $M_{0.5}Zr_2(PO_4)_3$ Phosphates

V. I. Pet'kov*, V. S. Kurazhkovskaya, A. I. Orlova*, and M. L. Spiridonova***

** Nizhniĭ Novgorod State University, pr. Gagarina 23, Nizhniĭ Novgorod, 603950 Russia*

e-mail: petkov@uic.nnov.ru

*** Moscow State University, Vorob'evy gory, Moscow, 119899 Russia*

Received October 1, 2001

Abstract—Double phosphates of zirconium and metals with an oxidation degree of +2 of the composition $M_{0.5}Zr_2(PO_4)_3$ (M = Mg, Ca, Mn, Co, Ni, Cu, Zn, Sr, Cd, and Ba) are synthesized and characterized by X-ray diffraction methods and IR spectroscopy. The crystal structures of all the compounds are based on three-dimensional frameworks of corner-sharing PO_4-tetrahedra and ZrO_6-octahedra. Phosphates with large Cd^{2+}, Ca^{2+}, Sr^{2+}, and Ba^{2+} cations octahedrally coordinated with oxygen atoms form rhombohedral structures (space group $R\bar{3}$), whereas phosphates with small tetrahedrally coordinated Mg^{2+}, Ni^{2+}, Cu^{2+}, Co^{2+}, Zn^{2+}, and Mn^{2+}-cations are monoclinic (space group $P2_1/n$). The effect of various structure-forming factors on the $M_{0.5}Zr_2(PO_4)_3$ compounds with a common structural motif but different symmetries are discussed. © *2002 MAIK "Nauka/Interperiodica".*

INTRODUCTION

Systematic studies of the crystal chemistry of groups of compounds that have a common sign (or common signs) are necessary for establishing the regularities of their formation and understanding the relation between their structures and properties and the analysis of the possible synthesis of compounds with new structure types.

Phosphates with a common structural motif but with different symmetries, in which PO_4-tetrahedra and LO_6-octahedra form mixed $\{[L_2(PO_4)_3]^{p-}\}_{3\infty}$ frameworks, are formed at the stoichiometric ratios L : P = 2 : 3. Depending on the charge of L and the condition providing phosphate electroneutrality, the cavities of their frameworks can be filled with cations of considerably different sizes and oxidation degrees ranging from +1 to +4 without considerable changes in the framework geometry.

These phosphates are characterized by the existence of stable individual groupings ("lanterns") consisting of two L-octahedra connected by three bridging P-tetrahedra along the ring and a small cavity in the shape of a trigonal prism between the octahedra that cannot be filled with cations (Fig. 1). The chemical bonds inside these groupings (Fig. 1a) are much stronger than the bonds formed by these groupings with one another and with cations filling the cavities of the framework and participating in the compound formation. Therefore, the above stable structural fragments can change their mutual spatial orientation under the effect of iso- and heterovalent substitutions of cations located in the positions inside the framework and in the cavities between the L- and P-polyhedra and also under the effect of various external factors such as temperature and pressure. The specific features of each structure type are determined by the packings of these groupings.

In widespread rhombohedral frameworks, these structure-forming fragments build columns along the $\bar{3}$-axes (Fig. 1b). In many instances, the symmetry of the compounds with $[L_2(PO_4)_3]_{3\infty}$ frameworks can be lowered to orthorhombic or even monoclinic (Fig. 1c). Theoretically, a monoclinic unit cell (sp. gr. $P2_1/n$) can be obtained from a rhombohedral one (in the hexagonal setting) by its slight deformation [1], and, therefore, the monoclinic structural motif can have columns similar to those singled out in rhombohedral frameworks. The symmetry relations between the large variety of phosphate structures with $\{[L_2(PO_4)_3]^{p-}\}_{3\infty}$ frameworks were established in our earlier study [2].

At present, the best studied phosphates are phosphates with mixed frameworks of the compositions $E^{I}L_2(PO_4)_3$ (where E^{II} is an alkali metal, L = Ge, Ti, Zr, Sn, and Hf) and $E^{I}_3L_2(PO_4)_3$ (where E^{I} = Li, Na, and L = Sc, Cr, Fe, and In) [3–8]. Quite a large number of studies are dedicated to the compounds $E^{II}_{0.5}L_2(PO_4)_3$ (where E^{II} is either an alkali earth or 3d-transition metal, and L = Ti or Zr) [9–13]. However, the structural studies of the latter compounds were usually reduced to obtaining diffraction patterns. Neither their space groups nor the character of the distribution of cations with an oxidation degree of +2 have been definitevely established. The information on the vibration spectra of $E^{II}_{0.5}Zr_2(PO_4)_3$ phosphates is also quite scarce. At the

same time, depending on the symmetry, the compounds characterized by similar structural motifs can give different vibration spectra. The use of factor-group analysis allows one to determine the number of active vibrations of anion groupings on the Raman-scattering and IR spectra and explain the differences in the vibration spectra associated with different chemical compositions and crystal symmetries.

Below, we generalize the X-ray diffraction and IR spectroscopy data for a series of phosphates with the composition $M_{0.5}Zr_2(PO_4)_3$, where M = Mg, Ca, Mn, Co, Ni, Cu, Zn, Sr, Cd, and Ba. We also perform factor-group analysis on vibrations of PO_4-tetrahedra in the structures of the compounds with $[L_2(PO_4)_3]_{3\infty}$ frameworks described by different space groups. Based on the experimental data obtained and consideration of the known data, we discuss the influence of various structure-forming factors on the specific characteristics of $M_{0.5}Zr_2(PO_4)_3$ phosphates.

EXPERIMENTAL

The synthesis of $M_{0.5}Zr_2(PO_4)_3$ phosphates performed by the sol–gel method was described in detail in our earlier publications [12, 13]. The starting materials were reagent-grade $M(NO_3)_2 \cdot xH_2O$ or $MCl_2 \cdot yH_2O$, $ZrOCl_2 \cdot 8H_2O$, and H_3PO_4. Electron probe analysis (a Camebax microprobe) showed that the samples were homogeneous, their compositions were close to the theoretical ones calculated by the formula $M_{0.5}Zr_2(PO_4)_3$, and they contained no noticeable amounts of any isomorphous impurities.

The X-ray diffraction analysis of the samples was made on a DRON-3M diffractometer (filtered CuK_α and CoK_α radiations, scanning rate 1 deg/min) at room temperature. The lattice parameters of the compounds synthesized were determined from their indexed diffraction patterns in the range of 2θ angles 8°–50° and then were refined by the least squares method. In those cases where the analysis of the systematic absences of reflections did not allow the unique establishment of space groups, the spectroscopic data were also analyzed.

The absorption spectra of the samples (finely dispersed films on KBr substrates) were recorded on a Specord 75 IR spectrophotometer in the frequency range 1800–400 cm^{-1}.

ANALYSIS OF VIBRATIONS OF A PHOSPHORUS TETRAHEDRON IN THE STRUCTURES OF COMPOUNDS WITH $[L_2(PO_4)_3]_{3\infty}$-TYPE FRAMEWORKS

Compounds of various compositions based on the $[L_2(PO_4)_3]_{3\infty}$ frameworks are crystallized in several space groups—$R\bar{3}c$, $R\bar{3}$, $R32$, $Pbca$, $Pbcn$, $Bb(Cc)$, $C2/c$, $P2_1/n$, $P\bar{1}$, and $P2_13$ [2]. Double phosphates of zirconium and elements with an oxidation degree of +2 are crystallized either in the rhombohedral (sp. gr. $R\bar{3}$) or monoclinic (sp. gr. $P2_1/n$) systems. Since the PO_4-tetrahedra in the structures of these phosphates are distorted to different degrees, one can expect the formation of different types of absorption bands active in the IR range of vibration spectra.

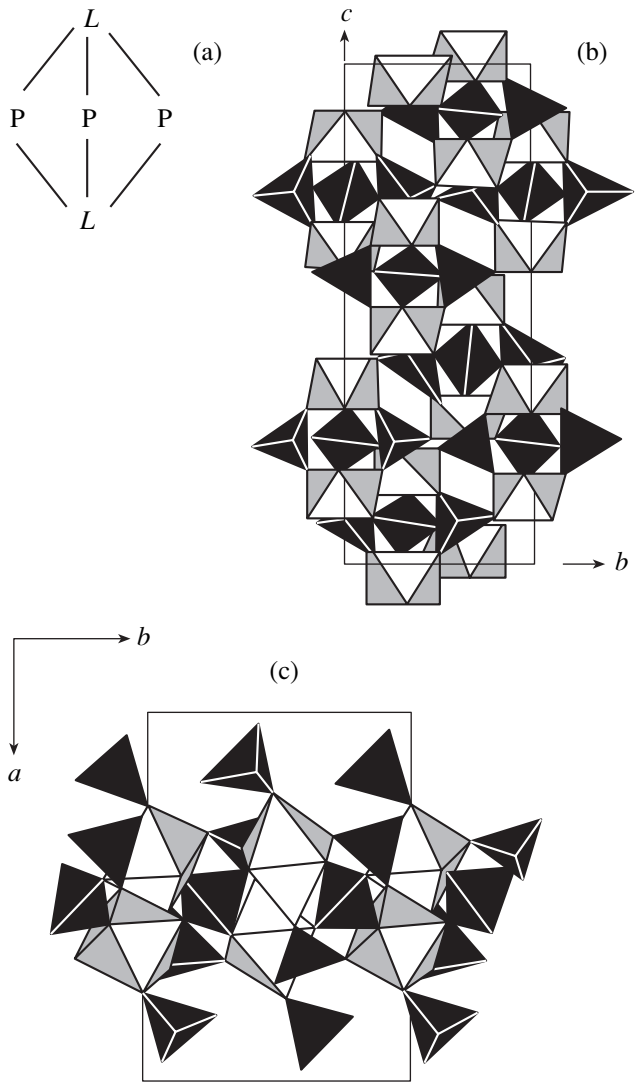

Fig. 1. Mixed $[L_2(PO_4)_3]_{3\infty}$ framework. (a) Schematic depiction of a lantern and lantern packing in (b) the rhombohedral framework and (c) its monoclinic modification.

In the vibration spectrum of an isolated PO_4-ion (the T_d symmetry), four bands are possible—a fully symmetric A_1 band (ν_1, ν_s, symmetric stretching vibration of a P–O bond), the degenerate E band (ν_2, δ_s is the symmetric deformation vibration of a P–O bond), and two threefold degenerate F_2 vibrations (ν_3, ν_{as} is the asymmetric stretching vibration and ν_4, δ_{as} is the asymmetric deformation vibration of a P–O bond). Of all

Table 1. Type and number of vibration bands for a PO_4-tetrahedron in rhombohedral and monoclinic phosphates of zirconium and elements with oxidation degree +2

Vibration type	T_d symmetry of an isolated tetrahedron	C_1 positional symmetry of a tetrahedron (RS and IR data)	Factor group C_{3i} ($R\bar{3}$)		Factor group C_{2h} ($P2_1/n$)	
			RS	IR	RS	IR
ν_1	A_1(RS)	A	$A_g + E_g$	$A_u + E_u$	$3A_g$	$3A_u$
ν_2	E(RS)	$2A$	$2A_g + 2E_g$	$2A_u + 2E_u$	$6A_g$	$6A_u$
ν_3, ν_4	F_2(RS, IR)	$3A$	$3A_g + 3E_g$	$3A_u + 3E_u$	$9A_g$	$9A_u$

Note: RS and IR indicate the bands in the Raman scattering and IR spectra, respectively, allowed by the selection rules.

Table 2. Indexing of the diffraction patterns of $M_{0.5}Zr_2(PO_4)_3$ compounds with M = Cd, Ca, Sr, and Ba (d, Å; I/I_0 %)

h k l	Cd			Ca			Sr			Ba		
	d_{obs}	d_{calcd}	I/I_0	d_{obs}	d_{calcd}	I/I_0	d_{obs}	d_{calcd}	I/I_0	d_{obs}	d_{calcd}	I/I_0
0 0 3	7.431	7.430	9	7.557	7.552	4	7.783	7.789	3	7.986	7.986	4
0 1 1	7.219	7.227	18	7.213	7.209	5	7.172	7.171	7	7.144	7.138	6
1 0 2	6.298	6.302	5	6.307	6.313	18	6.325	6.332	9	6.347	6.343	8
0 1 4	4.503	4.502	40	4.537	4.542	55	4.619	4.617	29	4.672	4.674	17
1 1 0	4.414	4.411	100	4.386	4.390	78	4.350	4.350	66	4.318	4.318	68
1 0 5	3.850	3.850	19	3.897	3.892	5	3.971	3.772	4	4.033	4.033	7
1 1 3	3.790	3.793	84	3.790	3.795	83	3.798	3.798	63	3.795	3.798	60
2 0 1	3.767	3.765	12	3.751	3.749	10	3.732	3.720	9	3.695	3.696	5
0 2 2	3.616	3.614	5	3.603	3.604	5	3.584	3.586	4	3.566	3.570	3
2 0 4	3.151	3.151	39	3.154	3.156	58	3.165	3.166	35	3.172	3.172	24
0 2 5	2.901	2.901	13	2.913	2.912	6	2.933	2.933	11	2.950	2.948	8
1 1 6	2.840	2.842	82	2.864	2.863	100	2.901	2.902	100	2.931	2.931	100
2 1 1	2.864	2.864	23	2.853	2.851	17	2.825	2.827	13	2.807	2.808	14
1 0 8	2.616	2.618	11	2.653	2.654	6	2.724	2.724	6	2.778	2.779	10
1 2 4	2.563	2.564	49	2.561	2.563	29	2.562	2.560	13	2.557	2.557	5
3 0 0	2.547	2.547	51	2.534	2.534	46	2.511	2.512	35	2.493	2.493	31
1 2 5	2.422	2.424	11	2.426	2.427	4	2.431	2.432	6	2.435	2.435	6
3 0 3	2.409	2.409	9	2.402	2.403	4	2.390	2.391	6	2.380	2.380	4
0 2 8	2.251	2.251	11	2.271	2.271	8	2.308	2.308	8	2.338	2.338	6
1 1 9	2.159	2.160	11	2.185	2.184	11	2.230	2.230	7	2.266	2.266	6
1 2 7	2.140	2.139	6	2.149	2.149	4	2.167	2.167	8	2.179	2.180	8
2 2 3	2.114	2.114	12	2.109	2.108	16	2.096	2.095	13	2.085	2.085	18
3 0 6	2.099	2.100	14	2.104	2.104	9	2.111	2.112	10	2.114	2.115	6
1 2 8	2.004	2.005	34	2.017	2.017	25	2.041	2.039	17	2.055	2.056	11
1 0 11	1.959	1.959	3	1.988	1.988	6	2.044	2.045	16	2.091	2.091	6
3 1 4	1.982	1.981	15	1.976	1.976	14	1.967	1.968	9	1.960	1.960	4
2 0 10	1.926	1.925	9	1.945	1.946	8	1.986	1.986	7	2.017	2.017	6
1 3 5	1.914	1.914	16	1.913	1.912	4	1.908	1.908	12	1.905	1.904	6
2 2 6	1.896	1.896	30	1.898	1.898	33	1.899	1.899	36	1.899	1.899	32
4 0 2	1.882	1.883	3	1.875	1.875	5	1.859	1.860	4	1.849	1.848	3
1 2 10	1.766	1.765	9	1.779	1.779	26	1.807	1.807	21	1.828	1.827	12

these vibrations, only the ν_3 and ν_4 vibrations are active in the IR range. Using the method of dividing the vibrations of a complex ion in a crystal into internal and external vibrations, we performed the group-factor analysis of vibrations of an orthophosphorus tetrahedron in the compounds described by the sp. gr. $R\bar{3}$ and $P2_1/n$. The positional symmetry of a complex PO_4-ion is lowered down to C_1 in both rhombohedral and monoclinic structures (phosphorous atoms are located in the general position). Then, the vibration ν_1 (A) becomes active and the ν_2 ($2A$), ν_3, and ν_4 ($3A$) vibrations become nondegenerate. The transition from the representation of the positional symmetry group of a tetrahedron, C_1, to the factor-group representations of the space groups C_{3i} ($R\bar{3}$) and C_{2h} ($P2_1/n$) is illustrated by Table 1.

In centrosymmetric crystals, the alternative selection rule for internal vibrations of a complex ion is preserved—vibrations symmetric with respect to the inversion center (the g vibrations) are active in the Raman spectrum but are inactive in the IR spectrum. Thus, the IR spectra of rhombohedral phosphates can have two bands of symmetric stretching vibrations ν_1 (A_u, E_u), four bands of symmetric deformation vibrations ν_2 ($2A_u$, $2E_u$), and six bands of asymmetric stretching and six bands of asymmetric deformation vibrations ν_3 and ν_4 ($3A_u$, $3E_u$). The unit cell of phosphates described by the sp. gr. $R\bar{3}$ has only one independent phosphorus position, 18f (at $Z = 6$, the unit cell contains 18 P atoms, the multiplicity of the position with the symmetry C_1 is 18). The monoclinic unit cell described by the sp. gr. $P2_1/n$ with $Z = 4$ contains 12 P atoms. The multiplicity of the general position is 4; the unit cell has three independent phosphorus positions. Thus, the selection rules for the monoclinic compounds allow the formation of much more bands in the IR spectra—three ν_1 ($3A_u$) bands, six ν_2 ($6A_u$) bands, and nine ν_3 and nine ν_4 ($9A_u$) bands.

RESULTS AND DISCUSSION

The X-ray phase analysis [12–14] showed the complex interactions between the components of the reactive mixtures, with the phase composition being essentially dependent on the temperature and the nature of divalent cations. The individual $M_{0.5}Zr_2(PO_4)_3$ compounds were formed in the temperature range from 730 to 1150°C.

The interplanar spacings in double phosphates of zirconium and alkali earth elements of the composition $M_{0.5}Zr_2(PO_4)_3$ and also in $Cd_{0.5}Zr_2(PO_4)_3$ are listed in Table 2, their crystallographic characteristics are indicated in Table 3.

Indexing of diffraction patterns from $M_{0.5}Zr_2(PO_4)_3$ polycrystals (M = Cd, Ca, Sr, and Ba) shows their structural analogy. The absences of the reflections of the type $h - k + l = 3n$ unambiguously indicate the R-lattice.

In the structures with a rhombohedral mixed framework (Fig. 1b), the lanterns are "beaded" onto the threefold inversion axes and occupy all the vertices of an elementary rhombohedron and also the position in its center; i.e., the rhombohedral unit cell includes two such lanterns—the initial one and the second one (in the rhombohedron center) inverted with respect to the initial one. It also connects six lanterns at the unit-cell vertices, thus forming a continuous anionic framework.

The framework has two types of cavities in the proportion 1 : 3. In the columns extended along the c-axis, octahedral cavities of the $M1$ type are formed between the two neighboring lanterns. Neighboring columns are connected by single PO_4-tetrahedra and, thus, create $M2$-type cavities of an irregular shape with c.n. 8.

The precision analysis of $Cd_{0.5}Zr_2(PO_4)_3$ [15] and $Ca_{0.5}Zr_2(PO_4)_3$ [11] structures based on the corresponding powder diffraction data showed that Cd^{2+} and Ca^{2+} cations are orderly distributed over the octahedra beaded onto threefold axes and occupy half of all the $M1$ cavities, while the $M2$ cavities are empty. The average lengths of the Cd–O and Ca–O bonds coincide within the error and are equal to 2.47 Å. The average distances in independent Zr-octahedra are 2.03 and 2.05 Å for $Cd_{0.5}Zr_2(PO_4)_3$ and 2.06 and 2.08 Å for $Ca_{0.5}Zr_2(PO_4)_3$. The P–O bond lengths in orthophosphorus tetrahedra range within 1.52–1.57 Å for cadmium-containing compound and within 1.52–1.54 Å for calcium-containing one.

It can be seen from Table 3 that in the series of $M_{0.5}Zr_2(PO_4)_3$ compounds with M = Cd, Ca, Sr, and Ba, the a-parameter decreases and the c-parameter increases with an increase in the radius of the M cation, whereas the unit-cell volume increases with it. These tendencies in the behavior of the unit-cell parameters can be interpreted as follows. Since M cations occupy the positions inside the columns between two faces of the neighboring ZrO_6-octahedra located along the c-axis (Fig. 1b), the introduction of a larger M-cation increases the c-parameter. This is accompanied by the correlated rotation of zirconium octahedra and phosphorus tetrahedra connecting the parallel columns, which, in turn, decreases the intercolumnar distances and, thus, also the a-parameter. Slight deformation of the structure (without any pronounced change of the initial motif) is possible because of the existence of large voids at a level of each Zr, P-lantern in the framework and along the $\bar{3}$ axes.

Figure 2 shows the IR-spectra of zirconium phosphates with large divalent Cd, Ca, Sr, and Ba cations. The bands in the range 1250–1000 cm^{-1} are attributed to asymmetric stretching vibrations ν_3 of a PO_4 ion. The intense high-frequency bands at 1250–1170 cm^{-1} are explained by the fact that, at large P–O–Zr bond angles, the electron density of small polarized considerably

Table 3. Crystallographic characteristic of the compounds

Chemical formula	Space group	*a*, Å	*b*, Å	*c*, Å	β, deg	*V*, Å^3	*Z*
$Cd_{0.5}Zr_2(PO_4)_3$	$R\bar{3}$	8.822(1)	–	22.291(3)	–	1502	6
$Ca_{0.5}Zr_2(PO_4)_3$	$R\bar{3}$	8.780(1)	–	22.653(3)	–	1512	6
$Sr_{0.5}Zr_2(PO_4)_3$	$R\bar{3}$	8.701(1)	–	23.370(4)	–	1532	6
$Ba_{0.5}Zr_2(PO_4)_3$	$R\bar{3}$	8.638(1)	–	23.950(3)	–	1548	6
$Ni_{0.5}Zr_2(PO_4)_3$	$P2_1/n$	12.385(3)	8.924(4)	8.840(3)	90.53(1)	977.0	4
$Mg_{0.5}Zr_2(PO_4)_3$	$P2_1/n$	12.384(3)	8.922(3)	8.844(3)	90.56(2)	977.1	4
$Cu_{0.5}Zr_2(PO_4)_3$	$P2_1/n$	12.389(3)	8.925(4)	8.841(3)	90.53(1)	977.4	4
$Co_{0.5}Zr_2(PO_4)_3$	$P2_1/n$	12.389(3)	8.928(3)	8.840(2)	90.54(1)	977.7	4
$Zn_{0.5}Zr_2(PO_4)_3$	$P2_1/n$	13.389(2)	8.929(3)	8.842(2)	90.54(1)	978.1	4
$Mn_{0.5}Zr_2(PO_4)_3$	$P2_1/n$	12.390(3)	8.931(4)	8.843(3)	90.55(1)	978.5	4

charged Zr^{4+}-ions is partly localized on a P–O bond, which results in high values of the force constants of this bond [16].This range has five (Cd, Sr, and Ba) or six (Ca) bands allowed by the selection rules. The bands in the range 1000–950 cm^{-1} are attributed to the symmetric ν_1 vibrations, which are represented by a broadened band with a shoulder. With an increase in cation size, the asymmetric stretching bands are shifted toward lower frequencies, and the symmetric stretching vibrations, in the opposite direction. As a result, the bands at 1025 cm^{-1} in the spectra of Sr- and Ba-containing phases are incompletely resolved and show a shoulder against the background of the band at 1045 cm^{-1}. The bands in the range 640–545 cm^{-1} are considered as deformation vibrations, ν_4, and the band in the vicinity of 425 cm^{-1}, as the deformation ν_2 vibrations of a PO_4-tetrahedron.

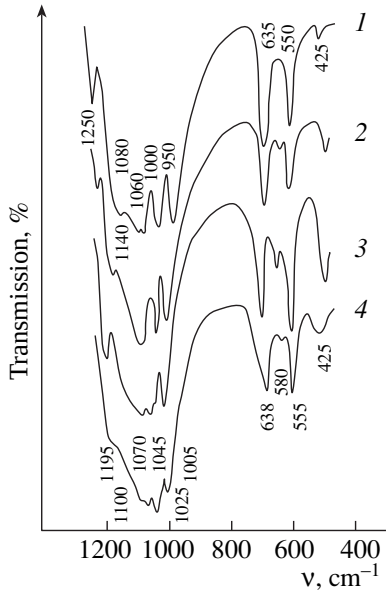

Fig. 2. IR spectra of $M_{0.5}Zr_2(PO_4)_3$ orthophosphates crystallized in the trigonal system (sp. gr. $R\bar{3}$): (*1*) $Cd_{0.5}Zr_2(PO_4)_3$, (*2*) $Ca_{0.5}Zr_2(PO_4)_3$, (*3*) $Sr_{0.5}Zr_2(PO_4)_3$, and (*4*) $Ba_{0.5}Zr_2(PO_4)_3$.

All the bands of symmetric vibrations of a PO_4-tetrahedron in the $M_{0.5}Zr_2(PO_4)_3$ phosphates with *M* = Cd, Ca, Sr, and Ba are intense and well resolved (Fig. 2). The spectrum in this range differs from the spectra of zirconium and alkali metal phosphates of the compositions $EZr_2(PO_4)_3$ with *E* = Na, K, Rb, and Cs, which are crystallized in the sp. gr. $R\bar{3}c$ [17], where the stretching vibrations are represented by only one broad band with some slightly distinguished maxima [18]. The well resolved bands confirm a high degree of atomic order in the structure. Indeed, Cd atoms are located in the 3*b* positions in the layers (sp. gr. $R\bar{3}$), whereas the 3*a* positions remain empty [15]. Based on the analogy of the spectra, one can state that in alkali-earth zirconium phosphates, the Ca, Sr, and Ba atoms occupy the layers of *M*1 cavities in the structure.

The interplanar spacings in $Mg_{0.5}Zr_2(PO_4)_3$ are listed in Table 4, while those for $M_{0.5}Zr_2(PO_4)_3$ phosphates with *M* = Mn, Co, Ni, Cu, and Zn were indicated in our earlier publication [13]. These compounds containing small cations with an oxidation degree of +2 are crystallized in the sp. gr. $P2_1/n$ (Table 3). The similarity of their chemical formulas, the closeness of the lattice parameters and unit-cell volumes, and the same symmetry indicate the common basis for the formation of their crystal structures and lead to the assumption that they are isostructural. Knowledge of the $Ni_{0.5}Zr_2(PO_4)_3$ phosphate structure [19] allows us to state that the structures of the $M_{0.5}Zr_2(PO_4)_3$ compounds (*M* = Mg, Mn, Co, Ni, Cu, and Zn) are established quite reliably.

The P unit cells of these structures are monoclinically distorted with respect to their *R* cells (Fig. 1). The

Table 4. Indexing of the diffraction patterns of $Mg_{0.5}Zr_2(PO_4)_3$ (d, Å; I/I_0, %)

$h\,k\,l$	d_{obs}	d_{calcd}	I/I_0	$h\,k\,l$	d_{obs}	d_{calcd}	I/I_0
1 0 –1	7.227	7.231	4	4 1 1	2.768	2.769	11
2 0 0	6.185	6.193	8	1 3 –1	2.747	2.750	17
1 1 –1	5.610	5.618	10	1 3 1		2.747	
0 2 0	4.458	4.460	21	2 3 –1	2.568	2.569	10
0 0 2	4.420	4.423	100	2 1 –3	2.561	2.559	24
2 1 1	4.387	4.394	52	4 2 0	2.542	2.543	42
0 1 2	3.954	3.962	12	4 0 2	2.526	2.524	8
1 1 –2	3.782	3.784	30	1 2 3	2.403	2.409	3
3 0 –1	3.757	3.754	39	5 1 –1	2.313	2.310	3
3 0 1	3.723	3.726	16	0 0 4	2.211	2.211	6
3 1 –1	3.456	3.461	6	4 2 2	2.196	2.197	3
2 2 –1	3.358	3.357	12	0 4 2	1.992	1.991	8
2 2 1	3.342	3.343	11	2 3 –3	1.987	1.988	8
0 2 2	3.145	3.141	43	2 3 3	1.980	1.979	17
4 0 0	3.099	3.096	32	1 4 2	1.965	1.965	14
1 2 –2	3.051	3.049	9	6 1 1	1.957	1.957	29
1 2 2	3.043	3.039	6	5 2 2	1.939	1.938	3
1 0 –3	2.875	2.874	9	6 2 0	1.870	1.873	5
3 2–1		2.872		5 3 –1	1.863	1.863	4
2 2 2	2.797	2.793	7	6 0 2			
4 1 –1	2.786	2.784	9	5 1 –3			

main building elements of the framework (lanterns) are located along the [102] and $[10\bar{2}]$ directions playing the role of quasi-threefold axes. As a result, the Zr-octahedra of two neighboring groupings form strongly distorted tetrahedral voids occupied by small cations. The *M*-ions occupy their positions with a probability of 0.5.

The cation–oxygen distances in the Ni^{2+}-tetrahedra in monoclinic $Ni_{0.5}Zr_2(PO_4)_3$ phosphate range from 1.89 to 2.26 Å, with the average distance being 2.11 Å [19]. The average Ni–O distance in polyhedra of the $Ni_{0.5}Zr_2(PO_4)_3$ phosphate is considerably longer than that predicted from the sum of the ionic radii $r_{IV}(Ni) + r_{IV}(O) = 0.55 + 1.36 = 1.91$ (Å) [20]. This indicates that the non-structure-forming Ni site can be occupied by cations with a somewhat larger size and an oxidation degree of +2, such as Mg, Cu, Co, Zn, and Mn. The average distances in each of the independent Zn octahedra of the $Ni_{0.5}Zr_2(PO_4)_3$ phosphate are equal to 2.08 Å. The average P–O lengths in the tetrahedra of this phosphate are 1.50, 1.51, and 1.53 Å.

In the range of ν_3 vibrations, the IR-spectra of these compounds (Fig. 3) have either all the nine bands allowed by the selection rules (the Ni, Zn phases) or have from six to seven bands (the Mg-, Co-, Cu-, and Mn-containing phases). In the range of ν_1 vibrations, all three allowed bands are formed in all the phases except for the Mn-containing ones, where only one band is formed. The spectra of ν_4 vibrations have only six or seven of the nine possible bands. The ν_2 vibrations recorded by a spectrophotometer are represented by two bands. The somewhat different form of the IR spectrum of $Mn_{0.5}Zr_2(PO_4)_3$ phosphate seems to be caused by a larger Mn-ion which "pushes apart" the tetrahedral positions of their location, which, in turn, affects the vibrations of phosphorus tetrahedra.

The above analysis of the vibrations in the related structures of double orthophosphates of Zr and the elements with an oxidation degree of +2 described by different space groups shows that the IR spectra of the phases with large and small cations differ in the character, number, and types of their bands both in the stretching and deformation regions.

Thus, the synthesized compounds with $\{[Zr_2(PO_4)_3]^-\}_{3\infty}$ frameworks containing Cd, alkali earth elements, Mg, and 3*d* elements have similar structures but different arrangements of cations with an oxidation degree of +2 located in the framework voids. The structures of these phosphates can be divided into two groups (Table 5)—zirconium phosphates with small cations (Ni, Cu, Mg, Co, Zn, and Mn) described by the sp. gr. $P2_1/n$ with *d*-elements and Mg occupying the tetrahedral voids and phosphates with orthorhombic

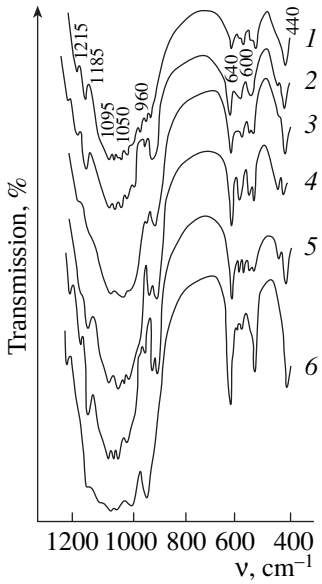

Fig. 3. IR spectra of $M_{0.5}Zr_2(PO_4)_3$ orthophosphates crystallized in the monoclinic system (sp. gr. $P2_1/n$)): (*1*) $Mg_{0.5}Zr_2(PO_4)_3$, (*2*) $Ni_{0.5}Zr_2(PO_4)_3$, (*3*) $Co_{0.5}Zr_2(PO_4)_3$, (*4*) $Cu_{0.5}Zr_2(PO_4)_3$, (*5*) $Zn_{0.5}Zr_2(PO_4)_3$, and (*6*) $Mn_{0.5}Zr_2(PO_4)_3$.

structures (sp. gr. $R\bar{3}$) and large Cd-, Ca-, Sr-, and Ba-cations characterized by an octahedral environment.

However, the size of the *M*-cation is not the only factor determining the formation of a certain structure type. Thus, the $Cu_{0.5}Zr_2(PO_4)_3$ phosphate has a stable rhombohedral structure at temperatures higher than 520°C [21]. According to the DTA data, with an increase in the temperature, $Mg_{0.5}Zr_2(PO_4)_3$ and $Zn_{0.5}Zr_2(PO_4)_3$ phosphates undergo a phase transition at 670°C [22]. The established phase transitions accompanied by the change of the symmetry are associated with the transformation of the crystal structure due to changes in the temperature. These reconstructive transitions are accompanied by the change in the coordination number of an *M* cation from 4 to 6, with the preservation of the main islandlike structural groupings—lanterns. In terms of structure, the polymorphism of $M_{0.5}Zr_2(PO_4)_3$ phosphates with *M* = Mg, Cu, and Zn seems to be associated with the easy deformability of the oxygen environment and unstable coordination of cations with an oxidation degree of +2, a rather flexible construction built by Zr- and P- coordination polyhedra (connected only via their vertices), and also with a more uniform distribution of the stresses arising at large amplitudes of atomic vibrations among various bonds. Thr different temperatures of these phase transitions are determined by the electronic structure and the stereochemical characteristics of the *M*-cation.

Table 5. Morphotropic series of phosphates of zirconium and divalent elements $M_{0.5}Zr_2(PO_4)_3$

Compound	Radius of *M*, Å	C.n. M^{2+}	Space group
$Ni_{0.5}Zr_2(PO_4)_3$	0.55	4	$P2_1/n$
$Cu_{0.5}Zr_2(PO_4)_3$	0.57	4	
$Mg_{0.5}Zr_2(PO_4)_3$	0.57	4	
$Co_{0.5}Zr_2(PO_4)_3$	0.58	4	
$Zn_{0.5}Zr_2(PO_4)_3$	0.60	4	
$Mn_{0.5}Zr_2(PO_4)_3$	0.66	4	
$Cd_{0.5}Zr_2(PO_4)_3$	0.95	6	$R\bar{3}$
$Ca_{0.5}Zr_2(PO_4)_3$	1.00	6	
$Sr_{0.5}Zr_2(PO_4)_3$	1.18	6	
$Ba_{0.5}Zr_2(PO_4)_3$	1.35	6	

The phenomenon of the high flexibility and stability of the $[L_2(PO_4)_3]_{3\infty}$ framework readily accommodating various combinations of cations and variations in the temperature and pressure seems to result from the combination of two competing structure-forming factors. The first one is associated with the existence of relatively rigid octahedral–tetrahedral fragments (lanterns); the second, with the tendency to a more uniform spatial distribution of tetrahedral phosphorus anions and cations that have different charges in the cationic and anionic parts of the structure, which is dictated by the requirement of the local valence balance. These two factors manifest themselves especially clearly at the ends of the series of compounds with $[L_2(PO_4)_3]_{3\infty}$ frameworks, which include the cations in the order of the change in their ionic radii when the composition of the anionic part (framework) of their structure is constant.

In the morphotropic series of zirconium phosphates of divalent elements, $M_{0.5}Zr_2(PO_4)_3$ (Table 5), the part of the series with small M^{2+}-cations (in comparison with Zr^{4+}-ions participating in the formation of the anionic $\{[Zr_2(PO_4)_3]^-\}_{3\infty}$ framework), the main structure-forming factor is the mixed octahedral–tetrahedral framework accommodating a smaller cation. In the part of the series with large Cd^{2+}-, Ca^{2+}-, Sr^{2+}-, and Ba^{2+}-cations, the atomic arrangement is determined mainly by the geometric factor—if the radius of a highly charged cation (Zr^{4+}) is much less than the radius of a less charged ion (M^{2+}), the general arrangement of these cations and tetrahedral oxo anions results in the "pushing-apart effect" of large MO_6 octahedra, which changes the structure geometry. The phase transitions in these compounds are accompanied by the rotation of PO_4 tetrahedra and some changes in the oxygen environment of *M* atoms, while the general features of the structure architecture are preserved.

ACKNOWLEDGMENTS

This study was supported by the Russian Foundation for Basic Research, project nos. 02-03-32181 and 01-03-33013.

REFERENCES

1. P. C. Christidis and P. J. Rentzeperis, Z. Kristallogr. **144**, 341 (1976).
2. V. I. Pet'kov, G. I. Dorokhova, and A. I. Orlova, Kristallografiya **46** (1), 76 (2001) [Crystallogr. Rep. **46**, 69 (2001)].
3. M. Sljukic, B. Matkovic, B. Prodic, and S. Scavnicar, Croat. Chem. Acta **39**, 145 (1967).
4. L. O. Hagman and P. Kierkegaard, Acta Chem. Scand. **22**, 1822 (1968).
5. V. I. Petkov, A. I. Orlova, and O. V. Egorkova, J. Struct. Chem. **37**, 933 (1996).
6. R. Perret and A. Boudjada, C. R. Seances Acad. Sci., Ser. C **282**, 245 (1976).
7. S. E. Sigarev, Kristallografiya **37** (4), 1055 (1992) [Sov. Phys. Crystallogr. **37**, 563 (1992)].
8. S. E. Sigarev, Kristallografiya **38** (3), 203 (1993) [Crystallogr. Rep. **38**, 399 (1993)].
9. N. G. Chernorukov, I. A. Korshunov, and T. V. Prokof'eva, Kristallografiya **23** (4), 844 (1978) [Sov. Phys. Crystallogr. **23**, 475 (1978)].
10. S. Senbhagaraman, T. N. Guru Row, and A. M. Umarji, Solid State Commun. **71**, 609 (1989).
11. J. Alamo and J. L. Rodrigo, Solid State Ionics **63–65**, 678 (1993).
12. V. I. Pet'kov, A. I. Orlova, and D. A. Kapranov, Zh. Neorg. Khim. **43**, 1534 (1998).
13. V. I. Pet'kov, A. I. Orlova, G. I. Dorokhova, and Ya. V. Fedotova, Kristallografiya **45** (1), 36 (2000) [Crystallogr. Rep. **45**, 30 (2000)].
14. V. I. Petkov and A. I. Orlova, J. Therm. Anal. **54**, 71 (1998).
15. R. Brochu, M. El-Yacoubi, M. Louer, *et al.*, Mater. Res. Bull. **32**, 15 (1976).
16. P. Tarte, A. Rulmont, and C. Merckaert-Ansay, Spectrochim. Acta A **42**, 1009 (1986).
17. H. Y.-P. Hong, Mater. Res. Bull. **11**, 173 (1976).
18. V. S. Kurazhkovskaya, A. I. Orlova, V. I. Pet'kov, *et al.*, Zh. Strukt. Khim. **41**, 74 (2000).
19. A. Jouanneaux, A. Verbaere, Y. Piffard, *et al.*, Eur. J. Solid State Inorg. Chem. **28**, 683 (1991).
20. R. D. Shannon, Acta Crystallogr., Sect. A: Cryst. Phys., Diffr., Theor. Gen. Crystallogr. **32**, 751 (1976).
21. A. El-Jazouli, M. Alami, R. Brochu, *et al.*, J. Solid State Chem. **71**, 444 (1987).
22. K. Nomura, S. Ikeda, K. Ito, and H. Einaga, J. Electroanal. Chem. **326**, 351 (1992).

Translated by L. Man

Crystallography Reports, Vol. 47, No. 5, 2002, pp. 744–747. Translated from Kristallografiya, Vol. 47, No. 5, 2002, pp. 810–813.

DIFFRACTION AND SCATTERING OF IONIZING RADIATION

Role of Sublattices in the Formation of Electron Density in Metal Nitrites

Yu. N. Zhuravlev and A. S. Poplavnoĭ

Kemerovo State University, ul. Krasnaya 6, Kemerovo, 650043 Russia

e-mail: zhur@phys.kemsu.ru

Received October 2, 2001

Abstract—The self-consistent valence electron densities of $NaNO_2$, $AgNO_2$, and their constituent sublattices are calculated on the basis of the theory of the local-density functional. The quantity characterizing the relation between different sublattices is introduced as the difference density resulting from the subtraction of the densities of the individual sublattices from the total electron density. The role of metal in the formation of electron density is established, and, in particular, it is shown that, in $AgNO_2$, anionic bonds have the covalent component formed at the expense of the electron density of the cation. It is also shown that, qualitatively, the difference density in $NaNO_2$ corresponds to the experimental deformation density. © *2002 MAIK "Nauka/Interperiodica".*

INTRODUCTION

Metal nitrites have numerous phases that exist under different pressures and temperatures. The order–disorder phase transitions in these nitrites have been extensively studied by various methods [1, 2]. One of the methods of studying crystal structures and phase transitions is the experimental determination or theoretical calculation of the deformation electron density. The deformation electron density characterizes the total effect of electron redistribution between various atoms and displacements of electrons from the atomic positions into interstitials. Traditionally, the effect of electron redistribution is interpreted in terms of the local approach, i.e., in terms of the hybridization of orbitals of the neighboring atoms, as is usually done in molecular quantum chemistry. But the role of the long-range order in chemical bonding in crystalline solids still remains unclear. To study this problem, we elaborated a new approach to the description of the changes in the electron density of free atoms caused by their incorporation into the crystal lattice, which is based on the notions of sublattices and difference density [3]. The application of this approach to crystals with mainly ionic chemical bonding allowed us to establish a number of electron-density characteristics associated with long-range interactions between equivalent atoms in the sublattices. Below, in order to establish the role of the sublattices in the formation of the valence electron density, we extend the method of sublattices [3] to $NaNO_2$ and $AgNO_2$ crystals where, along with the ionic component, there also exists a covalent component of chemical bonds inside the molecular NO_2 complex.

METHODS AND OBJECTS OF STUDY

The electron density was calculated by the method of nonempirical pseudopotential [4] in the basis of the numerical sp^3d^5 atomic pseudoorbitals. The atomic orbitals were calculated using the solution of the Schrödinger equation with the same pseudopotentials by fitting the occupation numbers to the well-known diagrams of the energy states of an electron in an atom. It was necessary to use of the virtual *p*- and *d*-states of metal and *d*-states of nitrogen and oxygen in the decomposition of crystal orbitals, because the former play an important role in the distribution of the valence electron charge. Taking account of the *d*-orbitals of nitrogen was necessary for the reliable reconstruction of the electron structure of an anion, whereas the diffuse *d*-orbitals of oxygen were taken into account because they are responsible for anion–anion interactions. The details of the numerical variant of the method can be found elsewhere [5].

In the method of sublattices, a crystal is divided into a set of symmetrically related atoms of one kind with the preservation of their real geometry and electroneutrality. Then, the self-consistent calculation of the electron density is performed for a crystal as a whole and for each of its constituent sublattices. The sublattice density automatically takes into account the hybridization effects of the equivalent atoms. Subtracting the sublattice densities from the crystal density, we obtain the difference density that can be either positive or negative and clearly illustrates the electron transport between the atoms of different kinds. The difference electron density thus determined differs from the deformation density, which is obtained by subtracting the

1063-7745/02/4705-0744$22.00

spherically symmetric atomic density from the experimental density. The difference is caused by the fact that, in our approach, one distinguishes the hybridization effects between the equivalent atoms that make up the sublattices and the hybridization effects between the sublattices themselves.

One of the selected objects is $NaNO_2$, a ferroelectric with the simplest crystal structure. Up to a temperature of 437 K, sodium nitrite has an orthorhombic lattice with the symmetry C_{2V}^{20}, then it undergoes the transition from the ferroelectric to the paraelectric phase described by the group D_{2h}^{25}. The experimental study of the deformation density in the vicinity of the phase-transition point in $NaNO_2$, the deformation density in its ferroelectric phase, and small deviations from it caused by the partial reorientation of the nitrite group were studied in [1]. The second object, $AgNO_2$, has an atomic structure similar to that of sodium nitrite but has been less studied both theoretically and experimentally. In order to establish the role played by cations in chemical bonding in metal nitrites, we calculated the crystal and sublattice valence densities in $NaNO_2$ and $AgNO_2$. The calculations were performed for the ordered ferroelectric phase with the symmetry C_{2V}^{20} and the lattice parameters determined earlier for $NaNO_2$ [6] and $AgNO_2$ [7].

CALCULATED RESULTS AND DISCUSSION

For convenience, we used the setting in which the *z*-axis was directed along the crystallographic *b*-axis, and the *y*-axis, along the *c*-axis [6]. The densities in both the text and the figure captions are given in e $Å^{-3}$ units.

The distribution of the crystal valence density and the sublattice densities in the *bc* plane in $NaNO_2$ are shown in Fig. 1. Consider first the crystal density. It is characterized by the obvious localization of the electron density at the anion and, in particular, oxygen atoms. The density at the nitrogen atom is about ~1, whereas at the oxygen maxima, which have the shape of *p*-orbitals oriented normally to the N–O bond, the density is about 2.5. The common density contours "embrace" oxygen atoms in NO_2^- with the density value ~1.5 and the closest anions with the density ~0.5. The common contours embracing the anions are also formed in the *ab* plane, whereas in the *ac* planes only the common contours connecting oxygen atoms in the NO_2^- complexes are formed. Such a density distribution is formed because of the overlapping wave functions of the nitrogen and oxygen of the neighboring anions. As is seen from Fig. 1, the nitrogen sublattice provides the maximum density at the atoms in the form of p_z orbitals, and the oxygen sublattice, in the form of

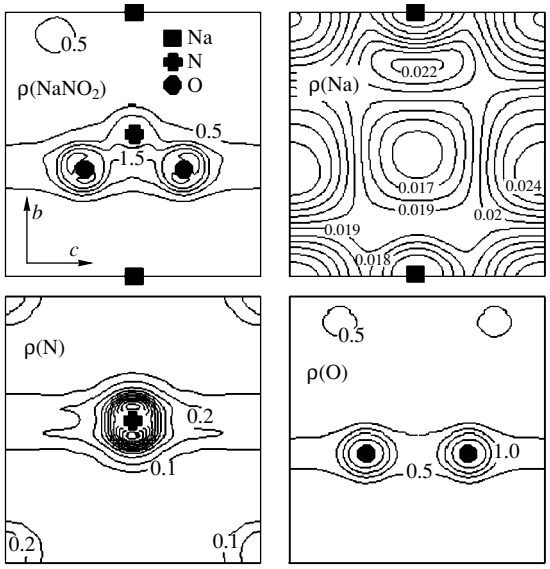

Fig. 1. Distributions of crystal electron density and sublattice densities due to Na, N, and O atoms in $NaNO_2$.

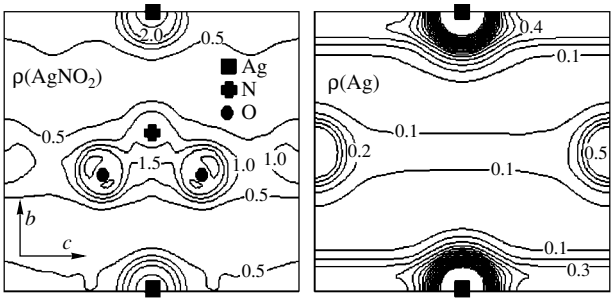

Fig. 2. Distribution of crystal electron density and sublattice density due to Ag atoms in $AgNO_2$.

p_{xy} orbitals. It is the hybridization of these orbitals that provides bonding in the anion. In this case, both sublattices share the density contours relating the atoms of the neighboring anions, which manifests itself in the crystal density. The density of the sodium sublattice is distributed rather uniformly, and its maxima are located in the region between the oxygen atoms of the nearest anions. Thus, an electron of the metal atom is transferred not to the anion but to the interanionic space. Therefore, one has to consider not the M^+–A^- ionic bond, but rather the ionic bond in terms of the whole crystal, as being formed not with the participation of individual atoms but with the participation of individual sublattices.

Figure 2 shows the distribution of the crystal valence density and the density of the silver sublattice in $AgNO_2$ in the same *bc* plane as in $NaNO_2$. It is seen from Figs. 1 and 2 that the crystal densities at the anions are close in both crystals; the density of the nitrogen and oxygen sublattices are also very close (they are not

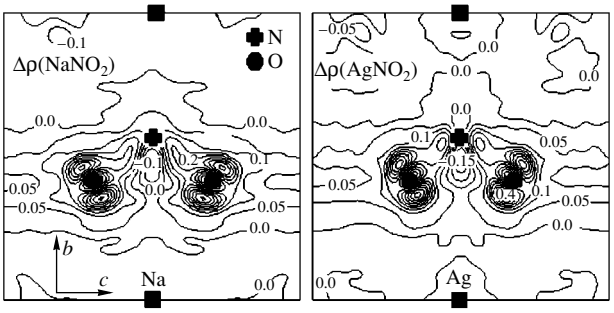

Fig. 3. Difference density in $NaNO_2$ and $AgNO_2$.

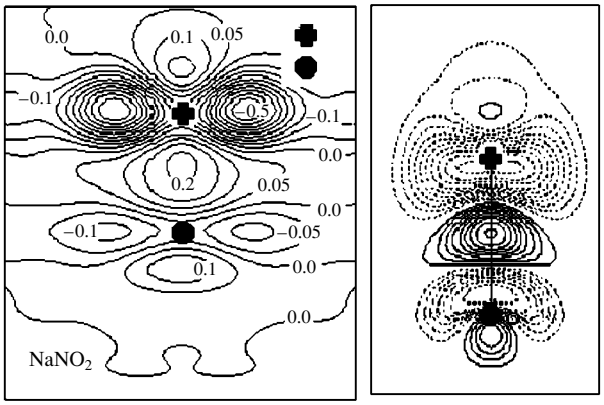

Fig. 4. Difference density in the plane normal to the N–O bond (on the left) and the experimental deformation density in $NaNO_2$ [6].

shown in Fig. 2 in order to save space). However, a considerably larger number of valence electrons at silver atoms (11, in our calculation) results in a drastic change in the density of the metal sublattice in $AgNO_2$ in comparison with the corresponding density in $NaNO_2$, which also manifests itself in the crystal density. First, the shared contours relating silver atoms are formed in $AgNO_2$. Silver transfers a considerably larger charge to the plane of anions than sodium, so that the noticeable charge density is formed in the interanionic region, which is also clearly seen from the crystal density. The existence of common electron-density contours for neighboring anions and also the small electron-charge maximum between these contours lead to the assumption that covalent bonding exists between the anions.

The charge redistribution between the sublattices is described by the difference density $\Delta\rho(\mathbf{r})$ shown for $NaNO_2$ and $AgNO_2$ in Fig. 3. It is seen that the difference densities in the vicinity of oxygen atoms and inside the anionic group are close for both compounds. The most pronounced differences are seen in the vicinity of the cations, which is quite natural because of the considerable difference in the numbers of valence electrons in sodium and silver.

The negative $\Delta\rho(\mathbf{r})$ values are in the direct vicinity of nitrogen and oxygen nuclei and in the vicinity of cations. The maxima of the difference density correspond to two points located symmetrically with respect to the N–O bond and also to the middle points of these bonds. The values of the two ending maxima are different. The larger value has the maximum located closer to the cation along the O–Na bond length. At the same time, the far maximum is deformed in a such way that it provides the maximum charge along the N–O bond. This distribution of the difference density is qualitatively similar to the experimental deformation density determined in [6, 8]. Thus, the sublattice interactions are most pronounced between the oxygen and nitrogen sublattices and result in the complicated redistribution of the electron charge between these sublattices, which can be considered as covalent bonding. The negative $\Delta\rho(\mathbf{r})$ values in the vicinity of the metal are explained by the charge transfer from the metal sublattice to the nitrogen and oxygen sublattices, which provides the formation of the ionic component of the chemical bond.

Now, compare in more detail the calculated difference density in $NaNO_2$ with the known experimental data.

The deformation density in $NaNO_2$ was studied by the X-ray diffraction method elsewhere [6, 8]. As was already indicated, in the vicinity of the nitrite group, the deformation-density maps obtained in these studies are qualitatively similar to the difference-density maps in the *bc* plane (Figs. 3 and 4). Figure 4 shows the calculated map of $\Delta\rho(\mathbf{r})$ for $NaNO_2$ in the plane perpendicular to the N–O bond (the left-hand side of Fig. 4) and the experimental deformation density obtained in the same plane in [6] (the right-hand side of Fig. 4). The negative values of the deformation density are indicated by dashed lines. This figure clearly shows the qualitative similarity of the difference and the deformation densities. The difference density is negative at the sites of nitrogen and oxygen nuclei and also in the regions that have the shape of *p*-orbitals oriented normally to the N–O bond. The maxima of difference density are located in the middle of this bond (the value 0.2) and lower than the nitrogen and oxygen nuclei (the value 0.1). Thus, the interaction between nitrogen and oxygen atoms in the crystal results in the electron-charge transfer from the peripheral regions of the atoms to the regions along the bond between them. This electron-charge redistribution is typical of covalent chemical bonding.

The similarity of the difference and deformation densities is explained by the fact that the most pronounced hybridization effects in nitrites take place between the nitrogen and oxygen sublattices, whereas

the hybridization between the other sublattices and inside the sublattices is much weaker.

ACKNOWLEDGMENTS

This work was supported by the "Russian Universities" Program, project no. UR 01.01.047.

REFERENCES

1. T. Gohda, M. Ichikawa, T. Gustafson, and I. Olovson, Phys. Rev. B **63**, 014101 (2001).
2. C. Duan, W. N. Mei, R. W. Smith, *et al.*, Phys. Rev. B **63**, 144105 (2001).
3. Yu. N. Zhuravlev and A. S. Poplavnoĭ, Zh. Strukt. Khim. **42** (5), 860 (2001).
4. G. H. Bachelet, D. R. Hamann, and M. Schluter, Phys. Rev. B **26**, 4199 (1982).
5. Yu. N. Zhuravlev, Yu. M. Basalaev, and A. S. Poplavnoĭ, Izv. Vyssh. Uchebn. Zaved., Fiz., No. 3, 96 (2000).
6. T. Gohda, M. Ichikawa, T. Gustafson, and I. Olovson, Acta Crystallogr., Sect. B: Struct. Sci. **56**, 11 (2000).
7. S. Ohba and Y. Saito, Acta Crystallogr., Sect. B: Struct. Crystallogr. Cryst. Chem. **37**, 1911 (1981).
8. M. Okuda, S. Ohba, Y. Saito, *et al.*, Acta Crystallogr., Sect. B: Struct. Sci. **46**, 343 (1990).

Translated by L. Man

Crystallography Reports, Vol. 47, No. 5, 2002, pp. 748–752. Translated from Kristallografiya, Vol. 47, No. 5, 2002, pp. 814–818.

STRUCTURES OF INORGANIC COMPOUNDS

Crystal Structure of Cation-Deficient Calciohilairite and Possible Mechanisms of Decationization in Mixed-Framework Minerals

D. Yu. Pushcharovskiĭ*, I. V. Pekov*, M. Pasero, E. R. Gobechiya*, S. Merlino**, and N. V. Zubkova***

**Faculty of Geology, Moscow State University, Vorob'evy gory, Moscow, 119899 Russia*

e-mail: dmitp@geol.msu.ru

***Department of Earth Sciences, University of Pisa, Pisa, 56126 Italy*

Received March 20, 2002

Abstract—The crystal structure of cation-deficient calciohilairite from the Lovozero massif (the Kola Peninsula) was established (Siemens P4 diffractometer, MoK_α radiation, 409 independent reflections with $|F| > 4\sigma(F)$, anisotropic refinement, $R(F) = 0.037$). Like other representatives of the hilairite structure type, calciohilairite is described by the space group $R32$ ($a = 10.498(2)$ Å, $c = 7.975(2)$ Å, $Z = 3$), whereas its unit-cell parameter c is reduced by a factor of two. Two positions in the cavities of the mixed zirconium–silicon–oxygen framework are occupied by Ca and Na cations in the ratio of 1 : 1 (partly occupied $A(1)$ position) and oxonium cations $(H_3O)^+$ and H_2O molecules in the ratio of 1 : 2 ($A(2)$ position). Different types of isomorphous replacement accompanying the formation of cation-deficient mixed-framework structures (lovozerite, vinogradovite–lintisite, labuntsovite–nenadkevichite, eudialyte, etc.) are considered. Based on the X-ray diffraction data, the following scheme of isomorphism in the structure of cation-deficient calciohilairite is suggested: $2Na^+ + H_2O \rightleftharpoons 0.5Ca^{2+} + 1.5\square + (H_3O)^+$, where $\square$ is a vacancy. © *2002 MAIK "Nauka/Interperiodica".*

INTRODUCTION

Calciohilairite $CaZrSi_3O_9 \cdot 3H_2O$ is a rare mineral attributed to the hilairite group according to its composition, X-ray diffraction data, and crystal morphology. This mineral was discovered in hydrothermalites of alkaline granites from the Golden Horn batholith (Washington, USA) [1] and was also found in the derivatives of the Mont-Saint-Hilaire and Saint-Amable agpaitic massifs (Quebec, Canada) [2]. Intermediate members of the calciohilairite–hilairite ($Na_2ZrSi_3O_9 \cdot 3H_2O$) series were discovered in the Strange Lake alkaline complex [3]. Recently, calciohilairite was found in the endocontact zone of the Lovozero alkaline massif (the Kola Peninsula), where it is the major zirconium-containing mineral of hydrothermalites developed in cavernous albitized murmanite–eudialyte lujavrites from the Flora Mountain. Isometric white and coffee-brown, usually split, crystals (up to 0.4 mm in size) of calciohilairite formed by the {012} faces of a rhombohedron and {110} faces of the hexagonal prism occur in vugs in association with aegirine, natrolite, lorenzenite, labuntsovite-Mn, kuzmenkoite-Mn, carbonate-fluorapatite, and vuoriyarvite-K [4].

The structures of several minerals of the hilairite group were studied, among which are hilairite [5], komkovite [6], sazykinaite-(Y) [7], pyatenkoite-(Y) [8], and calciohilairite [1]. The structure of hilairite was reported for the first time in [5] and was described as a mixed framework consisting of helical chains of $[Si_3O_9]$ linked via Zr-octahedra. The cavities of the framework are occupied by the Na cations and H_2O molecules. In addition to hilairite, the structures of its rare-earth analogue sazykinaite-(Y) [7], pyatenkoite-(Y) [8], and komkovite [6] were also established. In the crystal structure of sazykinaite-(Y), one of two Zr positions is occupied by Y and rare-earth cations. In pyatenkoite-(Y), the Zr ions in two positions are completely replaced by Y + *REE* and Ti + Nb. The structure of komkovite differs from hilairite in that Na atoms are replaced by Ba atoms in the ratio 2 : 1. The crystal structure of calciohilairite has not been established. In the first study of this mineral, which was devoted to its mineralogical description [1], it was only noted that the unit-cell parameter a of this mineral is twice as large as that of hilairite ($a = 20.870(4)$ Å, $c = 16.002(4)$ Å, space group $R32$). However, the poor quality of single crystals used in this investigation cast some doubt on the reliability of the crystallographic and geometric characteristics of calciohilairite. A new occurrence of calciohilairite at the Lovozero alkaline massif, where single crystals suitable for X-ray diffraction analysis were found, and the presently available X-ray facilities gave new impetus to the investigation of the structure of this mineral.

1063-7745/02/4705-0748$22.00 © 2002 MAIK "Nauka/Interperiodica"

EXPERIMENTAL

Electron microprobe analysis of seven calciohilairite crystals (Table 1) revealed the following characteristic features:

—the presence of Nb and Ti impurities, which, apparently, replace Zr; in all the analyses, the Si/Σ(Zr + Nb + Ti + Hf) ratio was approximately 3 : 1;

—very wide variations in the Ca : Na ratio, including variations within one crystal, which ranges from sodium-free zones (i.e., from virtually pure calciohilairite) to a calcium-containing variety of hilairite $(Na_{2-x},Ca_{x/2})ZrSi_3O_9 \cdot 3H_2O$, where $x < 1$; the latter is usually found in crystal cores;

—a substantial content of K and Sr impurities (often K > Na);

—an overall deficiency of large low-valence cations (Na + K + Ca + Sr + Mn + Zn); the sum of their formula coefficients ranges from 0.6 to 1.0 with respect to three Si atoms.

Thus, the mineral from the Lovozero massif is very compositionally inhomogeneous and, on the whole, can be assigned to a cation-deficient variety of calciohilairite.

A single crystal of calciohilairite of dimensions $0.30 \times 0.20 \times 0.22$ mm was selected using a Weissenberg camera. The X-ray diffraction data were collected from this crystal on an automated Siemens P4 diffractometer. The crystallographic characteristics and the details of X-ray data collection and structure refinement are listed in Table 2.

The parameters of the trigonal unit cell a = 10.498(2) Å, c = 7.975(2) Å were determined by the least-squares refinement with the use of the angular parameters of 30 reflections in the range $19° \le 2\theta \le 25°$. Both reduced parameters are approximately half as large as those reported earlier [1]. The ψ-scan empirical absorption correction was introduced. The structure was refined within the space group $R32$ using the SHELX97 program package [9] based on the modified atomic coordinates determined earlier [5]. The subsequent stages, including the refinement of the electron contents in three cation positions (A(1), A(2), and Zr) and the refinement based on the anisotropic thermal parameters, reduced the $R(F)$ factor to 0.037. The cation distribution thus obtained confirmed that the Zr position is completely occupied, whereas the intraframework position A(1) is occupied by the Ca and Na cations in the ratio 1 : 1 (calculated from the electron content) by only 33%. In spite of the shortened distances (~1.84(3) Å) between the symmetrically related (Ca,Na) atoms located in the A(1) position, the partial occupancy of the latter excludes any direct contact between these atoms. For this reason, the maximum occupancy of the A(1) position cannot be higher than 50% (one Ca atom per formula unit). An increase in the cation content in the A(1) position of the hilairite structure should be accompanied by a twofold increase in the unit-cell parameter c. The fact that the (Ca,Na) cations occupy the A(1) position is indirectly confirmed by the octahedral coordination of these cations. This coordination is formed by the water molecules located in the A(2) position and the O(1) anions. The A(1) position was also found in the structures of other minerals of the hilairite group, whereas the A(2) position in the new specimen, unambiguously revealed from a difference electron density synthesis, was observed for the first time. Taking into account the requirement of the electroneutrality of the structural formula and the presence of water in the mineral structure, we assumed that the A(2) position is occupied by oxonium cations H_3O^+ and water molecules in the ratio 1 : 2. The presence of the mobile cations (H_3O^+) in the A(2) position accounts for the high thermal parameter of the atoms in the A(2) position (Table 3). Recently, similar thermal parameters of the oxonium cations were found in the structure of tsepinite-(Na), a representative of the labuntsovite group [10]. The results of the X-ray diffraction analysis confirmed the formula $(Ca,Na)_{0.67}ZrSi_3O_9[H_2O,H_3O]_3$. The fact that this formula is slightly different from the average composition of the mineral (the right column in Table 1), in particular, the absence of K, is attributed to the individual features of the grain under investigation. On the whole, the weight contents of the components corresponding to the idealized structural formula (CaO, 4.79; Na_2O, 2.65; ZrO_2, 31.90; SiO_2, 46.66; H_2O,

Table 1. Variations in the chemical composition of the minerals of the calciohilairite–hilairite series from the Flora Mountain (Lovozero massif) according to the results of 17 electron microprobe analyses for seven crystals (Camebax SX 50)

Component	Ranges, wt %	Average compositions, wt %	Average cation content (with respect to Si = 3)
Na_2O	0.00–2.4	0.28	0.04
K_2O	0.4–3.2	2.09	0.18
CaO	4.1–11.5	6.96	0.50
SrO	0.00–1.3	0.67	0.03
MnO	0.00–0.9	0.89	0.01
ZnO	0.00–0.6	0.18	0.01
SiO_2	41.6–47.4	44.90	3
TiO_2	0.5–1.4	0.81	0.04
ZrO_2	26.8–31.1	29.23	0.95
HfO_2	0.0–0.8	0.31	0.01
Nb_2O_5	0.3–3.3	1.76	0.05
Sum		87.44	

Note: In all the analyses, the Ba, Mg, Fe, Al, *REE*, F, and Cl contents were lower than the detection limits.

Table 2. Crystallographic characteristics and details of the X-ray diffraction study

Formula	$(Ca,Na)_{0.67}ZrSi_3O_9[H_2O,H_3O]_3$
Unit-cell parameters, Å	a = 10.498(2), c = 7.975(2)
Space group; Z	$R32$; 3
Unit cell volume V, Å^3	761.1(2)
Calculated density ρ, g/cm^3	2.543
Absorption coefficient μ, mm^{-1}	1.679
Molecular weight	1165.54
F_{000}	565.0
Diffractometer	Siemens P4
Wavelength, Å	0.71073
$2\theta_{min}$, deg	6.80
$2\theta_{max}$, deg	59.72
Total number of reflections	1427
Total number of independent reflections	425
Number of independent reflections with $\|F\| > 4\sigma(F)$	409
R_{int}	0.044
Number of parameters used in the refinement	33
R_F	0.037
$w_R(F^2)$	0.089
GOOF	1.235
$\Delta\rho_{max}$, e/Å^3	0.80
$\Delta\rho_{min}$, e/Å^3	–0.48

14.00; Σ = 100 wt %) are close to the ranges of the composition variations of calciohilairite determined by the electron microprobe analysis (Table 1). The final coordinates of the basis atoms and thermal parameters are listed in Table 3. The results of the calculations of the valence balance [11, 12] are given in Table 4. The interatomic distances in the coordination polyhedra have standard values (the average Zr–O, Si–O, and (Ca,Na)–O distances are 2.077, 1.625, and 2.410 Å, respectively). The projection of the structure obtained using the ATOMS program [13] is shown in the figure.

RESULTS AND DISCUSSION

The crystal structure of cation-deficient calciohilairite is characterized by a twofold decrease in the size of the unit cell compared to the unit cells of other representatives of this mineralogical group (hilairite, komkovite, and pyatenkoite-(Y)), with the space group $R32$ being retained. In addition, the structure of the new mineral also has a position that is not found in other representatives of this group. This position is occupied by the H_3O^+ cations and water molecules. The configuration of the zirconium–silicon–oxygen mixed framework remains virtually unchanged. The presence of the Ca or Na cations in the $A(1)$ position excludes the simultaneous presence of the oxonium cation in the $A(2)$ position and, on the contrary, allows water molecules to occupy the latter position. The octahedral coordination of the (Ca,Na) cations is formed by three water molecules and three O(1) atoms at distances of 2.30(2) and 2.52(1) Å, respectively. Unlike the completely occupied $A(2)$ position, the existence of vacancies in the $A(1)$ position is favorable for the simultaneous presence of the large oxonium cations H_3O^+ in the $A(2)$ position. The oxonium cation in the $A(2)$ position is surrounded by the O^{2-} anions located at rather large distances (2.987(6) Å), which is consistent with the H_3O^+–O distance typical of this cation (~2.57 Å). In this case, the oxonium cations can form weak hydrogen

Table 3. Coordinates, multiplicities (Q), occupancies (q), and thermal parameters for the basis atoms

Position*	*x/a*	*y/b*	*z/c*	*Q*	*q*	$U_{eq}^{**} \times 10^2$, Å^2
Zr	0.0	0.0	0.0	0.1667	0.1667	1.61(3)
A(1)	0.0	0.0	0.615(2)	0.3333	0.1117	9.6(5)
A(2)	0.0	0.201(2)	0.5	0.5	0.5	14.8(5)
Si	0.4141(2)	0.4141(2)	0.5	0.5	0.5	1.90(5)
O(1)	0.0951(6)	0.1860(3)	0.8488(4)	1	1	2.55(7)
O(2)	0.6475(6)	0.0	0.0	0.5	0.5	3.8(2)

* $A(1)$ = Ca, Na; $A(2)$ = H_2O, H_3O.

** The parameters U_{eq} were calculated from the anisotropic atomic displacements.

bonds with O(1) atoms, which were taken into account in calculations of the valence balance [12].

The total water content in the *A*(2) position (H_3O^+ + $2H_2O$ per structural formula) is in complete agreement with the accepted formula of hilairite.

The constitution and the possible mechanism of the formation of cation-deficient calciohilairite are not only of interest by themselves but also might help one to elucidate the nature of partially decationized varieties of many zeolite-like minerals that are widespread in hydrothermally altered alkaline rocks and their derivatives.

The isomorphic relationship between hilairite and "full-cation" calciohilairite is rather simple ($2Na^+ \rightleftharpoons Ca^{2+} + \square$). This scheme often occurs in minerals, particularly in zeolites (analcime–wairakite, chabazite, gmelinite, etc.). In some specimens, the additional water molecules are located in the vacant cavities ($2Na^+ \rightleftharpoons Ca^{2+} + H_2O$) and, thus, lower the symmetry. As an example, we refer to zeolites of the natrolite $Na_2(Al_2Si_3O_{10}) \cdot 2H_2O$–scolecite $Ca(Al_2Si_3O_{10}) \cdot 3H_2O$ series [14].

However, the above schemes of isomorphism alone cannot explain the constitution of cation-deficient calciohilairite. Proceeding from the conditions of the local valence balance, it seems to be highly improbable that a deficiency of positive charge in this mineral (resulting from the overall deficiency of large extraframework cations) can be compensated with the partial replacement of O atoms in the framework by OH groups. The data on the occupancies of the extraframework positions and the cation–anion distances lead to the conclusion that the residual positive charge is accounted for by the oxonium cations. As a result, the general scheme of isomorphism, which leads from hilairite $Na_2ZrSi_3O_9 \cdot 3H_2O$ to cation-deficient calciohilairite, can be represented as follows: $2Na^+ + H_2O \longrightarrow 0.5Ca^{2+} + 1.5\square + (H_3O)^+$.

Taking into account the zonal structures of some crystals found at the Flora Mountain, it can be assumed that initially they consisted of hilairite. The subsequent decrease in alkalinity of hydrothermal solutions led to ion exchange resulting either in partial or complete leaching of Na and uptake of larger cations (Ca^{2+}, H_3O^+, K^+, Sr^{2+}), particularly in outer zones of individuals. The incorporation of the oxonium cations into the channels of the mineral structure seems to be highly probable, because it is well known that the acid–base equilibrium in solutions is displaced to the $(H_3O)^+$ ions under almost neutral conditions.

The fact that the leaching of Na from many zeolite-like rare-element minerals is a process readily occurring at the late-hydrothermal evolution stages of alkaline massifs is supported by abundant evidence, including numerous experimental data (for example, the information on steenstrupine [15]). In this case, a deficiency of positive charge can be compensated in a number of ways. For example, isomorphism according to the schemes $Na^+ + O^{2-} \longrightarrow \square + OH^-$ and $Na^+ + O^{2-} \longrightarrow H_2O + OH^-$ was substantiated for Zr and Ti silicates of the lovozerite group and for Ti silicates of the vinogradovite–lintisite polysomatic series [16–18].

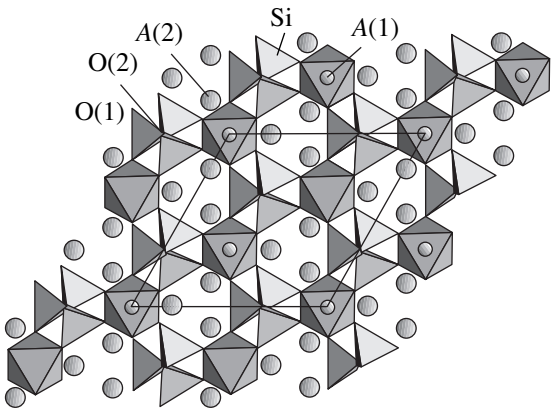

Structure of cation-deficient calciohilairite projected onto the (001) plane; *A*(1) = Ca, Na; *A*(2) = H_2O, H_3O.

The former scheme "accompanies" the transformation of vinogradovite $Na_4Ti_4(Si_2O_6)_2 \cdot [(Si,Al)_4O_{10}]O_4(H_2O,Na,K)_3$ into the so-called "vinogradovite II" $Na_2O_2Ti_4(Si_2O_6)(Si_4O_{10})O_2(OH)_2 \cdot 2H_2O$ [16].

These mechanisms seem to be the most probable also for the orthorhombic representatives of the labuntsovite group, whose structures contain narrow channels [19]. In contrast, the Na^+ cations in the structures of monoclinic labuntsovite-like phases and minerals of the eudialyte group with large cavities in the framework can be replaced by oxonium cations $(H_3O)^+$ [10, 20]. The leaching of Na accompanied by hydration is also typical of pyrochlore, catapleiite, gaidonnayite, elpidite, and a number of other minerals. However, the mechanism of this process should be elucidated for many of these minerals.

To summarize, the results of the study of cation-deficient calciohilairite from the Lovozero massif allowed us to propose the most crystallochemically probable structure model for an oxonium-stabilized partly decationized zeolite-like mineral with a mixed

Table 4. Calculated valence balance

Atom	O(1)	O(2)	H_2O
Ca, Na	0.057		0.108
Zr	0.687		
Si	1.044	$0.952^{[\times 2]}$	
H_3O^+	0.044		
Σ	1.832	1.904	0.108

(Zr,Nb,Ti)-Si-framework and describe one of the mechanisms of the "gentle" leaching of sodium from these compounds. This phenomenon is widespread in nature.

ACKNOWLEDGMENTS

We are grateful to R.K. Rastsvetaeva for valuable advice and helpful discussions.

This study was supported by the Russian Foundation for Basic Research (project nos. 00-05-65399 and 00-15-96633) and by the Program "Russian Universities". S. Merlino and M. Pasero acknowledge the support (40%) of the MURST project ("Structural Imperfections in Minerals: Microstructure, Modular Aspects, and Structure Modulation"). D.Yu. Pushcharovskiĭ acknowledges the support of the program existing within the framework of the Russian–Italian scientific cooperation (project no. 62).

REFERENCES

1. R. C. Boggs, Amer. Mineral. **73**, 1191 (1988).
2. L. Horvath, E. Pfenninger-Horvath, R. A. Gault, and P. Tarasoff, Mineral. Rec. **29** (2), 83 (1998).
3. T. C. Birkett, R. R. Miller, A. C. Roberts, and A. N. Mariano, Can. Mineral. **30**, 191 (1992).
4. I. V. Pekov, *Lovozero Massif: History, Pegmatites, Minerals* (Ocean Pictures Ltd, Moscow, 2000).
5. G. D. Ilyushin, A. A. Voronkov, N. N. Nevskiĭ, *et al.*, Dokl. Akad. Nauk SSSR **260** (5), 1118 (1981) [Sov. Phys. Dokl. **26**, 916 (1981)].
6. E. V. Sokolova, A. V. Arakcheeva, and A. V. Voloshin, Dokl. Akad. Nauk SSSR **320** (6), 1384 (1991) [Sov. Phys. Dokl. **36**, 666 (1991)].
7. R. K. Rastsvetaeva and A. P. Khomyakov, Kristallografiya **37** (6), 1561 (1992) [Sov. Phys. Crystallogr. **37**, 845 (1992)].
8. R. K. Rastsvetaeva and A. P. Khomyakov, Dokl. Akad. Nauk **351** (1), 74 (1996).
9. G. M. Sheldrick, *SHELX97: Program for the Solution and Refinement of Crystal Structures* (Siemens Energy and Automation, Madison, 1997).
10. R. K. Rastsvetaeva, N. I. Organova, I. V. Rozhdestvenskaya, *et al.*, Dokl. Akad. Nauk **371** (3), 336 (2000).
11. N. E. Brese and M. O'Keeffe, Acta Crystallogr., Sect. B: Struct. Sci. **47**, 192 (1991).
12. G. Ferraris and G. Ivaldi, Acta Crystallogr., Sect. B: Struct. Sci. **44**, 341 (1988).
13. E. Dowty, *Atoms 3.2: A Computer Program for Displaying Atomic Structures* (Kingsport, 1995).
14. G. Gottardi and E. Galli, *Natural Zeolites* (Springer-Verlag, Berlin, 1985).
15. E. Makovicky and S. Karup-Moller, Neues Jahrb. Mineral., Abh. **140** (3), 300 (1981).
16. S. Merlino and M. Pasero, EMU Notes Mineral. **1**, 297 (1997).
17. N. A. Yamnova, Yu. K. Egorov-Tismenko, and I. V. Pekov, Kristallografiya **46** (6), 1019 (2001) [Crystallogr. Rep. **46**, 937 (2001)].
18. U. Kolitsch, D. Yu. Pushcharovsky, I. V. Pekov, and E. Tillmans, in *Abstracts of the 19th European Crystallographic Meeting, Nancy, 2000*, p. 363.
19. I. V. Pekov, N. V. Chukanov, A. P. Khomyakov, *et al.*, Zap. Vseross. Mineral. O-va **128** (3), 72 (1999).
20. I. A. Ekimenkova, R. K. Rastsvetaeva, and N. V. Chukanov, Dokl. Akad. Nauk **371**, 5 (2000).

Translated by T. Safonova

Crystallography Reports, Vol. 47, No. 5, 2002, pp. 753–758. Translated from Kristallografiya, Vol. 47, No. 5, 2002, pp. 819–824.

STRUCTURES OF INORGANIC COMPOUNDS

Simulation of Defects Formed by Cations of Bivalent and Trivalent Metals in the Structure of Potassium Dihydrogen Phosphate: A Computational Technique

T. A. Eremina*, N. N. Eremin, V. A. Kuznetsov*, N. G. Furmanova*, and V. S. Urusov****

** Shubnikov Institute of Crystallography, Russian Academy of Sciences, Leninskiĭ pr. 59, Moscow, 11733 Russia*

e-mail: furm@ns.crys.ras.ru

*** Moscow State University, Vorob'evy gory, Moscow, 119899 Russia*

Received November 15, 2001

Abstract—This paper reports on the results of crystal chemical analysis and computer simulation of the defect structure of potassium dihydrogen phosphate (KDP) containing impurities of bivalent and trivalent metals. It is shown that these impurities can form defect centers of different types: isolated centers formed by M^{3+} and Ni^{2+} ions and, in part, by Co^{2+} ions at interstitial sites, chains composed of M^{2+} impurity ions with radii from ≈0.65 to ≈1.1 Å, and centers created through the substitution of large-sized bivalent cations for potassium ions either with the formation of additional potassium vacancies or through the heterovalent isomorphism mechanism. The calculations are performed using different-type interatomic interaction potentials, and a comparative analysis of the results obtained is carried out. © *2002 MAIK "Nauka/Interperiodica".*

INTRODUCTION

In order to elucidate how local stresses produced by impurities affect the crystallization (i.e., the structural mechanism of impurity effect), it is necessary to know the structure of defect regions and the strains induced by these regions in the crystal matrix. In this work, we performed a crystal chemical analysis of the structure of potassium dihydrogen phosphate (KDP) and a computer simulation of defect centers with the aim of revealing the mechanism of incorporation of bivalent and trivalent impurity metals (with ionic radii varying over a wide range) into the structure. We analyzed the variants of calculations within the purely ionic and ionic–covalent approximations (for bivalent and trivalent cations) and calculations with inclusion of the harmonic potential (for bivalent cations).

COMPUTATIONAL TECHNIQUE

The structure of KDP containing impurities of bivalent (Ni^{2+}, Co^{2+}, Fe^{2+}, Mn^{2+}, Ca^{2+}, Sr^{2+}, and Ba^{2+}) and trivalent (Al^{3+}, Fe^{3+}, Mn^{3+}, Y^{3+}, and La^{3+}) metals was simulated by minimizing the interatomic interaction energy according to the GULP software package [1]. The results obtained in our earlier work [2] concerned with the simulation of a perfect KDP structure were used in calculations. As in [2–4], the effective charges of impurity ions were taken equal to +2.7 e for M^{3+} cations and +1.9 e for M^{2+} cations. The ionic radii used in analysis were taken from [5]. In most cases, the radius of the region adjacent to a defect and characterized by considerable distortions was assumed to be 4.5 Å and the radius of the region beyond which the structure can be considered undistorted was 11.5 Å. The exceptions were the calculations of three-particle impurity clusters in which the above radii were increased to 6.5 and 16.5 Å, respectively.

Earlier [6], we performed a crystal chemical analysis of the KDP structure and demonstrated that impurity cations most probably occupy the interstitial holes *M*1 and *M*2 with the coordinates (0.25, 0.35, 0.125) and (0.75, 0.22, 0.125). Large-sized cations can substitute for K^+ cations. These variants of incorporating ions into the KDP structure were considered for all the cations studied (the calculations in the framework of the purely ionic model were described in detail in [3, 4]). Unlike [3, 4], in the present work, similar calculations were carried out with allowance made for a Morse potential (for bivalent and trivalent cations) and different models of calculating defect centers in the structure were analyzed comparatively.

In [3, 4], the M^{3+}–O bond was treated as purely ionic, even though this bond in the KDP structure is partly covalent in character. The calculations proved that the introduction of a covalent component (Morse potential) into the expression for the M^{3+}–O interatomic interaction potential does not lead to radical changes in the general pattern (Table 1). Therefore, the ionic approximation in the case of defect formation by trivalent metals in the *M*1 and *M*2 holes is quite adequate

Table 1. Energies (eV) of the defect formation by trivalent metals at the *M*1 and *M*2 sites according to partly covalent model 1 and ionic model 2

Ion	Ionic radius, Å	*M*1		*M*2	
		1	2	1	2
Al	0.53	–15.84	–6.90	–14.67	–5.15
Fe	0.55	–14.89	–5.71	–13.32	–4.67
Mn	0.58	–14.38	–5.05	–13.12	–3.13
Y	0.90	–12.11	–1.22	–10.49	0.88
La	1.03	–11.26	1.23	–9.49	2.89

Table 2. Parameters of the M^{3+}–O interatomic interaction potential in the framework of the partly covalent model*

M^{3+}	B_{ij}, eV	ρ_{ij}, eV/Å^6	D_{ij}, eV	σ_{ij}, Å^{-1}	R_0, Å
Al	580.93	0.3118	0.412	1.604	1.91
Mn^{3+}	655.48	0.3214	0.441	1.556	2.03
Fe^{3+}	636.35	0.3239	0.425	1.516	2.11
Y	700.92	0.3588	0.604	1.432	2.40
La	701.96	0.3651	0.676	1.369	2.53

* $V_{ij}(R_{ij}, f) = f^2[Z_iZ_j/R_{ij} + B_{ij}\exp(-R_{ij}/\rho_{ij})] - (1 - f^2)D_{ij}\{\exp[2\sigma_{ij}(R_{ij}^0 - R_{ij})] - 2\exp[\sigma_{ij}(R_{ij}^0 - R_{ij})]\}$.

Table 3. Parameters of the M^{2+}–O interatomic interaction potential in the framework of the partly covalent model

Cation	B_{ij}, eV	ρ_{ij}, eV/Å^6	D_{ij}, eV	σ_{ij}, Å^{-1}	R_0, Å
Ni	1582.5	0.2882	0.43	1.7349	2.11
Co	1491.7	0.2951	0.48	1.6943	2.14
Fe	1207.6	0.3084	0.53	1.6213	2.16
Mn	1007.4	0.3262	0.55	1.5328	2.21
Ca	1090.4	0.3437	0.60	1.4546	2.40
Sr	959.1	0.3721	0.59	1.3437	2.58
Ba	905.7	0.3976	0.69	1.2575	2.76

and quantitatively describes the character of distortions. The parameters of the M^{3+}–O interatomic interaction potential taking into account the Morse potential are listed in Table 2.

All the foregoing is valid only for the incorporation of trivalent impurities into the *M*1 and *M*2 sites, i.e., for the incorporation of ions into commensurate holes. In the case when M^{3+} cations occupy the K site with the M^{3+}–O distances obviously greater than the optimum for trivalent cations, the ionic model cannot correctly describe the incorporation pattern. Indeed, according to calculations within this model, a decrease in the ionic radius in a series of trivalent metals leads to a decrease in the energy of defect formation at the K site, which has no physical meaning. We did not consider the occupation of the K site by trivalent metals, because this situation virtually cannot occur in view of the small ionic radius of these metals.

The calculation of the energy of defects created by bivalent cations is a more complicated problem. The occurrence of cations with radii close to the radius of the potassium cation in the series of these metals requires considering not only the *M*1 and *M*2 sites but also the K sites as really possible. Therefore, in the case of bivalent cations, the M^{2+}–O bond should be treated only within the partly covalent approximation. The introduction of the Morse potential as the covalent term results in a certain rigidity of the metal–oxygen configuration, because this potential is not a function that monotonically decreases with an increase in the distance but rather exhibits a minimum at a distance that is optimum for a particular ion pair. The Morse potential is described by two coefficients, namely, the weighting factor D_{ij} and the softness coefficient σ_{ij} . Furthermore, the Morse potential is characterized by an optimum distance between ions involved in the bond, i.e., the optimum M^{2+}–O distance. This distance is approximately estimated as the sum of the corresponding radii. The parameter D_{ij} is evaluated as the dissociation energy of a single covalent bond with correction for the coordination number [7]. The softness parameter σ_{ij} and the corresponding stiffness parameter ρ_{ij} in the expression for the Born–Mayer potential are related by the known formula $\sigma_{ij} = 1/(2\rho_{ij})$ [8]. The bond ionicity *f* entering into the expression for the Morse potential can be easily estimated using the charges of ions involved in the bond. For example, the ionicity of a bivalent metal with a charge of +1.9 e is equal to 95% and the ionicity of an oxygen atom (–1.14 e) is 57%. As a result, the ionicity of the M^{2+}–O bond is equal to 76%. The M^{2+}–O interatomic interaction parameters thus obtained are given in Table 3. The energies of defect formation (calculated within this model) are presented in Fig. 1 and Table 4. However, it turns out that the results obtained have no physical meaning. Indeed, according to these data, the incorporation into the K site with the formation of a potassium vacancy is most favorable for all the bivalent cations. Therefore, even the inclusion of the Morse potential does not lead to an adequate description of the interactions at distances appreciably longer than the optimum distances.

The reason resides in the form of the Morse potential itself. This situation can be illustrated using the following example (Fig. 2). Let us assume that a cation *A* is in a tetrahedral oxygen environment and all the bond lengths are equal to the optimum distance. This ideal case corresponds to the minimum in the curve of the Morse pair potential. When a polyhedron is distorted (two bonds are shortened and two bonds are lengthened by the same distance ΔR), the energy increases by

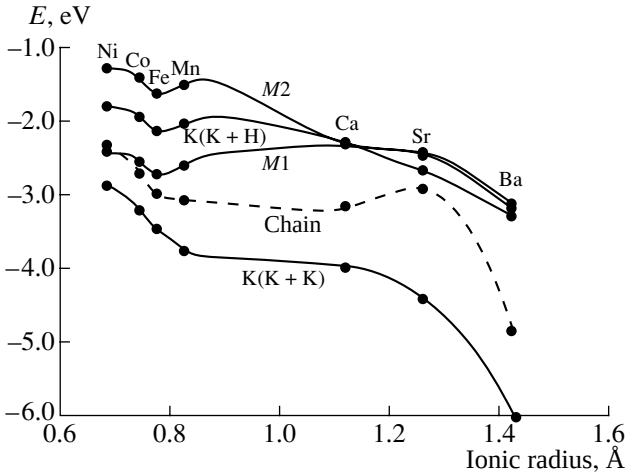

Fig. 1. Energies of the defect formation by bivalent metal ions at the K, *M*1, and *M*2 sites in the framework of the partly covalent model. The solid lines represent the energies of single defects, and the dashed line indicates the energies of clusters.

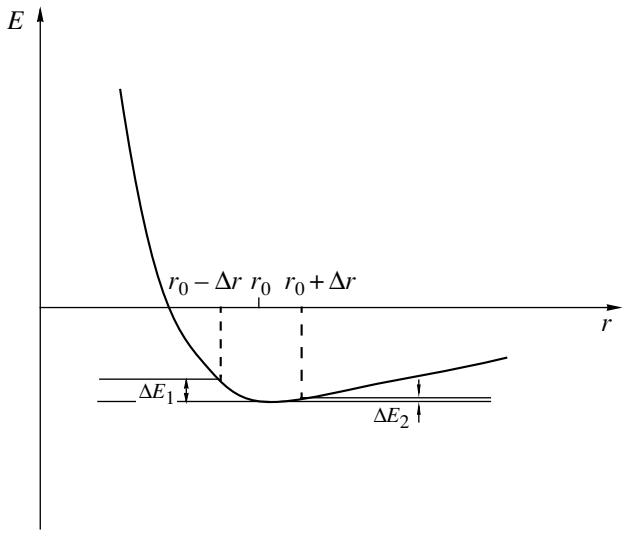

Fig. 2. Schematic representation of the Morse potential.

$2\Delta E1 + 2\Delta E2$. Note that this distortion leads to practically no change in the volume of the coordination polyhedron which remains suitable for the *A* cation. However, if all four distances are lengthened and the volume of the polyhedron becomes inappropriate for the given cation, the energy increases by a considerably smaller value, i.e., $4\Delta E2$ (due to a strong asymmetry of the Morse potential).

In order to solve the above problem, the second-order harmonic component in the form of a symmetric quadratic parabola was additionally introduced into the relationship for the potential. According to Burkert and Allinger [9], the harmonic potential can be used to change the length of covalent bonds. The total interaction potential has the form

$$V_{ij}(R_{ij}, f) = f^2[Z_iZ_j/R_{ij} + B_{ij}\exp(-R_{ij}/\rho_{ij})] - (1 - f^2)D_{ij}\{\exp[2\sigma_{ij}(R_{ij}^0 - R_{ij})] - 2\exp[\sigma_{ij}(R_{ij}^0 - R_{ij})]\} + k(R_{ij}^0 - R_{ij})^2.$$

Here, the optimum distance between the interacting ions and the stiffness parameter *k* are the parameters of the harmonic potential. The stiffness parameter was chosen to be equal to 2.39 in the course of calculations. The choice was governed by the stability of the simulated defects. In the case, when the interaction between ions is described by the harmonic potential, it is necessary to determine the parameter that reduces the range of this potential only to atoms of the first coordination sphere. Reasoning from the crystal chemical analysis of the structure, the last parameter was taken to be equal to 3 Å.

The defect energies calculated in terms of the model accounting for the contribution of the harmonic potential are presented in Fig. 3 and Table 5. Only within this approximation did we succeed in obtaining reasonable ratios between the energies of defect formation at different sites. It should be noted that, since independent criteria for the reliability of the M^{2+}–O interaction potentials including the Morse and harmonic potentials are absent, these potentials can be used only to compare the defect energies in series of bivalent and trivalent metals.

RESULTS AND DISCUSSION

As follows from the data obtained in our recent work [4] and those presented in Tables 4 and 5, the calculations within all three models offer similar results: an increase in the ionic radius in the series of bivalent metals leads to a change in the most favorable variant of incorporating the impurity into the crystal structure, namely, single defects give way to chains. Of the two sites *M*1 and *M*2, the former site is most favorable for all the cations. The *M*1 site corresponds to the minimum energies of defect formation by all trivalent and small-sized bivalent cations. The electroneutrality is provided by removing two potassium cations and one proton upon incorporation of M^{3+} and only two potassium cations upon incorporation of M^{2+} [3, 4]. In the latter case, the nearest hydrogen atom is displaced from the site with the coordinates (0.125, 0.161, 0.125) to the site with the coordinates (0.125, 0.099, 0.125). This leads to a distortion of the hydrogen bond (the O···H bond length increases from 1.27 to 1.29 Å, and the O···H···O angle decreases to 149°). According to calculations, other variants of compensating for the valence result in the instability of the simulated structure.

Table 4. Energies (eV) of the defect formation by bivalent metals at the K, *M*1, and *M*2 sites in the framework of the partly covalent model

Cation	Ionic radius, Å	K(K + H)*	K(K + K)**	*M*1	*M*2	Chain
Ni	0.69	–1.801	–2.86	–2.427	–1.287	–2.321
Co	0.75	–1.93	–3.21	–2.533	–1.416	–2.703
Fe	0.78	–2.147	–3.46	–2.73	–1.634	–3.012
Mn	0.83	–2.033	–3.75	–2.61	–1.511	–3.074
Ca	1.12	–2.331	–3.97	–2.36	–2.327	–3.173***
Sr	1.26	–2.683	–4.39	–2.479	–2.447	–2.915***
Ba	1.42	–3.288	–5.99	–3.21	–3.156	–4.821***

***** Incorporation into the K site with the removal of one potassium cation and hydrogen.
** Incorporation into the K site with the removal of two potassium cations.
*** Cluster consisting of three ions at the K sites.

Table 5. Energies (eV) of the defect formation by bivalent metals at the *K*, *M*1, and *M*2 sites in the framework of the partly covalent model with inclusion of the harmonic potential

Cation	Ionic radius, Å	K(K + H)*	K(K + K)**	*M*1****	*M*2****	Chain
Ni	0.69	0.63	–1.39	–2.40	–0.71	–1.94
Co	0.75	0.14	–1.58	–2.50	–0.92	–2.39
Fe	0.78	–0.31	–2.04	–2.69	–1.16	–2.82
Mn	0.83	–0.63	–2.37	–2.57	–1.08	–2.82
Ca	1.12	–1.75	–3.61	–2.32	–0.96	–2.81***
Sr	1.26	–2.01	–3.83	–2.01	–0.62	–2.38***
Ba	1.42	–3.17	–4.98			–3.92

***** Incorporation into the K site with the removal of one potassium cation and hydrogen.
** Incorporation into the K site with the removal of two potassium cations.
*** Cluster consisting of three ions at the K sites.
**** The last empty squares correspond to the displacement to the K site.

The energies of defect formation by trivalent cations in the framework of both the purely ionic and partly covalent models regularly increase with an increase in the ionic radius (Table 1). This suggests that the larger the size of cations, the harder their incorporation into the structure. Since the *M*1 sites in the KDP structure lie in the (100) planes [2], the occupation of a part of them by M^{3+} cations brings about the formation of sparse networks parallel to the (100) and (010) planes. These networks will be referred to as impurity networks of the *first type*. The intersection of these networks gives rise to channels that are extended along the *Z*-axis of the crystal and are filled with impurity ions (at the *A*–*G* sites in Fig. 4).

A more complex situation occurs with defects created by bivalent cations. A comparative analysis of these defects was performed in the framework of the partly covalent model with due regard for the harmonic potential. The calculations demonstrate that an increase in the ionic radius leads to a change in the defect type (Fig. 3, Table 5). Actually, for the smallest-sized Ni^{2+} cations, as for M^{3+} cations, the lowest energy of defect formation is observed in the case of the isolated *M*1 sites. At the same time, Fe^{2+} and Mn^{2+} cations with the highest probability form chain clusters of the *ABDE*… and *ABDF*… types. These chains can make an angle of 60°–75° with the *Z*-axis. The chain formation and its geometric prerequisites were considered in detail in [4]. Systems of these chains form impurity networks of the *second type* in the crystal. Most likely, Co^{2+} cations are statistically distributed over isolated sites and chains.

A closer examination revealed a number of characteristic features. In the case when Ni^{2+} or Co^{2+} cations form a three-particle cluster, they remain at the *M*1 sites. On the other hand, if chains are formed by Fe^{2+} or Mn^{2+} cations, the third participant of a cluster is displaced from the *D* site to the hole of a distant potassium cation (hereafter, the potassium hole) in the course of energy minimization. For Ca^{2+}, Sr^{2+}, and Ba^{2+} cations, all participants of a three-particle cluster are displaced to the potassium holes. Note that, in the framework of

the partly covalent model without regard for the harmonic potential, all participants of a three-particle cluster irrespective of their radius are displaced to the potassium holes. This displacement is explained by the fact that the K site (with the formation of a potassium vacancy) appears to be most favorable within the simple partly covalent model.

In the framework of the partly covalent model with inclusion of the harmonic potential, the displacement of small-sized cations (Fe^{2+} and Mn^{2+}) to the potassium holes can be explained in the following way. The elimination of a large number of atoms during the chain formation in the structure results in the formation of a local region of structural sparseness in which the larger part of the free space is occupied by potassium polyhedra freed from atoms. Therefore, the stabilization of the loose region with Fe^{2+} ions by placing one out of three ions in the potassium hole appears to be more favorable, even though the occupation of the *M*1 holes by these ions is more preferable from the standpoint of crystal chemistry. However, in real crystals, the transfer of the *D* ion from the *M*1 site to the potassium hole is limited by kinetic factors. Indeed, the formation of impurity chains is most likely a step-by-step process: the incorporation of the *A* impurity ion (Fig. 4) creates favorable conditions in the adjacent hole *B*. In turn, after the occupation of this hole, favorable conditions arise in the *D* (or *E*) hole. Consequently, the *D* cation is initially incorporated into the *M*1 site and then migrates to the K site through the channels formed by vacancies arising at potassium and hydrogen sites. This migration in the crystal can be hindered. As a consequence, the vast majority of impurity cations forming clusters occupy the crystal chemically preferable *M*1 sites. In this case, the *D* cations are in a nonequilibrium state and external factors, for example, the heating of the crystal, can facilitate their transfer to the potassium holes. It is quite possible that this is a reason for the improvement in the optical properties of KDP crystals and the relieving of internal stresses in them in the course of annealing at temperatures of 140–180°C [10, 11]. In [10, 11], the authors explained improvement in the crystal quality by the structural changes in internal defects without going into details of their structure.

For large-sized bivalent cations with a radius larger than 1.1 Å, the incorporation into the *M*1 sites is energetically unfavorable (Fig. 3, Table 5). These ions substitute for potassium ions in the structure and form defects of the *third type*. The compensation for the valence is provided by the formation of either potassium vacancies or hydrogen vacancies; in this case, the former variant is more preferable (Table 5). Moreover, it should be noted that the substitution of barium ions for potassium ions according to the heterovalent isomorphism mechanism $K^+ + P^{5+} = Ba^{2+} + Si^{4+}$ widely occurs in natural minerals. A similar substitution under conditions of laboratory experiments is confirmed by the continued presence of noticeable amounts of silicon

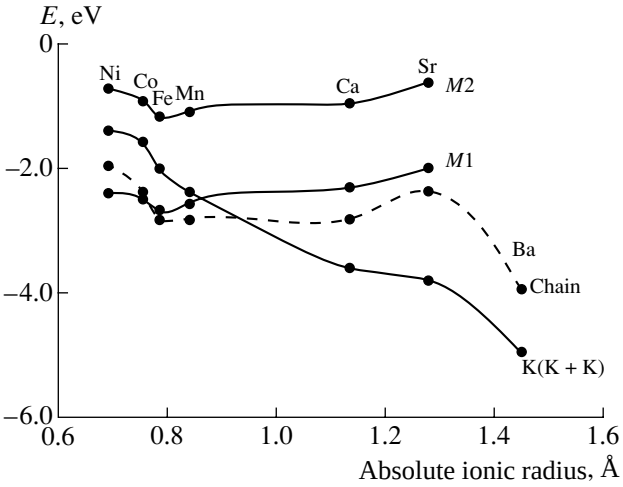

Fig. 3. Energies of the defect formation by bivalent metal ions at the K, *M*1, and *M*2 sites in the framework of the partly covalent model with inclusion of the harmonic potential. The solid lines represent the energies of single defects, the dashed line corresponds to the energies of clusters, and the closed circles indicate the energy of the defect formed through the heterovalent isomorphism mechanism.

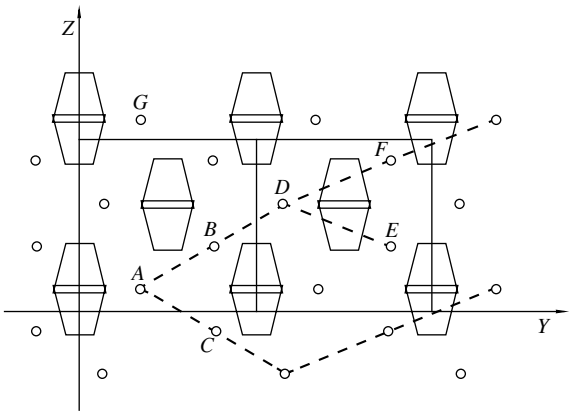

Fig. 4. Orientation of impurity chains in the (100) plane. Partly overlapping PO_4 tetrahedra are shown. ○ is an *M*1 interstitial site.

in KDP mother solutions. This variant of the substitution was calculated only for Ba^{2+} cations. It is found that the energy of formation of the double defect center is equal to –5.12 eV, which corresponds to the minimum energy for the barium cation.[1] The defect energy computed within the same model in the case of a simple substitution is equal to –4.98 eV; i.e., it is slightly higher than that for the substitution through the heterovalent isomorphism mechanism. It follows from Table 5 that, for large-sized bivalent cations, the minimum energies of defect formation are observed in the case when the defects are created upon incorporation of the impurity into the K site with removal of an addi-

[1] The calculations were carried out within the partly covalent model with allowance made for the harmonic potential.

tional potassium atom. Therefore, the K site appears to be preferable for large-sized cations. These cations are incorporated into the K sites and either substitute for the K^+ ions with the formation of additional potassium vacancies or form complex defect centers through the heterovalent isomorphism mechanism. It seems likely that, in real crystals, the incorporation proceeds according to both substitution mechanisms.

Thus, the impurity ions of bivalent and trivalent metals form defect centers of the following three types: (i) the isolated defect centers occupying channels along the *Z*-axis of the crystal (for M^{3+}, Ni^{2+}, and Co^{2+} cations), (ii) the impurity chain clusters oriented at an angle of 60°–75° with respect to the *Z*-axis of the crystal (for Fe^{2+}, Mn^{2+}, and, partly, Co^{2+} cations), and (iii) the defect centers created at the K sites both with the formation of potassium vacancies and through the heterovalent isomorphism mechanism.

The formation of different-type defect centers is responsible for different degrees of strain of the KDP crystal structure. A comparison of the energies of defect formation shows that, compared to M^{2+} ions, M^{3+} ions induce weaker local stresses in the structure.[2] Although Ni^{2+} and, partly, Co^{2+} ions form defect centers similar to those created by M^{3+} ions, bivalent ions produce stronger local stresses in the structure. Even stronger stresses arise when impurity chains are formed by M^{2+} cations. In contrast, the incorporation of Ba^{2+} cations into the K sites either with the formation of additional vacancies or through the heterovalent isomorphism mechanism ($K^+ + P^{5+} = M^{2+} + Si^{4+}$) generates weaker stresses in the series of bivalent metals. In the last case, a somewhat smaller radius of Ba^{2+} ions as compared to that of K^+ ions is compensated for by the larger size of SiO_4 polyhedra. Moreover, unlike the preceding cases, this variant of the substitution does not require the formation of additional vacancies.

CONCLUSIONS

The results of our investigation have demonstrated that the incorporation of trivalent impurities into the KDP structure is adequately described within the ionic approximation. At the same time, the mechanism of incorporation of bivalent cations has defied correct interpretation even in terms of the partly covalent model. In this respect, the potential involving the harmonic component was proposed for describing bivalent cations. The defects formed by trivalent cations were also considered in the framework of the partly covalent approximation. This made it possible to carry out a qualitative comparative analysis of the incorporation of bivalent and trivalent impurities.

The impurities of bivalent and trivalent metals form defect centers of different types in the KDP structure. These centers generate local stresses in the crystal matrix and, thus, produce different strains of the crystal structure. The calculated energies of defect formation and the performed analysis of distortions of the crystal structure in the nearest environment of impurity ions allowed us to draw the inference that the minimum stresses arise upon incorporation of trivalent cations. The bivalent metals, which either form impurity chains in the structure or substitute for the K^+ ions at the potassium sites (in the case of large-sized M^{2+} cations), give rise to stronger stresses.

[2] A comparison was performed within the partly covalent model, because the purely ionic model, as applied to bivalent cations, has no physical meaning and the harmonic potential was not used in analyzing trivalent ions.

ACKNOWLEDGMENTS

This work was supported by the Russian Foundation for Basic Research, project no. 99-03-32557.

REFERENCES

1. J. D. Gale, *GULP: User Manual* (Royal Institution and Imperial College, London, 1992–1994).
2. T. A. Eremina, V. A. Kuznetsov, T. M. Okhrimenko, *et al.*, Kristallografiya **43** (5), 906 (1998) [Crystallogr. Rep. **43**, 852 (1998)].
3. T. A. Eremina, N. N. Eremin, N. G. Furmanova, *et al.*, Kristallografiya **46** (1), 82 (2001) [Crystallogr. Rep. **46**, 75 (2001)].
4. T. A. Eremina, V. A. Kuznetsov, N. N. Eremin, *et al.*, Kristallografiya **46** (6), 1072 (2001) [Crystallogr. Rep. **46**, 989 (2001)].
5. R. D. Shannon and C. T. Prewitt, Acta Crystallogr., Sect. B: Struct. Crystallogr. Cryst. Chem. **25**, 925 (1969).
6. T. A. Eremina, V. A. Kuznetsov, T. M. Okhrimenko, *et al.*, Kristallografiya **41** (4), 717 (1996) [Crystallogr. Rep. **41**, 680 (1996)].
7. *Properties of Inorganic Compounds*, Ed. by A. I. Efimov (Khimiya, Leningrad, 1983).
8. V. S. Urusov and N. N. Eremin, Phys. Chem. Miner. **22** (3), 151 (1995).
9. U. Burkert and N. Allinger, *Molecular Mechanics* (American Chemical Society, Washington, 1982; Mir, Moscow, 1986).
10. K. Fujioka, S. Matsuo, T. B. Kanabe, *et al.*, J. Cryst. Growth **181**, 226 (1997).
11. Y.-J. Fu, Z.-S. Gao, S.-L. Wang, *et al.*, Cryst. Res. Technol. **35** (2), 177 (2000).

Translated by O. Borovik-Romanova

Crystallography Reports, Vol. 47, No. 5, 2002, pp. 759–767. Translated from Kristallografiya, Vol. 47, No. 5, 2002, pp. 825–833.

STRUCTURES OF INORGANIC COMPOUNDS

Precision X-ray Diffraction and Mössbauer Studies and Computer Simulation of the Structure and Properties of Malayaite $CaSnOSiO_4$

N. N. Eremin, V. S. Urusov, V. S. Rusakov, and O. V. Yakubovich

Moscow State University, Vorob'evy gory, Moscow, 119899 Russia

e-mail: neremin@mail.ru

Received January 11, 2002

Abstract—The structure and some physical properties of malayaite $CaSnOSiO_4$ have been studied by the precision X-ray diffraction, Mössbauer spectroscopy, and computer simulation of the structure. The unit-cell parameters $a = 7.152(2)$ Å, $b = 8.888(2)$ Å, $c = 6.667(2)$ Å, $\beta = 113.37(2)°$, $V = 389.0(3)$ Å^3, and $\mu r = 0.68$ are refined on a synthetic impurity-free sample. The distribution of the deformation electron density is analyzed in the basic fragments of the crystal structure forming an anionic framework. The constructed potentials of pair and three-particle interaction reproduced quite well the elastic, dielectric, and energy characteristics and allowed us to predict their numerical values, which are in good agreement with the limited available experimental data. © *2002 MAIK "Nauka/Interperiodica".*

INTRODUCTION

Malayaite $CaSnOSiO_4$ belongs to silicates containing isolated SiO_4-groups with additional anions (titanite group). This rare mineral was discovered in 1965 in Malaysia [1]. Later [2], it was found that this mineral forms a solid solution with isostructural high-temperature titanite (sphene) at elevated temperatures. Unlike the low-temperature titanite modification, the tin atoms in the malayaite structure at room temperature are located in the center of SnO_6-octahedra, which facilitates their crystallization in the space group $A2/a$ [3]. A fragment of the malayaite structure is shown in Fig. 1.

Recently, natural malayaite samples were studied by Raman spectroscopy, transmission electron microscopy, and various X-ray methods (powder diffractometry, the use of synchrotron radiation for studying single crystals) [4]. These data allowed us to obtain some additional information on their structure and crystal chemistry. Below, we describe our studies of synthetic malayaite by precision X-ray diffraction and Mössbauer spectroscopy and also theoretical studies by computer simulation of the structure.

PRECISION X-RAY STUDY

The X-ray refinement of the structure was made on a synthetic impurity-free sample synthesized hydrothermally and shaped to a sphere of radius 0.12 mm. The parameters of the monoclinic unit-cell of malayaite were refined using 15 reflections measured on an automated four-circle Syntex $P1$ diffractometer: $a = 7.152(2)$ Å, $b = 8.888(2)$ Å, $c = 6.667(2)$ Å, $\beta = 113.37(2)°$, $V = 389.0(3)$ Å^3, and $\mu r = 0.68$.

The intensities of 3614 reflections were measured within the $+h$, $\pm k$, $\pm l$ hemisphere of the reciprocal space (four equivalent reflections for each general-type reflection, Mo$K\alpha$ radiation, graphite monochromator).

We used 2θ–θ scanning at a rate of 2–24 deg/min up to $\sin\theta/\lambda = 1.2$ Å^{-1}. The scan angle increased from 2° to 3° with an increase in the scattering angle. To improve the accuracy and statistics, we also measured the reflections in the far range of the reciprocal space for another hemisphere, so that the number of the equivalent reflections for far general-type reflections increased to 8. After averaging the equivalent reflections and the removal of the control, spurious, and rejected reflections, the experimental data set consisted of 1517 independent reflections with $I > 1.96(\sigma I)$.

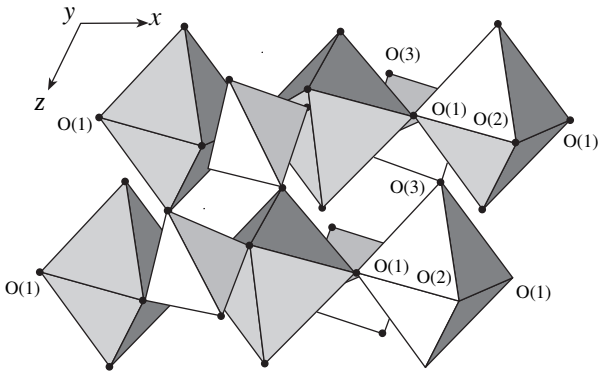

Fig. 1. A fragment of the malayaite structure. Tin atoms are located in octahedra and silicon atoms are located in tetrahedra. The positions of calcium atoms are not shown.

1063-7745/02/4705-0759$22.00 © 2002 MAIK "Nauka/Interperiodica"

Table 1. Coordinates of basic atoms and anisotropic temperature factors ($Å^2$) in malayaite

Atom	*x/a*	*y/b*	*z/c*	B_{11}	B_{22}	B_{33}	B_{12}	B_{13}	B_{23}
Ca	0.25	0.66295(5)	0.5	2.63(4)	0.32(1)	0.50(1)	0.00(0)	–0.14(1)	0.00(0)
Sn	0.5	0.5	0	0.26(1)	0.30(1)	0.30(1)	–0.01(0)	0.11(0)	0.00(0)
Si	0.75	0.68203(8)	0.5	0.35(2)	0.24(1)	0.26(2)	0.00(0)	0.11(1)	0.00(0)
O(1)	0.75	0.58690(18)	0	0.33(3)	0.46(3)	0.97(4)	0.00(0)	0.32(3)	0.00(0)
O(2)	0.91293(20)	0.56796(12)	0.67555(19)	0.73(2)	0.62(2)	0.41(2)	0.23(2)	0.14(2)	0.13(2)
O(3)	0.37180(19)	0.71195(12)	0.89014(19)	0.66(2)	0.46(2)	0.56(2)	0.20(2)	0.33(2)	0.06(1)

All the computations were performed by the MINEXTL program package [6]. After the introduction of the correction for absorption, the malayaite structure was refined within the framework of the superposition-type atomic model by the least squares method in the full-matrix approximation with due regard for the anisotropic harmonic atomic vibrations, the secondary extinction by Zachariasen (U_x = 3130 Å), and the anomalous scattering of tin atoms.

The refinement using the set of the experimental data from the high-angle range of the reciprocal space with $\sin\theta/\lambda > 0.95$ $Å^{-1}$ (407 reflections) was performed to $R = 0.0098$, $Rw = 0.0125$, and $S = 0.8727$. For the full set of 1517 reflections, $R = 0.0130$, $Rw = 0.0230$, and $S = 1.680$. The final coordinates of the basic atoms and their anisotropic thermal parameters are listed in Table 1.

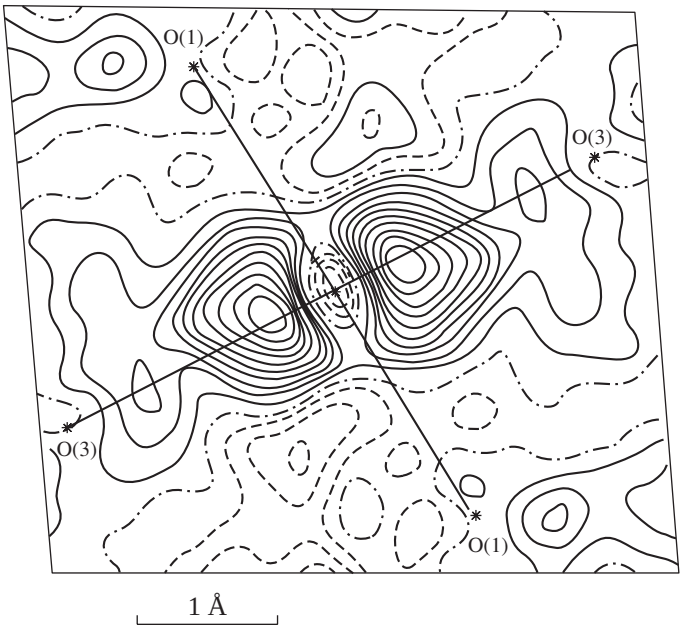

Fig. 2. Deformation electron-density map in the equatorial plane of the SnO_6-octahedron of malayaite. Hereafter, isolines are spaced by 0.1 e/$Å^3$; positive isolines are shown by solid lines; zero contour, by a dot-and-dash line; negative isolines, by a dashed line.

The errors in the deformation electron-density maps with respect to the superposition of neutral atoms estimated according to [7] showed that the error in the vicinity of the chemical bond is 0.02 e/$Å^3$, at the positions of Si atoms, 0.06; at the positions of O atoms, 0.04–0.08; and at Sn atoms about 0.30 e/$Å^3$. Such a pronounced error at the tin nucleus should affect the character of the electron distribution in the SnO_6 octahedron, therefore, the careful analysis of the deformation electron-density maps in this polyhedron was necessary. For other structural fragments, the deformation electron-density maps were expected to be more reliable.

The distribution of the deformation electron density $\Delta\rho$ in malayaite was analyzed in all the basic structural fragments forming the anionic framework. The deformation electron-density map passing through one Sn atom and four O atoms is shown in Fig. 2. The zero synthesis of the electron density confirmed our assumption that the pronounced peaks located at the distance of 0.5 Å from the tin atom are explained by the series termination. The deformation electron-density map is the most reliable at a distance of 0.8–0.9 Å from the tin nucleus. The most pronounced $\Delta\rho$ peak 0.3 e/$Å^3$ is located on the Sn–O(3) line at a distance of 1.6 Å from the tin atom and characterizes the σ-type bonds. On the Sn–O(2) line, the σ-type 0.2 e/$Å^3$-high peaks are also located at close distances from the tin nucleus. The bonding type in the Sn–O(1)–Sn chains along the octahedral column is somewhat different because the coordination number of the O(1) atom relative to Sn equals two. In this situation, the O(1) atom seems to be in the *sp*-hybridization, and, therefore, two additional electron-density peaks (0.2 e/$Å^3$) around this atom are found, whose displacement from the bond line can be explained by the effect of the lone electron pair. Thus, the malayaite structure has two types of Sn–O bonds, which is also confirmed by the interatomic distances (Sn–O(1) and Sn–O(2), Sn–O(3)).

Since the difference between the interatomic distances is explained by the different bond strengths s_{ij} [8], we simulated the s_{ij} distribution in the malayaite structure using the BONDVAL program. The results are indicated in Table 2. There is a pronounced difference between the bond strengths of two groups of the

Sn–O distances (0.78 for Sn–O(1) and, on average, 0.61 for Sn–O(2) and Sn–O(3)).

The construction of deformation electron-density maps passing through the SnO_6-octahedron can be considered as an attempt at visualizing the regions of excessive electron density, which were assumed to be responsible for a high electric-field gradient (EFG) at tin nuclei. Subtraction of the corresponding zero synthesis from the deformation electron-density map, where the effect of series termination is clearly seen, showed that the maxima of the excessive density $\Delta\rho$ really exist at the indicated points of the internuclear space. However, this method is not reliable, and the error of the determination of the deformation electron density in the vicinity of a tin nucleus makes the above explanation of the existence of a high EFG at the tin nucleus in malayaite only one of the possible explanations.

The $\Delta\rho$ map reflecting the redistribution of the electron density in the silicon–oxygen tetrahedron is shown in Fig. 3. Approximately in the center of the Si–O distance (0.8–0.9 Å from the Si atom), the 0.3 e/Å^3-high maximum is formed on all four bonds, which indicates that the silicon atom is sp^3-hybridized and that the bond is essentially covalent. This map is similar to the map with the analogous distribution of the maxima in titanite [9]. In both cases, despite the fact that all the Si–O distances in the tetrahedron are almost equal, there are two bond pairs that are slightly different from each other. In contrast to titanite, in malayaite the bond maxima are equal, but the maxima of excessive electron density on the Si–O(2) pair are slightly displaced from the bond line, which is not observed for the Si–O(3)

Table 2. Interatomic distances (Å) in the coordination polyhedra in the malayaite structure calculated by the method of bond-strength (s_{ij})

Bond	s_{ij}	R_{calcd}
Si–O(2)	1.039	1.610
Si–O(3)	0.961	1.639
Sn–O(1)	0.779	1.997
Sn–O(2)	0.649	2.065
Sn–O(3)	0.571	2.112
Ca–O(1)	0.442	2.270
Ca–O(2)	0.312	2.398
Ca–O(3)	0.234	2.505

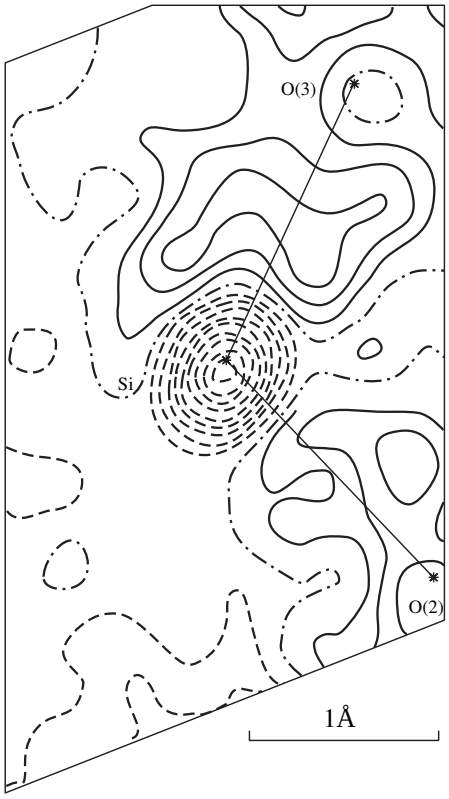

Fig. 3. Deformation electron-density map in the Si–O(3)–O(2) plane crossing the silicon–oxygen tetrahedron of malayaite.

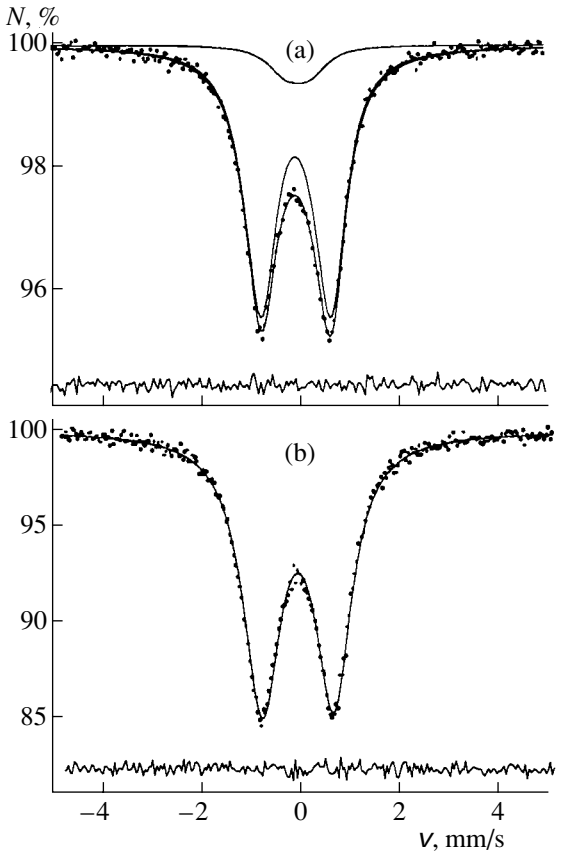

Fig. 4. Mössbauer spectra of (a) the SnO_2-doped malayaite sample synthesized from the solid phase and (b) the undoped malayaite sample obtained by hydrothermal synthesis.

Table 3. Hyperfine parameters of the Mössbauer spectra of malayaite synthesized by two different methods

Method of synthesis	Spectrometer	Model used in data processing	δ_I, mm/s	Δ, mm/s	χ^2
Solid-phase	NZ-640/2	Two quadrupole doublets	−0.049(2)	1.42(1)	0.97
Solid-phase	MS 1101E	Two quadrupole doublets	−0.047(2)	1.42(1)	0.99
Hydrothermal	MS 1101E	One quadrupole doublet	−0.058(6)	1.45(1)	0.93

Table 4. Calculated asymmetry parameter η of EFG tensor and quadrupole splitting Δ for ^{119}Sn nuclei in $CaSnOSiO_4$

Model	Sublattice					Δ, mm/s	η
	Sn	Si	Ca	O	Ω		
Formal charges	+4.00	+4.00	+2.00	−2.00	–	0.37	−0.50
Effective charges	+3.20	+2.40	+2.00	−1.52	–	0.28	−0.35
$x = 1.00\ x_0$	+3.20	+2.40	+2.00	−1.42	−0.25	0.70	−0.06
$x = 0.85\ x_0$	+3.20	+2.40	+2.00	−1.32	−0.50	0.82	−0.08
$x = 0.81\ x_0$	+3.20	+2.40	+2.00	−1.42	−0.40	1.20	+0.01
$x = 0.81\ x_0$	+3.50	+2.40	+2.00	−1.38	−0.50	1.38	−0.01
Experiment	?	?	?	?	?	1.42(2)	?

bonds. Possibly, this is associated with the π-component of the Si–O(2) bond, whose multiplicity (valence) slightly exceeds unity (1.04), whereas the multiplicity of the Si–O(3) bonds is lower than unity (0.96). The structural differences of the tetrahedron edges, O(3)–O(3) and O(2)–O(2), are similar to those in titanite; i.e., the O(3)–O(3) edge connects the octahedra of the same column, whereas the O(2)–O(2) edge connects the octahedra of two different columns.

The deformation electron-density distribution in the calcium polyhedron of malayaite is similar to its distribution in titanite [9]—a pronounced displacement of the 0.10–0.15 e/Å^3 maxima of oxygen atoms. This indicates the essentially ionic character of the chemical interaction.

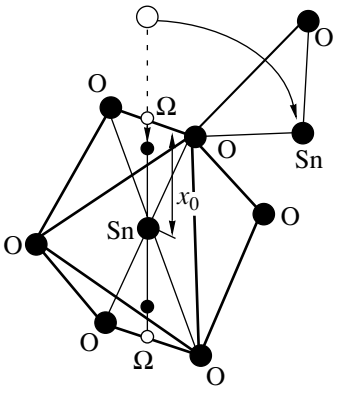

Fig. 5. Scheme explaining the shifts of Ω-regions toward the central tin atom in malayaite. The dashed circles show the positions of these regions and a neighboring Sn atom in cassiterite.

The data obtained from the deformation electron-density maps can be complemented with the total electron-density map, whose use allowed us to evaluate the radius of the optimum separation for the Sn atom (0.89 Å). This value is noticeably lower than in cassiterite (0.95–0.97 Å [10]). Different radii of tin atoms in these minerals lead to the assumption that the effective tin charge in malayaite is higher than in cassiterite, i.e., in the first case, the ionicity of the Sn–O bond is more pronounced.

MÖSSBAUER SPECTROSCOPY STUDY

The samples of synthetic malayaite synthesized hydrothermally [5] and from the solid phase were studied by Mössbauer spectroscopy. The solid-phase synthesis was performed as follows. A stoichiometric ground mixture of CaO, SiO_2, and SnO_2 was pressed, placed into a corundum crucible, and annealed in a muffle furnace for two weeks at a temperature ranging from 1250 to 850°C. The microanalysis showed that the sample contained 12.12 at. % Ca, 13.76 at. % Si, and 11.76 at. % Sn, which corresponded to the formula $CaSnOSiO_4$. To check the results of the synthesis, we analyzed the material by the X-ray phase analysis which showed a good agreement of the obtained X-ray diffraction pattern with the data in [11]. However, the model-based interpretation of the one quadrupole doublet of the Mössbauer spectrum of this sample using the SPECTR program [12] showed too high a value of the functional χ^2, which is characteristic of the presence of a small amount of the second phase. After the model-based fitting of the spectrum to two quadrupole doublets, the hyperfine parameters of the partial malayaite spectrum were determined and the presence of an SnO_2

impurity corresponding to 10.5 at. % Sn was established.

The Mössbauer spectrum of the malayaite sample obtained by the method of solid-state sintering is shown in Fig. 4a. The experiment was performed for 118 h (on a NZ-640/2 spectrometer) at the Laboratory of Solid-State Geochemistry at the Vernadsky Institute of Geochemistry and Analytical Chemistry of the Russian Academy of Sciences. The Mössbauer spectrum of the malayaite sample obtained hydrothermally is shown in Fig. 4b. The experiment was performed during 97 h (on a MS1101E spectrometer) at the Department of General Physics of Moscow State University. Since the microprobe analysis [5] showed the absence of a noticeable impurity concentration in the second case, the Mössbauer spectrum was fitted by one quadrupole doublet using the SPECTR program [12]. The sample synthesized from the solid phase was remeasured using the same device. Thus, three independent Mössbauer experiments were made on two malayaite samples using different spectrometers, which allowed us to check the reproducibility of the results and improve their reliability. In all the cases, the ^{119m}Sn source in the $BaSnO_3$ matrix with an activity of several mCi was used. To reduce the possible influence of texture, the measurements were made on a conic sample with a paraffin filler, with the normal to the sample surface forming an angle of ~54.7° with the direction of the γ-quanta flight. The processing of the experimental spectra yielded the results listed in Table 3.

A negative value of the isomer shift δ relative to cassiterite SnO_2 confirms the assumption that the ionicity of the Sn–O bond in malayaite is more pronounced than in standard cassiterite. However, the quadrupole splitting Δ is too high for tetravalent tin compounds (Δ = 0.49 mm/s in SnO_2). As was shown in [13], the main contribution to the quadrupole splitting of the SnO_2 Mössbauer line comes from the localized excessive electron density in the interatomic space at a distance shorter than the average distance to the anions of the first coordination sphere. In malayaite, the Δ value is three times higher than in SnO_2, thus indicating that the regions of excessive electron density in this compound are closer to the Sn nucleus. This assumption seems to be quite reasonable, because it takes into account the structural characteristics of malayaite: octahedra in a column share their vertices, and, hence, the region of the excessive electron density Ω has only one nearest tin atom at the edge of the oxygen octahedron instead of the two characteristic of cassiterite (Fig. 5), where the octahedra share their edges. Taking into account the electrostatic data, one can assume that the absence of the positively charged second cation should promote a displacement of the Ω region toward the tin nucleus, i.e., to the observation point of the EFG.

In order to calculate the EFG by the method of modified point charges using the LATTICE program [14], the following model was used. A point charge of the Ω region varied from 0.25 to 0.50 e, and this region was localized on a line connecting the center of the shortest edge of the oxygen octahedron with the observation point (Fig. 5). The EFG value in the vicinity of the ^{119}Sn nucleus was calculated as the resulting value of the charges of all atomic sublattices and the sublattice of the Ω regions. In each particular case, the values of the effective atomic charges were calculated proceeding from the neutrality principle with due regard for optimization performed by computer simulation (see Table 4). The position of the Ω region was fixed by the *x*-coordinate (Fig. 5). In all the calculations, the values of the nuclear quadrupole momentum $Q(^{119}\text{Sn}) = -0.109$ bar [15] and antishielding factor $\gamma_\infty = -10$ [16] were used.

Table 5. Parameters of the pair potentials of interatomic interactions used in malayaite simulation

Parameters	Model		
	ionic	shell	optimum
q(Sn)	4.00	2.42	3.20
q(Ca)	2.00	2.00	2.00
q(Si)	4.00	4.00	2.40
q(Sn–shell)		1.58	
q(O–shell)		–2.47	
A(O–O), eV	15123.6	15123.6	15123.6
A(Si–O), eV	3134.35	3134.35	1092.56
A(Ca–O), eV	1090.49	1090.49	1090.49
ρ(O–O), Å	0.2230	0.2230	0.2230
ρ(Sn–O), Å	0.2765	0.2765	0.2765
ρ(Si–O), Å	0.2730	0.2730	0.2730
ρ(Ca–O), Å	0.3437	0.3437	0.3437
C(O–O), eV/Å^6	28.430	28.430	28.430
K(Sn), eV/Å^2		2037.8	
K(O), eV/Å^2		23.09	
D(Sn–O), eV			0.3492
D(Si–O), eV			2.4448
β(Sn–O), Å^{-1}			2.8080
β(Sn–O), Å^{-1}			1.8315
r_0(Sn–O), Å			2.050
r_0(Sn–O), Å			1.620

It can be seen from Table 4 that the enormously high EFG value observed in malayaite is well simulated with the aid of the point charges of 0.4–0.5 e located at the distance of 0.9 Å from the Sn atom. This model becomes invalid for shorter distances because of the ambiguity in the antishielding factor γ_∞. Note that the

Table 6. Calculated and experimental atomic coordinates for malayaite

Atom	Coordinates	Shell model	Ionic model	Optimum model	Experiment*
Ca	*x*	0.2500	0.2500	0.2500	0.25
	y	0.9188	0.9251	0.9098	0.91295
	z	0.7499	0.7500	0.7500	0.75
Sn	*x*	0.5000	0.5000	0.5000	0.5
	y	0.7500	0.7500	0.7500	0.75
	z	0.2500	0.2500	0.2500	0.25
Si	*x*	0.7500	0.7500	0.7500	0.75
	y	0.9283	0.9245	0.9415	0.93203
	z	0.7506	0.7500	0.7497	0.75
O(1)	*x*	0.7507	0.7500	0.7500	0.75
	y	0.8385	0.8286	0.8028	0.83690
	z	0.2513	0.2500	0.2497	0.25
O(2)	*x*	0.9164	0.8883	0.8794	0.91293
	y	0.8093	0.8158	0.8349	0.81796
	z	0.9246	0.9242	0.9257	0.92555
O(3)	*x*	0.3801	0.3744	0.3836	0.37180
	y	0.9647	0.9668	0.9608	0.96195
	z	0.1412	0.1709	0.1804	0.14014

* In the simulation, we used another crystallographic setting that was dictated by the characteristics of the METAPOCS program; therefore, the experimental coordinates are brought into correspondence with the setting of the model.

simulated EFG tensor is almost symmetrical within the framework of this model. Thus, the considerable variation in the EFG values at tin nuclei in $CaSnSiO_5$ and SnO_2 can be explained on the basis of the essential structural and crystallochemical differences, and, in both cases, the main contribution to EFG comes from the electron redistribution in the SnO_6-octahedron.

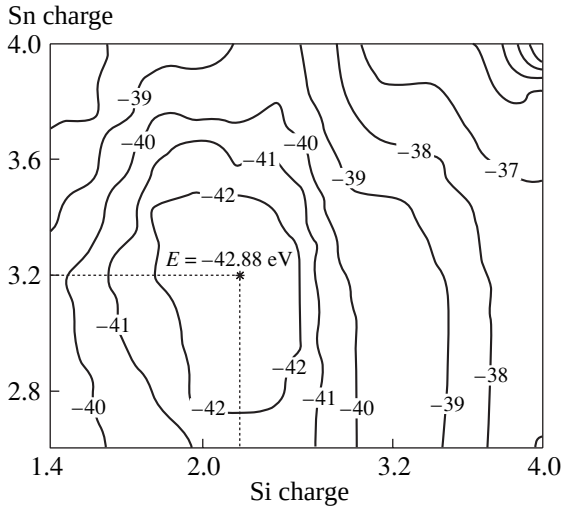

Fig. 6. The atomization energy distribution in malayaite depending on the charges of Si and Sn atoms.

THEORETICAL SIMULATION OF MALAYAITE STRUCTURE AND ITS PROPERTIES

The simulation was performed in a partly covalent approximation by the original method of the minimization of the atomization energy developed in [17] using the METAPOCS program [18]. This simulation was interesting in itself since the elastic and dielectric properties of this mineral have not yet been studied experimentally.

To describe malayaite, a set of pair Born–Mayer–Huggins potentials was used. The potentials of pair Ca–O and O–O interaction were taken from [19]. The potentials of the Sn–O and Si–O bonds with a varied ionicity degree were developed earlier and tested in [20] for the simulation of quartz and cassiterite.

To estimate the charges of the Sn and Si atoms, we performed several calculations using a complex potential in the form

$$V_{ij}(R_{ij}, q) = q^2 Z_i Z_j / R_{ij} + \lambda_{ij}^w \exp(-R_{ij}\rho_{ij}) + d_{ij}^w\{\exp[2\sigma_{ij}(R_{ij}^0 - R_{ij})] - 2\exp[\sigma_{ij}(R_{ij}^0 - R_{ij})]\} - C_{ij}/R_{ij}^6, \quad (1)$$

Table 7. Calculated and experimental interatomic distances (Å) in the structure of malayaite. The number of equivalent bonds is indicated in braces

Atoms	Distance	
	experiment	shell model
SiO_4-tetrahedron		
Si–O(2)	{2} 1.640(1)	1.680(7)
Si–O(3)	{2} 1.635(1)	1.671(2)
O(2)–O(2)	{1} 2.566(2)	2.592(2)
O(2)–O(3)	{2} 2.666(2)	2.693(1)
O(2)–O(3)	{2} 2.815(3)	2.823(4)
O(3)–O(3)	{1} 2.684(3)	2.758(2)
SnO_6-octahedron		
Sn–O(1)	{2} 1.948(1)	1.954(1)
Sn–O(2)	{2} 2.089(1)	2.079(1)
Sn–O(3)	{2} 2.096(1)	2.101(2)
O(1)–O(2)	{2} 2.840(1)	2.838(5)
O(1)–O(2)	{2} 2.872(1)	2.868(3)
O(1)–O(3)	{2} 2.742(1)	2.682(13)
O(1)–O(3)	{2} 2.976(1)	3.032(8)
O(2)–O(3)	{2} 2.942(1)	2.908(5)
O(2)–O(3)	{2} 2.976(1)	3.003(5)
CaO_7-polyhedron		
Ca–O(1)	{1} 2.241(8)	2.156(6)
Ca–O(2)	{2} 2.401(6)	2.418(6)
Ca–O(3)	{2} 2.746(5)	2.662(8)
Ca–O(3)	{2} 2.422(5)	2.438(6)

Table 8. Predicted properties of malayaite

Properties	Ionic model	Shell model	Model with partly covalent bonding
Elastic constants and modules (Mbar)			
C_{11}	1.348	2.361	2.288
C_{12}	1.430	1.322	0.929
C_{13}	0.276	0.866	0.825
C_{15}	0.366	0.685	0.584
C_{22}	5.274	5.041	4.071
C_{23}	1.493	1.478	1.160
C_{25}	0.077	0.011	0.024
C_{33}	3.426	3.715	2.848
C_{35}	−0.927	−0.487	−0.438
C_{44}	0.839	0.632	0.651
C_{46}	0.436	0.452	0.244
C_{55}	1.203	1.371	1.142
C_{66}	0.836	0.749	0.709
K	1.827	2.049	1.671
μ	1.032	1.047	0.920
Dielectric constants			
ε_{11}	6.494	6.901	5.731
ε_{22}	4.569	4.491	3.202
ε_{33}	6.768	6.882	6.633
$\varepsilon_{\infty}^{11}$	–	2.720	–
$\varepsilon_{\infty}^{22}$	–	2.652	–
$\varepsilon_{\infty}^{33}$	–	2.587	–
Energy characteristics (eV)			
U	−284.45	−285.68	−170.10
E	−32.01	−33.24	−42.88

where q is the degree of ionicity of the bond ($0 < q < 1$), Z_i and Z_j are formal ionic charges, R_{ij}^0 is the sum of covalent radii, and the empirical parameters λ and d are attributed by weights at each value of the ionicity degree. Two repulsion parameters ("softness" ρ and "stiffness" σ) are related by the well-known equation

$$\rho = \frac{1}{2}\sigma^{-1}. \quad (2)$$

To reduce the number of computations, we restricted the values of atomic charges from below—the tin charge was varied from +2.6 to +4.0 e and the silicon charge, from +1.4 to +4.0 e (the limit for tin corresponds to an underestimated cation charge in SnO_2 and for silicon, to that value in α-quartz). Within these limits, 64 model computations were performed for different combinations of the effective charges of Si and Sn. Taking into account that the Ca–O bond has a pronounced ionic nature, the calcium charge was taken to be +2.0 in all the cases. The oxygen charge was calculated proceeding from the unit-cell neutrality. For each set of atomic charges, the structure simulation was performed with a search for the minimum of the configuration and atomization energies E with due regard for a correction for the energy ΔE of charge transfer from cations to anions determined for each set of atomic charges from the data on the ionization energy of the atomic valence states as described in [17, 20].

The charges corresponding to the minimum of the atomization energy were taken to be optimal. To estimate the optimum charge set more precisely, 36 more cycles of simulation were performed, in which the tin charge varied from +3.0 to +3.4 e and the silicon charge, from +2.2 to +2.6 e.

To obtain data on high-frequency dielectric constants, we used a shell model of formal charges with due regard for the polarization of tin and oxygen atoms and three-particle O–Si–O interaction. The parameters of the harmonic potentials for Sn and O were taken from [19], and the parameters of three-particle potential, from [21].

The parameters of the different pair potentials for the ionic, shell, and "optimum" models are listed in Table 5. The predicted $CaSnOSiO_4$ atomic coordinates and new experimental data are listed in Table 6. Since the atomic coordinates obtained for different theoretical models differ only insignificantly, the experimental interatomic distances are compared only with the distances calculated based on the shell model (Table 7). The calculated components of the tensors of elastic and dielectric constants, as well as the structural, $U = \sum V_{ij}$, and atomization, E, energies, of malayaite are listed in Table 8. The bulk compression modulus K (by Voigt) and the shear modulus μ are calculated using the well-known relationships.

As is seen from Tables 6 and 7, the structural characteristics of malayaite are reproduced rather well using any of the three models. The Si, Sn, Ca, and O(1) atoms practically occupy the positions that were determined experimentally. The deviations from the experimental positions observed for the O(2) and O(3) atoms occupying the general positions are also small and do not exceed 0.2–0.3 Å. Using the harmonic potential in the shell model for Sn and O atoms, we could estimate the high-frequency dielectric constants ε_{ij} of malayaite. However, allowance for the polarization only for Sn and O atoms resulted in somewhat underestimated values of these constants, which is seen from the comparison of the experimental and calculated refractive indices n. For natural malayaite, the refractive indices are $n_p = 1.764$, $n_g = 1.798$, and $n_m = 1.783$ [22]. Hence, the ε_{ij} values in malayaite should be ~3.1–3.2 (compare with the data in Table 8). However, it is necessary to note that the n values are essentially dependent on the sample composition, and the refractive indices of pure malayaite can differ somewhat from the values indicated in handbooks of mineralogy.

Using 100 values of the atomization energy E obtained based on different models of charge distribution, we constructed the surface $E(Z_{Sn}, Z_{Si})$, which has a pronounced minimum at the charges Si = +2.40(4) e and Sn = +3.20(4) e (Fig. 6). These atomic charges were used in the "optimum" model. The E value at the minimum is equal to –42.88 eV or –4133 kJ/mol. The experimental E value obtained using the experimental value of enthalpy of the malayaite formation from simple components (ΔH_{298} = –2246 kJ/mol [5]) equals –4424 kJ/mol, i.e., differs from the theoretical estimate by 6.5%.

CONCLUSIONS

The following conclusions can be made from the precision X-ray diffraction and Mössbauer studies and computer simulation.

The effective tin charge in malayaite $CaSnOSiO_4$ is somewhat higher than in cassiterite SnO_2.

In malayaite, two types of Sn–O bonds exist—the bonds along the octahedral chain and the bonds directed toward the adjacent chains; in the silicon–oxygen octahedron, two pairs of bonds of different multiplicities based on sp^3-hybridization of the Si-orbitals are observed; the Ca–O bond is essentially ionic.

The anomalously high quadrupole splitting of the Mössbauer spectrum of ^{119}Sn nuclei in malayaite can be explained by the formation of regions characterized by the excessive electron density giving rise to charge redistribution on the Sn–O bonds.

The semiempirical sets of the parameters of the pair and three-particle interactions allow one to reproduce the structural features of malayaite and predict the values of its elastic, dielectric, and energy characteristics, which are in good agreement with the limited available experimental data on its properties.

REFERENCES

1. J. B. Alexander and B. H. Flinter, Miner. Mag. **35**, 622 (1965).
2. S. Takenouchi, Miner. Deposita **6**, 335 (1971).
3. J. B. Higgins and P. H. Ribbe, Am. Mineral. **62**, 801 (1977).
4. L. A. Groat, S. Kek, U. Bismayer, *et al.*, Am. Mineral. **81**, 595 (1996).
5. I. L. Khodakovskiĭ, A. Bart, Yu. V. Semenov, *et al.*, Geokhimiya **9**, 1298 (1982).
6. R. G. Gerr, T. N. Borovskaya, N. N. Lobanov, V. A. Strel'tsov, *et al.*, Zh. Strukt. Khim. **32**, 170 (1991).
7. N. N. Lobanov and V. G. Tsirel'son, in *Proceedings of the 1st All-Union Conference "Precision Structural Investigations of Crystals," Riga, 1989*, p. 79.
8. V. S. Urusov and I. P. Orlov, Kristallografiya **44**, 736 (1999) [Crystallogr. Rep. **44**, 686 (1999)].
9. V. S. Urusov, N. N. Eremin, and O. V. Yakubovich, Kristallografiya **40** (3), 485 (1995) [Crystallogr. Rep. **40**, 442 (1995)].
10. V. S. Urusov, N. N. Eremin, and O. V. Yakubovich, in *Extended Abstracts of the SAGAMORE XI, 1994*, P4-38, 237.
11. R. A. Eppler, J. Am. Ceram. Soc. **5**, 455 (1976).

12. V. I. Nikolaev and V. S. Rusakov, *Mössbauer Analysis of Ferrites* (Mosk. Gos. Univ., Moscow, 1985).
13. D. A. Khramov, V. S. Rusakov, N. N. Eremin, and V. S. Urusov, Izv. Akad. Nauk, Ser. Fiz. **58** (4), 30 (1994).
14. V. S. Rusakov, *Mössbauer Spectroscopy of Locally Heterogeneous Systems* (Inst. Yadernoĭ Fiziki Respubliki Kazakhstan, Almaaty, 2000).
15. H. Haas, M. Menninger, H. Andreasen, *et al.*, Hyperfine Interact. **15/16**, 215 (1983).
16. F. Borsa and R. G. Barns, Phys. Rev. Lett. **12**, 281 (1964).
17. V. S. Urusov and N. N. Eremin, Phys. Chem. Miner. **22**, 151 (1995).
18. G. D. Price and S. C. Parker, Phys. Chem. Miner. **10**, 209 (1984).
19. C. M. Freeman and C. R. A. Catlow, J. Solid State Chem. **85**, 65 (1990).
20. V. S. Urusov and N. N. Eremin, Phys. Chem. Miner. **23**, 216 (1996).
21. J. E. Post and C. W. Burnham, Am. Mineral. **71**, 142 (1986).
22. *Minerals: Reference Book*, Ed. by F. V. Chukhrov (Nauka, Moscow, 1972), Vol. 3, issue 1, p. 352.

Translated by T. Dmitrieva

Crystallography Reports, Vol. 47, No. 5, 2002, pp. 768–772. Translated from Kristallografiya, Vol. 47, No. 5, 2002, pp. 834–838.

STRUCTURES OF INORGANIC COMPOUNDS

Synthesis and Crystal Structures of Bimetallic Hydrogen Sulfates $M^IM^{II}[H(SO_4)_2](H_2O)_2$ (M^I = K, Cs; M^{II} = Zn, Mn) and Selenate $KMg[H(SeO_4)_2](H_2O)_2$

S. I. Troyanov*, I. V. Morozov*, and E. Kemnitz**

** Department of Chemistry, Moscow State University, Vorob'evy gory, Moscow, 119899 Russia*

e-mail: troyanov@thermo.chem.msu.ru

*** Department of Chemistry Research, Humboldt University of Berlin, Hessische strasse 1–2, D-10115 Berlin, Germany*

Received February 12, 2002

Abstract—Single crystals of acid salt hydrates $M^I\{M^{II}[H(XO_4)_2](H_2O)_2\}$, where M^I, M^{II}, and X are K, Zn, and S (**I**); K, Mn, and S (**II**); Cs, Mn, and S (**III**); or K, Mn, and Se (**IV**), respectively, were synthesized and studied by X-ray diffraction analysis. Compounds **I**–**IV** (space group $P1$) are isostructural to each other and to hydrate $KMg[H(SO_4)_2](H_2O)_2$ (**V**) studied earlier. Structures **I**–**V**, especially, the M^I–O, M^{II}–O, and X–O distances and the O···H···O (2.44–2.48 Å) and O_w–H··O (2.70–2.81 Å) hydrogen bonds, are discussed. © *2002 MAIK "Nauka/Interperiodica".*

INTRODUCTION

Considerable attention given to a class of acid salts of inorganic oxygen-containing acids stems from the interest in the characteristic features of hydrogen bonding in their crystal structures. In recent years, acid sulfates and selenates of mono- and divalent metals, including numerous adducts with acid H_2XO_4, were systematically studied [1, 2]. Some hydrogen alkali metal acid salts of the compositions M^IHXO_4 and $M^I_3H(XO_4)_2$ (M^I = Rb or Cs and X = S or Se) undergo phase transitions to form phases possessing high protonic conductivity [3]. The studies of phases containing mixed M^I cations showed that the phase-transition temperature and other characteristics of phase transitions are essentially dependent on the degree of replacement, for example, in the $Cs_{1-x}M^I_xHSO_4$ phases [4]. In some instances, these phases possess their own structure types. As an example, we refer to $K_{0.5}Rb_{0.5}HSO_4$ [5] or $Rb_4LiH_3(XO_4)_4$ [6].

Hydrogen salts with metal cations in different valence states were much less studied. Only one compound containing mono- and divalent metals, $KMg[H(SO_4)_2](H_2O)_2$ dihydrate, was structurally studied [7]. We performed a systematic study of the synthesis and crystal structures of such salts and managed to prepare hydrogen sulfate (selenate) hydrates possessing other combinations of mono- and divalent metals of the compositions $M^IM^{II}[H(XO_4)_2](H_2O)_2$ and $M^I_4M^{II}[H(SO_4)_2]_2(H_2O)_2$. Below, we report the results of our studies of four compounds of the first group.

EXPERIMENTAL

Synthesis. The $M^IM^{II}H(XO_4)_2(H_2O)_2$ compounds were prepared by crystallization from aqueous solutions of chalcogenates $M^I_2XO_4$ and $M^{II}XO_4$ and acid H_2XO_4. The molar ratio of the reagents was varied to optimize the conditions of the synthesis. It was found that the phases of the composition $M^IM^{II}H(SO_4)_2(H_2O)_2$, where M^I and M^{II} = K and Zn (**I**), K and Mn (**II**), or Cs and Mn (**III**), were crystallized, if sulfates were taken in the molar ratio 1 : 2 in the presence of a fivefold or sixfold excess (with respect to its stoichiometric amount) of sulfuric acid. Bimetallic hydrogen selenate $KMnH(SeO_4)_2(H_2O)_2$ (**IV**) was prepared with the use of an eightfold excess of selenic acid. In some syntheses, the corresponding acid sulfates were used instead of alkali sulfate, or alkali metal was introduced by dissolving its carbonate in an acid. The $M^I_2XO_4$ and $M^{II}XO_4$ salts or their mixtures were crystallized from less acidic solutions. Hydrogen chalcogenate M^IHXO_4 was present among the products of primary crystallization from solutions with an excess of alkali cations. The phase purity of the resulting samples were confirmed by X-ray powder diffraction analysis. In order to grow larger (up to 5 mm) single crystals, the solutions were concentrated, and crystallization occurred at 50°C. The crystals thus obtained were nonhygroscopic but they effloresced during storage for several weeks in air.

Analogous experiments on crystallization in the $M^I_2XO_4$–$M^{II}XO_4$–H_2XO_4 systems for the K–Cd–S, K–

1063-7745/02/4705-0768$22.00

Table 1. Crystallographic characteristics and the details of X-ray data collection and the refinement of structures **I**–**IV**

Compound	**I**, $KZn[H(SO_4)_2] \cdot 2H_2O$	**II**, $KMn[H(SO_4)_2] \cdot 2H_2O$	**III**, $CsMn[H(SO_4)_2] \cdot 2H_2O$	**IV**, $KMg[H(SeO_4)_2] \cdot 2H_2O$
Molecular weight	333.63	323.20	417.01	386.37
Crystal system	Triclinic	Triclinic	Triclinic	Triclinic
Space group	$P\bar{1}$	$P\bar{1}$	$P\bar{1}$	$P\bar{1}$
a, Å	4.563(3)	4.693(2)	4.788(2)	4.671(3)
b, Å	5.751(4)	5.816(3)	5.843(3)	5.882(3)
c, Å	8.149(5)	8.247(2)	8.577(4)	8.479(5)
α, deg	103.43(3)	103.49(3)	104.31(3)	103.15(3)
β, deg	99.63(8)	99.81(3)	95.99(3)	99.02(4)
γ, deg	95.37(3)	96.08(3)	93.80(3)	96.95(4)
V, Å^3/Z	203.1(2); 1	213.2(2); 1	230.2(2); 1	221.1(2); 1
ρ_{calcd}, g/cm^3	2.728	2.518	3.008	2.902
$\mu(MoK_\alpha)$, mm^{-1}	4.088	2.562	5.818	8.940
T, K	180(2)	180(2)	180(2)	170(2)
θ_{max}, deg	32.0	30.0	32.0	30.0
Number of measured and independent reflections	1836/1413	2525/1237	2828/1525	1883/1290
Number of reflections with $[I > 2\delta(I)]$	1345	1121	1431	903
Number of reflections and parameters in the least-squares refinement	1342/80	1126/80	1438/80	960/79
R_1 $[I > 2\delta(I)]/wR_2$ (all reflections)	0.0224/0.0717	0.0187/0.0577	0.0255/0.0772	0.0398/0.1188
$\Delta\rho_{max}/\Delta\rho_{min}$, $\bar{e}$/Å^3	0.990/–0.929	0.490/–0.443	1.763/–1.683	1.816/–1.712

Table 2. Coordinates of the basis atoms and the equivalent (isotropic for H atoms) thermal parameters in structures **I**–**IV**

Atom	x	y	z	U_{eq}, Å^2	Atom	x	y	z	U_{eq}, Å^2
I					**III**				
K	0	0	0.5	0.0204(1)	Cs	0	0	0.5	0.0166(1)
Zn	0	0	0	0.0073(1)	Mn	0	0	0	0.0106(1)
S	0.60871(7)	0.31795(6)	0.24169(4)	0.0063(1)	S	0.56694(11)	0.31480(9)	0.23521(6)	0.0100(1)
O(1)	0.7871(3)	0.1201(2)	0.2045(2)	0.0111(2)	O(1)	0.7250(4)	0.1087(3)	0.1825(2)	0.0158(3)
O(2)	0.3470(3)	0.2850(2)	0.1026(2)	0.0113(2)	O(2)	0.3019(4)	0.2887(3)	0.1278(3)	0.0207(4)
O(3)	0.7799(3)	0.5541(2)	0.2690(2)	0.0137(2)	O(3)	0.7238(4)	0.5391(3)	0.2448(3)	0.0204(4)
O(4)	0.5069(3)	0.3013(2)	0.4061(1)	0.0118(2)	O(4)	0.4989(5)	0.3082(3)	0.4022(3)	0.0207(4)
O(5)	0.2026(3)	0.7896(2)	0.1492(2)	0.0116(2)	O(5)	0.1785(5)	0.7717(4)	0.1439(3)	0.0199(4)
H(1)	0.509(15)	0.445(11)	0.469(8)	0.02(1)	H(1)	0.497(15)	0.445(10)	0.479(9)	0.02(1)
H(2)	0.0900(10)	0.673(8)	0.157(5)	0.04(1)	H(2)	0.0300(22)	0.659(18)	0.175(12)	0.07(2)
H(3)	0.362(13)	0.732(11)	0.131(7)	0.06(1)	H(3)	0.359(12)	0.736(10)	0.164(7)	0.03(1)
II					**IV**				
K	0	0	0.5	0.0306(1)	K	0	0	0.5	0.0268(4)
Mn	0	0	0	0.0095(1)	Mg	0	0	0	0.0104(4)
S	0.61755(6)	0.32218(5)	0.24745(3)	0.0087(1)	Se	0.62029(8)	0.31979(7)	0.24200(5)	0.0093(2)
O(1)	0.7943(2)	0.1305(2)	0.2119(1)	0.0154(2)	O(1)	0.8117(7)	0.1076(6)	0.2047(4)	0.0138(7)
O(2)	0.3635(2)	0.2851(2)	0.1083(1)	0.0154(2)	O(2)	0.3391(7)	0.2828(6)	0.0942(4)	0.0141(7)
O(3)	0.7833(2)	0.5586(2)	0.2758(1)	0.0189(2)	O(3)	0.8079(8)	0.5808(6)	0.2724(5)	0.0179(7)
O(4)	0.5159(2)	0.3034(2)	0.4089(1)	0.0153(2)	O(4)	0.5094(8)	0.2994(6)	0.4172(4)	0.0149(7)
O(5)	0.2010(2)	0.7766(2)	0.1505(1)	0.0162(2)	O(5)	0.2086(8)	0.7919(7)	0.1301(5)	0.0148(7)
H(1)	0.510(11)	0.448(8)	0.466(6)	0.02(1)	H(1)	0.569(29)	0.464(27)	0.471(16)	0.02(1)
H(2)	0.101(7)	0.668(6)	0.174(4)	0.044(7)	H(2)	0.125(17)	0.696(14)	0.160(9)	0.02(2)
H(3)	0.348(8)	0.715(6)	0.137(4)	0.048(8)	H(3)	0.369(24)	0.732(18)	0.100(12)	0.04(2)

Table 3. Interatomic distances *d* (Å) in the crystal structures of $M^{I}M^{II}[H(XO_4)_2](H_2O)_2$

	(*d*) **I**	(*d*) **II**	(*d*) **III**	(*d*) **IV**	(*d*) **V** [7]**
M^{I}(*r*, Å)*	K (1.55)	K (1.55)	Cs (1.81)	K (1.51)	K (1.55)
M^{II}(*r*, Å)*	Zn (0.745)	Mn (0.820)	Mn (0.820)	Mg (0.720)	Mg (0.720)
X	S	S	S	Se	S
M^{II}–O(1)	2.081(1)	2.161(1)	2.153(2)	2.073(4)	2.069(2)
M^{II}–O(2)	2.080(1)	2.156(1)	2.138(2)	2.067(4)	2.051(2)
M^{II}–O(5)	2.077(1)	2.175(1)	2.186(2)	2.057(4)	2.068(2)
M^{II}–O (average distance)	2.079	2.164	2.159	2.066	2.066
M^{I}–O (range)	2.71–3.16	2.72–3.21	3.13–3.26	2.71–3.14	2.76–3.22
M^{I}–O (average distance)	2.958	2.990	3.192	2.917	2.991
X–O(1)	1.464(2)	1.464(1)	1.466(2)	1.624(3)	1.465(2)
X–O(2)	1.467(2)	1.466(1)	1.465(2)	1.623(3)	1.458(2)
X–O(3)	1.452(2)	1.453(1)	1.446(2)	1.617(4)	1.452(2)
X–O(4)	1.510(2)	1.512(1)	1.511(2)	1.673(4)	1.508(2)
O(4)–H(1)···O(4')***	2.451(3)	2.461(2)	2.444(4)	2.476(7)	2.478(3)
O(5)–H(2)···O(3")***	2.695(2)	2.701(2)	2.813(3)	2.707(6)	2.738(3)

* Radii of the cations for M^{I} (c.n. 10), M^{II} (c.n. 6), and K^{+} (c.n. 8) in **IV** were taken from [10].

** The scheme of atomic numbering for the O and H atoms is brought into correspondence with that used in this study.

*** The O···O distances in hydrogen bonds. The symmetry codes for the O(4') and O(3") atoms: $1-x, 1-y, 1-z$ and $x-1, y, z$, respectively.

Zn–Se, and K–Mg–Se triads did not result in the growth of bimetallic hydrogen chalcogenates. Instead, basic or acid salts of M^{I} and M^{II} metals or their mixtures were detected by X-ray powder diffraction analysis in the crystallization products.

X-ray diffraction study. X-ray diffraction data for single crystals of **I**–**IV** were collected at a low temperature on an automated four-circle STADI-4 (Stoe) diffractometer (MoK_α radiation, graphite monochromator, λ = 0.71073 Å, ω–2θ scan technique). The crystallographic characteristics and details of the structure refinement are given in Table 1. Either the numerical absorption corrections taking into account the real crystal shape (**III**) or the empirical absorption corrections with the use of ψ-scan data for four to six reflections (**I**, **II**, and **IV**) were applied.

The coordinates of the non-hydrogen atoms were determined by the direct method [8] and then were refined by the full-matrix least-squares method with the anisotropic thermal parameters [9]. The positions of hydrogen atoms in the structures of **I**–**IV** were revealed from difference electron-density syntheses and refined by the least-squares method with the isotropic thermal parameters. One of three independent hydrogen atoms, H(1), appeared to be disordered over two positions around the center of inversion. The atomic coordinates in the structures of **I**–**IV** and their equivalent (isotropic for H atoms) thermal parameters are given in Table 2. Since all the compounds are isostructural, we used the unified atom numbering scheme. The interatomic distances for the coordination environments around the M^{I}, M^{II}, and *X* atoms and the hydrogen bond lengths are listed in Table 3.

RESULTS AND DISCUSSION

X-ray diffraction analysis demonstrated that hydrogen salt hydrates **I**–**IV** are isostructural to each other and to the salt $KMg[H(SO_4)_2](H_2O)_2$ (**V**) studied earlier [7]. The linear unit cell parameters vary according to the relative sizes of the cations (M^{I} and M^{II} [10]) and XO_4 anions (Table 1). The large M^{I} cations (K and Cs), smaller M^{II} cations (Zn, Mn, and Mg), compact XO_4 anions (*X* = S and Se), and water molecules can be considered as structural blocks (figure). The centrosymmetric coordination environment around the M^{I} cations is formed by the O atoms of the XO_4 groups located at shorter distances and the O(H) and O_w atoms located at longer distances (Table 3). If the size of the coordination polyhedron is limited by the maximum K–O distance (3.25 Å), the coordination number of the potassium atom in the structures of **I**, **II**, and **V** is equal to 10, whereas the coordination number of this atom in the structure of **IV** is equal to 8 (the K–O_w distance is 3.43 Å). In the structure of **III** containing the Cs atom with the coordination number 10, the corresponding distances are substantially larger in accordance with its larger, ionic radius.

The centrosymmetrical octahedral coordination about the M^{II} cations is formed by four O atoms of the

XO_4 groups [O(2) and O(3)] and two O(5) atoms of the water molecules. The M^{II}–O bond lengths have close values. The average M^{II}–O distances depend on the ionic radius of the metal atom. In the XO_4-tetrahedra, the *X*–O bond lengths are determined by the nature of the chalcogen atom and the additional structural functions of the oxygen atoms. On the whole, the S–O bonds are shorter by 0.16–0.17 Å than the analogous Se–O bonds, which is consistent with the analogous values observed in other structures containing XO_4 anions [1]. The structures under consideration are characterized by the presence of three *X*–O bonds of approximately equal lengths, whereas the fourth *X*–O(4) bond is noticeably longer (Table 3). The O(1) and O(2) atoms are involved not only in the formation of the *X*–O bonds but also in the coordination of the M^{II} atoms, which results in the virtually equal *X*–O(1) and *X*–O(2) bond lengths. The O(3) atom acts as an acceptor (*A*) of the hydrogen atom in the O(5)–H(2)···O(3") hydrogen bond, whereas the *X*–O(3) bonds are slightly shortened. The fact that the *X*–O bond length depends more substantially on the coordination of the metal atom (*M*) than on the acceptor function (*A*) is attributed to the relatively small radii of the M^{2+} dications. The structures of hydrogen chalcogenates containing singly-charged cations (K, Rb, or Cs) are characterized by the inverse ratio of the effects exerted by the *M* and *A* functions on the *X*–O bond lengths [1, 11]. Finally, the largest *X*–O(4) bond length is associated with the participation of the O(4) atom in the disordered O(4)–H(1)···O(4') hydrogen bond, where it plays the role of a half-donor (*D*) and half-acceptor of the H atom (1/2*D* + 1/2*A*).

The system of hydrogen bonds includes the short O(4)–H(1)···O(4') bonds (2.44–2.48 Å) that link two XO_4-tetrahedra into a dimer with the formation of isolated hydrated anions $\{[H(XO_4)_2](H_2O)_2\}^{3-}$, and longer O(5)–H(2)···O(3") bonds (2.70–2.81 Å) between dimers and water molecules. The H(1) atom involved in the strong hydrogen bond is disordered around the inversion center. In the structures of **I**–**III**, established with a higher accuracy, the O(4)–H(1) and H(1)···O(4') distances are 0.86–0.91 and 1.56–1.60 Å, respectively, and the O(4)–H(1)···O(4') angles are 172°–175°. Initially, proceeding from difference Fourier syntheses, we placed the H(1) atom in the structure of **I** into the inversion center. However, the subsequent refinement of the structure gave somewhat better results (the $U_{H(1)}$ parameter) for a model containing the disordered H(1) atom. Such disorder was also observed in structures **II**–**IV** studied at low temperatures and in structure **V** at room temperature [7]. One hydrogen atom of the water molecule is involved in the O(5)–H(2)···O(3") hydrogen bond, whereas another hydrogen atom, H(3), virtually does not participate in the hydrogen bonding, apparently, because of the fact that the O(1)–O(4) atoms perform some additional functions. A double acceptor function (2*A*), which is quite common in the structures of many acid salts, is not realized for the O(3) atom, presumably, because the O(5)–H(3) bond is directed toward the space between the oxygen atoms.

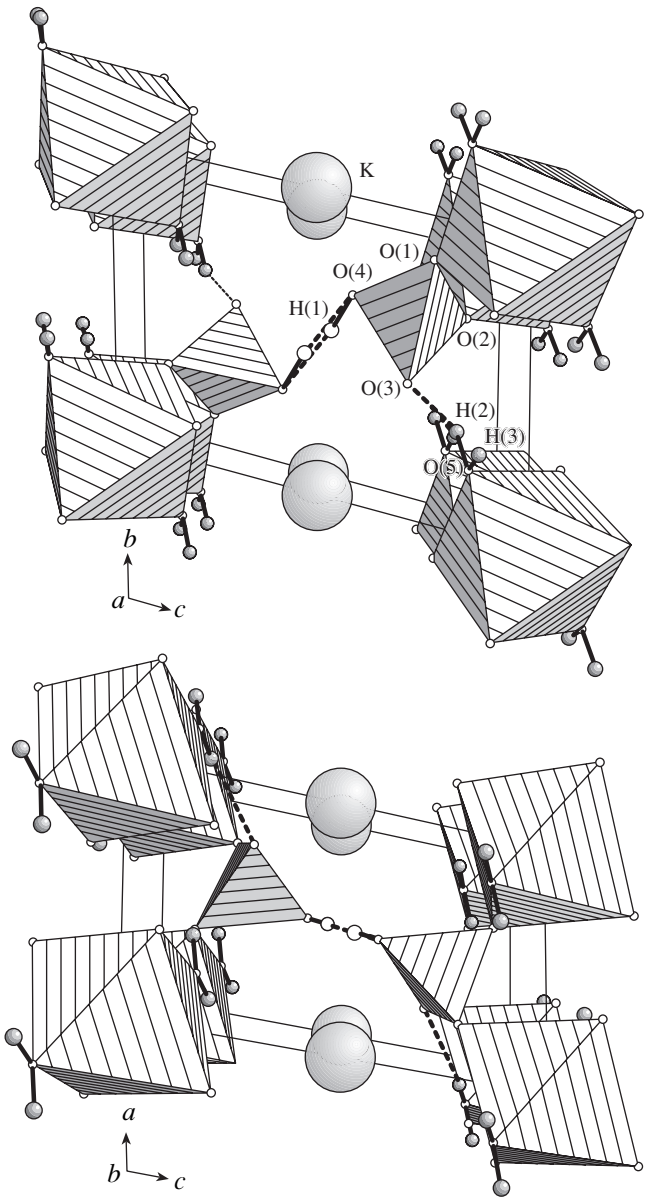

Crystal structure of $KMn[H(SO_4)_2](H_2O)_2$ (**II**) projected along the *a*-axis (at the top) and the *b*-axis (at the bottom). The coordination environments of Mn and S atoms are shown as octahedra and tetrahedra, respectively. The disordered H(1) atoms are indicated by empty circles.

The $M[H(XO_4)_2]$ salts with *M* = Na–Cs [12] are rather similar to the structure type under consideration. The structures of these salts are also characterized by the formation of the $[H(XO_4)_2]$ dimers via a symmetric hydrogen bond. Some of these compounds (*M* = Rb or Cs) undergo high-temperature phase transitions giving rise to phases with high protonic conductivity [13, 14]. The absence of water molecules in their structures is

responsible for the higher thermal stability of these compounds. In addition, the disordered arrangement of the XO_4-tetrahedra (necessary for the manifestation of high proton conductivity) is not suppressed by the formation of additional hydrogen bonds.

In the structures of hydrates that have close compositions, $M^{II}(HXO_4)_2 \cdot H_2O$ (M^{II} = Mg, Mn, or Cd [2, 15, 16]), no hydrogen bonds between the anions are formed, and the water molecules are both donors and acceptors of the H atoms (from the HXO_4 groups) in hydrogen bonds. In the structures of $M^{II}(HXO_4)_2$ containing no water molecules, the hydrogen bonds between the HXO_4^- anions lead to the formation of infinite zigzag chains [17].

REFERENCES

1. E. Kemnitz and S. I. Troyanov, Adv. Mol. Struct. Res. **4**, 79 (1998).
2. E. Kemnitz, S. I. Troyanov, and H. Worzala, Eur. J. Solid State Inorg. Chem. **30**, 629 (1993).
3. A. I. Baranov, L. A. Shuvalov, and N. M. Shchagina, Pis'ma Zh. Éksp. Teor. Fiz. **36**, 381 (1982) [JETP Lett. **36**, 459 (1982)].
4. T. Mhiri and P. Colomban, Solid State Ionics **44**, 227 (1991).
5. W. G. Mumme, Acta Crystallogr., Sect. B: Struct. Crystallogr. Cryst. Chem. **29**, 1076 (1973).
6. A. Petrazhko, M. Polomska, and A. Pavlovski, Izv. Akad. Nauk SSSR, Ser. Fiz. **55** (3), 529 (1991).
7. J. Maciček, S. Gradinarov, R. Bonchev, and C. Balarew, Acta Crystallogr., Sect. C: Cryst. Struct. Commun. **50**, 1185 (1994).
8. G. M. Sheldrick, *SHELXS86: Program for the Solution of Crystal Structures* (University of Göttingen, Göttingen, 1990).
9. G. M. Sheldrick, *SHELXL93: Program for the Refinement of Crystal Structures* (University of Göttingen, Göttingen, 1993).
10. R. Shannon and C. T. Prewitt, Acta Crystallogr., Sect. B: Struct. Crystallogr. Cryst. Chem. **35**, 745 (1969).
11. E. Kemnitz, C. Werner, and S. I. Troyanov, Eur. J. Solid State Inorg. Chem. **33**, 563 (1996).
12. W. Jowig, H. Fuess, and S. Ferraris, Acta Crystallogr., Sect. B: Struct. Crystallogr. Cryst. Chem. **38**, 2798 (1982).
13. A. I. Baranov, I. P. Makarova, L. A. Muradyan, *et al.*, Kristallografiya **32** (3), 682 (1987) [Sov. Phys. Crystallogr. **32**, 400 (1987)].
14. B. V. Merinov, A. I. Baranov, and L. A. Shuvalov, Kristallografiya **35** (2), 355 (1990) [Sov. Phys. Crystallogr. **35**, 200 (1990)].
15. I. V. Morozov, S. I. Troyanov, A. Stiewe, and E. Kemnitz, Z. Anorg. Allg. Chem. **624**, 135 (1998).
16. A. Stiewe, E. Kemnitz, and S. Troyanov, Z. Kristallogr. **213**, 654 (1998).
17. M. A. Simonov, S. I. Troyanov, E. Kemnitz, *et al.*, Kristallografiya **31**, 1220 (1986) [Sov. Phys. Crystallogr. **31**, 721 (1986)].

Translated by T. Safonova

Crystallography Reports, Vol. 47, No. 5, 2002, pp. 773–782. Translated from Kristallografiya, Vol. 47, No. 5, 2002, pp. 839–848.

STRUCTURES OF INORGANIC COMPOUNDS

Synthesis and Crystal Structure of New Double Indium Phosphates $M^{I}_3In(PO_4)_2$ (M^{I} = K and Rb)

M. G. Zhizhin*, A. A. Filaretov, A. V. Olenev*, V. V. Chernyshev*, F. M. Spiridonov*, and L. N. Komissarova***

** Moscow State University, Vorob'evy gory, Moscow, 119899 Russia*
e-mail: zhizhin@tech.chem.msu.ru
*** Kurnakov Institute of General and Inorganic Chemistry, Russian Academy of Sciences, Leninskiĭ pr. 31, Moscow, 119991 Russia*

Received April 18, 2002

Abstract—Double potassium indium and rubidium indium phosphates $K_3In(PO_4)_2$ (**I**) and $Rb_3In(PO_4)_2$ (**II**) are synthesized by solid-phase sintering at T = 900°C. The compounds prepared are characterized by X-ray powder diffraction (**I** and **II**), X-ray single-crystal diffraction (**II**), and laser-radiation second harmonic generation. Structure **I** is solved using the Patterson function and refined by the Rietveld method. Both compounds crystallize in the monoclinic crystal system. For crystals **I**, the unit cell parameters are as follows: a = 15.6411(1) Å, b = 11.1909(1) Å, c = 9.6981(1) Å, β = 90.119(1)°, space group $C2/c$, R_p = 4.02%, and R_{wp} = 5.25%. For crystals **II**, the unit cell parameters are as follows: a = 9.965(2) Å, b = 11.612(2) Å, c = 15.902(3) Å, β = 90.30(3)°, space group $P2_1/n$, R_1 = 4.43%, and wR_2 = 10.76%. Structures **I** and **II** exhibit a similar topology of the networks which are built up of $\{In[PO_4]_2\}$ (**I**) and $\{In_2[PO_4]_4\}$ (**II**) structural units.

INTRODUCTION

The crystal chemical features of double phosphates of composition $M^{I}_3M^{III}(PO_4)_2$ (where M^{I} = K and Rb) have been investigated in sufficient detail in the case of scandium, yttrium, and rare-earth elements. These compounds have been studied by different methods. It has been demonstrated that phosphates containing rare-earth elements hold considerable promise for use as laser and luminescent materials [1–3]. All the known double phosphates of composition $K_3M^{III}(PO_4)_2$ are structural analogues of arcanite β-K_2SO_4 (for M^{III} = Y, La–Yb) or glaserite $K_3Na(SO_4)_2$ (for M^{III} = Lu and Sc) [2–5]. Double phosphates $Rb_3M^{III}(PO_4)_2$ (where M^{III} = Y, Dy–Lu) belong to the $K_3Na(SO_4)_2$ structural type [4, 6]. Among the double indium phosphates $M^{I}_3In(PO_4)_2$, only the β and α modifications of the compound $Na_3In(PO_4)_2$ are known [7, 8]. The low-temperature β modification of $Na_3In(PO_4)_2$ belong to arcanite-like phosphates. The same is also true for the β-$Na_3M^{III}(PO_4)_2$ compounds (where M^{III} = La–Lu), whose structure is characterized by a combination of β-K_2SO_4 and Na_2CrO_4 structural motifs [9]. The role played by the structural motif of sodium chromate in the structure of the $Na_3In(PO_4)_2$ compound increases upon the β ⟶ α polymorphic transition (T = 700°C).

Until very recently, double phosphates $M^{I}_3In(PO_4)_2$ (where M^{I} = K and Rb) were unknown. However, reliable information on the structure of these compounds is required to elucidate how the size and structure of the electron shell of the trivalent cation and the size of an alkali cation affect the crystal structure of $M^{I}_3M^{III}(PO_4)$ phosphates in the series M^{III} = La– ⋯ –Lu–In–Sc–Fe.

In this respect, the purpose of the present work was to synthesize the compounds $K_3In(PO_4)_2$ (**I**) and $Rb_3In(PO_4)_2$ (**II**) and to perform the X-ray structure investigation.

EXPERIMENTAL

Synthesis. The compounds $K_3In(PO_4)_2$ (**I**) and $Rb_3In(PO_4)_2$ (**II**) were prepared by the solid-phase reaction from stoichiometric amounts of In_2O_3 (chemically pure), M_2HPO_4 (analytical grade), and M_2CO_3 (analytical grade) at a temperature of 900°C for 120 h. The synthesis was carried out in alundum crucibles in air. Every 24 hours, samples were ground in order to ensure homogenization of the mixture. The completeness of the reaction was controlled using X-ray diffraction. The samples were annealed at higher temperatures (up to T = 1250°C) with the aim of preparing single crystals and elucidating the character of melting of the relevant compounds. A rapid cooling of the melt of compound **I** to temperatures below 1200°C and a slow cooling of the melt of compound **II** from 950 to 900°C (at a rate of 5 K/h) led to the formation of transparent, light yellow crystals in the form of prismatic needles with a maximum length of 3 mm. The crystals prepared were

1063-7745/02/4705-0773$22.00

washed from the melt with a large amount of warm distilled water and dried in air at 50°C.

Attempts to synthesize these compounds under hydrothermal conditions (T = 200°C and p = 20 atm) in the range $7 \le pH \le 10$ were unsuccessful. The hydroxo phosphates $M^{I}In(OH)PO_4$ (where M^{I} = K and Rb) were formed over the entire range of pH [10, 11]. It should be noted that, in the case of compound **II**, we observed the cocrystallization with a phase of unknown composition whose fraction decreased with an increase in pH.

X-ray powder diffraction analysis was performed on an STOE diffractometer [CuK_{α_1} radiation; λ = 1.5406 Å; SiO_2 monochromator; 2θ step-scan mode; step width, 0.02° in 2θ; 2θ = 5°–80°].

X-ray structure analysis. The crystal structures of double phosphates were investigated using crystals of $K_3In(PO_4)_2$ (0.35 × 0.12 × 0.10 mm in size) and $Rb_3In(PO_4)_2$ (0.30 × 0.15 × 0.13 mm in size) that were chosen with the use of a polarizing microscope and mounted on the goniometer head of an Enraf–Nonius CAD4 four-circle diffractometer (MoK_α radiation, graphite monochromator). The unit cell parameters were determined with a sufficient number of well-resolved reflections measured in the course of initial data collection. In the case of single crystal **I**, among the twenty five reflections observed, five reflections were characterized by fractional indices *hkl*. This allowed us to assume that the high-temperature phase of compound **I** has a modulated crystal structure, which was subsequently confirmed by the X-ray single-crystal investigation [12]. However, the incommensurate modulated structure of single crystals **I** was not thoroughly investigated because of the limited technical potentialities of the diffractometer used in our experiments. The structure of single crystal **II** was solved and refined using a complete X-ray diffraction analysis (room temperature, ω–2θ scan mode). The initial processing of the intensities of diffraction reflections was carried out according to the XCAD [13] and PSICALC [14] software packages (the Lorentz and polarization effects were taken into account, and absorption correction was introduced using the azimuthal scanning of reflections with χ angles close to 90°). The space group $P2_1/n$ (no. 14) was uniquely determined from the conditions for absences of reflections ($h0l$: $h + l = 2n$; $0k0$: $k = 2n$; $h00$: $h = 2n$; and $00l$: $l = 2n$). The structure was solved by the direct method and refined on F^2 with the full-matrix least-squares procedure in the isotropic approximation and then in the anisotropic approximation for all the atoms (according to the SHELXS97 [15] and SHELXL97 [16] software packages). The final reliability factors are as follows: R_1 = 4.43% and wR_2 = 10.76% for F and F^2, respectively.

Intensities of experimental reflections used for determining the structure of compounds **I** and **II** synthesized at 900°C in the form of polycrystalline samples were collected on an STADI-P (STOE) powder diffractometer (transmission geometry, CuK_{α_1} radiation, λ = 1.5406 Å, germanium monochromator, position-sensitive detector) for **I** and a SIEMENS D500 powder diffractometer (reflection geometry, CuK_{α_1} radiation, SiO_2 monochromator) for **II**. The scanning was performed in the 2θ range 9(10)°–100° with a step of 0.01(0.02)° and an exposure time of ~30 min per point. The X-ray diffraction pattern of compound **I** was initially indexed in the orthorhombic crystal system [a = 15.638(1) Å, b = 11.192(1) Å, c = 9.694(1) Å, M_{20} = 38.7, and F_{20} = 67.8 (0.0085, 52)] with the use of the TREOR90 program [17]. A closer examination of large-angle reflections ($2\theta > 50°$) revealed a monoclinic distortion of the unit cell with the angle β = 90.13°. The conditions determined for the absences (hkl: $h + k = 2n$) indicated two possible space groups, namely, the Cc acentric (no. 9) and $C2/c$ centrosymmetric (no. 15) groups. The monoclinic unit cell parameters determined for compound **II** from the first 35 peaks [a = 9.967(1) Å, b = 11.616(1) Å, c = 15.902(1) Å, β = 90.32(1)°, M_{20} = 28.6, and F_{30} = 65.3 (0.0067, 69)] were close to the corresponding parameters obtained for the single crystal. The results of indexing of the X-ray diffraction patterns of compounds **I** and **II** have been deposited with the JCPDS–ICDD Powder Diffraction File.

The peak profiles were described by the modified (split-type) pseudo-Voigt function [18]. The background profile was approximated by the Chebyshev polynomial. The X-ray diffraction patterns were decomposed into individual peaks according to the full-pattern-decomposition (FPD) procedure with the MRIA software package [19]. In this case, the FPD reliability factors were χ^2 = 3.17% and R_p = 3.15% for compound **I** and χ^2 = 6.27% and R_p = 2.91% for compound **II**. When solving crystal structure **I**, the heaviest atoms (K, In, and P) were located by the Patterson method with the use of 613 $|F^2|$ values (according to the DIRDIF96 program [20]). The positions of the oxygen atoms were determined using a procedure with step-by-step displacement (with a step of 0.7 Å for translations along the a-, b-, and c-axes) and rotation (with a step of 20° for the ψ, φ, and κ angles) of the known fragment (PO_4^{3-} group) in the asymmetric part of the unit cell. The starting model for the refinement of structure **II** was based on the single-crystal data. The subsequent refinement of both structures by the Rietveld method with a gradual weakening of constraints on the bond lengths in the tetrahedra resulted in satisfactory reliability factors: χ^2 = 4.88%, R_p = 4.02%, and R_{wp} = 5.25% for compound **I** and χ^2 = 7.82%, R_p = 3.83%, and R_{wp} = 5.16% for compound **II**. After the refinement of all 100 parameters for compound **I** and all 150 parameters for compound **II** (these parameters included the structural, background, profile, and unit cell parameters and also the scale factor and zero-point shift) within the

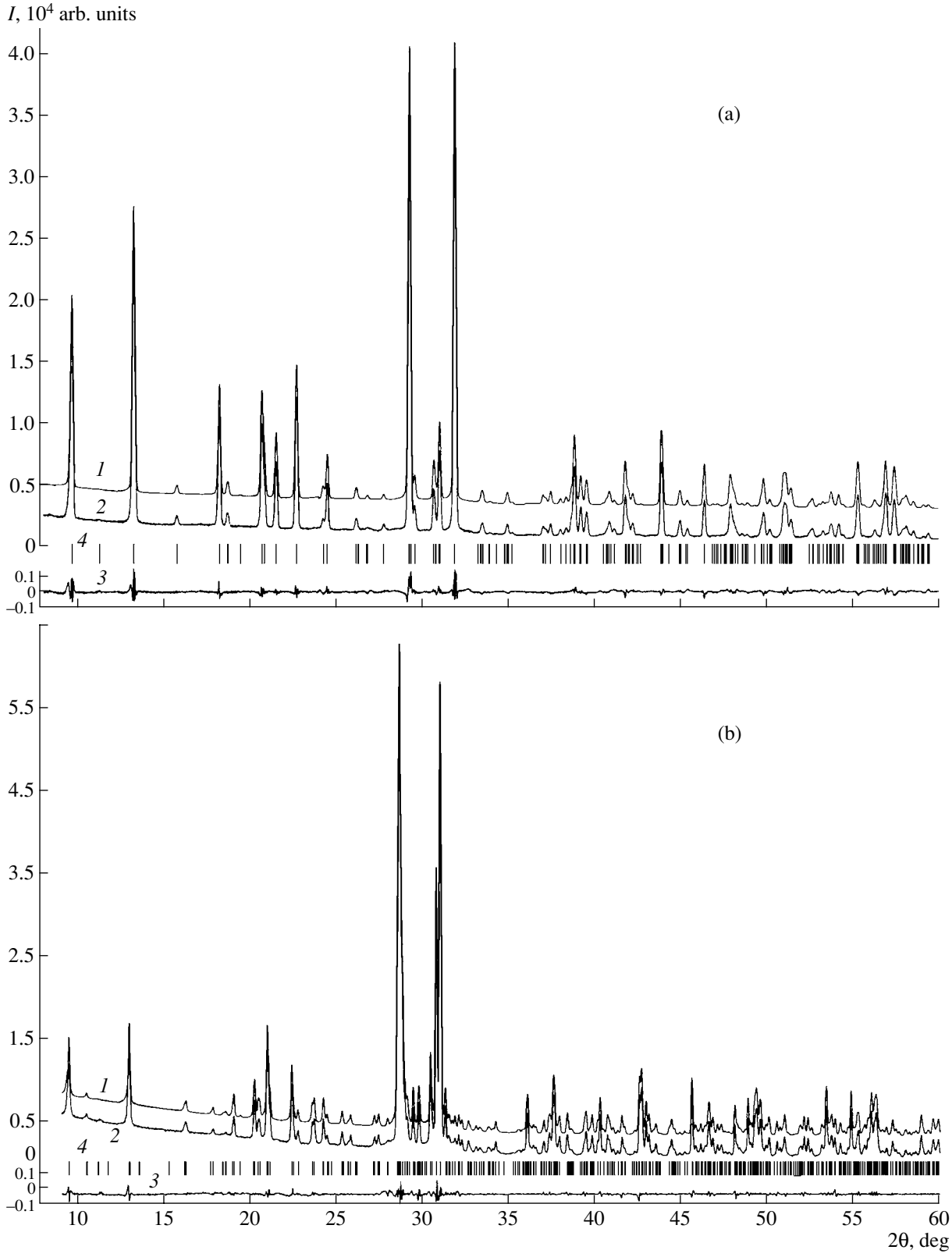

Fig. 1. Fragments of (*1*) calculated, (*2*) experimental, and (*3*) difference X-ray diffraction patterns and (*4*) positions of Bragg reflections for (a) $K_3In(PO_4)_2$ and (b) $Rb_3In(PO_4)_2$ compounds.

Table 1. Data collection and refinement parameters for $K_3In(PO_4)_2$ and $Rb_3In(PO_4)_2$ structures

Compound	$K_3In(PO_4)_2$ (powder)	$Rb_3In(PO_4)_2$ (crystal)
Diffractometer	STADI-P (STOE)	CAD-4 (Nonius)
Crystal system	Monoclinic	
Space group; Z	$C2/c$, 8	$P2_1/n$, 8
2θ (θ) range, deg	8–100 (2θ)	2–26(θ)
Unit cell parameters, Å:		
a	15.6411(1)	9.965(2)
b	11.1909(1)	11.612(2)
c	9.6981(1)	15.902(2)
β, deg	90.119(1)	90.30(3)
V, Å^3	1697.53(3)	1840.1(7)
Number of reflections	890	3625 [R_{int} = 0.023]
Number of unique reflections with $I > 2\sigma(I)$		2204
Number of refined parameters:		
structural	60	
other	40	253
Reliability factors, %:		
χ^2; R_p; R_{wp}^*	4.88; 4.02; 5.25	
R_1; wR_2^{**}		4.43; 10.76

* $R_p = (\Sigma|y_{i,\,\mathrm{exp}} - y_{i,\,\mathrm{calcd}}|)(\Sigma y_{i,\,\mathrm{exp}})$; $R_{wp} = \{(\Sigma w_i[y_{i,\,\mathrm{exp}} - y_{i,\,\mathrm{calcd}}]^2)/(\Sigma w_i[y_{i,\,\mathrm{exp}}]^2)\}^{1/2}$.

** $R_1 = \Sigma(|F_{\mathrm{exp}}| - |F_{\mathrm{calcd}}|)/\Sigma|F_{\mathrm{exp}}|$; $wR_2 = [\Sigma w(F_{\mathrm{exp}}^2 - F_{\mathrm{calcd}}^2)^2/\Sigma w(F_{\mathrm{exp}}^2)^2]^{1/2}$, $w^{-1} = \sigma^2(F_{\mathrm{exp}}^2) + (0.041P)^2$, $P = (F_{\mathrm{exp}}^2 + 2F_{\mathrm{calcd}}^2)/3$.

chosen model, the experimental and theoretical X-ray diffraction patterns were in good agreement (Figs. 1a, 1b).

The crystal data and refinement parameters for structures **I** and **II** are summarized in Table 1. The coordinates of the basis atoms, thermal parameters, and selected interatomic distances are listed in Tables 2 and 3.

Laser-radiation second harmonic generation in powders of the compounds prepared was measured in a reflection geometry with the use of an Nd : YAG laser as a radiation source (λ = 1064 nm, frequency ν = 6.25 kHz, pulse duration τ = 12 ns, mean power W = 9.5 MW). Finely crystalline quartz was used as a reference sample.

RESULTS AND DISCUSSION

Double phosphate **I** crystallizes in the monoclinic crystal system in the centrosymmetric space group $C2/c$. The choice of this space group is in agreement with the laser-radiation second harmonic generation data [$I_{2\omega}/I_{2\omega(\mathrm{SiO_2})} = 0.02$]. For compound **II**, zero laser-radiation second harmonic generation signal uniquely confirms the choice of the centrosymmetric unit cell (space group $P2_1/n$). All the atoms in structure **II** occupy general positions, whereas two atoms in structure **I** are located in special positions (on the twofold axis). The mean In–O distances in InO_6 octahedra (2.141 and 2.155 Å in **II** and 2.136 Å in **I**) are typical and comparable to those observed in other indium phosphates [7, 8]. All the InO_6 octahedra have a substantially distorted structure. It is seen from Table 3 that, in structure **II**, four In^{3+}–O interatomic distances in the $In(1)O_6$ octahedron fall in the range 2.072–2.150 Å and the distances to two oxygen atoms are equal to 2.219 and 2.218 Å. In the $In(2)O_6$ octahedron, two distant oxygen atoms are located at distances of 2.251 and 2.231 Å. In structure **I**, the spread in the In^{3+}–O distances is larger and the two longest distances are equal to 2.238 and 2.331 Å. This distortion of the indium polyhedra is associated with the necessity of attaining a balance of the bond valences at the oxygen anions in the presence of common edges between the InO_6 octahedra and the PO_4 tetrahedra (Fig. 2). The calculated sums of bond valences [21] at the In(1) (3.18) and In(2) (3.07) atoms in structure **II** and at the In atom (3.33) in structure **I** agree well with the formal oxidation number of indium.

The presence of two common oxygen atoms between the P(1) and In atoms in structure **I** [P(1) and In(1), P(4) and In(2) in structure **II**] is likely responsible for the insignificant distortion of the phosphate tet-

Table 2. Atomic coordinates and thermal parameters (Å^2) for $K_3In(PO_4)_2$ and $Rb_3In(PO_4)_2$ compounds

Atom	*x*	*y*	*z*	$B_{iso}/U_{eq} \times 10^2$****
		$K_3In(PO_4)_2$		
In	0.1251(1)	0.1377(1)	0.0747(1)	3.0(1)
K(1*a*)*	0.0918(2)	0.6085(3)	0.0966(4)	3.7(3)
K(1*b*)**	0.1828(3)	0.5985(4)	0.1009(6)	3.7(3)
K(2)	0.7532(1)	0.8824(2)	0.2915(2)	3.1(1)
K(3)	0	0.3755(4)	0.25	5.1(1)
K(4)	0	0.8854(3)	0.25	5.7(1)
P(1)	0.6525(1)	0.1498(3)	0.4274(3)	2.1(1)
P(2)	0.4001(1)	0.3684(2)	0.5835(3)	2.6(1)
O(11)***	0.5925(3)	0.0579(4)	0.3625(5)	2.8(1)
O(12)	0.6357(3)	0.2730(3)	0.3690(5)	3.1(2)
O(13)	0.6338(3)	0.1545(4)	0.5831(4)	3.2(2)
O(14)	0.7448(2)	0.1135(4)	0.4025(6)	2.8(2)
O(21)	0.4914(2)	0.3299(4)	0.5557(6)	3.2(1)
O(22)	0.3914(3)	0.4192(4)	0.7298(5)	3.0(2)
O(23)	0.3416(3)	0.2588(5)	0.5724(6)	7.0(2)
O(24)	0.3718(4)	0.4623(4)	0.4798(5)	5.7(2)
		$Rb_3In(PO_4)_2$		
In(1)	0.42228(7)	0.63098(7)	0.13117(5)	0.96(2)
In(2)	0.07342(7)	0.65243(7)	−0.11421(5)	0.98(2)
Rb(1)	0.2938(1)	0.8802(1)	−0.0079(1)	2.08(3)
Rb(2)	0.7397(1)	0.6071(1)	0.0009(1)	1.91(3)
Rb(3)	−0.1002(1)	0.8785(1)	0.0837(1)	2.59(3)
Rb(4)	0.7889(1)	0.5991(1)	0.2464(1)	2.09(3)
Rb(5)	0.1137(1)	0.5841(1)	0.3281(1)	2.71(3)
Rb(6)	0.3126(1)	0.3640(1)	0.2427(1)	2.27(3)
P(1)	0.4351(3)	0.6378(3)	0.3548(2)	1.13(6)
P(2)	0.0808(3)	0.6214(3)	0.1017(2)	0.93(6)
P(3)	0.4145(3)	0.6333(3)	−0.0943(2)	0.92(6)
P(4)	0.5550(3)	0.8408(2)	0.1624(2)	1.01(6)
O(11)	0.1209(8)	1.0422(7)	0.0884(5)	2.03(19)
O(12)	0.3986(9)	0.6066(7)	0.2643(5)	2.05(19)
O(13)	0.0891(7)	0.8440(6)	−0.1333(5)	1.35(17)
O(14)	−0.1250(8)	0.7408(7)	−0.1229(5)	1.81(18)
O(21)	0.0326(8)	0.6994(7)	0.1708(5)	1.78(18)
O(22)	0.0120(8)	0.4846(7)	−0.0943(5)	1.72(18)
O(23)	0.0791(8)	0.6893(7)	0.0183(5)	1.93(18)
O(24)	0.2242(8)	0.5742(7)	0.1215(5)	2.30(20)
O(31)	0.4428(9)	0.7449(6)	−0.1397(5)	2.38(21)
O(32)	0.4373(9)	0.6494(8)	0.0001(5)	2.81(22)
O(33)	0.2704(8)	0.5914(8)	−0.1105(5)	2.60(21)
O(34)	0.4903(8)	0.4626(7)	0.1249(5)	2.54(21)
O(41)	0.0755(9)	0.6221(7)	−0.2471(5)	2.52(21)
O(42)	0.3911(9)	1.0655(7)	−0.1051(5)	2.17(20)
O(43)	0.6176(7)	0.7210(6)	0.1448(4)	1.11(16)
O(44)	0.4023(7)	0.8198(7)	0.1480(5)	1.74(18)

***** Occupancy of the K(1*a*) site is equal to 0.58(3).
** Occupancy of the K(1*b*) site is equal to 0.42(3).
*** Designations of oxygen atoms: the first numeral is the number of the tetrahedron, and the second numeral is the number of the oxygen atom in the tetrahedron.
**** The thermal parameters B_{iso} are given for $K_3In(PO_4)_2$, and the equivalent thermal parameters U_{eq} calculated as a one-third of the orthogonal tensor U_{ij} are presented for $Rb_3In(PO_4)_2$.

Table 3. Selected interatomic distances and angles in $K_3In(PO_4)_2$ and $Rb_3In(PO_4)_2$ structures

Distance	*d*, Å	Distance	*d*, Å
$K_3In(PO_4)_2$			
In–O(12)	2.238(2)	K(2)–O(11)	3.264(2)
O(13)	2.331(4)	O(12)	2.637(2)
O(14)	2.064(1)	O(13)	2.780(3)
O(21)	2.130(1)	O(14)	2.804(3)
O(22)	2.017(3)	O(22)	3.157(3)
O(24)	2.033(4)	O(23)	2.539(2)
⟨In–O⟩	2.14	O(23')	3.351(3)
K(1*a*)–O(11)	2.965(4)	O(24)	2.750(3)
O(11')	2.640(4)	⟨K(2)–O⟩	2.91
O(11")	2.936(5)	K(3)–O(11) × 2	2.728(3)
O(12)	3.291(4)	O(13) × 2	2.670(3)
O(13)	3.019(6)	O(21) × 2	2.975(4)
O(21)	3.163(6)	O(23) × 2	3.368(3)
O(23)	2.571(4)	⟨K(3)–O⟩	2.94
⟨K(1*a*)–O⟩	2.94	K(4)–O(12) × 2	2.722(2)
K(1*b*)–O(11)	3.223(4)	O(21) × 2	3.032(5)
O(11')	2.942(4)	O(22) × 2	2.776(3)
O(13)	2.938(4)	O(24) × 2	3.122(3)
O(14)	3.084(6)	⟨K(4)–O⟩	2.91
O(14')	3.206(3)	P(2)–O(21)	1.615(5)
O(23)	2.487(6)	O(22)	1.535(4)
O(23')	2.966(4)	O(23)	1.534(2)
⟨K(1*b*)–O⟩	2.98	O(24)	1.520(3)
P(1)–O(11)	1.527(2)	⟨P(2)–O⟩	1.53
O(12)	1.513(3)		
O(13)	1.540(4)		
O(14)	1.520(5)		
⟨P(1)–O⟩	1.53		
Angle	ω, deg	Angle	ω, deg
∠(O(11)–P(1)–O(12))	110.7(3)	∠(O(21)–P(2)–O(22))	110.8(3)
∠(O(11)–P(1)–O(13))	108.0(0)	∠(O(21)–P(2)–O(23))	108.8(2)
∠(O(11)–P(1)–O(14))	109.7(2)	∠(O(21)–P(2)–O(24))	110.6(3)
∠(O(12)–P(1)–O(13))	107.6(3)	∠(O(22)–P(2)–O(23))	107.9(3)
∠(O(12)–P(1)–O(14))	110.4(3)	∠(O(22)–P(2)–O(24))	109.2(3)
∠(O(13)–P(1)–O(14))	110.3(3)	∠(O(23)–P(2)–O(24))	109.5(3)
⟨∠(O–P(1)–O)⟩	109.5	⟨∠(O–P(2)–O)⟩	109.5
$Rb_3In(PO_4)_2$			
In(1)–O(12)	2.150(8)	In(2)–O(13)	2.251(7)
O(24)	2.086(8)	O(14)	2.231(8)
O(32)	2.101(8)	O(22)	2.067(8)
O(34)	2.072(8)	O(23)	2.150(8)
O(43)	2.219(7)	O(44)	2.088(8)
O(44)	2.218(8)	O(41)	2.143(8)
⟨In(1)–O⟩	2.141	⟨In(2)–O⟩	2.115

Table 3. (Contd.)

Distance	*d*, Å	Distance	*d*, Å
		$Rb_3In(PO_4)_2$	
Rb(1)–O(11)	2.995(8)	Rb(2)–O(14)	2.851(8)
O(13)	2.876(7)	O(22)	3.070(8)
O(23)	3.110(8)	O(22')	3.423(8)
O(31)	3.017(8)	O(24)	2.890(9)
O(32)	3.041(9)	O(32)	3.054(9)
O(42)	2.824(8)	O(32')	3.461(9)
O(44)	2.790(8)	O(33)	2.893(9)
⟨Rb(1)–O⟩	3.093	O(34)	3.140(9)
Rb(3)–O(11)	2.886(8)	O(43)	2.915(7)
O(11')	2.956(9)	⟨Rb(2)–O⟩	3.077
O(13)	3.319(8)	Rb(4)–O(13)	2.845(7)
O(21)	2.824(8)	O(21)	2.955(8)
O(23)	3.020(8)	O(22)	3.284(8)
O(42)	2.992(9)	O(31)	2.981(8)
O(43)	3.496(7)	O(33)	3.146(8)
⟨Rb(3)–O⟩	3.07	O(41)	2.903(8)
Rb(5)–O(11)	2.990(8)	O(42)	3.200(8)
O(12)	3.032(9)	O(43)	2.739(7)
O(21)	2.947(8)	⟨Rb(4)–O⟩	3.007
O(31)	2.667(8)	Rb(6)–O(11)	3.467(8)
O(42)	3.015(8)	O(12)	2.964(8)
O(44)	3.097(8)	O(14)	2.927(8)
⟨Rb(5)–O⟩	2.958	O(21)	2.812(8)
P(1)–O(11)	1.521(8)	O(24)	3.229(8)
O(12)	1.527(8)	O(31)	3.204(8)
O(13)	1.560(8)	O(34)	2.827(9)
O(14)	1.573(8)	O(44)	2.813(8)
⟨P(1)–O⟩	1.545	⟨Rb(6)–O⟩	3.03
P(3)–O(31)	1.510(8)	P(2)–O(21)	1.504(8)
O(32)	1.529(8)	O(22)	1.543(8)
O(33)	1.537(8)	O(23)	1.544(8)
O(34)	1.543(8)	O(24)	1.561(8)
⟨P(3)–O⟩	1.530	⟨P(2)–O⟩	1.538
		P(4)–O(41)	1.515(8)
		O(42)	1.520(8)
		O(43)	1.550(7)
		O(44)	1.556(7)
		⟨P(4)–O⟩	1.535
Angle	ω, deg	Angle	ω, deg
∠(O(11)–P(1)–O(12))	107.7(5)	∠(O(21)–P(2)–O(22))	110.1(5)
∠(O(11)–P(1)–O(13))	112.9(5)	∠(O(21)–P(2)–O(23))	108.5(4)
∠(O(11)–P(1)–O(14))	111.5(5)	∠(O(21)–P(2)–O(24))	111.1(5)
∠(O(12)–P(1)–O(13))	112.0(5)	∠(O(22)–P(2)–O(23))	109.8(5)
∠(O(12)–P(1)–O(14))	109.7(5)	∠(O(22)–P(2)–O(24))	106.5(5)
∠(O(13)–P(1)–O(14))	103.1(4)	∠(O(23)–P(2)–O(24))	111.0(5)
⟨∠(O–P(1)–O)⟩	109.5	⟨∠(O–P(2)–O)⟩	109.5
∠(O(31)–P(3)–O(32))	109.7(5)	∠(O(41)–P(4)–O(42))	108.6(5)
∠(O(31)–P(3)–O(33))	111.6(5)	∠(O(41)–P(4)–O(43))	112.0(5)
∠(O(31)–P(3)–O(34))	110.6(5)	∠(O(41)–P(4)–O(44))	108.1(5)
∠(O(32)–P(3)–O(33))	109.7(5)	∠(O(42)–P(4)–O(43))	113.0(4)
∠(O(32)–P(3)–O(34))	108.0(5)	∠(O(42)–P(4)–O(44))	111.9(5)
∠(O(33)–P(3)–O(34))	107.1(5)	∠(O(43)–P(4)–O(44))	103.1(4)
⟨∠(O–P(3)–O)⟩	109.5	⟨∠(O–P(4)–O)⟩	109.5

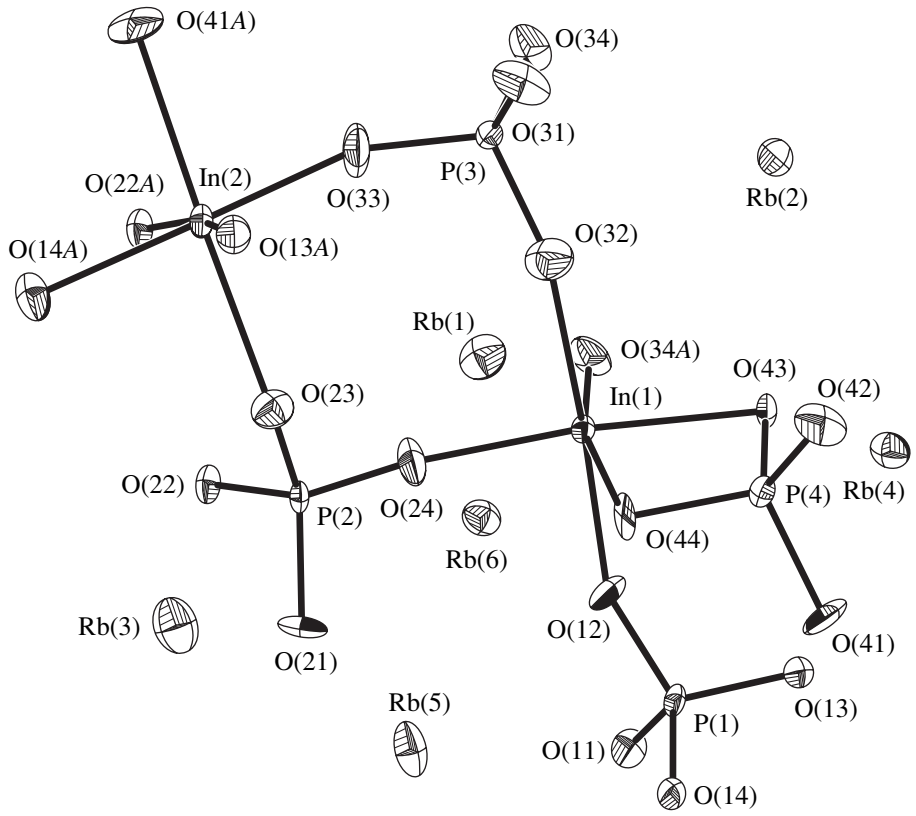

Fig. 2. A fragment of the crystal structure of the $Rb_3In(PO_4)_2$ compound. Bonds and atoms in the form of thermal ellipsoids at a 50% probability level are shown schematically.

rahedra (Table 3). The mean P–O distances correlate well with the sum of the relevant ionic radii (according to Shannon [22]).

The skeleton of structure **I** is a three-dimensional network consisting of InO_6 octahedra (isolated from each other) and PO_4 tetrahedra shared by vertices and edges. The network is built up of the characteristic structural units $\{In[PO_4]_2\}$ formed by three symmetrically independent polyhedra: one InO_6 octahedron and two PO_4 tetrahedra. In the *xy* plane, these units are linked together into parallel columns with the formation of pseudolayers. The columns of one pseudolayer are rotated with respect to the columns of the other pseudolayer, alternate along the *z*-axis, and form the $\{In[PO_4]_2\}_\infty$ framework (Fig. 3a). In structure **II**, the topologically identical framework of the same composition is comprised of six symmetrically independent polyhedra: two InO_6 octahedra and four PO_4 tetrahedra (Fig. 3b). The $P(2)O_4$ tetrahedra in **I** [the $P(2)O_4$ and $P(3)O_4$ tetrahedra in **II**] are involved in the bonding of the columns of adjacent pseudolayers. At the same time, the $P(1)O_4$ tetrahedra that have common edges with the indium polyhedra in **I** [the $P(1)O_4$ and $P(4)O_4$ tetrahedra in **II**] are responsible for the formation of columns. Along the main crystallographic directions, the channels are formed in the structures. The size and shape of these channels are governed by alkali cations.

In structure **I**, five crystallographically independent potassium atoms, as a rule, have an eightfold coordination. The sole exception is provided by the $K(1a)O_7$ and $K(1b)O_7$ polyhedra (Table 3). Their oxygen environment is characterized by two coordination spheres. The first coordination sphere is composed of four to six oxygen atoms located at distances of 2.487–3.084 Å. The second coordination sphere consists of two or three more distant oxygen atoms (3.122–3.368 Å). The K(1*a*) and K(1*b*) atoms statistically occupy two sites separated by a distance of 1.47 Å with occupancies of 0.58(3) and 0.42(3), respectively. Allowance made for this splitting of the K(1) position into two positions in the refinement of structure **I** leads not only to a considerable decrease in the factor R_p from 5.39 to 4.02% and a decrease in the thermal parameter B_{iso} for the K(1) atom from 12.5 to 3.7 $Å^2$ for each split position but also results in a certain increase in the anomalously short distance K(1)–O(23) from 2.394 Å to 2.571 Å for K(1*a*)–O(23) and to 2.487 Å for K(1*b*)–O(23). Most likely, this is responsible for the modulation of atomic positions in the structure of the high-temperature phase of compound **I**, which was obtained in the form of single crystals upon rapid cooling of the stoichiometric melt $K_3In(PO_4)_2$ to temperatures below 1200°C.

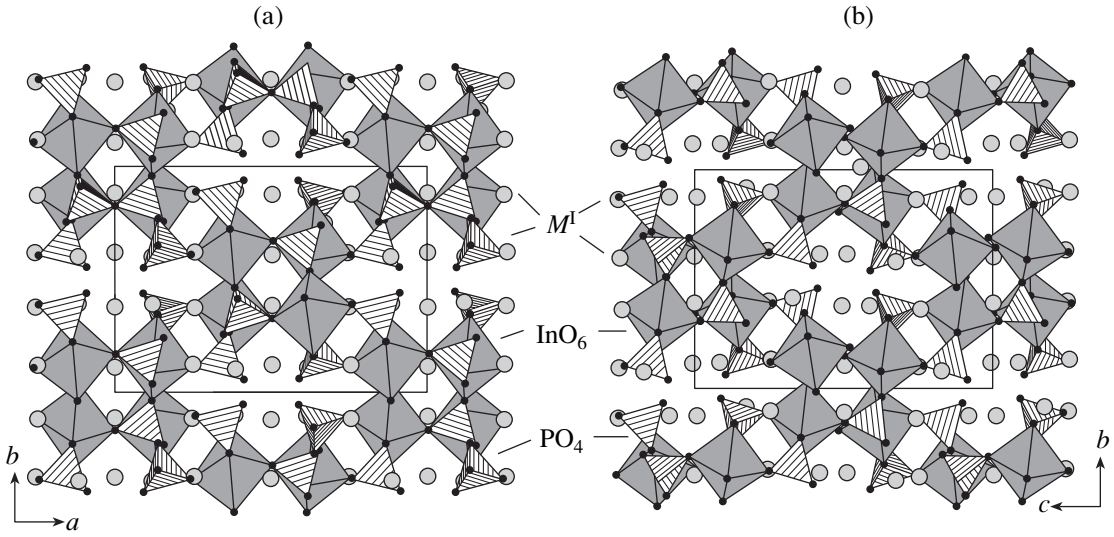

Fig. 3. Projections of the crystal structures of (a) $K_3In(PO_4)_2$ and (b) $Rb_3In(PO_4)_2$ compounds along the *z*- and *x*-axes.

In structure **II**, six crystallographically independent rubidium atoms form polyhedra with different coordination numbers (from 6 to 9). The Rb(5) atom is located in a distorted octahedron. This fact itself is very unusual because a coordination number of 6 is not characteristic of the environment of large-sized alkali cations (Rb^+ and Cs^+). In this case, the sixfold coordination can be associated with the position of the Rb(5) atom in the framework in which this atom, like the Rb(3) atom, occupies a niche between the columns of the pseudolayer. Similar positions of M^I cations in structure **I** are occupied by the K(1*a*) and K(1*b*) atoms, whereas the other atoms are located in the channels of the structures. In the $Rb(5)O_6$ polyhedron, the distances from the Rb(5) atom to five oxygen atoms vary from 2.947 to 3.097 Å and one oxygen atom is located at an anomalously short distance of 2.667 Å. Note that the contribution from this short Rb–O contact to the sum of the bond valences at the Rb(5) atom is equal to 0.34. The coordination numbers of the Rb(1) and Rb(3) atoms are equal to 7 (7 and 6 + 1, respectively). In the $Rb(1)O_7$ polyhedron, the distances from the Rb(1) atom to all seven oxygen atoms lie in the range 2.824–3.11 Å. At the same time, in the $Rb(3)O_7$ polyhedron, the distances from the Rb(3) atom to six oxygen atoms range from 2.824 to 3.319 Å and the seventh oxygen atom is located at a distance of 3.496 Å. According to Donnay and Allmann [23], this distance exceeds the limiting Rb–O bond length (3.42 Å). The contribution from this oxygen atom only slightly affects the sum of the bond valences at the Rb(3) atom and is equal to 0.04. The Rb(4) and Rb(6) atoms form eight-vertex polyhedra in which two coordination spheres can be distinguished. The nearest environment of these atoms is formed by five oxygen atoms located at distances of 2.739–2.981 and 2.8224–2.964 Å. The second coordination spheres each involve three oxygen atoms at distances of 3.146–3.284 and 3.204–3.467 Å. The nine-vertex polyhedron $Rb(2)O_9$ has a more complex geometry of the oxygen environment. In this case, it is possible to separate three rubidium coordination spheres (4 + 3 + 2), among which two oxygen atoms of the third sphere are located at distances of 3.423 and 3.461 Å. All the rubidium polyhedra are shared either by oxygen edges or by vertices. This permits us to draw the inference that the network composed of rubidium atoms is formed in the structure. The sums of the bond valences at the Rb(1)–Rb(6) atoms fall in the range 0.94–1.18, which is in agreement with the formal oxidation number of rubidium.

Therefore, the replacement of the K^+ cation by the larger sized Rb^+ cation is accompanied by an increase in the number of crystallographically independent positions of M^I atoms and a change in the coordination numbers and geometry of the M^IO_x coordination polyhedra. Moreover, unlike structure **I**, structure **II** is characterized by the complete occupation of sites by alkali cations. A comparison between the structures of double phosphates $M^I_3In(PO_4)_2$ (where M^I = K and Rb) demonstrates that, despite the lowering of the symmetry of the unit cell, the framework structures remain topologically similar.

It is of interest to compare the structural data obtained in our work for phosphates $M^I_3In(PO_4)_2$ (where M^I = K and Rb) with the data available in the literature for the compounds $Na_3In(PO_4)_2$, $K_3M^{III}(PO_4)_2$ (where M^{III} = Y, La–Lu, Sc), and $Rb_3M^{III}(PO_4)_2$ (where M^{III} = Y, Dy–Lu) [2–8]. The structural transformations in the previously known compounds with layered structures correlate with the ionic radii of cations. It seems

likely that no clear similarity in the structures of the β-$Na_3In(PO_4)_2$, $K_3In(PO_4)_2$, and $Rb_3In(PO_4)_2$ compounds is observed because of the substantial difference between the ionic radii of sodium and potassium (rubidium). For like compounds, such as $K_3M^{III}(PO_4)_2$ and $Rb_3M^{III}(PO_4)_2$, the structural topology almost completely depends on the radius of the M^{III} cation. In this regard, the series $K_3M^{III}(PO_4)_2$ is most significant. The crossover from an arcanite-like structure (typical of the majority of rare-earth elements) to a glaserite-like structure occurs upon changing over from ytterbium to lutecium in the lanthanide series and is attended by a rise in the symmetry of the unit cell from monoclinic (M^{III} = Y, Na–Yb) to trigonal (M^{III} = Lu and Sc). The latter symmetry is also observed in the case of the compounds $Rb_3M^{III}(PO_4)_2$ (where M^{III} = Y, Dy–Lu). The compounds $M^I_3In(PO_4)_2$ (where M^I = K and Rb) have specific structures of the framework type. On the other hand, judging only from the size factor [i.e., from the difference Δr between the ionic radii of M^+ and In^{3+} (r_{VI} = 0.79 Å), Lu^{3+} (r_{VI} = 0.85 Å), and Sc^{3+} (r_{VI} = 0.745 Å)], the indium compounds should belong to layered (glaserite-like) phosphates that are stable in the range 0.38 Å ≤ Δr ≤ 0.89 Å [24]. The difference between the crystal structures of $M^I_3In(PO_4)_2$ compounds and the glaserite-like structures of $M^I_3Lu(PO_4)_2$ (where M^I = K and Rb) and $K_3Sc(PO_4)_2$ is most likely associated with the specific features of the electronic structure of scandium, indium, and lutecium atoms.

ACKNOWLEDGMENTS

We are grateful to S.Yu. Stefanovich for measuring the laser-radiation second harmonic generation and A.V. Arakcheeva for her participation in discussions of the results and helpful remarks.

REFERENCES

1. M. Kloss, B. Finke, L. Schwarz, and D. Haberlandl, J. Lumin. **72–74**, 684 (1997).
2. H. Y.-P. Hong and S. R. Chinn, Mater. Res. Bull. **11**, 421 (1976).
3. B. I. Lazoryak, Usp. Khim. **65**, 307 (1996).
4. P. P. Mel'nikov and L. N. Komissarova, Koord. Khim. **12** (10), 1299 (1986).
5. L. N. Komissarova, A. P. Bobylev, A. N. Kirichenko, *et al.*, Zh. Neorg. Khim. **47**, 684 (2002).
6. V. B. Kalinin, Candidate's Dissertation in Chemistry (Moskow State University, Moscow, 1975).
7. M. G. Zhizhin, V. A. Morozov, A. P. Bobylev, *et al.*, J. Solid State Chem. **149**, 99 (2000).
8. K.-H. Lii, Eur. J. Solid State Inorg. Chem. **33**, 519 (1996).
9. J. K. Nimmo, Acta Crystallogr., Sect. B: Struct. Crystallogr. Cryst. Chem. **37**, 431 (1981).
10. J. A. Hriljac, C. P. Grey, A. K. Cheetham, *et al.*, J. Solid State Chem. **123**, 243 (1996).
11. K.-H. Lii, J. Chem. Soc., Dalton Trans., 815 (1996).
12. A. Arakcheeva, G. Chapuis, and M. Zhizhin, in *Book of Abstracts of Aperiodic Structures 2001, Krynica, 2001* (EJB, Krakow, 2001), p. 146.
13. *Enraf–Nonius CAD4 Operator Manual* (Enraf–Nonius, Delft, 1984).
14. P. McArdle, *PSICALC* (National University of Ireland I, Galway, 1999).
15. G. M. Sheldrick, *SHELXS97: Program for the Solution of Crystal Structures* (Univ. of Göttingen, Göttingen, 1997).
16. G. M. Sheldrick, *SHELXL97: Program for the Refinement of Crystal Structures* (Univ. of Göttingen, Göttingen, 1997).
17. P.-E. Werner, L. Erriksson, and M. Westdahl, J. Appl. Crystallogr. **18**, 367 (1985).
18. H. Torraya, J. Appl. Crystallogr. **19**, 440 (1986).
19. V. B. Zlokazov and V. V. Chernyshev, J. Appl. Crystallogr. **25**, 447 (1992).
20. P. T. Beurskens, G. Beurskens, W. P. Bosman, *et al.*, *The DIRDIF-96 Program System* (Univ. of Nijmegen, Nijmegen, 1996).
21. N. E. Brese and M. O'Keeffe, Acta Crystallogr., Sect. B: Struct. Sci. **47**, 192 (1991).
22. R. D. Shannon, Acta Crystallogr., Sect. A: Cryst. Phys., Diffr., Theor. Gen. Crystallogr. **32**, 751 (1976).
23. G. Donnay and R. Allmann, Am. Mineral. **55**, 1003 (1970).
24. V. A. Morozov, B. I. Lazoryak, A. P. Malakho, *et al.*, J. Solid State Chem. **160**, 377 (2001).

Translated by O. Borovik-Romanova

Crystallography Reports, Vol. 47, No. 5, 2002, pp. 783–790. Translated from Kristallografiya, Vol. 47, No. 5, 2002, pp. 849–855.

STRUCTURE OF ORGANIC COMPOUNDS

Crystal Structure of Calcium *trans*-*N*-(Nitrilotriacetato)(pyridine-2-carboxylato)cobaltate(III) Hexahydrate, $Ca[Co(Nta)(Pic)]_2 \cdot 6H_2O$

L. A. Zasurskaya*, I. N. Polyakova, T. N. Polynova*, A. L. Poznyak***, and V. S. Sergienko****

** Faculty of Chemistry, Moscow State University, Vorob'evy gory, Moscow, 119899 Russia*
e-mail: lar@lar.chem.msu.su

*** Kurnakov Institute of General and Inorganic Chemistry, Russian Academy of Sciences, Leninskiĭ pr. 31, Moscow, GSP-1, 119991 Russia*

**** Institute of Molecular and Atomic Physics, Belarussian Academy of Sciences, pr. F. Skoriny 70, Minsk, 220072 Belarus*

Received December 28, 2001

Abstract—Crystals of $Ca[Co^{III}(Nta)(Pic)]_2 \cdot 6H_2O$ (**I**) (where Nta^{3-} and Pic^- are the nitrilotriacetate and picolinate ions, respectively) are prepared and characterized by the X-ray diffraction technique. Crystals **I** are monoclinic, a = 18.599(4) Å, b = 12.556(3) Å, c = 14.042(3) Å, β = 102.90(3)°, V = 3196(1) Å^3, Z = 4, space group $P2_1/c$, $R1$ = 0.0278, $wR2$ = 0.0716, and $Goof$ = 1.054 for 4982 reflections with $I > 2\sigma(I)$. Structure **I** is built of the $\{Ca(H_2O)_4[Co(Nta)(Pic)]_2\}_{1\infty}$ polymer ribbons and molecules of crystallization water. One of the two symmetrically independent anionic complexes (*B*) is included in the chain and alternates with cationic units, whereas the other anionic complex (*A*) forms a branch of this chain. The cationic and anionic units are interlinked via the interactions of the Ca^{2+} cations with the carbonyl atoms of the main (Nta^{3-}) and additional (Pic^-) ligands. The octahedral environment of the Co(III) atoms consists of donor atoms of the Nta^{3-} (N + 3O) and Pic^- (N + O) ligands. The coordination polyhedron of the Ca atom (pentagonal bipyramid) includes two carbonyl O atoms of two Nta^{3-} ligands, one O_{Pic} atom, and four O_w atoms of water molecules. © *2002 MAIK "Nauka/Interperiodica".*

INTRODUCTION

Structural studies of transition metal (*M*) mixed-ligand complexes with monoaminocarboxylate (*L*) and additional (*L*') ligands have revealed that, at the ratio $n_M : n_L = 1 : 1$, donor atoms of the *L* ligand occupy only some of the sites in the coordination sphere of the metal atom and the remaining sites are occupied by atoms of the *L*' ligands [1]. In the presence of alkaline-earth cations (*M*'), the monoaminocarboxylate ligands, whose coordination capacity is potentially low, often form polymeric structures due to interactions between *M*' cations and O_L oxygen atoms of the ligands.

The structures of Co(III) mixed-ligand aminocarboxylates, namely, $Ca[Co(Nta)(En)(CN)]_2 \cdot 6H_2O$ (**II**) [2], $Ba[Co(Nta)(CN)_2] \cdot 3H_2O$ (**III**) [3], and $Ba[Co(Nta)(Gly)]ClO_4 \cdot 4H_2O$ (**IV**) [4], where *L*' is ethylenediamine (*En*), cyanide ion (CN^-), or glycinate ion (Gly^-), were reported earlier. In our recent work [5], we investigated the structure of $Ca[Co(Nta)(H_2O)]_2 \cdot 4H_2O$ (**V**) and revealed that, in the absence of additional ligands, the coordination sphere of the Co(II) atom includes, apart from the donor atoms of the Nta^{3-} ligand, a water molecule and the terminal O atom of an adjacent ligand. The latter bond links the anions into chains.

In order to determine the structural functions of the main and additional ligands and the role of the Ca^{2+} cations in the crystal structure formation, we performed an X-ray structure analysis of $Ca[Co^{III}(Nta)(Pic)]_2 \cdot 6H_2O$ (**I**), where Nta^{3-} and Pic^- are the nitrilotriacetate ($N(CH_2COO)_3^{3-}$) and picolinate (pyridine-2-carboxylate, $NC_5H_4COO^-$) ions, respectively.

EXPERIMENTAL

Synthesis. Crystals **I** were prepared as follows. A solution of $CoCl_2 \cdot 6H_2O$ containing an excess of hydrogen peroxide was cooled to 0°C and added dropwise to a mixture with an equimolar amount of H_3Nta and a fourfold amount of $KHCO_3$. After vigorous gas evolution, the $[Co(Nta)(CO_3)]^{2-}$ ions, which imparted a blue color to the solution, were formed. When the gas evolution terminated, picolinic acid (1 equivalent) was added to the solution. Heating of the mixture to 60°C resulted in a change in its color to dark rose, which is typical of $[Co^{III}Nta(Pic)]^-$ ions with nitrogen atoms of the main and additional ligands in the *trans* positions.

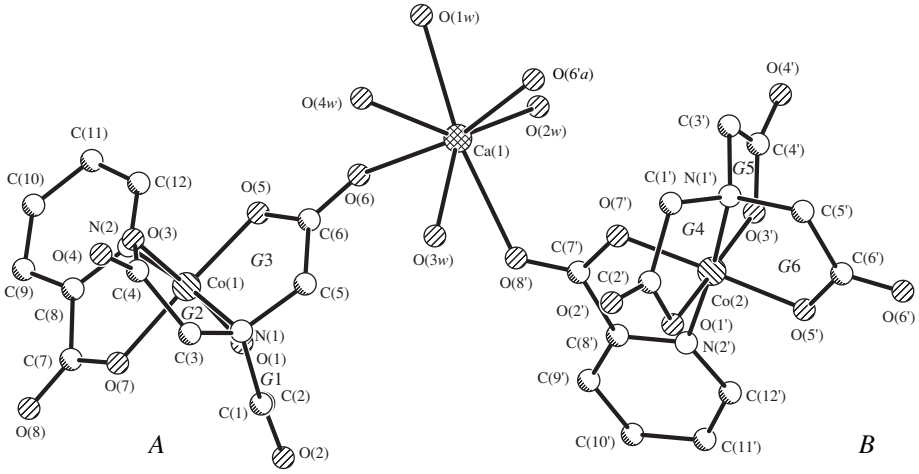

Fig. 1. A link of the $\{Ca(H_2O)_4[Co(Nta)(Pic)]_2\}_{1\infty}$ ribbon in structure **I**.

The solution was passed through a Sephadex G-10 column to remove low-molecular admixtures (KCl and others) and a column packed with a Sephadex DEAF-25 anion-exchange resin in the Cl^- form to separate the target ions from other complexes ($[Co(Pic)_3]$ and $[Co(Nta)_2]^{3-}$). A rose band of *trans-N*-$[Co(Nta)(Pic)]^-$ anions was eluated with a $CaCl_2$ solution (0.05 mol/l). The violet *cis-N*-$[Co(Nta)(Pic)]^-$ ions, which should be eluated before the *trans-N* isomer, were not observed in the column. Concentration of the eluate led to the precipitation of $Ca[Co^{III}(Nta)(Pic)]_2 \cdot 6H_2O$ (**I**) crystals.

X-ray diffraction study. Crystals **I** ($C_{24}H_{32}N_4O_{22}Co_2Ca_1$) are monoclinic; $a = 18.599(4)$ Å, $b = 12.556(3)$ Å, $c = 14.042(3)$ Å, $\beta = 102.90(3)°$, $V = 3196(1)$ Å^3, $\rho_{calcd} = 1.842$ g/cm^3, $\mu_{Mo} = 1.30$ mm^{-1}, $Z = 4$, and space group $P2_1/c$.

The diffraction data were obtained on an Enraf–Nonius CAD4 diffractometer (MoK_α radiation, graphite monochromator, ω scan mode, $\theta_{max} = 27°$). The structure was solved by the direct method. The calculations were performed with the SHELX86 [6] and SHELX97 [7] program packages. The non-hydrogen atoms were refined by the least-squares procedure in the anisotropic approximation. The hydrogen atoms were located from the difference Fourier synthesis and refined in the isotropic approximation. The hydrogen atoms of the *w*5 and *w*6 water molecules were refined in a rider model with U_{iso} values 1.2 times larger than the U_{eq} values of the $O_w(5)$ and $O_w(6)$ atoms. The refinement led to the following discrepancy factors: $R1 = 0.0479$, $wR2 = 0.0775$, and $Goof = 1.054$ for all the 6326 unique reflections; $R1 = 0.0278$, $wR2 = 0.0716$, and $Goof = 1.054$ for 4982 reflections with $I > 2\sigma(I)$. The residual electron density lies between –0.370 and 0.392 e/Å^3.

The atomic coordinates and thermal parameters (U_{eq} or U_{iso}) are listed in Table 1, and selected bond lengths are given in Table 2.

RESULTS AND DISCUSSION

The structure of mixed-ligand complex **I** is built of the $\{Ca(H_2O)_4[Co(Nta)(Pic)]_2\}_{1\infty}$ zigzag chains and crystallization water molecules. The structural formula of **I** is $\{Ca(H_2O)_4[Co(Nta)(Pic)]_2\}_{1\infty} \cdot 2H_2O$.

The Co(III) atoms occupy two symmetrically independent positions and form anionic complexes (*A* and *B*, Fig. 1) of the same composition, $[Co(Nta)(Pic)]^-$. The *B* anionic complex is included in the $\{Ca(H_2O)_4[Co(2) \cdot (Nta)(Pic)]\}^+_{1\infty}$ zigzag chain running along the twofold screw axis 2_1, and the *A* anionic complex, $[Co(1)(Nta)(Pic)]^-$, forms a branch of this chain. The anionic and cationic units that alternate in the chain are linked via the interactions between the Ca^{2+} cation and the carbonyl O(6'*a*) and O(8') atoms of the neighboring *B* complexes. The *A* anionic fragments are linked to the chains by the Ca–O(6) bonds to form broad ribbons (Fig. 2). All the Ca–O interactions are due to a bidentate bridging function of three carboxylate groups. A similar manner of formation of branched chains is observed in the structure of $Ca[Fe^{III}(Edds)]_2 \cdot 8H_2O$ (**VI**) (where $Edds^{4-}$ is the ethylenediaminedisuccinate anion) [8]; however, in this case, the chains are more compact.

In structure **I**, two Co(III) polyhedra have identical octahedral structures. The environment of the Co(1) and Co(2) atoms consists of donor atoms of the Nta^{3-} (N + 3O) and Pic^- (N + O) ligands. In the *A* and *B* complexes, the N atoms of the main and additional ligands are located in the *trans* positions, as is the case in structures **II** and **IV**.

Table 1. Atomic coordinates and thermal parameters in structure **I**

Atom	*x/a*	*y/b*	*z/c*	U_{eq}/U_{iso}, Å^2
Co(1)	0.56494(2)	0.04385(2)	0.71643(2)	0.0180(1)
Co(2)	0.05025(2)	0.32887(2)	0.68872(2)	0.0166(1)
Ca(1)	0.23626(2)	0.00169(4)	0.72005(3)	0.0209(1)
O(1)	0.5469(1)	0.1577(1)	0.6251(1)	0.0255(4)
O(2)	0.5553(1)	0.3341(2)	0.6331(1)	0.0363(4)
O(3)	0.5835(1)	−0.0581(1)	0.8177(1)	0.0258(4)
O(4)	0.6022(1)	−0.0658(2)	0.9796(1)	0.0376(5)
O(5)	0.4702(1)	−0.0122(1)	0.6641(1)	0.0227(4)
O(6)	0.3538(1)	−0.0041(1)	0.6764(1)	0.0303(4)
O(7)	0.6596(1)	0.1046(1)	0.7655(1)	0.0252(4)
O(8)	0.7706(1)	0.1152(2)	0.7317(1)	0.0352(4)
O(1')	0.0961(1)	0.3703(1)	0.8175(1)	0.0236(4)
O(2')	0.1276(1)	0.2966(2)	0.9648(1)	0.0364(5)
O(3')	−0.0029(1)	0.2785(1)	0.5667(1)	0.0250(4)
O(4')	−0.0702(2)	0.1428(2)	0.5007(2)	0.0590(7)
O(5')	−0.0226(1)	0.4341(1)	0.6837(1)	0.0227(4)
O(6')	−0.1302(1)	0.4639(1)	0.7213(1)	0.0334(4)
O(7')	0.1245(1)	0.2232(1)	0.6961(1)	0.0233(4)
O(8')	0.2379(1)	0.1978(1)	0.6748(1)	0.0273(4)
N(1)	0.5216(1)	0.1313(2)	0.8009(1)	0.0212(4)
N(2)	0.6136(1)	−0.0396(2)	0.6358(1)	0.0216(4)
N(1')	−0.0081(1)	0.2340(2)	0.7474(1)	0.0197(4)
N(2')	0.1136(1)	0.4134(2)	0.6283(1)	0.0187(4)
C(1)	0.5367(1)	0.2430(2)	0.7740(2)	0.0286(6)
C(2)	0.5467(1)	0.2484(2)	0.6695(2)	0.0233(5)
C(3)	0.5597(2)	0.0988(2)	0.9022(2)	0.0291(6)
C(4)	0.5828(1)	−0.0174(2)	0.9020(2)	0.0258(5)
C(5)	0.4411(1)	0.1064(3)	0.7810(2)	0.0335(6)
C(6)	0.4190(1)	0.0244(2)	0.7020(2)	0.0216(5)
C(7)	0.7095(1)	0.0749(2)	0.7203(2)	0.0248(5)
C(8)	0.6856(1)	−0.0150(2)	0.6493(2)	0.0224(5)
C(9)	0.7314(2)	−0.0666(2)	0.5995(2)	0.0311(6)
C(10)	0.7018(2)	−0.1449(2)	0.5327(2)	0.0345(6)
C(11)	0.6277(2)	−0.1689(2)	0.5184(2)	0.0317(6)
C(12)	0.5846(1)	−0.1147(2)	0.5711(2)	0.0253(5)
C(1')	0.0412(1)	0.2035(2)	0.8430(2)	0.0239(5)
C(2')	0.0924(1)	0.2963(1)	0.8798(1)	0.0234(5)
C(3')	−0.0277(2)	0.1454(1)	0.6755(1)	0.0269(5)
C(4')	−0.0358(2)	0.1907(1)	0.5725(1)	0.0290(6)
C(5')	−0.0740(1)	0.2945(1)	0.7617(1)	0.0266(5)
C(6')	−0.0772(1)	0.4054(1)	0.7188(1)	0.0223(5)
C(7')	0.1826(1)	0.2540(1)	0.6692(1)	0.0200(5)
C(8')	0.1778(1)	0.3644(1)	0.6277(1)	0.0188(5)
C(9')	0.2306(1)	0.4108(2)	0.5868(2)	0.0264(5)
C(10')	0.2155(2)	0.5094(2)	0.5427(2)	0.0314(6)
C(11')	0.1493(2)	0.5580(2)	0.5413(2)	0.0294(6)
C(12')	0.0991(1)	0.5082(2)	0.5854(2)	0.0246(5)

Table 1. (Contd.)

Atom	*x/a*	*y/b*	*z/c*	U_{eq}/U_{iso}, Å^2
O(1*w*)	0.2257(2)	–0.1798(2)	0.6538(2)	0.0422(5)
O(2*w*)	0.1634(1)	0.0158(2)	0.5629(2)	0.0439(6)
O(3*w*)	0.2824(1)	0.1107(2)	0.8615(2)	0.0455(6)
O(4*w*)	0.2962(1)	–0.1130(2)	0.8537(2)	0.0444(5)
O(5*w*)	0.6346(2)	0.3369(2)	0.9819(2)	0.0567(6)
O(6*w*)	0.7725(2)	0.2705(2)	1.0504(2)	0.0719(8)
H(1*A*)	0.494(2)	0.287(3)	0.776(2)	0.043(9)
H(1*B*)	0.584(2)	0.266(3)	0.816(2)	0.048(9)
H(3*A*)	0.527(2)	0.110(2)	0.948(2)	0.033(8)
H(3*B*)	0.601(2)	0.143(2)	0.923(2)	0.031(8)
H(5*A*)	0.430(2)	0.084(3)	0.842(3)	0.07(1)
H(5*B*)	0.410(2)	0.171(3)	0.760(2)	0.06(1)
H(9)	0.778(2)	–0.050(2)	0.612(2)	0.038(8)
H(10)	0.731(2)	–0.181(2)	0.497(2)	0.038(8)
H(11)	0.604(2)	–0.222(2)	0.476(2)	0.038(8)
H(12)	0.538(2)	–0.132(2)	0.567(2)	0.027(7)
H(1*A*')	0.068(2)	0.143(2)	0.833(2)	0.031(8)
H(1*B*')	0.012(1)	0.186(2)	0.893(2)	0.024(7)
H(3*A*')	–0.072(2)	0.110(2)	0.683(2)	0.035(8)
H(3*B*')	0.014(2)	0.100(3)	0.690(2)	0.042(9)
H(5*A*')	–0.074(2)	0.295(2)	0.828(2)	0.034(8)
H(5*B*')	–0.120(2)	0.251(3)	0.732(2)	0.041(8)
H(9')	0.275(2)	0.372(2)	0.591(2)	0.037(8)
H(10')	0.251(2)	0.544(2)	0.517(2)	0.034(8)
H(11')	0.136(1)	0.622(2)	0.512(2)	0.027(7)
H(12')	0.052(1)	0.534(2)	0.582(2)	0.016(6)
H(1*w1*)	0.234(2)	–0.238(4)	0.685(3)	0.07(1)
H(2*w1*)	0.216(3)	–0.189(4)	0.607(3)	0.08(2)
H(1*w2*)	0.133(2)	–0.033(3)	0.536(3)	0.08(1)
H(2*w2*)	0.154(2)	0.066(3)	0.538(2)	0.04(1)
H(1*w3*)	0.314(2)	0.088(4)	0.913(3)	0.08(1)
H(2*w3*)	0.273(4)	0.185(5)	0.858(5)	0.08(1)
H(1*w4*)	0.344(2)	–0.130(3)	0.867(3)	0.06(1)
H(2*w4*)	0.275(2)	–0.160(3)	0.872(3)	0.06(1)
H(1*w5*)	0.630	0.405	0.947	0.068
H(2*w5*)	0.602	0.338	1.026	0.068
H(1*w6*)	0.725	0.284	1.025	0.086
H(2*w6*)	0.790	0.321	1.099	0.086

In the *A* and *B* complexes, coordinated Nta^{3-} ligands form the *G*(1), *G*(2), *G*(3) and *G*(4), *G*(5), *G*(6) glycinate rings, respectively. The distortions observed in the bond angles in the Co(1) and Co(2) polyhedra due to the formation of three glycinate rings closed by the Nta^{3-} ligand are insignificant: the NCoO endocyclic angles lie between 86.43(8)° and 88.87(8)°. The O(1)Co(1)O(3) and O(1')Co(2)O(3') exocyclic angles [173.87(8)° and 173.49(7)°] deviate from the ideal value most of all. This is apparently associated with the fact that the atom pairs O(1), O(3) and O(1'), O(3') belong to the conjugated rings *G*(1), *G*(2) and *G*(4), *G*(5), respectively. In turn, these rings lie approximately in the equatorial planes of the *A* and *B* com-

Table 2. Bond lengths in the polyhedra of the Co and Ca atoms in structure **I**

Bond	Complex *A*	Complex *B*	Bond	*d*, Å
	d, Å	*d*, Å	Ca–O(6)	2.399(2)
Co(1)–O(1)	1.899(2)	1.893(2)	Ca–O(6'*a*)	2.349(2)
Co(1)–O(3)	1.886(2)	1.886(2)	Ca–O(8')	2.545(2)
Co(1)–O(5)	1.887(2)	1.882(2)	Ca–O_w(1)	2.453(2)
Co(1)–O(7)	1.901(2)	1.901(2)	Ca–O_w(2)	2.324(2)
Co(1)–N(1)	1.920(2)	1.917(2)	Ca–O_w(3)	2.406(2)
Co(1)–N(2)	1.911(2)	1.918(2)	Ca–O_w(4)	2.430(2)

Note: The symmetry transformation for the O(6'*a*) atom is as follows: $-x, y - 0.5, -z + 1.5$.

plexes, which were defined so by analogy with those in diaminocarboxylates [1].

The conjugated rings *G*(1), *G*(2) and *G*(4), *G*(5) in the *A* and *B* complexes are most strained as evidenced by the sums of endocyclic angles, which are equal to 529.4°, 530.6° and 527.9°, 529.3°, respectively. In the *G*(3) and *G*(6) rings, like the five-membered rings closed by the picolinate ions, the sums of endocyclic angles (540.0°, 539.8°, 539.4°, and 539.6°, respectively) are close to the ideal value (538.4°). In the pla-

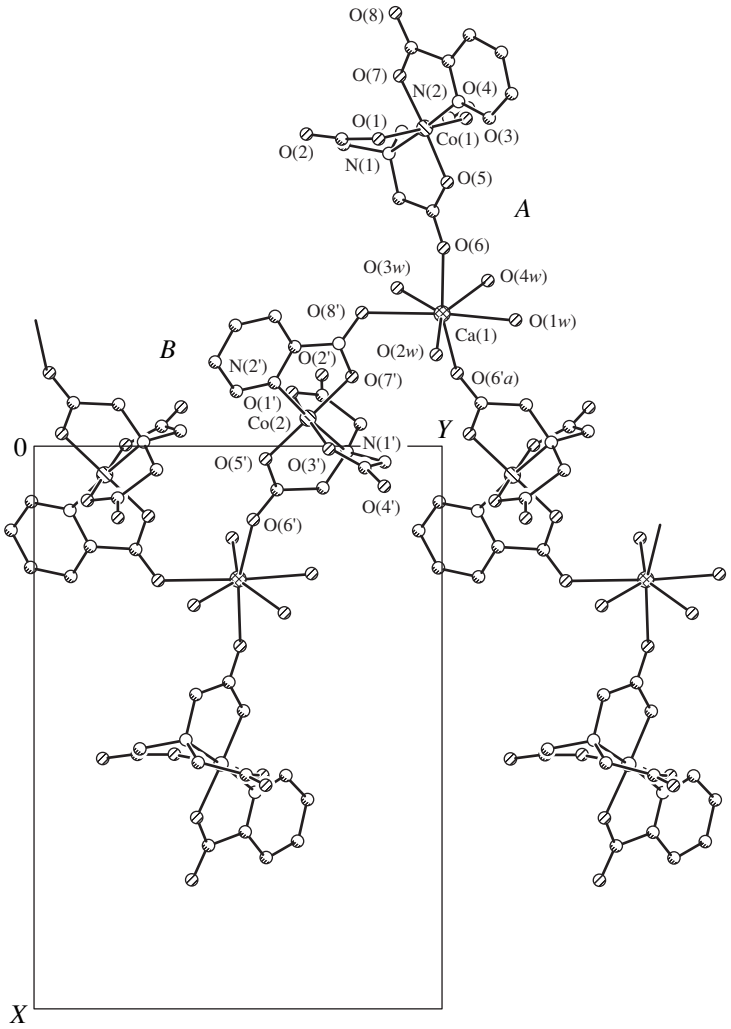

Fig. 2. Projection of the ribbon onto the (001) plane.

Table 3. Geometric characteristics of hydrogen bonds in structure **I***

A–H···*B* bond	Distance, Å			*AHB*, angle, deg	Position of the *B* atom
	A–H	H···*B*	*A*···*B*		
$O_w(1)$–$H(1)_{w1}$···O(8)	0.84(4)	2.20(5)	3.027(4)	167(5)	$-x+1, y-\frac{1}{2}, -z+\frac{3}{2}$
$O_w(1)$–$H(2)_{w1}$···O(6)	0.64(5)	2.33(5)	2.941(5)	159(6)	$-x+1, y-\frac{1}{2}, -z+\frac{3}{2}$
$O_w(2)$–$H(1)_{w2}$···O(4')	0.86(4)	1.81(4)	2.660(4)	171(4)	$-x, -y, -z+1$
$O_w(2)$–$H(2)_{w2}$···O(2')	0.72(4)	2.02(4)	2.734(3)	178(4)	$x, -y+\frac{1}{2}, z-\frac{1}{2}$
$O_w(3)$–$H(1)_{w3}$···O(4)	0.87(4)	1.93(4)	2.788(4)	166(6)	$-x+1, -y, -z+2$
$O_w(3)$–$H(2)_{w3}$···O(8')	0.95(7)	2.52(7)	2.791(3)	141(5)	x, y, z
$O_w(4)$–$H(1)_{w4}$···O(2)	0.89(4)	1.93(4)	2.807(4)	169(4)	$-x+1, y-\frac{1}{2}, -z+\frac{3}{2}$
$O_w(4)$–$H(2)_{w4}$···$O_w(6)$	0.78(4)	2.08(6)	2.850(5)	167(5)	$-x+1, -y, -z+2$
$O_w(5)$–$H(1)_{w5}$···O(6)	0.99	2.16	3.031(4)	148	$-x+1, y+\frac{1}{2}, -z+\frac{3}{2}$
$O_w(5)$–$H(1)_{w5}$···O(5)	0.99	2.38	3.132(4)	133	$-x+1, y+\frac{1}{2}, -z+\frac{3}{2}$
$O_w(5)$–$H(2)_{w5}$···O(1)	0.96	1.90	2.859(4)	174	$x, -y+\frac{1}{2}, z+\frac{1}{2}$
$O_w(6)$–$H(1)_{w6}$···$O_w(5)$	0.90	1.78	2.664(5)	168	x, y, z
$O_w(6)$–$H(2)_{w6}$···O(8)	0.93	2.13	2.930(4)	143	$x, -y+\frac{1}{2}, z+\frac{1}{2}$

* The hydrogen atoms in the *w*5 and *w*6 water molecules were refined in a rider model.

nar six-membered picolinate rings, the sums of angles are equal to the ideal value [720.0(2)°], within the experimental error. In structures **III–V**, in which all the three arms of the Nta^{3-} ligand are coordinated, the sums of endocyclic angles can also be divided into two groups.

In the *A* complex, the Co–$N(1)_{Nta}$ bond (Table 2) is slightly longer than the Co–$N(2)_{Pic}$ bond, whereas in the *B* complex, the corresponding bond lengths are virtually equal to each other. The Co–O_{Nta} bonds in the *A* and *B* complexes have mean lengths of 1.891(2) and 1.887(2) Å, respectively, and are shorter than the Co–O_{Pic} bond. On the whole, the lengths of the Co–N and Co–O bonds formed by the Nta^{3-} and Pic^{-} ligands in the *A* and *B* complexes of structure **I** are close to each other and comparable to those in structures **II**–**IV**.

In the Nta^{3-} ligands, the C(sp^3)–C(sp^3) bonds are the shortest [1.502(4) and 1.514(4) Å in the least distorted axial *G*(3) and *G*(6) rings, respectively] and are approximately equal [mean, 1.524(4) Å] in the *G*(1), *G*(2), *G*(4), and *G*(5) equatorial rings. The mean C(sp^2)–C(sp^2) bond lengths in the pyridine rings in the *A* and *B* complexes are 1.382(4) and 1.377(4) Å, respectively.

The N–C(sp^3) bond lengths in the Nta^{3-} ligand have normal values. Their mean values are 1.496 and 1.494(4) Å in the *A* and *B* complexes, respectively. The N(2)–C(8) and N(2)–C(12) bond lengths in the pyridine rings are slightly different [1.346 and 1.337(3) Å in the *A* complex and 1.345 and 1.333(3) Å in the *B* complex].

The difference between the C–O_c and C–O_u bond lengths (O_c and O_u are the oxygen atoms involved and not involved in the Co coordination, respectively) varies from 0.037 to 0.082 Å. The minimum values of Δ_{C-O} are observed for the *G*(3) and *G*(6) rings [0.037 and 0.039(3) Å], in which the $O_u(6)$ and $O_u(6'a)$ atoms coordinate the Ca atom at the *trans* positions in its polyhedron. The decrease in the Δ_{C-O} values (equalizing the C–O bond lengths) suggests a redistribution of the electron density due to the Ca–O_u interaction. For comparison, we note that, in the framework structure **V**, in which all the O terminal atoms of the Nta^{3-} ligand coordinate metal atoms (one of them forms the Co–O_u bond, and two other form the Ca–O_u bonds), the largest value of Δ_{C-O} is only 0.020(2) Å.

A comparison of the symmetrically independent anionic fragments *A* and *B* with the use of the SUSY program [9] showed that these fragments are closely allied geometrically. The differences between the *A* and *B* anions are quantitatively characterized by the criterion *s* (0.11 Å) and the discrepancies R_i, that is, the distances between the corresponding atoms of the anions under comparison at their closest coincidence. The maximum discrepancy (0.25 Å) is observed for the O(4) and O(4') terminal carbonyl atoms of the Nta^{3-} ligand. These atoms are not involved in the Ca coordination, but the O(4') atom forms the shortest hydrogen bond with the *w*2 water molecule [O···O, 2.660(4) Å] in structure **I**, which leads to a decrease in the Δ_{C-O} value to 0.046(3) Å [in the *A* complex, the corresponding value is 0.064(3) Å].

The environment of the Ca^{2+} cation (C.N. = 7, distorted pentagonal bipyramid) includes two carbonyl oxygen atoms of the Nta^{3-} ligands of the *A* and *B* complexes [$O_u(6)$ and $O_u(6'a)$], the $O_u(8')$ atom of the Pic^- ion of the *B* complex, and four water molecules (*w*1–*w*4). The O(1*w*)–O(4*w*) atoms and the $O_u(8')$ atom lie in the base of the pentagonal bipyramid, whereas the $O_u(6)$ and $O_u(6'a)$ atoms occupy its axial sites. The $O_u(6)CaO_u(6'a)$ angle is equal to 165.35(7)°, and the angles formed by the Ca–O bonds in the base of the pentagonal bipyramid range between 68.54(9)° and 74.36(9)°. The Ca–O_{Nta} distances [2.349 and 2.399(2) Å] are significantly shorter than the Ca–O_{Pic} distance [2.545(2) Å] but comparable to the Ca–O_w distances [2.324(2)–2.453(2) Å]. In structure **II** ($C.N._{Ca}$ = 8, polyhedron of an irregular shape), the Ca–O_{Nta} distances [2.36–2.60(1) Å], with two exceptions, are longer than the Ca–O_w distances [2.36 and 2.37(1) Å]. The shortest Ca–O_{Nta} distance [2.271(1) Å] is observed in the centrosymmetric octahedral Ca polyhedron in structure **V**; the other Ca–O_{Nta} distance is 2.420(2) Å, and the Ca–O_w distance is 2.351(2) Å. The Ca polyhedron (C.N. = 7, pentagonal bipyramid), which most closely resembles the polyhedron in structure **I**, is observed in structure **VI**. As in **I**, it is formed by three terminal O_u atoms and four O_w atoms. However, in structure **VI**, all the three O_u atoms are located in the base of the pentagonal bipyramid and the Ca–O_{Edds} distances [2.41–2.48(1) Å] are significantly longer than the Ca–O_{Nta} distances in **I**.

In structure **I** (Fig. 2), the polymer ribbons $\{Ca(H_2O)_4[Co(Nta)(Pic)]_2\}_{1\infty}$ run along the twofold screw axes 2_1 and form layers that are parallel to the (001) coordinate plane and pass at $z = 1/4$ and 3/4. The *B* anionic complexes, which are included in the polymer chains, are located along the twofold screw axes 2_1 at $x = 0$, and the *A* fragments (branches of the chains) are located at $x = 1/2$. The cationic units lie between them ($x \approx 1/4$) in conventional layers aligned parallel to the (100) plane.

The system of hydrogen bonds (Table 3) links ribbons into layers and the layers into a three-dimensional framework. In the Ca polyhedron, the *w*1 and *w*4 molecules each form one hydrogen bond with an oxygen atom of the *A* complex [$O_u(8)$ and $O_u(2)$, respectively] inside the layer and the other hydrogen bond with the *w*6 crystallization water molecule. The *w*6 molecule, in turn, forms the hydrogen bond with the $O_u(8)$ atom of the adjacent layer. As a result, the continuous hydrogen-bond chain $\cdots O_u(8)\cdots H–O_w(1)–H\cdots O_w(6)–H\cdots O_u(8)\cdots$ is formed. The *w*6 molecule forms one more bond with the *w*5 crystallization water molecule, which links the *A* anionic fragments inside the layer via the hydrogen bond with the $O_c(1)$ atom and via the bifurcate bond with the $O_c(5)$ and $O_u(6)$ atoms of the same carboxylate group. Two water molecules from the Ca environment form hydrogen bonds between the layers: the *w*2 molecule is bound to the $O_u(2')$ and $O_u(4')$ atoms of the *B* complexes, and the *w*3 molecule is bound to the $O_u(4)$ atom. The *w*5 and *w*6 molecules are linked by the short hydrogen bond [2.664(5) Å] and play an important role in the structure formation: these molecules are located in holes between layers of polymer ribbons and, thus, stabilize the layers and link them via hydrogen bonds [O···O, 2.664(4)–3.132(4) Å] into a three-dimensional structure.

CONCLUSIONS

For the *A* and *B* complexes of structure **I**, the total coordination capacity of the Nta^{3-} ligand (D_{Nta}), by which we mean the total number of bonds formed by the ligand with the transition and alkaline-earth metal atoms, is equal to five: each Nta^{3-} ligand is tetradentate relative to the Co atoms ($D_{Co} = 4$) and monodentate relative to Ca^{2+} ($D_{Ca} = 1$). The Pic^- ligand is bidentate in the *A* complex ($D_{Co} = 2$) and tridentate in the *B* complex ($D_{Co} = 2$ and $D_{Ca} = 1$).

In complexes **II**, **III**, and **IV**, which also have a polymer-type structure, the total coordination capacity of the D_{Nta} ligand is larger than that in complex **I** (bidentate bridging), because the carboxylate groups of the Nta^{3-} ligands have more complex functions (tridentate bridging–cyclic). For example, in chainlike structure **IV**, $D_{Nta} = 7$ ($D_{Co} = 4$ and $D_{Ba} = 3$). In chainlike structure **II**, which contains rods built only of the bonds between the Ca atom and the oxygen atoms of the uncoordinated acetate arm of the Nta^{3-} ligand, $D_{Nta} = 6$ ($D_{Co} = 3$ and $D_{Ca} = 3$). In framework structure **III**, $D_{Nta} = 8$ ($D_{Co} = 4$ and $D_{Ba} = 4$). In structure **V**, one of the carboxylate groups links two Co atoms in the anionic chain ($D_{Co} = 4 + 1$). This structural function is rather uncommon for aminocarboxylates. In addition, the ligand forms two bonds with the Ca^{2+} cations ($D_{Ca} = 2$), thus linking the anionic chains into a framework and increasing the coordination capacity of the Nta^{3-} ligand to seven.

ACKNOWLEDGMENTS

This study was supported in part by the Belarussian Republican Foundation for Basic Research, project no. F98-243.

REFERENCES

1. M. A. Porai-Koshits, Sov. Sci. Rev., Sect. B: Chem. **10**, 91 (1987).
2. O. P. Gladkikh, T. N. Polynova, A. L. Poznyak, and M. A. Poraĭ-Koshits, Koord. Khim. **19** (2), 133 (1993).
3. O. P. Gladkikh, T. N. Polynova, M. A. Poraĭ-Koshits, and A. L. Poznyak, Koord. Khim. **18** (12), 1125 (1992).
4. O. P. Gladkikh, T. N. Polynova, M. A. Poraĭ-Koshits, and A. L. Poznyak, Koord. Khim. **18** (10–11), 1156 (1992).
5. L. A. Zasurskaya, I. N. Polyakova, T. N. Polynova, *et al.*, Koord. Khim. **27** (4), 294 (2001).
6. G. M. Sheldrick, Acta Crystallogr., Sect. A: Found. Crystallogr. **46** (6), 467 (1990).
7. G. M. Sheldrick, *SHELX97: Program for the Solution and the Refinement of Crystal Structures* (Univ. of Göttingen, Göttingen, 1997).
8. F. Pavelcik and V. Kettman, Collect. Czech. Chem. Commun. **48** (5), 1376 (1983).
9. T. N. Kukina and P. M. Zorky, Vestn. Mosk. Univ., Ser. 2: Khim. **22** (3), 248 (1981).

Translated by I. Polyakova

Crystallography Reports, Vol. 47, No. 5, 2002, pp. 791–797. Translated from Kristallografiya, Vol. 47, No. 5, 2002, pp. 856–862.

STRUCTURE OF ORGANIC COMPOUNDS

X-ray Diffraction Investigation of *trans*-2,8-Dihydroxy-2,4,4',6,6',8,10,10',12,12'-Decamethyl-5,11-Dicarbacyclohexasiloxane and *trans*-1,4-Dihydroxy-1,4-Dimethyl-1,4-Disilacyclohexane

A. P. Polishchuk*, N. N. Makarova, T. V. Astapova**, and I. M. Petrova****

** Institute of Physics, National Academy of Sciences of Ukraine, pr. Nauki 46, Kiev, 03028 Ukraine*

*** Nesmeyanov Institute of Organoelement Compounds, Russian Academy of Sciences, ul. Vavilova 28, Moscow, 119991 Russia*

e-mail: nmakar@ineos.ac.ru

Received December 13, 2001

Abstract—The crystal structures of two organosilicon compounds are studied by X-ray diffraction. Crystals of *trans*-2,8-dihydroxy-2,4,4',6,6',8,10,10',12,12'-decamethyl-5,11-dicarbacyclohexasiloxane, $C_{12}H_{36}O_6Si_6$, (**I**) are studied at 293 K [$a = b = 16.310(4)$ Å, $c = 9.849(3)$ Å, $V = 2620(1)$ Å^3, $d_{calcd} = 1.128$ g/cm^3, space group $P4(2)/n$, $Z = 4$, 3370 reflections, $wR2 = 0.1167$, $R1 = 0.0472$ for 2291 reflections with $F > 4\sigma(F)$]. Crystals of *trans*-1,4-dihydroxy-1,4-dimethyl-1,4-disilacyclohexane, $C_6H_{16}O_2Si_2$, (**II**) are studied at 110 K [$a = 6.8253(5)$ Å, $b = 9.5495(8)$ Å, $c = 12.0064(10)$ Å, $\alpha = 101.774(2)°$, $\beta = 102.203(2)°$, $\gamma = 95.068(2)°$, $V = 741.8(1)$Å^3, $d_{calcd} = 1.184$ g/cm^3, space group $P\bar{1}$, $Z = 3$, 6267 reflections, $wR2 = 0.1052$, $R1 = 0.0421$ for 3299 reflections with $F > 4\sigma(F)$]. It is found that the conformation of the ring in compound **I**, which contains two methylene groups in the cyclohexasiloxane ring, differs from those in its analogues containing only oxygen atoms or one methylene group in the ring. The noticeable difference between the SiCSi angle [123.0(2)°] and the tetrahedral angle is characteristic of cyclohexasiloxanes. Structure **II** contains three independent molecules with very close conformations. The cyclohexane rings adopt a chair conformation. The methylene groups in **II**, in distinction to those in **I**, are characterized by a standard tetrahedral coordination. © *2002 MAIK "Nauka/Interperiodica".*

INTRODUCTION

The ability of cyclolinear polyorganosiloxanes to self-organize into the mesomorphic state and to form monomolecular Langmuir–Blodgett films at the air–water interface was reported for the first time in [1, 2]. This self-organization was observed in cyclolinear polyorganosiloxanes with cyclosiloxane rings of various sizes in homopolymers and copolymers. It was found that the ability to self-organize is retained upon the replacement of some oxygen atoms by the methylene groups in both the ring and the linking fragment (bridge) between the rings [3, 4]. This opens the way to control the properties of cyclolinear polyorganosiloxanes by varying the Si–O/Si–CH_2 ratio. Apparently, the aforementioned properties depend on the size and conformation of the monomers and the nature of the substituents at the Si atoms. The conformational ability of the monomers and, hence, the polymers depends on the SiOSi and SiCSi angles.

In particular, the X-ray diffraction study of two bicyclic monomers, namely, 2,2',4,4',6,8,8',10,10',12-decamethylbicyclo[5.5.1]hexasiloxane and 2,2',4,4',6,8,8',10,10',12-decamethylbicyclo[5.5.1]-9-car-bahexasiloxane, showed that the replacement of one oxygen atom by the methylene group is accompanied by the conformational changes in the bicycle, which are not very significant but are still noticeable, and the deviation of the SiCSi angle [121.0(1)°] from the tetrahedral value [5]. Similar conformational changes in the cyclosiloxane ring and a close value of the SiCSi angle [122.1(1)°] were found in the structure of 2,8-dihydroxy-2,4,4',6,6',10,10',12,12'-decamethyl-5-carbahexacyclosiloxane [6]. Moreover, the structural data for 2,8-dihydroxy-2,8-diphenyl-4,4',6,6',10,10',12,12'-octa-methyl-cyclohexasiloxane [6] indicate that the conformation of the cyclohexasiloxane ring changes upon the replacement of substituents at the Si atom by substituents that differ in nature, in particular, the replacement of methyl groups by phenyl groups. With the purpose of elucidating the specific conformational features of the cyclohexasiloxane ring containing two CH_2 groups, we preformed X-ray diffraction analysis of the crystal structures of *trans*-2,8-dihydroxy-2,4,4',6,6',8,10,10',12,12'-decamethyl-5,11-dicarbacyclohexasiloxane (**I**) and *trans*-1,4-dihydroxy-1,4-dimethyl-1,4-disilacyclohexane (**II**).

EXPERIMENTAL

Compound **I** was prepared by the reaction of step-by-step condensation followed by the hydrolysis of a mixture of compounds **Ia** and **Ib** according to the following scheme:

$$Cl_2MeSiOSiMe_2CH_2SiMe_2OSiMeCl_2 + HOMe_2SiCH_2SiMe_2OH$$

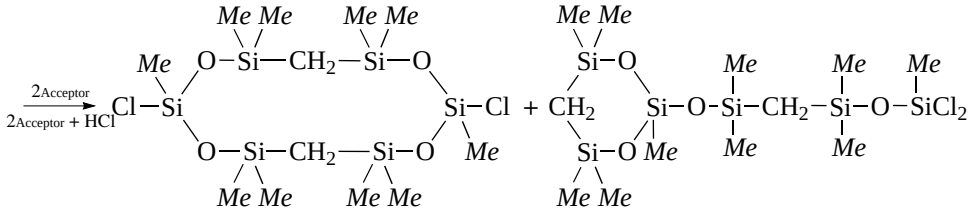

Ia **Ib**

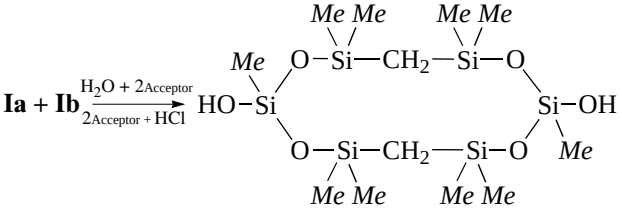

I

A solution containing a mixture of isomers **Ia** and **Ib** (0.95 g, 1.97 mmol) in diethyl ether (6 ml) was added to a mixture of aniline (0.42 g, 4.53 mmol) and water (0.073 g, 4.3 mmol) in ether (6 ml). The reaction mass was stirred for 1 h at a temperature between 0 and +5°C and filtered to remove $C_6H_5NH_2HCl$. After the ether was distilled off, the reaction product (0.8 g) was separated and dissolved in pentane (2.5 ml). Crystals (0.25 g, 28%) with T_m = 82–83°C precipitated at –10°C. Single crystals of compound **I** were obtained by recrystallization from pentane. NMR spectra (*D*-acetone), ^{1}H δ: 0.011 (s, 4H, CH_2); 0.042 (s, 6H, CH_3); 0.142, 0.16 (2s *cis*/*trans*, 24H, CH_3); 2.88, 2.91 (2s *cis*/*trans*, 2H, OH). ^{29}Si δ: 5.76 (s, 4Si, $SiCH_2Si$); –55.60; 55.73 (2s, 2Si, SiOH).

Single crystals of compound **II**, which was synthesized according to the procedure in [7], were obtained by slow evaporation of a hexane solution. The main crystal data and experimental parameters at 293 and 110 K for **I** and **II**, respectively, are listed in Table 1. The processing of the experimental data and subsequent calculations were carried out with the SAINT [8] and SHELXTL97 [9] program packages.

Both structures were solved by the direct method, and the non-hydrogen atoms were refined in the full-matrix anisotropic approximation. All the hydrogen atoms were located from the difference Fourier syntheses and refined in the isotropic approximation. The coordinates and equivalent isotropic thermal parameters of the non-hydrogen atoms are listed in Tables 2 and 3.

RESULTS AND DISCUSSION

In structures **I** and **II**, the molecules occupy special positions at the centers of symmetry. The characteristic feature of compound **I** is the presence the oxygen atoms and two methylene groups in the siloxane ring (Fig. 1). Certainly, this determines the difference between the conformation of this ring and the conformations of the rings in the purely oxygen analogue and the compound with one methylene group (2,8-dihydroxy-2,4,4',6,6',10,10',12,12'-decamethyl-5-carbahexacyclosiloxane). The SiOSi angles [143.8(1)° and 144.2(2)°] are characteristic of cyclosiloxanes and actually coincide with the corresponding angles in an oxygen analogue of compound **I**, namely, the *trans* isomer of 2,8-dihydroxy-2,4,4',6,6',8,10,10',12,12'-decametylcyclohexasiloxane (144.9°, 145.6°, and 146.8°) [10]. Note that, in the *cis* isomer of this compound, four SiOSi angles (145.7°–150.2°) are characteristic of most cyclosiloxanes and two angles increase to 173.6° and 174.1° [10]. In the structure of 2,8-dihydroxy-2,4,4',6,6',10,10',12,12'-decamethyl-5-carbahe-xacyclo-siloxane studied earlier, which contains one methylene group in the ring [6],

Table 1. Crystallographic parameters and experimental data for structures **I** and **II**

Parameter	**I**	**II**
Empirical formula	$C_{12}H_{36}O_6Si_6$	$C_6H_{16}O_2Si_2$
M_r	444.94	176.37
Crystal system	Tetragonal	Triclinic
Space group	$P4(2)/n$	$P\bar{1}$
Z	4	3
a, Å	16.310(4)	6.8253(5)
b, Å	16.310(4)	9.5495(8)
c, Å	9.849(3)	12.0064(10)
α, deg	90	101.774(2)
β, deg	90	102.203(2)
γ, deg	90	95.068(2)
V, Å^3	2620(1)	741.8(1)
d_{calcd}, g/cm^3	1.128	1.184
μ, mm^{-1}	0.338	0.309
$F(000)$	960	288
Diffractometer	Siemens P3/PC	Smart 1000 CCD
λ, Å	0.71073	0.71073
T, K	293(2)	110(2)
θ_{max}, deg	28.06	30.05
Total number of reflections	3370	6267
Number of reflections with $F > 4\sigma(F)$	2291	3299
Refinement on	F_2	F_2
$R1$	0.0472	0.0421
$wR2$	0.1167	0.1052
S	1.094	0.979

Table 2. Coordinates ($\times 10^4$) and isotropic thermal parameters (Å$^2 \times 10^3$) of the non-hydrogen atoms in structure **I**

Atom	x	y	z	U_{eq}
Si(1)	8875(1)	4280(1)	8367(1)	55(1)
Si(2)	9129(1)	6110(1)	7659(1)	50(1)
Si(3)	9497(1)	6682(1)	10589(1)	56(1)
O(1)	8708(1)	5227(1)	7884(2)	70(1)
O(2)	9614(1)	6397(1)	9004(2)	66(1)
O(3)	8373(1)	6726(1)	7336(3)	73(1)
C(1)	8344(4)	3595(3)	7159(6)	104(1)
C(2)	8432(2)	4149(3)	10085(4)	82(1)
C(3)	9855(3)	6106(3)	6242(4)	85(1)
C(4)	8381(2)	6709(3)	10978(6)	97(1)
C(5)	9964(4)	7705(2)	10807(5)	94(1)
C(6)	9995(2)	4094(2)	8335(4)	65(1)

Table 3. Coordinates ($\times 10^4$) and isotropic thermal parameters (Å$^2 \times 10^3$) of the non-hydrogen atoms in structure **II**

Atom	x	y	z	U_{eq}
Si(1*A*)	−3219(1)	1461(1)	749(1)	17(1)
O(1*A*)	−3483(2)	1618(1)	2114(1)	20(1)
C(1*A*)	−1207(3)	2898(2)	720(2)	25(1)
C(2*A*)	−2591(2)	−383(2)	194(1)	19(1)
C(3*A*)	−5742(2)	1623(2)	−146(1)	20(1)
Si(1*B*)	976(1)	−15(1)	3792(1)	16(1)
O(1*B*)	313(2)	1473(1)	3396(1)	19(1)
C(1*B*)	2335(3)	−994(2)	2754(2)	24(1)
C(2*B*)	2569(2)	451(2)	5325(1)	20(1)
C(3*B*)	−1428(2)	−1128(2)	3758(1)	20(1)
Si(1*C*)	4625(1)	−5296(1)	3513(1)	18(1)
O(1*C*)	3707(2)	−7042(1)	3098(1)	21(1)
C(1*C*)	4740(3)	−4561(2)	2202(2)	25(1)
C(2*C*)	2868(2)	−4411(2)	4344(2)	21(1)
C(3*C*)	7186(2)	−5067(2)	4523(1)	21(1)

two SiOSi angles [145.3(2)° and 145.8(2)°] also nearly coincide with the corresponding angles in **I**, but the third angle increases to 161.7(5)°.

As was expected, the Si(1)–C(6)–Si(3) ($-x + 2, -y + 1, -z + 2$) bond angle in **I** [123.0(2)°] differs noticeably from the tetrahedral value; however, it is close to the values determined earlier in the structures of 2,8-dihydroxy-2,4,4',6,6',10,10',12,12'-decamethyl-5-carbahexacyclosiloxane [122.1(1)°] [6] and 2,2',4,4',6,8,8',10,10',12-decamethylbicyclo[5.5.1]-9-carbahexasiloxane [121.0(1)°] [5]. The Si(1) and Si(3) atoms have a standard tetrahedral coordination and normal Si–C and Si–O bond lengths (1.830–1.860 and 1.610–1.638 Å, respectively). Note that, in 2,2',4,4',6,8,8',10,10',12-decamethylbicyclo[5.5.1]hexasiloxane, the SiOSi bond angle at the oxygen atom that occupies the position of the methylene group in its analogue (2,2',4,4',6,8,8',10,10',12-decamethylbicyclo[5.5.1]-9-carbahexasiloxane) is 146.4(1)° [5].

The deviation of the SiCSi angle from the normal value is observed in the linear monomer of bis(hydroxydimethylsilyl)methane [11], in which the Si atoms are characterized by a standard tetrahedral coordination and the SiCSi angle is 118.1(3)°.

The shape of the cyclohexasiloxane ring in **I** can be described as a crown: the Si atoms alternately deviate from the mean plane of the ring in opposite directions

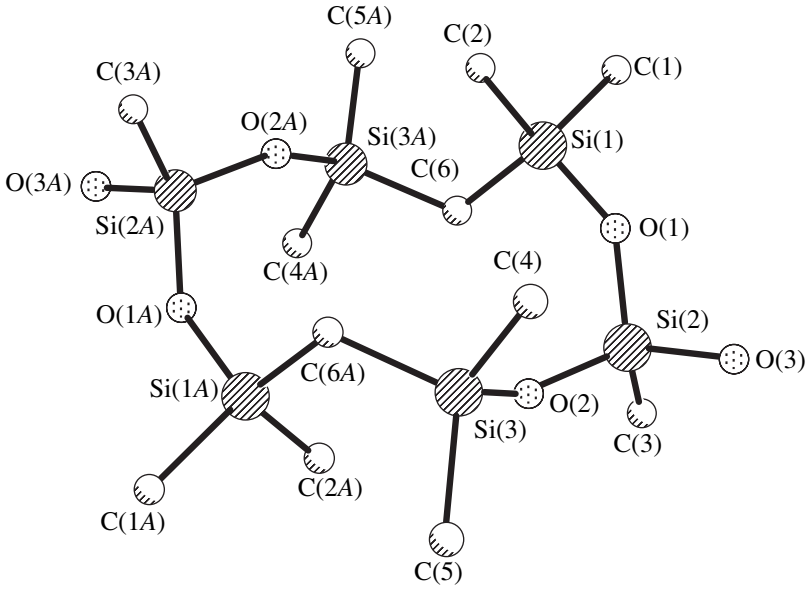

Fig. 1. Structure of molecule **I**.

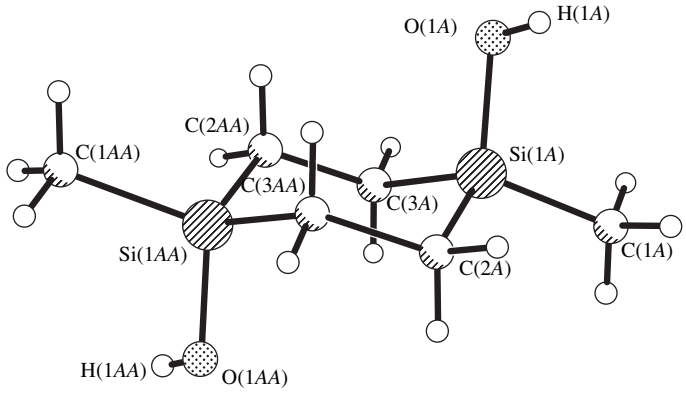

Fig. 2. Structure of molecule **II** (*A*).

(Fig. 1); however, in most compounds, these rings have complex puckered conformations, which can hardly be described by some standard shape. The exception is provided by the *cis* isomer of 2,8-dihydroxy-2,4,4',6,6',8,10,10',12,12'-decametylcyclohexasiloxane whose ring adopts a boat conformation [10] due to increased SiOSi angles (173.6° and 174.1°).

In structure **II**, the molecules are located at different centers of symmetry ($-x - 1, -y, -z$; $-x, -y, -z + 1$; and $-x + 1, -y - 1, -z + 1$), so that there are three crystallographically independent molecules (*A*, *B*, and *C*). The torsion angles indicate that all three molecules have closely similar conformations. The six-membered rings adopt chair conformations (Fig. 2): the silicon atoms in molecules *A*, *B*, and *C* deviate from the mean plane of the carbon atoms by 0.809, 0.787, and 0.804 Å, respectively.

In structure **II**, the bond angles at the carbon and silicon atoms in the six-membered rings have standard tetrahedral values. At the same time, in the structure of a cyclic monomer, namely, 1,3-dihydroxy-1,3-dimethyl-1,3-disilacyclobutane, which contains two independent molecules with planar four-membered rings and close geometric characteristics [12], the SiCSi angle is 88.2(2)°. In the latter structure, the Si atoms have a distorted tetrahedral coordination in which the endocyclic CSiC angle decreases to 91.2(2)°. This angle is close to the CSiC angle (92.8°) in 1,3-diphenyl-1,3-dimethyl-1,3-disilacyclobutane, in which the SiCSi angle is 86.6° [13]. Note that the above angles (close to 90°) are characteristic of strained 1,3-disilacyclobutane systems [14–20]. Apparently, the six-membered rings in structure **II**, in which the angles are characterized by tetrahedral values, are less strained than the cyclobutane systems.

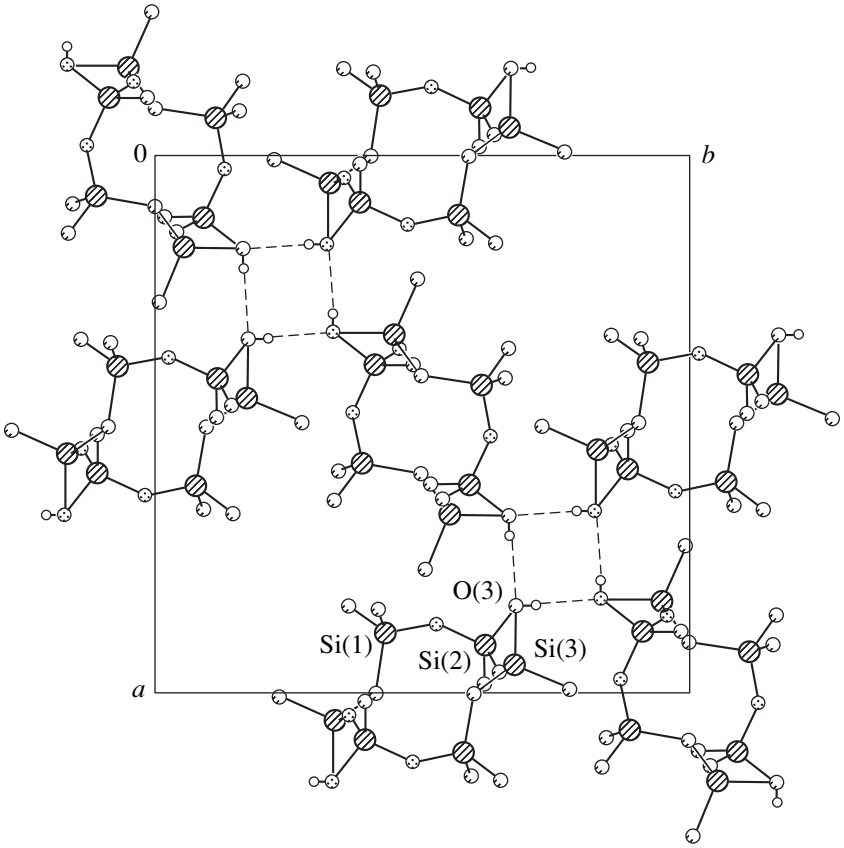

Fig. 3. Projection of the molecular packing in crystal **I** onto the *ab* plane. Dashed lines indicate intermolecular hydrogen bonds that link the molecules into tetramers.

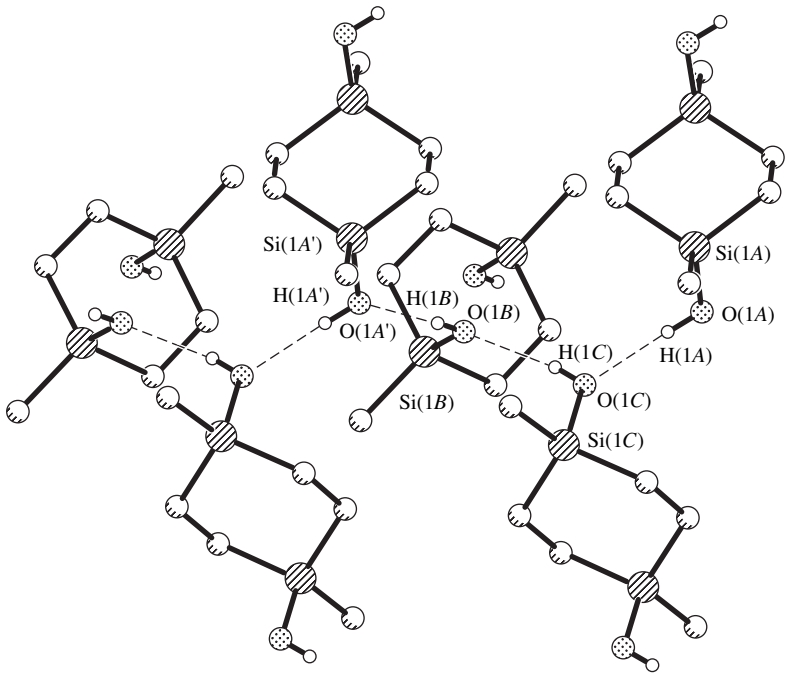

Fig. 4. System of hydrogen bonds in structure **II**.

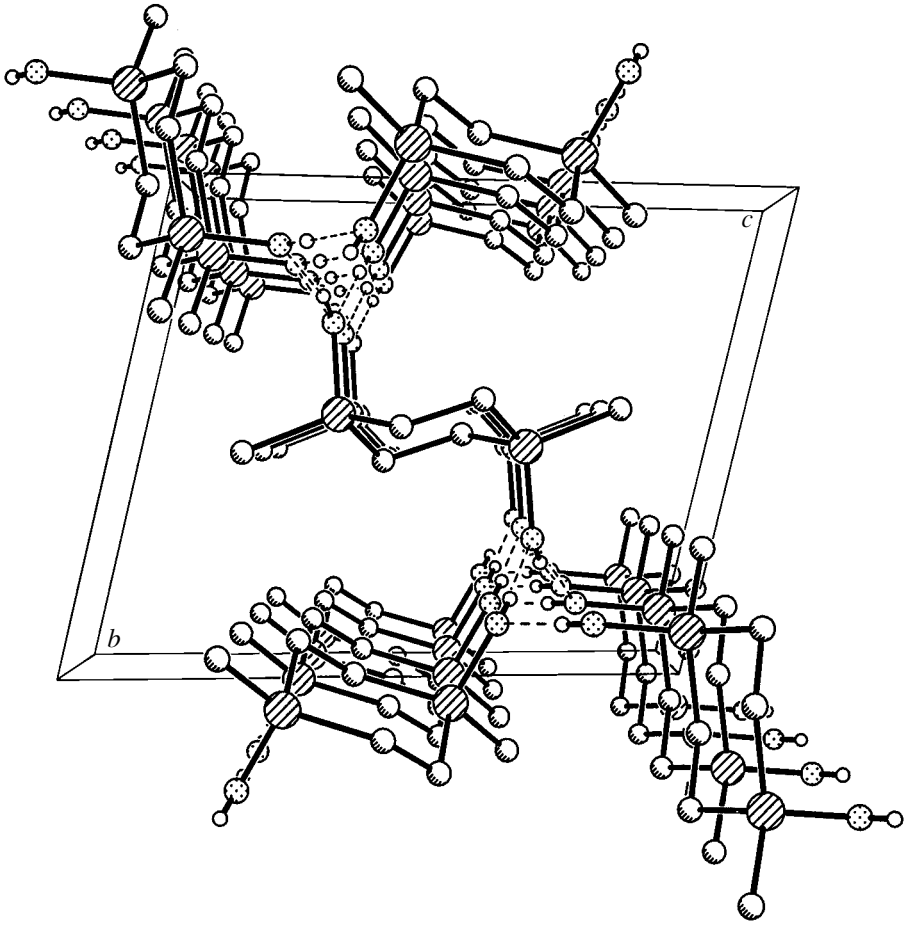

Fig. 5. Projection of the molecular packing in crystal **II** onto the *bc* plane. Dashed lines indicate intermolecular hydrogen bonds that link the molecular columns along the *x*-axis.

The molecular packing in crystal **I** (Fig. 3) is similar to that in the crystal of 2,8-dihydroxy-2,4,4',6,6',10,10',12,12'-decamethyl-5-carbahexacyclosiloxane [6]. The molecules are associated into tetramers through the intermolecular hydrogen bonds O(3)···O(3) (–*y* + 1.5, *x*, –*z* + 1.5) [2.709(3) Å] around the fourfold inversion axes. This molecular arrangement was also observed in the *trans* isomer of 2,8-dihydroxy-2,4,4',6,6',8,10,10',12,12'-decametylcyclohexasiloxane [10]. The same space groups, the closeness of the unit cell parameters, and similarity of the packings in **I**, the *trans* isomer of 2,8-dihydroxy-2,4,4',6,6',8,10,10',12,12'-decametylcyclohexasiloxane, and 2,8-dihydroxy-2,4,4',6,6',10,10',12,12'-decamethyl-5-carbahexacyclosiloxane indicate that this type of molecular packing is efficient for these compounds. Note that, although the crystals of **I** and 2,8-dihydroxy-2,4,4',6,6',10,10',12,12'-decamethyl-5-carbahexacyclosiloxane have close structures, they are not isostructural.

In crystal **II**, an infinite system of intermolecular hydrogen bonds [O(1*A*)···O(1*B*), 2.750(4) Å; O(1*B*)···O(1*C*) (*x*, *y* + 1, *z*), 2.735(4) Å; and O(1°C)···O(1*A*) (*x* + 1, *y* – 1, *z*), 2.737(4) Å] (Fig. 4) interlinks molecular columns running along the *x*-axis (Fig. 5).

CONCLUSIONS

In structure **I**, the presence of two methylene groups in the cyclohexasiloxane ring results in a change in the conformation of the ring as compared to the *cis* and *trans* isomers of the oxygen analogue and the 2,8-dihydroxy-2,4,4',6,6',10,10',12,12'-decamethyl-5-carbahexacyclosiloxane molecule, which contains one methylene group. This conformational difference is due to the different electron nature of the oxygen atoms and the methylene groups and, apparently, shows itself geometrically in different values of the SiOSi and SiCSi angles. The latter angles differ significantly from the standard tetrahedral value. As was noted above, the conformational flexibility makes the variation of physicochemical properties of cyclolinear polyorganosiloxanes possible.

In structure **II**, which contains three conformationally close independent molecules, the cyclohexane

rings adopt a chair conformation and the methylene groups, in contrast to **I**, have a standard tetrahedral coordination.

The data on the SiCSi angles indicate that they vary over a wide range. In the cyclosiloxane systems, these angles vary from ~90° in 1,3-disilacyclobutanes to ~123° in 2,8-dihydroxydecaorganocyclohexasiloxanes.

ACKNOWLEDGMENTS

This study was carried out within the INTAS European program, project no. 97-0485.

REFERENCES

1. N. N. Makarova and Yu. K. Godovsky, Prog. Polym. Sci. **22**, 1001 (1997).
2. S. I. Belousov, T. Sautter, Yu. K. Godovsky, *et al.*, Vysokomol. Soedin. **38** (9), 1538 (1996).
3. N. V. Chizhova, N. N. Makarova, Yu. K. Godovsky, and A. I. Buzin, Vysokomol. Soedin. **42** (11), 1797 (2000).
4. T. V. Astapova, E. V. Matukhina, P. V. Petrovskiĭ, *et al.*, Vysokomol. Soedin. **41** (4), 581 (1999).
5. A. P. Polishchuk, N. N. Makarova, T. V. Astapova, and É. B. Rusanov, Kristallografiya **46** (6), 1035 (2001) [Crystallogr. Rep. **46**, 953 (2001)].
6. A. P. Polishchuk and N. N. Makarova, Kristallografiya **47** (5), 863 (2002) [Crystallogr. Rep. **47**, 798 (2002)].
7. L. M. Volkova, I. M. Petrova, N. V. Chizhova, *et al.*, Izv. Akad. Nauk, Ser. Khim., No. 9, 1734 (1999).
8. *SMART Version 5.051 and SAINT Version 5.00: Area Detector Control and Integration Software* (Bruker AXS Inc., Madison, 1998).
9. G. M. Sheldrick, *SHELXTL97, Versions 5.10: An Integrated System for Solving, Refining, and Displaying Crystal Structures from Diffraction Data* (Bruker AXS Inc., Madison, 1997).
10. N. G. Furmanova, V. I. Andrianov, and N. N. Makarova, Zh. Strukt. Khim. **28**, 113 (1987).
11. K. Yu. Suponitsky, K. A. Lyssenko, T. V. Astapova, *et al.*, Liq. Cryst. **25**, 179 (1998).
12. K. A. Lyssenko, T. V. Astapova, M. Yu. Antipin, and N. N. Makarova, Mendeleev Commun., 87 (1998).
13. K. Hayakawa, M. Tachikawa, T. Suzuki, *et al.*, Tetrahedron Lett. **36**, 3181 (1995).
14. C. Eaborn, J. D. Smith, P. B. Hitchcock, and S. E. Sozerli, J. Chem. Res., 566 (1998).
15. N. Wiberg, C. M. M. Finger, T. Passler, *et al.*, Z. Naturforsch. B **51**, 1744 (1996).
16. N. Auner, W. Ziche, and E. Herdtweck, J. Organomet. Chem. **426** (1), 1 (1992).
17. K. M. Baines, A. G. Brook, P. D. Lickiss, and J. E. Sawyer, Organometallics **8**, 709 (1989).
18. C. Krempner, H. Reinke, and H. Oehme, Angew. Chem. Int. Ed. Engl. **33**, 1615 (1994).
19. J. Braddock-Wilking, M. Y. Chiang, and P. P. Gaspar, Organometallics **12**, 197 (1993).
20. K. Schmohl, M. Blach, H. Reinke, *et al.*, Eur. J. Inorg. Chem., 1667 (1998).

Translated by I. Polyakova

Crystallography Reports, Vol. 47, No. 5, 2002, pp. 798–804. Translated from Kristallografiya, Vol. 47, No. 5, 2002, pp. 863–868.

STRUCTURE OF ORGANIC COMPOUNDS

X-ray Diffraction Investigation of *trans*-2,8-Dihydroxy-2,8-Diphenyl-4,4',6,6',10,10',12,12'-Octamethylcyclohexasiloxane and *trans*-2,8-Dihydroxy-2,4,4',6,6',8,10,10',12,12'-Decamethyl-5-Carbahexacyclosiloxane

A. P. Polishchuk*, N. N. Makarova, and T. V. Astapova****

** Institute of Physics, National Academy of Sciences of Ukraine, pr. Nauki 46, Kiev, 03028 Ukraine*

*** Nesmeyanov Institute of Organoelement Compounds, Russian Academy of Sciences, ul. Vavilova 28, Moscow, 119991 Russia*

e-mail: nmakar@ineos.ac.ru

Received September 20, 2001

Abstract—The crystal structures of two organosilicon compounds are studied by X-ray diffraction. Crystals of *trans*-2,8-dihydroxy-2,8-diphenyl-4,4',6,6',10,10',12,12'-octamethylcyclohexasiloxane, $C_{20}H_{36}O_8Si_6$, (**I**) are triclinic; at 110 K, a = 11.476(1) Å, b = 12.106(1) Å, c = 13.636(1) Å, α = 94.337(1)°, β = 112.669(1)°, γ = 112.216(1)°, space group $P\bar{1}$, Z = 2, and R = 0.057 for 5069 reflections with $F > 4\sigma(F)$. Crystals of *trans*-2,8-dihydroxy-2,4,4',6,6',8,10,10',12,12'-decamethyl-5-carbahexacyclosiloxane, $C_{11}H_{34}O_7Si_6$, (**II**) are tetragonal; at 293 K, $a = b$ = 15.487(3) Å, c = 11.364(3) Å, space group $P4_2/n$, Z = 4, and R = 0.055 for 955 reflections with $F > 4\sigma(F)$. It is found that the structure of compound **I**, in which the substituents at the Si(1) atom differ in volume and inductive effect, contains two crystallographically independent molecules with different conformations of the hexasiloxane ring. In structure **II**, the oxygen atom and the methylene group are statistically disordered as a result of the location of the molecule at the center of symmetry. Although the SiCSi angle [122.1(1)°] differs noticeably from the tetrahedral angle, its value is characteristic of cyclohexasiloxanes and is not related to the disorder. © *2002 MAIK "Nauka/Interperiodica".*

INTRODUCTION

Among the numerous organosilicon compounds, cyclolinear polyorganosiloxanes, that is, compounds whose macromolecules consist of rings differing in size and connected through oxygen atoms or other flexible links, are of particular interest. The properties of cyclolinear polyorganosiloxanes can change considerably depending on the number of flexible elements in both the ring and the linear chain, as well as on the ring size. In particular, the liquid-crystal properties of cyclolinear polyorganosiloxanes and their application to LB technologies are to a large degree determined by the conformational flexibility of monomers and polymers as a whole [1].

In the previous paper [2], we discussed the conformational characteristics of two bicyclic monomers, namely, 2,2',4,4',6,8,8',10,10',12-decamethylbicyclo-[5.5.1]hexasiloxane and 2,2',4,4',6,8,8',10,10',12-decamethylbicyclo[5.5.1]-9-carbahexasiloxane, which differ in the number of SiOSi and $SiCH_2Si$ groups. With the goal of determining the effect of the substituents at the Si atom on the conformation of cyclohexasiloxanes and revealing the conformational changes upon replacement of the oxygen atom by the methylene group, we performed X-ray diffraction studies of two compounds, namely, *trans*-2,8-dihydroxy-2,8-diphenyl-4,4',6,6',10,10',12,12'-octamethylcyclohexasiloxane (**I**) and *trans*-2,8-dihydroxy-2,4,4',6,6',8,10,10',12,12'-decamethyl-5-carbahexacyclosiloxane (**II**).

EXPERIMENTAL

Single crystals of compounds **I** and **II**, which were synthesized according to the procedure described in [3, 4], were grown by slow evaporation of heptane solutions. The main crystal data and experimental parameters for **I** at 110 K and **II** at 293 K are listed in Table 1. The processing of the experimental data and the subsequent calculations were carried out with the SAINT [5] and SHELXTL97 [6] program packages. Both structures were solved by the direct method, and the nonhydrogen atoms were refined in the full-matrix anisotropic approximation.

At the beginning of the refinement, the methylene group was replaced by the oxygen atom, because molecule **II** occupies the center of symmetry. Upon the refinement of the structure, one more peak of the electron density was revealed near this oxygen atom and assigned to the carbon atom of the methylene group. For these atoms, the site occupancy G is equal to 0.5.

Table 1. Crystallographic parameters and experimental data for structures **I** and **II**

Parameter	**I**	**II**
Empirical formula	$C_{20}H_{36}O_8Si_6$	$C_{11}H_{34}O_7Si_6$
M_r	573.03	446.92
Crystal system	Triclinic	Tetragonal
Space group	$P\bar{1}$	$P4_2/n$
Z	2	4
a, Å	11.476(1)	15.487(3)
b, Å	12.106(1)	15.487(3)
c, Å	13.636(1)	11.364(3)
α, deg	94.337(1)	90
β, deg	112.669(1)	90
γ, deg	112.216(1)	90
V, Å^3	1563.2(2)	2726(1)
d_{calcd}, g/cm^3	1.217	1.089
μ, mm^{-1}	0.304	0.328
F(000)	608	960
Diffractometer	Smart 1000 CCD	Siemens P3/PC
λ, Å	0.71073	0.71073
T, K	110(2)	293(2)
θ_{max}, deg	30.08	25.05
Total number of reflections	8882	2301
Number of reflections with $F > 4\sigma(F)$	5069	955
Refinement on	F^2	F^2
$R1$	0.057	0.055
$wR2$	0.148	0.129
S	0.872	0.879

Table 2. Coordinates ($\times 10^4$) and isotropic thermal parameters (Å$^2 \times 10^3$) of the non-hydrogen atoms in structure **I**

Atom	Molecule *A*				Atom	Molecule *B*			
	x	y	z	U_{eq}		x	y	z	U_{eq}
Si(1)	6486(1)	7170(1)	2033(1)	44(1)	Si(1)	527(1)	1463(1)	3862(1)	52(1)
Si(2)	5334(1)	4387(1)	1940(1)	48(1)	Si(2)	2754(1)	506(1)	4448(1)	55(1)
Si(3)	7505(1)	7148(1)	167(1)	48(1)	Si(3)	–1213(1)	1910(1)	4971(1)	56(1)
O(1)	7801(2)	8236(2)	3101(2)	66(1)	O(1)	–566(3)	344(2)	2780(2)	88(1)
O(2)	5962(2)	5882(1)	2351(1)	54(1)	O(2)	1910(2)	1281(2)	4594(2)	62(1)
O(3)	7066(2)	7084(2)	1158(2)	66(1)	O(3)	–119(2)	1566(2)	4697(2)	71(1)
O(4)	3796(2)	3907(2)	911(2)	71(1)	O(4)	2078(3)	–812(2)	4664(2)	98(1)
C(1)	5057(2)	7642(2)	1508(2)	45(1)	C(1)	1054(3)	2889(2)	3409(2)	56(1)
C(2)	5317(3)	8799(3)	1321(3)	68(1)	C(2)	155(5)	3040(4)	2467(3)	93(1)
C(3)	4254(4)	9172(3)	929(1)	88(1)	C(3)	581(9)	4173(6)	2182(5)	119(2)
C(4)	2909(3)	8377(3)	715(3)	80(1)	C(4)	1872(7)	5112(4)	2823(5)	115(2)
C(5)	2619(3)	7229(3)	880(3)	71(1)	C(5)	2765(6)	4970(4)	3755(6)	110(1)
C(6)	3674(2)	6853(3)	1270(2)	55(1)	C(6)	2348(4)	3882(3)	4037(4)	82(1)
C(7)	5147(5)	3745(4)	3072(4)	80(1)	C(7)	4593(4)	1398(6)	5490(5)	103(2)
C(8)	6490(3)	3984(3)	1521(3)	64(1)	C(8)	2595(6)	268(5)	3058(3)	92(1)
C(9)	7894(5)	8687(3)	–90(1)	89(1)	C(9)	–139(9)	3323(7)	6075(8)	167(4)
C(10)	8997(4)	6769(4)	528(4)	84(1)	C(10)	–2422(7)	2138(9)	3756(6)	136(2)

Table 3. Coordinates ($\times 10^4$) and isotropic thermal parameters ($Å^2 \times 10^3$) of the non-hydrogen atoms in structure **II**

Atom	*x*	*y*	*z*	U_{eq}
Si(1)	5997(1)	4041(1)	1815(1)	82(1)
Si(2)	5793(1)	6021(1)	2107(1)	71(1)
Si(3)	5704(1)	6643(1)	–512(1)	86(1)
O(1)	6198(2)	5059(2)	2060(3)	95(1)
O(2)	5440(2)	6300(2)	812(3)	104(1)
O(3)	5054(3)	3806(8)	1280(10)	123(3)
O(4)	6589(2)	6643(2)	2520(4)	99(1)
C(1)	6331(7)	3417(5)	3111(7)	204(4)
C(2)	6640(5)	3703(5)	498(7)	160(3)
C(3)	4880(4)	6125(4)	3174(6)	142(3)
C(4)	6855(5)	6400(5)	–797(7)	175(3)
C(5)	5498(4)	7815(3)	–564(6)	129(2)
C(6)	4822(1)	4000(10)	1650(10)	75(4)

Table 4. Torsion angles (deg) in structures **I** and **II**

Angle	**I**(*A*)	**I**(*B*)	Angle	**II**
	τ	τ		τ
O(4)–Si(2)–O(2)–Si(1)	–64.4(2)	–87.6(2)	O(3)–Si(1)–O(1)–Si(2)	8.7(7)
O(3)–Si(1)–O(2)–Si(2)	–27.2(2)	142.0(2)	C(6)–Si(1)–O(1)–Si(2)	–7.4(7)
O(2)–Si(1)–O(3)–Si(3)	139.8(7)	167.3(3)	O(2)–Si(2)–O(1)–Si(1)	–62.7(5)
O(4)*–Si(3)–O(3)–Si(1)	–82.0(8)	130.5(3)	O(1)–Si(2)–O(2)–Si(3)	–77.3(5)
O(2)–Si(4)–O(4)–Si(3)*	161.0(3)	–15.2(8)	O(1)–Si(1)–C(6)–Si(3)*	138(1)
Si(2)–O(3)–Si(3)*–O(3)*	–77.4(5)	14.0(6)	O(1)–Si(1)–O(3)–Si(3)*	140(4)
			O(3)*–Si(3)–O(2)–Si(2)	148.7(5)
			C(6)*–Si(3)–O(2)–Si(2)	131.4(5)
			Si(1)–O(3)–Si(3)*–O(2)*	–67(1)
			Si(1)–C(6)–Si(3)*–O(2)*	–63(1)

Note: In molecules *A* and *B* of structure **I**, the asterisked atoms are related to the reference atoms by the symmetry operations ($-x + 1, -y + 1, -z$) and ($-x, -y, -z + 1$), respectively. In structure **II**, the asterisked atoms are related to the reference atoms by the symmetry operation ($-x + 1, -y + 1, -z$).

Note that the refinement of structure **II**, in which the oxygen atom and the methylene group were disordered over two positions, led to worse geometric parameters of the molecule.

The presence of the methylene group in **II** is confirmed by the NMR spectrum, which contains signals characteristic of the $–CH^{2–}$ group in the cyclic fragment [4].

The positions of the hydrogen atoms in the methylene group ($G = 0.5$) in **II** were calculated from geometric considerations. All the remaining hydrogen atoms in structures **I** and **II** were located from the difference Fourier syntheses. All the hydrogen atoms were refined isotropically. The coordinates and equivalent isotropic thermal parameters of the non-hydrogen atoms in **I** and **II** are presented in Tables 2 and 3, respectively. The torsion angles are listed in Table 4.

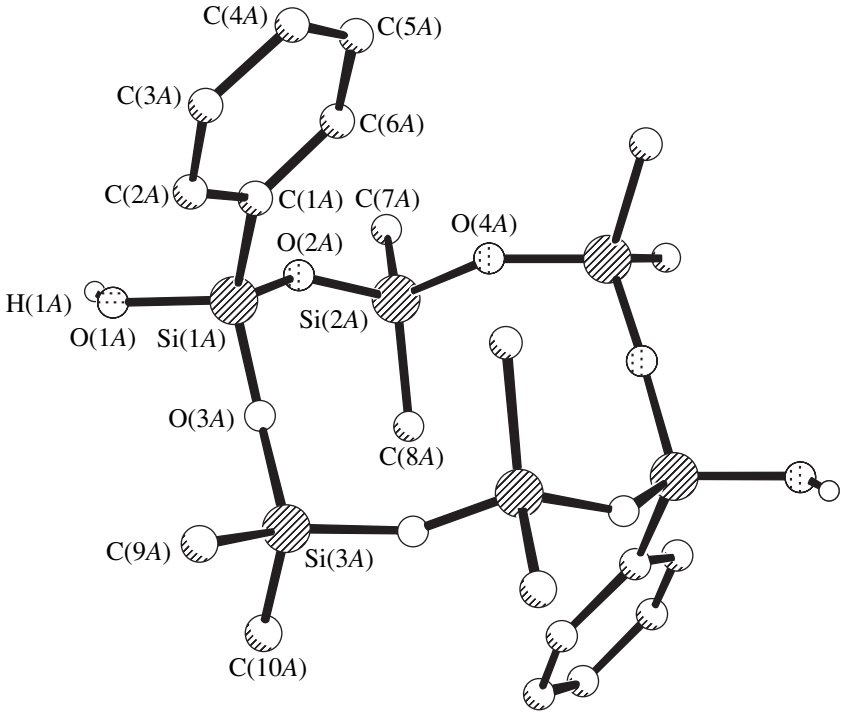

Fig. 1. Structure of molecule **I**(*A*).

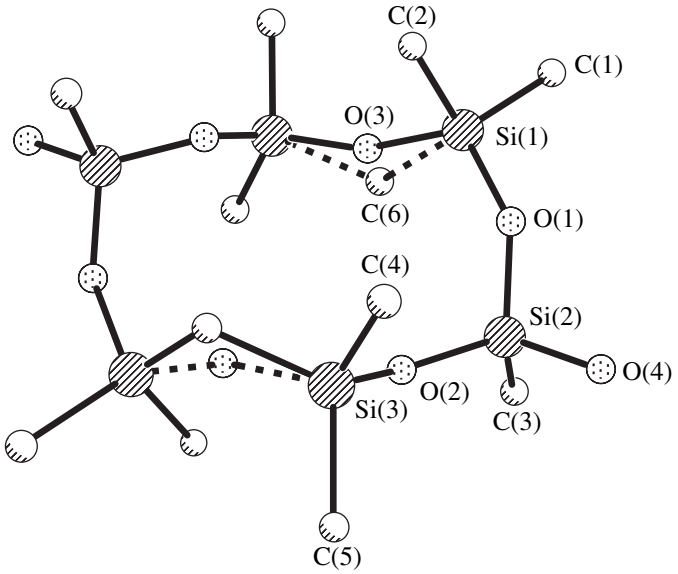

Fig. 2. Structure of molecule **II**.

RESULTS AND DISCUSSION

In structures **I** and **II**, the molecules occupy special positions at the centers of symmetry. In structure **I** (Fig. 1), the molecules are located at different centers of symmetry ($-x + 1, -y + 1, -z$; $-x, -y, -z + 1$); therefore, there are two crystallographically independent molecules. The difference in the endocyclic torsion angles (Table 4) indicates that the two molecules have different conformations. This agrees with the wide scatter of SiOSi bond angles [145.7°–169.1° in **I**(*A*) and 139.1°–162.7° in **I**(*B*)].

The specific feature of structure **II** is the location of the O(3) oxygen atom and the C(6) carbon atom of the methylene group at the same link of the ring (Fig. 2)

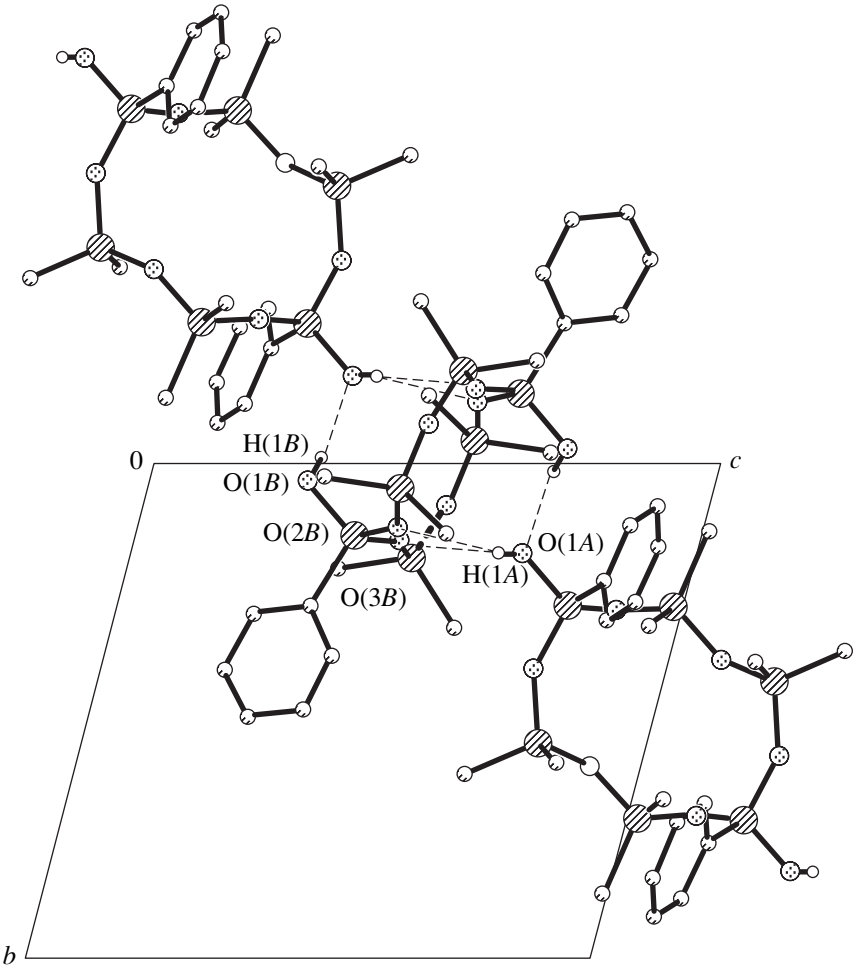

Fig. 3. Projection of the molecular packing in crystal **I** onto the *bc* plane. Dashed lines indicate intermolecular hydrogen bonds.

because of the centrosymmetric position of the molecule. Most probably, this is explained by the statistical arrangement of the enanthiomers which form the centrosymmetric packing in crystal **II**.

Although the centrosymmetric siloxane ring in **II** is disordered, the Si(1)O(3)Si(3)* bond angle [161.7(5)°] lies in the range of values reported [7] and the Si(1)C(6)Si(3)* bond angle [122.1(1)°] is close to the angle [121.0(1)°] observed in the structure of 2,2',4,4',6,8,8',10,10',12-decamethylbicyclo[5.5.1]-9-carbahexasiloxane [2]. The other two angles [145.3(2)° and 145.8(2)°] at the oxygen atoms in the ring actually coincide with the corresponding angles [144.9°, 145.6°, and 146.8°] in an oxygen analogue of compound **II**, namely, the *trans* isomer of 2,8-dihydroxy-2,4,4',6,6',8,10, 10'12,12'-decamethylcyclohexasiloxane [8]. Note that, in the *cis* isomer of 2,8-dihydroxy-2,4,4',6,6',8,10,10,',12,12'-decamethylcyclohexasiloxane, four SiOSi angles (145.7°–150.2°) are characteristic of the majority of cyclosiloxanes and the two angles increase to 173.6° and 174.1° [8].

In the structures studied, the rings have puckered conformations that can hardly be described by some standard shape. This is characteristic of most compounds of this type. The exception is provided by the *cis* isomer of 2,8-dihydroxy-2,4,4',6,6',8,10,10'12,12'-decamethylcyclohexasiloxane, in which increased SiOSi angles (173.6° and 174.1°) enable the ring to adopt a boat conformation [8].

The hydroxyl groups in the structures studied are involved in hydrogen bonding. In structure **I**, the hydroxyl groups form intermolecular hydrogen bonds with each other and with two oxygen atoms of the ring [O(1*B*)···O(1*A*) ($x-1, y-1, z$), 2.721(4) Å; O(1*A*)···O(2*B*) ($-x+1, -y+1, -z+1$), and 3.016(3) Å; O(1*A*)···O(3*B*) ($-x+1, -y+1, -z+1$), 3.066(3) Å]. The molecules are linked through the hydrogen-bond system into infinite chains (Fig. 3).

In crystal **II**, similar to the structure of the *trans* isomer of 2,8-dihydroxy-2,4,4',6,6',8,10,10'12,12'-decamethylcyclohexasiloxane, the intermolecular hydrogen bonds O(4)–H···O(4) ($y, -x+1.5, -z+0.5$) form squares with sides of 2.740(4) Å, so that the molecules are asso-

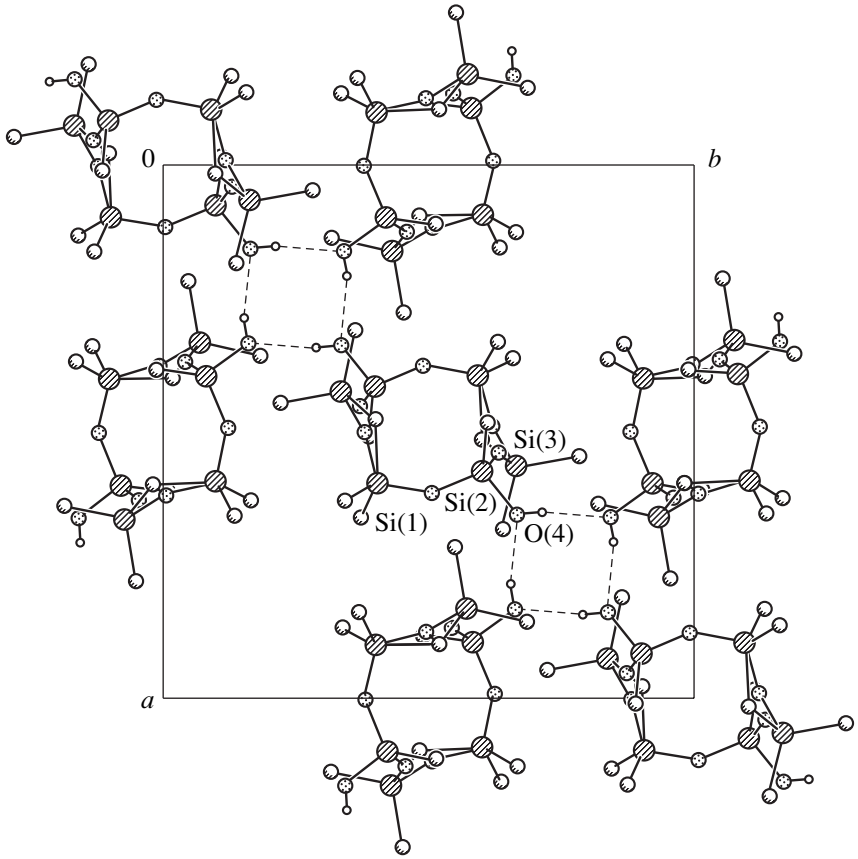

Fig. 4. Projection of the molecular packing in crystal **II** onto the *ab* plane. Dashed lines indicate intermolecular hydrogen bonds.

ciated into tetramers around the fourfold inversion axes (Fig. 4).

Thus, it was found that the structure of compound **I**, in which the substituents at the Si(1) atom differ in volume and inductive effect, consists of two crystallographically independent molecules with different conformations of the hexasiloxane ring. As in the bicyclic systems 2,2',4,4',6,8,8',10,10',12-decamethylbicyclo [5.5.1]hexasiloxane and 2,2',4,4',6,8,8',10,10',12-decamethylbicyclo[5.5.1]-9-carbahexasiloxane [2], in structure **II**, the replacement of one O atom by the CH_2 group is accompanied by slight conformational changes (Table 4). We assume that the accumulation of monomers with a slightly changed conformation in cyclolinear polyorganosiloxanes should result in changes in the physicochemical properties. This makes it possible to control the physicochemical properties by selecting the conformational characteristics of the monomers, in particular, with consideration for the different hydrophilic–hydrophobic nature of the O atoms and the CH_2 groups.

Moreover, the structural studies of molecules **I** and **II** confirmed again the wide variability of SiOSi bond angles and revealed a noticeable difference between the SiCSi angle [122.1(1)°] and the tetrahedral angle. Taking into account that the SiCSi angles in 1,3-disilacyclobutane systems are close to 90° [9–16], we can state with confidence that the SiCSi angles in cyclosiloxane systems exhibit a rather wide variability.

ACKNOWLEDGMENTS

This study was carried out within the INTAS European program, project no. 97-0485.

REFERENCES

1. N. N. Makarova and Yu. K. Godovsky, Prog. Polym. Sci. **22**, 1001 (1997).
2. A. P. Polishchuk, N. N. Makarova, T. V. Astapova, and É. B. Rusanov, Kristallografiya **46** (6), 1035 (2000) [Crystallogr. Rep. **46**, 953 (2000)].
3. N. N. Makarova, B. D. Lavrukhin, T. V. Timofeeva, and V. N. Zelencheva, Izv. Akad. Nauk SSSR, Ser. Khim., No. 5, 1114 (1985).
4. N. V. Chizhova, T. V. Astapova, P. V. Petrovskiĭ, and N. N. Makarova, Izv. Akad. Nauk, Ser. Khim., No. 8, 1436 (2000).
5. *SMART Version 5.051 and SAINT Version 5.00: Area Detector Control and Integration Software* (Bruker AXS Inc., Madison, 1998).
6. G. M. Sheldrick, *SHELXTL97, Versions 5.10: An Integrated System for Solving, Refining, and Displaying*

Crystal Structures from Diffraction Data (Bruker AXS Inc., Madison, 1997).

7. V. E. Shklover, Yu. T. Struchkov, I. V. Karpova, *et al.*, Zh. Strukt. Khim. **26**, 125 (1985).
8. N. G. Furmanova, V. I. Andrianov, and N. N. Makarova, Zh. Strukt. Khim. **28**, 113 (1987).
9. K. A. Lyssenko, T. V. Astapova, M. Yu. Antipin, and N. N. Makarova, Mendeleev Commun., 87 (1998).
10. K. Hayakawa, M. Tachikawa, T. Suzuki, *et al.*, Tetrahedron Lett. **36**, 3181 (1995).
11. C. Eaborn, J. D. Smith, P. B. Hitchcock, and S. E. Sozerli, J. Chem. Res., 566 (1998).
12. N. Wiberg, C. M. M. Finger, T. Passler, *et al.*, Z. Naturforsch. B **51**, 1744 (1996).
13. N. Auner, W. Ziche, and E. Herdtweck, J. Organomet. Chem. **426** (1), 1 (1992).
14. C. Krempner, H. Reinke, and H. Oehme, Angew. Chem. Int. Ed. Engl. **33**, 1615 (1994).
15. J. Braddock-Wilking, M. Y. Chiang, and P. P. Gaspar, Organometallics **12**, 197 (1993).
16. K. Schmohl, M. Blach, H. Reinke, *et al.*, Eur. J. Inorg. Chem., 1667 (1998).

Translated by I. Polyakova

Crystallography Reports, Vol. 47, No. 5, 2002, pp. 805–811. Translated from Kristallografiya, Vol. 47, No. 5, 2002, pp. 869–875.

STRUCTURE OF ORGANIC COMPOUNDS

Molecular and Crystal Structures of 1*R*,4*R*-*cis*-2-(4-Hydroxybenzylidene)-*p*-Menthan-3-one

V. I. Kulishov*, A. S. Tolochko*, M. Yu. Antipin, V. V. Vashchenko***, and L. A. Kutulya*****

** Institute of Physics, National Academy of Sciences of Ukraine, pr. Nauki 46, Kiev, 03650 Ukraine*

e-mail: kulishov@iop.kiev.ua

*** Nesmeyanov Institute of Organoelement Compounds, Russian Academy of Sciences, ul. Vavilova 28, Moscow, GSP-1, 119991 Russia*

**** Institute of Single Crystals, National Academy of Sciences of Ukraine, pr. Lenina 60, Kharkov, 61001 Ukraine*

Received March 6, 2001; in final form, February 19, 2002

Abstract—The molecular and crystal structures of chiral 1*R*,4*R*-*cis*-2-(4-hydroxybenzylidene)-*p*-menthan-3-one (**I**) are determined by X-ray diffraction analysis. Single crystals of **I** are orthorhombic, $a = 8.997(2)$ Å, $b = 11.314(2)$ Å, $c = 14.847(3)$ Å, $V = 1511.3(5)$ Å^3, $Z = 4$, and space group $P2_12_12_1$. The cyclohexanone ring in molecules of compound **I** has a chair-type conformation with the axial methyl and equatorial isopropyl groups. The enone and benzylidene groupings are nonplanar. The considerable distortion of bond angles at the sp^2 carbon atoms of the benzylidene grouping and the puckering parameters of the cyclohexanone ring in the structure of **I** are close to those observed for the previously studied compound with the *p*-methoxy substituent. In the crystal, molecules **I** are linked by very short intermolecular hydrogen bonds >C=O··HO–. © *2002 MAIK "Nauka/Interperiodica".*

INTRODUCTION

The molecular and crystal structures of a number of derivatives of chiral cyclic ketones, namely, 1*R*,4*R*-*cis*- and 1*R*,4*S*-*trans*-*p*-menthan-3-ones, were investigated by X-ray diffraction in our earlier works. In particular, we determined the structures of diastereomeric 2-arylidene substituted compounds with substituents of different electronic nature in the arylidene fragment [1–7] and stereoisomeric β-hydroxy ketones with different configurations of the C(2) and exocyclic chiral centers and the same 1*R*,4*S* configuration [8–10]. It has been found that the molecular structures of diastereomeric 2-arylidene substituted compounds have a number of common features: (i) nonplanarity of the enone and arylidene groupings, which substantially depends on the electronic nature of the *para* substituent; (ii) considerable distortion of bond angles at the sp^2 carbon atoms of the arylidene fragment; and (iii) shortened intramolecular contacts between the atoms of the benzene ring (in the *ortho* position with respect to the vinyl bond) and the atoms of the C(1)HCH_3 group. In crystals of 1*R*,4*R*-*cis* diastereomers, the cyclohexanone ring adopts a chair-type conformation (with the axial methyl and equatorial isopropyl groups), which is significantly distorted in the case of derivatives with electron-donor substituents [OCH_3, $N(CH_3)_2$, and C_6H_5]. In crystals of the compounds with the 1*R*,4*S*-*trans* configuration, the cyclohexanone ring exhibits either a chair-type conformation with axial alkyl groups (*p*-carbomethoxy substituted compound [7]) or a twist conformation (*p*-phenyl derivative [3]). According to the results of molecular mechanics calculations and ^{1}H NMR spectroscopic data [3, 11], these compounds in solutions exist in the form of an equilibrium mixture of both conformers. The structural features of different 2-arylidene derivatives of *p*-menthan-3-ones and cyclohexanone are interpreted by assuming the combined influence of two factors, namely, conjugation and steric effects [5, 6]. The first factor (conjugation) favors a flattening of the cinnamoyl fragment, which, in turn, causes a distortion of the cyclohexanone ring toward a half-chair conformation and gives rise to a steric strain of the molecules, as judged from the shortened intramolecular contacts. At the same time, by virtue of the second factor (steric effects), the cyclohexanone ring shows a tendency to retain a chair-type conformation.

In β-hydroxy ketones with the chiral 1*R*,4*S*-*p*-menthan-3-one fragment, the hydrogen bonds differ in character depending on the configurations of the C(2) and exocyclic chiral centers. It is revealed that their structures can involve the strong intramolecular hydrogen bonds –OH··OC< (1*R*,2*R*,4*S*,1'*S* [9] and 1*R*,2*R*,4*S*,1'*R* [10] derivatives) and the cooperative bonds –OH··OH··OH [8].

In the present work, we carried out X-ray diffraction investigation of the molecular and crystal structures

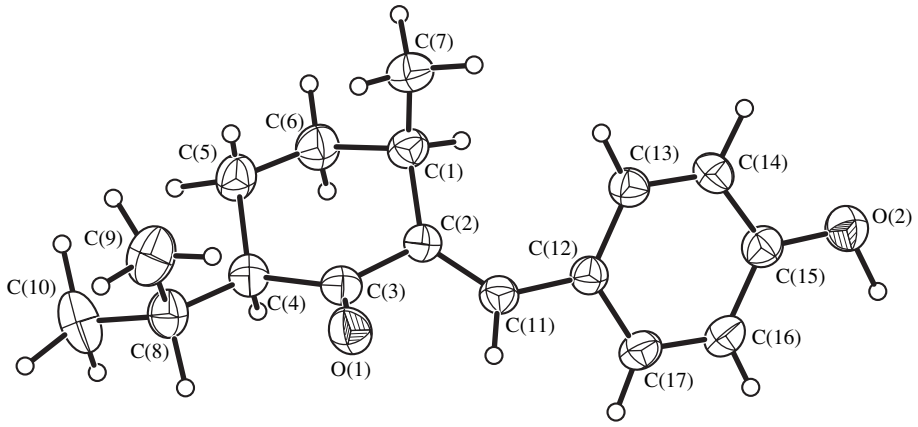

Fig. 1. Molecular structure of compound **I**.

of 1*R*,4*R*-*cis*-2-(4-hydroxybenzylidene)-*p*-menthan-3-one (**I**):

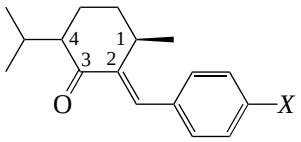

X = OH (**I**),
X = OCH_3 (**II**) [1]; X = $N(CH_3)_2$ (**III**) [5],
X = C_6H_5 (**IV**) [6].

It was of interest to compare the molecular structure of **I** and the molecular structures of the derivatives with the same 1*R*,4*R*-*cis* configuration and different electron-donor substituents (such as OCH_3, $N(CH_3)_2$, and C_6H_5 groups) with the aim of elucidating how the *p*-hydroxy substituent involved in hydrogen bonding affects the molecular geometry (especially, the geometry of the cyclohexanone fragment). Moreover, it was important to determine the type of intermolecular hydrogen bonds (–OH··OC< or –OH··OH··OH) formed in crystals of compound **I** with a considerable steric screening of the carbonyl group.

EXPERIMENTAL

Compound **I** was synthesized through condensation of (–)-menthone with 4-tetrahydropyranylhydroxybenzaldehyde according to a procedure similar to that described in the patent [12] followed by the removal of the tetrahydropyranyl group [13] and was then purified by crystallization from acetonitrile (T_m = 154–155°C). Colorless transparent single crystals suitable for X-ray diffraction analysis were grown from hexane with a small addition of isopropanol. A single crystal 0.5 × 0.4 × 0.3 mm in size was chosen for X-ray structure analysis. Crystals of compound **I** are orthorhombic, $C_{17}H_{22}O_2$, M = 258.35, a = 8.997(2) Å, b = 11.314(2) Å, c = 14.847(3) Å, V = 1511.3(5) Å^3, Z = 4, d_{calcd} = 1.135 g/cm^3, $\mu(MoK_\alpha)$ = 0.073 mm^{-1}, and space group $P2_12_12_1$.

X-ray diffraction analysis was performed on an Enraf–Nonius CAD4 automated diffractometer (MoK_α radiation, graphite monochromator, θ-5/3θ scan mode, θ_{max} = 25°). The intensities of 3113 reflections were measured in the index ranges $0 < h < 10$, $0 < k < 13$, and $-17 < l < 17$. After averaging of the equivalent reflections, the final data set included 2660 independent reflections (R_{int} = 0.0298), which were used in further calculations. The structure was solved by the direct method and refined by the full-matrix least-squares procedure on F_{hkl}^2 in the anisotropic approximation for the non-hydrogen atoms. The hydrogen atoms were located from the difference Fourier synthesis and refined in the isotropic approximation. The final discrepancy factors were as follows: $R1$ = 0.0387 (calculated from F_{hkl} for 2008 reflections with $I > 2\sigma(I)$), $wR2$ = 0.1259 (calculated from F_{hkl}^2) for all 2660 reflections used in the refinement), and *Goof* = 0.937. The absolute configuration was determined from the known *R* configuration of the C(1) chiral center. All the calculations were performed using the SHELXTL PLUS 5.2 software package. The atomic coordinates are listed in Table 1.

RESULTS AND DISCUSSION

Figure 1 shows the molecular structure of compound **I**, which was determined from the X-ray diffraction data. The bond lengths are presented in Table 2. The bond angles are listed in Table 3. The selected torsion angles are given in Table 4. For comparison, the selected torsion angles in molecules of compounds **II**–**IV** are also presented in Table 4.

As in the previously studied structures **II**–**IV**, the cyclohexanone ring in structure **I** has a chair-type conformation [the signs of the endocyclic torsion angles

Table 1. Atomic coordinates ($\times 10^4$) and equivalent isotropic thermal parameters U_{eq} ($\times 10^3$) for structure **I**

Atom	*x*/*a*	*y*/*b*	*z*/*c*	U_{eq}, Å^2
O(1)	−3845(2)	5870(2)	5813(1)	72(1)
O(2)	1984(2)	9027(2)	9529(1)	76(1)
C(1)	−4319(3)	6475(2)	8180(2)	55(1)
C(2)	−3576(2)	6668(2)	7274(1)	51(1)
C(3)	−4450(3)	6331(2)	6467(2)	54(1)
C(4)	−6091(3)	6636(2)	6461(2)	56(1)
C(5)	−6797(3)	6372(3)	7368(2)	70(1)
C(6)	−5929(3)	6911(3)	8141(2)	69(1)
C(7)	−4227(4)	5170(2)	8442(2)	70(1)
C(8)	−6909(3)	6146(2)	5634(2)	68(1)
C(9)	−7006(5)	4808(3)	5642(3)	93(1)
C(10)	−8463(4)	6677(4)	5544(3)	101(1)
C(11)	−2240(2)	7149(2)	7119(2)	54(1)
C(12)	−1140(2)	7615(2)	7762(1)	53(1)
C(13)	−875(3)	7129(2)	8610(2)	60(1)
C(14)	165(3)	7604(2)	9175(2)	63(1)
C(15)	977(3)	8592(2)	8927(2)	59(1)
C(16)	752(3)	9072(2)	8088(2)	61(1)
C(17)	−281(3)	8589(2)	7514(2)	60(1)
H(1)	−3750(30)	6970(20)	8621(17)	55(6)
H(4)	−6070(30)	7450(30)	6460(17)	65(7)
H(5*A*)	−7820(40)	6680(30)	7240(20)	106(10)
H(5*B*)	−6820(30)	5550(20)	7482(17)	60(7)
H(6*A*)	−5920(30)	7890(30)	8102(18)	77(8)
H(6*B*)	−6380(40)	6730(30)	8720(20)	82(9)
H(7*A*)	−3180(40)	4920(30)	8570(20)	79(8)
H(7*B*)	−4770(30)	4700(20)	7950(20)	71(8)
H(7*C*)	−4720(40)	5060(30)	8990(20)	83(9)
H(8)	−6310(30)	6440(20)	5020(20)	76(8)
H(9*A*)	−5920(40)	4530(40)	5660(20)	89(9)
H(9*B*)	−7490(50)	4590(30)	5100(30)	129(15)
H(9*C*)	−7820(50)	4500(30)	6040(30)	122(14)
H(10*A*)	−9020(70)	6180(50)	6120(40)	180(20)
H(10*B*)	−8290(40)	7630(20)	5470(20)	111(11)
H(10*C*)	−8980(40)	6520(20)	4870(20)	96(9)
H(11)	−1990(30)	7260(20)	6506(18)	56(6)
H(13)	−1360(30)	6400(20)	8814(15)	54(6)
H(14)	370(30)	7220(20)	9805(17)	69(7)
H(16)	1250(40)	9630(30)	7850(20)	94(10)
H(17)	−480(40)	9090(30)	7010(20)	91(9)
H(O2)	2570(40)	9760(30)	9250(20)	84(9)

Note: The equivalent isotropic thermal parameters U_{eq} for non-hydrogen atoms are calculated from the anisotropic thermal parameters U_{ij} (for hydrogen atoms, $U_{eq} = U_{iso}$).

Table 2. Bond lengths in structure **I**

Bond	*d*, Å	Bond	*d*, Å
C(1)–C(2)	1.518(3)	C(8)–C(9)	1.516(4)
C(1)–C(6)	1.531(4)	C(8)–C(10)	1.528(4)
C(1)–C(7)	1.530(4)	C(11)–C(12)	1.473(3)
C(2)–C(3)	1.483(3)	C(12)–C(13)	1.394(3)
C(2)=C(11)	1.340(3)	C(12)–C(17)	1.395(3)
C(3)–O(1)	1.230(3)	C(13)–C(14)	1.367(4)
C(3)–C(4)	1.516(3)	C(14)–C(15)	1.386(4)
C(4)–C(5)	1.518(4)	C(15)–C(16)	1.374(4)
C(4)–C(8)	1.535(3)	C(15)–O(2)	1.364(3)
C(5)–C(6)	1.517(4)	C(16)–C(17)	1.375(4)

φ_1–φ_6 alternate (Fig. 1, Table 4)]. The alkyl substituents are characterized by the *cis* orientation with respect to the cyclohexanone ring. The methyl group occupies the axial position, and the propyl group is in the equatorial position (see the torsion angles φ_7–φ_{10}). It should be noted that, as in the earlier-studied compounds [1, 5, 14], the *R* configuration of the C(1) center in the initial (–)-menthone remains unchanged during synthesis of the compound under investigation. Therefore, the *cis* orientation observed for 1,4-alkyl substituents unambiguously indicates that the C(4) chiral center also has an *R* configuration. Consequently, compound **I** belongs to the 1*R*,4*R* diastereomers.

The conformation of the cyclohexanone ring in structure **I** can be described, with a high accuracy, as a chair-3,6, because the atoms of the opposite bonds in this ring [C(1)–C(2) and C(4)–C(5)] are coplanar to within 0.02 Å and the C(3) and C(6) atoms deviate from the root-mean-square plane by 0.48 and 0.66 Å, respectively. Judging from the calculated puckering parameters [15, 16], the distortion of the chair-type conformation due to the presence of two sp^2 carbon atoms in the cyclohexanone ring in the structure under investigation is insignificant and similar to that observed in the methoxy substituted compound **II** (Table 4), which contains a relatively weak electron-donor substituent in the arylidene grouping. The relatively small difference between the torsion angles φ_7 and φ_8 (or φ_9 and φ_{10}) in compound **I** also indicates a slight distortion of the chair-type conformation of the cyclohexanone ring as compared to those in structures **III** and **IV** in which the difference between these angles is approximately equal to 20° (Table 4).

The enone grouping in the studied compound is substantially nonplanar: the φ_{11} torsion angle is equal to 40.4°. This angle slightly exceeds the corresponding angle in the methoxy substituted compound **II** and is considerably larger than the φ_{11} torsion angle in compounds **III** and **IV** (Table 4). Similar regularities are observed for the φ_{12} torsion angle in the twisted arylidene grouping.

The structure of compound **I** is characterized by a considerable distortion of the bond angles at the sp^2 carbon atoms, specifically of the bond angles C(1)C(2)C(11) (ω_α) and C(2)C(11)C(12) (ω_β) (Table 3), as is the case in structures **II**–**IV** and a number of other derivatives of 2-arylidenecyclohexanones studied earlier in [1–7, 17]. In [5], it was noted that changes in the ω_β bond angles in the series of substituted 2-arylidene-*p*-menthan-3-ones and 2-arylidenecyclohexanones are associated with changes in the

Table 3. Bond angles (ω, deg) in structure **I**

Bond angle	ω	Bond angle	ω
C(2)–C(1)–C(6)	109.7(2)	C(4)–C(8)–C(9)	122.4(3)
C(2)–C(1)–C(7)	109.9(2)	C(4)–C(8)–C(10)	111.5(2)
C(6)–C(1)–C(7)	111.8(2)	C(9)–C(8)–C(10)	109.9(3)
C(1)–C(2)–C(3)	116.4(2)	C(2)–C(11)–C(12)**	129.5(2)
C(1)–C(2)–C(11)*	127.3(2)	C(11)–C(12)–C(13)***	124.0(2)
C(3)–C(2)–C(11)	116.2(2)	C(11)–C(12)–C(17)	118.9(2)
C(2)–C(3)–C(4)	117.6(2)	C(13)–C(12)–C(17)	117.1(2)
C(2)–C(3)–O(1)	120.8(2)	C(12)–C(13)–C(14)	121.1(2)
C(4)–C(3)–O(1)	121.6(2)	C(13)–C(14)–C(15)	121.0(2)
C(3)–C(4)–C(5)	111.0(2)	C(14)–C(15)–C(16)	118.8(2)
C(3)–C(4)–C(8)	112.9(2)	C(15)–C(16)–C(17)	120.3(2)
C(5)–C(4)–C(8)	116.0(2)	C(12)–C(17)–C(16)	121.7(2)
C(4)–C(5)–C(6)	112.1(2)	O(2)–C(15)–C(14)	117.9(2)
C(1)–C(6)–C(5)	112.8(2)	O(2)–C(15)–C(16)	123.3(2)

Note: In structures **II**, **III**, and **IV**, the asterisked bond angle is equal to (*) 130.4°, 125.9°, and 126.1°; (**) 130.0°, 131.5°, and 134.1°; and (***) 124.4°, 127.0°, and 127.3°, respectively [1, 5, 6].

Table 4. Selected torsion angles (φ_i, deg) according to the X-ray diffraction data and calculated puckering parameters for compounds **I–IV**

Angle	φ_i			
	I	**II**	**III**	**IV**
φ_1, C(1)C(2)C(3)C(4)	41.2(3)	39.2	21.6(6)	20.8(4)
φ_2, C(2)C(3)C(4)C(5)	−42.6(3)	−46.1	−23.1(6)	−27.2(4)
φ_3, C(3)C(4)C(5)C(6)	50.5(3)	60.4	42.1(6)	46.2(3)
φ_4, C(4)C(5)C(6)C(1)	−58.6(3)	−66.3	−60.5(6)	−61.1(3)
φ_5, C(5)C(6)C(1)C(2)	53.5(3)	57.7	56.7(5)	53.4(3)
φ_6, C(6)C(1)C(2)C(3)	−44.7(3)	−44.4	−37.5(5)	−32.7(4)
φ_7, C(7)C(1)C(2)C(3)	78.7(3)	82.3	87.9(5)	92.5(3)
φ_8, C(7)C(1)C(6)C(5)	−68.7(3)	–	−68.2(5)	−70.0(3)
φ_9, C(8)C(4)C(3)C(2)	–174.8(2)	–170.6	–156.8(4)	–159.4(3)
φ_{10}, C(8)C(4)C(5)C(6)	–178.9(2)	–	174.0(4)	177.1(2)
φ_{11}, O(1)C(3)C(2)C(11)	40.4(3)	34.9	20.2(7)	13.0(4)
φ_{12}, C(2)C(11)C(12)C(13)	35.9(4)	31.7	23.2(8)	4.9(5)
Puckering parameters				
θ, deg	6.79	9.76	19.59	19.00
Ψ, deg	20.24	24.70	6.53	19.66
S	1.00	1.09	0.89	0.88

degree of nonplanarity of the arylidene grouping with variations in the electronic properties of the *para* substituent. The results obtained for structure **I** are completely consistent with the observed tendency of the ω_β bond angle to increase when the φ_{12} torsion angle decreases. According to these two characteristics, structure **I** and the methoxy substituted structure **II** are similar to each other. Moreover, a comparison of the angles ω_β and φ_{12} in compounds **I** and **II** shows that the electron-donor effect of the hydroxyl group involved in the formation of an intermolecular hydrogen bond in the crystal is less pronounced than that of the methoxy substituent.

Unlike the sterically strained structures **III** and **IV**, which contain either the strong electron-donor *p*-dimethylamino substituent (compound **III**) or the biphenyl grouping (compound **IV**), structure **I** can be considered substantially less strained. This follows from the aforementioned distortion of the bond angles, the weak distortion of the chair-type conformation of the cyclohexanone ring, and the analysis of the intramolecular contacts between the atoms of the benzene ring and the $>$C(1)HCH$_3$ fragment (Table 5). The H(1)···H(13) intramolecular contacts are shortened in structures **III** (2.13 Å [5]) and **IV** (1.93 Å [6]) and are close to the sum of the van der Waals radii of hydrogen atoms (2.32 Å [18]) in structures **I** [2.26(4) Å] and **II** (2.38 Å [1]). A similar situation is observed for the C(13)···H(1) and C(1)···H(13) intramolecular contacts, which are close to the sum of the van der Waals radii of carbon and hydrogen atoms (2.87 Å [18]) in structure **I** [2.77(3) and 2.83(3) Å, respectively] and are shortened in structures **III** (2.64 and 2.68 Å [5]) and **IV** (2.65 and 2.66 Å [6]). In the aforementioned molecular fragment of structure **I**, as in structures **II–IV**, only the intramolecular contact C(1)···C(13) [3.25(4) Å] is noticeably

Table 5. Shortened intramolecular contacts (*d*, Å) in structures **I–IV**

Contact	*d*			
	I	**II**	**III**	**IV**
H(1)···H(13)	2.26(4)	2.38	2.13	1.93
H(1)···C(13)	2.77(3)	2.75	2.64	2.65
H(13)···C(1)	2.83(3)	2.69	2.68	2.66
C(1)···C(13)	3.25(4)	3.19	3.35	3.28
H(1)···C(12)	2.77(3)			
H(5*A*)···C(10)	2.58(3)			
H(5*A*)···H(10*A*)	2.06(7)			
H(5*B*)···C(7)	2.77(3)			
H(5*B*)···H(7*B*)	2.19(4)			
H(7*B*)···C(5)	2.77(3)			
H(9*A*)···C(3)	2.71(3)			
H(9*A*)···O(1)	2.42(4)			
H(9*C*)···H(10*A*)	2.19(7)			
H(10*A*)···C(5)	2.73(6)			

Note: The sums of the van der Waals radii are as follows [18]: H···H, 2.32 Å; H···C, 2.87 Å; H···O, 2.45 Å; and C···C, 3.42 Å.

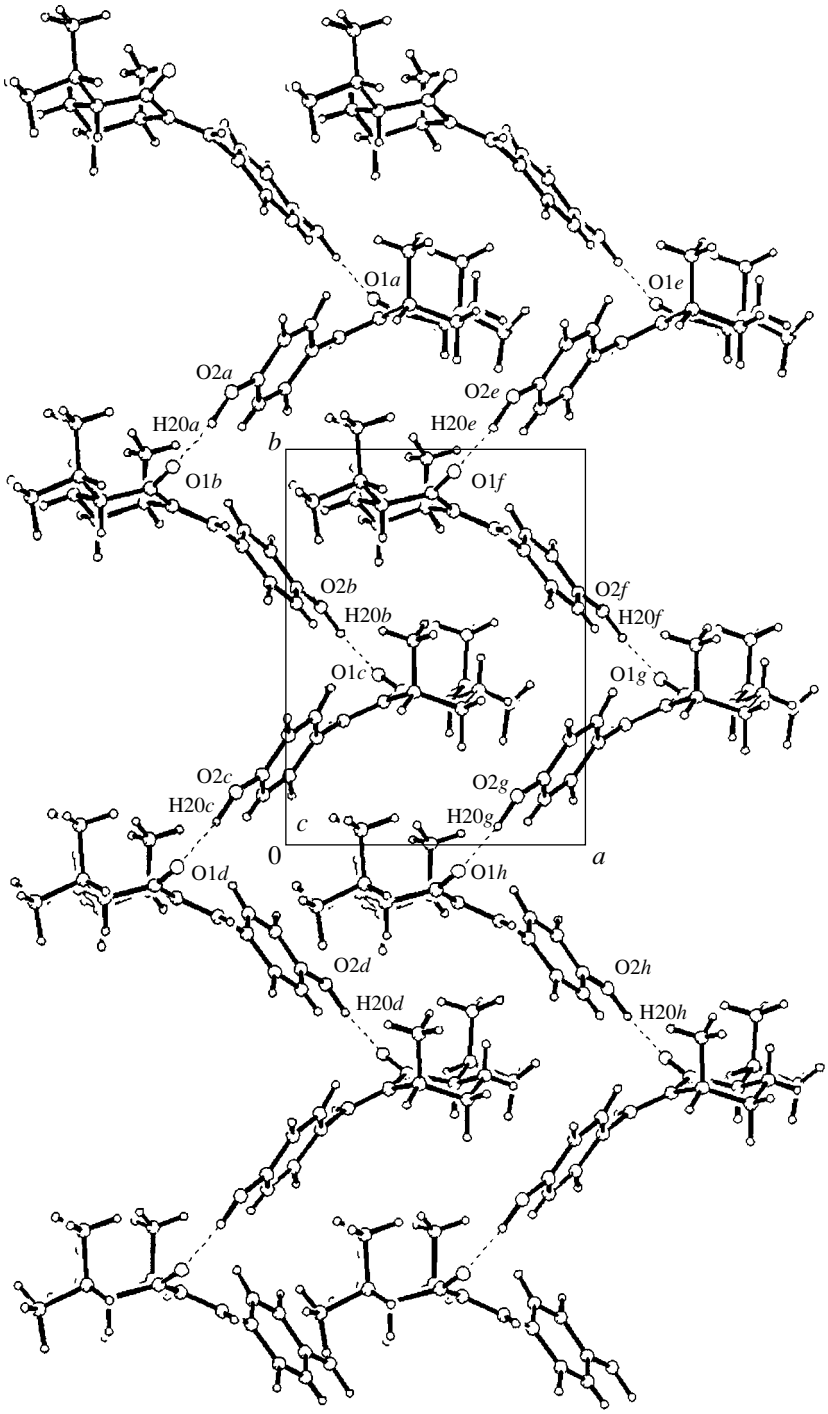

Fig. 2. Projection of a fragment of the molecular packing in crystal structure **I** along the *c*-axis. Hydrogen bonds are shown by dashed lines.

shortened (the sum of the van der Waals radii of carbon atoms is equal to 3.42 Å [18]). A comparison of the available data for structures **I**–**IV** and a number of other 1*R*,4*R*-2-arylidene-*p*-menthan-3-ones [5, 17] demonstrates that the presence of shortened intramolecular contacts between the atoms of the $CH_3HC(1)C(2)=CHC_6H_4X$ fragment—an indication of its steric strain—correlates with the degree of nonplanarity of the benzylidene grouping, which is characterized by the φ_{12} torsion angle (Table 4). Actually, the shortest contacts, especially the H(1)···H(13) contacts, are observed in structures **III** and **IV** with the smallest torsion angles φ_{12}. However, the H(1)···H(13) contact (2.28 Å) is not shortened in the related compound con-

taining the substituent $X = NO_2$ [5] and the substantially nonplanar arylidene group ($\varphi_{12} = 42.4°$). Therefore, the relation between the steric strain of the molecular fragment under consideration and the electronic nature of the *para* substituent in the aryl group is beyond question.

The conformation of the isopropyl fragment in the structure of compound **I** is virtually identical to that in the structures of other 1*R*,4*R*-2-arylidene-*p*-menthan-3-ones studied earlier in [5, 6]. In crystal **I**, the H(4)–C(4) and H(8)–C(8) bonds exhibit a *gauche* orientation [the torsion angle is equal to 61.1(2)°]. One methyl group is in the *trans* position with respect to the H(4)–C(4) bond [the torsion angle is 177.8(2)°], and the other methyl group is in the *gauche* position to this bond [the torsion angle is –53.9(2)°]. In this conformation, both methyl groups of the isopropyl fragment are significantly distant from the carbonyl group (Fig. 1), even though the shortened intramolecular contacts are observed between the atoms of the methyl group in the *trans* position with respect to the C(4)–H(4) bond and the atoms of the 5-methylene fragment: H(5*A*)···C(10), 2.58(3) Å; H(10*A*)···C(5), 2.73(6) Å; and H(5*A*)···H(10*A*), 2.06(7) Å (Table 5). On the other hand, the intramolecular contact between the H(9*A*) atom of the *gauche*-methyl group and the carbonyl carbon atom is considerably shortened [H(9*A*)···C(3), 2.71(3) Å], whereas the H(9*A*)···O(1) contact [2.42.(4) Å] is close to the sum of the van der Waals radii of hydrogen and oxygen atoms (2.45 Å [18]).

In the crystal structure of compound **I**, the molecules are linked by the hydrogen bonds –OH···O=C< (Fig. 2). The parameters of the hydrogen bonds are given below.

D–H···*A*	*d*(D–H)	*D*(H···*A*)	*d*(D···H)	<(*DHA*)
O(2)–H(20)···O(1) –*x*, 0.5 + *y*, 1.5 – *z*	1.07 Å	1.70 Å	2.72 Å	158°.

The length of the hydrogen bond OH···O, on the whole, is typical of the hydrogen bonds formed by the hydroxyl group of the benzene fragment with the carbonyl grouping of α,β-unsaturated ketones in both the *s–cis* and *s–trans* conformations [19]. Such a short (and, correspondingly, strong) hydrogen bond is undeniably associated with the "phenol" origin of the hydroxyl group in the compound under investigation.

ACKNOWLEDGMENTS

We are grateful to Z.A. Starikova for her assistance in the performance of this investigation and active participation in discussions of the results.

This work was supported by the International Association of Assistance for the promotion of cooperation with scientists from the New Independent States of the former Soviet Union, project no. INTAS-1997-1730.

REFERENCES

1. V. I. Kulishov, L. A. Kutulya, V. E. Kuz'min, *et al.*, Zh. Obshch. Khim. **61** (1), 155 (1991).
2. L. A. Kutulya, V. P. Kuznetsov, E. E. Lakin, *et al.*, Kristallografiya **38** (5), 86 (1993) [Crystallogr. Rep. **38**, 630 (1993)].
3. L. A. Kutulya, V. P. Kuznetsov, L. D. Patsenker, *et al.*, Kristallografiya **39** (5), 860 (1994) [Crystallogr. Rep. **39**, 782 (1994)].
4. L. A. Kutulya, V. V. Vashchenko, V. P. Kuznetsov, *et al.*, Kristallografiya **40** (6), 1015 (1995) [Crystallogr. Rep. **40**, 941 (1995)].
5. L. A. Kutulya, V. P. Kuznetsov, V. I. Kulishov, *et al.*, Kristallografiya **44** (3), 475 (1999) [Crystallogr. Rep. **44**, 435 (1999)].
6. A. S. Tolochko, V. I. Kulishov, L. A. Kutulya, *et al.*, Kristallografiya **46** (2), 254 (2001) [Crystallogr. Rep. **46**, 214 (2001)].
7. S. V. Shishkina, T. G. Drushlyak, L. A. Kutulya, *et al.*, Kristallografiya **46** (5), 860 (2001) [Crystallogr. Rep. **46**, 786 (2001)].
8. L. A. Kutulya, L. D. Patsenker, V. V. Vashchenko, *et al.*, Izv. Akad. Nauk, Ser. Khim., No. 7, 1247 (1995).
9. V. P. Kuznetsov, L. D. Patsenker, L. A. Kutulya, *et al.*, Kristallografiya **40** (1), 47 (1995) [Crystallogr. Rep. **40**, 40 (1995)].
10. L. A. Kutulya, V. V. Vashchenko, O. V. Shishkin, *et al.*, Izv. Akad. Nauk, Ser. Khim., No. 11, 2251 (1998).
11. T. G. Drushlyak, L. A. Kutulya, N. S. Pivnenko, *et al.*, Mol. Cryst. Liq. Cryst. Sci. Technol., Sect. A **364**, 691 (2001).
12. V. V. Vashchenko and L. A. Kutulya, Ukr. Patent No. 33753A (2001).
13. P. van de Witte, J. C. Galan, and J. Lub, Liq. Cryst. **24** (6), 819 (1998).
14. L. A. Kutulya, Doctoral Dissertation in Chemistry (Kharkov, 1992).
15. N. S. Zefirov and V. A. Palyulin, Dokl. Akad. Nauk SSSR **252** (1), 111 (1980).
16. N. S. Zefirov, V. A. Palyulin, and E. E. Dashevskaya, J. Phys. Org. Chem. **3**, 147 (1990).
17. V. P. Kuznetsov, V. I. Kulishov, L. A. Kutulya, *et al.*, Kristallografiya **44** (2), 229 (1999) [Crystallogr. Rep. **44**, 196 (1999)].
18. Yu. V. Zefirov and P. M. Zorky, Usp. Khim**. 64**, 446 (1995).
19. *The Cambridge Structural Database* (Cambridge, 2001).

Translated by O. Borovik-Romanova

Crystallography Reports, Vol. 47, No. 5, 2002, pp. 812–814. Translated from Kristallografiya, Vol. 47, No. 5, 2002, pp. 876–878.

LATTICE DYNAMICS AND PHASE TRANSITIONS

Formation of an Internal Bias Field in Chromium- and *L*, α-Alanine-Doped Triglycine Sulfate Crystals

S. D. Milovidova, A. S. Sidorkin, O. V. Rogazinskaya, and A. A. Sidorkin

Voronezh State University, Universitetskaya pl. 1, Voronezh, 394893 Russia

e-mail: sidorkin@dom.vsu.ru

Received July 26, 2001

Abstract—The unipolar state of a chromium- and *L*, α-alanine-doped ferroelectric triglycine sulfate (TGS) crystal has been studied. The experimental data on the distribution of internal bias fields with respect to a seed are considered. The possible mechanisms of the formation of an internal bias field during the growth of TGS crystals with a low impurity concentration are considered. © *2002 MAIK "Nauka/Interperiodica".*

The unipolar state of a ferroelectric crystal is characterized by only one of several equiprobable polarization states. The static unipolarity is determined by the ratio of the areas of the domains of opposite signs. The most popular method of estimating the degree of the dynamic unipolarity in ferroelectrics is the determination of the value of the so-called internal bias field, for example, from the displacement of the dielectric-hysteresis loop along the *E* axis.

At present, it is assumed that the defects produced by different external factors (e.g., the surface treatment or material irradiation with the quanta of different energies) are responsible for the unipolar state of ferroelectrics, together with the dopants that are specially introduced into a crystal during its growth [1–4]. In most cases, the causes of the formation of the unipolar state in ferroelectric crystals by these defects are not quite clear.

The study of the formation of the unipolar state in TGS, TGS + Cr^{3+}, and TGS + *L*,α-alanine [4] showed that this state can be formed due to the nonsymmetrical incorporation of the dopant into a crystal. To refine the above assumptions, we studied the laws of the formation of an internal bias field E_b during the growth of a TGS crystal double doped with chromium ions and *L*,α-alanine molecules.

A double-doped TGS crystal and crystals doped either with chromium ions or *L*,α-alanine molecules, which were compared, were grown in the ferroelectric phase by the method of decreasing the saturated-solution temperature. To prepare the samples from the crystals grown, a ~40-mm-long bar in the shape of a rectangular parallelepiped was sawn from the crystal whose long axis coincided with the polar *Y*-axis and the 5×5 mm^2 cross section was in the *XZ* plane. Then the bar was cleaved along the cleavage planes into ~1-mm-thick samples. The samples of a TGS crystal located at different distances from the seed were studied. We used the silver electrodes deposited in vacuum. The intensity and sign of the internal bias field were determined from the displacement of the loops of dielectric hysteresis.

In Cr-doped crystals, the concentration of chromium ions (Cr^{3+}) was 0.03 mol %, whereas the concentration of *L*,α-alanine molecules in solution was 1 mol %. We chose such concentrations to ensure almost equal internal bias fields (~50 V/cm) in crystals with different dopants (Fig. 1). To compare the influence of one impurity with the influence of two impurities, the concentrations of chromium and double-doped *L*,α-alanine were chosen to be the same as in the material doped with only one dopant (chromium or *L*,α-alanine).

As is seen from Fig. 1, the signs of the field E_b for a nominally pure TGS crystal and a chromium-doped TGS crystal on different sides of the seed were opposite, but were the same for a *L*,α-alanine-doped TGS crystal, in accordance with [4]. In both cases, the field E_b increases with the distance from any side of the seed. In a double-doped crystal (Fig. 2, curve *1*), the dependence of E_b on the distance from the seed is qualitatively the same as the dependence of the sum of the fields formed in a Cr-doped TGS crystal or *L*,α-alanine-doped TGS crystal (Fig. 1, curve *3*). However, the intensity of this field in a double-doped crystal is essentially higher (up to ~260 V/cm) than total field E_b (up to ~60 V/cm) in a chromium- or *L*,α-alanine-doped TGS crystal (Fig. 2, curve *2*). This discrepancy is observed for all the samples located at different distances from the seed and ranges approximately from 100 and 200 V/cm.

The internal bias fields evaluated from the displacement of the dielectric-hysteresis loop agree with the degree of unipolarity evaluated from the ratio of the areas of the opposite-sign domains. The sample unipolarity does not exceed 70% on the one side of the seed, but reaches 90% on its other side.

The occurrence of the internal bias field can be explained as follows. Because of different trapping

1063-7745/02/4705-0812$22.00

coefficients and mobilities of different impurities associated with their different dimensions and characteristics of their electronic structure, the crystallization front is a surface which efficiently separates the impurities whose charges have opposite signs. This results in the formation of the electric field E_f along the direction normal to the crystallization front and the separation of a certain direction in a growing ferroelectric crystal, thus promoting the formation of an internal bias field in the crystal.

In a crystal with charged point defects (for example, in a chromium-doped TGS crystal and in a nominally pure TGS crystal that still contains a certain number of such defects), the composite dipole configurations are formed from the present impurities of opposite signs (or an impurity and its vacancy) during crystal growth, because their formation reduces the electrostatic energy of the crystal.

The average orientation of the axes of such dipoles in the field E_f is determined either by the growth direction or the direction closest to it determined by the crystal structure; in other words, this orientation will be completely determined. The energies of the polarized defects in the domains of opposite signs are different, which promotes the formation of the preferred polarization direction, i.e., the formation of the unipolar state.

Now, evaluate the internal bias field thus formed. According to [2], the internal field in a crystal with oriented polar defects is

$$E_b = 4\pi\kappa d N \eta_0, \quad (1)$$

where κ is the correlation constant, d is the defect size, N is the concentration of the dipole impurity in a crystal, and η_0 is the order parameter fixed at the defect nucleus. To evaluate E_b, it is necessary to set the concentration of the dipole impurity in the crystal dependent on the electric field intensity at the crystallization front. The field E_f was calculated in [6] using the boundary layer method [5]. Using these data, we obtain the expression for the internal bias field as

$$E_b = 4\pi\gamma\kappa d p^2 N^2 / e L_D \sqrt{k_{min}}. \quad (2)$$

Here, L_D is the Debye screening length, γ is the numerical factor [2] entering the expression for the order parameter $\eta_0 = \gamma \bar{p} N$, in which $\bar{p}$ is the average value of electrical moment of the dipole complex that is formed during crystal growth and whose orientation is influenced by the field E_f.

If this complex has only two possible orientational states (along the direction of growth of the face and in the opposite direction), then $\bar{p}$ acquires the form

$$\bar{p} \cong p^2 E_f / T, \quad (3)$$

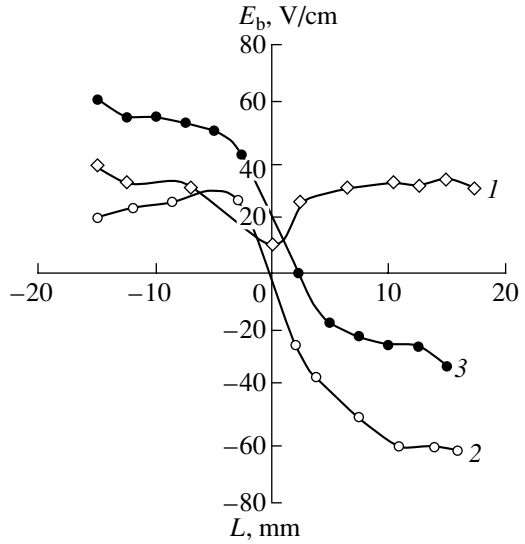

Fig. 1. Distribution of internal bias fields E_b with respect to the seed in a TGS crystal doped either with (*1*) *L*,α-alanine molecules or (*2*) chromium ions. Curve *3* is obtained by interpolation of the sum of curves *1* and *2* at discrete points.

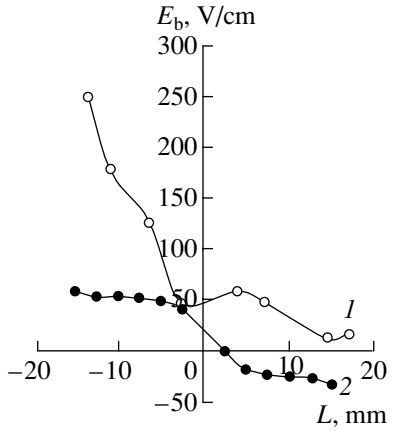

Fig. 2. Distribution of internal bias fields E_b with respect to the seed in a TGS crystal double doped with *L*,α-alanine molecules and chromium ions: (*1*) experimental data and (*2*) calculation data.

where p is the dipole moment of the composite dipole complex and T is the temperature.

The evaluation of E_b using formula (2) at $\kappa \sim 10^{-15}$ cm^2, $L_D \sim 10^{-6}$ cm, $\gamma \sim 1$, $d \sim 10^{-7}$ cm, $N \sim 10^{19}$ cm^{-3}, and $p \sim 10^{-17}$ yields ~50 V/cm [4], which coincides with the experimentally observed value for a nominally pure TGS crystal and a TGS crystal with a low concentration of chromium ions (Fig. 1).

Note that, according to the model under consideration, the internal field induced on the opposite faces should be opposite in sign. This corresponds to the experimental situation with a nominally pure crystal and a crystal with a chromium impurity (Fig. 1).

The above mechanism also works in a crystal doped with *L*,α-alanine. However, in this case, the orientation of dipole complexes "frozen" into a crystal lattice is essentially dependent on an increase in the system energy due to the formation of the orientations of "head to head" and "tail to tail" type in the complexes, which leads to the same orientations of the dipole complexes over the whole growing crystal.

In a TGS crystal simultaneously doped with chromium and *L*,α-alanine, both the above mechanisms should work simultaneously. However, in such crystals, the intensities of internal bias fields determined experimentally are somewhat higher than their calculated intensities (Fig. 1, curve *2*). The absence of such a simple "superposition" of the mechanism can be caused by the mechanical stresses arising in the crystals because of the large dimensions of *L*,α-alanine molecules (in comparison with the replaced glycine molecules) incorporated into the crystal during its growth. These stresses increase the unit-cell volume in such crystals [7, 8], which, in turn, increases the correlation constant and, hence, the intensity of the field E_b.

ACKNOWLEDGMENTS

This study was supported by the Netherlands Organization on Scientific Studies (NWO) project "Nonlinear Dielectric Films for Nanotechnology" and the Russian Foundation for Basic Research, project no. 01-02-16828.

REFERENCES

1. S. R. Fletcher, E. T. Keve, and A. S. Skapski, Ferroelectrics **14**, 789 (1976).
2. A. P. Levanyuk, V. V. Osipov, A. S. Sigov, and A. A. Sobyanin, Zh. Éksp. Teor. Fiz. **76** (1), 345 (1979) [Sov. Phys. JETP **49**, 176 (1979)].
3. V. K. Novik, N. D. Gavrilova, and G. T. Galstyan, Kristallografiya **28** (6), 1165 (1983) [Sov. Phys. Crystallogr. **28**, 684 (1983)].
4. B. M. Darinskii, A. S. Sidorkin, and S. D. Milovidova, Ferroelectrics **142**, 45 (1993).
5. A. A. Chernenko, Dokl. Akad. Nauk SSSR **153** (5), 1129 (1963).
6. A. A. Chernov and A. M. Mel'nikova, Kristallografiya **16** (3), 477 (1971) [Sov. Phys. Crystallogr. **16**, 404 (1971)].
7. S. D. Milovidova, I. I. Evseev, I. V. Vavresyuk, and S. A. Aleshin, Kristallografiya **42** (6), 1137 (1997) [Crystallogr. Rep. **42**, 1060 (1997)].
8. S. D. Milovidova, I. I. Evseev, and I. V. Vavresyuk, Kristallografiya **37** (2), 497 (1992) [Sov. Phys. Crystallogr. **37**, 258 (1992)].

Translated by T. Dmitrieva

Crystallography Reports, Vol. 47, No. 5, 2002, pp. 815–823. Translated from Kristallografiya, Vol. 47, No. 5, 2002, pp. 879–887.

PHYSICAL PROPERTIES OF CRYSTALS

Modern Application Packages for Rigorous Solution of Problems of Light Propagation in Anisotropic Layered Media: II. Optically Active Crystals

A. F. Konstantinova*, B. V. Nabatov*, E. A. Evdishchenko*, and K. K. Konstantinov**

** Shubnikov Institute of Crystallography, Russian Academy of Sciences, Leninskiĭ pr. 59, Moscow, 117333 Russia*

e-mail: afkonst@usa.net

*** Institute of Mechanical Engineering, Russian Academy of Sciences, Malyĭ Khariton'evskiĭ per. 4, Moscow, 101830 Russia*

Received April 26, 2002

Abstract—The matrix **Δ** suggested by Berreman for optically active crystals of various symmetry classes has been calculated with the use of the Mathematica-4.1 package. It is shown that the eigenvalues of this matrix are the refractive indices, whereas its eigenvectors determine the polarization states of eigenwaves propagating in the crystal. The relation between the components of the gyration tensors obtained on the basis of various constitutive equations is established. The essential differences in the optical activity described on the basis of these equations are also discussed. *© 2002 MAIK "Nauka/Interperiodica".*

INTRODUCTION

Earlier [1], we described in detail the Berreman method [2, 3] and the possibilities provided by the use of this method in combination with computer mathematics—the Mathematica-4.1 package. Below, we describe a detailed study of the matrix **Δ** for optically active nonmagnetic crystals of various symmetry classes.

The matrix **Δ** is obtained from the optical matrix **M** 6×6 of a medium characterized by an arbitrary set of optical properties determined by the dielectric constant, electrical conductivity, magnetic susceptibility, and gyration tensors written in the general form. The form of the matrix **M** and, therefore, also that of the matrix **Δ**, depend on the form of the constitutive equation used in the consideration of the Maxwell equations. The application of different forms of the constitutive equations in different studies is explained by the allowance for the optical activity of crystals and the form of the gyration tensor. Some authors believe that the gyration tensor can have symmetric or antisymmetric components, whereas other state that the nondiagonal elements can only be symmetric. We cannot discuss here all the relevant publications and, therefore, mention only the articles most often cited and used in the solution of various problems.

Generally speaking, the form of the gyration tensor is independent of the constitutive equations, because it is determined by the crystal symmetry. Voigt was one the first to obtain the components of the gyration tensor for crystals of 18 symmetry classes, in which this tensor had any form [4]. The same gyration tensor was also used by F.I. Fedorov and his students and followers [5–7].

Historically, the optical activity of crystals was described in the same way as in the Born study [8], i.e., on the basis of the symmetric gyration tensor [9–12]. As a result, the antisymmetric tensors were ignored, and only the crystals of 15 symmetry classes were considered to be optically active. The optical activity in almost all the experimental studies was described based on the symmetric gyration tensor and was represented in the form of gyration surfaces [13], although it is quite clear that gyration surfaces cannot describe the specific rotation of the polarization plane, because they correspond only to the symmetric components of the gyration tensor.

In addition to different forms of the gyration tensor used in different studies, the constitutive equations themselves are also written in different forms. Probably, this fact is not worth mentioning here, but the authors of the theoretical and experimental studies describe the optical activity in different ways, which can result in incredible confusion. Different descriptions of the optical activity in various theories is of fundamental importance, which has been ignored because, in many instances, the theoretical and experimental studies are performed almost independently. At first glance, it may seem that one can use any form of constitutive equations. However, it is absolutely obvious that, first, one has to establish the relation between the tensors used in different studies and, second, to determine the applicability range of each of these theories. This problem can be solved by different methods. Below, we use the Berreman method and the Mathe-

1063-7745/02/4705-0815$22.00

matica-4.1 package to consider the matrix $\mathbf{\Delta}$ for crystals of various symmetry classes in the analytical form, establish the boundaries of various theories in the description of optical activity, and determine the appropriate approximation that can be used in each specific instance.

VARIOUS FORMS OF CONSTITUTIVE EQUATIONS USED TO DESCRIBE THE OPTICAL ACTIVITY OF CRYSTALS

The elements of the matrix $\mathbf{\Delta}$ and the result of the solution of the boundary problems are essentially dependent on the form of the constitutive equations and the method of the formation of the block optical matrix **M**. Now, consider in detail different forms of the constitutive equations with allowance for the optical activity. In the general form, each of the tensors in the constitutive equations has nine components.

In [5], which constitutive equations provide the correct description of the optical activity was determined. The same constitutive equations were obtained in [14]. These equations were also used in [15–26]. Hereafter, we refer to these equations as the Condon–Fedorov equations,

$$D_j = \varepsilon_{jk}E_k + i\alpha_{jk}H_k, \quad B_j = \mu_{jk}H_k - i\tilde{\alpha}_{jk}E_k. \qquad (1)$$

In [8, 9], the constitutive equations have the form

$$D_j = (\varepsilon_{jk} + ie_{jkl}g_{lm}n_m)E_k, \quad B_j = \mu_{jk}H_k \qquad (2)$$

and are considered as approximate equations, hereafter referred to as the Born–Landau equations, where e_{jkl} is the Levi–Civita tensor and n_m are the directional cosines of the wave normal.

In [27], the so-called Drude constitutive equations are suggested, which are also used in [2, 3, 28] and have the form

$$D_j = \varepsilon_{jk}E_k + i\gamma_{jk}H_k, \quad B_j = \mu_{jk}H_k. \qquad (3)$$

In the above constitutive equations, the second-rank pseudotensors α_{jk}, g_{lm}, and γ_{jk} are used, which describe the optical activity in different ways and which are therefore named differently by different authors. As was indicated earlier [1], all these pseudotensors are referred to as simply gyration tensors.

For optically active crystals, constitutive equations (1)–(3) are written as [2, 3]

$$\mathbf{D} = \varepsilon\mathbf{E} + \rho\mathbf{H}, \quad \mathbf{B} = \mu\mathbf{H} + \rho'\mathbf{E}. \qquad (4)$$

It can be seen from Eqs. (4) how one can write the relation between the field vectors **E**, **H** and the induction vectors **D**, **B** for their use in the Berreman method and which blocks should be possessed by the optical matrix **M** in this case [2], namely,

$$\begin{bmatrix}\mathbf{D}\\ \mathbf{B}\end{bmatrix} = \mathbf{M}\begin{bmatrix}\mathbf{E}\\ \mathbf{H}\end{bmatrix}, \quad \mathbf{M} = \begin{pmatrix}\varepsilon & \rho\\ \rho' & \mu\end{pmatrix}. \qquad (5)$$

As was indicated above, we consider here nonmagnetic crystals, and therefore the tensor μ is assumed to be the unit tensor in all the constitutive equations.

It was shown in [5] that the use of Eqs. (2) and (3) in solving the boundary problem on light propagation through an optically active plate results in the violation of the law of energy conservation—the sum of the intensities of the transmitted and reflected waves differs from the intensity of the incident one. Therefore, the theory of the optical activity based on constitutive equations (2) and (3) is only an approximate one, whereas the theory based on constitutive equations (1) is rigorous, although up to now many authors have described the optical activity based on constitutive equations (2) and (3). Below, we indicate the expressions which would allow one to justify the use of the approximate theory in the computations or interpretation of the results obtained for concrete crystals.

At present, we face a situation in which the components of the gyration tensor g_{jk} are calculated in the experimental studies of optically active crystals based on Eqs. (2) and the relationships derived from these equations, whereas the use of Eqs. (1) would result in different descriptions of the same results, with this difference being of essential importance. Therefore, it is necessary to consider the relation between the components of the gyration tensors α_{jk}, g_{jk}, and γ_{jk} entering constitutive equations (1)–(3).

We shall show the results to which the differences between the equations indicated above lead in the calculation of the refractive indices and polarization parameters of eigenwaves in crystals of various symmetry classes.

PHYSICAL MEANING OF EIGENVALUES AND EIGENVECTORS OF THE MATRIX $\mathbf{\Delta}$

In principle, the differences in the description of the optical activity with the aid of constitutive equations (1)–(3) can be seen quite clearly by examining either the equations of the normals that are necessary for the calculation of refractive indices or the polarization of the waves propagating in a crystal (eigenwaves). The corresponding procedure is rather time- and labor-intensive. However, as has already been indicated, one can analyze the matrix $\mathbf{\Delta}$ using different constitutive equations. First, clarify the physical meaning of the eigenvalues and eigenvectors of this matrix, which are not simply a secondary result of the calculations but also a source of useful information on the optical properties of the medium. Moreover, upon the calculation of the matrix $\mathbf{\Delta}$, one can also determine the characteristic equation of this matrix and its eigenvalues and eigenvectors.

We derived the characteristic equation of the matrix $\mathbf{\Delta}$ for optically active uniaxial crystals using the constitutive equations from [5]. Comparing this equation with the rigorous equation of the normals also given in

[5], we established that the coefficients of both fourth-order equations coincide. Thus, at normal light incidence, the characteristic equation of the matrix $\mathbf{\Delta}$ determines the refractive indices of the waves propagating in the crystal, whereas, at oblique incidence, it determines the projections of the refractive indices of these waves on the direction of the normal, *z*, to the plate.

Consider this statement in more detail. Earlier [5], it was shown that at oblique light incidence, the projections of the refraction vectors of all the waves (incident, refracted, and reflected) on the *x*-axis are equal and are determined by the refractive index n_i of the ambient (incidence) medium and the incidence angle ϕ_i. Now, write the refraction vectors $\mathbf{m}_j$ ($j = 1, \ldots, 4$) of the waves propagating in the crystal as was suggested in [5]

$$\mathbf{m}_j = \xi \mathbf{e}_x + \eta_j \mathbf{e}_z = n_j \mathbf{n}_j, \quad (6)$$

where $\xi = n_i \sin\phi_i$, $\mathbf{e}_x$ and $\mathbf{e}_z$ are the unit vectors along the *x* and *z* directions, respectively; η_j are the projections of the vectors $\mathbf{m}_j$ on the *z*-axis; and n_j and $\mathbf{n}_j$ are the refractive indices and the unit vectors of the wave normal of the respective waves. The relationship

$$m_j^2 = n_j^2 = \xi^2 + \eta_j^2 \quad (7)$$

uniquely relates the refractive indices of the waves propagating in a crystal and the quantities η_j corresponding to the eigenvalues of the matrix $\mathbf{\Delta}$ at the oblique incidence. The positive η_j-values correspond to all the waves propagating along the "forward" direction, i.e., the waves propagating from the upper to the lower face, whereas the negative ones, to the waves propagating in the "backward" direction. Obviously, at normal light incidence onto the crystal ($\xi = 0$), the eigenvalues of $\mathbf{\Delta}$ completely determine the refractive indices of the waves propagating in the crystal.

We should like to emphasize once again that the η_j values calculated from the rigorous equation of normals [5] obtained based on constitutive equations (1) fully coincide with the eigenvalues of the matrix $\mathbf{\Delta}$.

The eigenvectors $\mathbf{\psi}_j = [E_{xj}, H_{yj}, E_{yj}, -H_{xj}]$ of the matrix $\mathbf{\Delta}$ are the generalized vectors of the fields of eigenwaves (refracted and reflected) propagating inside the crystal. The eigenwave polarization is determined by the mutual spatial orientation of the crystal and the refraction vector of the incident wave. The vectors $\mathbf{\psi}_j$ determine the *x* and *y* components of the electric and magnetic fields of the corresponding waves. The vectors corresponding to the positive eigenvalues of the matrix $\mathbf{\Delta}$ describe the "forward" waves, whereas the negative ones describe the "backward" waves. At normal light incidence and the coincidence of the axes of the chosen coordinate system with the principal axes of the tensor ε_{jk} and the gyration tensor (α_{jk}, g_{jk}, or γ_{jk}), the relationships

$$k_E = E_{yj}/E_{xj} \quad \text{and} \quad k_H = H_{yj}/H_{xj} \quad (8)$$

determine the polarization state of the fields $\mathbf{E}_j$ and $\mathbf{H}_j$ of the *j*th eigenwave in the crystal corresponding to the refractive index n_j [see Eq. (7)], i.e., determine the ellipticity of the eigenwaves in the crystal. At oblique incidence, the above relationships determine the ellipticity of the projections of the polarization ellipses of eigenwaves on the surface of the crystalline plate.

Thus, it is obvious that the matrix $\mathbf{\Delta}$ contains all the information on the optical properties of the medium, including the information on the polarization of eigenwaves and their refractive indices.

COMPARISON OF THE REFRACTIVE INDICES AND POLARIZATION OF EIGENWAVES DETERMINED FROM DIFFERENT CONSTITUTIVE EQUATIONS

As was indicated above, upon writing the constitutive equations, one can obtain the expressions for determining the refractive indices of the waves propagating in a crystal from the equation of the normals or the characteristic equation of the matrix $\mathbf{\Delta}$. Now, consider the differences between these expressions in the case of constitutive equations (1)–(3).

Crystals of Classes 32, 422, and 622

First, consider in detail the optically active crystals whose dielectric constant tensors ε_{jk} and gyration tensors α_{jk}, g_{jk}, and γ_{jk} that describe the optical activity in various constitutive equations (1)–(3) have the same diagonal form. These are the crystals of the axial symmetry classes *32*, *422*, and *622* ($\varepsilon_{11} = \varepsilon_{22} \neq \varepsilon_{33}$, $\alpha_{11} = \alpha_{22} \neq \alpha_{33}$, $g_{11} = g_{22} \neq g_{33}$, and $\gamma_{11} = \gamma_{22} \neq \gamma_{33}$) and the crystals of the cubic classes *23* and *432* whose diagonal tensor components ε, α, *g*, and γ are equal.

In the majority of experimental studies, the refractive indices n_1 and n_2 were calculated from the equations of the normals obtained based on the constitutive equations (2)

$$(n^2 - n_{01}^2)(n^2 - n_{02}^2) = G^2, \quad (9)$$

whose solution has the form

$$n_{1,2}^2 = \{(n_{01}^2 + n_{02}^2) \mp [(n_{01}^2 - n_{02}^2)^2 + 4G^2]^{1/2}\}/2, \quad (10)$$

where

$$n_{01}^2 = \varepsilon_{11}, \quad n_{02}^2 = \varepsilon_{11}\varepsilon_{33}/(\varepsilon_{11}\sin^2\theta + \varepsilon_{33}\cos^2\theta), \quad (11)$$

n_{01} and n_{02} are the refractive indices of the eigenwaves propagating in the crystal with no allowance for the optical activity, and *G* is the scalar gyration parameter

$$G = g_{ik} n_i n_k. \quad (12)$$

In unaxial crystals, $g_{22} = g_{11}$ and *G* takes the form

$$G = g_{11}\sin^2\theta + g_{33}\cos^2\theta, \quad (13)$$

where θ is the angle between the wave normal and the optic axis; consequently, at a normal incidence, is the angle betwrrn the optic axis and the normal to the surface of the plate.

Now, write the expressions for $n_{1,2}^2$ obtained from the characteristic equation of the matrix $\mathbf{\Delta}$ based on constitutive equations (1). If the optic axis of the crystal is parallel to the direction $\{\sin\theta, 0, \cos\theta\}$, this expression has the form

$$\begin{aligned} n_{1,2}^2 &= \{(\varepsilon_{11} + \varepsilon_{33} + 2\alpha_{11}\alpha_{33})r_1\sin^2\theta \\ &+ 2(\varepsilon_{11} + \alpha_{11}^2)r_3\cos^2\theta \mp [(\varepsilon_{33} - \varepsilon_{11})^2 r_1^2\sin^4\theta \\ &+ 4((\alpha_{11} + \alpha_{33})(\alpha_{11}\varepsilon_{33} + \alpha_{33}\varepsilon_{11})r_1^2\sin^4\theta \\ &+ 4\alpha_{11}^2\varepsilon_{11}r_3^2\cos^4\theta + 2\alpha_{11}(\varepsilon_{11}(\alpha_{11} + \alpha_{33}) \\ &+ (\alpha_{11}\varepsilon_{33} + \alpha_{33}\varepsilon_{11}))r_1r_3\sin^2\theta\cos^2\theta)]^{1/2}\}/(2z), \end{aligned} \tag{14}$$

where $z = (\varepsilon_{11}\sin^2\theta + \varepsilon_{33}\cos^2\theta) - (\alpha_{11}\sin^2\theta + \alpha_{33}\cos^2\theta)^2$, $r_1 = \varepsilon_{11} - \alpha_{11}^2$, $r_3 = \varepsilon_{33} - \alpha_{33}^2$.

As was shown in [29], constitutive equations (2), (3) describe the phenomenon of optical activity within an accuracy of the product of the anisotropy parameters by the gyrotropy parameters. We shall show that it is with precisely this accuracy that expression (14) of the rigorous theory is transformed into expression (10) of the approximate theory. With this aim, we write

$$\varepsilon_{11,33} = \bar{\varepsilon} \mp \Delta\varepsilon, \tag{15}$$

where $\bar{\varepsilon} = (\varepsilon_{11} + \varepsilon_{33})/2$ and $\Delta\varepsilon = (\varepsilon_{33} - \varepsilon_{11})/2$. Ignoring the terms of the order $(\Delta\varepsilon\,\alpha)$ in (14) and the terms $(\alpha_{ii}\,\alpha_{jj})$ in the expressions of the form $(\varepsilon_{kk} \pm \alpha_{ii}\,\alpha_{jj})$ and taking into account Eq. (11), we can transform expression (14) into the form

$$\begin{aligned} n_{1,2}^2 &= \{(n_{01}^2 + n_{02}^2) \mp [(n_{01}^2 - n_{02}^2)^2 \\ &+ 4[\sqrt{\bar{\varepsilon}}(\alpha_{11} + \alpha_{33})\sin^2\theta \\ &+ 2\alpha_{11}\sqrt{\varepsilon_{11}}\cos^2\theta]^2\bar{\varepsilon}^2/(\varepsilon_{11}\sin^2\theta + \varepsilon_{33}\cos^2\theta)^2]^{1/2}\}/2. \end{aligned} \tag{16}$$

It is clearly seen that the notation

$$g_{11} = \sqrt{\bar{\varepsilon}}(\alpha_{11} + \alpha_{33}), \quad g_{33} = 2\alpha_{11}\sqrt{\varepsilon_{11}} \tag{17}$$

transforms Eq. (16) into Eq. (10) with an accuracy up to the factor $\bar{\varepsilon}/(\varepsilon_{11}\sin^2\theta + \varepsilon_{33}\cos^2\theta)$. We emphasize once again that the angle θ in the expressions of the approximate theory is formed by the wave normal and the optic axis of the crystal, whereas, in the expressions of the rigorous theory, this angle is formed by the optic axis and the normal to the plate surface. In both theories, this angle has the same meaning only for uniaxial crystals at normal light incidence.

Now, compare the expressions for the refractive indices obtained using constitutive equations (1), (2), and (3) for the two most important cases—the light incidence along the optic axis and normal to it.

Consider, first, the light propagation along the optic axis and tabulate the results obtained. It should be indicated that the expressions for the eigenvector components given below are written within the accuracy of a constant. One also has to bear in mind that, in constitutive equations (2), the tensor ε_{jk} is written in a different form from that in constitutive equations (1), namely,

$$\varepsilon = \begin{pmatrix} \varepsilon_{11} & -ig_{33} & 0 \\ ig_{33} & \varepsilon_{11} & 0 \\ 0 & 0 & \varepsilon_{33} \end{pmatrix}. \tag{18}$$

In other words, the components ε_{jk} are complex quantities, whereas the existence of the optical activity is determined by their imaginary parts.

Even this simplest case shows that the refractive indices are calculated in different ways depending on the constitutive equations used, and the relation between these refractive indices has the form

$$\begin{aligned} n_{1,2} &= \sqrt{\varepsilon_{11}} \mp \alpha_{11} \approx \sqrt{\varepsilon_{11}} \mp g_{33}/(2\sqrt{\varepsilon_{11}}) \\ &\approx \sqrt{\varepsilon_{11}} \mp \gamma_{11}/2. \end{aligned} \tag{19}$$

One should pay attention to the fact that $n_{1,2}$ values calculated by constitutive equations (1) are accurate, whereas their values calculated from constitutive equations (2), (3) are only approximate (resulting from the approximate evaluation of the square root). Expression (19) yields the following relation between the components of the gyration tensors used in various constitutive equations:

$$\alpha_{11} = g_{33}/(2\sqrt{\varepsilon_{11}}) = \gamma_{11}/2. \tag{20}$$

It should be emphasized that the use of any of constitutive equations (1)–(3) provides the ellipticity of the eigenwaves, $k_E = E_{yj}/E_{xj} = \pm i$; in other words, the eigenwaves are circularly polarized with opposite bypass directions despite the fact that all the equations are written differently.

Now, write the expressions of the refractive indices resulting from the use of constitutive equations (1) and (2) for a plate cut out parallel to the optic axis ($\theta = 90°$), i.e., for light propagating normally to the optic axis

$$\begin{aligned} n_{1,2}^2 &= (\varepsilon_{11} + \varepsilon_{33} + 2\alpha_{11}\alpha_{33} \\ &\mp \sqrt{(\varepsilon_{33} - \varepsilon_{11})^2 + 4(\alpha_{11} + \alpha_{33})(\alpha_{11}\varepsilon_{33} + \alpha_{33}\varepsilon_{11})})/2, \end{aligned} \tag{21}$$

$$n_{1,2}^2 = (\varepsilon_{11} + \varepsilon_{33} \pm \sqrt{(\varepsilon_{33} - \varepsilon_{11})^2 + 4g_{11}^2})/2. \tag{22}$$

Comparing the refractive indices obtained, we see that

$$g_{11} = (\alpha_{11} + \alpha_{33})\bar{n}, \tag{23}$$

where $\bar{n} = \sqrt{(\varepsilon_{11} + \varepsilon_{33})/2}$ under the condition that quantity $(2\alpha_{11}\alpha_{33})$ is negligible in comparison with $(\varepsilon_{11} + \varepsilon_{33})$ and that the quantities of the order of the product of the gyration-tensor components by crystal anisotropy are also ignored. It has already been indicated that the approximate theory of the optical activity is valid just under these approximations [29]. We do not indicate here the expressions for the refractive indices which follows from other constitutive equations.

As in the previous case of light propagation along the optic axis, the most important factor in the case of light propagation normally to the optic axis is the essential difference in the description of the optical activity based on different constitutive equations. The rotation of the polarization plane through the angle χ in the case of light propagation along the optic axis is determined by different gyration-tensor components and the use of different constitutive equations, namely:

$$\begin{aligned}\chi &= \pi d(n_2 - n_1)/\lambda = \pi d 2\alpha_{11}/\lambda \\ &\approx \pi d g_{33}/(\lambda\sqrt{\varepsilon_{11}}) = \pi d\gamma_{11}/\lambda.\end{aligned} \quad (24)$$

Using constitutive equations (2) in the case of light propagation along the optic axis, the difference in the refractive indices and, therefore, also the rotation of the polarization plane are determined by the component g_{33}, which differs from two other equal components. In the description of the optical activity by constitutive equations (1), the rotation of the polarization plane is determined by two equal components of the gyration tensor, α_{11}. In the description of the optical activity along the direction normal to the optic axis, all the optical parameters in the case of constitutive equations (2), including the refractive indices and the ellipticity of eigenwaves, are determined by two equal components of the gyration tensor, $g_{11} = g_{22}$. In the case of constitutive equations (1), these optical parameters are determined by the sum of the tensor components $(\alpha_{11} + \alpha_{33})$. The approximate relation between these components is established by relationship (23). This is the essential difference in the description of the optical activity by various constitutive equations. This should be kept in mind in the consideration of the phenomenon of optical activity when using various constitutive equations.

We believe that the relation between the gyration-tensor components in different descriptions of the optical activity was first noticed in [29], where the equations of the normals obtained with the aid of constitutive equations (1) and (2) were compared and the relationships between the gyration tensors used in different equations were established. However, at that time, no importance was given to this result.

It should be underlined once again that at present, it is commonly believed that the constitutive equations suggested in [5, 14] are quite rigorous and used mainly in theoretical studies, whereas the constitutive equations suggested in [8, 9] are approximate and used in experimental studies. When selecting the constitutive equations, one has to bear in mind the applicability range of the approximate equations and also the relationships between the gyration-tensor components used in various constitutive equations.

Different constitutive equations, refractive indices $n_{1,2}$, generalized field vectors $\psi_{1,2}$ of the eigenwaves, and the form of the Δ matrices for optically active isotropic crystals of the classes *23*, *432* and uniaxial crystals of the classes *32*, *422*, and *622* along the direction of the optic axis ($\theta = 0°$) in the case of normal light incidence

Authors, references, constitutive equations, $n_{1,2}$, $\psi_{1,2}$	Δ matrix
Fedorov, Condon [5, 14] $D_j = \varepsilon_{jk}E_k + i\alpha_{jk}H_k$, $B_j = \mu_{jk}H_k - i\tilde{\alpha}_{jk}E_k$ $n_{1,2} = \sqrt{\varepsilon_{11}} \mp \alpha_{11}$ $\psi_{1,2} = [\pm i/\sqrt{\varepsilon_{11}}, \pm i, 1/\sqrt{\varepsilon_{11}}, 1]$	$\begin{bmatrix} 0 & 1 & -i\alpha_{11} & 0 \\ \varepsilon_{11} & 0 & 0 & -i\alpha_{11} \\ i\alpha_{11} & 0 & 0 & 1 \\ 0 & i\alpha_{11} & \varepsilon_{11} & 0 \end{bmatrix}$
Born, Landau [8, 9] $D_j = (\varepsilon_{jk} + ie_{jkl}g_{lm}n_m)E_k$, $B_j = \mu_{jk}H_k$ $n_{1,2} = \sqrt{\varepsilon_{11} \mp g_{33}}$ $\psi_{1,2} = [\pm i/\sqrt{\varepsilon_{11} \mp g_{33}}, \pm i,$ $1/\sqrt{\varepsilon_{11} \mp g_{33}}, 1]$	$\begin{bmatrix} 0 & 1 & 0 & 0 \\ \varepsilon_{11} & 0 & ig_{33} & 0 \\ 0 & 0 & 0 & 1 \\ -ig_{33} & 0 & \varepsilon_{11} & 0 \end{bmatrix}$
Berreman, Drude [2, 27] $D_j = \varepsilon_{jk}E_k + i\gamma_{jk}H_k$, $B_j = \mu_{jk}H_k$ $n_{1,2} = \sqrt{\varepsilon_{11} + \gamma_{11}^2/4} \mp \gamma_{11}/2$ $\psi_{1,2} = [i(\pm\sqrt{\varepsilon_{11} + \gamma_{11}^2/4} + \gamma_{11})/\varepsilon_{11},$ $\pm i, 1/(\sqrt{\varepsilon_{11} + \gamma_{11}^2/4} \mp \gamma_{11}), 1]$	$\begin{bmatrix} 0 & 1 & 0 & 0 \\ \varepsilon_{11} & 0 & 0 & -i\gamma_{11} \\ 0 & 0 & 0 & 1 \\ 0 & i\gamma_{11} & \varepsilon_{11} & 0 \end{bmatrix}$

Thus, we described in detail the calculation of the refractive indices for the crystals described by the axial classes *32*, *422*, and *622*. These calculations for the crystals described by other symmetry classes are not considered in such detail. For the latter crystals, only some essential features of the use of various constitutive equations are considered.

Crystals of Classes 3, 4, 6 and 3m, 4mm, and 6mm

Unlike crystals of the classes *32*, *422*, and *622*, the gyration tensor of the crystals of the classes *3*, *4*, and *6* has, in addition to diagonal components, also antisymmetric ones, $\alpha_{21} = -\alpha_{12}$ [5]. When using constitutive equations (2), we assumed that the gyration tensor is completely symmetric. Therefore, crystals of the classes *32*, *422*, *622* and *3*, *4*, *6* were described by the same diagonal gyration tensor, whereas the components $\alpha_{21} = -\alpha_{12}$ were assumed to be zeroes [8]. The matrix Δ for the crystals of these classes in the case of the oblique light incidence $\theta = 0°$ (the optic axis is normal to the plate plane), $\psi = 0°$, and an arbitrary angle φ

has the form

$$\Delta = \begin{pmatrix} -i\alpha_{12} & \dfrac{\varepsilon_{33}-\alpha_{33}^2-\xi^2}{\varepsilon_{33}-\alpha_{33}^2} & -\dfrac{i(\alpha_{11}(\varepsilon_{33}-\alpha_{33}^2)+\alpha_{33}\xi^2)}{\varepsilon_{33}-\alpha_{33}^2} & 0 \\ \varepsilon_{11} & i\alpha_{12} & 0 & -i\alpha_{11} \\ i\alpha_{11} & 0 & -i\alpha_{12} & 1 \\ 0 & \dfrac{i(\alpha_{11}(\varepsilon_{33}-\alpha_{33}^2)+\alpha_{33}\xi^2)}{\varepsilon_{33}-\alpha_{33}^2} & \dfrac{\varepsilon_{11}(\varepsilon_{33}-\alpha_{33}^2)-\varepsilon_{33}\xi^2}{\varepsilon_{33}-\alpha_{33}^2} & i\alpha_{12} \end{pmatrix}. \quad (25a)$$

Hereafter, the angles φ, θ, and ψ determine the position of the orthogonal system of the principal axes of the tensor in the laboratory coordinate system *xyz*. In the Mathematica-4.1 package, the transition from one coordinate system to another is performed via three successive rotations: by angle φ around the *z*-axis, then by angle θ around the *x*-axis, and, finally, by angle ψ around the *z*-axis.

In the case θ = 90° (the optic axis lies in the plate plane), with the other conditions being the same, **Δ** is written as

$$\Delta = \begin{pmatrix} -\dfrac{\alpha_{11}\alpha_{12}\xi}{\varepsilon_{11}-\alpha_{11}^2} & \dfrac{\varepsilon_{11}-\alpha_{11}^2-\xi^2}{\varepsilon_{11}-\alpha_{11}^2} & -\dfrac{i[\alpha_{33}(\varepsilon_{11}-\alpha_{11}^2)+\alpha_{11}\xi^2]}{\varepsilon_{11}-\alpha_{11}^2} & \dfrac{i\alpha_{12}\xi}{\varepsilon_{11}-\alpha_{11}^2} \\ \dfrac{\varepsilon_{11}(\varepsilon_{11}-\alpha_{11}^2-\alpha_{12}^2)}{\varepsilon_{11}-\alpha_{11}^2} & -\dfrac{\alpha_{11}\alpha_{12}\xi}{\varepsilon_{11}-\alpha_{11}^2} & -\dfrac{i\varepsilon_{11}\alpha_{12}\xi}{\varepsilon_{11}-\alpha_{11}^2} & -\dfrac{i\alpha_{11}(\varepsilon_{11}-\alpha_{11}^2-\alpha_{12}^2)}{\varepsilon_{11}-\alpha_{11}^2} \\ \dfrac{i\alpha_{11}(\varepsilon_{11}-\alpha_{11}^2-\alpha_{12}^2)}{\varepsilon_{11}-\alpha_{11}^2} & -\dfrac{i\alpha_{12}\xi}{\varepsilon_{11}-\alpha_{11}^2} & \dfrac{\alpha_{11}\alpha_{12}\xi}{\varepsilon_{11}-\alpha_{11}^2} & \dfrac{\varepsilon_{11}-\alpha_{11}^2-\alpha_{12}^2}{\varepsilon_{11}-\alpha_{11}^2} \\ \dfrac{i\varepsilon_{11}\alpha_{12}\xi}{\varepsilon_{11}-\alpha_{11}^2} & \dfrac{i[\alpha_{33}(\varepsilon_{11}-\alpha_{11}^2)+\alpha_{11}\xi^2]}{\varepsilon_{11}-\alpha_{11}^2} & \dfrac{\varepsilon_{33}(\varepsilon_{11}-\alpha_{11}^2)-\varepsilon_{11}\xi^2}{\varepsilon_{11}-\alpha_{11}^2} & \dfrac{\alpha_{11}\alpha_{12}\xi}{\varepsilon_{11}-\alpha_{11}^2} \end{pmatrix}. \quad (25b)$$

The above matrices are applicable to the crystals of the classes *32*, *422*, and *622* under the condition $\alpha_{12} = \alpha_{21} = 0$; the crystals of the classes *3m*, *4mm*, *6mm* under the condition $\alpha_{11} = \alpha_{22} = \alpha_{33} = 0$; and the crystals of the classes *23* and *432* under the conditions $\alpha_{11} = \alpha_{22} = \alpha_{33}$ and $\alpha_{12} = \alpha_{21} = 0$.

In the crystals of the symmetry classes *3*, *4*, and *6*, the component α_{12} enters the expressions of the refractive indices (here, they are given for the cases θ = 0° and θ = 90°, respectively):

$$n_{1,2} = \sqrt{\varepsilon_{11}-\alpha_{12}^2} \pm \alpha_{11}; \quad (26a)$$

$$n_{1,2}^2 = \frac{\varepsilon_{11}-\alpha_{11}^2-\alpha_{12}^2}{\varepsilon_{11}-\alpha_{11}^2}(\varepsilon_{11}+\varepsilon_{33}+2\alpha_{11}\alpha_{33} \pm \sqrt{(\varepsilon_{33}-\varepsilon_{11})^2+4(\alpha_{11}+\alpha_{33})(\alpha_{11}\varepsilon_{33}+\alpha_{33}\varepsilon_{11})})/2. \quad (26b)$$

Obviously, if $\alpha_{12} = 0$, expressions (26) are transformed into the corresponding expressions for the classes *32*, *422*, and *622*.

The crystals of the classes *3m*, *4mm*, and *6mm* have been believed to be optically inactive for quite a long time, because their optical activity is described by fully antisymmetric gyration tensor, $\alpha_{21} = -\alpha_{12}$ and $\alpha_{11} = \alpha_{22} = \alpha_{33} = 0$. However, it was shown [30] that the optical activity of these crystals manifests itself only in the case of oblique light incidence (the ellipticity of the eigenwaves has the nonzero value), despite the fact that it is seen from expressions (26) that, even at normal light incidence, the refractive indices depend on the component α_{12}.

Crystals of Classes ($\bar{4}$, $\bar{4}2m$)

In crystals of the class $\bar{4}$, the components of the gyration tensors are $\alpha_{22} = -\alpha_{11}$, $\alpha_{33} = 0$, and $\alpha_{21} = \alpha_{12}$.

In crystals of the class $\bar{4}2m$, the gyration tensor $\alpha_{12} = \alpha_{21} = 0$ differs from the gyration tensor of the remaining uniaxial crystals. This difference reduces to the fact that only one axis of the tensor α coincides with the axis of the tensor α, and both axes coincide with the direction of the optic axis of the crystal. If the direction of the optic axis coincides with the direction of the *z*-axis of the chosen laboratory coordinate system, then two other principal axes of the tensor α are directed along the *x*- and *y*-axes, respectively, whereas two other orthogonal principal axes of the tensor α are rotated by a certain angle around the *x*- and *y*-axes, respectively. If the expressions of the refractive indices are to contain the nondiagonal components of the tensor α, the system of the principal axes of tensors α and ε should be rotated by an angle φ around the *z*-axis. We should like to draw attention to the fact that, in uniaxial crystals of other classes, this rotation by the angle φ does not change the form of the tensors α and ε at $\theta = 0°$ and $\theta = 90°$ irrespective of normal or oblique light incidence, whereas in crystals of the classes $\bar{4}$ and $\bar{4}2m$, the rotation by an angle φ plays a decisive role in the calculation of the refractive index at $\theta = 90°$, with the tensor ε remaining constant. The matrix $\mathbf{\Delta}$ for these crystal at normal light incidence at $\theta = \psi = 0°$ and an arbitrary value of the angle φ is

$$\mathbf{\Delta} = \begin{pmatrix} -i\alpha_{12} & 1 & i\alpha_{11} & 0 \\ \varepsilon_{11} & i\alpha_{12} & 0 & -i\alpha_{11} \\ i\alpha_{11} & 0 & i\alpha_{12} & 1 \\ 0 & -i\alpha_{11} & \varepsilon_{11} & -i\alpha_{12} \end{pmatrix}. \quad (27a)$$

Under the same conditions but at $\theta = 90°$, the matrix $\mathbf{\Delta}$ has the form

$$\mathbf{\Delta} = \begin{pmatrix} 0 & 1 & 0 & 0 \\ \frac{v\varepsilon_{11}}{z} & 0 & 0 & -\frac{iuv}{z} \\ \frac{iuv}{z} & 0 & 0 & \frac{v}{z} \\ 0 & 0 & \varepsilon_{33} & 0 \end{pmatrix}, \quad (27b)$$

where $u = \alpha_{11}\cos 2\varphi + \alpha_{12}\sin 2\varphi$, $v = \varepsilon_{11} - \alpha_{11}^2 - \alpha_{12}^2$, and $z = \varepsilon_{11} - u^2$.

These matrices provide the determination of the refractive indices in the form

$$n_{1,2}^2 = \varepsilon_{11} - \alpha_{11}^2 - \alpha_{12}^2 \quad (28a)$$

at $\theta = 0°$, and

$$n_{1,2}^2 = \frac{\varepsilon_{11} - \alpha_{11}^2 - \alpha_{12}^2}{2(\varepsilon_{11} - [\alpha_{11}\cos 2\varphi + \alpha_{12}\sin 2\varphi]^2)}(\varepsilon_{11} + \varepsilon_{33} \mp \sqrt{(\varepsilon_{33} - \varepsilon_{11})^2 + 4[\alpha_{11}\cos 2\varphi + \alpha_{12}\sin 2\varphi]^2\varepsilon_{33}}) \quad (28b)$$

at $\theta = 90°$.

Using constitutive equations (2), one arrives at the expression for $n_{1,2}$ at $\theta = 90°$ in the form

$$n_{1,2}^2 = (\varepsilon_{11} + \varepsilon_{33} \mp \sqrt{(\varepsilon_{33} - \varepsilon_{11})^2 + 4[g_{11}\cos 2\varphi + g_{12}\sin 2\varphi]^2})/2. \quad (29)$$

Comparing expressions (28b) and (29), we clearly see which approximations and which relations for the components were used in the rigorous and approximate theories:

$$g_{11} = \alpha_{11}\bar{n}, \quad g_{12} = \alpha_{12}\bar{n}. \quad (30)$$

Crystals of Orthorhombic Class 222

In the general case, all the components of the tensors ε and α have nonzero values. In this case, the tensor ε is symmetric, while the tensor α can be of an arbitrary form. Using the Mathematica-4.1 package, the matrix $\mathbf{\Delta}$ can be obtained in a general but rather cumbersome form and, therefore, is not indicated here. Moreover, this general matrix is characteristic of only one class of crystals—triclinic crystals of class *1*. For crystals of the classes 2, *m*, and *mm*2, the gyration tensor has nondiagonal components. Only one of its principal axis coincides with one of the principal axes of the tensor ε, whereas the orthogonal pairs of two other principal axes of each tensor are located in the *xOy* plane and are rotated by different angles around the *x*- and *y*-axes, respectively. In order to obtain the correct dependence of the refractive indices of eigenwaves on angle φ, one has to perform transformations similar to those made for crystals of class $\bar{4}$. The corresponding expressions are too cumbersome and, therefore, are not given here.

Consider the crystals of the orthorhombic class *222*. Here, the directions $\mathbf{u}_1$, $\mathbf{u}_2$, and $\mathbf{u}_3$ ($|\mathbf{u}_j| = 1$) of the principal axes of the tensors ε and α coincide with the symmetry axes 2 of the crystal. In the laboratory coordinate system, these tensors are diagonal ($\varepsilon_{11} \neq \varepsilon_{22} \neq \varepsilon_{33} \neq 0$, $\varepsilon_{jk} = 0$, $\alpha_{11} \neq \alpha_{22} \neq \alpha_{33} \neq 0$, $\alpha_{jk} = 0$, $j \neq k$) if $\mathbf{u}_1 \parallel \mathbf{e}_x$, $\mathbf{u}_2 \parallel \mathbf{e}_y$, $\mathbf{u}_3 \parallel \mathbf{e}_z$ (the Eulerian angles are $\varphi = \theta = \psi = 0°$). In

this case, the matrix $\mathbf{\Delta}$ at oblique incidence has the form

$$\mathbf{\Delta} = \begin{pmatrix} 0 & \dfrac{\varepsilon_{33} - \alpha_{33}^2 - \xi^2}{\varepsilon_{33} - \alpha_{33}^2} & -\dfrac{i(\alpha_{22}(\varepsilon_{33} - \alpha_{33}^2) + \alpha_{33}\xi^2)}{\varepsilon_{33} - \alpha_{33}^2} & 0 \\ \varepsilon_{11} & 0 & 0 & -i\alpha_{11} \\ i\alpha_{11} & 0 & 0 & 1 \\ 0 & \dfrac{i(\alpha_{22}(\varepsilon_{33} - \alpha_{33}^2) + \alpha_{33}\xi^2)}{\varepsilon_{33} - \alpha_{33}^2} & \dfrac{\varepsilon_{22}(\varepsilon_{33} - \alpha_{33}^2) - \varepsilon_{33}\xi^2}{\varepsilon_{33} - \alpha_{33}^2} & 0 \end{pmatrix}. \quad (31)$$

At the normal light incidence, the refractive indices are

$$n_{1,2}^2 = (\varepsilon_{11} + \varepsilon_{22} + 2\alpha_{11}\alpha_{22} \mp \sqrt{(\varepsilon_{22} - \varepsilon_{11})^2 + 4(\alpha_{11} + \alpha_{22})(\alpha_{11}\varepsilon_{22} + \alpha_{22}\varepsilon_{11})})/2. \quad (32)$$

If $\varphi = 0°$ and $\theta = \psi = 90°$, then $\mathbf{u}_2 \parallel \mathbf{e}_z$, and if $\varphi = \theta = 90°$ and $\psi = 0°$, then $\mathbf{u}_1 \parallel \mathbf{e}_z$. Therefore, the subscripts of the ε_{ij} and α_{ij} of the matrices $\mathbf{\Delta}$ and, naturally, in the refractive indices corresponding to each of the above cases are changed by cyclic permutation. With due regard for this approximation, the relation between the gyration-tensor components g_{ii} and α_{jj} can be written as

$$g_{11} \approx (\alpha_{22} + \alpha_{33})\sqrt{\frac{\varepsilon_{22} + \varepsilon_{33}}{2}},$$
$$g_{22} \approx (\alpha_{11} + \alpha_{33})\sqrt{\frac{\varepsilon_{11} + \varepsilon_{33}}{2}}, \quad (33)$$
$$g_{33} \approx (\alpha_{11} + \alpha_{22})\sqrt{\frac{\varepsilon_{11} + \varepsilon_{22}}{2}}.$$

In the above expression, the relation between the components is analogous to the relation established for the crystals of the classes *32*, *422*, and *622* in expression (23) and is also valid in the same approximation.

CONCLUSIONS

The analytical form of the matrix $\mathbf{\Delta}$ and the specific features of its characteristics for optically active crystals of different symmetry classes was obtained and analyzed by the Berreman method using the Mathematica-4.1 package. It is shown that the matrix $\mathbf{\Delta}$ is in itself of interest for studying crystals, since its eigenvalues are the refractive indices and its eigenvectors determine the polarization state of the waves propagating in crystals.

The relation between the components of the gyration tensors used in the description of the optical activity in some commonly used theories is established. It is shown that the rigorous Condon–Fedorov constitutive equations, most often used in theoretical studies, describe the phenomenon of the optical activity in a way that is essentially different from the approximate Born–Landau constitutive equations used in the experimental studies. The expressions obtained for refractive indices based on different constitutive equations provide the determination of the applicability ranges of the approximate theory.

REFERENCES

1. A. F. Konstantinova, K. K. Konstantinov, B. V. Nabatov, and E. A. Evdishchenko, Kristallografiya **47** (4), 702 (2002) [Crystallogr. Rep. **47**, 645 (2002)].
2. D. W. Berreman, J. Opt. Soc. Am. **62** (4), 502 (1972).
3. R. M. Azzam and N. M. Bashara, *Ellipsometry and Polarized Light* (North-Holland, Amsterdam, 1977; Mir, Moscow, 1981).
4. W. Voigt, Nachriechten, 156 (1903).
5. F. I. Fedorov, *Theory of Gyrotropy* (Nauka i Tekhnika, Minsk, 1976).
6. B. N. Grechushnikov, in *Modern Crystallography*, Vol. 4: *Physical Properties of Crystals*, Ed. by B. K. Vainshtein, A. A. Chernov, and L. A. Shuvalov (Nauka, Moscow, 1981; Springer-Verlag, Berlin, 1988).
7. A. F. Konstantinova, B. N. Grechushnikov, B. V. Bokut', and E. G. Valyashko, *Optical Properties of Crystals* (Nauka i Tekhnika, Minsk, 1995).
8. M. Born, *Optik* (Springer, Berlin, 1933; GNTIU, Kiev, 1937).
9. L. D. Landau and E. M. Lifshitz, *Course of Theoretical Physics*, Vol. 8: *Electrodynamics of Continuous Media* (Nauka, Moscow, 1982; Pergamon, New York, 1984).
10. J. F. Nye, *Physical Properties of Crystals: Their Representation by Tensors and Matrices* (Clarendon, Oxford, 1957; Inostrannaya Literatura, Moscow, 1960).
11. A. Yariv and P. Yeh, *Optical Waves in Crystals: Propagation and Control of Laser Radiation* (Wiley, New York, 1984; Mir, Moscow, 1987).
12. Yu. I. Sirotin and M. P. Shaskol'skaya, *Fundamentals of Crystal Physics* (Nauka, Moscow, 1975; Mir, Moscow, 1982).
13. A. V. Shubnikov, *Principles of Optical Crystallography* (Akad. Nauk SSSR, Moscow, 1958; Consultants Bureau, New York, 1960).
14. E. U. Condon, Rev. Mod. Phys. **9**, 432 (1937).
15. V. N. Aleksandrov, Kristallografiya **15** (5), 996 (1970) [Sov. Phys. Crystallogr. **15**, 867 (1970)].

16. B. V. Bokut', A. N. Serdyukov, and F. I. Fedorov, Kristallografiya **15** (5), 1002 (1970) [Sov. Phys. Crystallogr. **15**, 871 (1970)].
17. L. M. Barkovskiĭ, G. N. Borzdov, and F. I. Fedorov, Dokl. Akad. Nauk BSSR **19** (4), 305 (1975).
18. E. Georgieva, J. Opt. Soc. Am. A **12** (10), 2203 (1995).
19. M. P. Silverman and J. Badoz, J. Opt. Soc. Am. A **7** (7), 1163 (1990).
20. S. Bassiri, C. H. Papas, and N. Engheta, J. Opt. Soc. Am. A **5** (9), 1450 (1988).
21. A. Lakhtakia, V. V. Varadan, and V. K. Varadan, J. Opt. Soc. Am. A **5** (2), 175 (1988).
22. A. H. Sihvola and I. V. Lindell, Microwave Opt. Technol. Lett. **4** (8), 295 (1991).
23. W. S. Weiglhofer and A. Lakhtakia, J. Phys. D **26**, 2117 (1993).
24. I. V. Lindell, A. H. Sihvola, S. A. Tretyakov, and A. J. Viitanen, *Electromagnetic Waves in Bi-Isotropic and Chiral Media* (Artech House, Boston, 1994).
25. A. A. Gevorgyan, Opt. Spektrosk. **91** (5), 812 (2001) [Opt. Spectrosc. **91**, 762 (2001)].
26. I. J. Lalov and N. A. Kojouharova, Bulg. J. Phys. **27** (2), 66 (2000).
27. P. K. L. Drude, *Theory of Optics* (Longmans, London, 1902; ONTI, Moscow, 1935).
28. Y. Sah and J. G. Krishna, J. Opt. Soc. Am. A **18** (6), 1388 (2001).
29. E. A. Evdishchenko, A. F. Konstantinova, and B. N. Grechushnikov, Kristallografiya **36** (4), 842 (1991) [Sov. Phys. Crystallogr. **36**, 470 (1991)].
30. A. F. Konstantinova and B. V. Nabatov, Kristallografiya **40** (2), 219 (1995) [Crystallogr. Rep. **40**, 197 (1995)].

Translated by L. Man

Crystallography Reports, Vol. 47, No. 5, 2002, pp. 824–828. Translated from Kristallografiya, Vol. 47, No. 5, 2002, pp. 888–892.

PHYSICAL PROPERTIES OF CRYSTALS

Inverse Faraday Effect in Anisotropic Media

P. V. Volkov and M. A. Novikov

Institute for Physics of Microstructures, Russian Academy of Sciences, GSP-105, Nizhni Novgorod, 603950 Russia

e-mail: volkov@ipm.sci-nnov.ru

Received November 15, 2001;
in final form, April 18, 2002

Abstract—The inverse Faraday effect in anisotropic media has been studied theoretically. All the 32 symmetry classes of crystals are considered at various relative orientations of the optic axes and directions of light propagation. The specific features of the inverse Faraday effect in uni- and biaxial crystals are considered. *© 2002 MAIK "Nauka/Interperiodica".*

INTRODUCTION

Nonlinear optical phenomena still attracts great attention among experts in laser optics and its various applications. Among these phenomena, a special group is formed by the dc effects (the effects of optical rectification). One of these effects, the so-called inverse Faraday effect [1], consists in the induction of dc magnetization in a dielectric by circularly polarized light, i.e., magnetic optical rectification (detection), which was first predicted by Pitaevskiĭ [2]. An interesting feature of this effect is its manifestation in nonabsorbing media, which is of primary importance for quantum optics in the case of nondestructive measurements [3].

GENERAL THEORY OF INVERSE FARADAY EFFECT IN CRYSTALS

The inverse Faraday effect in nonabsorbing media can be conveniently described by the Pershan energy method based on the free-energy function [4]. This approach showed that it follows from the law of energy conservation that the rotation of the polarization plane in a magnetic field, the Faraday effect, and the inverse Faraday effect are described by the same tensor.

Let a light wave propagate through a nonabsorbing medium in a constant magnetic field. Then the free energy of the medium F has the form

$$F = -\frac{1}{2}(\chi_{ijk}(\omega, \omega, 0)E_i^*(\omega)E_j(\omega)H_k(0) + \chi_{ijk}^*(\omega, \omega, 0)E_i(\omega)E_j^*(\omega)H_k(0)), \quad (1)$$

where $\mathbf{E}(\omega)$ is the electric field of the wave, $\mathbf{H}(0)$ is the applied constant magnetic field, and χ is a third-rank pseudotensor that describes the interaction of the field with the material.

For crystals that are invariant with respect to the time reversal, i.e., that have no magnetic order, the following condition is valid [4]:

$$\chi_{ijk} = -\chi_{ijk}^* = i|\chi_{ijk}|; \quad (2)$$

in other words, the pseudotensor χ is purely imaginary. It follows from the symmetry of Eq. (1) with respect to the permutation of the electric-field components of the incident wave that

$$\chi_{ijk} = \chi_{jik}^*. \quad (3)$$

Combining conditions described by Eqs. (2) and (3), we have

$$\chi_{ijk} = ie_{ijl}A_{lk}, \quad (4)$$

where e_{ijl} is the totally antisymmetric Levi–Civita pseudotensor and $\mathbf{A}$ is the real second-rank tensor dual to the tensor χ.

According to the definition of the free energy, the polarization $\mathbf{P}(\omega)$ induced by the incident wave and responsible for the Faraday effect has the form:

$$P_i(\omega) = -\frac{\partial F}{\partial E_i^*} = ie_{ijl}A_{lk}E_j(\omega)H_k(0). \quad (5)$$

Differentiating free energy described by Eq. (1) with respect to $H_k(0)$, we obtain the induced magnetization $\mathbf{M}(0)$ in the field of the light wave $\mathbf{E}$,

$$M_k(0) = -\frac{\partial F}{\partial H_k^*(0)} = ie_{ijl}A_{lk}E_iE_j^*. \quad (6)$$

Comparing Eqs. (5) and (6), we see that the induced polarization and magnetization are described by the same tensor.

As far as we know (see, e.g., [5]), all the previous studies considered only the isotropic media, for which the A_{lk} tensor becomes a scalar. Then, Eq. (5) describes the rotation of the polarization plane of a wave in a transverse constant magnetic field, while Eq. (6), the magnetization of the medium along the direction of

propagation of a circularly polarized wave. Below we consider a more general case of the inverse Faraday effect in anisotropic crystals for various geometries of the mutual orientation of the wave vector and the crystal axes.

To study the inverse Faraday effect, we use the tensor notation that is not based on coordinates [6]. For isotropic media of symmetry $\infty\infty\infty m$ and gyrotropic media of symmetry $\infty\infty\infty$ and also for cubic crystals of the symmetry classes 23, $m3$, 432, $m3m$, and $\bar{4}3m$, the tensor A_{lk} has the form

$$\mathbf{A} = A\mathbf{e}_i\mathbf{e}_i, \tag{7}$$

where $\mathbf{e}_i$ are the unit vectors along the coordinate axes of the crystallophysical basis and A is the constant that describes the Faraday effect.

For trigonal crystals of the classes 32, $3m$, and $\bar{3}m$; tetragonal crystals of the classes 422, $4mm$, $\bar{4}2m$, and $4/mmm$; hexagonal crystals of the classes 622, $6mm$, $\bar{6}m2$, and $6/mmm$; the textures of the classes $\infty 2$, ∞m, and ∞/mm, we have

$$\mathbf{A} = A_1\mathbf{e}_i\mathbf{e}_i + A_2\mathbf{e}_3\mathbf{e}_3. \tag{8}$$

For trigonal crystals of the classes 3 and $\bar{3}$; tetragonal crystals of the classes 4, $\bar{4}$, and $4/m$; hexagonal crystals of the classes 6, $\bar{6}$, and $6/m$; and textures of the classes ∞ and ∞/m, we have

$$\mathbf{A} = A_1\mathbf{e}_i\mathbf{e}_i + A_2\mathbf{e}_3\mathbf{e}_3 + A_3(\mathbf{e}_1\mathbf{e}_2 - \mathbf{e}_2\mathbf{e}_1). \tag{9}$$

For all the orthorhombic crystals of the classes 222, mm, and mmm, we have

$$\mathbf{A} = A_1\mathbf{e}_1\mathbf{e}_1 + A_2\mathbf{e}_2\mathbf{e}_2 + A_3\mathbf{e}_3\mathbf{e}_3. \tag{10}$$

For monoclinic crystals of the classes 2, m, and $2/m$ ($2 \parallel X_3$, $m \perp X_3$), we have

$$\begin{aligned}\mathbf{A} &= A_1\mathbf{e}_1\mathbf{e}_1 + A_2\mathbf{e}_2\mathbf{e}_2 + A_3\mathbf{e}_3\mathbf{e}_3 \\ &+ A_4(\mathbf{e}_1\mathbf{e}_2 + \mathbf{e}_2\mathbf{e}_1) + A_5(\mathbf{e}_1\mathbf{e}_2 - \mathbf{e}_2\mathbf{e}_1).\end{aligned} \tag{11}$$

For monoclinic crystals of the classes 2, m, and $2/m$ ($2 \parallel X_2$, $m \perp X_2$), we have

$$\begin{aligned}\mathbf{A} &= A_1\mathbf{e}_1\mathbf{e}_1 + A_2\mathbf{e}_2\mathbf{e}_2 + A_3\mathbf{e}_3\mathbf{e}_3 \\ &+ A_4(\mathbf{e}_1\mathbf{e}_3 + \mathbf{e}_3\mathbf{e}_1) + A_5(\mathbf{e}_1\mathbf{e}_3 - \mathbf{e}_3\mathbf{e}_1).\end{aligned} \tag{12}$$

For triclinic crystals of the classes 1 and $\bar{1}$, we have

$$\begin{aligned}\mathbf{A} &= A_1\mathbf{e}_1\mathbf{e}_1 + A_2\mathbf{e}_2\mathbf{e}_2 + A_3\mathbf{e}_3\mathbf{e}_3 \\ &+ A_4(\mathbf{e}_1\mathbf{e}_2 + \mathbf{e}_2\mathbf{e}_1) + A_5(\mathbf{e}_1\mathbf{e}_2 - \mathbf{e}_2\mathbf{e}_1) \\ &+ A_6(\mathbf{e}_1\mathbf{e}_3 + \mathbf{e}_3\mathbf{e}_1) + A_7(\mathbf{e}_1\mathbf{e}_3 - \mathbf{e}_3\mathbf{e}_1) \\ &+ A_8(\mathbf{e}_2\mathbf{e}_3 + \mathbf{e}_3\mathbf{e}_2) + A_9(\mathbf{e}_2\mathbf{e}_3 - \mathbf{e}_3\mathbf{e}_2).\end{aligned} \tag{13}$$

According to (6) and (7), for isotropic media $\infty\infty\infty m$, gyrotropic media $\infty\infty\infty$, and cubic crystals of the classes 23, $m3$, 432, $m3m$, and $\bar{4}3m$, the induced magnetization has the form

$$\begin{aligned}\mathbf{M}(0) &= iA((E_2^*E_3 - E_2E_3^*)\mathbf{e}_1 \\ &+ (E_3^*E_1 - E_3E_1^*)\mathbf{e}_2 + (E_1^*E_2 - E_1E_2^*)\mathbf{e}_3),\end{aligned} \tag{14}$$

where E_i is the ith component of the electric field of the electromagnetic wave in the crystal physical basis.

In the general case, the phase anisotropy associated with the birefringence of the crystal should also be taken into account. In order to determine the electric-field components, it is necessary to solve a standard problem of the propagation of light in an anisotropic medium [7].

Since the phase shift of the field components in Eq. (14) is constant during light propagation, the magnetization $\mathbf{M}(0)$ can be written as

$$\mathbf{M}(0) = iA[\mathbf{E} \times \mathbf{E}^*]. \tag{15}$$

One can readily see that the induced magnetization is aligned along the wave vector, with the effect having the nonzero value only at a nonlinear polarization of the incident wave. In other words, we obtained a result similar to the result for isotropic media.

INVERSE FARADAY EFFECT IN UNIAXIAL CRYSTALS

Consider normal light incidence for uniaxial crystals.

For trigonal crystals of the classes 32, $3m$, and $\bar{3}m$; tetragonal crystals of the classes 422, $4mm$, $\bar{4}2m$, and $4/mmm$; hexagonal crystals of the classes 622, $6mm$, $\bar{6}m2$; and $6/mmm$, and textures of the classes $\infty 2$, ∞m, and ∞/mm, the magnetization is written as

$$\mathbf{M}(0) = iA_1[\mathbf{E} \times \mathbf{E}^*] + iA_2(E_1E_2^* - E_1^*E_2)\mathbf{e}_3. \tag{16}$$

Assume the wave vector is directed along the optic axis. Then (16) takes the form

$$\mathbf{M}(0) = iB[\mathbf{E} \times \mathbf{E}^*]\mathbf{e}_3, \tag{17}$$

where $B = A_1 + A_2$.

As in the previous case, the induced magnetization is parallel to the wave vector and necessarily has a circular component of the incident-wave polarization.

Assume now that the light propagates normally to the optic axis. Then, the induced magnetization has the form

$$\mathbf{M}(0) = A_1E_oE_e\sin((\mathbf{k}_o - \mathbf{k}_e)\mathbf{r} + \varphi)\mathbf{s}, \tag{18}$$

where $\mathbf{k}_o$ and $\mathbf{k}_e$ are the wave vectors of the ordinary and extraordinary waves, respectively, $\mathbf{s}$ is the unit vector parallel to the wave vector of the incident wave,

E_o and E_e are the components of the ordinary and extraordinary waves in the incident field, and φ is the phase shift between these components at the interface.

It is seen from Eq. (18) that the magnetization $\mathbf{M}(0)$ is parallel to the wave vector. We should like to emphasize that, unlike isotropic media, in this case the inverse Faraday effect takes place also for the linear polarization of the incident wave because of two normal orthogonally polarized waves propagating with different velocities. Hence, the polarization of the wave propagating in a crystal periodically changes in space from circular to linear with the period $\lambda/\Delta n$, where λ is the wavelength in a free space and Δn is the difference in the refractive indices of the ordinary and extraordinary waves. The periodic variation in the wave polarization results in the spatial oscillations of magnetization, which is reflected in Eq. (18).

Now, consider a more general case where light propagates at an arbitrary angle to the optic axis. Here, the induced magnetization is not parallel to the wave vector, because the electric field vector of the extraordinary wave forms a certain angle with the wave vector.

For uniaxial crystals, the refractive indices and the unit vectors of the electric field of the ordinary and extraordinary waves can be represented as [7]

$$n_o = \sqrt{\varepsilon_1}, \quad n_e = \frac{\varepsilon_1\varepsilon_3}{(\varepsilon_1 + (\varepsilon_3 - \varepsilon_1)(\mathbf{sc})^2)^{1/2}}, \tag{19}$$

$$\begin{aligned} \mathbf{e}_o &= \frac{[\mathbf{s}\times\mathbf{c}]}{(1-(\mathbf{sc})^2)^{1/2}}, \\ \mathbf{e}_e &= \frac{1}{(1-((\mathbf{sc})/\varepsilon_1)^2)^{1/2}}\left(\frac{\mathbf{s}(\mathbf{sc})}{\varepsilon_1} - \mathbf{c}\right), \end{aligned} \tag{20}$$

where $\mathbf{s}$ and $\mathbf{c}$ are the unit vectors along the wave vector of the incident wave and the optic axis, respectively, and ε_1 and ε_3 are the eigenvalues of the permittivity tensor.

Substituting Eq. (20) into the general expression for magnetization, (16), we arrive at

$$\begin{aligned} \mathbf{M}(0) &= A_1[\mathbf{e}_o\times\mathbf{e}_e]\sin((\mathbf{k}_o-\mathbf{k}_e)\mathbf{r}+\varphi)E_oE_e \\ &+ A_2((\mathbf{e}_o\mathbf{e}_1)(\mathbf{e}_e\mathbf{e}_1)+(\mathbf{e}_e\mathbf{e}_1)(\mathbf{e}_o\mathbf{e}_2)) \\ &\times \sin((\mathbf{k}_o-\mathbf{k}_e)\mathbf{r}+\varphi)E_oE_e\mathbf{e}_3. \end{aligned} \tag{21}$$

The first term is similar to Eq. (18) for light propagation normal to the optic axis, but, because of the longitudinal component of the electric field of the extraordinary wave, the induced magnetization is not parallel to the wave vector. The second term accounts for magnetization along the optic axis of the crystal which oscillates in space.

Now, consider the next group of crystals. We can write the following expression for the magnetization of trigonal crystals of the classes 3 and $\bar{3}$, tetragonal crystals of the classes 4, $\bar{4}$, and 4/*m*, hexagonal crystals of the classes 6, $\bar{6}$, and 6/*m*, and textures of the classes ∞ and ∞/m:

$$\begin{aligned} \mathbf{M}(0) &= iA_1[\mathbf{E}\times\mathbf{E}^*] + iA_2(E_1E_2^* - E_1^*E_2)\mathbf{e}_3 \\ &+ A_3((E_3E_2^* - E_2E_3^*)\mathbf{e}_2 - (E_1E_3^* - E_3E_1^*)\mathbf{e}_1). \end{aligned} \tag{22}$$

Consider two particular cases where light propagates along the optic axis and normally to it.

In the first case, the result obtained is similar to (16), and induced magnetization is parallel to the wave vector.

The second case, where light propagates normally to the optic axis, is more interesting. Representing the electric field of the incident wave in the form

$$\mathbf{E} = E_o(1/\sqrt{2})[\mathbf{s}\times\mathbf{c}] + E_e(1/\sqrt{2})\exp(i\varphi)\mathbf{e}_3, \tag{23}$$

we arrive at

$$\begin{aligned} \mathbf{M}(0) &= A_1E_oE_e\sin((\mathbf{k}_o-\mathbf{k}_e)\mathbf{r}+\varphi)\mathbf{s} \\ &+ A_3E_oE_e[\mathbf{s}\times\mathbf{c}]\sin((\mathbf{k}_o-\mathbf{k}_e)\mathbf{r}+\varphi). \end{aligned} \tag{24}$$

It can be seen (24) that induced magnetization is not parallel to the wave vector. The first term contributes to the longitudinal component of magnetization, while the second term, to the transverse component. Comparing Eqs. (24) and (9), we see that longitudinal magnetization is described by the symmetric part of the tensor A_{lk}, whereas transverse magnetization, by the antisymmetric one.

At an arbitrary angle between the wave vector and the optic axis, we use Eq. (21) to obtain

$$\begin{aligned} \mathbf{M}(0) &= A_1[\mathbf{e}_o\times\mathbf{e}_e]\sin((\mathbf{k}_o-\mathbf{k}_e)\mathbf{r}+\varphi)E_oE_e \\ &+ A_2((\mathbf{e}_o\mathbf{e}_1)(\mathbf{e}_e\mathbf{e}_2)+(\mathbf{e}_e\mathbf{e}_1)(\mathbf{e}_o\mathbf{e}_2)) \\ &\times \sin((\mathbf{k}_o-\mathbf{k}_e)\mathbf{r}+\varphi)E_oE_e\mathbf{e}_3 \\ &+ A_3((\mathbf{e}_o\mathbf{e}_3)(\mathbf{e}_e\mathbf{e}_2)+(\mathbf{e}_e\mathbf{e}_3)(\mathbf{e}_o\mathbf{e}_2)) \\ &\times \sin((\mathbf{k}_o-\mathbf{k}_e)\mathbf{r}+\varphi)E_oE_e\mathbf{e}_2 \\ &+ A_3((\mathbf{e}_o\mathbf{e}_3)(\mathbf{e}_e\mathbf{e}_1)+(\mathbf{e}_e\mathbf{e}_3)(\mathbf{e}_o\mathbf{e}_1)) \\ &\times \sin((\mathbf{k}_o-\mathbf{k}_e)\mathbf{r}+\varphi)E_oE_e\mathbf{e}_1. \end{aligned} \tag{25}$$

INVERSE FARADAY EFFECT IN BIAXIAL CRYSTALS

For all the orthorhombic crystals of the classes 222, *m*, and *mmm*, we have

$$\begin{aligned} \mathbf{M}(0) &= A_1(E_3E_2^* - E_2E_3^*)\mathbf{e}_1 \\ &+ A_2(E_1E_3^* - E_3E_1^*)\mathbf{e}_2 + A_3(E_2E_1^* - E_1E_2^*)\mathbf{e}_3. \end{aligned} \tag{26}$$

Generally, the magnetization direction is not parallel to the direction of a wave propagation. In this case,

spatial oscillations of magnetization with the period dependent on the direction of light propagation are observed. The only exception is the case of the configurations in which the wave vector is parallel to one of the optic axes.

As is well known, the optic axes in orthorhombic crystals lie in the *xz*-plane symmetrically with respect to the *z*-axis and form an angle β with it. This angle is defined by the equation

$$\tan\beta = \pm\sqrt{\frac{1/\varepsilon_x - 1/\varepsilon_y}{1/\varepsilon_y - 1/\varepsilon_z}}, \quad (27)$$

where $\varepsilon_x < \varepsilon_y < \varepsilon_z$ are the principal values of the permittivity tensor. If the wave vector is parallel to one of the optic axes, the electric-field components are related by the following expressions:

$$E_x\sin\beta + E_z\cos\beta = 0,\ E_x^2(1 + \tan^2\beta) + E_y^2 = E^2. \quad (28)$$

Substituting Eq. (28) into Eq. (26), we obtain

$$M_c(0) = E_x\sqrt{E^2 - E_x^2/\cos^2\beta}((A_1 + A_3)\sin\beta), \quad (29)$$

$$M_\perp(0) = E_x\sqrt{E^2 - E_x^2/\cos^2\beta}(A_1\tan^2\beta - A_3)\cos\beta, \quad (30)$$

where M_c is the magnetization induced along the optic axis, and $M_\perp$ is the magnetization induced normally to this axis.

An interesting feature of the inverse Faraday effect is observed if the electric field has all the three components. Then, the induced magnetization is not parallel to the wave vector because of the crystal anisotropy, despite the absent spatial oscillations. In this case, the incident wave should be circularly polarized.

For the monoclinic crystals of classes 2, *m*, and 2/*m* ($2 \parallel X_3$, $m \perp X_3$), we have

$$\begin{aligned}\mathbf{M}(0) &= A_1(E_2E_3^* - E_2^*E_3)\mathbf{e}_1 \\ &+ A_2(E_3E_1^* - E_3^*E_1)\mathbf{e}_2 + A_3(E_1E_2^* - E_1^*E_2)\mathbf{e}_3 \\ &+ A_4((E_3E_2^* - E_2E_3^*)\mathbf{e}_2 + (E_1E_3^* - E_3E_1^*)\mathbf{e}_1) \\ &+ A_5((E_3E_2^* - E_2E_3^*)\mathbf{e}_2 - (E_1E_3^* - E_3E_1^*)\mathbf{e}_1).\end{aligned} \quad (31)$$

If light propagates along the X_3-axis, the induced magnetization is also parallel to this axis. In all the other cases, the wave vector and magnetization are not parallel. As in the case of orthorhombic crystals, a circularly polarized wave propagating along one of the optic axes induces magnetization that is constant in space, but not parallel to the wave vector.

For triclinic crystals of the classes 1 and $\bar{1}$, we have

$$\begin{aligned}\mathbf{M}(0) &= A_1(E_2E_3^* - E_2^*E_3)\mathbf{e}_1 \\ &+ A_2(E_3E_1^* - E_3^*E_1)\mathbf{e}_2 + A_3(E_1E_2^* - E_1^*E_2)\mathbf{e}_3 \\ &+ A_4((E_3E_2^* - E_2E_3^*)\mathbf{e}_2 + (E_1E_3^* - E_3E_1^*)\mathbf{e}_1) \\ &+ A_5((E_3E_2^* - E_2E_3^*)\mathbf{e}_2 - (E_1E_3^* - E_3E_1^*)\mathbf{e}_1) \\ &+ A_6((E_3E_2^* - E_2E_3^*)\mathbf{e}_3 + (E_2E_1^* - E_1E_2^*)\mathbf{e}_1) \\ &+ A_7((E_3E_2^* - E_2E_3^*)\mathbf{e}_3 - (E_2E_1^* - E_1E_2^*)\mathbf{e}_1) \\ &+ A_8((E_1E_3^* - E_3E_1^*)\mathbf{e}_3 + (E_2E_1^* - E_1E_2^*)\mathbf{e}_2) \\ &+ A_9((E_1E_3^* - E_3E_1^*)\mathbf{e}_3 - (E_2E_1^* - E_1E_2^*)\mathbf{e}_2).\end{aligned} \quad (32)$$

The anisotropy is most pronounced in triclinic crystals, because these crystals have no axes or planes of the crystallographic symmetry. In these crystals, the induced magnetization and the wave vector, as follows from Eq. (32), are not parallel, regardless of the configuration. As in the two previous cases, the magnetization is constant in space if light propagates along one of the optic axes. In all the other cases, spatial oscillations of the induced magnetization with a period dependent on the direction of light propagation are observed.

CONCLUSIONS

Thus, we considered the specific features of the inverse Faraday effect in anisotropic crystalline media. Because of birefringence, the inverse Faraday effect also takes place if the incident light is linearly polarized, but then the magnetization oscillates in space. In this case, a one-dimensional magnetic lattice is formed. It is also worth noting that the inverse Faraday effect in biaxial crystals has a specific feature. If light propagates along one of the optic axes, the induced spatially constant magnetization is not parallel to the wave vector of the incident wave. Using additional optical beams propagating along other directions, one can create two- and three-dimensional periodic magnetic structures. These structures can be used for the creation of photon crystals, which presently attract much attention.

Finally, let us consider the numerical value of the above effects. Magnetization in isotropic media has the form [8]

$$M = V\lambda I\xi/2\pi^2 cn, \quad (33)$$

where V is the Verdet constant, λ is the light wavelength, I is the intensity of the incident wave, ξ is the degree of the wave ellipticity, c is the light velocity in vacuum, and n is the refractive index of the medium.

The Verdet constant for a ZnSe crystal at the wavelength 600 nm is about 300 rad T^{-1} m^{-1} [9]. Modern femtosecond lasers can emit nondestructive pulses with a power of up to several TW. According to Eq. (33), the induced magnetization is of the order of 0.5×10^4 A/m, which corresponds to the magnetic field with the induction of 0.05 T. The period of the spatial oscillations of

the magnetization is $\lambda/\Delta n$, i.e., 10–100λ. A resolution of several microns in the measurements of these fields has long been available [10]. Thus, one can hope that the inverse Faraday effect in crystals will soon be experimentally detected and used in practice.

REFERENCES

1. J. P. van der Ziel, P. S. Pershan, and L. D. Malmstrom, Phys. Rev. Lett. **15**, 190 (1965).
2. L. P. Pitaevskiĭ, Zh. Éksp. Teor. Fiz. **39** (5), 1450 (1960) [Sov. Phys. JETP **12**, 1008 (1960)].
3. V. B. Braginsky and F. Ya. Khalili, Rev. Mod. Phys. **68**, 1 (1996).
4. P. S. Pershan, Phys. Rev. **130**, 919 (1963).
5. A. Shigeyuki, Int. J. Quantum Chem. **75**, 33 (1999).
6. V. I. Fedorov, *Theory of Gyrotropy* (Nauka i Tekhnika, Minsk, 1976).
7. Yu. I. Sirotin and M. P. Shaskol'skaya, *Fundamentals of Crystal Physics* (Nauka, Moscow, 1975; Mir, Moscow, 1982).
8. N. G. Kalugin and G. Wagniere, J. Opt. B **3**, 1 (2001).
9. J. A. Wunderlich and L. G. Deshazer, Appl. Opt. **16**, 1584 (1977).
10. S. Jeffers, M. A. Novikov, and G. Hathaway, in *Proceedings of the Symposium "The Present Status of the Quantum Theory of Light," Toronto, 1995* (Kluwer Academic Publishers, Dordrecht, 1996), p. 131.

Translated by A. Zolot'ko

Crystallography Reports, Vol. 47, No. 5, 2002, pp. 829–831. Translated from Kristallografiya, Vol. 47, No. 5, 2002, pp. 893–895.

PHYSICAL PROPERTIES OF CRYSTALS

Optical Properties of Oxides and Fluorides with a Rutile-type Structure in Terms of the Point-Dipole Model

D. Yu. Popov

Institute of Chemistry, Far East Division, Russian Academy of Sciences, pr. Stoletiya Vladivostoka 159, Vladivostok, 690022 Russia

e-mail: popov@ich.dvo.ru

Received September 25, 2001; in final form, March 13, 2002

Abstract—The polarizabilities of ions in the MgF_2, ZnF_2, TiO_2, and SnO_2 compounds have been calculated based on the point-dipole model. It is shown that cation polarizabilities produce a stronger effect on the birefringence of AX_2(X = F, O) compounds than anion polarizabilities. *© 2002 MAIK "Nauka/Interperiodica".*

The point-dipole model [1–7] allows one to calculate theoretically the parameters of the optical indicatrix of a crystal knowing its structure data and polarizabilities of structural units. The latter can be optimized so as to reduce to a minimum the differences between the calculated and experimentally measured optical properties. This study is devoted to modeling optical properties in the point-dipole approximation and refining the polarizabilities of ions in AX_2(X = F, O) compounds with a rutile-type structure.

In terms of the point-dipole model, atoms in a crystal are considered as dipoles, whose dimensions are negligibly small in comparison with the interatomic distances. In this approximation, the local electric field induced by a light wave in the position k of the unit cell has the form [1]

$$\mathbf{F}(k) = \mathbf{E} + \sum_{k'} \mathbf{L}(kk')\mathbf{P}(k')/\varepsilon_0 v, \qquad (1)$$

where $\mathbf{E}$ is the macroscopic field, $\mathbf{P}(k')$ is the dipole moment in the position k', v is the unit cell volume, and $\mathbf{L}(kk')$ is the Lorenta-factor tensor, which depends on the geometry of the structure.

The dipole moment in the k' position is related to the local electric field $\mathbf{F}(k')$ in the same position by the equation

$$\mathbf{P}(k') = \varepsilon_0 \alpha(k')\mathbf{F}(k'), \qquad (2)$$

where $\alpha(k')$ is the polarizability. Substituting Eq. (2) into Eq. (1), we obtain the system of linear equations with respect to the components of the $\mathbf{F}$ vector. Solving this system and summing up the components of the vector $\mathbf{F}$ multiplied by the corresponding polarizabilities over all the k positions, one obtains the tensor relating the total dipole moment of the unit cell to the vector of the macroscopic field. Dividing the components of this tensor into the unit-cell volume, one obtains the dielectric susceptibility tensor and can pass to the dielectric constant tensor.

To perform such a calculation, I wrote a program entitled AnRef. The input data are the parameters of an elementary parallelepiped, the fractional coordinates of all the atoms in the unit cell, and their polarizabilities. The Lorenta-factor tensor is calculated by the method stated in [1]. If the calculated dielectric-constant tensor is not diagonal, the program reduces it to the principal axes; then, the principal refractive indices equal to square roots of the diagonal components are calculated.

For the crystals of intermediate systems, to which the AX_2 compounds are related, two of the diagonal components of the dielectric-constant tensor are equal to the squared refractive index *No* of an ordinary ray and one diagonal component is equal to the squared refractive index *Ne* of an extraordinary ray.

Using the AnRef program, we determined the polarizabilities of R-ions in the MgF_2, ZnF_2, TiO_2, and SnO_2 compounds (see table), with due regard for their structural data [8] and also the principal refractive indices for the D line (λ_D = 589 nm) [9]. All the AX_2 compounds with a rutile structure are isostructural and crystallize in the tetragonal sp. gr. $P4_2/mnm$ [8].

Numerous calculations were made using different polarizabilities of cations and anions until the attainment of the good agreement between the calculated and experimentally measured *No* and *Ne* values. The uniqueness of such a choice was provided by the fact that the number of calculated polarizabilities coincided with the number of independent components in the dielectric-constant tensor. It is important that each ion or cation, for which the polarizability was determined, occupies only one position in the crystallographically independent region of the unit cell.

The polarizabilities of ions depend on many factors, e.g., on the bond polarity. As a consequence, they are essentially different in different compounds but remain

1063-7745/02/4705-0829$22.00

Optimized ion polarizabilities

Compound	N_o, N_e	Ion	R_0, cm^3	R*, cm^3	$(V_0–V)$, Å^3	$(R_0–R)/(V_0–V)$
MgF_2	1.378	Mg^{2+}	0.5	1.22	2.858	–0.252
	1.390	F^-	2.0	1.64	–1.430	–0.252
ZnF_2	1.510	Zn^{2+}	1.7	1.69	3.011	0
	1.526	F^-	2.0	2.22	–1.506	0.1
TiO_2	2.6211	Ti^{4+}	1.7	7.443	2.800	–2.1
	2.9085	O^{2-}	3.8	1.432	–1.400	–1.7
SnO_2	2.0006	Sn^{4+}	3.6	5.823	3.072	–0.7
	2.0972	O^{2-}	3.8	1.887	–1.536	–1.2

* $R=N_A\alpha/3\varepsilon_0$ where N_A is the Avogadro number and α is the polarizability in Eq. (2).

close to the ionic refraction R_0 of the corresponding chemical elements [10].

The optimized cation polarizabilities for all the compounds except for ZnF_2 (where the selected polarizabilities are close to the refraction values) are much higher, and the anion polarizabilities are less than the corresponding refraction values. It should be indicated that the volume V of the Voronoĭ–Dirichlet polyhedron of the cation [11] is smaller, whereas that of the anion is larger than the average volume per atom in the crystal. Nevertheless, the cation and the anion in each compound have comparable $(R_0 – R)/(V_0 – V)$ ratios.

The anions in the crystals of the compounds with a rutile-type structure form a slightly distorted close packing. The close packed layers of anions in AX_2 are corrugated in such a way that the fourfold symmetry axes are parallel to the layers and the optic axis is parallel to these symmetry axes. Since the optic axis is parallel to the layers of the anion packing, which has pseudohexagonal symmetry, the variation in the principal birefringence in various AX_2 compounds should be caused mainly by the different polarizabilities of cations and not of anions. The problem of the most pronounced influence of cation polarizability on birefringence is of special importance because the polarizability of a cation can be evaluated based on the value of birefringence ignoring the principal refractive indices. The method is very advantageous for estimating polarizability because it is relatively simple in comparison with measurements of the principled refraction indices.

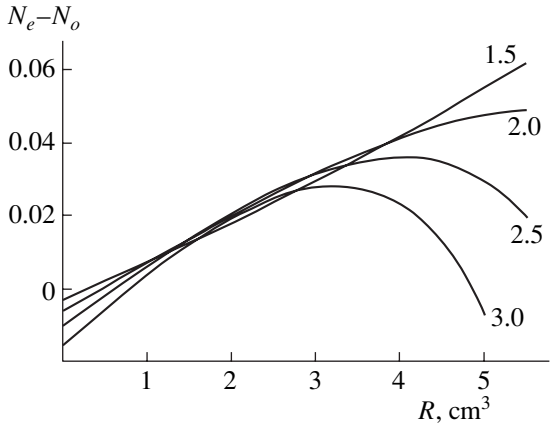

Birefringence of AX_2 crystals as a function of cation polarizabilities at various anion polarizabilities (indicated at the corresponding curves).

The principal refractive indices for various ion polarizabilities for CoF_2, NiF_2, ZnF_2, MnF_2, MgF_2, FeF_2, SnO_2, TiO_2, GeO_2, and MnO_2 compounds were calculated with the aid of the AnRef program and structural data [8]. For each compound, the plots of birefringence as a function of a cation polarizability were constructed at different anion polarizabilities. Since these compounds are isostructural, the plots thus constructed reflect the influence of cation polarizability on birefringence.

The $N_e – N_o$ dependences as functions of cation polarizability calculated for the MnF_2 structure are shown in the figure. Each curve corresponds to a certain value of anion polarizability (1.5–3.0). Within the range of cation polarizability from 1.0 to 3.0, the curves lie close to one another.

The plots obtained for other AX_2 structures are similar to the one considered above. To determine the slope of the curves, we calculated the change in birefringence per unit polarizability of the cation $\Delta(N_e – N_o)/\Delta R$ for the curve corresponding to anion polarizability equal to 1.5. In the range of cation polarizability from 1.0 to 1.5, $\Delta(N_e – N_o)/\Delta R$ varies from 0.010 to 0.015 for fluorides AX_2 and from 0.017 to 0.030 for oxides. The close curve positions at the cation polarizability 1.5 is characterized by the difference in birefringence $\Delta(N_e – N_o)$, which correspond to anion polarizabilities 2.5 and 1.5 for fluorides and 3.5 and 1.5 for oxides. The value of $\Delta(N_e – N_o)$ is considerably lower than the value of $\Delta(N_e – N_o)/\Delta R$ and is equal to 0.0009–0.0024 for AX_2 fluorides, and 0.0045–0.0118 for oxides. The point of intersection of the curve for anion polarizability equal to 1.5 with the vertical coordinate axis is characterized

by birefringence ΔN_0 when the cation polarizability is equal to zero. The value of ΔN_0 varies from –0.0042 to –0.0032 for AX_2 fluorides and from –0.0056 to –0.0035 for oxides.

Two compounds, FeF_2 and MnO_2, are of special interest. They have a much lower value of $\Delta(N_e - N_o)/\Delta R$ and a much higher value of $\Delta(N_e - N_o)/\Delta R$ than all the other compounds. The value of $\Delta(N_e - N_o)/\Delta R$ is equal to 0.002 for FeF_2 and to 0.012 for MnO_2; the value of $\Delta(N_e - N_o)$ is equal to 0.009 for FeF_2 and to 0.035 for MnO_2.

REFERENCES

1. P. G. Cummins, D. A. Dunmur, R. W. Munn, and R. J. Newham, Acta Crystallogr., Sect. A: Cryst. Phys., Diffr., Theor. Gen. Crystallogr. **32**, 847 (1976).
2. D. Pohl, J. C. Eck, and K. H. Klaska, Acta Crystallogr., Sect. A: Cryst. Phys., Diffr., Theor. Gen. Crystallogr. **34**, 1027 (1978).
3. D. Pohl and R. Rath, Acta Crystallogr., Sect. A: Cryst. Phys., Diffr., Theor. Gen. Crystallogr. **35**, 694 (1979).
4. G. A. Lager, Th. Armbruster, and D. Pohl, Phys. Chem. Miner. **14**, 177 (1987).
5. R. N. Abbott, Am. Mineral. **78**, 952 (1993).
6. R. N. Abbott, Can. Mineral. **32**, 909 (1994).
7. R. N. Abbott, Can. Mineral. **34**, 595 (1996).
8. R. W. G. Wyckoff, *Crystal Structures* (Interscience, New York, 1963, 2nd ed.), Vol. 1, p. 250.
9. A. N. Winchell and H. Winchell, *The Microscopical Characters of Artificial Inorganic Solid Substances: Optical Properties of Artificial Minerals* (Academic, New York, 1964; Mir, Moscow, 1967).
10. S. S. Batsanov, *Structural Chemistry: Facts and Dependences* (Mosk. Gos. Univ., Moscow, 2000).
11. A. F. Wells, *Structural Inorganic Chemistry* (Clarendon, Oxford, 1984; Mir, Moscow, 1987), Vol. 1.

Translated by A. Zalesskiĭ

Crystallography Reports, Vol. 47, No. 5, 2002, pp. 832–836. Translated from Kristallografiya, Vol. 47, No. 5, 2002, pp. 896–900.

PHYSICAL PROPERTIES OF CRYSTALS

Absorption and Circular-Dichroism Spectra of Iron-Doped Berlinite Crystals

V. I. Burkov*, A. V. Egorysheva*, Yu. F. Kargin, A. I. Motchanyĭ***, and P. P. Shvanskiĭ*****

** Moscow Institute of Physics and Technology, Institutskiĭ per. 9, Dolgoprudnyĭ, Moscow oblast, 141700 Russia*

e-mail: anna_egorysheva@rambler.ru

*** Kurnakov Institute of General and Inorganic Chemistry, Russian Academy of Sciences, Leninskiĭ pr. 31, Moscow, 117907 Russia*

**** All-Russia Research Institute of Synthesis of Mineral Materials, Institutskaya ul. 1, Aleksandrov, Vladimir oblast, 601600 Russia*

Received July 11, 2001; in final form, January 28, 2002

Abstract—Absorption and circular-dichroism spectra of iron-doped $AlPO_4$ crystals have been studied. For the first time, the experimental data on the electronic states of the $[FeO_4]^{5-}$ complex are obtained in the range from 190 to 350 nm with due regard for the interactions that cannot be described within the one-electron approximation. The bands observed in the absorption and circular-dichroism spectra are attributed to corresponding electronic transitions. The advantages of the use of crystal-field-induced circular dichroism in comparison with other spectroscopic methods in the analysis of the electronic states of impurity ions in gyrotropic crystalline matrices are considered on the $[FeO_4]^{5-}$ complex. © *2002 MAIK "Nauka/Interperiodica".*

INTRODUCTION

Berlinite ($AlPO_4$) crystals are a promising material for acoustic devices [1–3], which has stimulated the study of its crystallization conditions, the growth of large perfect berlinite crystals [4–9], and their characterization [10–15]. It is well known that impurities essentially change the physical properties of crystals, which is also true for berlinite crystals. In this study, we detected impurity iron ions in a crystal by the method of circular dichroism along with the conventional method of adsorption spectroscopy. For optically active crystals, this method provides additional information on the forbidden electronic transitions of the *d*- and *f*-elements [16].

Berlinite crystals are structurally similar to quartz (sp. gr. $P3_121$ (D_3^4) or $P3_221$ (D_3^6), a = 4.93, c = 10.94 Å, Z = 3) [17]. The Al and P atoms alternately occupy equivalent positions with symmetry 2 in the centers of slightly distorted oxygen tetrahedra around the 3_1 or 3_2 axes forming the chains in the crystal structure. If the iron atoms isomorphously replace aluminum atoms, then the electronic transitions of a Fe^{3+} ion in a chiral crystalline field can be active in the formation of circular-dichroism spectra.

Below, we describe the study of the absorption and circular-dichroism spectra of undoped and iron-doped $AlPO_4$ crystals. The choice of an iron activator is explained by the specific features of hydrothermal synthesis, which make iron the most probable impurity that can be isomorphously incorporated into the berlinite crystal lattice.

Undoped berlinite crystals were grown from a solution of orthophosphoric or sulfuric acids under different conditions. The growth conditions are described in detail elsewhere [7, 8]. Iron-doped berlinite crystals were grown from a sulfuric-acid solution. The iron concentration in crystals determined by flame photometry varied from 0.1 to 0.001 wt %. The measurements were made on plane-parallel plates cut out from single crystals with different iron content normal to the optic axis.

The absorption spectra were measured on a Specord M-40 spectrophotometer; the circular-dichroism spectra were measured on a Mark-3 (Jobin–Yvon) dichrometer in the spectral range from 190 to 800 nm.

ABSORPTION AND CIRCULAR-DICHROISM SPECTRA

The absorption and circular-dichroism spectra of iron-doped $AlPO_4$ crystals recorded at room temperature showed the bands caused by a presence of Fe^{3+} iron ions (Figs. 1, 2). The experimental data obtained are listed in the table. Data [18] on the polarized ($\pi(E \parallel c)$ and $\sigma(E \perp c)$) orthoaxial spectra of iron-doped $AlPO_4$, $GaPO_4$, $AlAsO_4$, and SiO_2 crystals are also indicated in this table. In general, our absorption spectra are consistent with the data in [18]. However, the number of the registered bands in our axial spectra exceeds their number in [18]. The last column of the table indicates the

1063-7745/02/4705-0832$22.00 © 2002 MAIK "Nauka/Interperiodica"

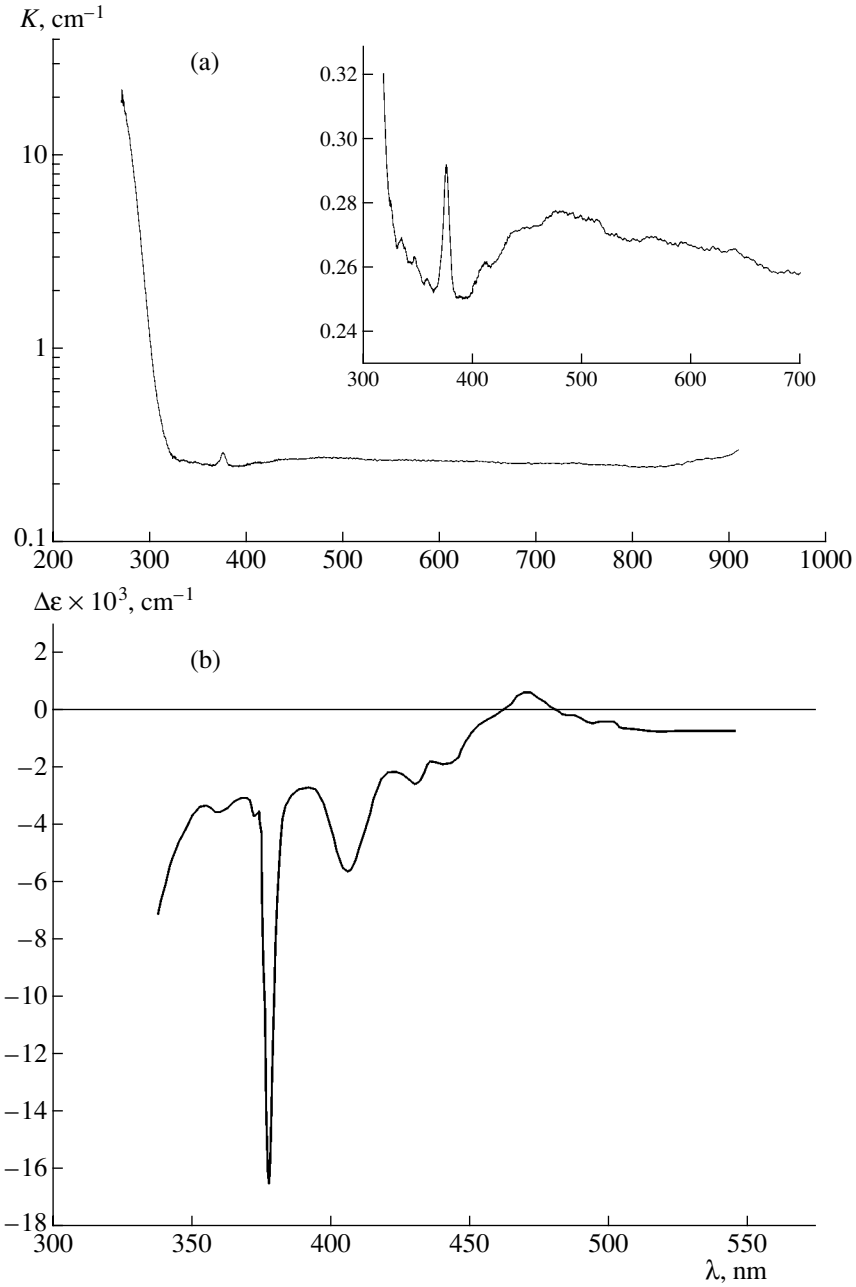

Fig. 1. (a) Absorption and (b) circular-dichroism spectra of iron-doped $AlPO_4$ crystals in the range of *d–d* transitions.

possible identification of the bands observed with the corresponding electronic transitions.

With due regard for the close ionic radii of Al^{3+} and Fe^{3+} ions [19] and the isostructurality of $AlPO_4$ and $FePO_4$ crystals [20], one could expect that iron atoms replace aluminum atoms in the oxygen octahedra in the berlinite lattice. Taking into account all the above data, we shall interpret the obtained spectra based on the data on electronic states of the tetrahedral $[FeO_4]^{5-}$ complex. The energies of the Fe^{3+} electronic states ($3d^5$-configuration) in a tetrahedral crystalline field are calculated in [21]. It is well known that the ground state of the Fe^{3+} ion in a tetrahedral crystalline field is the $^6A_1$-state. All the excited states are either quartets or doublets. Thus, the transitions in the crystalline field are parity- and spin-forbidden. The simultaneous influence of different mechanisms of acquiring the intensity, such as spin-orbital interaction, the distortion of tetrahedra, etc., results in a low resolution of the transitions to the quartet states. It is seen from the spectra shown in Fig. 1a that, as in [18], the absorption-band intensities in the range from 300 to 800 nm are weak. First, as was

Absorption and circular-dichroism bands due to electronic transitions of Fe^{3+} ions in tetrahedral crystalline field and bands due to transitions with charge transfer in iron-doped $AlPO_4$ crystals

Positions of the band maxima						Terms and transitions
absorption spectra		circular-dichroism spectra		absorption spectra [17]		
λ, nm	ν, cm^{-1}	λ, nm	ν, cm^{-1}	λ, nm	ν, cm^{-1}	
				543	18400 ($^4T_1$)	
		505	19420			$^4T_1(G)$
		495	20202			$^2T_2(G)$
		485	20685			
473	21141	470	21276	474	21100 ($^4T_2$)	$^4T_2(G)$
445	22472	445	22472			
430	23256	430	23256	432	23100 ($^4A_1$,^4E)	$^4T_1$, $^4E(G)$
405	24690	406	24630	406	24500 ($^4T_2$)	$^4T_2$ (D)
377	26525	376	26580	376	26580 (^4E)	^4E (D)
360	27777	362	27425			$^4T_2$ (P)
337	29673	335	29851			$^2A_2$, $^2T_1(F)$
		275	36363			$^6A_1 \longrightarrow {}^4T_1$
246	40650	252	39683			$^6A_1 \longrightarrow {}^6T_1$ ($t \longrightarrow 2e$)
218	45870	225	44444	218	45900 ($t \longrightarrow 2e$)	$^6A_1 \longrightarrow {}^6T_2$

already noted, all the electronic transitions of Fe^{3+} ions in the tetrahedral crystalline field (*d–d* transitions) are forbidden, and, second, the iron concentration in our crystals is very low ($C_{Fe} < 0.1$ wt %). In the circular-dichroism spectra obtained (Fig. 1b), these forbidden transitions are seen to be much better. All circular-dichroism bands of dextrotating light in the range of 300–800 nm have a negative sign, except for the low-intensity band at 470 nm ($\nu \approx 21276$ cm^{-1}).

As is shown in a number of studies (e.g., [22]), the transitions of the $[FeO_4]^{5-}$ complex occurring with charge transfer are in the range $\lambda < 300$ nm (or $\nu > 33000$ cm^{-1}). Indeed, in the UV-range (Fig. 2a), the intensity of the absorption band is two orders of magnitude higher than the intensity of the bands considered above, and, therefore, it can be attributed to transitions proceeding with charge transfer (probably, $t_1 \longrightarrow 2e$ [22]). Unlike the data in [18], a weak inflection is observed at the long-wave wing of the absorption band, which indicates that this band consists of several overlapping bands. The decomposition of the contour of this band into Gaussian components allowed us to select at least three bands, two of which have maxima at 218 and 246 nm. The third band has a maximum at $\lambda < 190$ nm. The circular-dichroism spectra clearly show (Fig. 2b) that, in the absorption range, three bands are formed, at 225, 252, and 275 nm, one of which has the maximum at $\lambda = 252$ nm and a sign opposite to the sign of the other bands.

The formation of two bands in the range of transition with charge transfer at 218 and 246 nm can be explained as follows. Consider a transition with charge transfer $t \longrightarrow 2e$. The state with the lowest ^5E energy of the excited $(e)^3(t_2)^3$ configuration provides the formation of two sextet and two quartet states $^6T_1$, $^6T_2$, $^4T_1$, and $^4T_2$ because of the interaction with a hole at the ligand orbital. The transition $^6A_1 \longrightarrow {}^6T_2$ is allowed in the electrical dipole approximation and determines the band intensity in the absorption spectrum. The intensity of the transition $^6A_1 \longrightarrow {}^6T_1$ (allowed in the magnetic dipole approximation) should be essentially lower in the absorption spectra. However, the intensities of the transitions to $^6T_2$ and $^6T_1$ in the circular-dichroism spectrum can be comparable if the symmetry is reduced from T_d to T. Since Fe^{3+} ions are located at the points with the C_2 symmetry, all the degenerate states of these ions are split and also mixed, so that the symmetry of the states formed is either A or B. Within the framework of the C_2 symmetry, the transition from the ground state to any excited state would be allowed in terms of the symmetry in the electrical-dipole and magnetic-dipole approximation and, hence, it would be active in the circular-dichroism spectrum. Thus, the presence of two bands in the absorption spectrum and three bands in the circular-dichroism one is caused by splitting the tetrahedral states and mixing the split components within the C_2 symmetry. The presence of the *d–d* transition $^6A_1 \longrightarrow {}^4T_1$ in the circular-dichroism spectrum is, apparently, explained by the spin-orbital mechanism of the intensity transfer from the $^6A_1 \longrightarrow {}^4T_2$ transition. It should be noted that experimental data on the electronic

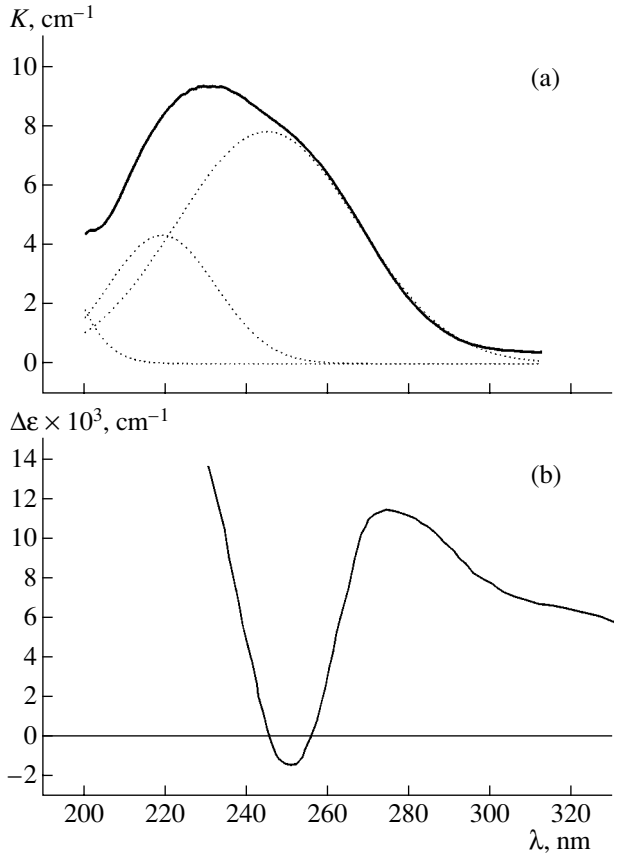

Fig. 2. (a) Absorption and (b) circular-dichroism spectra of iron-doped $AlPO_4$ crystals in the range of transitions with charge transfer. Dashed lines show the decomposition of the band contour into Gaussian components.

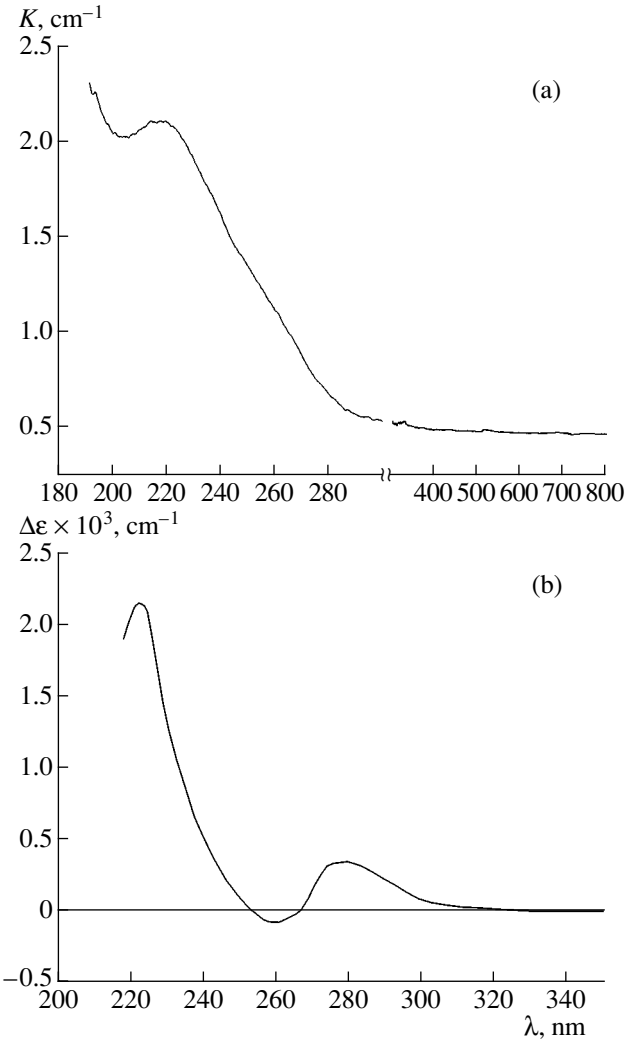

Fig. 3. (a) Absorption and (b) circular-dichroism spectra for undoped $AlPO_4$ crystals.

states of iron in the range from 190 to 350 nm are obtained for the first time.

As is shown experimentally, the absorption and circular-dichroism spectra of undoped berlinite crystals (Fig. 3) in the range 190–300 nm have bands similar to those observed in the spectra of iron-doped crystals, but they have a much lower intensity. It can be seen that the wavelengths of the maxima of these bands slightly differ from the wavelengths of corresponding maxima of analogous bands in the spectra of doped crystals. Since berlinite crystals are grown by hydrothermal synthesis from acid solutions in metal autoclaves under "severe" conditions, we cannot exclude the presence of other metals in crystals along with iron. Thus, the above changes in the positions of the band maxima can be explained by the presence in "pure" $AlPO_4$ crystals of small amounts of other metal ions and defects along with iron, which provide the formation of typical bands in the absorption and circular-dichroism spectra in this spectral range [23]. The presence of defects and a number of metals in undoped berlinite crystals was also observed in [24].

It should be emphasized that when studying different iron-doped crystals, we established that, despite the isostructurality of $AlPO_4$ and $FePO_4$ and close ionic radii of Al^{3+} and Fe^{3+}, iron-doped berlinite crystals are characterized by a nonuniform distribution of Fe^{3+} ions over the sample volume (which is apparently caused by the varying conditions of growth of single crystals). Moreover, according to local X-ray spectroscopy analysis (MS-46 Cameca), the crystals had some (mainly, iron) inclusions (≤1 μm in size).

CONCLUSION

It is shown that berlinite crystals can be a convenient gyrotropic matrix for studying induced circular dichroism in the range of the allowed electronic transitions of the 3*d*-elements. For the first time, data on the interactions that cannot be described within the one-electron approximation are obtained by the method of induced

circular dichroism for transitions with charge transfer in a $[FeO_4]^{5-}$ complex.

REFERENCES

1. Y. P. Chang and G. H. Barsch, IEEE Trans. Sonics Ultrason. **SU-23**, 127 (1976).
2. R. M. O'Connel and P. H. Carr, IEEE Trans. Sonics Ultrason. **SU-24**, 376 (1977).
3. D. G. Morency, W. Soluch, J. F. Vetelino, *et al.*, Appl. Phys. Lett. **33** (2), 117 (1978).
4. E. D. Kolb and R. A. Laudise, J. Cryst. Growth **43** (3), 313 (1978).
5. E. Philippot, A. Goiffon, and M. Maurin, J. Cryst. Growth **104** (3), 713 (1990).
6. V. I. Lyutin, A. I. Motchanyĭ, and P. P. Shvanskiĭ, Tr. Vseross. Nauchno-Issled. Inst. Sint. Miner. Syr'ya **14**, 22 (1997).
7. P. P. Chvansky, B. N. Kolodiev, S. V. Kolodieva, *et al.*, Ann. Chim. (Paris) **22** (8), 81 (1997).
8. A. I. Motchanyĭ and P. P. Shvanskiĭ, *Production of Berlinite Single Crystals. Synthesis of Minerals* (VNIISIMS, Aleksandrov, 2000), Vol. 1, p. 468.
9. A. I. Mottchanyi and P. P. Chvanski, in *Proceedings of the 3rd European Workshop on Piezoelectric Materials: Crystal Growth, Properties and Prospects, Montpellier, France, 2000.*
10. A. A. Shternberg, G. S. Mironova, and O. V. Zvereva, Kristallografiya **31** (6), 1206 (1986) [Sov. Phys. Crystallogr. **31**, 712 (1986)].
11. L. D. Kislovskiĭ, A. A. Shternberg, G. S. Mironova, *et al.*, Opt. Spektrosk. **63** (1), 114 (1987) [Opt. Spectrosc. **63**, 65 (1987)].
12. A. Yu. Klimova, A. A. Shternberg, G. S. Mironova, *et al.*, Kristallografiya **32** (3), 786 (1987) [Sov. Phys. Crystallogr. **32**, 463 (1987)].
13. L. N. Dem'yanets, O. V. Zvereva, Yu. M. Mininzon, *et al.*, Kristallografiya **37** (6), 1569 (1992) [Sov. Phys. Crystallogr. **37**, 850 (1992)].
14. B. N. Kolodiev, V. I. Lyutin, A. I. Motchanyĭ, and P. P. Shvanskiĭ, Neorg. Mater. **35** (7), 871 (1999).
15. M. L. Meilman, I. D. Ryabov, A. I. Mottchanyi, and P. P. Chvanski, in *Proceedings of the 3rd European Workshop on Piezoelectric Materials: Crystal Growth, Properties and Prospects, Montpellier, France, 2000.*
16. V. I. Burkov, Neorg. Mater. **30** (1), 12 (1994).
17. D. Schwarzenbach, Z. Kristallogr. **123** (3–4), 161 (1966).
18. G. Lehmann, Z. Phys. Chem. (Leipzig) **72**, 272 (1970).
19. R. D. Shannon and C. T. Prewitt, Acta Crystallogr., Sect. B: Struct. Crystallogr. Cryst. Chem. **25**, 925 (1969).
20. R. G. Grebenshchikov, in *Advances in Physics and Chemistry of Silicates* (Nauka, Leningrad, 1978), p. 162.
21. D. L. Wood and J. P. Remeika, J. Appl. Phys. **36** (5), 1249 (1965).
22. A. B. P. Lever, *Inorganic Electronic Spectroscopy* (Elsevier, Amsterdam, 1984, 2nd ed.).
23. L. G. Vanquickenborne and E. Verdonck, Inorg. Chem. **15** (2), 454 (1976).
24. L. E. Halliburton, L. A. Kappers, A. F. Armington, and J. Larkin, J. Appl. Phys. **51** (4), 2193 (1980).

Translated by T. Dmitrieva

Crystallography Reports, Vol. 47, No. 5, 2002, pp. 837–841. Translated from Kristallografiya, Vol. 47, No. 5, 2002, pp. 901–905.

PHYSICAL PROPERTIES OF CRYSTALS

A Technique for the Characterization of Crystal Homogeneity

O. V. Kachalov

Shubnikov Institute of Crystallography, Russian Academy of Sciences, Leninskiĭ pr. 59, Moscow, 117333 Russia

Received March 4, 2002

Abstract—A technique for the characterization of crystal homogeneity is proposed. It is based on the analysis of three-dimensional patterns corresponding to the intensity distributions of the Rayleigh component of scattered light $3DI_R(\mathbf{r})$. The potentialities of this technique are analyzed in comparison with those of the transmission tomography. Its efficiency is demonstrated by the study of a set of natural calcite samples. These samples were certified according to the conventional scheme used in geology. In this technique, the dynamic range of the inhomogeneity-parameter variation exceeds 10^4. The method for finding the simple growth shape based on the processing of $3DI_R(\mathbf{r})$ patterns is described. The proposed technique for the characterization of crystal homogeneity involves the quantitative description of the zonal structure of crystals including the contrast and the main period. *© 2002 MAIK "Nauka/Interperiodica".*

INTRODUCTION

The spectroscopy of scattered light is an efficient method of studying crystal homogeneity. Indeed, any distortion of the crystal structure results in a change in polarizability of a volume element of the crystal, which, in turn, contributes to the intensity of the unbiased component I_R of scattered light. The inelastic part, of the intensity, in particular, I_{MB} (the Mandelshtam–Brillouin component), is provided by the scattering of light by thermal excitations in the crystal. Their parameters Ω and $\mathbf{k}$ are determined from the conservation laws of the momentum and energy. The intensity I_{MB} is given by the relationship I_{MB} $(\sim n^8 p^2 \omega^4/\rho v^2)$ [1], where n is the refractive index, p are the photoelastic constants, ρ is the density, and v is the sound velocity. It is important that I_{MB} only slightly depends on the defect concentration in the crystal over a rather wide range of its variation, which allows one to use I_{MB} as an internal standard of the intensity I_R, which is taken to be a measure of crystal inhomogeneity, as was suggested in [2, 3]. Another, not less important, feature of the experiments on light scattering is the possibility of obtaining three-dimensional patterns of $I_R(\mathbf{r})$ distribution by limiting the dimensions of the scattering volume, which is especially important in studies of crystals possessing large-scale inhomogeneities comparable with the crystal size, such as its zones and sectors [4]. It is well known that the distributions Δn and Δk, the static variations in the real and imaginary parts of the dielectric constant ε, respectively, are determined by tomographic methods [5]. However, the tomographic techniques are insufficiently efficient for rather perfect crystals because of their low contrast. Figure 1 and Table 1 show the comparative characteristics of the transmission tomography and the method proposed in the present paper.

The main drawback of transmission tomography is its low contrast, because the receiver records all the radiation transmitted by the sample. The technique suggested here practically excludes this drawback because of the special geometry of the experiment and the spectral analysis of the transmitted light. In other words, we measure experimentally the quantity I_R, whose level is almost determined by the static perturbations Δn. The high contrast of this method, in turn, requires the use of a high-sensitive recording system, which seems to be the main drawback of this method.

RESULTS AND DISCUSSION

The three-dimensional (3D) patterns of the I_R distributions were recorded on a high-resolution spectrome-

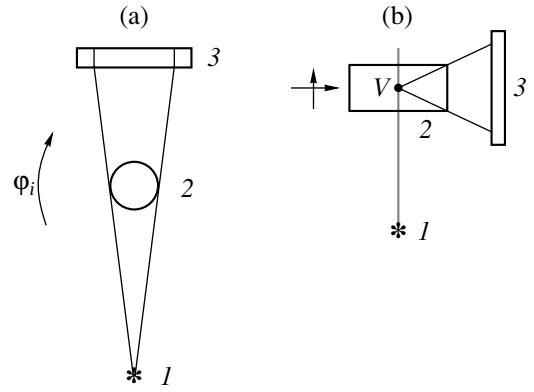

Fig. 1. Schematic diagram for tomography (a) in the transmitted and (b) scattered light: *1*, light source; *2*, sample; *3*, radiation receiver. (a) Scanning of the sample: rotation of the sample through fixed angles φ_i; (b) sample displacements along the Cartesian axes. The linear dimension of the scattering volume v is about 0.2 mm.

1063-7745/02/4705-0837$22.00 © 2002 MAIK "Nauka/Interperiodica"

Table 1. Comparison of tomography characteristics in the (a) transmitted and (b) scattered light

Experiment	a	b
	Set of data on the projections of the sample at the fixed rotation angles φ_i	Recording of the intensity of the Rayleigh component scattered from a limited volume v of the sample during scanning along the Cartesian coordinates
Processing of experimental data	Reconstruction of $F(\Delta\varepsilon)$ by solving the Radon problem	Obtaining the image of $F(\Delta n)$ in the direct experiment
Contrast	Low	High
The level of the analyzed radiation	$\sim I_0$	$\sim 10^{-4}$–$10^{-7}\ I_0$

ter based on a scanning Fabri–Perot interferometer. The cooled photomultiplier was used as a receiver of scattered light. The recording system was based on the method of counting photons. The source of light excitation was a He–Ne laser. The spectrometer had such a sensitivity that the signal-to-noise ratio was of the order of $\sim 10^2$ for the longitudinal component in quartz in the $x(zz)y$ scattering geometry (at a laser power of about 20 mW and a time constant of the system of about 4s). The sample was mounted on a three-axis table. The spatial images of the $I_R(\mathbf{r})$ distribution, were recorded using the following type of scanning: it was continuous along the x-axis (the direction of the propagation of the exciting light waves) and stepwise along the two other axes, with a step of about 0.1 mm. The 3D patterns corresponding to the $I_R(\mathbf{r})$ distributions over the xz sections were recorded automatically (here, the z-axis coincides with the direction normal to the scattering plane xy). The translation of the sample along the x- and z-axes was provided by step motors.

An example of the 3D pattern of the $I_R(\mathbf{r})$ distribution in twinned natural calcite is shown as a stereoscopic pair in Fig. 2. The low level of $I_R(\mathbf{r})$ corresponds to the twin boundary. Note that the patterns similar to the pattern shown here were also observed in some other crystals. This fact clearly demonstrates the obviously insufficient characterization of the crystal homogeneity by only one parameter η proposed in [2, 3]. Here, we suggest the use of the following set of numerical parameters characterizing the observed $I_R(\mathbf{r})$ distribution: $\tilde{\eta}$, the I_R/I_{MB} value averaged over the crystal; $M = \tilde{\eta}_{max}/\tilde{\eta}_{min}$, the ratio of average maximum and minimum η values; and $\tilde{\tau}$, the average value of the main oscillations period in $I_R(\mathbf{r})$. This set of parameters provides only the general characteristics (without details) of the homogeneity of the crystal. Its main "goal" is to yield initial information for the comparison of the characteristics of different samples. The exhaustive analysis of the internal morphology of the sample is performed by processing the pattern of the spatial $I_R(\mathbf{r})$ distribution.

To examine the efficiency of the proposed technique of characterization of the crystal homogeneity, we studied a set of natural Iceland spar samples (calcite $CaCO_3$) certified according to the conventional scheme currently adopted in geology and based on the classification of the samples over certain classes according to the given level of light transmission in the ultraviolet, visible, and infrared ranges. The homogeneity was

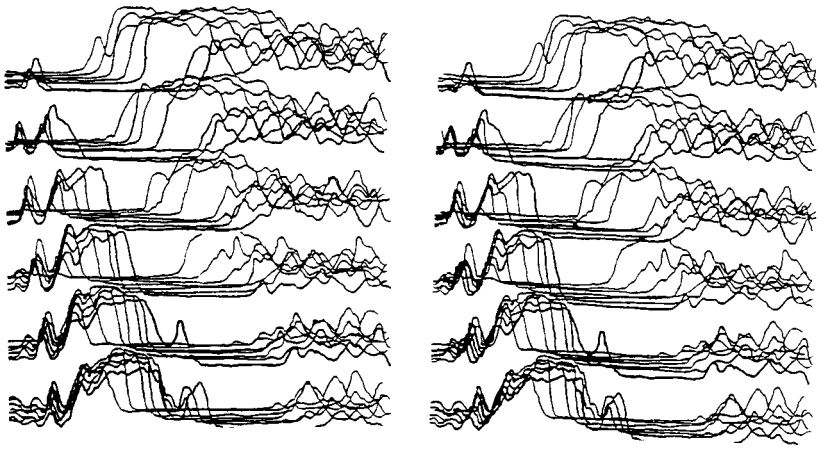

Fig. 2. Stereoscopic pair of the spatial distribution of the Rayleigh component $I_R(\mathbf{r})$ in natural twinned calcite ($CaCO_3$). The scanning step along the 0x and 0z axes is 0.5 mm. The low $I_R(\mathbf{r})$ level corresponds to the twin boundary.

Table 2. Comparative characteristics of a number of natural calcite crystals (Iceland spar) obtained according to the scheme adopted in geology (grade) and by the method proposed in this paper ($2\eta_{av}$)

Sample	Type, grade	η_{av}	M_{av}	τ_{av}	Sample	Type, grade	η_{av}	M_{av}	τ_{av}
1	ISU,"unique"	1.6	–	–	8	ISU, 1	1.5(50)	1.3	–
2	ISO,"unique"	1(4)	2.5	1	9	ISI, 1	2.5×10^3	1.4	0.3
3	ISI,"unique"	1.4(8.6)	3(10)	1(0.5)	10	ISU, II	1.9×10^4	12	0.5
4	ISU,"extra"	460	1.5	1	11	SU, II	5×10^3	4.3	0.5
5	ISO, "extra"	1.5	4.0	0.5	12	ISI, II	54(600)	–	–
6	ISI, "extra"	49(220)	1(2)	(0.5)	13	ISU, III	40	–	–
7	ISU, 1	920	2	0.4	14	ISI, III	2.4×10^4	4.0	0.7

Note: IS is Iceland spar, ISU is Iceland spar studied in the ultraviolet range, ISO is Iceland spar studied in the optical range, ISI is Iceland spar studied the infrared range.

evaluated visually according to the intensity level of scattered light and the samples were divided into five grades (in the order of increase of I_{scat}): "unique," "extra," and classes I, II, and III. Table 2 summarizes the results for a set of natural Iceland spar samples certified according to this scheme. The samples were studied by the method proposed in the present paper. The examples of the $I_R(x)$ distributions for some samples are shown in Fig. 3. The comparison was performed based on $\tilde{\eta}$ data and the sample class in each grade. The numbers in brackets correspond to the different parts of the same sample (different simple growth forms). The data presented in Table 2 demonstrate that the homogeneity characterization according to both techniques yields rather close results. Some discrepancies seem to be explained by the subjective evacuation of the scattered-light intensity based on visual examination. As an example, consider here a few of the most typical cases. Sample 5 should be classified as unique. Samples 9 and 12 should be interchanged in the grade classification. Sample 13 should be classified as extra. Sample 8 consists of crystals of two grades—unique and extra. It is necessary to note that the visual inspection involves not only a subjective source of errors but also an objective one—the radiation provided by the inelastic processes (such as the Mandelshtam–Brillouin and Raman scattering) and, in some cases, also the luminescence. The effect of the two latter phenomena can be eliminated by the use of a narrow-band filter in the channel between the trace of the laser beam in the crystal and the eye of the observer, whereas the effect of I_{MB} can hardly be eliminated because of small values of the I_{MB} shift with respect to I_R (of the order of 0.1 cm^{-1}). This fact is of special importance for highly homogeneous crystals ($\tilde{\eta}$ of the order of unity and less). Despite poor metrological potentialities, the visual method of control is very popular as a technique for the rapid analysis of crystal quality.

Up to now, we evaluated crystal homogeneity with the aid of only one parameter, $\tilde{\eta}$. Being a measure of the average level of the defect content in a crystal, it plays the most important role among all the parameters included in the set of numerical parameters if only because of the fact that its value should be determined for all kinds of $I_R(\mathbf{r})$ distributions.

Now, let us discuss the characteristics of 3D $I_R(\mathbf{r})$ patterns and the information obtained from their processing. In turn, this allows one to understand better the physical sense of the parameters τ and M. Earlier [6], we proposed the method of passage from continuous distributions to discrete data, which allowed us to find the type of simple growth form of the samples. The procedure of the graphical construction of the discrete set can be illustrated based on the actual 2D $I_R(y, z)$ pattern shown in Fig. 4a and characteristic of the sample cut out from one sector of the simple growth form and of the scanning type used in our study—continuous scanning along the *y*-axis and at discrete steps along the *z*-axis. This distribution corresponds to the system of dots which are the projections of the $I_R(y, z)$ maxima onto the abscissa in each scan (Fig. 4b). Thus, the system of dots constructed has two main periods, δ and τ_1. They are of different nature—the first parameter is purely technological and depends on researcher choice, whereas the second one is determined by the internal structure of the crystal. In fact, with a decrease in δ, the dot density increases in the $\chi_i\chi_i'$ direction but remains unchanged in the *y* direction (it is shown by smaller dots). In the $\delta \longrightarrow 0$ limit, the set of dots belonging to the $\in \chi_i\chi_i'$ is transformed into a straight line—a trace of the intersection of the face of the simple growth form and the scanning plane *zy*. Thus, we obtain the first characteristic angle $\rho_{av} = 54.4°$. Upon a similar construction for the cross-section perpendicular to *zy*, for example *xy*, we find the second characteristic angle, $\varphi_{av} = 0°15'$. The angles φ and ρ unambiguously determine the type of the simple growth form for the given sample orientation.

In the above example, the angle values correspond to a π-rhombohedron (the tabulated angles are $\varphi = 0°$ and $\rho = 54°4'$). Thus, the observed spatial intensity

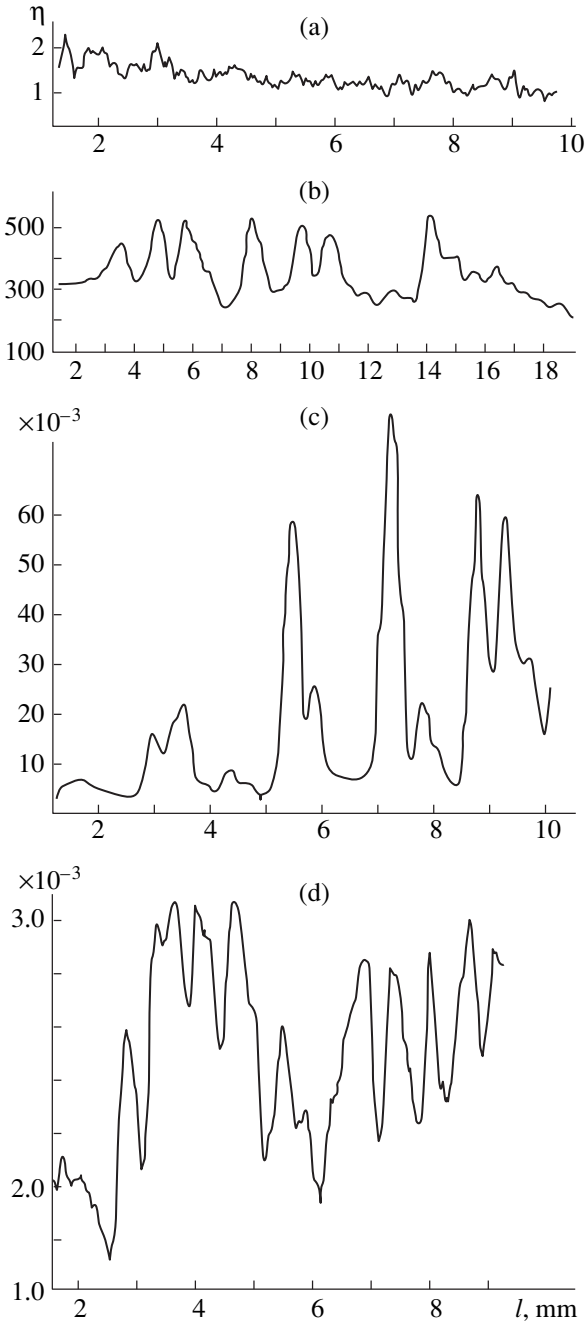

Fig. 3. Examples of individual scans of $I_R(x)$ for a number of $CaCO_3$ samples: (a) 1, (b) 4 (c) 10, and (d) 9 are the samples indicated in Table 2.

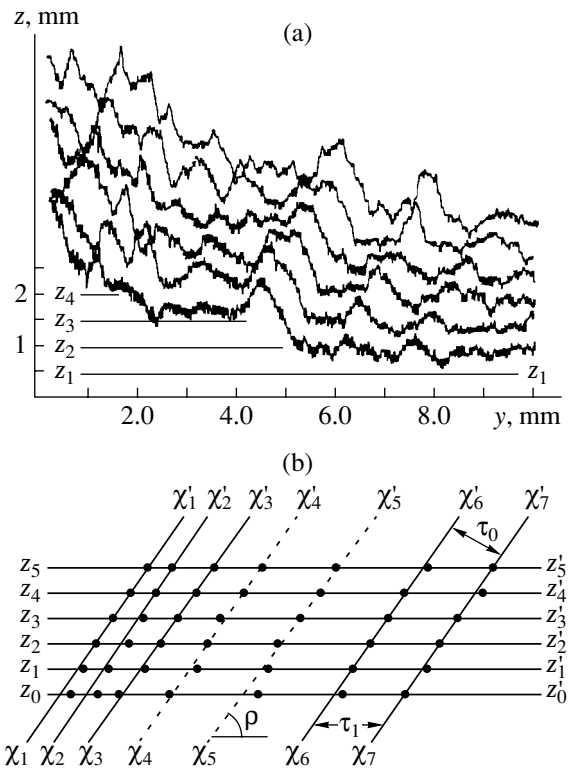

Fig. 4. An example of the determination of a simple growth form. (a) Two-dimensional $I_R(yz)$ distribution for a natural calcite sample cut out from one sector of the π-rhombohedron; $z_i z_i'$ are the zero-level lines for $I_R(y)$. The scanning step along the 0z axis is 0.5 mm; (b) a family of dots corresponding to the projections of the $I_R(yz)$ maxima onto the $z_i z_i'$ lines; $\chi_i\chi_i'$ are the characteristic straight lines passing through the maxima of dot density; these straight lines are the intersections of a face of the π-rhombohedron by the *yz* plane; ρ is the polar angle; τ_0 is the main period of the zonal structure. The scheme shows the change of the pattern with a fivefold increase in the scanning step and the area limited by $\chi_4\chi_4'$ and $\chi_5\chi_5'$ lines.

oscillations of the Rayleigh component or the defect-density waves are the manifestations of the zonal structure of the crystal. Therefore, hereafter the lattice constructed in such a way is called a zonal lattice. Its regular nature for the real crystal is determined by the stability of growth conditions. In practice, the $\Delta\tau$ value can be used as an additional parameter characterizing the degree of homogeneity and also a measure for the stability of growth conditions. It is possible to propose at least two methods for determining the characteristic directions. The first (static, at $\delta \longrightarrow 0$) method yields the characteristic direction corresponding to the maximum dot density. The second method (dynamic, which can be efficient for computer-based data processing) yields the characteristic direction corresponding to the maximum derivative of the dot density with respect to δ.

Now, consider the contrast of the zonal structure, or, in terms of the suggested system, the modulation depth *M* of the $I_R(\mathbf{r})$ distribution. In early studies of the zonal structure [4], some known impurities were introduced into the crystal to increase the contrast. In practice, in studies of crystal homogeneity one has to solve the inverse problem—to identify the types of defects that give rise to crystal inhomogeneity. This problem cannot be solved by the Rayleigh scattering method alone.

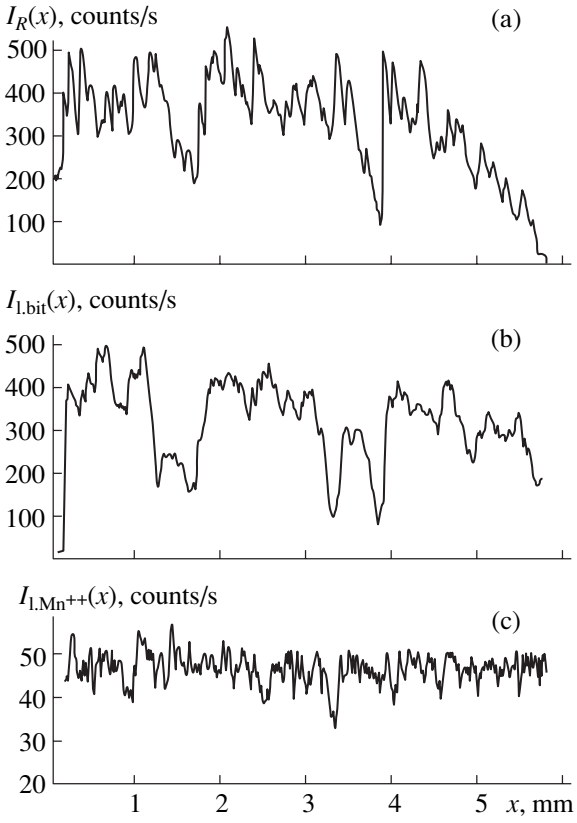

Fig. 5. Spatial distributions of the intensity of (a) the Rayleigh component $I_R(x)$, (b) luminescence from bitumens $I_{l.bit}(x)$, and (c) of Mn^{2+} ions $I_{l.Mn^{++}}(x)$ from the same sample of natural calcite.

Indeed, as was mentioned above, any defect contributes only to the intensity of the Rayleigh component.

One of the methods of solving this problem is to obtain the 3D distribution of the concentration of a certain kind of defects and then to compare this distribution with the $I_R(\mathbf{r})$ patterns to reveal the contribution made by these defects to the observed inhomogeneity.

This approach is illustrated by the study of single crystals of natural calcite. It is well known that the main defects in these crystals are ions of transition elements of the iron group and organic impurities (bitumens). The study of the luminescence spectra and the comparison of the results obtained with the data from [7] allowed us to identify the defects. These are Mn^{++} ions and bitumens with characteristic spectral bands. The Mn^{++} ions yield one band centered at 580 nm with the halfwidth of 40 nm. Bitumens, yield two bands centered at 400 and 525 nm with halfwidths of 120 and 100 nm, respectively. It is important that these bands do not overlap. The spatial distributions of the luminescence intensities $I_{l.Mn^{++}}(x)$ and $I_{l.bit}(x)$ and the $I_R(x)$ pattern obtained by the scanning of the same volume of the $CaCO_3$ crystal are shown in Fig. 5. The $I_R(x)$ pattern demonstrates the distribution of inhomogeneities over the crystal or, in fact, its zonal structure, whereas $I_{l.Mn^{++}}(x)$ and $I_{l.bit}(x)$ show the distributions of these defects over the same crystal volume.

The curves in Figs. 5a and 5b have analogous features: the same spatial phase relations and close values of the parameter M of their low-frequency harmonics (the fine structure of zonal pattern requires a special consideration). The above facts indicate the key role played by bitumens in the formation of the inhomogeneity distribution in the samples. On the other hand, the comparison of the curves in Figs. 5a and 5c show that Mn^{++} ions play a minor role in the formation of inhomogeneity because of the close values of the binding energies for Ca^{++} and Mn^{++} ions in calcite crystals. This example demonstrates the dominant role of non-isomorphic defects in the formation of the contrast in the zonal structure (or the M value).

Thus, the technique for evaluation of crystal homogeneity suggested above and involving the consideration of three-dimensional images of the crystals in scattered light and the set of numerical parameters η_{av}, $\tilde{\tau}_0$, and M, provides information on the internal structure of the crystals and the determination of the type of simple growth form. The suggested set of the numerical parameters has a clear physical meaning: η_{av} is the average degree of inhomogeneity in the units of I_{MB} and τ_0 and M are the quantitative characteristics of the zonal structure of the crystal, i.e., the main period and the contrast, respectively.

REFERENCES

1. G. P. Motulevich, Izv. Akad. Nauk SSSR, Ser. Fiz. **11**, 390 (1947).
2. T. C. Rich and D. A. Pinnow, Appl. Phys. Lett. **20** (7), 264 (1972).
3. Yu. L. Danileĭko, A. A. Manenkov, V. S. Nechitaĭlo, *et al.*, Kvantovaya Élektron., No. 8, 1812 (1974).
4. G. G. Lemmleĭn, *Sectorial and Zonal Structure of Crystals* (Nauka, Moscow, 1973).
5. G. T. Herman, *Image Reconstruction from Projection: The Fundamentals of Computerized Tomography* (Academic, New York, 1980; Mir, Moscow, 1983).
6. O. V. Kachalov, in *Abstracts of the XII European Crystallographic Meeting (ECM), Moscow, 1989*, Vol. 1, p. 351.
7. A. N. Tarashan, *Luminescence of Minerals* (Naukova Dumka, Kiev, 1978).

Translated by K. Kugel

Crystallography Reports, Vol. 47, No. 5, 2002, pp. 842–848. Translated from Kristallografiya, Vol. 47, No. 5, 2002, pp. 906–913.

PHYSICAL PROPERTIES OF CRYSTALS

Plastic Fragmentation in Crystals of Diamond-Like Hexagonal BN- and SiC-Phases

G. S. Oleĭnik and N. V. Danilenko

Institute of Problems of Materials Science, National Academy of Sciences of Ukraine, Kiev, Ukraine

e-mail: dep20@ipms.kiev.ua

Received April 11, 2001; in final form, March 28, 2002

Abstract—The processes of plastic macro- and microchanges in the shape of 2H-BN and 6H-SiC crystals during their deformation under high pressures (7.7 GPa) and temperatures (1200–1600°C) have been studied by transmission electron microscopy. It is established that deformation in crystals with a high density of basal stacking faults is induced by the rotations in the individual regions of the crystals. The shape changes are associated with rotation, tilt, bending, and displacement of the crystal regions of various dimensions. The localized crystallographic shears along the pyramidal $\{10\bar{1}2\}$ planes and the rotations about the [0001] axis are revealed. It is shown that all the above processes result in crystal fragmentation. © *2002 MAIK "Nauka/Interperiodica".*

INTRODUCTION

Earlier [1, 2], it was shown that the main mechanism of the translation deformation of the crystals of the wurtzite 2H-BN and 6H-SiC phases under high temperatures and quasihydrostatic-compression pressures consists in plastic shears caused by glide of split *a*/3 $[1\bar{1}00]$-type dislocations in the basal planes of the crystals. This deformation also causes the development of the intracrystallite layer-by-layer transition of the initial wurtzite phase into the sphalerite one (3C). Our subsequent studies showed that this transition is preceded by two stages of structural transformations in crystals—disordering along the [0001] direction caused by the accumulation of randomly distributed basal stacking faults and the formation of multilayer polytypes. The first stage proceeds over the whole crystal volume, whereas the second one is accompanied by the transformation into the 3C phase occurring during the formation of the misorientation boundaries in crystals with stacking faults. Below, we present the results obtained in the study of the nature of plastic deformation in crystals associated with the formation of such boundaries.

INITIAL MATERIALS AND EXPERIMENTAL METHODS

We studied polycrystalline samples 5 mm in diameter and 8 mm in height obtained by sintering powder particles in a "toroid"-type high-pressure chamber under conditions of quasihydrostatic compression providing the uniaxial compression along the sample height. Sintering was carried out under a pressure of 7.7 GPa in the temperature ranges 1200–1600°C for 2H-BN and 1200–1800°C for 6H-SiC. The dimension of the initial single-crystal 6H-SiC particles ranged within 10–20 μm, and the samples usually had the shape of polyhedra and, in some rare instances, platelets. The 2H-BN particles had the shape of platelets parallel to the (0001) plane with dimensions ranging within 1–3 μm and thickness, within 300–700 Å. Most of the 2H-BN particles were single crystals or slightly fragmented crystals with the azimuthal misorientation of the fragments in the (0001) plane not exceeding 5°–7°. The 2H-BN samples were either randomly oriented particles or oriented packings. In the latter case, the specimens were textured, because the particles were oriented with their basal planes parallel to one another.

The samples in the form of thin foils obtained by ion sputtering were studied by transmission electron microscopy. We studied the prismatic $\{11\bar{2}0\}$ sections of the crystals. This allowed us to observe the changes in the shape of plateletlike crystals and the formation of a microrelief on the faceting planes. These sections showed the fringe contrast of basal stacking faults (the traces of the basal layers). The corresponding microdiffraction patterns had rows of nodal 00*l* and *h*0*l* reflections, whose analysis provided the diagnostics of the structural state of the crystals. The diffuse streaks observed between the rows of the nodal reflections indicated disorder along the [0001] axis, whereas the systems of additional spot reflections indicated the formation of multilayer polytypes. The change in the stacking-fault fringes and contrast (its decrease or complete disappearance) and the microdiffraction patterns allowed us to determine the nature of the formation of the misoriented regions (fragments) in the crystals. The following typical cases were observed.

In the case of the group (i.e., relating to individual regions of the crystals) smooth tilts or sharp bends of the basal layers, the microdiffraction patterns had the intersecting rows of 00*l* and *h*0*l* reflections indicating

the misorientation of the individual microregions in the crystal (Figs. 1a, 1b). The angles formed by the intersecting rows of one type and the corresponding angles of the intersection of the regular stacking-fault fringes on the images corresponded to the misorientation angles of the *c*-axis of the matrix crystal and the crystal region determined from the tilt or bend of the basal layers (Fig. 1c). Obviously, in this case, the misorientation is caused by the rotation of the basal layers around the axes lying in the (0001) plane. If the *h*0*l* rows are intersected at the nodal *h*00 reflections, the *a*-axes of the matrix crystal and the misoriented regions are parallel (Fig. 1a); in all the other cases, these axes are misoriented (Fig. 1b). The misorientation of the *a*-axes because of the rotation around the *c*-axis is also seen from the weakening or complete disappearance of the fringe contrast of stacking faults in some regions in the crystal section. The weakening of the contrast is observed at the rotation angle up to 19°, i.e., prior to the formation of the $\{14\bar{5}0\}$ orientation indicated by the characteristic presence of the *h*0*l* rows at distances that are not multiples of the interplanar spacing $d_{(100)}$ on the microdiffraction patterns (Fig. 1d). The rotation by angles exceeding 19° results in the disappearance of the stacking-fault fringes and the formation of new orientations, including those of prismatic $\{1\bar{1}00\}$ type (Fig. 1e) corresponding to the rotation of the crystal region by an angle of 30°.

RESULTS AND DISCUSSION

Studying crystalline platelets of 2H-BN crystals with a high stacking-fault density, we established that their deformation occurs with a pronounced change in the shape of the well-developed (basal) surface without the loss of continuity. The most typical deformation of 2H-BN crystals is shown in Fig. 2. The $\{11\bar{2}0\}$ sections of almost all the 2H-BN and 6H-SiC samples showed group bends, kinks, displacements (Figs. 2f, 3, 4), and also rotations of the basal layers (Fig. 5).

The above specific features of the substructure are evidence of the fact that the plastic change in the shape of the crystals with high stacking-fault densities occur due to the displacements of individual microregions in the crystal bulk. This signifies that the rotational or cooperative plastic deformation typical of metals [3–5] takes place, which is a certain relaxation process occurring under the effect of the applied load under conditions of constrained deformation and the suppression of the translational plasticity. Two mechanisms of rotational plasticity proceeded via kink formation (irregular rotation), and the formation of the misorientation fringe formation was conditionally suggested in [4].

The development of the rotational deformation (kink formation) is studied in detail for nonmetal crystals with ionic bonding [6]. In some studies, it was established that such deformation at high temperatures can also occur in crystals with ionic–covalent (Al_2O_3 [7], SiC [8]) and covalent (diamond, 3C-BN [9]) bonding. For ionic crystals, such deformation is also possible at room temperature.

We distinguish between several individual processes of rotational deformation in the 2H-BN and 6H-SiC crystals.

I. Kink formation is observed either as a global process resulting in macroscopic changes in particle shape (Fig. 2) or as a local process occurring in the individual volumes of the crystals (Figs. 1c–1e, 3, 4). As is seen from the changes in the shape of the stacking-fault contrast, both cases are characterized by the group tilt of the basal layers with respect to the axes lying in the (0001) plane, i.e., in the main acting glide plane. In the local processes, the basal layers can acquire sharp kinks, including those accompanied by the formation of wedgelike misoriented regions with rectilinear interfaces (Figs. 1a, 1c) and the bends of various complexity up to the formation of vortex-like elements (Fig. 3). The rotation angles of the individual regions, even in an individual crystal, can vary from several degrees to tens of degrees (Figs. 1c, 3, 5). The kink formation can either proceed over the whole section of the crystal or can be decelerated in this section. In the latter case, complicated changes in the shape of the basal layers are observed. In the misoriented volume formed as a result of the kink formation, new bends or kinks of the basal layers can be formed, including those accompanied by rotations (Figs. 1c, 3).

II. Formation of misorientation fringes. Three characteristic cases of the formation of such fringes without changes in the shape of flat surfaces of particle faceting are distinguished: sharp rotations of individual regions about the [0001] axis or the axes tilted to it [the rotation angle of these regions can vary quite pronouncedly along the crystal section (Fig. 6)]; local rotations about arbitrary axes (Fig. 1d); and a combination of rotation around the [0001] axis with the tilt with respect to the axes lying in the basal plane (Fig. 4).

III. Localized crystallographic shears were revealed only in 2H-BN crystals from the presence of rectilinear boundaries in the $(11\bar{2}0)$ section against the background of stacking-fault fringes. Usually, these boundaries limit the regions in the shape of isosceles triangles whose base is parallel to the trace of the (0001) plane. On the corresponding electron-microscopy images, the angle at the vertex of this triangle is about 90°, whereas the angle of intersection of the side surfaces with the basal plane is about 45° (Fig. 7). These angles are close to the calculated angles formed by the $(\bar{1}012)$ and $(10\bar{1}2)$ planes with the basal plane in the 2H-BN lattice (Fig. 8). The angles were calculated at the lattice parameters $a = 0.255$ nm and $c = 0.423$ nm [10]. These data lead to the conclusion that the formation of the boundaries is provided by shears occurring simultaneously along two pyramidal planes.

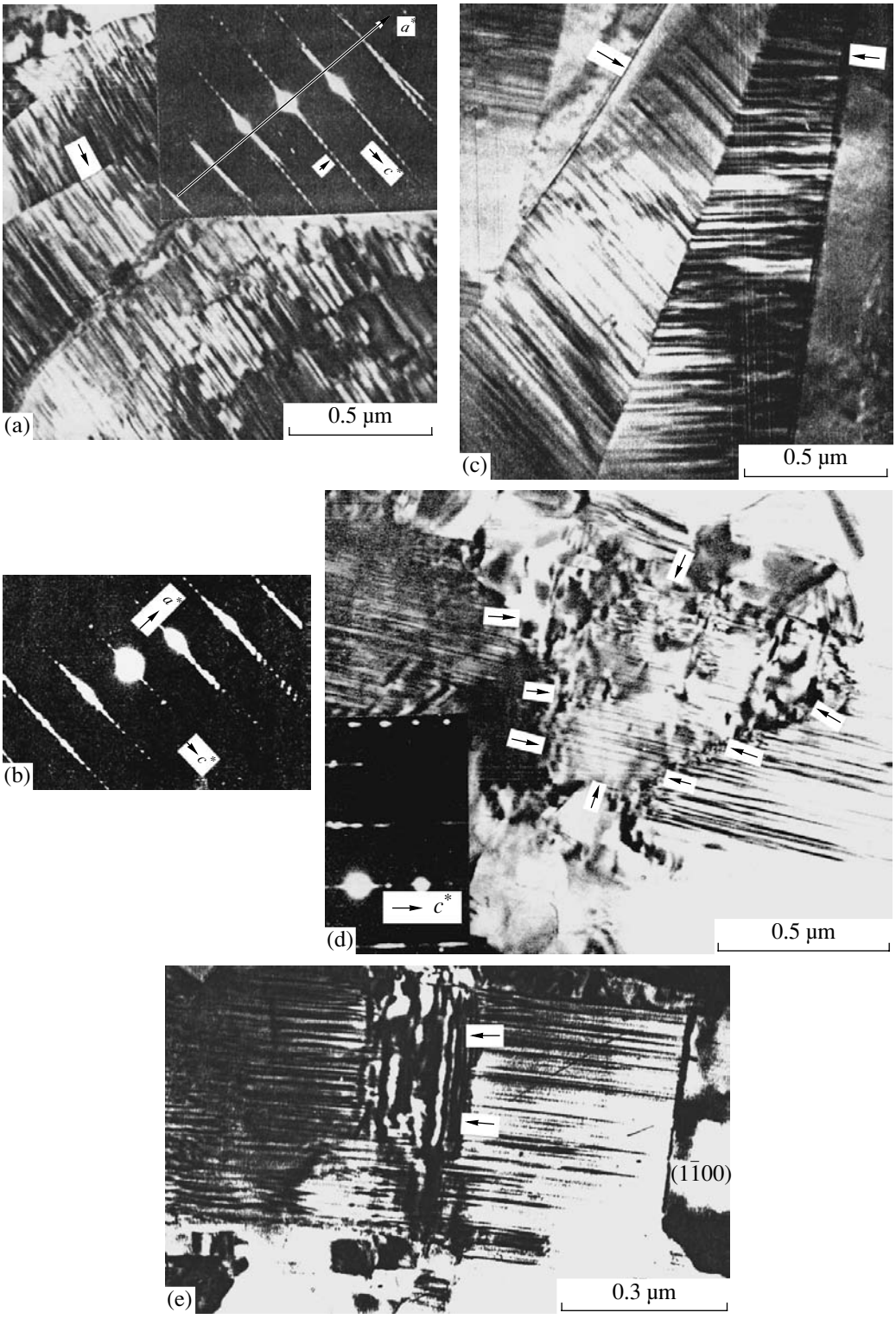

Fig. 1. Typical substructures of deformed crystals with basal stacking faults in $(11\bar{2}0)$. (a) The portion of a 6H-SiC crystal with weak kinks and rotations of basal layers. The corresponding microdiffraction pattern shows split *h*0*l* reflections and their intersections along the *a*-axis. The arrows indicate streaks between the nodal reflections; (b) microdiffraction pattern with the intersected *h*0*l* rows along the direction inclined to the *a*-axis; (c) micrographs of a sharp kink of basal layers, which provides the formation of wedgelike fragments; the arrows indicate the high-angle boundaries between the fragments; (d) the region with $(14\bar{5}0)$-type orientation in the section of the 2H-BN crystal (indicated by arrows). The corresponding diffraction pattern shows a row of nodal reflections parallel to the *h*0*l* rows of the matrix; (e) the region of the section of a 2H-BN crystal with the region of the $(1\bar{1}00)$-type orientation separated by the rectilinear boundary and extinction bend contours (indicated by arrows).

IV. Localized crystallographic rotations. The most typical case is sharp rotations of 30° of the crystal microregions about the [0001] axis over the whole crystal thickness resulting in the formation of fragments with $(1\bar{1}00)$ misorientation in the $(11\bar{2}0)$ section of the crystal. The conjugation boundaries between the fragments and the matrix are rectilinear and perpendicular to the basal plane (Figs. 1e, 9).

V. Processes of particle shaping allows the formation of a microrelief on the (0001) surface. These processes occur because of the displacement of microvolumes in the particles without a break in their continuity. Two cases are the most typical.

(1) The displacement of microvolumes in the crystal without a change in their orientations and the formation of misoriented interlayers. Most often, this takes place either along the [0001] axis or the axes tilted to it. Then, a microrelief consisting of steps of different heights is formed (Figs. 4f, 9) on the initial (0001) surface. We also observed the displacement of the structural elements with the triangular sections in the observation plane proceeding along the side planes and accompanied by the formation of ledges on the flat surfaces of particle faces (Fig. 4b).

(2) The displacement of microvolumes along the [0001] axis and the axes tilted to it in combination with their rotation about the [0001] axis (Fig. 9).

Structural transformations I–V in polycrystalline samples with high stacking-fault densities occur practically simultaneously. One can state that at $t = 1200$°C, the change in the shape of a crystal as a whole and the change in the shapes of the local volumes are provided mainly by kink formation, the formation of bends, and kinks in the (0001) plane with respect to the axes located in the basal plane, including the formation of the wedgelike structural elements. With an increase in temperature, the transformations in the crystals occur with the participation of localized shears and rotations.

Macro- and microchanges of crystal shape were observed both in the cases of random packing and the oriented packing characteristic of the 2H-BN-based samples. In the latter case, the most frequent processes were shear with the formation of fragments with triangular sections, rotations with the formation of linear boundaries, and the displacements of microvolumes parallel to the [0001] axis.

The above characteristics of the changes in crystal shape can be interpreted with the use of well-known data on the plastic deformation of anisotropic crystals.

It is well known that in crystals with a wurtzite structure, the action of different glide systems at high temperature is determined (as was proven by the example of ZnO [11]) by the angle θ of the deviation of the acting uniaxial stress from the [0001] axis. In the angular range $0° < \theta < 67°$, mainly glide in the basal plane takes place, whereas in the angular range $67° < \theta < 90°$, prismatic glide is most important. If the above direc-

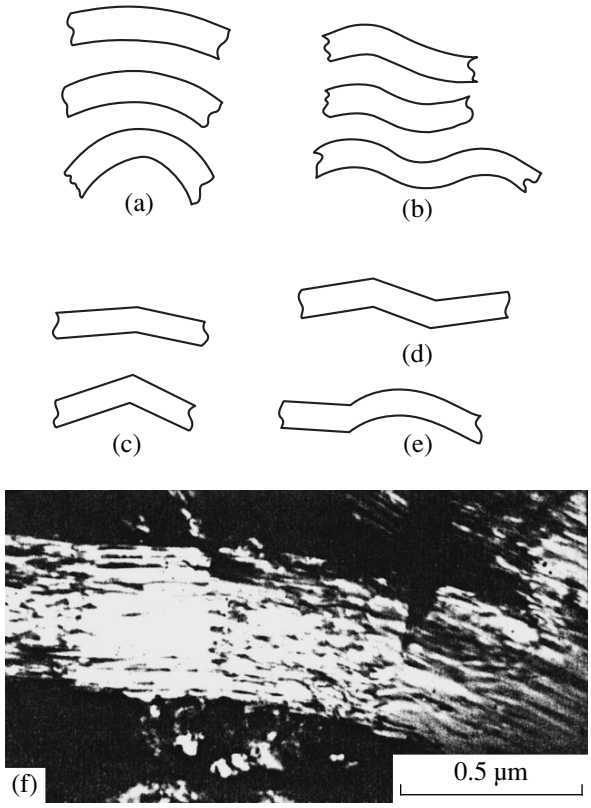

Fig. 2. Most typical cases of the changes in the shape of a 2H–BN crystal. (a, b) Bends; (c, d) kinks; (e) combinations of bends and kinks, (f) the dark-field image of a bent crystal.

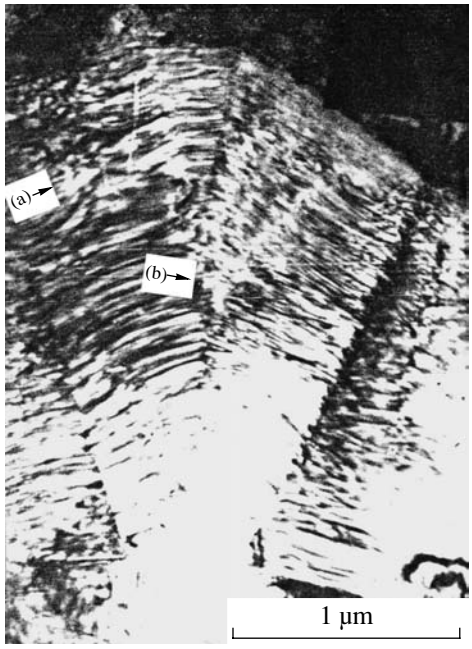

Fig. 3. Image of a bent 6H-SiC crystal, $(11\bar{2}0)$ section. (a) Complicated bend of the basal layers and (b) the region of the decelerated kink.

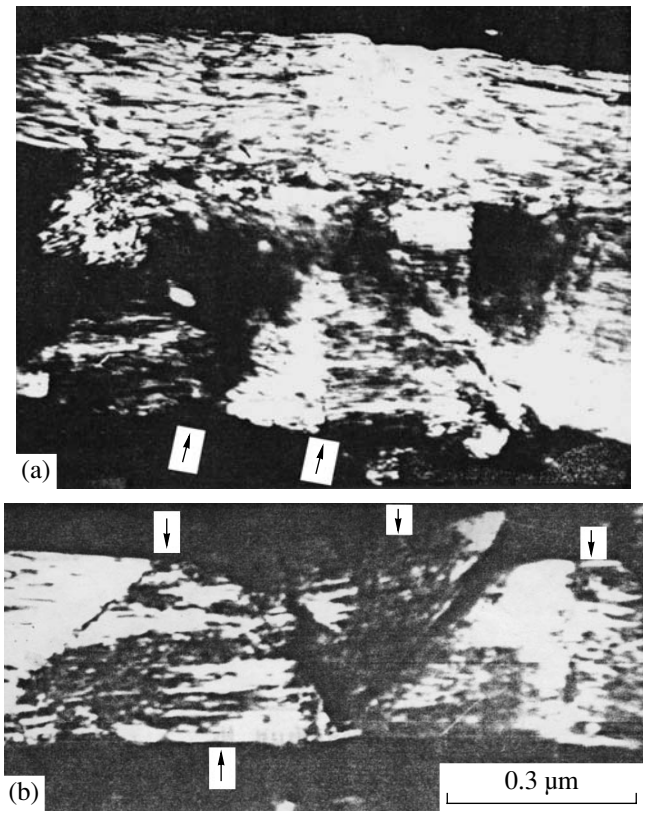

Fig. 4. Dark-field image of the $(11\bar{2}0)$ section of 2H-BN crystals obtained in the 100 reflection with different changes in the shape of the faces caused by the displacement of fragments (the arrows show the traces of the basal planes) of (a) an arbitrary shape and (b) the triangular section.

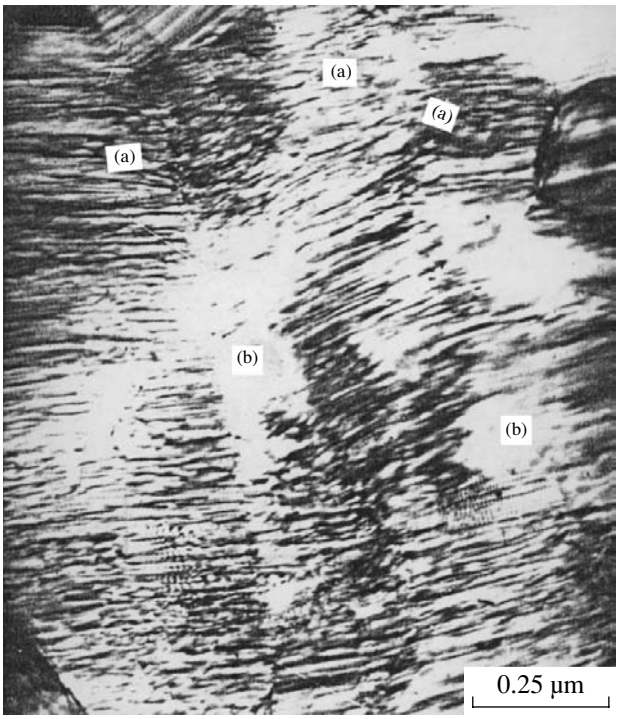

Fig. 5. Typical image of the $(11\bar{2}0)$ section of a 6H-SiC crystal (a) with group tilts and (b) rotations of the basal layers with respect to the [0001] axis.

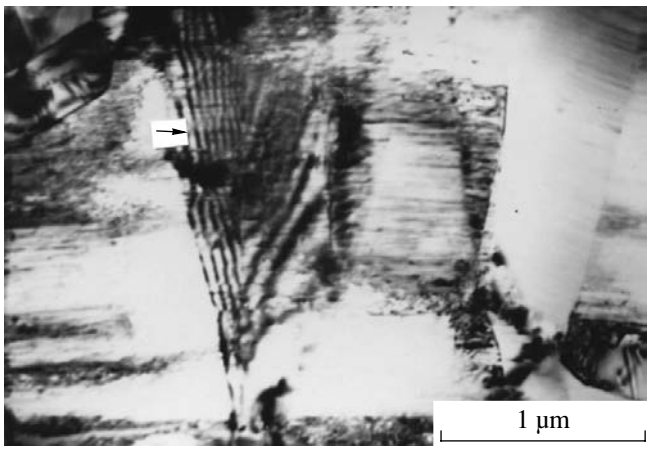

Fig. 6. High-angle misorientation boundary (indicated by arrows) in the $(11\bar{2}0)$ section of a 6H-SiC crystal formed because of the rotation with respect to the tilted axis.

tions coincide, only pyramidal glide is possible, whereas at the intersection of these directions at an angle of 90°, a combined pyramidal and prismatic glide takes place. As was indicated above, the translational deformation in the 6H-SiC and 2H-BN crystals during their thermobaric treatment is provided only by the glide of the basal split dislocations. Thus, one can conclude that such glide in the crystals studied (as well as in hexagonal close packed structures) is the easiest glide, which is provided by the low energy of basal stacking faults. As a result, the action of other glide systems and dislocation climb are hindered. Upon the completion of the action of the basal glide system, i.e., at high stacking-fault density, the rotational plastic deformation of crystals takes place.

Kink formation as an elementary event of plastic deformation in crystals can be caused by the local bending stresses orthogonal to the (0001) plane, i.e., can occur in cases where no basal glide is possible. It is under these conditions that kink formation on the surfaces of hcp metal crystals takes place [12].

The localized shears accompanied by the formation of structural elements with sections in the shape of isosceles triangles (Fig. 7) seem to take place under the most favorable conditions for pyramidal glide. Since deformation occurs in crystals with high stacking-fault densities, this glide can occur only under pronounced stresses, which give rise to the shear of microvolumes along the pyramidal planes. This is confirmed by the data on textured 2H-BN samples in which the (0001) surfaces of the platelet crystals were located during deformation normally to the compression axis. The displacement of microvolumes along the direction close to

the [0001] axis (Fig. 9) can be caused by the crystal orientation favorable for prismatic glide. Similar to the case of shear along the pyramidal planes, this glide in a crystal with a high stacking-fault density occurs as a microshear. The high levels of stresses along the [0001] axis are also indicated by the extinction bend contours observed in the $(11\bar{2}0)$ section (Fig. 1e).

Rotations about the [0001] axis in the macro- and microvolumes of the crystals with the preservation of their continuity (Fig. 1e) seem to proceed under conditions of blocking all the glide systems and the action of the uniaxial compression stress. The formation of the linear boundaries of the fragments parallel to the traces of the prismatic planes during these rotations seems to be caused by either preceding or accompanying shears along these planes. These shears can really occur via the formation of prismatic stacking faults. Indeed, we observed such stacking faults in 2H-BN [1].

The above structural transformations lead to crystal fragmentation because of their "saturation" with the misorientation boundaries.

One distinguishes the following types of boundaries.

High-angle boundaries. Plane boundaries appear already at $t = 1200°C$ because of sharp shears, localized shears, and rotations (Figs. 1c, 6, 9). The boundaries of arbitrary shapes are formed as a result of the restructuring of the dislocation boundaries at $t \geq 1600°C$ in the course of deformation (Fig. 10).

Boundaries in the shape of plane and volume dislocation pileups. Boundaries in the substructures with smoothly varying misorientations. These substructures were studied in detail in [5]. Their typical features are the spreading of nodal reflections on the microdiffraction patterns into arcs, the formation of fringes (relief edges) on dark-field images of the fragments (Fig. 4a), the change in the positions of the fragments when the samples are tilted in an electron microscope, and the presence of dislocation pileups in the form of extinction bend contours (Fig. 10). These substructures are formed in the 2H-BN and 6H-SiC crystals during the development of geometrically arbitrary or decelerated kinks and also during the formation of the reorientation fringes.

In some crystals, it is possible to reveal the boundaries with different misorientation angles and structural states. The most typical manifestation is the formation of boundaries because of sharp and smooth kinks of different strengths (Figs. 3, 5); the manifestation of the latter case is the formation of the boundaries at the stage of the dynamic rearrangement of their substructure (Fig. 10).

The most interesting fact is the appearance of plane high-angle boundaries at low temperatures (1200°C), where the diffusion processes are suppressed because of mainly covalent bonding in the crystals, whereas high pressures reduce the diffusion mobility. The for-

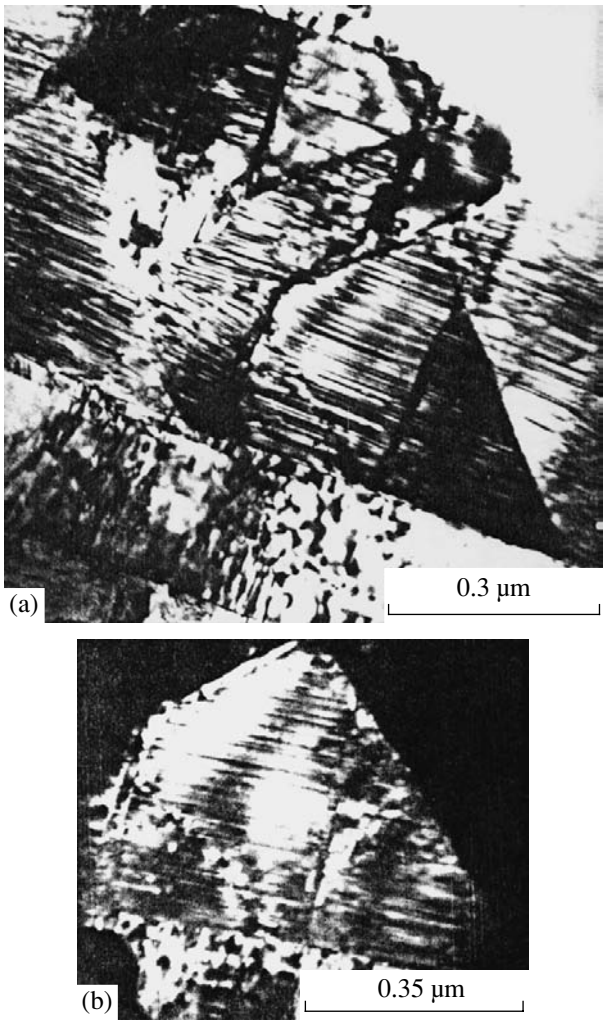

Fig. 7. Image of the fragments in a 2H-BN crystal. (a) General view, (b) dark-field image in the 100 reflection of the unit fragment with a triangular section.

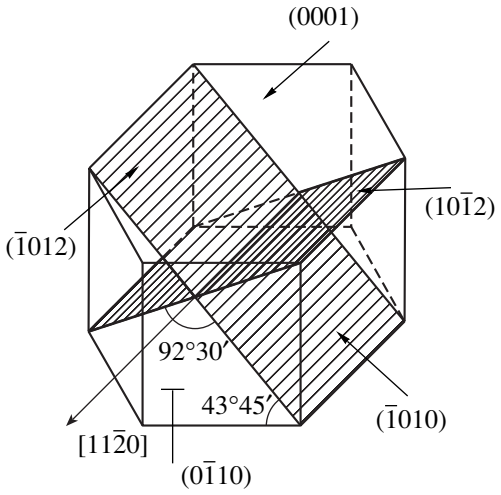

Fig. 8. Scheme of the intersection of the planes in the 2H-BN lattice.

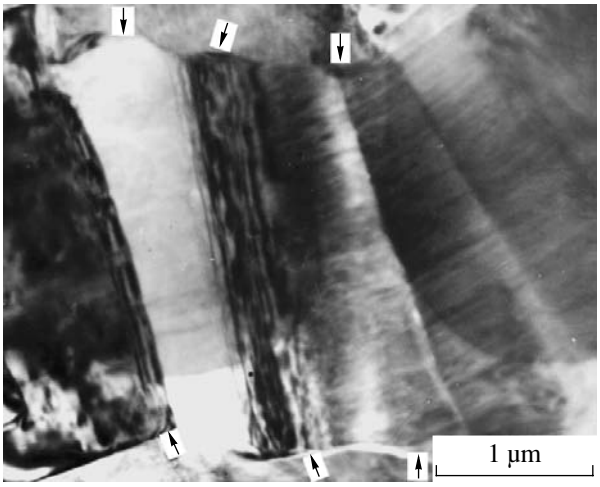

Fig. 9. Electron micrograph of the section of a platelet 6H-SiC crystal upon the displacement and rotations of the fragments with respect to the [0001] axis or the axes tilted to it (the arrows indicate the traces of the basal planes).

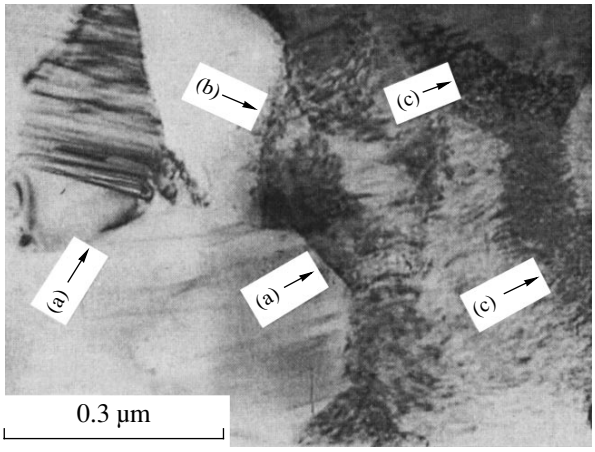

Fig. 10. Image of a 6H-SiC crystal with (a) high-angle boundaries, (b) the boundaries in the form of dislocation pileups, and (c) the boundaries with the region of the substructure with continuously varying misorientation. The arrows indicate of extinction bend contours.

mation of these boundaries can be explained based on the well-known concepts of the physical nature of the rotational plasticity and the crystal fragmentation induced by it. According to [3, 4], rotations are caused by the collective motion of the groups of interacting dislocations considered as a new element of the dislocation substructure—a disclination. It is the development of disclination-induced kinks that can provide the formation of the plane high-angle boundaries [3] (the so-called deformation knife boundaries) observed in molybdenum.

CONCLUSIONS

As is clear from the above, fragmentation of the 2H-BN and 6H-SiC crystals during thermobaric treatment is caused by their deformation as a result of the development of rotational plasticity at the stage of translation-shear suppression. This type of plasticity results from kink formation, the appearance of reorientation fringes, the rotations and displacements of microvolumes on different scales, localized crystallographic shears along the pyramidal planes, and rotations along the prismatic planes. The above transformations lead to the appearance of misorientation boundaries of various types in the crystals—from the boundaries characteristic of the substructures with continuously varying misorientation to high-angle boundaries. Our studies showed [13] that the subsequent transformations taking place in such fragmented crystals under thermobaric treatment occur via translational deformation caused by the glide of split dislocations in the (0001) planes proceeding independently in each fragment and promoting the phase transition from the wurtzite to the sphalerite structure type. Transformations can also take place as a result of structural rearrangements on the conjugating surfaces of the fragments with the appearance of high-angle boundaries. The latter stage determines the development of primary recrystallization.

REFERENCES

1. A. N. Pilyankevich, G. S. Oleĭnik, and V. F. Britun, Sverkhtverd. Mater., No. 1, 18 (1988).
2. V. F. Britun, G. S. Oleĭnik, and A. N. Pilyankevich, Ukr. Fiz. Zh. **33** (5), 791 (1988).
3. V. V. Rybin, *Pronounced Plastic Deformations and Fracture of Metals* (Metallurgiya, Moscow, 1986).
4. V. I. Vladimirov, *Cooperative Deformation Processes and Localization of Deformation* (Naukova Dumka, Kiev, 1989), p. 101.
5. V. E. Panin, Yu. V. Grinyaev, V. I. Danilov, *et al.*, *Structural Levels of Plastic Deformation and Fracture* (Nauka, Novosibirsk, 1990).
6. A. A. Urusovskaya, Itogi Nauki i Techn., Fiz.-Mat. Nauki **3**, 75 (1960).
7. V. G. Govorkov, E. P. Kozlovskaja, G. V. Berezhkova, and N. N. Voinova, Phys. Status Solidi A **7** (1), 277 (1971).
8. H. Suemotsu, T. Suzuki, and T. Iseki, J. Am. Ceram. Soc. **74** (1), 173 (1991).
9. G. S. Oleĭnik and N. V. Danilenko, *Electron Microscopy and Strength* (Inst. Problem Materialovedeniya Akad. Nauk Ukr., Kiev, 1999), p. 106.
10. A. S. Golubev, A. V. Kurdyumov, and A. N. Pilyankevich, *Boron Nitride* (Naukova Dumka, Kiev, 1987).
11. W. Funk and H. G. Sochel, Sci. Ceram. **9**, 519 (1977).
12. I. V. Gektina, A. V. Gektina, and F. F. Lavrent'ev, Metallofizika **9** (2), 3 (1987).
13. G. S. Oleĭnik, N. V. Danilenko, A. V. Kotko, and A. A. Bochechka, Fiz. Tekh. Vys. Davleniĭ **6** (4), 20 (1996).

Translated by L. Man

Crystallography Reports, Vol. 47, No. 5, 2002, pp. 849–855. From Kristallografiya, Vol. 47, No. 5, 2002, pp. 914–921.

LIQUID CRYSTAL

Lamellar Polymorphism in Multicomponent Lyotropic Amphiphilic Systems Based on Alkyltrimethylammonium Bromide Detergents[1]

E. O. Kiirend*, S. P. Chumakova, and T. J. Pehk***

** National Institute of Chemical Physics and Biophysics, Akadeemia 23, Tallinn, 2b Estonia*

*** Shubnikov Institute of Crystallography, Russian Academy of Sciences, Leninskiĭ pr. 59, Moscow, 117333 Russia*

Received August 10, 2001

Abstract—Lamellar polymorphism in multicomponent lyotropic systems based on alkyltrimethylammonium bromide detergents has been studied by polarization microscopy and ^{1}H-, ^{2}H-, and ^{13}C-NMR spectroscopy. The $L_{\alpha 1}$, $L_{\alpha 1\text{-}h}$, and $L_{\alpha h}$ lamellar phases are revealed, identified, and characterized. The alignment of the $L_{\alpha 1\text{-}h}$ lamellar phase in high magnetic fields is established. *© 2002 MAIK "Nauka/Interperiodica".*

INTRODUCTION

As is well known, molecules of detergents in aqueous solutions are prone to association. The formation of different structures and aggregates results in lyotropic polymorphism. This rich polymorphism is often associated with changes in temperature, component concentration, and the application of external electric and magnetic fields [1, 2]. There exist nematic disklike (N_D) [3–7], cylindrical (N_C) [4–8], hexagonal (H) [9], and several types of lamellar (L) phases [10–12]. A structural unit in lamellar phases is a bilayer associate of detergent molecules surrounded by water. The structural basis of cell membranes is a lipid bilayer, and, therefore, the lamellar phases are simple universal models of cell membranes [13–15]. On heating, the cubic C and lamellar L_α phases are destabilized and, as a result, the reversed hexagonal phase H_{II} is formed in the model lipids systems [15]. The interest in studies of the lamellar phase is associated with the intermediate L_α/H_{II} phase transformation. This type of transformation may play an important role in the functioning of biomembranes [16].

In the two-component didodecyldimethylammonium bromide–water system, the lamellar phase observed consists of two phases: $L_{\alpha 1}$ and $L_{\alpha 2}$. The $L_{\alpha 1}$ phase (Helfrich phase) is characterized by a pseudoisotropic texture and the accompanying Maltese crosses. The $L_{\alpha 2}$ lamellar phase with a mosaic texture is more structurized than the $L_{\alpha 1}$ phase [11, 17].

The $L_{\alpha 1}$, $L_{\alpha 1\text{-}h}$, and $L_{\alpha h}$ lamellar phases are established in the mixtures of C_{12} and C_{14} alkylpolyglycosides [18, 19]. In this case, only the $L_{\alpha h}$ phase is characterized by a pseudoisotropic texture with the homeotropically oriented micelles [19]. The $L_{\alpha 1\text{-}h}$ phase is characterized by a woven texture-like thermotropic S_C phases [20] or a schlieren texture characteristic of the nematic N_C lyomesophases with cylindrical micelles [19].

The changes in the bilayer structure result in the formation of the vesicular, planar smectic L_α, or sponge L_3 phases [21]. Moreover, in the lamellar phases, the bilayers can be rearranged and form various supramolecular structures [10, 22–25].

At present, the focal conic domains of the first type (FCD-I) with a negative Gaussian curvature (texture with oily streaks) are considered as the main structural elements in the classical L_α ($L_{\alpha h}$) lamellar phases. The focal conic domains of the second type (FCD-II) with a positive Gaussian curvature are characteristic of the $L_{\alpha 1}$ (L_α) phases [23, 25]. The textures of lamellar the $L_{\alpha 1}$ (onion) phase show the characteristic Maltese crosses [22, 26]. For the first time, spherical domains were observed in the Gomati lamellar phases [24]. Sometimes, the lamellar phases are subdivided into classical L_α and swollen L_α^H phases [12, 26–28].

The study of lamellar phases in multicomponent lyotropic molecular systems broadens our knowledge of the variety of the phases and their transformations in lyotropic liquid crystals (LC). The mixture of C_{12}, C_{14}, C_{16}-alkyltrimethylammonium bromides, NaBr, *n*-decyl alcohol, and D_2O is known to form lamellar, nematic and other phases forming different textures, including schlieren [6, 7] and marble textures. The identification and study of the textures in this system is hindered because of the possible phase transformation of the classical $L_{\alpha h}$ lamellar phase under the effect of the steady shear flow with the formation of the multilamellar vesicular $L_{\alpha 1}$ phase [29]. The lamellar phases with

[1] This article was presented by the authors in English.

bilayer structural elements can display different flow-induced orientational effects [30]. The orientation of the bilayer can give rise to the formation of the multilamellar onion phase. Thus, the identification of the lamellar phases in synthetic lyotropic systems is an important step in the studies of LC systems. We analyzed these phases using NMR spectroscopy and optical polarizing microscopy.

EXPERIMENTAL

Multicomponent cetyltrimethylammonium bromide (CTAB)–*n*-decanol–NaBr–D_2O mixtures were prepared within the concentration ranges corresponding to nematic phases [4]. ^{13}C NMR analysis showed that CTAB from Serva was really a mixture of dodecyl- (25 mol %), tetradecyl- (65 mol %), and hexadecyltrimethylammonium (10 mol %) bromides. This mixture is also of interest from the theoretical standpoint, because it was established that different lengths of the alkyl chain in the detergent molecules influence the formation, structure, and properties of the phases formed [31]. The reference detergent was cetyltrimethylammonium bromide (CTAB) (100 mol %) from Merck, because NaBr and *n*-decanol (chemically pure, Reakhim, USSR) could be used without any additional purification. Water contained more than 99.8% of D_2O (Izotop, USSR). The ingredients were mixed in several cycles of centrifugation in sealed glass ampoules 9 mm in diameter with a narrow 2–3 mm neck until the formation of a homogeneous mixture. The samples with a low *n*-decanol concentration were heated up to 60–70°C. The use of the mixed alkyltrimethylammonium bromide-based detergent (Serva) resulted in the faster formation of homogeneous mixtures. Samples with the ampoules were placed into standard 10-mm-long NMR sample tubes. The ^1H, ^2H, and ^{13}C NMR spectra were measured on a Bruker AMX-500 instrument at frequencies of 500.1, 76.8, and 125.8 MHz in a polarizing magnetic field of 11.7 T without sample rotation. The temperature was controlled by a B-VT-1000 unit (Bruker). The ^1H, ^2H, and ^{13}C NMR measurements were made using a lock resonance circuit and without change of the measuring head, which provided fast switching of the NMR spectrometer to all three nuclei under observation. The quadrupole splitting of the water signal in the ^2H NMR spectrum indicated the formation of lyomesophase in the mixture. The temperature dependence of this spectrum gave information about the phase transformations in the samples. The simultaneous presence of two phases in the sample was indicated by the formation of doublets with different $\Delta\nu_D$ values in the ^2H NMR spectra. The ^{13}C NMR spectra were useful for establishing long-range interactions and atom mobility in the detergent molecules of the lyomesophases. The prepared mesophases were characterized with the aid of polarization microscopy on POLAM L-311 and MIN-8 instruments.

RESULTS

Studying aggregation in lyotropic amphiphilic systems, we took into account the possible formation of isotropic solutions, micelles, and various LC and solid phases. These aggregational effects are reflected in the NMR spectra. Figure 1 shows the NMR spectra of different phases of a multicomponent CTAB–*n*-decanol–NaBr–D_2O system obtained at temperatures close to room temperature. The NMR spectrum of the deuterochloroform solution of CTAB–*n*-decanol mixture (a) is compared with the NMR spectra of the micellar solution (b), N_C phase with the marble texture (c), and the solid phase (d). The NMR spectra of the latter three states were obtained from sample 1 of the composition given in the table. The real solution provided the formation of sharp signals. The existence of two types of organic molecules in the ^1H spectrum can be determined only from the analysis of the integrated intensities of different absorption bands (Fig. 1, Ia). At the same time, the ^{13}C NMR spectrum provided the resolution of the signals from almost all the atoms of CTAB

Identification of the lyomesophases and types of their textures using the data of optical-polarizing microscopy and the compositions of the mixtures and the characteristic split of the NMR signal from ^2H nuclei of water in the samples studied

Sample	Phase	Texture type (Fig. 2)	*T*, K	Δν, Hz	Mixture composition, wt %				
					detergent CTAB (Serva)	detergent CTAB (Merck)	NaBr	*n*-decanol	D_2O
1	Micellar		297		32.36		3.06	3.88	60.70
1	N_C	c	286	14	32.36		3.06	3.88	60.70
2	$L_{\alpha h}$ (FCD-I)	a	297	43	32.84		4.95	6.38	55.83
3	$L_{\alpha 1}$ (FCD-II)	b	297	68		32.90	9.25	5.54	52.31
4	$L_{\alpha 1\text{-}h}$	d, e	297	42	26.85		7.04	5.08	61.03
5	H_I	b	297	26		34.99			65.01
6	Micellar		297		35.00				65.00

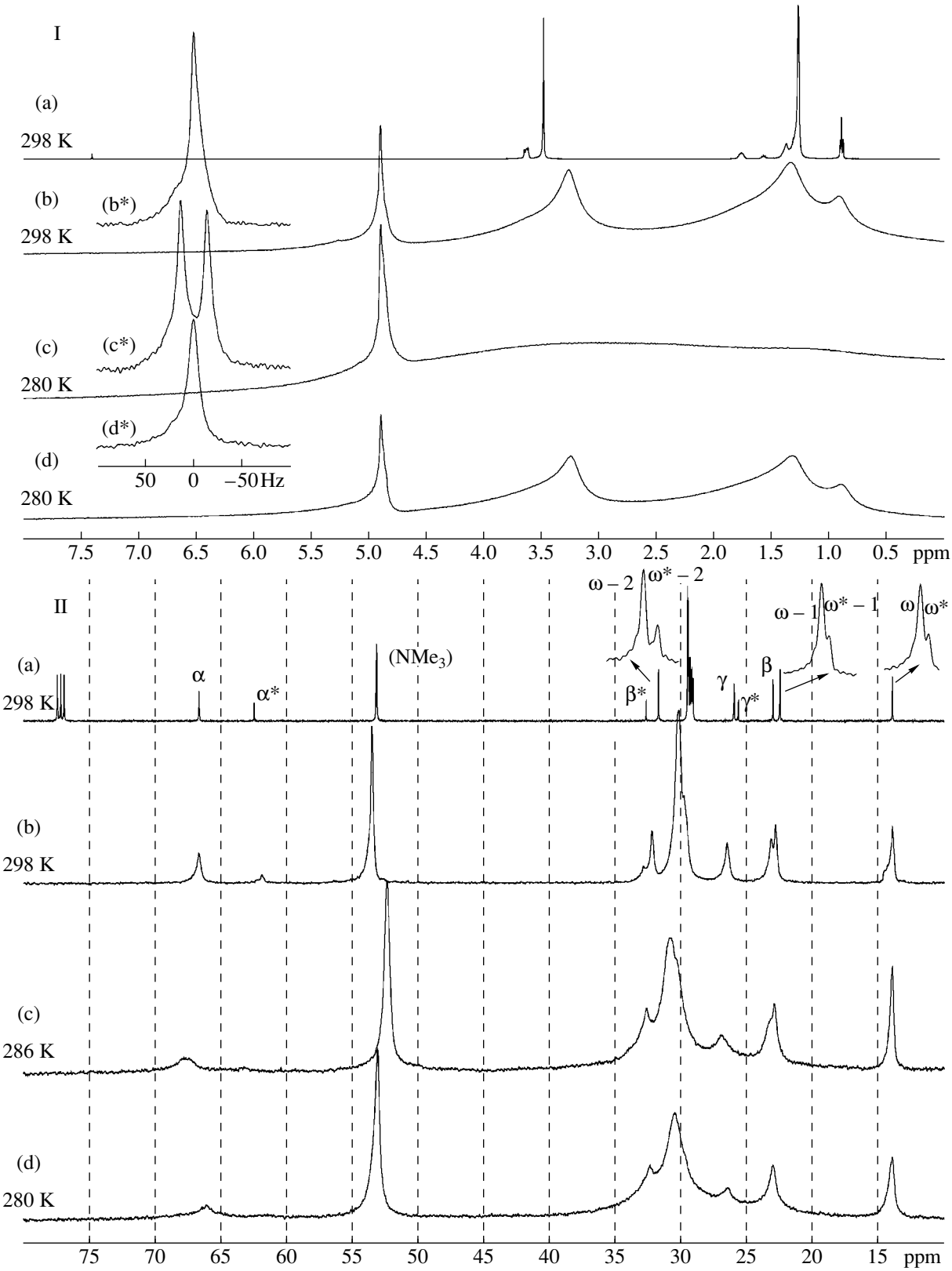

Fig. 1. (I) The ^{1}H and ^{2}H and (II) ^{13}C NMR spectra of different aggregate states of the CTAB–*n*-decanol–NaBr–D_2O system (sample 1). (a) Isotropic solution in $CDCl_3$; (b) micellar phase; (c) LC N_C phase with the marble texture; (d) solid-state phase. Here, α, β, and γ are the signals of the ^{13}C NMR spectrum of the atoms in the α- , β-, and γ-positions of the functional group (–OH, $–NMe_3$) and ω, ω – 1, and ω – 2 are the signals in the α- , β-, and γ-positions of the end atoms of the alkyl chains of the molecules.

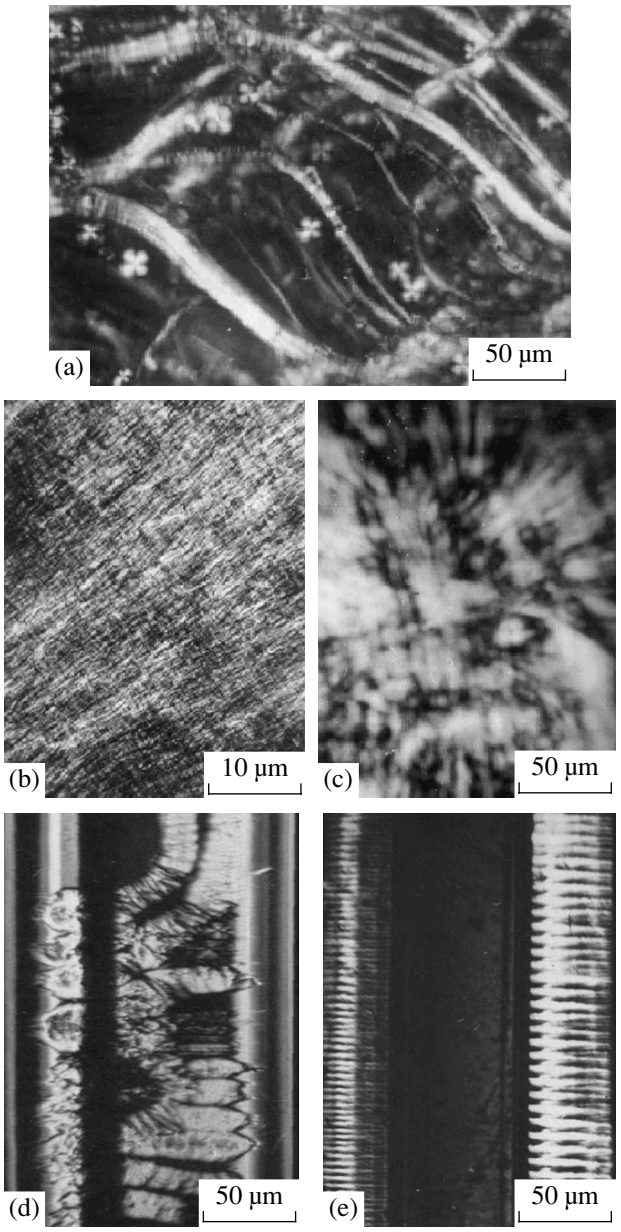

Fig. 2. Lyomesophase textures in the CTAB–*n*-decanol–NaBr–D_2O system: (a) homeotropic texture with oily streaks of the $L_{\alpha h}$ phase (sample 2), ×45; (b) texture of the $L_{\alpha 1}$ phase (sample 3); (c) marble texture (sample 1), ×45; (d) smectic-like texture with focal conics of the lamellar $L_{\alpha h\text{-}1}$ phase (sample 4), ×60; (e) oriented confocals of the $L_{\alpha h\text{-}1}$ phase in a capillary (sample 4), ×60.

and *n*-decanol (Fig. 1, IIa; signals from *n*-decanol are marked with asterisks). The lines due to all the central atoms from the alkyl chains were difficult to identify because of their overlap. However, different chemical shifts of the end atoms of the alkyl chain ($\Delta\delta_\omega$ = 0.01 ppm, $\Delta\delta_{\omega-1}$ = 0.01 ppm, and $\Delta\delta_{\omega-2}$ = 0.02 ppm) show the sensitivity of the ^{13}C NMR shielding to the long-range effects (Fig. 1, IIa).

The ^1H NMR spectrum of the micellar phase (Fig. 1, Ib) results in the strong broadening of the signals and, therefore, only three broad bands are seen—those of α protons from the hydrophilic end groups, end protons of methyl group, and other protons of the alkyl groups of molecules (Fig. 1, Ib). A relatively narrow signal at 4.8 ppm is attributed to water. The ^2H NMR spectrum of micellar solution showed no quadrupolar splitting. The ^{13}C NMR spectrum of the micellar phase has also broadened signals, but the presence of two types of organic molecules is still clearly seen (Fig. 1, Ib*). The most pronounced broadening is observed for α carbons of heteroatoms. The formation of micelles induces important selective effects in chemical shifts of carbon atoms ^{13}C. We observed the shifts of N-methyl and alkyl chains and the middle carbon atoms of the alkyl chains toward lower fields, which is characteristic of micelle formation (this was established by the NMR studies of various micellar solutions) (our unpublished data). This seems to be explained by the presence of *trans* alkyl conformers in the middle carbon atoms of alkyl chains.

The formation of a LC phase is clearly seen from the NMR spectra of both hydrogen isotopes: in the ^1H spectrum, in addition to a relatively narrow water signal, there is also an unstructured broad absorption band. In the ^2H spectrum, quadrupole splitting with strong temperature dependence is observed (Fig. 1, Ic, Ic*). The changes observed in the ^{13}C NMR spectrum are less dramatic and are associated with a further broadening of the signals and further shifts of the middle carbon atoms of alkyl chains toward low fields and the shift of the signals of carbon atoms of N-methyl toward high fields. At lower temperatures, the solid phase is formed, the quadrupole splitting of the D_2O ^2H NMR signal is no longer observed, and the ^1H spectrum resembles that of the micellar phase (Fig. 1, Ic*). The ^{13}C NMR spectrum still has broadened signals that are especially well pronounced for the α-carbon atoms. Signals from the central atoms of the alkyl chains and the carbons of N-methyl groups are shifted in the opposite directions, which is characteristic of the micellar phase (Fig. 1, IIc).

The compositions of the mixtures (see table) were selected in such a way that they would include the nematic region of the known phase diagram [4, 7]. The nematic lyomesophases in this system were studied in [4, 6, 7]. The composition of the lyotropic systems forming the lamellar phases (27–33 wt % of detergent, 4–6 wt % of *n*-decanol, 4–9 wt % of NaBr, and 55–65 wt % of D_2O) is close to those of the nematic phases. At the same time, the lamellar phases also exist at lower temperatures than the nematic ones and are characterized by higher viscosity. The characteristic feature of these phases are high values of quadrupole splitting of $\Delta\nu_D$ in the ^2H NMR spectra [6, 7].

Fig. 3. The ^{13}C NMR spectra from the (a) $L_{\alpha h}$, (b, c) $L_{\alpha 1}$, and (d) $L_{\alpha h\text{-}1}$ phases. The spectrum of the $L_{\alpha 1}$ phase indicates the formation of two phases on cooling from the temperature of the isotropic state (360 K) to initial room temperature (295 K).

The identification of the LC phases was made by polarization microscopy. The textures of different lamellar phases prepared from the multicomponent lyotropic mixtures are shown in Fig. 2. The texture of the classical lamellar phase $L_{\alpha h}$ (table, sample 2) is shown in Fig. 2a and is a typical pseudoisotropic texture with oily streaks and focal conic domains of the first type and negative Gaussian curvature (FCD-I). In the ^{13}C NMR spectra of the lamellar $L_{\alpha h}$ phase (Fig. 3a), the lines are broadened much more than those observed in the LC N_C phase from sample 1 (Fig. 1, IIc). The signals from α carbon atoms of the $L_{\alpha h}$ phase are so broadened that they cannot be identified against the background noise of the zero line. The quadrupolar splitting

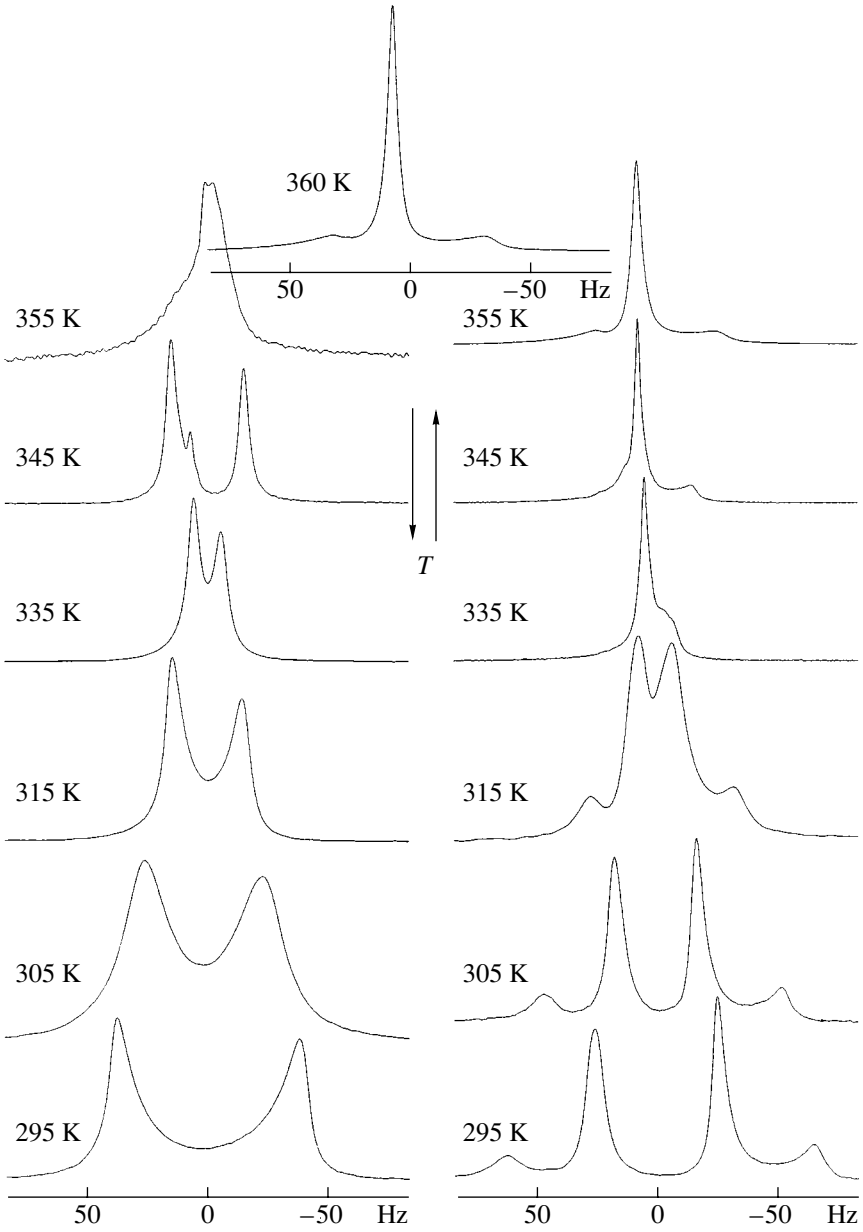

Fig. 4. Temperature dependence of the ^{2}H NMR spectrum of the lamellar $L_{\alpha 1}$ phase (sample 3) in the 11.7 T magnetic field in the heating and cooling cycles.

of the line of the $L_{\alpha h}$ phase in the ^{2}H spectrum (~43 Hz) is more pronounced than that for nematic lyomesophases (~18–20 Hz) [4, 7, 32].

At lower c/s (cosurfactant/surfactant) ratios in the lyotropic systems, one observes the formation of the lamellar $L_{\alpha 1}$ phase with an FCD-II-type texture and positive Gaussian curvature [23, 25]. The woven texture of the lamellar phase from sample 3 is shown in Fig. 2b. The temperature dependence of the ^{2}H NMR spectrum of this phase was studied on heated and cooled samples in a spectrometer (Fig. 4). The sample at room temperature was heated up to the temperature of the transition to the isotropic phase, T_c, and then was cooled back to room temperature (^{2}H NMR spectra in Fig. 3). In this case, the memory effect by the LC phase was observed. The quadrupole splitting $\Delta\nu_D$ at the given temperature depended (Fig. 4) on the history of the sample; cooling the sample in a magnetic field of the NMR spectrometer resulted in the formation of some additional phases. This behavior is also reflected in the ^{13}C NMR spectra: cooling the sample in a magnetic field provides the formation of two absorption bands from the main peak of alkyl chains and their

($\omega - 1$) atoms (cf. Figs. 3b, 3c). Thus, the $L_{\alpha 1}$ phase is transformed from the isotropic state in a strong magnetic field back into the mixture of two LC phases. The memory effect observed is of a complicated nature. The ratio of the two phases formed depends on the cooling conditions of the sample. The details of this process need additional studies.

In $L_{\alpha 1\text{-}h}$ phase (sample 4), the transformation of the smectic phase with the focal conics into the texture (Fig. 2d) with highly oriented confocals (Fig. 2e) was observed. This may be associated with the orientation of the lamellar phases at temperatures lower than $<T_c$. Recently, the orientation of the lamellar phases in strong magnetic fields was observed [33, 34]. The ^{13}C NMR spectrum of the $L_{\alpha 1\text{-}h}$ phase show a slight broadening of the lines in comparison with the lines of the $L_{\alpha h}$ phase (Figs. 3a, 3d).

The viscosity of the samples prepared from the detergent produced by Merck was higher than that of the samples based on the detergent produced by Serva, while the compositions of all the other components were the same. The samples prepared from CTAB gave the lamellar $L_{\alpha 1}$ phase (sample 3) and the hexagonal H_I phase (sample 5). Both phases have similar woven textures (Fig. 2b). The most viscous hexagonal H_I phase is very stiff; however, the ^{13}C NMR spectra indicate that the mobility of alkyl chains in the hexagonal phase is higher than in the lamellar phases. Thus, the micromobility determined from the NMR spectra is inconsistent with the macromobility determined from the viscosity measurements. The ^{13}C NMR spectrum from sample 6 practically coincides with that of the N_C phases (Fig. 1, Ic). This signifies that the mobilities of alkyl chains in the micellar and nematic N_C phases have close values.

CONCLUSION

The data reported here show the complex nature of the aggregational processes occurring in the lyotropic amphiphilic systems based on alkyltrimethylammonium bromide detergents. Different aggregational states and their mutual transformations can be studied with the aid of multinuclear NMR spectroscopy and optical polarization microscopy. In the present study, several lamellar phases, $L_{\alpha 1}$, $L_{\alpha 1\text{-}h}$, and $L_{\alpha h}$, have been identified and characterized. The alignment of the lamellar phases in strong magnetic fields has also been established.

REFERENCES

1. W. H. Gelbert, A. Ben-Shaul, and D. Roux, *Micelles, Membranes, Microemulsions and Monolayers* (Springer-Verlag, New York, 1994).
2. D. Attwood and A. T. Florence, *Surfactant Systems, Their Chemistry, Pharmacy and Biology* (Chapman and Hall, London, 1983).
3. K. D. Lawson and T. J. Flautt, J. Am. Chem. Soc. **89**, 5489 (1967).
4. B. J. Forrest and L. W. Reeves, Chem. Rev. **1**, 1 (1981).
5. L. Q. Amaral, O. Santin Filho, G. Taddei, *et al.*, Langmuir **13** (19), 5016 (1997).
6. É. O. Kiĭrend, S. P. Chumakova, and T. I. Pekhk, Kristallografiya **31** (4), 732 (1986) [Sov. Phys. Crystallogr. **31**, 432 (1986)].
7. É. O. Kiĭrend, S. P. Chumakova, and N. R. Ivanov, Kristallografiya **38** (6), 201 (1993) [Crystallogr. Rep. **38**, 817 (1993)].
8. L. Q. Amaral, C. A. Pimentel, M. R. Tavares, *et al.*, J. Chem. Phys. **71**, 2940 (1979).
9. C. V. Teixeira, R. Itri, and L. Q. Amaral, Langmuir **15** (4), 936 (1999).
10. K. M. McGrath, Langmuir **13** (7), 1987 (1997).
11. M. Monduzzi, F. Caboi, F. Larche, *et al.*, Langmuir **13** (8), 2184 (1997).
12. J. Gustafsson, G. Oradd, G. Lindblom, *et al.*, Langmuir **13** (4), 852 (1997).
13. I. G. Chistyakov, *Liquid Crystals* (Nauka, Moscow, 1966).
14. G. H. Brown and J. J. Wolken, *Liquid Crystals and Biological Structures* (Academic, New York, 1979; Mir, Moscow, 1982).
15. J. Borne, T. Nylander, and A. Khan, Langmuir **16** (26), 10044 (2000).
16. C. J. Chu and F. C. J. Szoka, J. Liposome Res. **4** (1), 361 (1994).
17. F. Caboi and M. Monduzzi, Langmuir **12** (15), 3548 (1996).
18. G. Platz, C. Thunig, and H. Hoffmann, Ber. Bunsenges. Phys. Chem. **96** (5), 667 (1992).
19. G. Platz, J. Polike, C. Thunig, *et al.*, Langmuir **11** (11), 4250 (1995).
20. G. Platz and C. Thunig, Langmuir **12** (7), 1906 (1996).
21. W. Helfrich, Z. Naturforsch. C **28**, 693 (1973).
22. H. Hoffmann, C. Thunig, P. Schmiedel, *et al.*, Langmuir **10**, 3972 (1994).
23. Ph. Boltenhagen, O. D. Lavrentovich, and M. Kleman, Phys. Rev. A **46** (4), 1743 (1992).
24. R. Gomati, J. Appell, P. Bassereau, *et al.*, J. Phys. Chem. **91**, 6203 (1987).
25. O. Regev and F. Guillement, Langmuir **15** (13), 4357 (1999).
26. J. Oberdisse, C. Couve, J. Appell, *et al.*, Langmuir **12** (5), 1212 (1996).
27. M. C. Holmes, M. S. Leaver, and A. M. Smith, Langmuir **11** (1), 356 (1995).
28. S. S. Funari, M. C. Holmes, and G. J. T. Tiddy, J. Phys. Chem. **98**, 3015 (1994).
29. P. Panizza, D. Roux, V. Vuillaume, *et al.*, Langmuir **12** (2), 248 (1996).
30. J. I. Escalante, M. Gradzielski, H. Hoffmann, *et al.*, Langmuir **16** (23), 8653 (2000).
31. C. C. Ruiz and J. Aguiar, Langmuir **16** (21), 7946 (2000).
32. B. E. Weiss-Lopez, C. Gamboa, and A. S. Tracey, Langmuir **11** (12), 4844 (1995).
33. G. Briganti, A. L. Segre, D. Capitani, *et al.*, J. Phys. Chem. B **103** (5), 825 (1999).
34. M. A. Firestone, D. M. Tiede, and S. Seifert, J. Phys. Chem. B **104** (11), 2433 (2000).

Crystallography Reports, Vol. 47, No. 5, 2002, pp. 856–858. Translated from Kristallografiya, Vol. 47, No. 5, 2002, pp. 922–924.

LIQUID CRYSTAL

Phenomenological Model of Phase Transitions between Isotropic, Nematic, and Smectic Phases in Liquid Crystals

A. E. Prostakov

Rostov State University, pr. Stachki 194, Rostov-on-Don, 344104 Russia

e-mail: eslarin@ip.rsu.ru

Received March 28, 2002

Abstract—The existence of the biaxial smectic phase SmA_b has been proved in the model of the Landau potential with two (nematic and smectic) interacting order parameters. © *2002 MAIK "Nauka/Interperiodica".*

INTRODUCTION

The symmetry of liquid-crystal phases is characterized by the orientational and positional order in the molecule arrangement [1, 2]. According to the Friedel classification, the phases in liquid crystals with achiral calamitic molecules are divided into two types—nematics and smectics [2]. The isotropic liquid has the complete orientational ($O(3)$) and translational ($T(3)$) symmetry of the group $G = O(3) \times T(3)$. At the transition to the nematic (*N*) phase, the translational symmetry is retained, while the rotational symmetry is violated, which provides the formation of two types of nematic phases—the uniaxial phase N_u ($G = D_{\infty h} \times T(3)$) and the biaxial phase N_b ($G = D_{2h} \times T(3)$). In nematics, the molecules are aligned along the director **n**. Smectic (*Sm*) liquid-crystal phases exhibit a layered structure in which the molecules are characterized not only by the orientational but also by some positional order. The simplest example of a smectic phase is the SmA_u phase with the symmetry $G = D_{\infty h} \times T(2)$ and the director perpendicular to the smectic layers. Within the layers, the centers of gravity of the molecules are disordered as in a conventional liquid. The violation of $D_{\infty h}$ symmetry leads to various smectic phases. For example, the director tilt with respect to the smectic layers gives rise to the formation of the *SmC* phase ($G = C_{2h} \times T$). Another example is the SmA_b phase ($G = D_{\infty h} \times T(2)$), in which the director of biaxial molecules is perpendicular to the layers. The possibility of the existence of this phase was first pointed out by McMillan [3, 4]. Within the context of the phenomenological Landau theory, the possibility of the direct transition from the isotropic to smectic (*SmA* and *SmC*) phases was studied in [5]. However, the transition to the SmA_b phase has not yet been studied theoretically. Below, we consider the simplest theoretical model of the Landau–de Gennes phase transitions, which describes the transitions from the isotropic (*I*) to the N_u, SmA_u, and SmA_b phases. Although the transition from *I* to *N* phase was widely studied both theoretically and experimentally [1], the direct transition from isotropic (*I*) to the *SmA* and SmA_b phases (*I–A* transition) was not observed experimentally until recently (see [6] and references). A simple model of Landau thermodynamic potential that allows one to describe the *I–A* transition was proposed in [6]. However, a number of errors did not allow the authors [6] to study this model in more detail. Below, we perform the detailed analysis of this model.

THE MODEL OF LANDAU THERMODYNAMIC POTENTIAL

The order parameter that describes the transition to the *N* phase is a traceless tensor [1]

$$Q_{ik} = 1/2\eta_1(3n_in_j - \delta_{ik}) + \sqrt{3}/2\eta_2(m_im_j - l_il_j), \quad (1)$$

where **n**, **m**, and $\mathbf{l} = \mathbf{n} \times \mathbf{m}$ are the orthogonal eigenvectors Q_{ij} corresponding to the eigenvalues

$$\eta_1, -1/2(\eta_1 + \sqrt{3}\eta_2), -1/2(\eta_1 - \sqrt{3}\eta_2), \quad (2)$$

respectively. The quantities η_1 and η_2 define the uniaxial ($\eta_1 \neq 0$ and $\eta_2 = 0$) and biaxial ($\eta_1 \neq 0$ and $\eta_2 \neq 0$) order. The smectic order can be described by the imaginary order parameter

$$\Psi(\mathbf{r}) = |\Psi(\mathbf{r})|e^{-iqu(\mathbf{r})}, \quad (3)$$

where $q = 2\pi/d$, and *d* is the layer thickness [1]. In the simplest case of the *SmA* phase, the wave vector is parallel to the *z*-axis

$$\Psi(z) = |\Psi|e^{-iqz}. \quad (4)$$

Generally, the thermodynamic potential has the form

$$\Phi = \Phi_1(Q_{ik}) + \Phi_2(|\Psi|, \nabla\Psi) + \Phi_3(Q_{ik}, |\Psi|, \nabla\Psi), \quad (5)$$

where $\Phi_1(Q_{ik})$ is the thermodynamic potential of the *N* phase, Φ_2 is the thermodynamic potential of the *SmA* phase, and Φ_3 is the potential corresponding to the

interaction between the order parameters. Retaining the simplest invariants in Φ_3, we obtain

$$\Phi_3(Q_{ik}, |\Psi|, \nabla\Psi) = \gamma_1 Q_{ik}(\nabla_i\Psi)(\nabla_k\Psi) + \gamma_2 Q_{ik}Q_{ik}|\Psi|^2. \quad (6)$$

Then, the simplest fourth-order potential with respect to the order parameters has the form (in notation suggested in [6])

$$\Phi = 1/2AQ_{ik}Q_{ik} - 1/3BQ_{ij}Q_{jk}Q_{ki} + 1/4C(Q_{ik}Q_{ik})^2 + 1/2\alpha|\Psi|^2 + 1/4\beta|\Psi|^4 + 1/4\delta|\Psi|^2Q_{ik}Q_{ik} + 1/2b_1(\nabla_i\Psi)^2 + 1/4b_2(\Delta\Psi)^2 + 1/2e_1Q_{ik}(\nabla_i\Psi)(\nabla_k\Psi). \quad (7)$$

The invariant $Q_{ik}(\nabla_i\Psi)(\nabla_k\Psi)$ is the trace of the product of two symmetric second-rank tensors that can simultaneously be reduced to the diagonal form ($D_{\infty h}$ symmetry). Here, the eigenvalues of the matrix $(\nabla_i\Psi)(\nabla_j\Psi)$ are ξ_1, $-1/2(\xi_1 + \sqrt{3}\xi_2)$, and $-1/2(\xi_1 - \sqrt{3}\xi_2)$, where

$$\xi_1 = \frac{1}{\sqrt{6}}\left[\left(\frac{\partial\Phi}{\partial z}\right)^2 - \left(\frac{\partial\Phi}{\partial x}\right)^2 - \left(\frac{\partial\Phi}{\partial y}\right)^2\right],$$
$$\xi_2 = \frac{1}{\sqrt{2}}\left[\left(\frac{\partial\Phi}{\partial x}\right)^2 - \left(\frac{\partial\Phi}{\partial y}\right)^2\right]. \quad (8)$$

Then, the invariant $Q_{ik}(\nabla_i\Psi)(\nabla_k\Psi)$ is

$$\gamma_1(\eta_1\xi_1 + \eta_2\xi_2). \quad (9)$$

From Eqs. (4) and (8), we obtain $\xi_1 = q^2|\Psi|^2$ and $\xi_2 = 0$. According to [7],

$$Q_{ik}Q_{ik} = 3/2(\eta_1^2 + \eta_2^2),$$
$$Q_{ij}Q_{jk}Q_{ki} = 3/4(\eta_1^3 - 3\eta_1\eta_2^2), \quad (10)$$

and, hence, the thermodynamic potential is

$$\Phi = a_1(\eta_1^2 + \eta_2^2) + b_1(\eta_1^3 - 3\eta_1\eta_2^2) + a_2(\eta_1^2 + \eta_2^2)^2 + \alpha_1|\Psi|^2 + \alpha_2|\Psi|^4 + \lambda_1|\Psi|^2q^2 + \lambda_2|\Psi|^2q^4 + \gamma_1\eta_1q^2|\Psi|^2 + \gamma_2(\eta_1^2 + \eta_2^2)|\Psi|^2q^2. \quad (11)$$

If the model of potential (11) is to meet the condition of the global minimality (the values of the order parameters should be finite irrespective of the changes in the parameters) [8], the parameters of the model before the higher powers of the expansion in the order parameters should satisfy certain relations. In [6], the sequence of the relations was determined erroneously. Using the method stated in [6], we obtain

$$\alpha_2 > 0, \quad a_2 > 0, \quad \lambda_2 > 0,$$
$$\gamma_2 > -2\sqrt{a_2\alpha_2} + \gamma_1^2/4\lambda_2. \quad (12)$$

Within model (11), the variable parameters are a_1, b_1, α_1, and λ_1, which depend on the external conditions, e.g., the temperature and pressure. For the sake of simplicity, we put $b_1 = \text{const} < 0$.

ANALYSIS OF THE SYSTEM OF THE EQUATIONS OF STATE FOR THE MODEL OF THE THERMODYNAMIC POTENTIAL

The system of the equations of state for thermodynamic potential (11) has the form

$$\frac{\partial\Phi}{\partial\eta_1} = 2a_1\eta_1 + 3b_1(\eta_1^2 - \eta_2^2) + 4a_2(\eta_1^2 + \eta_2^2)\eta_1 + \gamma_1|\Psi|^2q^2 + \gamma_2|\Psi|^2\eta_1 = 0,$$
$$\frac{\partial\Phi}{\partial\eta_2} = 2\eta_2[a_1 - 3b_1\eta_1 + 2a_2(\eta_1^2 + \eta_2^2) + \gamma_2|\Psi|^2] = 0,$$
$$\frac{\partial\Phi}{\partial|\Psi|} = 2|\Psi|[\alpha_1 + 2\alpha_2|\Psi|^2 - 2\lambda_2q^4 + \gamma_2(\eta_1^2 + \eta_2^2)] = 0,$$
$$\frac{\partial\Phi}{\partial q} = 2|\Psi|^2q(\lambda_1 + 2\lambda_2q^2 + \gamma_1\eta_1) = 0. \quad (13)$$

The solutions of this system correspond to four phases:

$$I: \eta_1 = \eta_2 = 0, \quad |\Psi| = 0, \quad q = 0,$$
$$N_u: \eta_1 \neq 0, \quad \eta_2 = 0, \quad |\Psi| = 0, \quad q = 0,$$
$$SmA_u: \eta_1 \neq 0, \quad \eta_2 = 0, \quad |\Psi| \neq 0, \quad q \neq 0,$$
$$SmA_b: \eta_1 \neq 0, \quad \eta_2 \neq 0, \quad |\Psi| \neq 0, \quad q \neq 0. \quad (14)$$

It is important that only the first three phases were considered in [6]. The fourth-order potential with respect to Q_{ik} includes no biaxial phase N_b; in order to describe this phase, one has to take into account the sixth-order term. However, because of the interaction with the smectic parameter ($\gamma_1\eta_1|\Psi|^2q^2$), system of equations (13) admits of the following solution with $\eta_2 \neq 0$ at $|\Psi| \neq 0$ and $q \neq 0$:

$$\eta_2^2 - 3\eta_1\eta_2^2 = \gamma_1|\Psi|^2q^2/3b_1. \quad (15)$$

If $\gamma_1 = 0$ (or $|\Psi| = 0$ and $q = 0$), the solutions $\eta_2^2 - 3\eta_1^2 = 0$ correspond to the domains of the N_u phase. The analysis of the phase stability in the space of the variable parameters $R^3 = (a_1, \alpha_1, \lambda_1)$, ($b_1 = \text{const} < 0$) involves the determination of the degeneracy conditions for the matrix of the second derivatives

$$\|H_{ij}\| = \left\|\frac{\partial^2\Phi}{\partial g_i\partial g_j}\right\|, \quad (16)$$

where $g_i \in \{\eta_1, \eta_2, |\Psi|, q\}$ and $i, j = 1, \ldots, 4$.

The derivatives in Eq. (16) are found by substituting the solutions of Eq. (13) for each phase. For phase I, the stability conditions are

$$\alpha_1 \geq 0, \quad a_1 \geq 0. \quad (17)$$

The determinant $\|H_{ik}\|$ in the phase N_u has the form

$$\det\|H_{ik}\| = (-9b_1\eta_1)\eta_1(3b_1 + 8a_2\eta_1)(\alpha_1 + \gamma_2\eta_1^2). \quad (18)$$

As follows from Eq. (18), in model (13) we have

$$-9b_1\eta_1 \geq 0, \quad (19)$$

and if $b_1 < 0$, then $\eta_1 > 0$.

Two other degeneracy conditions for $\|H_{ik}\|$ are given by the equations in R^3

$$a(\mathrm{I})_1 = -\frac{3}{2}b_1\sqrt{-\frac{\alpha_1}{\gamma_2}} + 2a_2\frac{\alpha_1}{\gamma_2}, \quad (20)$$

$$a(\mathrm{II})_1 = \frac{9b_1^2}{32a_2}. \quad (21)$$

Condition (21) specifies the coexistence region of the I and N_u phases, in which the I–N_u first-order transition occurs at

$$a_1(I\text{–}N) = b_1^2/4a_2. \quad (22)$$

Curves (20) and (21) in the space $R^2 = (a_1, \alpha_1)$ are tangential to one another at the point ($\alpha_1 = -\gamma_2 9b_1^2/64a_2^2$, $a_1 = 9b_1^2/32a_2$). For the SmA_u phase, the degeneracy condition for $\|H_{ik}\|$ has the form

$$32|\Psi|^4q^2\left(-9b_1\eta_1 + \frac{\gamma_1\Psi^2q^2}{\eta_1}\right)\left[4\lambda_2\Delta_1\eta_1^2\right.$$
$$+ 2\lambda_2(3\alpha_2b_1 - 2\gamma_1\gamma_2q^2)\eta_1 - \gamma_1^2(\lambda_2q^4 + \alpha_2|\Psi|^2) \quad (23)$$
$$\left. - \frac{2\lambda_1\lambda_2\Psi^2q^2}{\eta_1}\right] = 0,$$

where $\Delta_1 = 4\alpha_2a_2 - \gamma_2^2$. The condition

$$-\left(9b_1\eta_1 + \gamma_1\frac{\Psi^2q^2}{\eta_1}\right) \geq 0 \quad (24)$$

differs from Eq. (19) for the N_u phase and specifies a curve in the plane $R^2 = \{a_1, \alpha_1\}$. This condition determines the stability of the SmA_u phase in relation to the formation of the SmA_b phase. Condition (23) also specifies the region of the real solutions for the SmA_u phase. In this case, there is a region where the I, SmA_u, and N_u phases coexist. In this region, the first-order I–SmA_u, I–N, and SmA_u–N_u phase transitions take place, which converge to a triple point.

The degeneracy conditions for H_{ik} in the SmA_b phase with the lowest symmetry have the form

$$64|\Psi|^4q^2\eta_2^2[4\lambda_2\Delta_1\eta_1^2 + (\Delta_1|\Psi|^4 - 4\lambda_2\gamma_1^2q^4$$
$$+ 3b_1(\gamma_1\gamma_2q^2 + 3\alpha_2b_1))\eta_1 \quad (25)$$
$$+ 2\lambda_2(3b_1\eta_2^2 - \gamma_1\Psi^2q^2)\Delta_1] = 0.$$

The analysis of conditions (23) and (25) showed that both second-order transitions along curve $\eta_2 = 0$ [Eq. (24)] and first-order transitions between the SmA_u and SmA_b phases are possible. In addition, the direct first-order transition from the I to the A_b phase is also possible.

CONCLUSIONS

Thus, we have analyzed the simplest model of thermodynamic potential (11). The study of the solutions of system of equations (14) and their stability showed that the model describes four phases, I, N_u, SmA_u, and SmA_b. The SmA_b phase is optically biaxial; one of the axes coincides with the normal to the smectic layers z, while the other two axes ξ and η, lying in (x, y) plane, are not equivalent:

$$Q_{zz} \neq 0, \quad Q_{\xi\xi} \neq Q_{\eta\eta} \neq 0,$$
$$Q_{\xi\eta} = Q_{\eta z} = Q_{\xi z} = 0. \quad (26)$$

The effective potential described by (13) was studied in [6] at $\eta_2 = 0$; it was assumed that conditions (19) are satisfied. In this case, the phase diagram has a region of parameter values such that no solutions of the equations of state can exist, which shows that this approach is erroneous.

ACKNOWLEDGMENTS

The author is grateful to E.S. Larin for formulating the problem. The calculations were performed with the use of the program Maple V Release 5. The author is also grateful to E.B. Loginov, who attracted his attention to publication [5].

REFERENCES

1. P. G. de Gennes, *The Physics of Liquid Crystals* (Clarendon, Oxford, 1993).
2. G. Friedel, Ann. Phys. **18**, 273 (1922).
3. W. L. McMillan, Phys. Rev. A **4**, 1238 (1971).
4. R. I. Meyer and W. L. McMillan, Phys. Rev. A **9**, 899 (1974).
5. E. E. Gorodetskiĭ and V. É. Podnek, Kristallografiya **29** (6), 1054 (1984) [Sov. Phys. Crystallogr. **29**, 618 (1984)].
6. P. K. Mukherjee, H. Pleiner, and H. R. Brandt, Eur. Phys. J. E **4**, 293 (2001).
7. M. I. Freiser, Phys. Rev. Lett. **24**, 1041 (1970).
8. Yu. M. Gufan, E. S. Larin, and M. B. Stryukov, Izv. Akad. Nauk, Ser. Fiz. **65**, 1102 (2001).

Translated by A. Zolot'ko

Crystallography Reports, Vol. 47, No. 5, 2002, pp. 859–866. Translated from Kristallografiya, Vol. 47, No. 5, 2002, pp. 935–932.

CRYSTAL GROWTH

Fluctuations in the Step Velocity and the Generation of a Dislocation Spiral on the (101) Face of Monoclinic Lysozyme Crystals

L. N. Rashkovich*, N. V. Gvozdev*, M. I. Sil'nikova*, and A. A. Chernov**

** Physics Department, Moscow State University, Leninskie gory, Moscow, 119899 Russia*

e-mail: rashk@polc49.phys.msu.su

*** NASA Marshall Space Flight Center, Huntsville, AL 35812, USA*

Received February 20, 2002

Abstract—The generation of a dislocation spiral and fluctuations in the step velocity on the (101) face of monoclinic lysozyme crystals have been studied by *in situ* atomic force microscopy (AFM). It is shown that the (101) face grows by the dislocation mechanism and that the steps move via the formation of one-dimensional nuclei. The velocity of a part of the step fluctuates, with the fluctuations increasing proportionally to the fourth-order root of time. In the process of spiral generation, a segment of the step attains a certain critical length and then moves with a constant velocity. Even under constant supersaturation, the fluctuations can give rise to changes in the segment length. The interstep distance in the step echelon also varies. © *2002 MAIK "Nauka/Interperiodica".*

INTRODUCTION

Studying the processes of crystallization of the orthorhombic lysozyme modification, we have established that the kink density on the steps of this crystal is rather low and that the steps move via the formation of one-dimensional nuclei [1, 2]. We also studied the fluctuations in the step velocity [3] and established that the velocity is independent of the step length. This phenomenon is of special interest because it is inconsistent with the thermodynamic Gibbs–Thomson equation. Obviously, this phenomenon can be associated with the kinetics of the process [4]. It was expedient to verify whether the step velocity is really independent of the step length also on some other crystals.

Lysozyme, like other proteins, has a propensity to polymorphism and forms several modifications crystallizing under different chemical conditions within a narrow temperature range. Growth of the tetragonal and orthorhombic modifications has been studied in sufficient detail, whereas the mechanism and kinetics of crystallization of the monoclinic phase have not been studied as yet and, therefore, we selected this modification as the object of our study.

EXPERIMENTAL METHOD

The crystals were obtained from sixfold recrystallized lysozyme (Seikagaku, Japan) by the method described in detail in [5].

The approximately 1-mm-long crystals were well faceted (Fig. 1). According to [5], the unit-cell parameters of the crystals are a = 2.80 nm, b = 6.25 nm, c = 6.09 nm, $\beta = 90.8°$, $z = 4$, space group $P2_1$. The twofold axis coincides with the b-axis of the crystals.

The experiments were performed in a liquid cell of a Nanoscope-3 atomic-force microscope (Digital Instruments) in the contact mode using Si_3O_4 tips in the shape of tetrahedral pyramids with the angle at the vertex equal to 70°. The cantilever in the shape of an 100-μm-high isosceles triangle had a rigidity of 0.12 N/m. In order to obtain adequate images, we had to maintain a constant force applied to the tip (at a level of about 10^{-10} N). The temperature of the experiment was about 25°C. Because of a slight variation in the solution composition (in comparison with the composition recommended in [5]), the solubility curve suggested in [5] cannot be used, and, thus, we could not determine the supersaturation, but it remained constant during the whole experiment, which was confirmed by the constant average step velocity.

EXPERIMENTAL RESULTS

Morphology of a Growing Surface

It was rather easy to reveal the growth sources in the form of single and double spirals and also the Frank–Read sources on the (010) face (Fig. 2). In most of the cases, the step rise had an elementary height of 2.5 nm corresponding to the interplanar spacing d_{101}. The spirals had an almost rectangular shape, but the average distances between the spiral turns were different along four directions. Along one of the directions, the steps perpendicular to the b-axis were essentially rough. In

1063-7745/02/4705-0859$22.00 © 2002 MAIK "Nauka/Interperiodica"

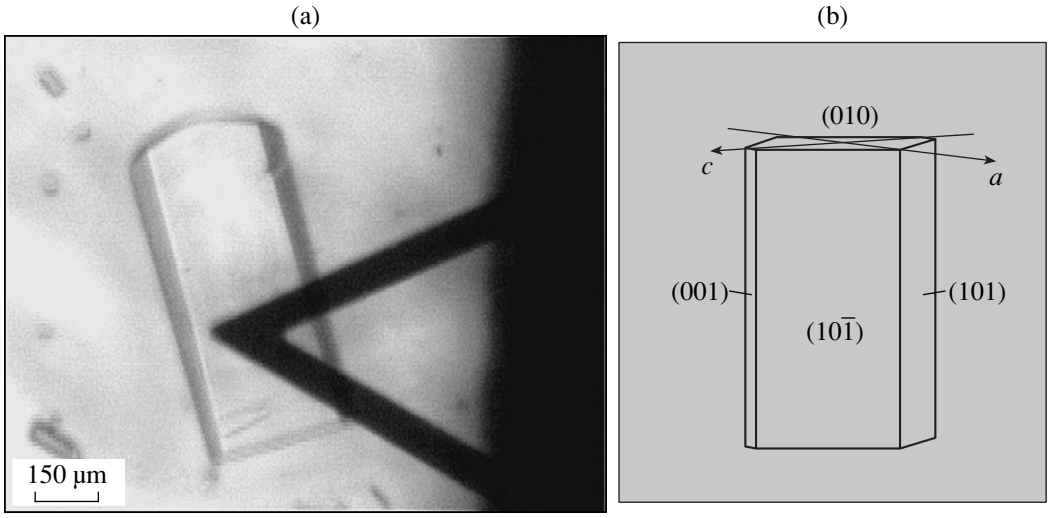

Fig. 1. (a) Photograph of a monoclinic lysozyme crystal in a liquid cell of an AFM; (b) crystal habit according to [5].

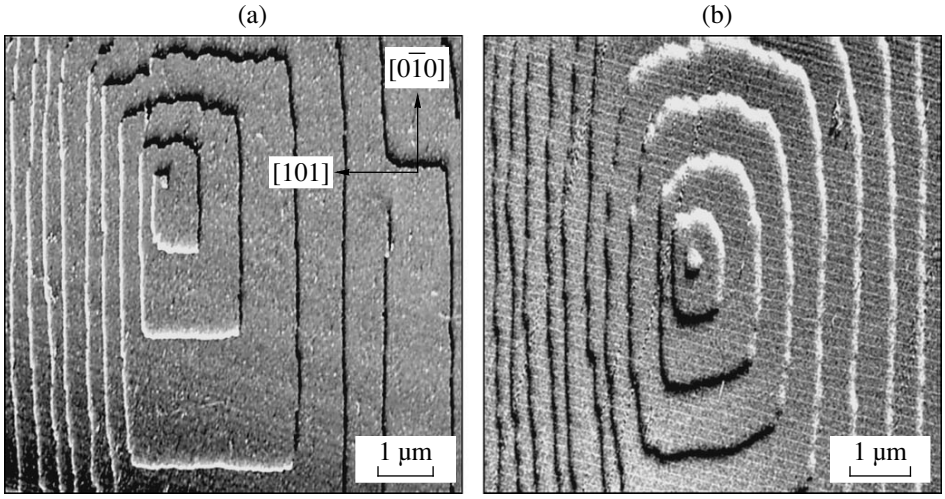

Fig. 2. AFM images of (a) a single spiral and (b) a Frank–Read source. The step shape in the second image is slightly distorted because of the smaller difference between the velocities of a step and a tip.

accordance with [5], this direction was taken to be the negative direction of the *b*-axis.

The image of a step parallel to the *b*-axis at a larger magnification is shown in Fig. 3. One can distinctly see the kinks whose depth (6.7 nm) corresponds to the unit-cell dimension along the [101] direction. Unlike the case of an orthorhombic crystal, there were almost no kinks of multiple or half depth. The number of the kinks is rather small and they are distributed nonuniformly. This pattern is typical of the step motion via the formation of one-dimensional nuclei [1, 6].

At a larger magnification, one can also see the molecular structure of the face (Fig. 4). The characteristic dimensions between the rows of the unit cells are consistent with the corresponding X-ray data. No surface reconstruction was revealed, although it cannot be excluded that the neighboring rows of the cells are somewhat shifted along the *b* axis.

Fluctuations in Step Velocity

Figure 5 shows the atomic-force microscopy image of two steps obtained in the mode of one-line scanning. In this mode, the slow motion of the AFM scanner is switched off, so that one can observe the changes in the position of a small (in our case, ~0.3-nm-long) step segment. Thus, it is possible to measure the time upon which the step starts moving forward or backward along the normal to itself (for one lattice parameter). Using a successive series of similar images, we recorded 150 attachment (86) and detachment (64) events. As a result of each event, the step moved forward or backward for one lattice parameter (6.7 nm). The step displacement x as a function of time t is shown

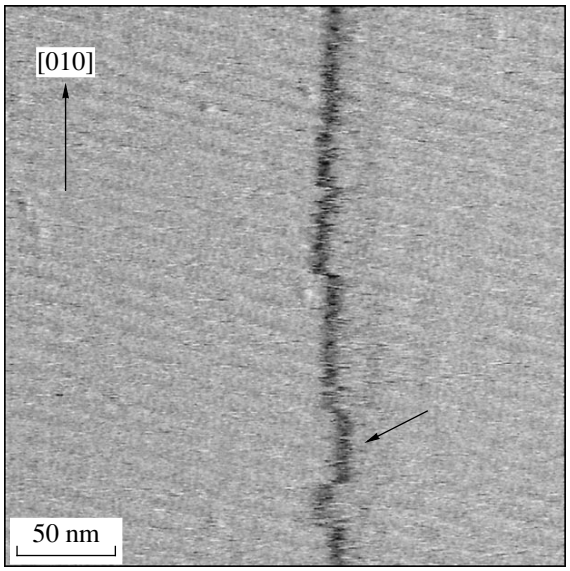

Fig. 3. The portion of a step of elementary height. The step moves slowly from left to right via the attachment of building blocks to the kinks and the formation and growth of one-dimensional nuclei. The arrows show a new row of the elementary cells of the step.

in Fig. 6 with the indication of the experimental values of step positions at different moments of time. The average slope of $x(t)$ is the average step velocity, v_{st} = 0.23 nm/s. In addition to the total increase of x with time, one can also see three plateaux in $x(t)$ with the centers at $t \approx 150$, 300, and 500 s (Fig. 6), which may correspond to the fluctuations of a kink in the vicinity of the scanning site. Then the average local slopes in the transition from one plateau to the following one would correspond to the kink velocity.

The average time interval between the kink arrival was 4.42 s. It should be noted that the average time of the appearance of a new unit cell upon its detachment was five times shorter than the average time of the remaining events (1.3 and 6.5 s, respectively). The forward motion of a step signifies the arrival of a new kink to the scanning site (line). Then, the fluctuation "retreat" of the kink immediately upon this "attack" would be immediately recorded. Each next attack is associated with the arrival of a new kink, which takes a longer time (of the order of the time necessary for a kink to pass the distance equal to the interkink distance on a step). This pattern seems to be formed only under noticeable supersaturations, because, in this case, the kink attack is more probable than its retreat.

The distribution function of the time of the new kink arrival (τ) follows from the lengths of the horizontal steps of the staircase (Fig. 6). It should characterize the distribution of the distances between the neighboring kinks (x) because $\tau = x/v$, where v is the kink velocity assumed to be constant. At a random kink distribution on a step, the probability $P(x)$ that a kink would be

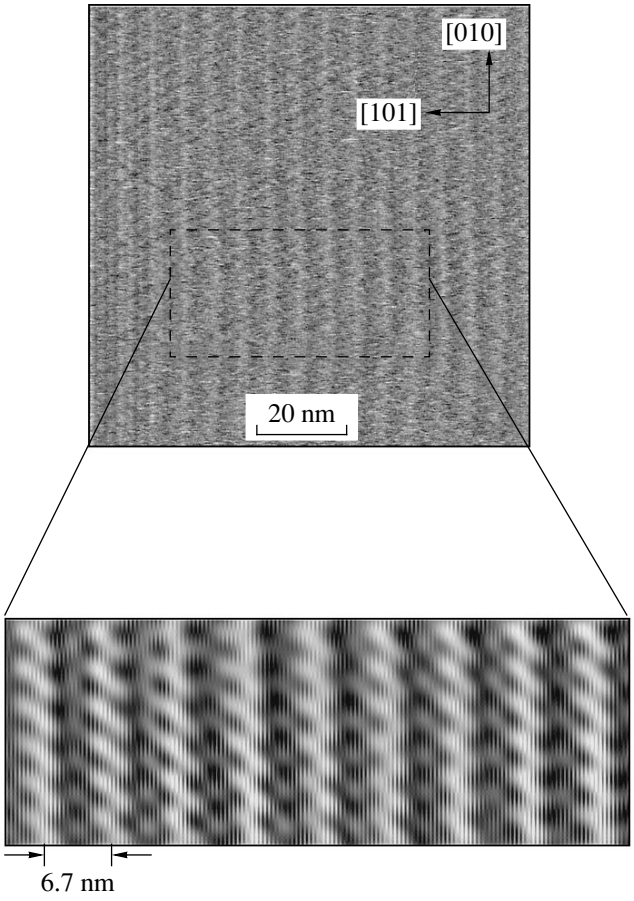

Fig. 4. The structure of the face at a high resolution. Below, a portion of the upper image filtered from noise by the Fourier method is shown; 512 scans, 30.5 Hz.

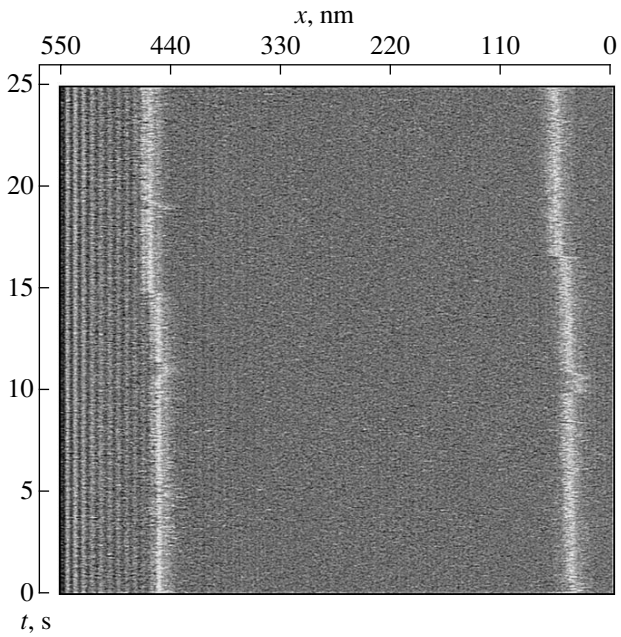

Fig. 5. The image of two steps parallel to the b-axis obtained in the one-row scanning mode. Kink depth 6.7 nm, 512 scans, 20.3 Hz.

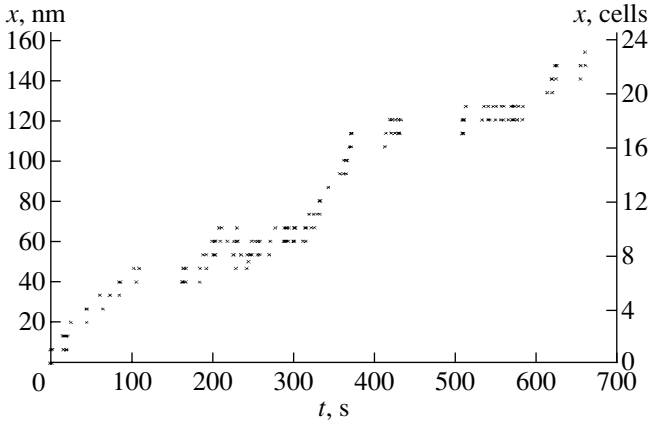

Fig. 6. The change in the position of the portion of a step with time. The origin of the coordinates system corresponds to the first attachment of a building block.

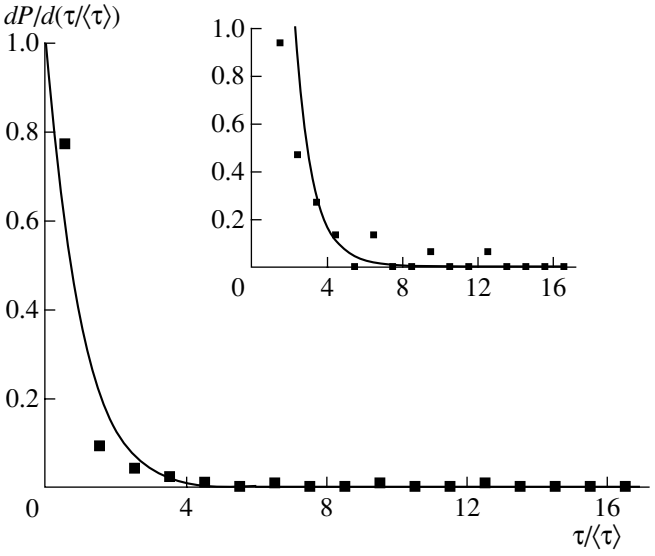

Fig. 7. The distribution function of the time of the kink arrival to the chosen step portion. The curve is exponential. In the inset: the range of small $dP/d(\tau/\langle\tau\rangle) = n/N\Delta$ values. Here n is the number of points in the corresponding range of $\tau/\langle\tau\rangle$ values ($\Delta = 1$); $N = 150$, $\langle\tau\rangle = 4.42$ s.

encountered in the vicinity of its neighbor at a distance ranging from x to $x + dx$ has the density

$$dP/d(x/\langle x\rangle) = \exp(-x/\langle x\rangle),$$

where $\langle x\rangle$ is the average interkink distance. The calculated probability density $dP/d(\tau/\langle\tau\rangle)$ as a function of $\tau/\langle\tau\rangle$ is shown in Fig. 7. It considerably differs from the exponential dependence, especially at high $\tau/\langle\tau\rangle$ values. This can be associated with both nonrandom kink distribution on the step and the dependence of the kink velocity on the distance from one kink to the neighboring one. Both factors could have been caused by impurities; however, we revealed no signs of impurity presence, which is also confirmed by the constant depth of all the kinks.

To analyze the fluctuations in the position of the step segment, we assumed, in the first approximation, that the step velocity was constant, $v_{st} = 0.23$ nm/s. The fluctuation-induced deviation of the step position from its average value δx depending on time t was calculated as the difference between the real step position at the moment t and the coordinate of the corresponding point on the line approximating the whole staircase (Fig. 6). Then, it became possible to construct the autocorrelation function of the dependence of $\langle(\delta x)^2\rangle$ on time in the form

$$\langle(\delta x)^2\rangle = \langle[\delta x(t) - \delta x(t + \Delta t)]^2\rangle. \quad (1)$$

Averaging was made over all the t values at the constant Δt. The data in Fig. 6 were approximated by the linear dependence insufficiently well, and, therefore, we limited the consideration to the maximum Δt value, $\Delta t = 8$ s. Expression (1) characterizes the change in the squared fluctuation amplitude of the step position for the time Δt. This dependence is shown on the double logarithmic scale in Fig. 8 and is described sufficiently well by a straight line whose slope calculated by the LS method equals 0.47 ± 0.01, i.e., is close to 0.5. Therefore, it was assumed that $\langle(\delta x)^2\rangle$ increases proportionally to the square root of time

$$\langle(\delta x)^2\rangle = (\chi t)^{1/2}. \quad (2)$$

The proportionality coefficient was determined as $\chi = 35.7$ nm^4/s $= 3.57 \times 10^{-27}$ cm^4/s. The proportionality of δx to the fourth-order root of time was predicted by Voronkov long ago [7] and was experimentally observed in KDP, the orthorhombic modification of lysozyme [3], and potassium hydrogen phthalate (KAP) [8]. Voronkov's theory allows one to determine a number of the fundamental parameters of crystallization from the χ value. We do not make these calculations here because it is still unclear what a building is block and what sizes it has, which is necessary for performing these calculations.

Formation of a Dislocation Spiral

To consider the formation of a perfect turn of the spiral in detail, it is necessary to obtain the largest possible number of images within the time necessary for the formation of one turn. This problem is far from simple, because the typical time necessary for taking one AFM image ranges from 30 to 50 s, whereas the time necessary for the formation of one spiral turn, even at low supersaturations, is of the order of 100 s [which corresponds to the rate of face growth of about 1 μm /day (24 h)]. At shorter times of image recording, the image quality and, thus, the measurement accuracy, are much lower. We obtained about 70 images reflecting the development of two turns of a spiral. The recording conditions were as follows. The frame dimensions were

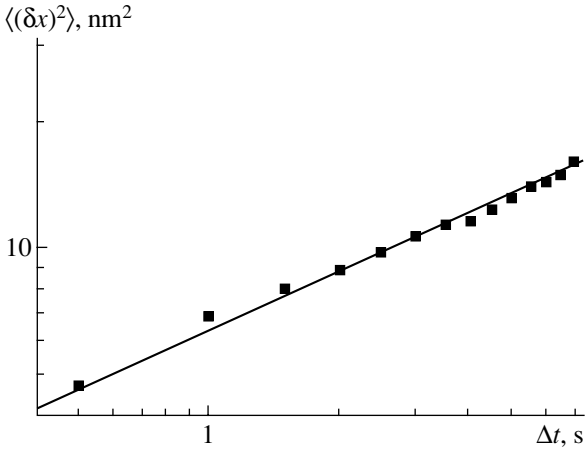

Fig. 8. Autocorrelation function (1) of the dependence of the mean squared fluctuations on time on a double logarithmic scale.

3.67×3.67 μm, the scanning frequency was 20.34 Hz, and the number of scans was 128 (we recorded only half of the frame). As a result, the total time necessary for recording one image was 3.147 s, and the accuracy of measuring the distances (a recording step) was 28.7 nm. Although the velocity of a measuring tip was 100 times higher than the step velocity, we observed a slight change (<5°) in their orientations in the upward or downward scanning, and, therefore, only half of all the images scanned along one direction were measured. Figure 9 shows nine frames characterizing the formation of one turn of a spiral. The step and all its segments shown in this figure are of the same height. One of the frames in Fig. 9 shows the numbering of the step segments.

Considering Fig. 9, one has to pay attention to the following facts. The distances between the turns are not the same, which is clearly seen from the positions of the first segments of different turns. The segments of the first and third orientations are not rigorously rectilinear, and large kinks on these segments in different frames are located in different sites. The segments of the second orientation are extremely curved. One can see the extended protrusions and hollows on these segments. As a rule, the angles formed by the adjacent segments are rounded off. In the vicinity of the dislocation outcrop, where the segment lengths are rather small, this results in the fact that the length of the rectilinear portion of the segment is considerably less than the length of the segment itself.

More details on the formation of a new spiral turn can be obtained from Fig. 10. To construct this figure, we measured the lengths of all the segments during the time necessary for the formation of two spiral turns. This is only a scheme, because it does not reflect the deviations of the segments from the rectilinear shape clearly seen in Fig. 9. Each newly formed step segment first increases in length due to the motion of the neighboring segment, but it is not displaced as a whole along the normal to itself. Only upon the attainment of a certain critical length does the new segment start moving itself. This is the moment of the beginning of the forma-

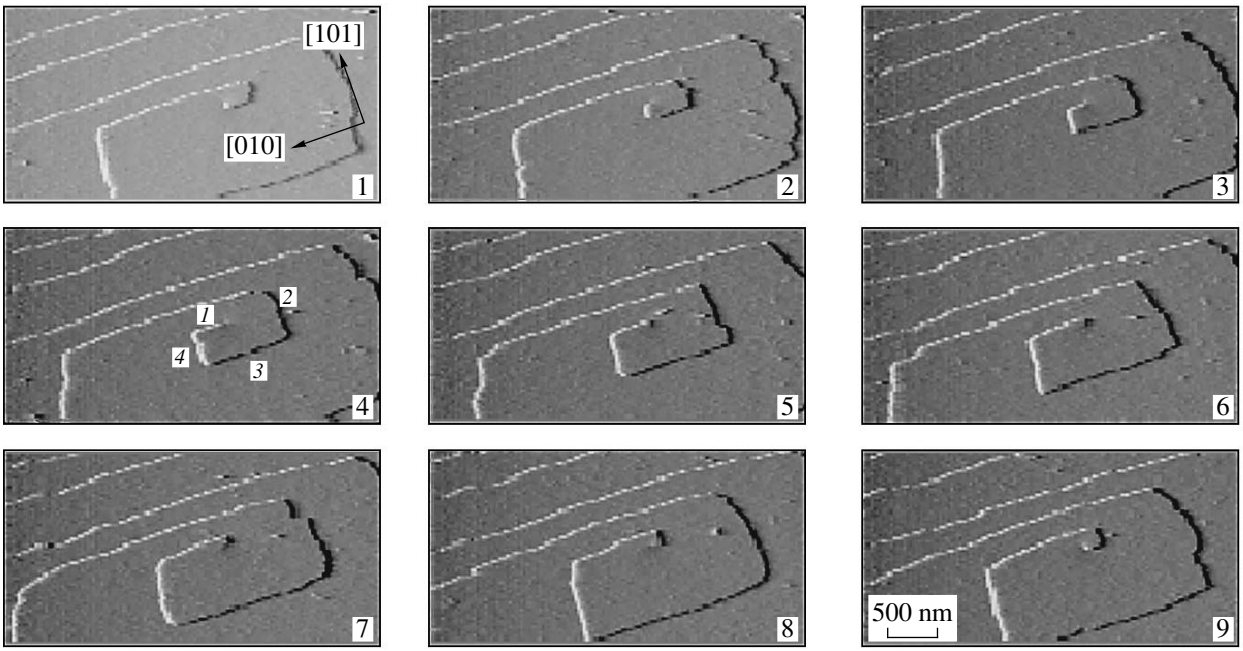

Fig. 9. The successive AFM images illustrating the formation of a new turn of a spiral. The time between the frames is 12.6 s. Light and dark squares at the step ends reflect the discreteness of image recording. The first segment appears in the time interval between frames 2 and 3; the second, between frames 6 and 7; the third, between frames 7 and 8; and the forth, between frames 1 and 9.

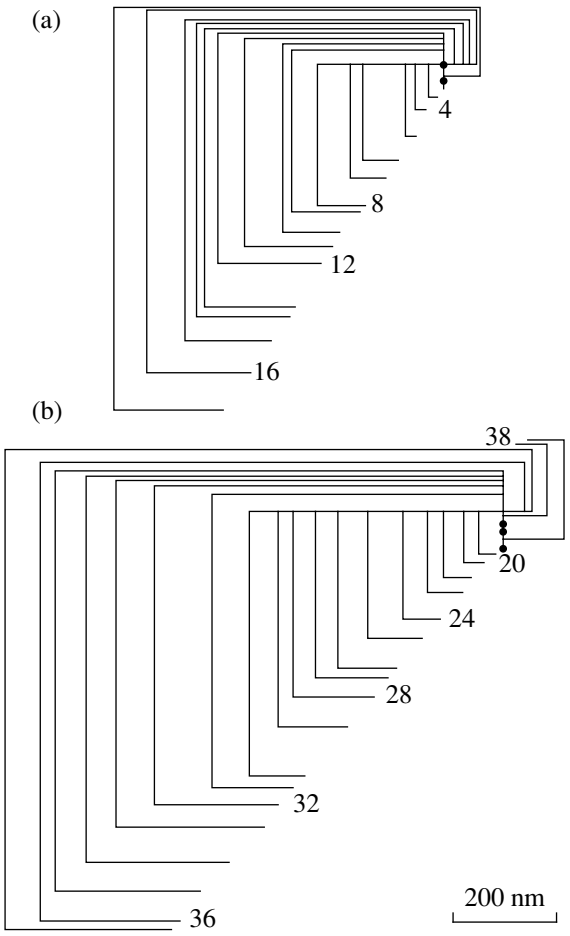

Fig. 10. The step motion during the formation of (a) the first and (b) the second turns of the spiral. The time interval between the neighboring step positions is 6.29 s. The figure is drawn by using the segment length measured with an accuracy of ±20 nm from 39 successive images of the spiral. Position 17 relates to the second turn, positions 37–39, to the third. The numbers of nine frames in Fig. 9 correspond to odd numbers from 3 to 19.

tion of another segment. When the latter attains its critical value and starts moving, the velocity of the lengthening of the first segment also increases, because now it is determined by the displacements of two neighboring segments. This process can be described in the following way. Denote the length of the segments and their average velocity as l_i and v_i, respectively, where $i = 1, 2, 3, 4$, in full accordance with the segment enumeration in Fig. 9, $l_{c,i}$ is the critical length, and t is the time. Then, we have $l_{i-1} < l_{c,i-1}$, $l_i = dl_i/dt = 0$; at $l_{i+1} < l_{c,i+1}$ $dl_i/dt = v_{i-1}$; at $l_{i+1} > l_{c,i+1}$ $dl_i/dt = v_{i-1} + v_{i+1}$; at $l_{i+1} = 0$ $l_i = l_{c,i}$.

The subscript $i - 1$ at $i = 1$ corresponds to segment 4 of the previous turn, and the subscript $i + 1$ at $i = 4$, to segment 1 of the following turn.

Using this characteristic fact, we measured the values of $l_{c,i}$ and v_i for two successive turns of the spiral from the images shown in Figs. 10a and 10b.

Segment, i	4	1	2	3
		First turn		
$l_{c,i}$, nm	60	300	70	75
v_i, nm/s	7.8	2.4	3.4	6.4
		Second turn		
$l_{c,i}$, nm	75	505	75	75
v_i, nm/s	7.6	2.4	5.4	7.6

As we can see, the critical length of the first segment became considerably larger at the second turn, with the critical lengths of the remaining segments being constant within the accuracy of our measurements. The velocity is changed only slightly and in an irregular way: it increases for segments 2 and 3 and remains practically constant for segments 1 and 4. It should be indicated that the first turn was formed for 94.5 ± 1.5 s, the second one, for 135 ± 1.5 s. Such a pronounced increase in the growth time of one spiral turn is associated mainly with an increase in the critical length of the first segment and, thus, requires more time for its formation. The turn started growing with the appearance of segment 4. Measuring the time from the appearance of another segment, we obtain different values: from the appearance of the first one, 104 s; from the appearance of the third, 142 s. This result is explained by the occurrence of fluctuations in $l_{c,i}$ and v_i, and, therefore, the time necessary for the formation of the same segment of the critical length is different for different spiral turns.

Considering Fig. 10, one can notice that the first range of the distances between the successive positions of mutually parallel segments is not less than the others. This signifies that even at a slight increase in the segment length above its critical value, its velocity is not less than at the pronounced segment length. In other words, the segment velocity is independent of its length. This conclusion is confirmed by a simple calculation. If the segment acquires a constant velocity immediately upon the attainment of the critical length, the spiral turn is formed for the time

$$T = l_{c4}/v_3 + l_{c1}/v_4 + l_{c2}/v_1 + l_{c3}/v_2.$$

Substituting the values obtained for the first turn into the above expression, we obtain $T = 97.2$ s, i.e., the time which practically coincides with the real time of the formation of this turn. This time would have been considerably longer if, with an increase in l/l_c, the velocity had gradually increased from zero to a certain constant value in accordance with the thermodynamic Gibbs–Thomson equation.

DISCUSSION

The ideas about the formation of a polygonal dislocation spiral at low kink density that were developed in [9] were based on the fact that a segment whose length

equals the length of the side of a two-dimensional critical nucleus has only a small rectilinear portion, because the angles of the critical nucleus should be rounded off. If the length of this portion is comparable with the average interkink distance, it may have no kinks at all for quite a long time. With an increase in the length of such a segment, it is the rectilinear portion that starts determining its velocity. It was shown [9] that, in this case, even a slight increase in l above l_c can drastically increase both the length and velocity of the rectilinear portion.

However, the analysis performed in [7, 9] is essentially based on the assumption that there is dynamic equilibrium between the rectilinear portion of the step and its environment. Meanwhile, the attainment of such an equilibrium requires sufficient time for the diffusion exchange of the kinks between the opposite ends of the rectilinear portion. This is the only mechanism which can let one end of a finite segment know about the existence of another, in other words, the mechanism relating the segment velocity with its length.

The exchange of the kinks between the segment ends requires that the kink that was detached from one segment end diffuse along the segment either to reach the other end or to encounter somewhere a kink of the opposite sign detached from the opposite end. The annihilation of these kinks provides the gain in the linear energy during dissolution of a short step in the solution with concentration equilibrium with respect to the kink (infinitely large crystal), because the time for kink diffusion along the rectilinear segment in equilibrium is unlimited. In a supersaturated solution, the situation is different. The segment ends "communicate" via kink annihilation only if the segment length is less than the length of a one-dimensional nucleus (the fluctuation length of the kink [6]) $l < 2b/s$. Here, $b = 6.25$ nm is the distance between the building blocks and s is the supersaturation. Thus, this situation is possible only under low supersaturations $s < 2b/l$ (≈10% for l of the order of 100 nm). The supersaturation in the experiments described above was unknown, but, using the analogy with orthorhombic lysozyme, where at a step velocity of about 2 nm/s $s = 170\%$ [4], the supersaturation would be considerably higher than 10%. In this situation, the Gibbs–Thomson equation is hardly applicable. Therefore, we believe that the critical segment length with a low kink density is determined not by the thermodynamics but rather by the kinetics of the attainment of the steady-state kink density.

It can be seen from Fig. 9 that, unlike other segments, the first one acquires a rather extended rectilinear portion upon the attainment of the critical length. The critical length of the first segment seems to be so large because it has no kinks at all. The pronounced fluctuations in the kink number on the first segment considered above should inevitably follow from the random changes in its critical length during the formation of the successive turns of the spiral. Therefore, even under a constant supersaturation (and constant v_i), the time necessary for the formation of a spiral turn would vary and change the distance between the turns equal to Tv_i, which was confirmed experimentally.

The fast attainment of a constant velocity under a small excess of the critical length of the segments is explained by the fast attainment of the steady-state (although fluctuating) kink density. Unfortunately, the calculations of the duration of the period of nonstationarity as a function of the length of one end of the segment fixed at the point of the dislocation outcrop, the rate of the kink formation, and the velocity of their motion have not yet been completed. The dependence of the segment velocity on its length should exist in any case, but its detailed study requires new experiments at different known supersaturations. Moreover, one cannot completely exclude the possibility that the end of a growing step can have a structure that differs from the structure of a step growing in the steady-state mode.

The experimentally observed fluctuations in the velocity of segments and their shape could have been explained by the effect of impurities, but, as has already been indicated, the experiment gave no grounds for this explanation. We assume that these phenomena are associated rather with the low fluctuating kink density on the steps.

CONCLUSION

Growth of the most developed (101) face of monoclinic lysozyme has been studied by the *in situ* AFM method under a constant supersaturation. The morphology of the face is described at both a high and low resolution. We observed fluctuations in the step velocity also at the stage of formation of the dislocation spiral. Two results seem to be important.

The portions of the steps move alternatively in the backward and forward directions. Fluctuations increase with time according to the law $[\langle(\delta x)^2\rangle]^{1/2} \approx (t)^{1/4}$. Along with KDP, KAP, and orthorhombic lysozyme, this law has already been established on the fourth (monoclinic lysozyme) crystal. The law is common for both low- and high-molecular compounds and is valid at a low and high kink density on the steps.

In formation of a dislocation spiral, the critical length of the segment with a low kink density, upon the attainment of which the segment starts moving, is determined not by the thermodynamics, but rather by the kinetics of the attainment of the stationary kink density on the segment. The segment is immobile unless it acquires kinks. Fluctuations in the kink densities result in differences in the critical lengths, variations in the time necessary for the formation of a spiral turn, and the distance between its turns even under low supersaturations.

ACKNOWLEDGMENTS

This study was supported by the Russian Foundation for Basic Research, project no. 00-02-016701 and NASA, project no. NAG8-3556.

REFERENCES

1. L. N. Rashkovich, N. V. Gvozdev, and I. V. Yaminskiĭ, Kristallografiya **43** (4), 745 (1998) [Crystallogr. Rep. **43**, 696 (1998)].
2. A. A. Chernov, L. N. Rashkovich, I. V. Yaminski, and N. V. Gvozdev, J. Phys.: Condens. Matter **11**, 9969 (1999).
3. L. N. Rashkovich, T. G. Chernevich, N. V. Gvozdev, *et al.*, Surf. Sci. Lett. **492**, L717 (2001).
4. L. N. Rashkovich, N. V. Gvozdev, M. I. Sil'nikova, *et al.*, Kristallografiya **46**, 934 (2001) [Crystallogr. Rep. **46**, 860 (2001)].
5. H. Hondon, G. Sazaki, S. Miyashita, *et al.*, Cryst. Growth Des. **1**, 327 (2001).
6. V. V. Voronkov, Kristallografiya **15** (1), 13 (1970) [Sov. Phys. Crystallogr. **15,** 8 (1970)].
7. V. V. Voronkov, in *Crystals*, Vol. 9: *Modern Theory of Crystal Growth I*, Ed. by A. A. Chernov and H. Müller-Krumbhaar (Springer-Verlag, Berlin, 1983), pp. 74–111.
8. L. N. Rashkovich, E. V. Petrova, O. A. Shustin, and T. G. Chernevich, Fiz. Tverd. Tela (St. Petersburg) (2002) (in press) [Phys. Solid State (2002) (in press)].
9. V. V. Voronkov, Kristallografiya **18** (1), 32 (1973) [Sov. Phys. Crystallogr. **18**, 19 (1973)].

Translated by L. Man

Crystallography Reports, Vol. 47, No. 5, 2002, pp. 867–870. Translated from Kristallografiya, Vol. 47, No. 5, 2002, pp. 933–936.

CRYSTAL GROWTH

Analysis of the Kinetics of Crystal Growth and Epitaxy in the Framework of the Multilayer Model of Mass Crystallization

A. M. Ovrutsky and O. A. Posylaeva

Dnepropetrovsk National University, Naukovy per. 13, Dnepropetrovsk, 49050 Ukraine
e-mail: metal@ff.dsu.dp.ua
e-mail: olya_pos@mail.ru

Received October 5, 2001; in final form, January 23, 2002

Abstract—The method for calculating the kinetics of crystal growth and epitaxy based on the two-dimensional model of the mass crystallization in many atomic layers has been developed. The kinetics of crystal growth is analyzed with due regard for the initial (critical) size of two-dimensional nuclei, the dependence of the growth rate of two-dimensional nuclei on their size, and the non-steady-state frequency of the formation of two-dimensional nuclei. The effect of characteristic parameters of crystallization on the kinetics of formation of epitaxial films and structure is also studied. © *2002 MAIK "Nauka/Interperiodica".*

Two-dimensional nucleation is the major mechanism of growth of atomically smooth crystal surfaces at rather high relative supersaturations $\sigma = \Delta\mu/kT$ ($\Delta\mu$ is the difference between the chemical potentials of the phases, k is the Boltzmann constant, and T is the temperature). Under such conditions, the multiple formation and growth of two-dimensional nuclei in the growing atomic layers take place; in other words, two-dimensional mass crystallization occurs almost in each layer. The simplest and the most elegant solution of the problem of three-dimensional crystallization was found by Johnson and Mehl [1]. In the particular case of spherical nuclei, this solution coincides with a more accurate solution obtained by Kolmogorov [2, 3]. Epitaxial growth in microscopic areas can proceed by the mechanism of two-dimensional nucleation even under rather low supersaturations if these areas have no defects providing the formation of steps. Liquid-phase epitaxial growth proceeds at rather high supersaturations [4]. The processes of epitaxial growth are quite complicated, and, therefore, their theoretical study is currently performed by modeling [5]. The approximations necessary for the analytical solution of this problem are considered in [3], where it is also indicated that, in fact, one can readily take into account anchoring when analyzing multilayer epitaxial growth.

Theoretical estimates of the growth rate for a crystal growing by the mechanism of two-dimensional nucleation were made only for very low or rather high supersaturations. Under low supersaturations, we have [6]

$$V_{\mathrm{I}} = (L^2/a^3)\beta\sigma^{1/2}\exp(a\gamma^2/\sigma), \qquad (1)$$

where L^2 is the face area, a is the crystal-lattice parameter, β is the kinetic coefficient for a straight step ($V_{\mathrm{st}} = \beta\sigma$ is the growth rate of a straight step), and γ is the free energy of the step edge per atom in the kT units. At high supersaturations, we have

$$V_{\mathrm{II}} = \beta\sigma^{5/6}\exp(a\gamma^2/3\sigma). \qquad (2)$$

Equation (1) corresponds to the kinetic mode of crystal growth in which there is almost no nucleation and the supersaturation is almost constant over the whole crystal surface. In multiple nucleation, σ is the local surface supersaturation. However, in the case of growth from melt or vapor, the supersaturation above the crystal surface can be more or less uniform. Equation (2) does not take into account the competition between various growth centers (the "multihead" growth [6]) and their possible mergure.

To describe crystal growth, we invoked the Johnson and Mehl idea [1] of the elimination of the fictitious part of the increment of the crystalline phase. The two-dimensional nuclei arise and grow in many atomic layers (Fig. 1). First, we assume that nucleation can occur at any point of the given layer even if the corresponding portion has already been crystallized. Calculating the increment of the crystalline phase within the given time interval, we eliminate the increments due to fictitious nuclei and the regions where the non-fictitious centers overlap (white regions in Fig. 1).

The number of two-dimensional centers of crystallization per unit area formed in the zth layer within the time interval $[t_k - j\Delta t,\ t_k - (j-1)\Delta t]$ is equal to $I_z\Delta t$ (t_k is the current moment of time, $1 \le j \le k$, Δt is a small time step such that its decrease produces almost no effect on the calculated results). Here $I_z = I_0\exp(-\tau/t)$ is the non-steady-state rate of two-dimensional nucleation [7] (τ is the characteristic time of the non-steady-

1063-7745/02/4705-0867$22.00

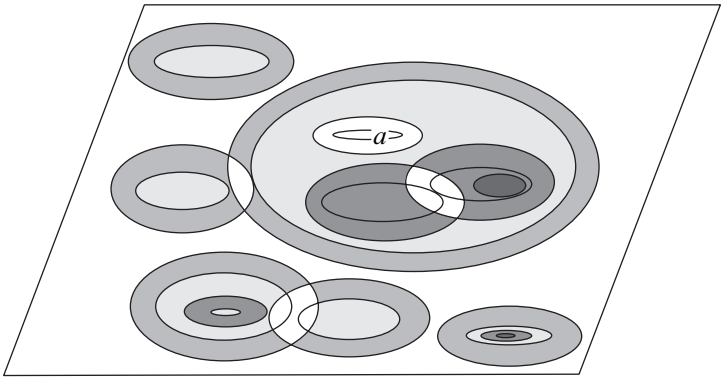

Fig. 1. Schematic illustration of the Mehl–Johnson model of multilayer crystallization; *a* is a fictitious nucleus.

state process, t is the time passed from the onset of crystallization in the given layer), and $I_0 = (1/a)^3\beta\sigma^{1/2} \times \exp(-\pi\gamma^2/\sigma)$ is the steady-state nucleation rate [4]. An increase in the area of all crystallization centers in the zth layer $\Delta Q_{z,k}$ for the face area ($L^2 = 1$) within the time interval $[t_k - \Delta t, t_k]$ can be written as

$$\Delta Q_{z,k} = (Q_{z-1,k-1} - Q_{z,k-1})Q_{z-1,k-1} \times \sum_{j=1}^{k-1} I_z(t_j)\Delta t 2\pi r_{k-j}\Delta r_{k-j}, \quad (3)$$

where $Q_{z,k}$ is the fraction of the crystalline phase in the zth layer at time moment t_k, r_{k-j} is the radius of the crystallization center formed earlier within the time interval ranging from t_{k-j-1} to t_{k-j}. To calculate the dependence of the size of crystallization centers on time, we used the relationship for the growth rate of a curved step reported in [8]. The increments in their radii were determined with due regard for the Gibbs–Thomson shift with respect to supersaturation as $\Delta r_i = \beta\sigma(1 - r^*/r_{i-1})\Delta t$, where $1 \le i \le k$, $r^* = a\gamma/\sigma$. The initial size r_0 of the crystallization center was assumed to be equal to $r_0 = r^* + \delta r$, where $\delta r = a(\pi\sigma)^{-1/2}$ is the addition that reduces the free energy of nucleation by kT. The factor $(Q_{z-1,k-1} - Q_{z,k-1})$ implies the elimination of the fictitious increments in the areas of the crystallization centers (including fictitious nuclei). The factor $Q_{z-1,k-1}$ takes into account the whole two-dimensional volume assessable for crystallization. The increments in the fraction of the crystalline phase, $\Delta Q_{z,k}$, in Eq. (3) should be summed over all the time intervals $[t_k - \Delta t, t_k]$ up to the moment of time under consideration. The subsequent summation of all the obtained Q_z values over all the layers yields the total amount of the crystalline phase Q as the conditional number of the fully occupied atomic layers.

It is very difficult to take into account the rate of non-steady-state nucleation for two-dimensional centers of crystallization. For the first layer, time t in the formula of nucleation rate (see above) indicates the time passed from the onset of crystallization. However, clusters in the following layers can start forming only upon the appearance of the crystalline phase in the lower layer. To find the self-consistent solutions in the mode of steady-state nucleation, we assumed that t is half the average time t_{av} of existence of each portion of the surface uncovered with the next layer. This time was chosen based on several solutions in such a way that the desired solution would yield the same result $t_{av} = a/V$ (V is the determined growth rate). The nonstationarity time τ was determined as the time necessary for the attainment of such a size distribution for clusters whose average size $n_{av} = \langle n^2\rangle^{1/2}$ would correspond to the equilibrium nucleus-size distribution. Thus, we have $\tau \cong \langle n^2\rangle/2B(n_{av}/2)$, where $B(n_{av}/2)$ is the diffusion coefficient corresponding to random walks of nuclei in the size space. With due regard for the analysis performed in [9], we found that $B(n_{av}/2) = (\pi n_{av}/2)^{1/2}\beta/a$. The initial stages of epitaxy were analyzed in the approximation of the steady-state rate of nucleation.

At constant nucleation, $I = I_0$, and growth rates $V = V_{st}$ ($r_0 = 0$), our calculations for a single layer agree quite well with the analytical solution of the two-dimensional problem of mass crystallization obtained by the Mehl–Johnson method, $Q = 1 - \exp(-t^3/\tau_m^3)$, $\tau_m = (\pi V^2 I_0/3)^{-1/3}$ (see curve *1* in Fig. 2). Curves *2* and *3* in Fig. 2 illustrate the time dependence of Q for an infinite number of layers. Curve *2* was calculated for a steady-state nucleation rate of two-dimensional nuclei and a constant rate of their growth. Curve *3* was obtained for nuclei with due regard for the dependence of their growth rate on size. The parameters used in the calculations, $\gamma = 0.5$ and $\beta = 0.1$ m/s, are typical of the crystallization from melt. The curves are plotted versus normalized time t/τ_m ($\tau_m = 1.7 \times 10^{-6}$ s). The growth rate can be determined from the curve slopes. If the growth rate is constant, the structure of the interphase boundary ceases to change; in other words, the continuous crystalline film has already been formed. In our solutions obtained at different parameters β and γ ($\beta = 0.05$

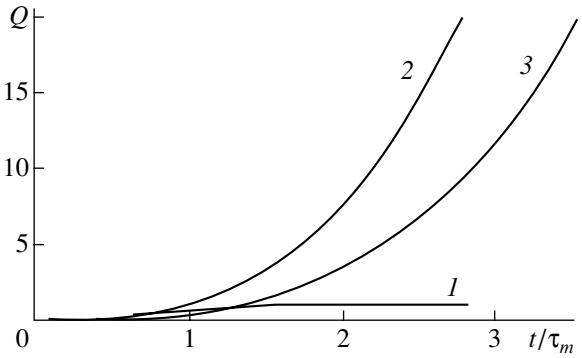

Fig. 2. Total amount of the crystallized phase versus normalized time at $\gamma = 0.5$, $\beta = 0.1$ m/s, and $\sigma = 0.08$: (*1*) calculations for a single layer; (*2*, *3*) unlimited number of layers at (*2*) $I = I_0$ and $V = V_{st}$ and (*3*) $I = I_0$ and $V = V_{st}(1 - r^*/r)$.

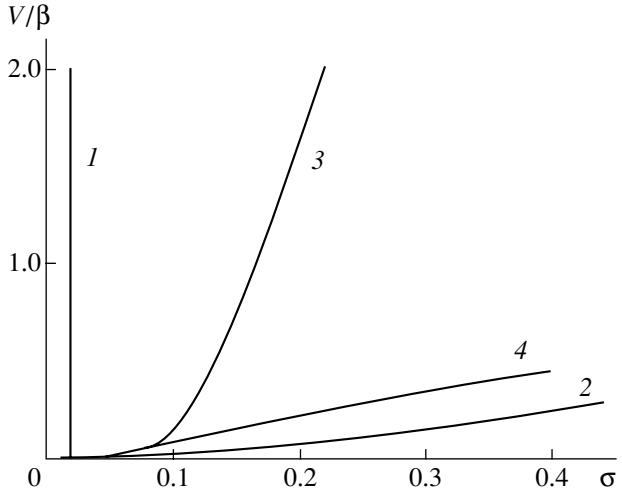

Fig. 3. Crystallization rate versus supersaturation. (*1*) According to (1); (*2*) according to (2); (*3*, *4*) numerical results: (*3*—steady-state nucleation rate ($I = I_0$), *4*—$I = I_0\exp(-\tau/t)$).

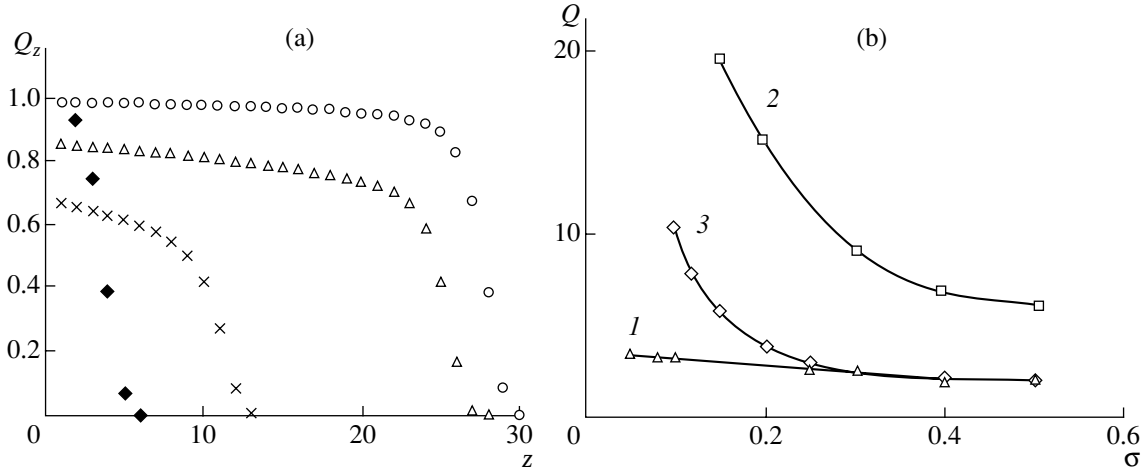

Fig. 4. (a) Relative filling of a layer with the crystalline phase as a function of layer number and (b) total amount of the crystallized phase as a function of supersaturation: ◆ homoepitaxy, $Q_1 = 0.99$ and $\sigma = 0.05$; □ epitaxy, $Q_1 = 0.99$ and $\sigma = 0.30$; △ epitaxy, $Q_1 = 0.90$ and $\sigma = 0.15$; × epitaxy, $Q_1 = 0.67$ and $\sigma = 0.15$; (*1*) homoepitaxy, $Q_1 = 0.99$; (*2*) epitaxy, $Q_1 = 0.90$; (*3*) epitaxy, $Q_1 = 0.67$. For homoepitaxy, $\gamma_1 = \gamma_2 = 0.5$, $\beta_1 = \beta_2 = 10$ cm/s; for epitaxy, $\gamma_1 = 0.6$, $\gamma_2 = 0.5$, $\beta_1 = 5$ cm/s, and $\beta_2 = 10$ cm/s.

and 0.10 m/s, $\gamma = 0.5$, 0.6, 0.8. and 1.0) and different supersaturations σ ($\sigma = 0.15$–0.40), the constant rate was observed at $Q = 25$–35.

The plots of growth rate versus supersaturation are shown in Fig. 3 at $\beta = 0.1$ m/s and $\gamma = 0.5$. Curves *1* and *2* correspond to the analytical Eqs. (1) and (2). Curve *3* was obtained by our method at $I = I_0$ and curve *4*, with allowance for the non-steady-state behavior of the rate of two-dimensional nucleation. It can be seen that curve *3* (in the steady-state approximation) is located above curve *2*, because we took into account the initial size of two-dimensional nuclei and the contribution from the sideward growth of the crystallization centers (Eq. (2) was derived in the approximation of a single growth center). The additional allowance for the non-steady-state processes considerably reduce the growth rate, so that curve *4* approaches curve *2*.

The variations in the kinetic coefficient do not affect the $Q(t/\tau_m)$ curves because the increments ΔQ_z in Eq. (3) are proportional to β and $\tau_m \approx 1/\beta$. On the conventional time scale, the growth rate is proportional to β. An increase in the edge energy γ affects $Q(t/\tau_m)$ curves in the same way as the lowering of supersaturation.

In our calculations of epitaxy, we assumed that the free edge energy of the steps in the first layer (γ_1) is slightly higher than that for the subsequent ones (γ_2)

and that the threshold supersaturation (below which no growth is observed) is always overestimated. The expectation time of the appearance of the crystalline phase (the characteristic time τ_m for the first layer is longer than for the subsequent layers) also increases. The distributions of the fraction of the crystalline phase (Q_z) over atomic layers are quite different in epitaxy and homoepitaxy ($\gamma_1 = \gamma_2$). In epitaxy, $\gamma_1 > \gamma_2$ and, at relatively low supersaturations, the total amount of the crystalline phase is practically proportional to the filling of the first layer for quite a long period of time. This indicates the formation of three-dimensional crystals and the absence of a continuous film.

Figure 4a shows several Q_z–$Q(z)$ curves for epitaxy and homoepitaxy at the given filling of the first layer. The total amount of the crystalline phase at moments when the filling of the first layer attains the given value (0.67, 0.90, 0.99) as a function of supersaturation is shown in Fig. 4b. The number of atomic layers corresponding to the most dramatic decrease in Q_z is associated with the phase-boundary width, which is relatively small (3–5 layers) and depends on supersaturation. These data show that the formation of continuous films in epitaxy takes more time so that such a film can be formed only at considerable thicknesses of the coating. At relatively low supersaturations, no continuous film can be obtained at all (in growth by the mechanism of two-dimensional nucleation).

The above approach to the description of crystal-growth kinetics and epitaxy is advantageous because it allows one to take into account all the characteristic features of the growth mechanism and the substrate properties. The method allows one to calculate the growth kinetics at any supersaturations and at all the values of the parameters β and γ related to the atomic structure of the crystal surface. In epitaxy, one can also calculate the structural parameters of the films depending on the crystallization conditions. The computer programs designed based on Delphi and Mathcad packages can also be used for mixed growth mechanisms by taking into account the contribution made by dislocation-like growth centers.

REFERENCES

1. W. A. Johnson and R. F. Mehl, Trans. Am. Inst. Min., Metall. Pet. Eng. **135**, 416 (1939).
2. A. N. Kolmogorov, Izv. Akad. Nauk SSSR, Ser. Mat., No. 3, 355 (1937).
3. V. Z. Belen'kiĭ, *Geometric–Probabilistic Models of Crystallization* (Nauka, Moscow, 1980).
4. L. V. Abramov, N. G. Deryagin, M. G. Mil'vidsky, *et al.*, Kristallografiya **40** (6), 906 (1995) [Crystallogr. Rep. **40**, 840 (1995)].
5. P. Schulze and E. Weinan, J. Cryst. Growth **222**, 414 (2001).
6. A. A. Chernov, in *Modern Crystallography*, Vol. 3: *Crystal Growth*, Ed. by B. K. Vainshtein, A. A. Chernov, and L. A. Shuvalov (Nauka, Moscow, 1980; Springer-Verlag, Berlin, 1984).
7. Ya. B. Zel'dovich, Zh. Éksp. Teor. Fiz. **12**, 565 (1940).
8. W. K. Burton, N. Cabrera, and F. C. Frank, Philos. Trans. R. Soc. London, Ser. A **243**, 299 (1951).
9. V. V. Voronkov, Kristallografiya **15** (6), 1120 (1970) [Sov. Phys. Crystallogr. **15**, 979 (1970)].

Translated by K. Kugel

Crystallography Reports, Vol. 47, No. 5, 2002, pp. 871–878. Translated from Kristallografiya, Vol. 47, No. 5, 2002, pp. 937–944.

CRYSTAL GROWTH

Growth of Single Crystals of NaH_2PO_4 (NaDP), $NaH_2PO_4 \cdot H_2O$ ($NaDP \cdot H_2O$), and $NaH_2PO_4 \cdot 2H_2O$ ($NaDP \cdot 2H_2O$) Sodium Dihydrogenphosphate Based on the Analysis of the Na_2O–P_2O_5–H_2O Phase Diagram

L. V. Soboleva and A. É. Voloshin

Shubnikov Institute of Crystallography, Russian Academy of Sciences, Leninskiĭ pr. 59, Moscow, 117333 Russia

e-mail: labsol@ns.crys.ras.ru

Received March 12, 2001; in final form, April 15, 2002

Abstract—The crystallization conditions for the NaH_2PO_4, $NaH_2PO_4 \cdot H_2O$, and $NaH_2PO_4 \cdot 2H_2O$ solid phases have been established from the analysis of the phase diagram of solubility of the ternary Na_2O–P_2O_5–H_2O system in the temperature range from 0 to 100°C. Based on these data, the methods for growing sodium dihydrogenphosphate single crystals of the above compositions are developed. The initial components for preparing mother solutions were H_3PO_4 and NaOH solutions taken in certain weight ratios. For the first time, NaDP, $NaDP \cdot H_2O$, and $NaDP \cdot 2H_2O$ single crystals were grown on a seed by the method of temperature decrease. The habits of the NaDP and $NaDP \cdot H_2O$ single crystals are determined. *© 2002 MAIK "Nauka/Interperiodica".*

INTRODUCTION

The growth and study of the properties of potassium, rubidium, cesium, and ammonium dihydrogenphosphates single crystals are considered in numerous publications. These crystals, which possess valuable physical properties, are widely used in laser technology as elements for control of modulator beams and optical shutters for generating giant light pulses in solid-state lasers, orthogonal switchers of light polarization, discrete light deflectors, and nonlinear frequency transducers (up to the fourth harmonic). However, there is no published data on the growth of sodium dihydrogenphosphate single crystals of the compositions NaDP, $NaDP \cdot H_2O$, and $NaDP \cdot 2H_2O$. The synthesis of these crystals seems to be very interesting both for practice and also for studying the characteristics of the variations of their properties in the homologous series of alkali metal dihydrogenphosphates.

The present study was aimed at developing methods of growing sodium dihydrogenphosphates crystals and the synthesis of NaH_2PO_4, $NaH_2PO_4 \cdot H_2O$, and $NaH_2PO_4 \cdot 2H_2O$ single crystals in the dynamic mode.

Earlier [1], we developed a general approach to the choice of crystallization conditions for growing single crystals of complicated compounds of various chemical classes. This approach was based on the preliminary analysis of the phase diagrams of solubility of ternary systems. The main characteristic of this approach is the use of simple components for preparing mother solutions of the required chemical composition, a feature that is very important for crystallization along the preliminarily chosen optimum trajectory. In particular, this approach was used to grow KH_2PO_4 [2] and, for the first time, LiH_2PO_4 single crystals [3].

ANALYSIS OF THE PHASE DIAGRAM OF THE Na_2O–P_2O_5–H_2O SYSTEM AND SELECTION OF CONDITIONS FOR GROWTH OF NaDP, $NaDP \cdot H_2O$, AND $NaDP \cdot 2H_2O$ SINGLE CRYSTALS

The growth of single crystals of complex compositions from aqueous solutions is associated with certain difficulties because of the specific characteristics of their solubility (congruent or incongruent) and the stability of their existence only within certain temperature ranges. An increase or decrease in the solution temperature can change the chemical composition of these solutions and the nature of solubility. Moreover, the crystallization process in ternary systems with the participation of a solvent (in particular, water) proceeds mainly in the dynamic mode. The considerable amount of the mother solution is consumed during the formation of a crystal either as a result of the solvent evaporation or a decrease in the solution temperature. In turn, this changes the component ratio in the solution, whereas the composition of the solid phase formed in a ternary system depends mainly on the solution composition.

Despite the nonequilibrium nature of crystal growth (although very close to equilibrium), the appropriate method and conditions necessary for the growth of sin-

1063-7745/02/4705-0871$22.00 © 2002 MAIK "Nauka/Interperiodica"

gle crystals can readily and successfully be determined from the equilibrium solubility phase diagram of ternary systems.

In a ternary system, to each solid phase there corresponds its own crystallization region whose solubility curve has nonvariant singular points (eutonics and transient points) at which two different solid phases are simultaneously crystallized. Then, it follows that the optimum composition of the solution for the crystallization of a solid phase should be located at the maximum distance from the points of nonvariant equilibria, because, in this case, the probabilities of the cocrystallization of the adjacent phases or a transition to the crystallization region of another phase are lower. This condition can be formulated more rigorously as follows:

(i) when growing single crystals of congruently or incongruently dissolving solid phases by the methods of temperature decrease or isothermal evaporation, one has to use the saturated solutions of the compositions located in the middle part of the solubility curve (i.e., lying at the maximum possible distance from the points of nonvariant equilibria);

(ii) for congruently dissolving solid phases, one can use the saturated solution of the compositions located at the point of the intersection of the solubility curve and the singular solid-phase–water secant under the condition that this secant passes far from the point of nonvariant equilibria.

The above approach is quite justified in complicated systems possessing several crystallizing phases of different compositions in which either the crystallization region of each phase is rather small or the composition of the phase is temperature-dependent.

The compositions of the saturated solutions thus determined usually provide the most favorable conditions for growing single crystals of complicated compositions in ternary systems and, thus, can be considered as the optimum conditions. It was shown [1, 4, 5] that the largest amount of a solid phase in the ternary system is crystallized from the saturated solutions corresponding to the middle part of the solubility curve of a complicated chemical compound. On the contrary, the closer the compositions of the saturated solutions to the compositions of the nonvariant points, the more pronouncedly the component ratio of the solution differs from the stoichiometric component ratio in the solid phase and the smaller the amount of solid phase crystallized from the solution.

The developed approach essentially simplifies the technology of crystal growth and is more economical because no time is needed for the experimental selection of the mother solution, the determination of the temperature limits of the crystallization, and the choice of the growth method. Also, there is no need to synthesize an expensive initial complicated compound, because the initial mother solution is prepared from simple components of the system. Moreover, the experimental study of the dependence of the composition and quality of single crystals on the position of the points corresponding to different compositions of saturated solutions on the solubility curves of solid phases for a number of systems [1–4] showed that the compositions of the solution chosen by the suggested method provide the best quality of the crystals grown.

The principle of determining the optimum composition and temperature of the mother solution from the solubility diagrams of various ternary systems is of a general character and can be applied to the seeded growth of single crystals of complicated compounds of various chemical classes [1, 3, 6–8]. In the present study, we used this method for selecting growth conditions for sodium dihydrogenphosphate single crystals.

The ternary Na_2O–P_2O_5–H_2O system was studied in the temperature range from 25 to 100°C [9]. The number of the solid phases formed in the system and their compositions are shown in Fig. 1.

There are three sodium dihydrogenphosphate-based phases with different amounts of crystal water in the unit cell.

The centrosymmetric monoclinic NaH_2PO_4 phase has a pseudo-orthorhombic unit cell (sp. gr. $P2_1/C$) with the lattice parameters a = 6.808 Å, b = 13.491 Å, c = 7.331 Å, β = 92.88°, and Z = 8 [10]. Its crystal structure is characterized by strong asymmetric hydrogen bonding.

The noncentrosymmetric orthorhombic $NaH_2PO_4 \cdot H_2O$ phase (space group $Pna2_1$) has the lattice parameters a = 7.616 Å, b = 7.899 Å, c = 7.382 Å, and Z = 4. A water molecule forms two very weak hydrogen bonds [11].

The noncentrosymmetric $NaH_2PO_4 \cdot 2H_2O$ phase is described by the space group $P2_12_12_1$ and has the lattice parameters a = 7.275 Å, b = 11.384 Å, c = 6.06 Å, and Z = 4 [12].

Now, consider the physicochemical characteristics of crystallization of NaH_2PO_4, $NaH_2PO_4 \cdot H_2O$, and $NaH_2PO_4 \cdot 2H_2O$ solid phases in the temperature range from 25 to 100°C. The concentration and temperature conditions of their stable crystallization are indicated in Table 1. It follows from Fig. 1 and Table 1 that the $NaH_2PO_4 \cdot 2H_2O$ solid phase is dissolved congruently at 25°C and, probably, also at 0°C. The branch of the solubility curve is rather extended, lies in a wide region of the Na_2O and P_2O_5 concentrations, and has a singular point.

The $NaH_2PO_4 \cdot H_2O$ solid phase exists in the temperature range from 40 to 25°C. The congruent solubility at 40°C becomes incongruent at 25°C. The extended branch of the solubility curve at 40°C has a singular point; at 25°C, a short curve of the incongruent solubility is formed. At 100 and 60°C, the NaH_2PO_4 solid phase has a long branch of the congruent solubility curve, especially in a wide range of P_2O_5 concentra-

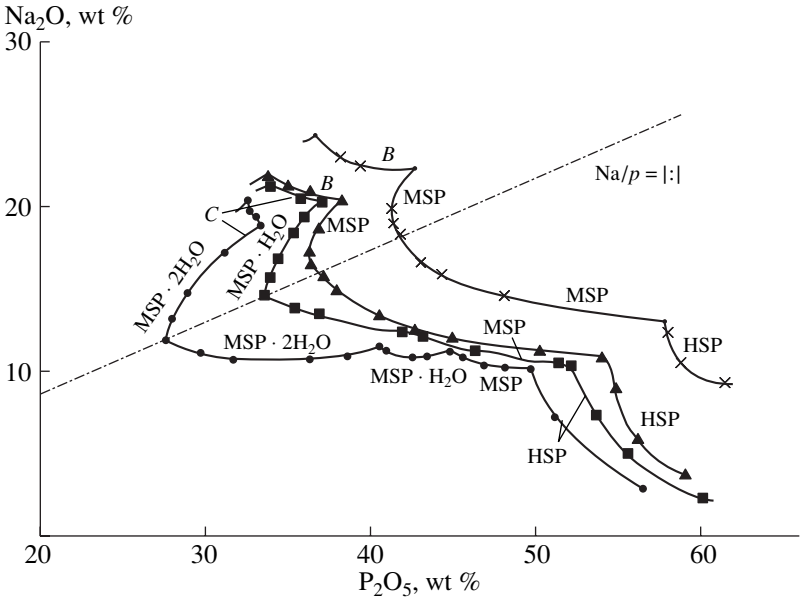

Fig. 1. Phase diagram of solubility Na_2O–P_2O_5–H_2O in the range 25–100°C. Notation: MSP = NaH_2PO_4, HSP = $NaH_3(PO_4)_2$, B = $Na_2HPO_4 \cdot NaH_2PO_4$, C = $Na_2HPO_4 \cdot 2NaH_2PO_4 \cdot H_2O$, ● 25°C, ■ 40°C, ▲ 60°C, × 100°C.

tions. At 40 and 25°C, the solubility branches become shorter, and the transition to incongruent solubility is observed.

To determine the optimum compositions of the mother solutions for growing NaDP, NaDP · H_2O, and NaDP · $2H_2O$ crystals, we represented the data for the ternary Na_2O–P_2O_5–H_2O system (25–28°C) [9] as triangular Gibbs diagrams (Figs. 2–4).

Figure 2 shows the solubility curves of NaH_2PO_4 at 100, 60, 40, and 25°C. Point *1* corresponds to the composition of the saturated solution at the maximum distance from the eutonics on the solubility branches of the isotherms at 25 and 40°C. Point *2* corresponds to the composition of the mother solution at the maximum distance from the eutonics E_1 and E_2 at 60°C. Point *3* indicates the composition of the saturated solution at the intersection of the NaH_2PO_4–H_2O line with the solubility curve at 60°C.

Figure 3 shows the solubility curve of $NaH_2PO_4 \cdot H_2O$ at 25 and 40°C. Point *4* corresponds to the composition of the saturated solution at the maximum distance from the euthonics at 25°C. Point *5* is the composition of the mother solution at the maximum distance from the eutonics E_1 and E_2 at 40°C.

Point *6* in Fig. 4 corresponds to the composition of the saturated solution at the point of intersection of the $NaH_2PO_4 \cdot 2H_2O$–H_2O line with the solubility curve at

Table 1. Temperature and concentration conditions of the crystallization of sodium dihydrogenphosphates in the Na_2O–P_2O_5–H_2O system

Solid phase	*T*, °C	Composition of liquid phase, wt %			Solubility nature
		Na_2O	P_2O_5	H_2O	
$NaH_2PO_4 \cdot 2H_2O$	0	9.36	21.43	69.21	
	25	17.28–11.41	31.20–40.51	51.52–48.08	Congruent
$NaH_2PO_4 \cdot H_2O$	25	11.33–11.31	40.95–44.85	47.72–43.84	Incongruent
	40	20.44–12.53	35.90–42.27	43.66–45.20	Congruent
NaH_2PO_4	25	11.31–10.19	44.85–49.80	43.84–40.01	Incongruent
	40	12.25–10.66	42.73–51.35	45.02–37.99	Incongruent
	60	20.74–10.89	38.20–54.09	41.06–35.02	Congruent
	100	22.40–13.14	13.31–9.25	64.29–76.97	Congruent

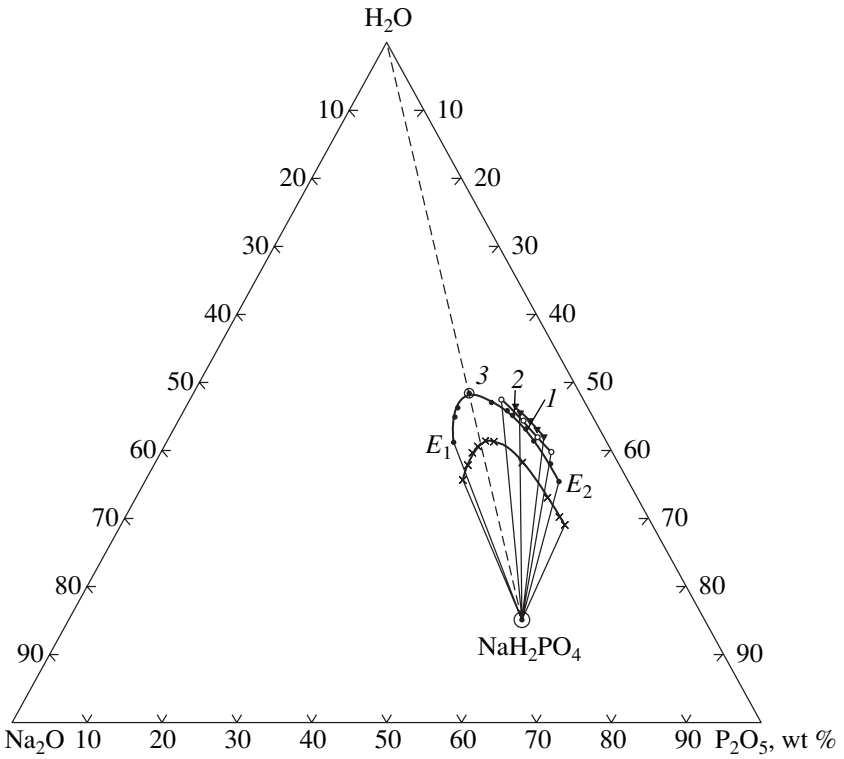

Fig. 2. Solubility isotherms of NaH_2PO_4 in the Na_2O–P_2O_5–H_2O system. Notation: –×–×– 100°C, –●–●– 60°C, –○–○– 40°C, –▲–▲– 25°C, E_1 and E_2 are eutonics, point *1* indicates the composition of the saturated solution at the maximum distance from the eutonics at the solubility branches of the isotherms at 25 and 40°C; point *2* indicates the composition of the mother solution at the maximum distance from eutonics E_1 and E_2 at 60°C; point *3* indicates the composition of the saturated solution at the intersection of the straight line NaH_2PO_4–H_2O with the solubility curve at 60°C.

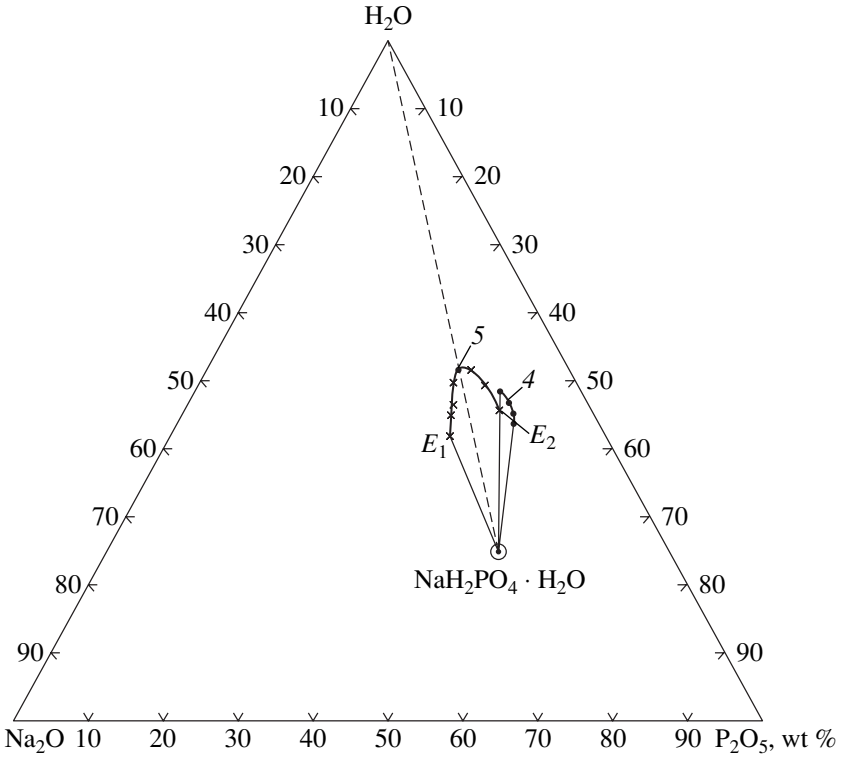

Fig. 3. Solubility isotherms of $NaH_2PO_4 \cdot H_2O$ in the Na_2O–P_2O_5–H_2O system; –●–●– 25°C, –×–×– 40°C, E_1 and E_2 are eutonics, point *4* is the composition of the saturated solution at the maximum distance from the eutonics at 25°C, point *5* is the composition of the mother solution at the maximum distance from the eutonics E_1 and E_2 at 40°C.

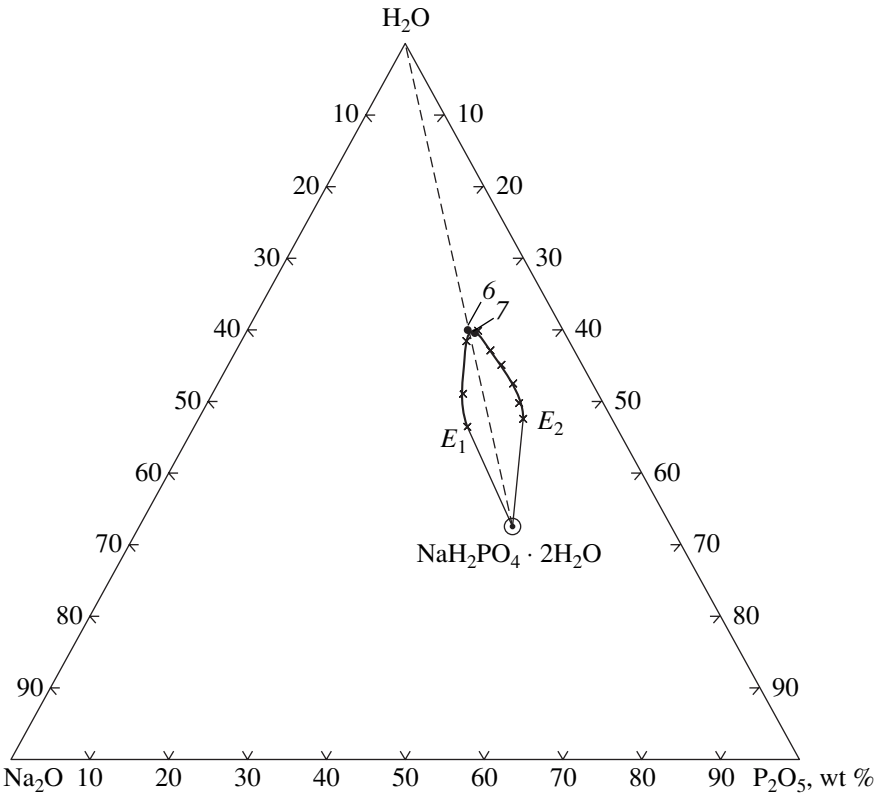

Fig. 4. Solubility isotherm of $NaH_2PO_4 \cdot 2H_2O$ in the Na_2O–P_2O_5–H_2O system. –×–×– 25°C, E_1 and E_2 are eutonics, point *6* indicates the composition of the saturated solution corresponding to the point of intersection of the straight line $NaH_2PO_4 \cdot 2H_2O$–H_2O with the solubility curve at 25°C; point *7* indicates the composition of the mother solution at 35°C.

25°C. Point *7* corresponds to the composition of the mother solution at 35°C.

Table 2 lists the growth conditions for NaH_2PO_4, $NaH_2PO_4 \cdot H_2O$, and $NaH_2PO_4 \cdot 2H_2O$ crystals chosen based on data obtained in the analysis of the physicochemical characteristics of crystallization under equilibrium conditions for the NaDP, NaDP · H_2O, and NaDP · $2H_2O$ phases in the ternary system with due regard for the approach developed for growing crystals in the dynamic mode.

GROWTH OF NaDP, NaDP · H_2O, AND NaDP · $2H_2O$ SINGLE CRYSTALS

The mother solutions were prepared from NaOH and H_3PO_4 chemicals of special purity grade and distilled water. The compositions of the NaDP, NaDP–H_2O, and NaDP–$2H_2O$ solutions are indicated in Table 2. To provide the necessary supersaturation of the mother solutions, we used a sodium hydroxide powder instead of a NaOH solution.

The technology of preparing mother solutions for growing crystals of all the compositions was as follows. Small portions of the NaOH powder were added to a cooling H_3PO_4 solution in a vessel under constant stirring. The reaction between the components was of an exothermic nature and proceeded according to the scheme

$$NaOH + H_3PO_4 + H_2O \longrightarrow NaH_2PO_4 \cdot nH_2O + H_2O$$
$$(n = 0, 1, 2).$$

The solution thus obtained was cooled, filtered through Schott filter no. 2, and poured into a crystallizer with a seed whose composition corresponded to the composition of the crystal to be grown. The seeds were prepared from the solutions used for the growth of NaDP, NaDP · H_2O, and NaDP · $2H_2O$ crystals. The solutions were poured into a crystallizer at the initial temperature equal to the growth temperature. The temperature modes used in growth are indicated in Table 2. The prepared solutions had a pH ranging from 1 to 2. All the mother solutions were rather viscous and preserved the set supersaturation for quite a long time. To make the solution bulk homogeneous, the constant stirring of the solution was started immediately upon its pouring into the crystallizer.

Although the physicochemical nature of NaH_2PO_4, $NaH_2PO_4 \cdot H_2O$, and $NaH_2PO_4 \cdot 2H_2O$ crystallization (associated with the change of their solubility from congruent to incongruent with a lowering of the temperature from 60 to 25°C and from 40 to 20°C, respectively) and the range of existence of $NaH_2PO_4 \cdot 2H_2O$

Table 2. Optimum growth conditions for NaDP, NaDP · H_2O, and NaDP · $2H_2O$ crystals grown from the solutions in the Na_2O–P_2O_5–H_2O system in the temperature range 25–80°C

Crystal	Isotherm		Mother solution					Growth temperature, °C	Figure
	T, °C	point	wt %			*V*, ml			
			Na_2O	P_2O_5	H_2O	NaOH	H_3PO_4		
NaDP	40, 25	1	11.80	47.00	41.20	89.75	54.65	40, 25	2
						d = 1.13	*d* = 1.46		
	60	2*	13.00	43.00	44.00			60	
	60	3	15.00	36.50	48.50	85.30	87.64	60	
						d = 1.17	*d* = 1.33		
NaDP · H_2O	25	4	10.93	42.70	46.37			25	3
	40	5*	14.66	33.62	51.72	86.60	80.72	40	
						d = 1.16	*d* = 1.29		
NaDP · $2H_2O$	25	6	12.00	27.60	60.40			25	4
	35	7*	13.00	29.80	57.20	113.00	59.41	35	
						d = 1.12	*d* = 1.25		

Note: Point *1*, the composition of the saturated solution at the maximum distance from the eutonic, corresponds to the solubility branches of isotherms at 40 and 25°C; point *2* indicates the composition of the mother solution at the maximum distance from the eutonic at 60°C; point *3* indicates the composition of the saturated solution corresponding to the point of intersection of the line NaH_2PO_4–H_2O with the solubility curve at 60°C; point *4* indicates the composition of the saturated solution at the maximum distance from the eutonic at 25°C; point *5* indicates the composition of the saturated solution corresponding to the intersection of the straight line $NaH_2PO_4 \cdot H_2O$–H_2O with the solubility curve at 40°C; point 6 indicates the composition of the saturated solution corresponding to the intersection of the straight line $NaH_2PO_4 \cdot 2H_2O$–H_2O with the solubility curve at 25°C; and point 7 indicates the probable composition of the mother solution NaDP–$2H_2O$ at 35°C; * indicates the compositions of the mother solutions used for crystal growth, and *d* is the solution density in g/cm^3.

only from 25 to 0°C dictated the growth of the crystals by the method of isothermal evaporation, the considerable viscosity and acidity of the mother solutions and rather low initial growth temperature nevertheless meant that no solvent evaporation was observed.

Thus, we had to use the method of temperature decrease from 70, 47, and 35°C down to room temperature to grow NaDP, NaDP · H_2O, and NaDP · $2H_2O$ crystals, respectively. The initial rate of temperature decrease was 0.01°C/day (24 h).

As a result, we obtained transparent colorless $25 \times 22 \times 8$ mm^3 NaDP, $35 \times 30 \times 35$ mm^3 NaDP · H_2O, and $35 \times 30 \times 18$ mm^3 NaDP · $2H_2O$ crystals.

The NaDP crystals were stable stored in air, whereas NaDP · H_2O and NaDP · $2H_2O$ crystals were unstable and rapidly lost their transparency and became turbid.

We assume that these transformations are caused by the reactions

$$NaH_2PO_4 \cdot H_2O + H_2O \longrightarrow NaH_2PO_4 \cdot 2H_2O,$$

$$NaH_2PO_4 \cdot 2H_2O \longrightarrow NaH_2PO_4 \cdot H_2O + H_2O;$$

in other words, the following reversible reaction takes place:

$$NaH_2PO_4 \cdot H_2O + H_2O \rightleftharpoons NaH_2PO_4 \cdot 2H_2O.$$

This transition associated with the absorption and loss of water is confirmed by the data of the X-ray diffraction study of the products of the reversible reaction [11]. It is also shown that the packing density of the crystalline NaH_2PO_4, $NaH_2PO_4 \cdot H_2O$, and $NaH_2PO_4 \cdot 2H_2O$ phases decreases with an increase in hydration.

The crystals grown are shown in Fig. 5. Because of the pronounced instability of a $NaH_2PO_4 \cdot 2H_2O$ crystals (Fig. 5c) in air, the crystal changed its shape already after several hours of being stored in air, which did not allow us to determine its habit.

The habit of the NaDP crystal (Fig. 6a) determined by goniometric measurements is described by the symmetry class 2/*m* and consists of the following simple forms: two pinacoids ({010} and {001}) and two rhombic prisms ({110} and {011}).

The habit of the NaDP · H_2O crystal is shown in Fig. 6b. It should be emphasized that it is inconsistent with the sp. gr. $Pna2_1$ determined in [11]. Our measurements showed that its symmetry class is *m* (monoclinic system) and that the crystal has the following simple forms: pinacoid {010}, seven domatic dihedra $\{\bar{1}10\}$, $\{01\bar{1}\}$, $\{11\bar{1}\}$, $\{\bar{1}1\bar{1}\}$, $\{\bar{1}11\}$, {124}, {421}, and five monohedra {101}, {100}, $\{\bar{1}00\}$, {001}, $\{00\bar{1}\}$. The monoclinicity angle formed by the (100) and (001) faces equals $\beta \approx 93.5°$. It should also be indicated that the faces of the {110} dihedron and the (011) faces are degenerate, probably because their growth essentially depends on the growth conditions. The cause of the inconsistency between the results obtained in our study

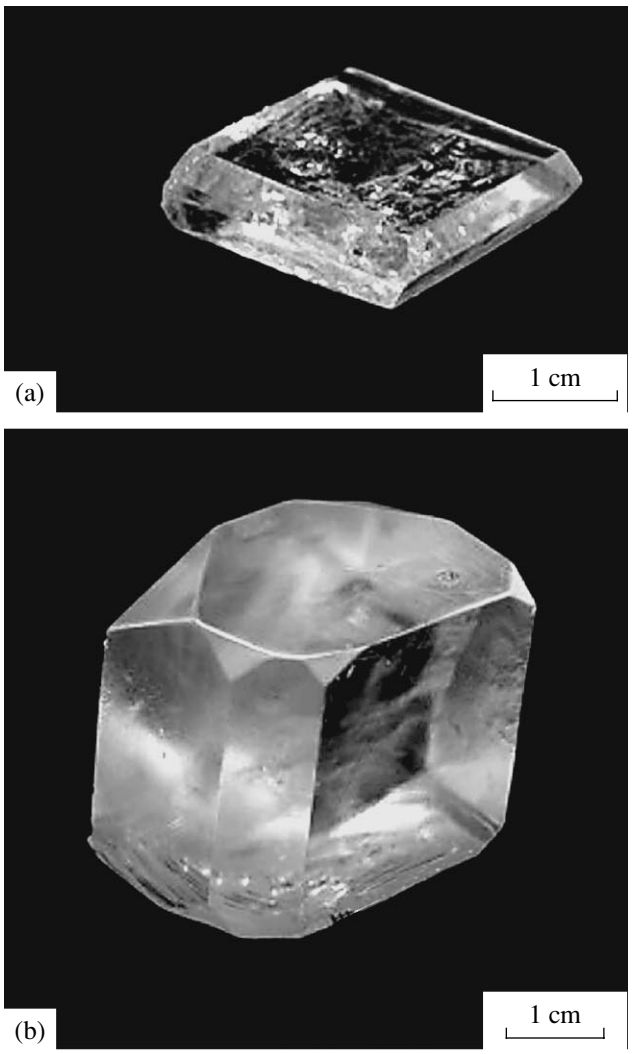

Fig. 5. Single crystals of (a) NaDP, (b) NaDP · H_2O, and (c) NaDP · $2H_2O$.

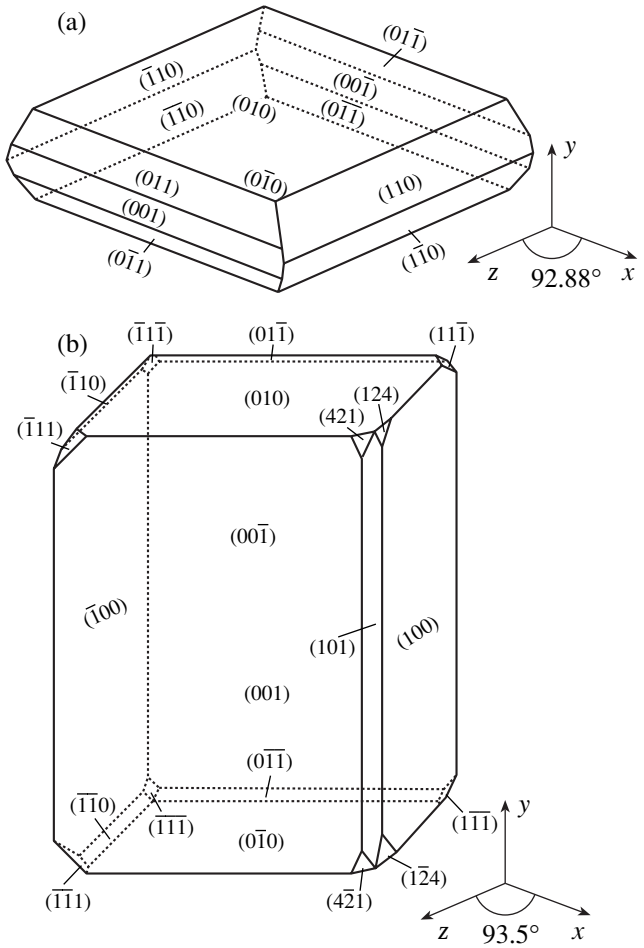

Fig. 6. Habit of (a) NaDP and (b) NaDP · H_2O single crystals.

and in [11] is still unclear. Among the possible causes are the following. Possibly, the inconsistency is explained by the different compositions of the phases obtained in [11] and in our study (most probably, different number of the molecules of crystal water). Another reason is that, as was indicated above, the NaDP · H_2O crystals, being pronouncedly unstable, rapidly change their composition in air. These facts can results in erroneous X-ray diffraction data because of the varying number of molecules of crystal water in the sample during the experiment. To remove this discrepancy, some additional X-ray studies are necessary.

CONCLUSION

The analysis of the phase diagram of solubility of the ternary Na_2O–P_2O_5–H_2O system in the temperature range from 0 to 100°C allowed us to determine the nature of solubility and establish the conditions of crystallization for the NaH_2PO_4, NaH_2PO_4 · H_2O, and $NaH_2PO_4 \cdot 2H_2O$ solid phases under equilibrium conditions—the compositions of the saturated solutions and the temperature limits of their stable crystallization.

Based on the data obtained, we managed to grow on seed transparent NaDP, $NaDP \cdot H_2O$, and $NaDP \cdot 2H_2O$ single crystals by the method of temperature decrease. The NaDP crystals are stable and can be stored in air, whereas the $NaDP \cdot H_2O$ and $NaDP \cdot 2H_2O$ crystals are unstable, rapidly lose transparency, and become turbid. This transition seems to be associated with the absorption of water by sodium dihydrogenphosphate monohydrate and the loss of water by sodium dihydrogenphosphate dihydrate. The habit of NaDP and $NaDP \cdot H_2O$ crystals is determined. The discrepancy is also revealed between the symmetry class determined for a $NaDP \cdot H_2O$ crystal and the space group determined for this crystal earlier.

REFERENCES

1. L. V. Soboleva, Neorg. Mater. **31** (5), 614 (1995).
2. L. V. Soboleva, Neorg. Mater. **32** (8), 1007 (1996).
3. L. V. Soboleva and I. L. Smol'skiĭ, Kristallografiya **42** (4), 762 (1997) [Crystallogr. Rep. **42**, 700 (1997)].
4. L. V. Soboleva, Neorg. Mater. **27** (4), 822 (1991).
5. V. A. Anosov and S. A. Pogodin, *Basic Principles of Physicochemical Analysis* (Akad. Nauk SSSR, Moscow, 1947).
6. L. V. Soboleva, E. B. Rudneva, and I. L. Smol'skiĭ, Kristallografiya **43** (4), 756 (1998) [Crystallogr. Rep. **43**, 706 (1998)].
7. L. V. Soboleva and L. F. Kirpichnikova, Kristallografiya **46** (2), 350 (2001) [Crystallogr. Rep. **46**, 306 (2001)].
8. L. V. Soboleva, A. É. Voloshin, V. A. Kirikov, and M. V. Biglova, Kristallografiya **47** (1), 140 (2002) [Crystallogr. Rep. **47**, 130 (2002)].
9. B. Wendrow and K. A. Kobe, Ind. Eng. Chem. **44** (6), 1439 (1952).
10. M. Gatti and G. Ferraris, Acta Crystallogr., Sect. B: Struct. Crystallogr. Cryst. Chem. **30**, 1 (1974).
11. M. Gatti and G. Ferraris, Acta Crystallogr., Sect. B: Struct. Crystallogr. Cryst. Chem. **32**, 359 (1976).
12. H. Bartl, M. Gatti, and G. Ferraris, Acta Crystallogr., Sect. B: Struct. Crystallogr. Cryst. Chem. **32**, 987 (1976).

Translated by L. Man

Crystallography Reports, Vol. 47, No. 5, 2002, pp. 879–884. Translated from Kristallografiya, Vol. 47, No. 5, 2002, pp. 945–949.

CRYSTAL GROWTH

Growth and Study of Single Crystals of the (Na,Li)NbO_3 Solid Solutions

I. P. Raevskiĭ, L. A. Reznichenko, V. G. Smotrakov, V. V. Eremkin, M. A. Malitskaya, L. A. Shilkina, and E. S. Gagarina

Research Institute of Physics, Rostov State University, pr. Stachki 194, Rostov-on-Don, 344090 Russia

e-mail: smotr@ip.rsu.ru

Received May 16, 2001; in final form, April 3, 2002

Abstract—Plateletlike transparent (Na,Li)NbO_3 (NLN) single crystals with up to 7 mol % $LiNbO_3$ possessing a perovskite structure are synthesized by the method of spontaneous crystallization from $NaBO_2$ flux. Based on the X-ray diffraction data and dielectric measurements of these single crystals, the phase *x–T* diagram of these solid solutions is constructed in the vicinity of the $NaNbO_3$ composition. It differs from the *x–T* diagrams established for the $Na_{1-x}Li_xNbO_3$ ceramic. © *2002 MAIK "Nauka/Interperiodica".*

INTRODUCTION

$Na_{1-x}Li_xNbO_3$ (NLN) solid solutions of the antiferroelectric $NaNbO_3$ (NN) with a perovskite structure and the ferroelectric $LiNbO_3$ with a pseudoilmenite structure are widely used in the form of ceramics [1–3]. Sodium niobate undergoes six phase transitions [1, 4], which considerably complicates the *x–T* phase diagram of the NLN solid solutions. Since many phase transitions in lithium niobate give rise to weak anomalies in the structural, electrophysical, and optical parameters, the data on the *x–T* diagram of NLN, which are based, as a rule, on the studies of ceramic samples [3–13], are rather contradictory. Since no data on the structure and properties of perovskite NLN single crystals are published (the only exception is the data at $x \approx 0.02$–0.03 [5, 7]), the present study is aimed at the synthesis of these solid solutions in the form of single crystals of a quality appropriate for optical and electrical measurements over a wide range of *x* values and the refinement of the NLN phase *x–T* diagram in the concentration range in the vicinity of $NaNbO_3$.

SYNTHESIS OF CRYSTALS AND METHODS OF MEASUREMENTS

The NLN single crystals were synthesized by the method of mass crystallization from flux. The solvent was $NaBO_2$ [8]. The initial charge consisting of the mixture of high-purity grade Na_2CO_3, Li_2CO_3, Nb_2O_5, and B_2O_3 was loaded into a platinum crucible and kept there for two to three hours at 1060°C. Then, the mixture was cooled down to 930–860°C at a rate of 6–7 K/h, the melt was poured out, and the synthesized crystals were washed with hot water. The crystals were colorless transparent platelets with a thickness ranging within 50–200 μm and an area of several square millimeters. Some crystals were isometric and had 2 mm-long edges. All the single crystals were faceted with (001) planes of perovskite basis and were twinned at room temperature.

The X-ray diffraction studies were performed on powder samples obtained upon crystals crushing on a DRON-3 diffractometer (FeK_α radiation, Mn filter). The dielectric constant was measured at frequencies ranging within 1–100 kHz with the aid of a R5083 ac bridge during continuous heating or cooling at a rate of 2–3 K/min. The Aquadag electrodes were applied onto the natural (001) faces of the crystals.

EXPERIMENTAL RESULTS

Figure 1a shows the $\varepsilon(T)$ dependences for an NN single crystal and some of the synthesized NLN crystals. The ceramic NN samples usually show only a spread maximum $\varepsilon(T)$ corresponding to the phase transition between two antiferromagnetic orthorhombic phases, *P* and *R* (hereafter all the phases are indicated in the Meroy notation [4]). The $\varepsilon(T)$ dependence of NN crystals showed two major anomalies—a step corresponding to the phase transition between the low-temperature ferroelectric rhombohedral phase *N* and the antiferroelectric orthorhombic phase *P*, and the maximum in the range of the $P \rightleftharpoons R$ phase transition. In accordance with the data obtained earlier for the ceramic [3, 9], the temperature T_m of the maximum of $\varepsilon(T)$ for NLN single crystals, first, decreases with an increase in the $LiNbO_3$ content and then increases with it. The concentration dependences of the average unit-cell parameter $a^* = V^{1/3}$ (where *V* is the unit-cell volume) of the ceramic NLN samples are nonmonotonic [3, 9, 10]. Therefore, the use of the dependences $a^*(x)$ and $T_m(x)$ obtained on NLN ceramic samples for estimating the composition of single crystals is far from simple.

1063-7745/02/4705-0879$22.00 © 2002 MAIK "Nauka/Interperiodica"

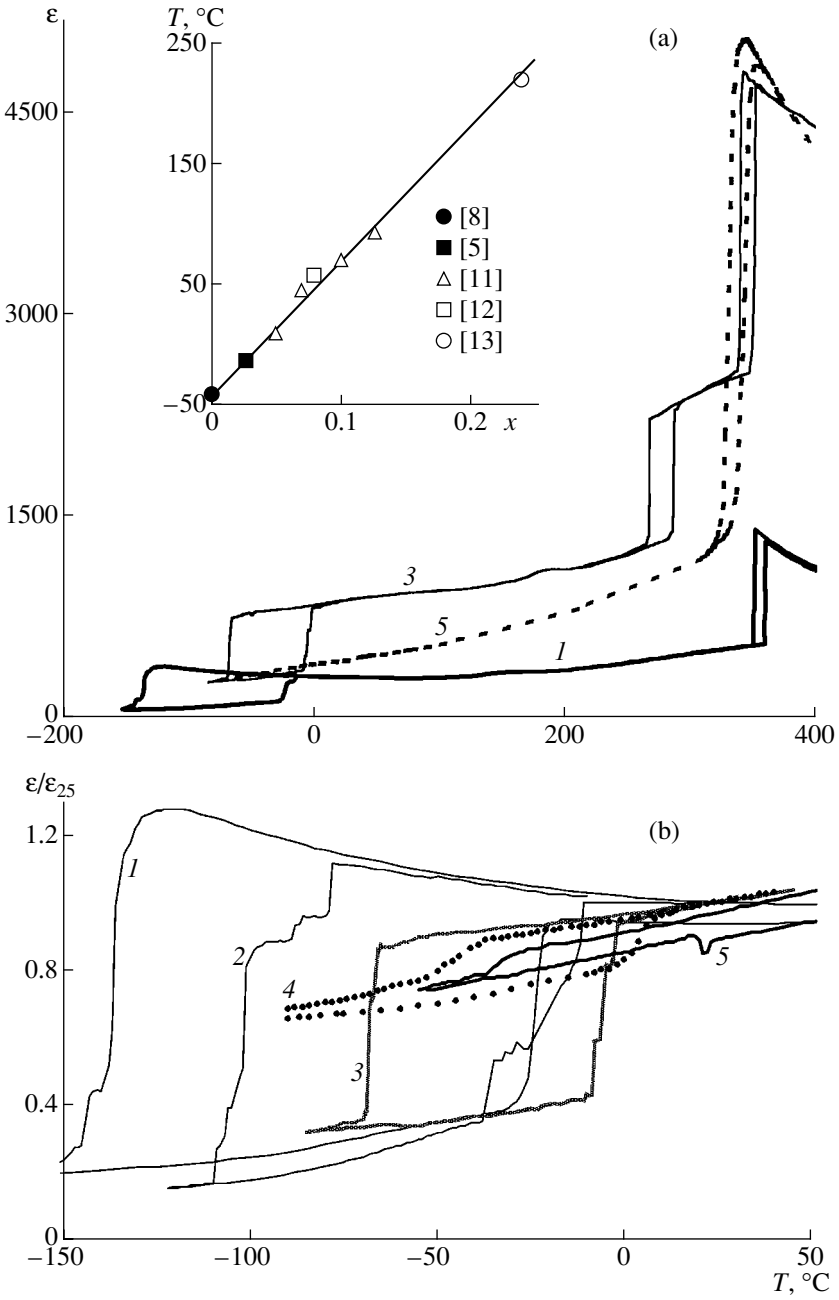

Fig. 1. The change in the form of the ε(*T*) dependences for $Na_{1-x}Li_xNbO_3$ crystals with an increase in the $LiNbO_3$ content in the melt (in molar fractions): (*1*) 0, (*2*) 0.05, (*3*) 0.2, (*4*) 0.45, and (*5*) 0.6. The measurement frequency is 100 kHz, and ε_{25} is the ε-value at 25°C. The inset shows the concentration dependence of the $N \longrightarrow P$ ($x < 0.02$) and $N \longrightarrow Q$ ($x > 0.02$) transitions constructed by the known data for the $Na_{1-x}Li_xNbO_3$ crystals (filled circles) and ceramic (empty circles).

Figure 1b shows the anomalies in ε(*T*) for the synthesized NLN crystals corresponding to the transition between the *N* and *P* phases (at $x < 0.02$) or to the ferroelectric orthorhombic *Q* phase formed at $x > 0.02$ [1, 3, 9]. It can be seen from Fig. 1b that the temperature of the phase transition, both under heating and cooling, monotonically increases with the $LiNbO_3$ content in the melt. Therefore, in order to determine the composition of the single crystals synthesized, we used the concentration dependences for the $N \longrightarrow P$ ($x < 0.02$) and $N \longrightarrow Q$ ($x > 0.02$) transitions constructed by the data obtained for NLN ceramics [7–13] (inset in Fig. 1a).

Figure 2a shows the concentration dependence of a^* for the synthesized NLN crystals at room temperature. It can be seen that a^* is practically independent of *x* in the range $x \le 0.03$ and has a jump in the range $0.03 \le x \le 0.04$. In the range $0.02 \le x \le 0.05$, the *P* and *Q* phases coexist. As is seen from Fig. 2b, in this case, the

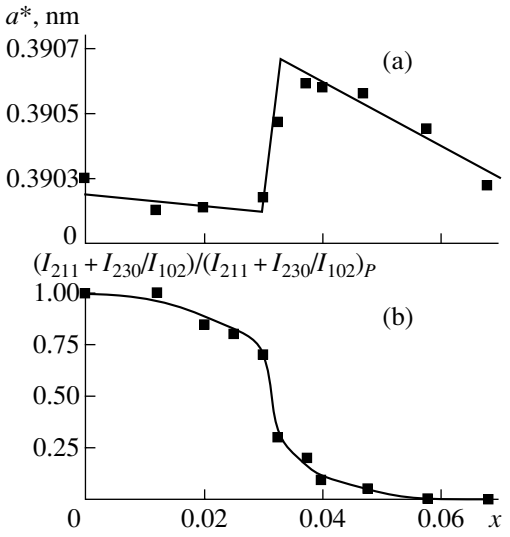

Fig. 2. (a) Concentration dependences of the average parameter of the perovskite unit cell and (b) the value of the $(I_{211} + I_{230}/I_{102})/(I_{211} + I_{230}/I_{102})_P$ ratios for the 211, 230, and 102 diffraction reflections proportional to the content of the *P* phase for $Na_{1-x}Li_xNbO_3$ single crystals at room temperature.

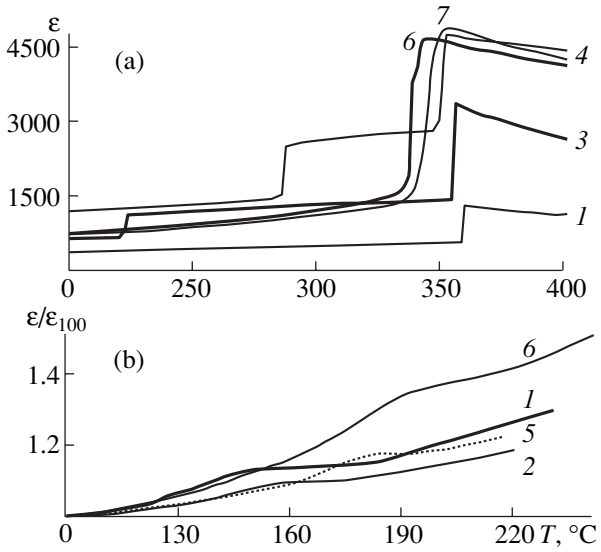

Fig. 3. (a, b) The change of the form of the anomalies in $\varepsilon(T)$ in the $Na_{1-x}Li_xNbO_3$ single crystals observed with an increase in the lithium content in various temperature ranges (ε_{100} is the ε value at 100°C). The measurements were made in the heating mode at a frequency of 100 kHz. x = (*1*) 0, (*2*) ~0.01, (*3*) ~0.02, (*4*) ~0.04, (*5*) ~0.05, (*6*) ~0.06, and (*7*) ~0.07.

relative content of the phase *P* estimated from the relationship $(I_{211} + I_{230}/I_{102})/(I_{211} + I_{230}/I_{102})_P$, where I_{211}, I_{230}, and I_{102} are the experimental intensities of the superstructural 211 and 230 reflections observed only in the *P* phase and the 102 reflection observed in both phases (the indices of the reflections are given in the orthorhombic setting), drastically decreases with an increase in x in the range $0.03 \le x \le 0.04$. The appearance of the lines corresponding to the *Q* phase on the X-ray diffraction patterns at $x \approx 0.02$ correlates with the appearance of the additional anomalies in $\varepsilon(T)$ at 220 and 80°C (Figs. 3a, 4). The anomaly in $\varepsilon(T)$ observed at $x \approx 0.02$ at temperatures in the region of 220°C has the form of a step whose temperature monotonically increases with an increase in x, whereas at $x \approx 0.06$, it merges with the maximum in ε (Figs. 1a, 3a). At $x >$ 0.06, the X-ray diffraction patterns of the crystals showed weak lines corresponding to the rhombohedral phase, whereas the maximum in $\varepsilon(T)$ became more diffuse (Figs. 1a, 3a).

Earlier, many authors observed a weak anomaly in $\varepsilon(T)$ at temperatures in the region of 150°C both in NN crystals and ceramics [17–20], however it was ignored because of its very low value. As is seen from the comparison of Figs. 1a and 3b, this anomaly becomes noticeable only on an appropriate scale. The NLN crystals also show this anomaly at a temperature which increases with an increase in x and attains the value of ~190°C at $x \approx 0.06$ (Fig. 3b).

DISCUSSION OF RESULTS

According to [4], in the temperature range from –150 to 400°C, NN crystals undergo two phase transitions to which the structural transformations $N \rightleftharpoons P$ and $P \rightleftharpoons R$ correspond.

The maximum of $\varepsilon(T)$ corresponding to the $P \rightleftharpoons R$ phase transition increases with an increase in x, which correlates quite well with the stabilization of the ferroelectric properties with an increase in the Li content [1]. The value of the temperature hysteresis of $\varepsilon(T)$ is practically constant (Fig. 1); in other words, here we are dealing with a first-order phase transition.

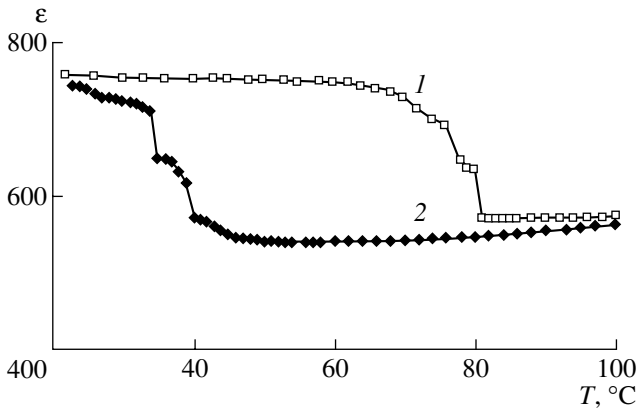

Fig. 4. The $\varepsilon(T)$ dependence for a $Na_{0.975}Li_{0.025}NbO_3$ crystal measured at a frequency of 100 kHz in the course of (*1*) heating and (*2*) subsequent cooling.

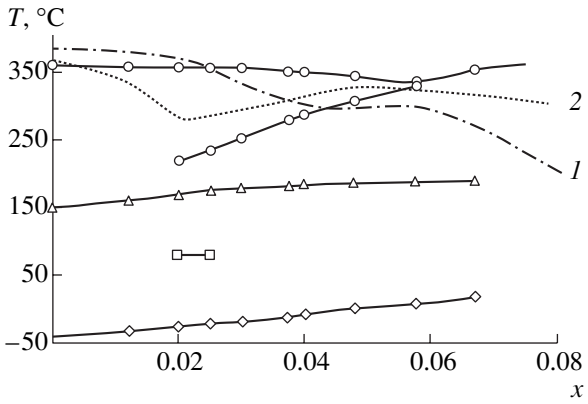

Fig. 5. The tentative *x–T* phase diagram for the $Na_{1-x}Li_xNbO_3$ solid solutions constructed by the data of dielectric measurements on single crystals (solid lines). The dashed and dashed–dotted lines show the lines of the phase transitions corresponding to the maximum of $\varepsilon(T)$ determined in [3] (curve *1*) and [9] (curve *2*) constructed by the experimental data for ceramic samples.

As was indicated in [1, 4, 14], the difference in the structural parameters of the *N* and *P* phases is quite pronounced, and, therefore, the $N \rightleftharpoons P$ phase transition is characterized by an unusually high value of temperature hysteresis. As is seen from Fig. 1b, in real NN crystals, this transition usually cannot occur simultaneously in the whole volume, and the $\varepsilon(T)$ dependence has jumps corresponding to the phase transitions occurring in different regions of the crystal. Such jumps are also observed in the NLN crystals with a low Li content. With an increase in *x*, the anomaly in $\varepsilon(T)$ corresponding to the $N \rightleftharpoons P(Q)$ phase transition decreases and becomes blurred, and the hysteresis temperature also decreases, i.e., the difference in the parameters of the high- and low-temperature phases becomes smoother.

Unlike other anomalies in $\varepsilon(T)$ observed in all the crystals studied, the anomaly at 80°C was observed only in the crystals with $0.020 \le x \le 0.025$ containing a small amount of the *Q* phase (Fig. 4), with the temperature of this anomaly being almost independent of *x*. Earlier, the anomalies observed at temperatures of 75–190°C in the temperature dependences of the unit-cell parameter of NN crystals, which contained an impurity of the *Q* phase in addition to the *P* phase, were attributed to the $P \rightleftharpoons Q$ phase transition [16]. These phase transformations were first-order transitions, which was confirmed, in particular, by the high value of temperature hysteresis. It seems that the anomalies in ε in the vicinity of 80°C observed in the NLN crystals with a small amount of the *Q* phase (characterized by a high value of temperature hysteresis (Fig. 4)) are also caused by the $P \rightleftharpoons Q$ phase transitions. This assumption is supported by the fact that, unlike other anomalies in $\varepsilon(T)$, this anomaly is characterized by a decrease in ε with an increase in the temperature *T*. Indeed, in the ferroelectric phase, the existence of pronounced internal fields makes the dielectric susceptibility lower than in the antiferroelectric phase, and one can expect a decrease in ω in the $P \longrightarrow Q$ transition, as is the case of the $P \longrightarrow N$ transition in NN (Fig. 1).

The anomaly observed on the $\varepsilon(T)$ curve in the form of a step for the NLN crystals with $0.02 \le x \le 0.06$ in the temperature range 220–330°C was not observed in the corresponding ceramic [3, 9]. The existence of the corresponding line of phase transitions on the phase *x–T* diagram of NLN crystals could have been assumed only based on the experimental data on the pyroelectric effect and $\varepsilon(T)$ [6, 7, 15] for $Na_{1-x}Li_xNbO_3$ crystals with $x \approx 0.02$. It should be noted that, in the crystals studied in [15], the step on the $\varepsilon(T)$ dependence was hardly seen, which seems to be associated with the insufficiently high quality of these crystals. In the NLN crystals synthesized in [15], the step on the $\varepsilon(T)$ dependence had a pronounced jump in ε and also a pronounced temperature hysteresis (Fig. 1a); in other words, in [15], a first-order phase transition was observed. This is also confirmed by the results of the studies of NLN crystals in polarized light. At temperatures corresponding to the step of the $\varepsilon(T)$ dependence, a change in the domain structure, motion of the phase fronts, and jumps in birefringence were observed [6, 7, 20]. At the same time, the X-ray diffraction studies of NLN powders showed [7, 9, 20] the absence of any changes in the symmetry of the perovskite unit cell in the temperature range from 25 up to 330–350°C. At temperatures corresponding to the step on $\varepsilon(T)$, only insignificant changes in the slope of the temperature dependence of the *a*, *b*, and *c* parameters and the monoclinicity angle β of the perovskite unit cell were observed.

Similar relatively weak changes in the slope of the temperature dependences of the perovskite unit-cell parameters also correspond to a weak anomaly in $\varepsilon(T)$ observed in the vicinity of 150°C for NN crystals and in the range 155–190°C for NLN crystals [7, 20, 21]. The absence of the temperature hysteresis of this anomaly on $\varepsilon(T)$ indicates that it may be independent of the $P \rightleftharpoons Q$ phase transition mentioned above [16]. Despite the fact that the anomalies in $\varepsilon(T)$ in the temperature range 155–190°C are rather diffuse, their temperatures are practically independent of the measuring-field frequency in the range from 1 to 100 kHz. Along with the absence of the phase-front motion and the change of the extinction in the polarized light for the crystals, these results allow one to assume that the phase transitions observed in NLN crystals in the range 150–190°C are similar to second-order phase transitions. This conclusion is consistent with the change in the slope of the temperature dependence of birefringence in $Na_{0.98}Li_{0.02}NbO_3$ crystals in the range 150–170°C recorded in [7].

The study of the Raman spectra [22] brought the authors to the conclusion that a second-order phase transition exists between the antiferroelectric orthorhombic phases in the vicinity of 190°C in NN crystals.

Taking into account the rather low accuracy of the determination of the transition temperature from the changes observed in the diffuse Raman spectra, one can assume that the anomalies on the $\varepsilon(T)$ dependence in the vicinity of 150°C observed in our studies of NN crystals correspond precisely to this transition.

Figure 5 shows the phase x–T diagram of the NLN solid solutions in the region of low $LiNbO_3$ content constructed on the basis of the data of dielectric measurements of single crystals in the temperature range from –150 to 400°C. For comparison, the same figure also shows the concentration dependences of the phase-transition temperature corresponding to the maximum of $\varepsilon(T)$ constructed from the data obtained for the ceramic NLN samples [3, 9]. The x–T diagrams obtained differ from those reported in [1, 3, 6, 9] in that they have a line of phase transitions corresponding to the above anomalies in the electrophysical and structural parameters in the range 150–200°C. Moreover, the studies of the single crystals provided the determination of the position of the phase-transition line on the phase x–T diagram of NLN in the range from 220 to 330°C, which has never been recorded for ceramics.

The considerable difference between the phase x–T diagram of the NLN solid solutions and the known x–T diagrams constructed on the basis of the data for ceramic samples [3, 6, 9] seems to be explained by the repeatedly indicated strong dependence of the structure and properties of the alkali metal-based niobates on the conditions of their synthesis. In particular, in the (Na, Li)NbO_3 system, one of the causes of such a strong influence may be the coexistence of the substitutional and interstitial solid solutions over a wide range of x values [10, 23].

A more detailed study of the phase transitions and properties of single crystals of the $NaNbO_3$-based solid solutions is the subject of our further investigations.

CONCLUSION

Thus, both in the (Na,Li)NbO_3 crystals and in the corresponding ceramic, one observes the coexistence of the antiferroelectric (P) and ferroelectric (Q) orthorhombic phases over a wide range of x values (morphotropic region). The characteristic feature of two-phase crystals is the existence of the anomalies in $\varepsilon(T)$ with the corresponding pronounced temperature hysteresis in the vicinity of 80°C caused by the $P \rightleftharpoons Q$ phase transitions.

The results of the dielectric measurements made on single crystals of $Na_{1-x}Li_xNbO_3$ solid solutions indicate that, in addition to the well-known six phase transitions in $NaNbO_3$, there exists one more transition that is similar to a second-order phase transition which occurs at about 150°C, presumably between the two antiferroelectric orthorhombic phases. The temperature of the latter transition increases with the Li content. Moreover, the appearance in the crystals with $x \geq 0.02$ of the ferroelectric phase Q is accompanied by the formation of an additional anomaly in $\varepsilon(T)$ in the form of a step in the vicinity of 220°C. The temperature of the latter anomaly in $\varepsilon(T)$ monotonically increases with x and, at $x \approx 0.06$, this anomaly merges with the maximum of ε.

The occurrence of a phase transition in $NaNbO_3$ and its solid solutions in the range from 30 to 200°C (coinciding with the working temperature interval of numerous functional materials) can considerably influence the temperature and time stability of their characteristics. This should necessarily be taken into account when designing new $NaNbO_3$-materials for various purposes.

ACKNOWLEDGMENT

This study was supported by the Russian Foundation for Basic research, projects nos. 99-02-17575 and 01-03-33119.

REFERENCES

1. G. A. Smolenskiĭ, V. A. Bokov, V. A. Isupov, *et al.*, *Physics of Ferroelectric Phenomena* (Nauka, Leningrad, 1985).
2. A. Ya. Dantsiger, O. N. Razumovskaya, L. A. Reznichenko, and S. I. Dudkina, *High-Performance Piezoceramic Materials. Optimization of Search* (Paĭk, Rostov-on-Don, 1995).
3. T. Nitta, J. Am. Ceram. Soc**. 51** (11), 626 (1968).
4. H. D. Megaw, Ferroelectrics **7** (1–4), 87 (1974).
5. W. L. Zhong, P. L. Zhang, H. S. Zhao, *et al.*, Phys. Rev. B **46**, 10583 (1992).
6. A. Sadel, R. Von der Muhll, and J. Ravez, Mater. Res. Bull. **18**, 45 (1983).
7. A. Sadel, R. Von der Muhll, J. Ravez, *et al.*, Solid State Commun. **44** (3), 345 (1982).
8. O. A. Zhelnova, V. G. Smotrakov, I. P. Raevskiĭ, and E. G. Fesenko, Kristallografiya **28** (5), 1052 (1983) [Sov. Phys. Crystallogr. **28**, 623 (1983)].
9. L. A. Shilkina, L. A. Reznichenko, M. F. Kupriyanov, and E. G. Fesenko, Zh. Tekh. Fiz. **47** (10), 2173 (1977) [Sov. Phys. Tech. Phys. **22**, 1262 (1977)].
10. E. S. Gagarina, L. A. Shilkina, L. A. Reznichenko, *et al.*, Izv. Akad. Nauk, Ser. Fiz. **65** (6), 778 (2001).
11. R. R. Zeyfang, R. M. Henson, and W. J. Maier, J. Appl. Phys. **48** (7), 3014 (1977).
12. M. N. Palatnikov, K. J. Borman, V. Samulyonis, *et al.*, Acta Univ. Latv. **559**, 34 (1991).
13. V. B. Nalbandyan, B. S. Medvedev, N. G. Sudorgin, *et al.*, Fiz. Tverd. Tela (Leningrad) **30** (9), 2661 (1988) [Sov. Phys. Solid State **30**, 1533 (1988)].
14. C. N. W. Darlington and H. D. Megaw, Acta Crystallogr., Sect. B: Struct. Crystallogr. Cryst. Chem. **29**, 2171 (1973).
15. A. Sadel, R. Von der Muhll, J. Ravez, and P. Hagenmuller, Ferroelectrics **47** (1–4), 169 (1983).

16. I. Lefkowitz, K. Lukaszewicz, and H. D. Megaw, Acta Crystallogr. **20**, 670 (1966).
17. N. N. Kraĭnik, Fiz. Tverd. Tela (Leningrad) **2** (4), 685 (1960) [Sov. Phys. Solid State **2**, 633 (1960)].
18. L. Pardo, P. Duran-Martin, J. P. Mercurio, *et al.*, J. Phys. Chem. Solids **58** (9), 1335 (1997).
19. K. Konieczny, Mater. Sci. Eng. B **60**, 124 (1999).
20. I. P. Raevskiĭ, L. A. Reznichenko, V. G. Smotrakov, *et al.*, Pis'ma Zh. Tekh. Fiz. **26** (16), 97 (2000) [Tech. Phys. Lett. **26**, 744 (2000)].
21. A. Molak, M. Pawelczyk, and J. Kwapulinski, J. Phys.: Condens. Matter **6**, 6833 (1994).
22. X. B. Wang, Z. X. Shen, Z. P. Hu, *et al.*, J. Mol. Struct. **385**, 1 (1996).
23. L. A. Shilkina, I. V. Pozdnyakova, S. I. Dudkina, *et al.*, in *Proceedings of the 8th International Conference "Semiconductors–Ferroelectrics," Rostov-on-Don, 1998*, p. 149.

Translated by L. Man

Crystallography Reports, Vol. 47, No. 5, 2002, pp. 885–890. Translated from Kristallografiya, Vol. 47, No. 5, 2002, pp. 950–954.

CRYSTAL GROWTH

Mathematical Modeling of Impurity Distribution in the Melt Meniscus in the Growth of Profiled Sapphire Crystals

V. A. Borodin*, A. V. Zhdanov, and D. N. Frantsev****

** Experimental Factory of Scientific Engineering, Russian Academy of Sciences, Chernogolovka, Moscow oblast, 142432 Russia*

e-mail: faramir@ezan.ac.ru

*** Institute of Solid State Physics, Russian Academy of Sciences, Chernogolovka, Moscow oblast, 142432 Russia*

Received May 16, 2001; in final form, January 23, 2002

Abstract—The distribution of impurities in the growth of profiled sapphire crystals is simulated. The distribution of impurities was calculated with the use of the diffusion equation with convective terms. The melt flow was found by solving the Navier–Stokes equation. The distributions of impurities over the melt meniscus are obtained at different crystallization rates. The maximum concentration supersaturation in the meniscus is studied as a function of its geometric parameters. © *2002 MAIK "Nauka/Interperiodica".*

INTRODUCTION

Depending on the growth conditions, different types of voids are formed in profiled sapphire crystals [1]. Most of the voids can be removed by appropriate technological procedures except for gaseous inclusions formed by the Tiller mechanism [2]. In a profiled sapphire crystal, this type of inclusions has the form of bubbles appearing in the melt saturated with a gaseous impurity in the region of the elevated concentration density at the crystallization front, which are trapped by growing crystals. The formation of these defects with sizes ranging from 1 to 15 μm is practically inevitable if the growth rate exceeds a certain critical value [3–6]. In sapphire ribbons and tubes, these defects are located at a distance 50–100 μm from the side surface of the crystal [3–8]. The study of the structure of the decanted front and the corresponding distribution of bubbles showed that their trapping occurs within the reentrant angles of the faceted cells at the crystallization front [4, 7]. The cellular structure of the growth front is formed at violations of the morphological stability of a planar interface if the crystallization rate exceeds a certain critical value [9]. It was found [4, 10] that it is the loss of stability of the plane crystallization front that determines the critical rate of bubble trapping in profiled sapphire crystals.

Because the cellular structure and, therefore, the bubble trapping at growth rates of 0.5 to 3.0 mm/min are observed on the local regions of the crystallization front, one can assume that the impurity concentration in the melt in the vicinity of these regions is higher than in the remaining volume. The supersaturation of the melt with the gaseous impurity in these regions creates the conditions for nucleation and the growth of bubbles.

The present study aims to simulate the impurity distribution in the growth of profiled crystals, determine the regions of the meniscus with the maximum impurity concentration, and compare the data obtained with the experimentally observed distribution of gaseous inclusions in crystals.

FORMULATION OF THE PROBLEM

A growing crystal is a planar ribbon with a pronounced thickness-to-width ratio, which allows us to consider the problem as two-dimensional. The region for calculation is formed by the intersection of the meniscus, the crystal, and the draw plate with the plane orthogonal to the working surface of the draw plate and the crystal sides (Fig. 1).

The impurity, together with the melt from the crucible, enters the meniscus through a capillary. The initial concentration is C_0. In the course of melt crystallization, the impurity is forced back by the crystallization front and enriches the melt.

To find the impurity concentration at each point of the meniscus, one has to solve the steady-state diffusion equation with the convective terms

$$U\frac{\partial C}{\partial x} + V\frac{\partial C}{\partial y} = D\left(\frac{\partial^2 C}{\partial x^2} + \frac{\partial^2 C}{\partial y^2}\right), \qquad (1)$$

where U and V are the x and y components of the melt-flow velocity, C is the impurity concentration, and D is the diffusion coefficient.

1063-7745/02/4705-0885$22.00

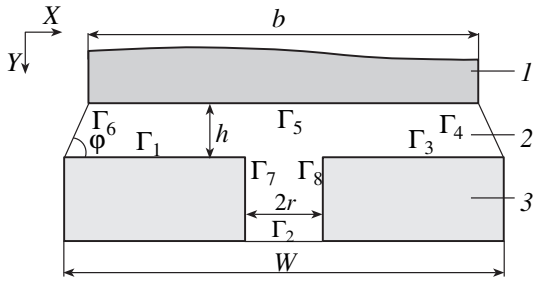

Fig. 1. Geometry of the calculational model: (*1*) crystal, (*2*) meniscus, and (*3*) die.

To solve the diffusion equation, one has to determine the distribution of the flow velocities in the meniscus by solving the steady-state Navier–Stokes equation for an incompressible viscous liquid

$$\mathrm{curl}[\mathbf{V}\,\mathrm{curl}\mathbf{V}] + \mu\Delta\mathrm{curl}\mathbf{V} = 0, \tag{2}$$

$$\rho\,\mathrm{div}\,\mathbf{V} = 0, \tag{3}$$

where ρ is the density and μ is the dynamic viscosity of the melt.

To estimate the character of the melt flow in the meniscus, we calculate the Reynolds number

$$\mathrm{Re} = \frac{V_0 h}{\nu} \approx 1.667 \times 10^{-4} \ll 1, \tag{4}$$

where V_0 is the pulling rate of the crystal ($V_0 = 1 \times 10^{-5}$ m/s), h is the meniscus height ($h = 3 \times 10^{-4}$ m), and ν is the coefficient of kinematic viscosity (for sapphire, $\nu = 1.8 \times 10^{-5}$ m^2/s [11]).

Now, evaluate the Marangoni and the Grashof numbers:

$$\mathrm{Ma} = \frac{\partial\sigma}{\partial T}\frac{\partial TL}{\rho\nu a} \approx 11.5 \ll 10^2, \tag{5}$$

$$\mathrm{Gr} = \frac{\beta g L^3 \Delta T}{\nu^2} \approx 1.46 \times 10^{-3} \ll 1, \tag{6}$$

where $\partial\sigma/\partial T = 2 \times 10^{-4}$ J/m^2 K is the temperature derivative of the surface tension, $\Delta T = 5$ K is the maximum temperature difference in the meniscus, $L = h$, $\rho = 3.03 \times 10^3$ kg/m^3 is the melt density, $a = 4.8 \times 10^{-7}$ m^2/s is the thermal diffusivity, and $\beta = 3.56 \times 10^{-4}$ 1/K is the thermal expansion coefficient [11].

Since the Marangoni and Grashof numbers are small [12], we can ignore the contributions due to the Marangoni and Grashof convections.

Moreover, since the Reynolds number is much less than unity (Re $\ll$ 1), the Navier–Stokes equation can essentially be simplified by ignoring the nonlinear term

$$\mu\Delta\left(\frac{\partial U}{\partial y} - \frac{\partial V}{\partial x}\right) = 0. \tag{7}$$

In the two-dimensional case, the continuity equation for a liquid flow (3) allows one to introduce the stream function $\psi(x, y)$

$$\frac{\partial\psi(x,y)}{\partial x} = \psi_x = -V, \qquad \frac{\partial\psi(x,y)}{\partial y} = \psi_y = U \tag{8}$$

and reduce Eq. (7) to the form

$$\Delta^2\psi = 0. \tag{9}$$

The following boundary conditions are used to solve the systems of equations for the concentration and the velocity distribution (Fig. 1).

The boundary Γ_1 corresponds to the left face of the draw plate and is defined as a wall (impermeable to melt and impurity), where the following condition of the melt adhesion should be fulfilled:

$$\frac{\partial\psi}{\partial n} = 0, \quad \psi_x = 0, \quad \psi_y = 0, \qquad \frac{\partial C}{\partial n} = 0. \tag{10}$$

The boundary Γ_2 corresponds to the lower boundary of the capillary. To solve the problem of convective diffusion in the meniscus, the calculations should be performed in a region with a small capillary section; however, it is not expedient to calculate the distribution of the liquid flow velocity along the whole capillary. Therefore, adding a small portion of the capillary to the calculation region, we assume that the flow in the capillary will obey the equation for a steady-state boundary layer

$$V_y(x) = AV_0\left[1 - \left(\frac{x}{r}\right)^2\right], \quad x \in [0, 2r], \tag{11}$$

where V_0 is the rate of crystal pulling from the melt, r is the capillary radius, b is the diameter of a growing crystal, and A is the constant taking into account the balance of the mass to be crystallized and the mass passed through the capillary,

$$A = \frac{3}{4r}\left[b + \int_0^b f'(x)^2 dx\right], \tag{12}$$

where $f(x)$ is a function of the meniscus profile. For the planar front, Eq. (12) is simplified,

$$A = \frac{3}{4r}b. \tag{13}$$

Proceeding from Eq. (11) of the velocity distribution over the capillary cross section, we arrive at the following boundary conditions:

$$\psi = -\frac{4}{3}AV_0\left(r + x - \frac{r^3 + x^3}{3r^2}\right),$$
$$\psi_x = -AV_0\left(1 - \left(\frac{x}{r}\right)^2\right), \quad \psi_y = 0, \quad x \in [0, 2r], \tag{14}$$
$$C = C_0.$$

The boundary Γ_3 corresponds to the right-hand face of the draw plate and is defined as a wall impermeable to melt and impurity.

$$\psi = -\frac{4}{3}ArV_0, \quad \psi_x = 0, \quad \psi_y = 0,$$
$$\frac{\partial C}{\partial n} = 0. \tag{15}$$

The boundary Γ_4 corresponds to the right-hand meniscus boundary. The boundary profile is assumed to be planar, since $h \in [0.1, 0.3]$ mm. At this boundary, the normal component of the velocity equals zero. In addition, the boundary conditions at the points of conjunction of boundaries 3–4 and 4–5 should be continuous. With this aim, we assume that the tangential velocity of the melt flow varies linearly along the meniscus boundary from $V = 0$ (at the junction with boundary 3) to $V = V_0\cos\varphi$ (at the junction with the crystallization front).

$$\psi = -\frac{4}{3}ArV_0, \quad \psi_x = -V_0(h - y)\sin\varphi,$$
$$\psi_y = V_0(h - y)\cos\varphi, \quad y \in [0, h], \tag{16}$$
$$\frac{\partial C}{\partial n} = 0.$$

The boundary Γ_5 corresponds to the crystallization front. Assuming the front to be planar, we obtain

$$\psi = V_0\left(-\frac{4}{3}Ar + b - x\right), \quad \psi_x = V_0, \quad \psi_y = 0,$$
$$-D\frac{\partial C}{\partial y} = C(1 - k_0)V_0. \tag{17}$$

The boundary Γ_6 corresponds to the left-hand surface of the meniscus. All the arguments used at boundary 4 hold true for boundary 6.

$$\psi = 0, \quad \psi_x = -V_0(h - y)\sin\varphi,$$
$$\psi_y = -V_0(h - y)\cos\varphi, \quad y \in [0, h], \tag{18}$$
$$\frac{\partial C}{\partial n} = 0.$$

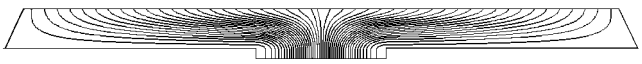

Fig. 2. Isolines of the stream function.

The boundary Γ_7 is the left-hand capillary wall impermeable to the impurity and melt.

$$\psi = 0, \quad \psi_x = 0, \quad \psi_y = 0,$$
$$\frac{\partial C}{\partial n} = 0. \tag{19}$$

The boundary Γ_8 is the right-hand capillary wall impermeable to the impurity and melt.

$$\psi = -\frac{4}{3}ArV_0, \quad \psi_x = 0, \quad \psi_y = 0,$$
$$\frac{\partial C}{\partial n} = 0. \tag{20}$$

Since the problem is symmetric, one only needs to solve the diffusion equation within half the calculation region. To do so, introduce a mirror boundary (where the condition $\frac{\partial C}{\partial n} = 0$ is satisfied) in the middle of the meniscus.

Thus, we determined the calculation region and the boundary conditions. The systems of equations will be solved numerically by the finite-difference method. With this aim, we have to divide the calculation region into subregions that have simple forms. We shall use a rectangular grid. The finite-difference system obtained for Eq. (1) will be solved by the iteration method; that for Eq. (9), by the Gauss method. In calculations, we used a 350×3 grid.

CALCULATION RESULTS

Figure 2 shows the isolines of the stream function obtained by solving Eq. (9) with the parameters $h = 0.2$, $W = 3$, $b = 2.8$, $r = 0.3$ mm, and $V_0 = 1$ mm/min. The impurity distribution was calculated for pulling rates ranging from 0.2 to 3 mm/min (corresponding to the usual pulling rates). For convenience, the data obtained were normalized to the initial impurity concentration in the melt, C_0. Figure 3 shows the distribution of the C/C_0 ratio over the meniscus volume. The diffusion coefficient of an impurity in a sapphire crystal was assumed to be $D = 2 \times 10^{-9}$ m^2/s; the impurity distribution coefficient was taken to be $K_0 = 0.3$.

Now, consider the behavior of the impurity distribution in the meniscus at a varying pulling rate (Fig. 3) and compare it with the dependence of the maximum C/C_0 ratio on V_0 (Fig. 4).

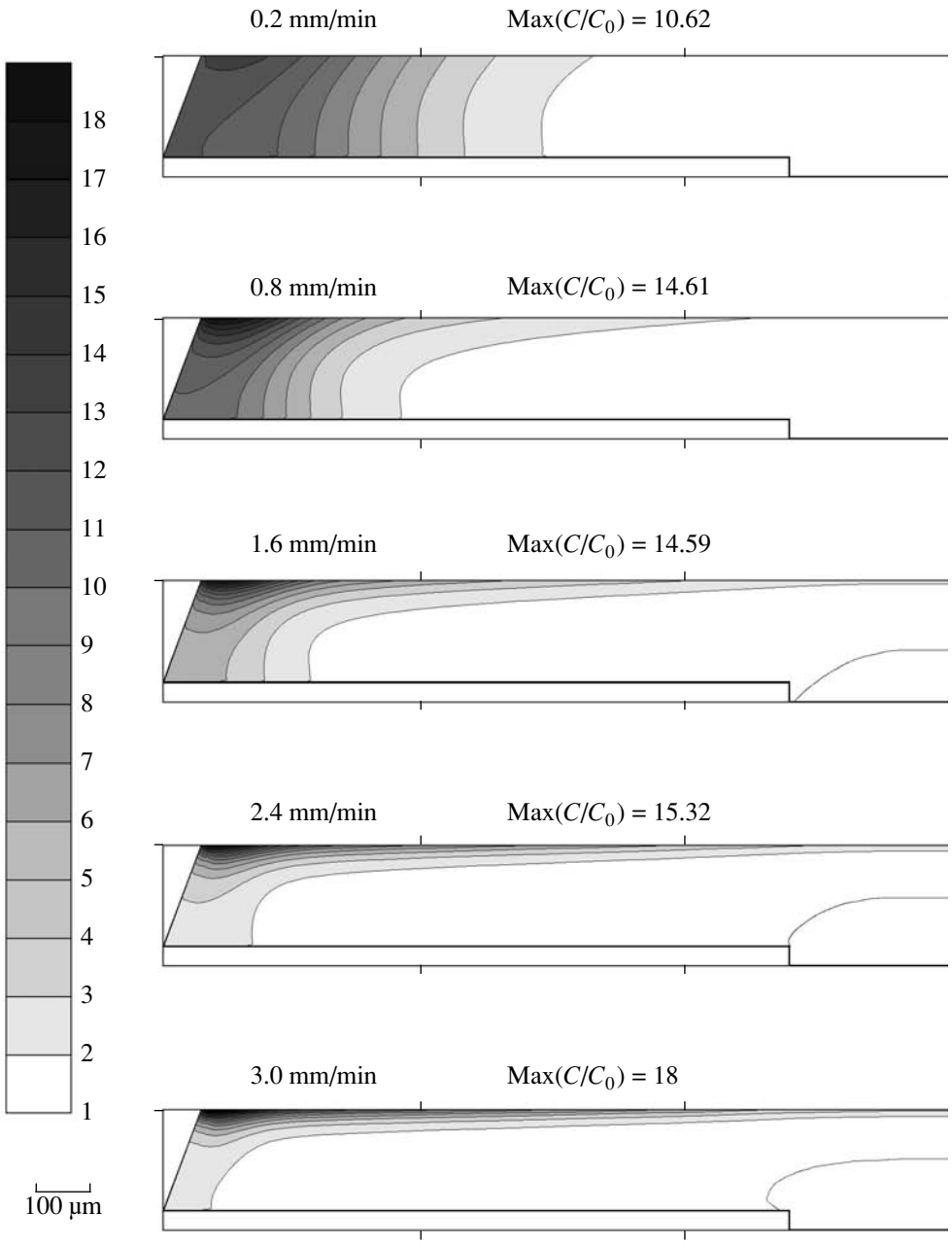

Fig. 3. Distributions of the C/C_0 ratio over the meniscus volume at various pulling rates. Isolines are drawn with a step equal to unity.

At low rates (up to 0.8 mm/min), the concentration gradient is parallel to the crystallization front. The region with the maximum concentration are located close to the side meniscus boundaries. With an increase in the pulling rate from 0.2 to 0.8 mm/min, the horizontal "compaction" of the supersaturation region also increases, which is accompanied by a substantial increase in the C/C_0 ratio (Fig. 4).

At pulling rates ranging from 0.8 to 1.8 mm/min, the horizontal compaction is almost completed, and an increase in the pulling rate leads to a slow vertical compaction in this region. This process is associated with a slight increase in the C/C_0 ratio, and the concentration gradient turns from the horizontal direction to the direction normal to the crystallization front.

Finally, at pulling rates exceeding 2.4 mm/min, the compaction of the impurity region is completed, and one observes a dramatic increase in the impurity concentration. It should be indicated that at these pulling rates the region of impurity supersaturation extends

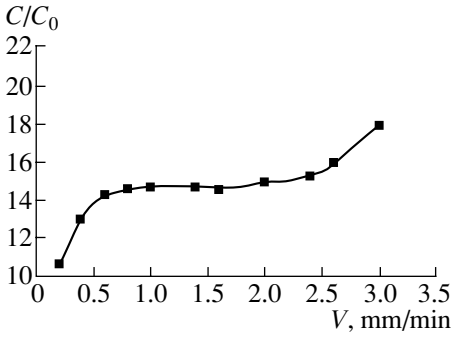

Fig. 4. C/C_0 ratio as a function of the pulling rate of the crystal *V*.

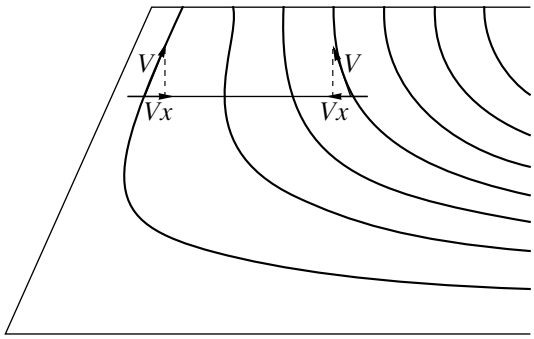

Fig. 5. Melt streamlines close to the side boundary of the meniscus.

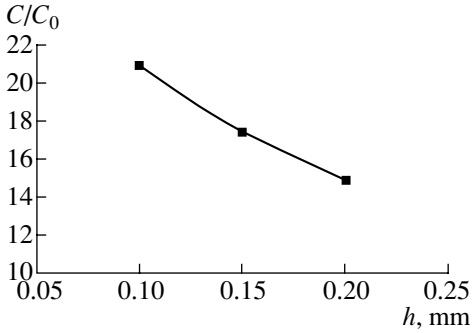

Fig. 6. C/C_0 ratio as a function of meniscus height *h*.

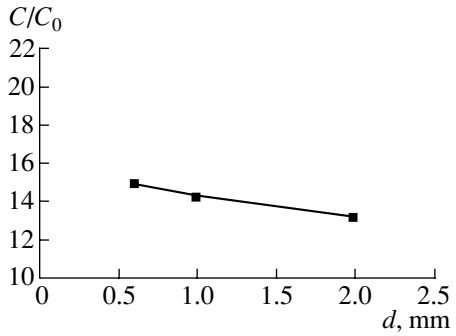

Fig. 7. C/C_0 ratio as a function of capillary diameter *d*.

over the whole meniscus width, which often results in the formation of the bubbles and their being trapped over the whole crystallization front (as described in [13]).

Calculations showed that the impurity concentration approaches its maximum value at the crystallization front at a distance of 25–45 μm from the side boundary of the meniscus, which is consistent with the experimental data [3–8]. If a pulling rate increases from 0.2 to 3.0 mm/min, the concentration maximum is slightly displaced from the crystal edge along the *X*-axis by a distance from 45 to 25 μm.

The fact that the impurity concentration attains its maximum at a certain distance from the side edge of the crystal probably can be associated with the horizontal counterflow of the melt near the side edge of the meniscus (Fig. 5).

We also calculated the maximum C/C_0 ratio as a function of the meniscus height and the capillary diameter (see Figs. 6, 7).

CONCLUSIONS

It is shown that the impurity concentration attains its maximum value at the crystallization front at a distance of 25–45 μm from the side boundary of the meniscus. The change in the pulling rate of the crystal from 0.2 to 3.0 mm/min leads to no noticeable shift of the concentration maximum.

It is also established that the dependence of the maximum supersaturation on the pulling rate has a plateau. The corresponding range of the growth rates can be recommended for growth processes.

It is worth noting that, at a certain critical pulling rate dependent on the geometric parameters of the meniscus, the supersaturation region extends over the whole meniscus width.

It is evident from Figs. 6 and 7 that the supersaturation can be considerably reduced by increasing either the capillary diameter or the meniscus height at a constant pulling rate.

REFERENCES

1. T. N. Yalovets, L. V. Bondarenko, V. A. Borodin, and T. A. Steriopolo, in *Proceedings of the All-Union Conference on Production of Profiled Crystals and Product by the Stepanov Method and Their Use in Peoples Economy, Leningrad, 1988*, p. 47.
2. W. A. Tiller, in *The Art and Science of Growing Crystals*, Ed. by J. J. Gilman (Wiley, New York, 1963; Metallurgizdat, Moscow, 1968).
3. V. F. Perov, V. S. Papkov, and I. A. Ivanov, Izv. Akad. Nauk SSSR, Ser. Fiz. **43** (9), 1977 (1979).
4. V. A. Tatarchenko, T. N. Yalovets, G. A. Satunkin, *et al.*, J. Cryst. Growth **50** (1), 335 (1980).

5. R. E. Novak, R. Metzl, A. Dreeben, and S. Berkman, J. Cryst. Growth **50** (1), 143 (1980).
6. K. Wada and K. Hoshikawa, J. Cryst. Growth **50** (1), 151 (1980).
7. S. E. Azoyan, L. P. Egorov, and L. M. Zatulovskiĭ, Izv. Akad. Nauk SSSR, Ser. Fiz. **43** (9), 1953 (1979).
8. V. A. Borodin, T. A. Steriopolo, V. A. Tatarchenko, and T. N. Yalovets, in *Crystal Growth* (Nauka, Moscow, 1986), Vol. 15, p. 157.
9. A. A. Chernov, in *Modern Crystallography*, Vol. 3: *Crystal Growth*, Ed. by B. K. Vainshtein, A. A. Chernov, and L. A. Shuvalov (Nauka, Moscow, 1980; Springer-Verlag, 1984).
10. J. T. A. Pollock, J. Mater. Sci. **7**, 649 (1972).
11. M. A. Maurakh and B. S. Mitin, *Liquid Refractory Oxides* (Metallurgiya, Moscow, 1979).
12. G. Z. Gershuni and E. M. Zhukhovitskiĭ, *Convective Stability of Incompressible Fluids* (Nauka, Moscow, 1972).
13. V. D. Perov, V. S. Papkov, and I. A. Ivanov, Izv. Akad. Nauk SSSR, Ser. Fiz. **43** (9), 1977 (1979).

Translated by A. Zolot'ko

Crystallography Reports, Vol. 47, No. 5, 2002, pp. 891–892. Translated from Kristallografiya, Vol. 47, No. 5, 2002, pp. 955–956.

ANNIVERSARIES

Mikhail Grigor'evich Mil'vidsky (on the Occasion of His 70th Birthday)

Today, Russia, always glorious with its talents, is losing "its own Platos and Newtons." Only the most steadfast people, our pride and "our everything" stay in Russia. Preserving their honor and dignity, they also defend with their heroic labor the honor and dignity of Russian science and determine its face and reputation in the world. Among these remarkable people, we justly include Mikhail Grigor'evich Mil'vidsky, doctor of technical sciences, professor, and academician of the Russian Academy of Natural Sciences, who will celebrate his 70th birthday on August 2, 2002, St. Elias' day. Perhaps, it was under the guidance of the Prophet Elias, who holds sway over natural forces, that Mil'vidsky obtained his powerful intellect, intuition, and bright temperament—qualities so important for a scientist.

Mil'vidsky's life's work was the study of semiconductors. The results of his scientific activity are very impressive—he is the author of 4 monographs, more than 500 scientific articles, a major discovery, and more than a 140 inventions, of which more than 40 were subsequently used in a number of industrial enterprises of the Russian Federation and the ex-Soviet republics. Forty-three candidate's dissertations were successfully defended under Mil'vidsky's guidance, and four of his former students defended doctoral dissertations. However, these figures only partly reflect the scale of his personality and scientific activity.

Mil'vidsky is a gifted scientist who made an essential contribution to the development of the technology and materials science of semiconductors and also to the creation of a national industry for manufacturing semiconductor-based elements. He performed a large complex of original studies concerning the growth of silicon single crystals, the behavior of dopants in these crystals, and the characteristics of defect formation in dislocation-free single crystals; he also developed the technology of the growth of silicon single crystals, the most important semiconductor material.

Mil'vidsky also performed himself or headed fundamental studies on the growth of gallium and indium arsenides and the epitaxial structures of solid solutions based on these arsenides. The main laws of the behavior of dopants and structural defects in these materials were established. Original technologies for growing gallium and indium arsenide single crystals and the epitaxial heterostructures based on the solid solution of the A_3B_5 compounds were also developed.

Mil'vidsky studied the role of isovalent impurities as a new class of dopants of semiconductors and their behavior in gallium arsenide and silicon single crystals, as well as in epitaxial structures. He gained important information on the growth of semiconductor single crystals under conditions of microgravity in space flights.

Mil'vidsky is the creator of a famous scientific school in the field of technology and the materials science of semiconductors. The studies performed by Mil'vidsky and his students and followers are well known and recognized by the scientific community. He was awarded the Major Prize of the International Academic Publishing Company Nauka/Interperiodica for the best scientific publication in 1997.

The success of his publications lies not only in their deep contents but also in his masterly command of language, the clarity and brevity of his style. The concentrated energy of his voice and his skill of emphasizing important points and singling out priorities make him a

1063-7745/02/4705-0891$22.00 © 2002 MAIK "Nauka/Interperiodica"

brilliant lecturer. All the subjects considered in his lectures become visible and tangible.

Mil'vidsky has spent a lot of time on scientific–organizational work. He is a member of the Scientific–Technological Council and a number of scientific councils of several institutes of the Russian Academy of Sciences, as well as a member of the editorial boards of several journals. He has been an organizer of, and participant in, numerous national and international conferences and meetings.

Mil'vidsky's creative work has been crowned with state awards: he was awarded the Lenin Prize, two State Prizes, the Order of the Sign of Honor, and several medals. He holds the titles of Honorary Scientist of the Russian Federation and Honorary Metallurgist of the Russian Federation.

The editorial board of *Kristallografiya* (Crystallography Reports) and numerous colleagues and friends congratulate Professor Mil'vidsky on his birthday and wish him good health, happiness, many years of creative work, and new achievements in science.

Translated by L. Man

Crystallography Reports, Vol. 47, No. 5, 2002, pp. 891–892. Translated from Kristallografiya, Vol. 47, No. 5, 2002, pp. 955–956.

ANNIVERSARIES

Mikhail Grigor'evich Mil'vidsky (on the Occasion of His 70th Birthday)

Today, Russia, always glorious with its talents, is losing "its own Platos and Newtons." Only the most steadfast people, our pride and "our everything" stay in Russia. Preserving their honor and dignity, they also defend with their heroic labor the honor and dignity of Russian science and determine its face and reputation in the world. Among these remarkable people, we justly include Mikhail Grigor'evich Mil'vidsky, doctor of technical sciences, professor, and academician of the Russian Academy of Natural Sciences, who will celebrate his 70th birthday on August 2, 2002, St. Elias' day. Perhaps, it was under the guidance of the Prophet Elias, who holds sway over natural forces, that Mil'vidsky obtained his powerful intellect, intuition, and bright temperament—qualities so important for a scientist.

Mil'vidsky's life's work was the study of semiconductors. The results of his scientific activity are very impressive—he is the author of 4 monographs, more than 500 scientific articles, a major discovery, and more than a 140 inventions, of which more than 40 were subsequently used in a number of industrial enterprises of the Russian Federation and the ex-Soviet republics. Forty-three candidate's dissertations were successfully defended under Mil'vidsky's guidance, and four of his former students defended doctoral dissertations. However, these figures only partly reflect the scale of his personality and scientific activity.

Mil'vidsky is a gifted scientist who made an essential contribution to the development of the technology and materials science of semiconductors and also to the creation of a national industry for manufacturing semiconductor-based elements. He performed a large complex of original studies concerning the growth of silicon single crystals, the behavior of dopants in these crystals, and the characteristics of defect formation in dislocation-free single crystals; he also developed the technology of the growth of silicon single crystals, the most important semiconductor material.

Mil'vidsky also performed himself or headed fundamental studies on the growth of gallium and indium arsenides and the epitaxial structures of solid solutions based on these arsenides. The main laws of the behavior of dopants and structural defects in these materials were established. Original technologies for growing gallium and indium arsenide single crystals and the epitaxial heterostructures based on the solid solution of the A_3B_5 compounds were also developed.

Mil'vidsky studied the role of isovalent impurities as a new class of dopants of semiconductors and their behavior in gallium arsenide and silicon single crystals, as well as in epitaxial structures. He gained important information on the growth of semiconductor single crystals under conditions of microgravity in space flights.

Mil'vidsky is the creator of a famous scientific school in the field of technology and the materials science of semiconductors. The studies performed by Mil'vidsky and his students and followers are well known and recognized by the scientific community. He was awarded the Major Prize of the International Academic Publishing Company Nauka/Interperiodica for the best scientific publication in 1997.

The success of his publications lies not only in their deep contents but also in his masterly command of language, the clarity and brevity of his style. The concentrated energy of his voice and his skill of emphasizing important points and singling out priorities make him a

1063-7745/02/4705-0891$22.00 © 2002 MAIK "Nauka/Interperiodica"

brilliant lecturer. All the subjects considered in his lectures become visible and tangible.

Mil'vidsky has spent a lot of time on scientific–organizational work. He is a member of the Scientific–Technological Council and a number of scientific councils of several institutes of the Russian Academy of Sciences, as well as a member of the editorial boards of several journals. He has been an organizer of, and participant in, numerous national and international conferences and meetings.

Mil'vidsky's creative work has been crowned with state awards: he was awarded the Lenin Prize, two State Prizes, the Order of the Sign of Honor, and several medals. He holds the titles of Honorary Scientist of the Russian Federation and Honorary Metallurgist of the Russian Federation.

The editorial board of *Kristallografiya* (Crystallography Reports) and numerous colleagues and friends congratulate Professor Mil'vidsky on his birthday and wish him good health, happiness, many years of creative work, and new achievements in science.

Translated by L. Man

Crystallography Reports, Vol. 47, No. 5, 2002, pp. 893–894. Translated from Kristallografiya, Vol. 47, No. 5, 2002, pp. 957–958.

MEMORIAL DATA

Nikolaĭ Naumovich Sheftal (on the 100th Anniversary of His Birth)

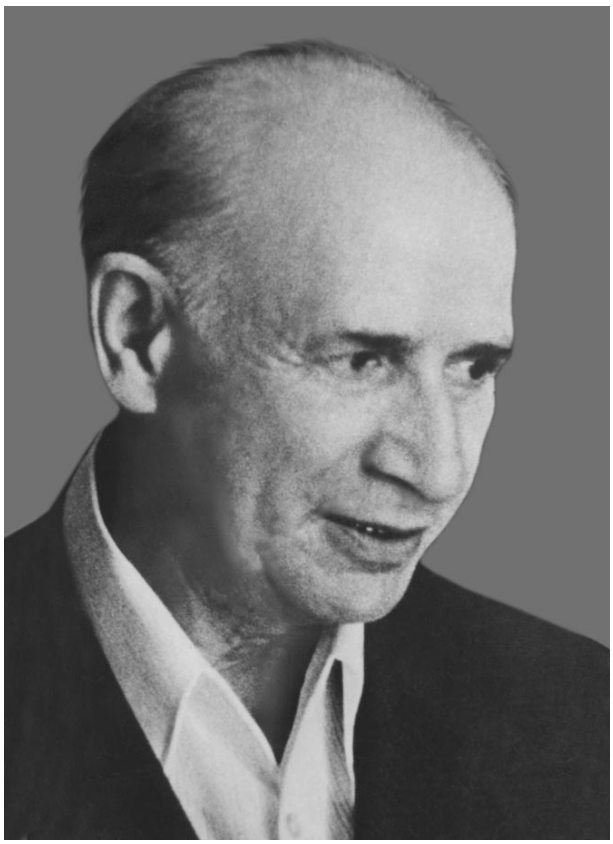

Nikolaĭ Naumovich Sheftal, an outstanding Soviet crystallographer, professor, and doctor of geology and mineralogy, was born on December 2, 1902, in Moscow into the family of a well-known engineer and inventor.

The scientific activity of Sheftal was dedicated to only one subject—crystal growth—which he knew in every detail, from experiments to their interpretation and generalization of the results, from teaching to scientific–organizational work. Sheftal went from a descriptive mineralogical view of crystal growth in his early studies to the solution of the problem of the active control of crystallization processes. He was one of the first enthusiasts of the industrial growth of crystals.

Sheftal spent more than half a century working at the Institute of Crystallography of the USSR Academy of Sciences. He started his experimental work at the Laboratory of Crystallography of the Lomonosov Institute, where, on the advice of A.V. Shubnikov, he was engaged in the synthesis of homogeneous saccharose crystals in order to replace the deficit quartz crystals with saccharose. In 1939, Sheftal managed to grow Seignette salt crystals on a large scale. This achievement promoted the organization of a special plant that produced many tons of these crystals, which, in turn, allowed one to manufacture several million piezoelectric elements for the needs of defense. In the period from 1945 to 1951, Sheftal performed the first successive experiments in the Soviet Union on the growth of high-quality synthetic quartz appropriate for manufacturing piezoelectric elements.

The sphere of Sheftal's research interests was very large and included diverse materials, methods, and applications. In addition to saccharose, Seignette salt, and quartz crystals, he was also interested in the growth of micas and various semiconductors, large bulky crystals and epitaxial films, crystallization from solutions, melts, and vapors, various crystallization mechanisms, and problems of twinning and geometric crystallography.

Against this background of his interests, two fundamental and somewhat related studies performed by Sheftal are especially important—the growth of epitaxial semiconductor films (in the 1950s) and artificial epitaxy (in the 1970s).

In 1953, Sheftal and his colleagues were the first in the world to grow epitaxial silicon and germanium films by the method of chloride crystallization from the vapor phase. These results were published in a scientific journal. An analogous result was obtained in the USA only in 1961 and paved the way for the use of epitaxial films in microelectronics.

The concept of artificial epitaxy was formulated by Sheftal in the early 1960s and was implemented experimentally in 1972. Similar works abroad were started only several years later. Then, artificial epitaxy (or graphoepitaxy) was developed as a new area of science and technology. Recently, artificial epitaxy has proved to be promising in connection with the problem of the growth of biological crystalline films on inorganic substrates.

Sheftal gave a lot of his time and energy to scientific–organizational work associated with crystal growth. In the period from 1955 to 1969, he was vice-chairman of the Scientific Council on Crystal Formation of the USSR Academy of Sciences. He was also an organizer of the first All-Union Meetings on crystal

1063-7745/02/4705-0893$22.00

growth (in 1957, 1959, 1963, and 1966), which are still held as conferences in our country (the last conference took place in 2001).

Sheftal was an initiator of the publication of the well-known collections of articles entitled *Crystal Growth.* Sheftal founded this publication in 1959 and was the editor of the first ten volumes. At present, there are 21 volumes of this series altogether, and all of them are also published in English abroad.

Sheftal was always surrounded by his students. Many groups of people interested in crystal growth in the Soviet Union were organized and developed under his ideological influence. More than 20 of his students defended their candidate's dissertations, and some of them also defended their doctoral dissertations. Sheftal was for many years professor at Moscow State University and headed the Laboratory of Crystal Growth at the Department of Crystallography and Crystal Chemistry of the Faculty of Geology.

Sheftal was a very benevolent person and this created around him an atmosphere favorable for scientific work. His passion, purposefulness, and enthusiasm for science were transmitted to all those around him. He was devoted to science till the very last days of his life.

Sheftal passed away in 1987.

All those who knew Sheftal, a pioneer of the science of crystal growth, will always remember him.

Translated by L. Man

Crystallography Reports, Vol. 47, No. 5, 2002, pp. 895–896. Translated from Kristallografiya, Vol. 47, No. 5, 2002, pp. 959–960.

MEMORIAL DATA

In Memory of Nikolaĭ Mitrofanovich Melankholin (on the 100th Anniversary of His Birth)

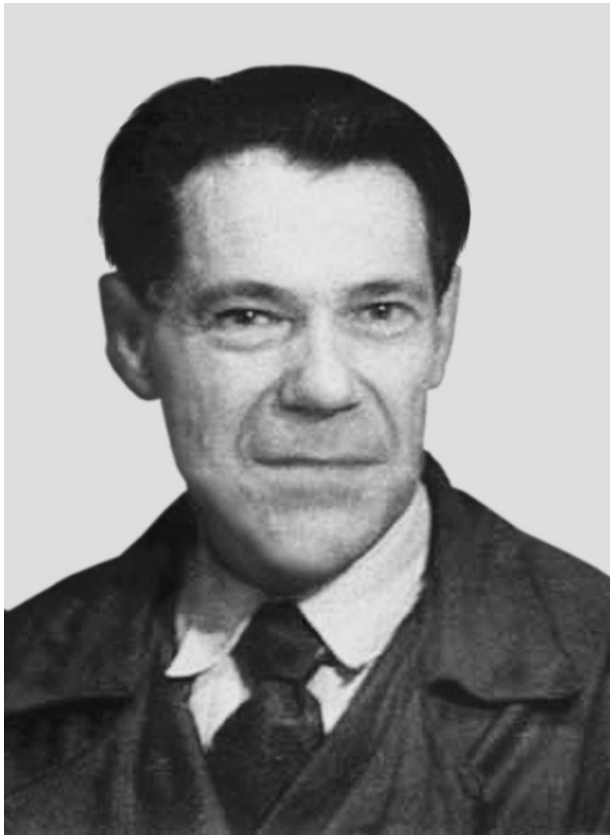

On April 11, 2002, Nikolaĭ Mitrofanovich Melankholin, an outstanding expert in the field of crystal optics, author of numerous scientific publications and inventions, a man of high culture, and a charming and modest person, would have celebrated his 100th birthday.

Melankholin was born on March 29, 1902 (according to the Old Style), in the village of Os'makovo in the province of Voronezh into the large family of a priest. After the premature death of his father, Melankholin began studying in Voronezh theological school and then in a Soviet labor school. He started earning his living at the age of 17, working as a librarian and an accounts clerk; he also gave private lessons. Upon graduating from the school, he entered the Novokhopersk Pedagogical Training College, which was famous for its broad educational program. There, the young man strove for knowledge, read a lot, wrote verse, took photographs, edited a manuscript journal, and delivered lectures both to his peers in the college and also to peasants. Melankholin earned the nickname "professor." Upon graduating from the college, Melankholin was recommended to enter Voronezh University. His recommendation letter read, "Melankholin possesses outstanding abilities and, being gifted in all disciplines, has an obvious inclination to the physical–mathematical sciences. Under favorable conditions, citizen Melankholin may become a prominent scientist."

After one year of studying in Voronezh, Melankholin arrived (or, to be precise, came on foot) to Moscow University. As a son of a priest, he was accepted in the Faculty of Physics and Mathematics only as an auditor. However, circumstances turned out to be favorable for him, and a year later Melankholin, by petition of S.I. Vavilov, became a full-time student and studied in Vavilov's group of theoretical physics. Upon graduating from the university in 1930, Melankholin and other students of Vavilov were recommended to work at the optical laboratory of the Institute of Applied Mineralogy. The situation continued to be very favorable; the former students started their research on crystal optics with great enthusiasm under the guidance of such remarkable scientists as V.V. Arshinov and N.E. Vedeneeva.

Vavilov continued to show interest in the work of his students. In 1940, Melankholin defended his candidate's dissertation dedicated to the measurement of refractive indices under a microscope (immersion method). Later, he published a book based on his dissertation. The following year, he became a senior research worker. Even in his dissertation, Melankholin improved on known research methods, developed the technique of fast precision measurements of dispersion in the refractive indices of crystals, and designed new apparatus. These designs and inventions and their further development until they were mass produced, together with consultations and the teaching of researchers from various institutes, industrial laboratories, and geological organizations became characteristic of Melankholin's activity.

Melankholin worked at the Institute of Applied Mineralogy (later, the All-Union Institute of Mineral Raw Material (VIMS)) until 1945, the time of the organization of the Laboratory of Crystal Optics at the Institute of Crystallography, where he started working under the guidance of Vedeneeva. As he had done earlier in VIMS, Melankholin continued his research work in two main directions—the study of the optical prop-

1063-7745/02/4705-0895$22.00

erties of crystals and the development of new optical methods for studying crystals and designing the appropriate apparatus. Studying the absorption spectra of some minerals and crystals of some dyes, Melankholin established new characteristics in the absorption spectra of absorbing crystals. In the crystals of various dyes, he revealed, and for the first time studied quantitatively, the dispersion of the indicatrix axes. He also performed a number of fundamental works on the pigmentation and dichroism of minerals; for example, he studied the absorption spectra of impurities in micas and feldspars. He also successfully applied the methods of crystal optics to the studies of the quality of newly grown crystals. With the advent of lasing crystals, Melankholin used all his knowledge to establish and study their optical properties.

In 1954, Melankholin in coauthorship with S.V. Grum-Grzhimaĭlo published a book entitled *Methods of Studying the Optical Properties of Crystals*, which since then has become a standard work of reference for all those studying crystals. Melankholin also paid great attention to the improvement of the qualifications of research workers and helped people working in various fields of research and industrial laboratories to use new methods of crystal optics.

Melankholin was also engaged in the study of plastic deformation and the fracture of crystals. He obtained valuable results in his studies of liquid crystals in the solutions of various dyes, whose study also required the creation of new methods. In particular, Melankholin established that substances with plane molecules can also form liquid crystals (earlier, the formation of liquid crystals was observed mainly for the substances with elongated molecules). His work on liquid crystals was highly regarded by the Scientific Council of the Institute of Crystallography; a documentary film made by Melankholin about the formation of the liquid crystals of dyes was recommended to be shown at the Anniversary Session of the Fedorov Society.

Melankholin had a golden touch. Any apparatus or device designed by him was developed to perfection. New devices designed by Melankholin were manufactured on an industrial scale and were used in numerous laboratories. Some of his devices and apparatuses are still used in crystallo-optical and petrographic studies. Some of these devices were reconstructed in 1980 by B.N. Grechushnikov.

Melankholin was extremely consistent and purposeful in his research. He combined the discipline of a scientist with the perception of an artist. As an extremely modest person, he surprised everybody with the power of his observation, his clarity, and the depth of his judgements.

Academician N.V. Belov wrote: “Melankholin is one of our most prominent experts in crystal optics, in particular, in applied optics.” Academician I.V. Obreimov said: “Melankholin, a student of Vavilov, seems to be the most outstanding expert in crystals optics. One might say that he is a man not of this world. For him, there exists nothing but science.” According to Academician A.V. Shubnikov, “Melankholin was really worthy of being called a doctor of sciences despite the fact that he did not write a doctoral dissertation. His 60 articles are equivalent to a doctoral dissertation.”

Melankholin was also an expert in art, in particular, in engravings. He delivered a course of lectures on the history of art for members of the Institute of Crystallography and illustrated his lectures with slides and pieces from his rich collection. These lectures are still remembered by many people.

After a serious illness, Melankholin continued his research work till the last years of his life. He also continued writing a book entitled *Methods of Studying the Optical Properties of Crystals*. The preparation of the second edition of this book was interrupted by his death on October 21, 1967. The book, completed by his wife, Nataliya Petrovna Smirnova, was published in 1970.

Melankholin’s scientific traditions are continued by his son, a botanist, and his daughter, a geologist.

Numerous students and followers will always remember Melankholin as a gifted scientist and an extremely modest and benevolent man.

Translated by L. Man